DESIGN, SYNTHESIS, AND PROPERTIES OF NICKEL COMPLEXES THAT REPLICATE THE STRUCTURAL AND ELECTRONIC PROPERTIES OF THE N3S2 DONOR SET OF NI-CONTAINING SUPEROXIDE DISMUTASE

by

PHAN TRIEU TRUONG

(Under the Direction of Todd C. Harrop)

ABSTRACT

Nickel superoxide dismutase (NiSOD) is a metalloenzyme that can catalyze the disproportionation of superoxide ($O_2^{\bullet-}$) to O_2 and H_2O_2 at the diffusion-controlled rates. In the NiSOD active site, the Ni ion is situated in a mixed amine/peptide thiolates N_3S_2 coordination environment. The unique NiSOD active site promotes facile Ni(III/II) redox while prevents the oxidation/oxygenation of thiolates by the substrate and products of $O_2^{\bullet-}$ disproportionation. This has prompted the development of relatively small synthetic analogues of NiSOD by our group and others to understand the role of mixed N/S donors in NiSOD. We reported the first five-coordinate (5C) analogue, K[Ni(N_3S_2)] (**1**), that replicates the N_3S_2 donor set of NiSOD structurally and electronically with a pendant pyridine as potential fifth ligand to Ni in the axial position. However, oxidation of **1** by ferrocenium hexafluorophosphate ($FcPF_6$) yielded a disulfide-bridged complex. The increased in basicity as well as steric enforcement by incorporation of *gem*-$(CH_3)_2$ moiety in the second-generation analogue, Na[Ni($N_3S_2^{Me2}$)] (**2**), is expected to promote Ni-based redox while preventing disulfide formation at the S *trans* to carboxamide. However, the increase in steric enforcement in **2** led to a new oxidation pathway that yielded a thiazolidine ring rearrangement

product that was not observed in **1**. Since coordination of axial N-ligand to Ni is critical in promoting Ni-based redox in NiSOD, the pendant pyridine is replaced with *N*-ethylmorpholine (NEM) moiety in the third-generation analogue, Na[Ni($N_3S_2^{NEM}$)] (**3**). The more Lewis basic N-donor in **3** is expected to coordinate to both Ni^{2+} and Ni^{3+} oxidation state to promote Ni-based redox. Reactions of **3** with oxidants (air, $FcPF_6$, and KO_2) and Lewis acid (i.e. tris(pentafluorophenyl) borane) yielded stair-step trimetallic species with N-NEM poised to coordinate to terminal [NiN_3S_2] centers. CV of these trimetallic species exhibited multiple reversible redox couples assigned to the terminal [NiN_3S_2] centers. These results show that while **1**-**3** can replicate NiSOD active site electronically and structurally, reversible Ni(III/II) redox couple is not achievable unless the electron density on S-thiolates is sequestered by Lewis acids (i.e., Ni^{2+} and borane), which mimics the H-bond interactions in NiSOD active site.

INDEX WORDS: Nickel; superoxide dismutase; thiolate; metalloenzyme; sulfur

DESIGN, SYNTHESIS, AND PROPERTIES OF NICKEL COMPLEXES THAT REPLICATE THE STRUCTURAL AND ELECTRONIC PROPERTIES OF THE N3S2 DONOR SET OF NI-CONTAINING SUPEROXIDE DISMUTASE

by

PHAN TRIEU TRUONG

B.A., Kenyon College, 2011

A Dissertation Submitted to the Graduate Faculty of The University of Georgia in Partial Fulfillment of the Requirements for the Degree

DOCTOR OF PHILOSOPHY

ATHENS, GEORGIA

2018

DESIGN, SYNTHESIS, AND PROPERTIES OF NICKEL COMPLEXES THAT REPLICATE THE STRUCTURAL AND ELECTRONIC PROPERTIES OF THE N3S2 DONOR SET OF NI-CONTAINING SUPEROXIDE DISMUTASE

by

PHAN TRIEU TRUONG

Major Professor:	Todd C. Harrop
Committee:	Michael K. Johnson
	Jeffrey L. Urbauer

Electronic Version Approved:

Suzanne Barbour
Dean of the Graduate School
The University of Georgia
August 2018

DEDICATION

To my parents, Kim Truong and Linh K. Phung

ACKNOWLEDGEMENTS

First and foremost, I would like to thank my advisor, Professor Todd C. Harrop, for providing guidance, support, and a place for me to do research in his lab. Todd, thank you for pushing me to be a better writer, a better presenter, and a better researcher. I would also want to thank Michael K. Johnson and Jeffrey L. Urbauer for their expertise in EPR and NMR, respectively. Thank you for your participation as my graduate committee members, your letters of recommendation, and continued support.

I was also fortunate to have been able to share a laboratory with exceptional former and current Harrop lab members: Dr. Eric Gale, Dr. Vivian Ezeh, Dr. Brian Sanders, Dr. Melody Walter, Dr. Ellen Broering, Dr. Ramsey Steiner, Yi Liu, Sydney Hallenbeck, Kristine Martin, David Bishop, Rachel Downs, Christian Cremo, and Amelia Reid. You have made the bad days tolerable and the good days exceptional. My experience would not be the same without you. I also want to acknowledge friends I have made during the course of my graduate career who have contributed to years that I will never forget.

I would like to thank Dr. Dennis Phillips and Dr. Chauwen Chou for help with MS, Dr. Greg Wylie and Dr. Dongtao Cui for help with NMR, and Dr. Pingrong Wei for help with X-ray crystallography. Financial support for my research was provided by the National Science Foundation (CHE-1506375 and CHE-0953102).

I must thank my parents and siblings for their unwavering support throughout the years. Last but not least, I would like to thank my best friend, my soulmate, and my wife , Amanda M. Myers, for supporting me unconditionally in all that I do.

TABLE OF CONTENTS

Page

CHAPTER

Chapter 1

OVERVIEW: NICKEL IN BIOLOGY

1.1 Overview: Nickel in Biology

The majority of Earth's Ni is found in the core with trace amounts found in crustal rocks.[1-3] Nickel was brought up to the surface via volcanic eruptions during the anoxic Archaean eon (>2.5 billion years), which supplied an abundant amount of Ni to seawater.[4] Geologic records suggest that Ni concentrations in seawater decreased drastically approximately half a billion years ago,[4] which explains the abundance of Ni metalloenzymes in strict anaerobes for the metabolism of H_2, CO, and CH_4. Ni metalloenzymes found limited use in eukaryotes. The utilization of Ni as a cofactor for early anaerobes highlight the ancient history of Ni in biology.[5] Although metalloenzymes that utilize Ni have not been identified in humans, Ni is found distributed in various tissues throughout the body.[6] Ni is ingested through many types of food[7] and deprivation of dietary nickel was found to have negative impact on animal physiology.[6] While not utilized by mammalian cells, Ni is found to be a key component to the virulence of human bacterial pathogens such as *Proteus mirabilis*,[8] *Helicobacter pylori*,[9] *Mycobacterium tuberculosis*,[10] *Yersinia enterocolitica*,[11] and *Cryptococcus neoformans*.[12]

To date, nine different Ni containing enzymes have been identified with lactase racemase as the newest addition in 2014.[13-15] While detailed reviews of these enzymes have been reported,[13,14] they will be briefly discussed in this chapter. The Ni dependent enzymes are primarily found in anaerobes where they catalyze a wide range of reactions, some of which are important to

the global N, C, and H cycles (Table 1.1). The Ni containing enzymes can be categorized into: (i) non-S-coordinated and (ii) S-coordinated, in which S donor atom originates from either Cys-S or sulfide from [FeS] cluster in the nickel active site. While the non-S-coordinated Ni enzymes utilize Ni^{2+} as a Lewis acid catalyst, S-coordinated Ni enzymes are redox-active and utilize $Ni^{+/2+/3+}$ states to catalyze a wide range of reactions that span redox potentials over 1.5 V.[13,14] An overview of the nine known Ni enzymes, their functions, and metal coordination environments is presented herein.

Table 1.1 List of Ni-containing metalloenzymes, role of Ni in catalysis, and a summary of their functions

Enzyme name (abbreviation)	Role	Enzyme function
Urease	Lewis acid	Urea hydrolysis
Glyoxalase I (GlxI)	Lewis acid	Detoxification of methylglyoxal
Acireductone dioxygenase (ARD)	Lewis acid	Methionine salvage pathway
Lactase racemase (LarA)	Unclear	Racemization of D- and L-lactic acid
Methyl-CoM reductase (MRC)	Redox	Synthesis of methane
CO dehydrogenase (CODH)	Redox	Reversible CO ↔ CO_2 conversion
Acetyl-CoA synthase (ACS)	Redox	Synthesis of acetyl-CoA
[NiFe] hydrogenase ([NiFe] H_2ase)	Redox	Reversible $H_2 \leftrightarrow 2H^+$ conversion
Ni superoxide dismutase (NiSOD)	Redox	Disproportionation of superoxide ($O_2^{\bullet-}$)

1.2 Nickel containing enzymes

1.2.1 Non-S-coordinated Ni enzymes

Urease

Ureases catalyze the hydrolytic decomposition of urea to ammonia and carbamate, which spontaneously decomposes to yield another equivalent of ammonia (Scheme 1.1). Urease plays an important role in the global nitrogen cycle and is found in a wide variety of organisms.[16-18] The crystal structures of urease have been solved from several model organisms including *Canavalia ensiformis*,[19] *Klebsiella aerogenes*,[20] *and Bacillus pasteurii*[21] with essentially identical active sites. The X-ray structure of urease from *B. pasteurii* (PBD: 2UBP) at 2 Å resolution reveals a trimer of trimers of $(\alpha\beta\gamma)_3$, where the Ni active sites are found in the α subunits (Figure 1.1) (Ref). An important feature in the α subunit is the helix-turn-helix motif that flank the active site cleft, which contains the catalytically essential His323 residue (numbering based on *B. pasteurii* sequence). In the active, a dinuclear Ni active site was found with the two Ni ions located 3.5-3.7 Å apart. The Ni ions are bridged by the carbamylated Lys220 residue and a hydroxide (Figure 1.1). In addition to the bridging ligands, Ni1 is coordinated by His249, His275, and a terminal H_2O ligand in a distorted square-pyramidal geometry. The remaining Ni, Ni2, is additionally coordinated by H137, His139, Asp363, and H_2O to in a distorted octahedral geometry.

Scheme 1.1 General Reaction Catalyzed by Urease

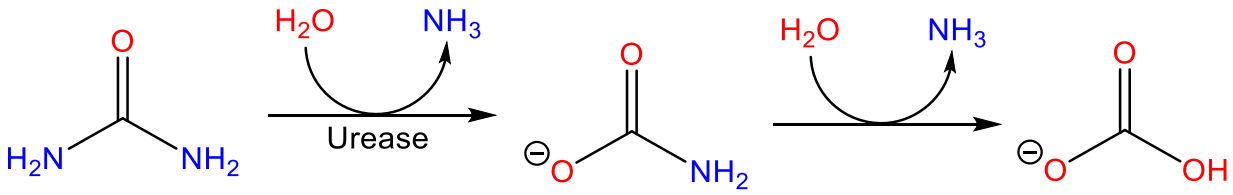

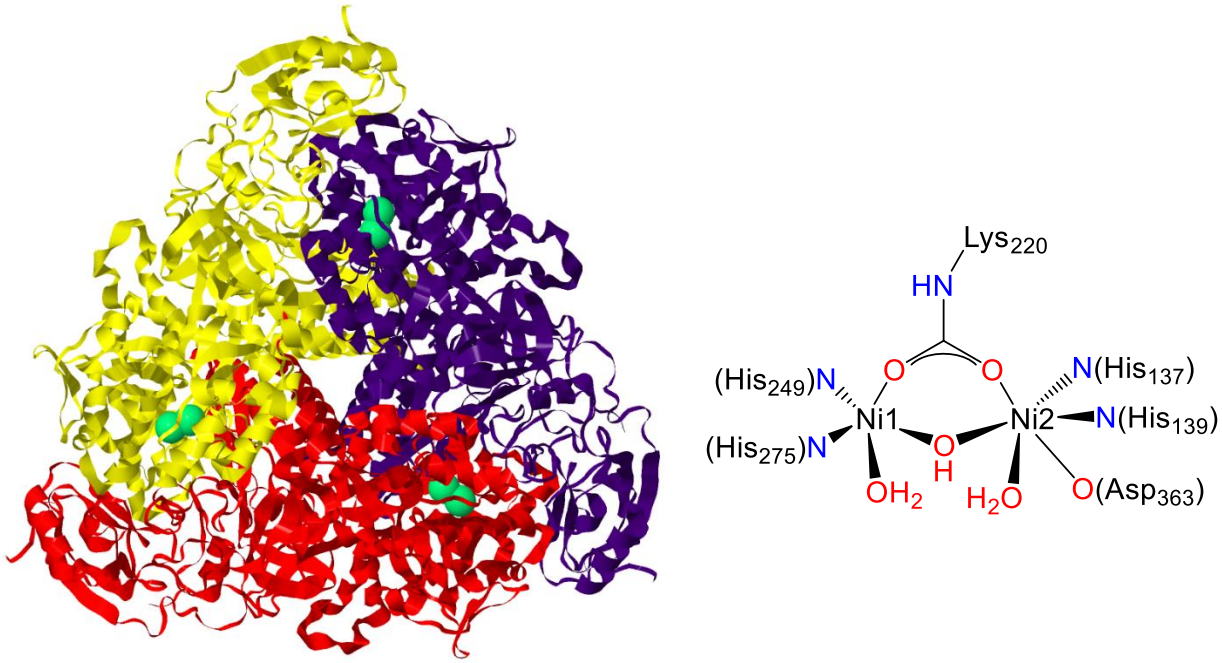

Figure 1.1 (*Left*) Structure of the trimer of trimers from *B. pasteurii* urease at 2 Å resolution (PDB: 2UBP). Image was prepared with Jmol.[22] Nickel atoms are depicted as green spheres. (*Right*) ChemDraw depiction of the dinuclear Ni active site.

During catalysis, the Ni ions remain in the 2+ oxidation state and act as a Lewis acid to activate the substrate. The first step of the mechanism is the binding of the O-atom of urea to the coordinately unsaturated Ni1 position, leading to the loss of three H_2O molecules in the active site (Scheme 1.2). This interaction is further stabilized by an H-bonding interaction of urea with His222, His323 and Ala366 upon the closure of the helix-turn-helix flap adjacent to the active site cleft. This intermediate is consistent with docking and DFT studies.[23] With enhanced basicity from H-bonding interactions, the $–NH_2$ of urea coordinates to Ni2. This binding mode is supported by crystal structure with citrate[24] and $B(OH)_3$[25] (isoelectronic to urea), bound with both Ni ions in a bidentate fashion. Subsequently, nucleophilic attack by the bridging hydroxide results in the formation of a tetrahedral intermediate. Proton transfer followed by collapse of the tetrahedral

intermediate yields carbamate and ammonia, which is released with the opening of the helix-turn-helix flap.

Scheme 1.2 Proposed urease catalytic mechanism.

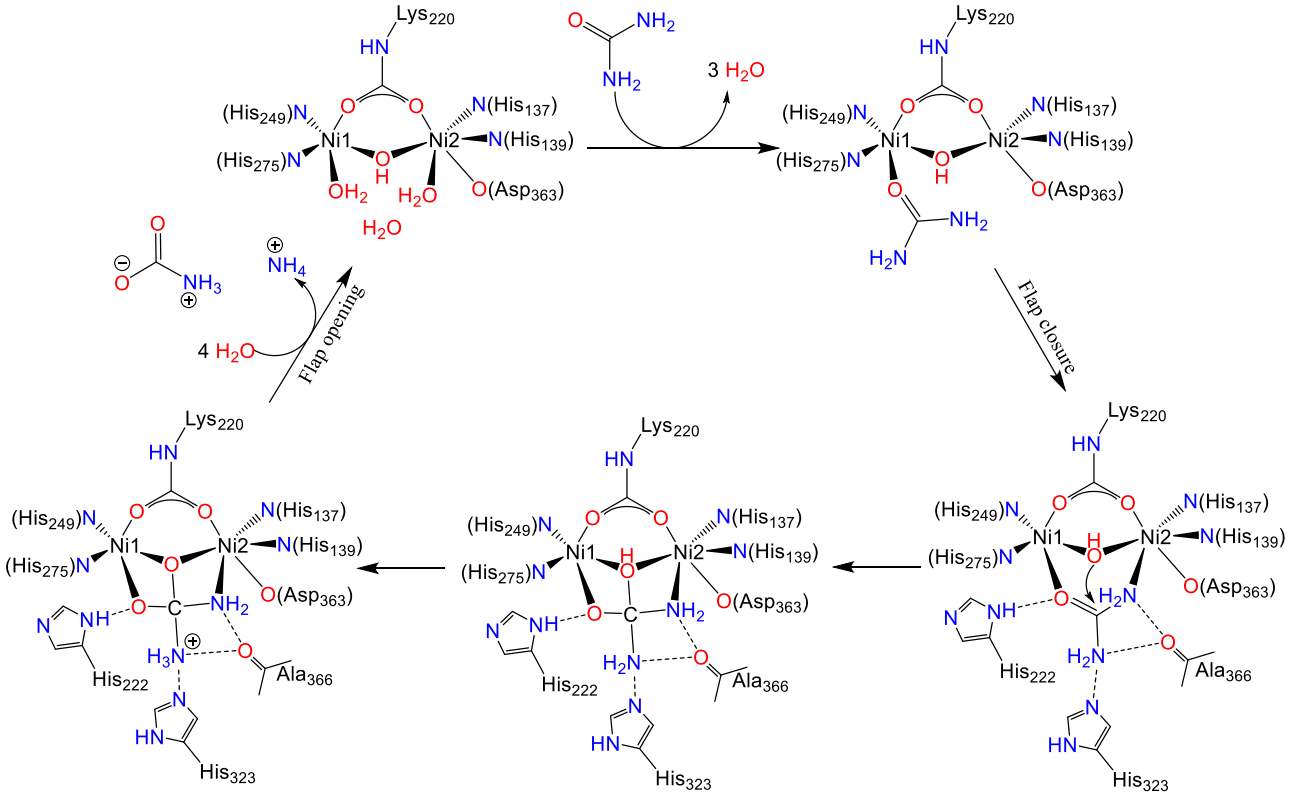

Glyoxylase I

Methylglyoxal (MG) can be generated from interconversion of dihydroxyacetone phosphate (DHAP) to glyceraldehyde-3-phosphate catalyzed by triosephosphate isomerase.[26] MG can also be generated by methylglyoxal synthase[27] and monoamine oxidase.[28] The glyoxylase system is a two-enzyme detoxifying system that catalyze the conversion of MG to the

corresponding 2-oxycarboxylic acid with the help of glutathione (GSH). The substrate for Glyoxylase I (GlxI) is a hemithioacetal that forms from non-enzymatic reaction between GSH and MG. GlxI catalyzes the isomerization of the hemithioacetal into the corresponding S-*D*-lactoylglutathione. Glyoxylase II (GlxII) then catalyzes the hydrolysis of the S-*D*-lactoylglutathione to 2-oxycarboxylic acid with the regeneration of GSH (Scheme 1.3).

Scheme 1.3 Methylglyoxal Detoxification by Glyoxylase System

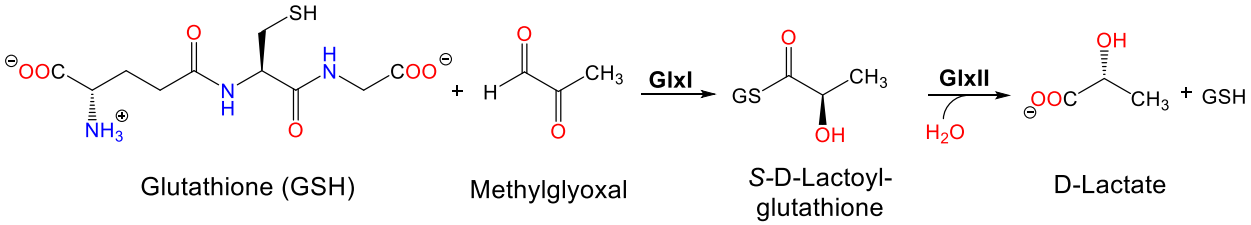

Glutathione (GSH) | Methylglyoxal | *S*-D-Lactoyl-glutathione | D-Lactate

GlxI can be separated into class I (Zn^{2+} activated) or class II (Ni^{2+} activated). Generally, GlxI from eukaryotes fall under class I, while GlxI from bacteria fall into class II.[29] Interestingly, GlxI from *E. coli* is inactive with bound Zn^{2+} and is only activated in the presence of Ni^{2+}.[30] The 135-amino acid GlxI from *E. coli* is a homodimer, where the Ni^{2+} ion is coordinated by His5, Glu56, His74, and Glu122 (His5 and Glu56 are from one monomer, while His74 and Glu122 are from another) and two water molecules in an almost ideal octahedral geometry at the interface between the two monomers (Figure 1.2).

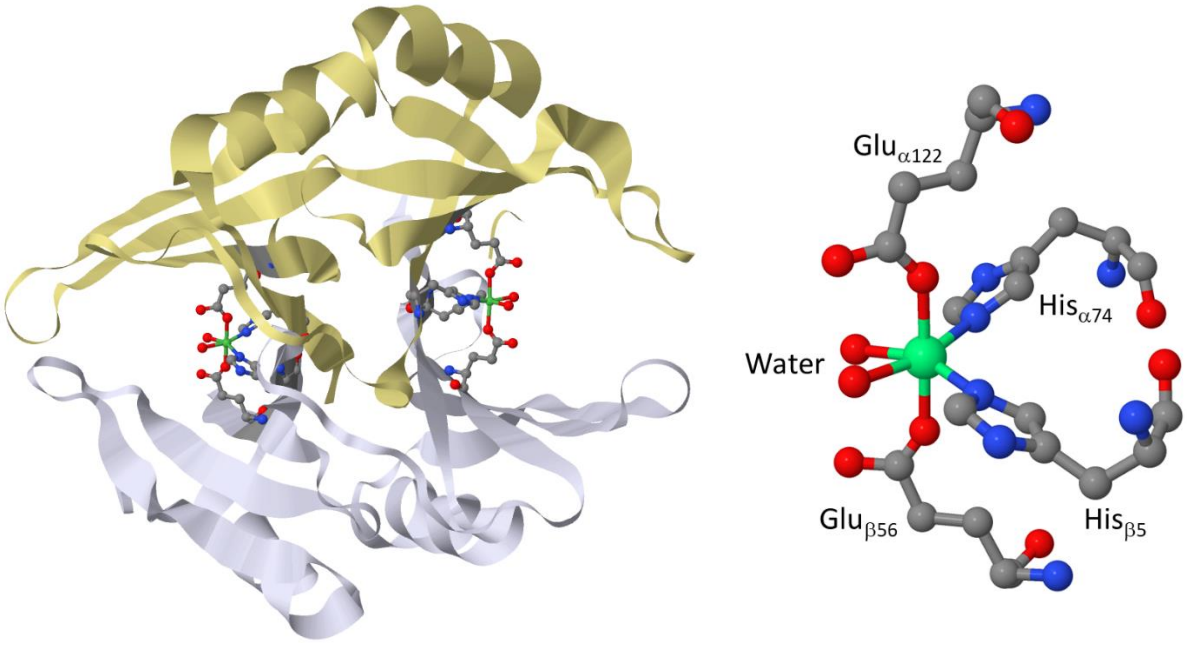

Figure 1.2 (*Left*) The structure of homodimeric GlxI from *E. coli* at 1.5 Å resolution (PDB: 1F9Z). (*Right*) The active site of GlxI with Ni coordinated by His74 and Glu122 from the α-subunit, His5 and Glu56 from the β-subunit, and two water ligands. H atoms are omitted for clarity. Images generated by Jmol.[22] Atom colors: green (nickel), red (oxygen), blue (nitrogen), and gray (carbon).

GlxI operates via the formation of an enediol(ate) intermediate (Scheme 1.4). Upon binding, the hemithioacetal substrate displaces two metal-bound water ligands and Glu122 to yield a square pyramidal complex with Glu122 as the general acid/base that facilitates the conversion of the hemithioacetal to S-*D*-lactoylglutathione. The Ni center remains in the 2+ oxidation state throughout catalysis, which indicates GlxI as a non-redox Ni enzyme. This proposed mechanism of GlxI was supported by kinetics and XAS studies of *E. coli* GlxI in the presence of inhibitors[31] and the crystal structure of Zn-containing human GlxI with the transition state analogue, *S*-(*N*-hydroxy-*N*-*p*-iodophenylcarbamoyl)glutathione.[32]

Scheme 1.4 Proposed mechanism for GlxI that involves coordination of substrate.

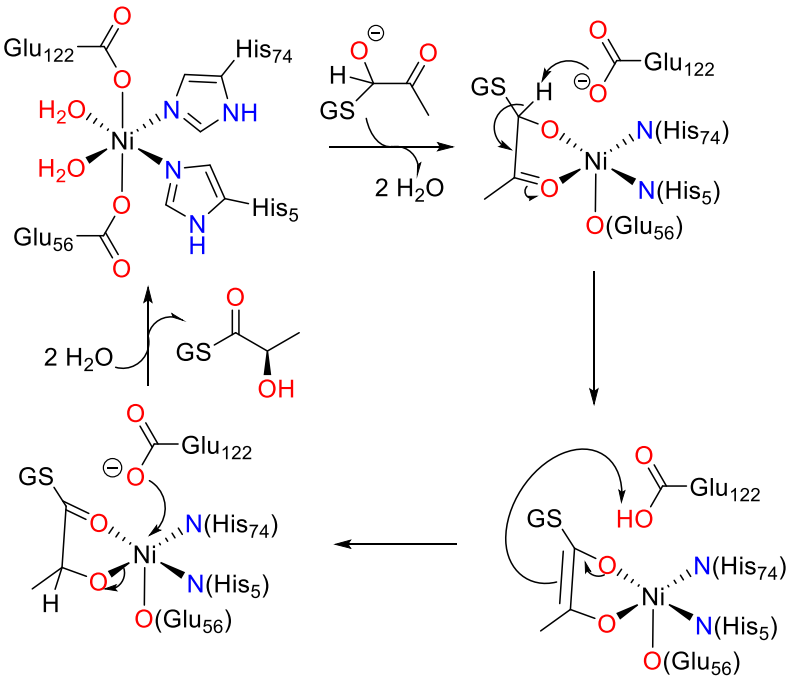

Acireductone Dioxygenase

The methionine salvage pathway (MSP) regulates several important metabolites in both eukaryotes and prokaryotes. The reaction of methionine and ATP yields *S*-adenosylmethionine, which is used in the biosynthesis of polyamines and in ethylene production in plants.[33,34] Polyamines are important to cell growth and proliferation while ethylene is important for the development of plants. Methylthioadenosine (MTA) is a byproduct of these processes and is a strong inhibitor of polyamine biosynthesis.[35] The penultimate intermediate in the MSP is acireductone, which is a derivative of MTA and the substrate for acireductone dioxygenase (ARD) (Scheme 1.5).[36,37] ARD from *Klebsiella oxytoca* utilize the same apoprotein is the only metalloenzyme that utilize the same apoprotein, but different metal (Ni^{2+} or Fe^{2+}), to catalyze two distinct chemical reactions (Scheme 1.5).[37-39] While FeARD catalyzes the on-pathway oxidation

of acireductone to the ketoacid precursor of methionine and formate, the other form, NiARD, catalyzes the off-pathway oxidation of acireductone with formation of CO, formate, and 3-(methylthio)propionate.

Scheme 1.5 Methionine salvage pathway. Numbers in pink label the C positions.

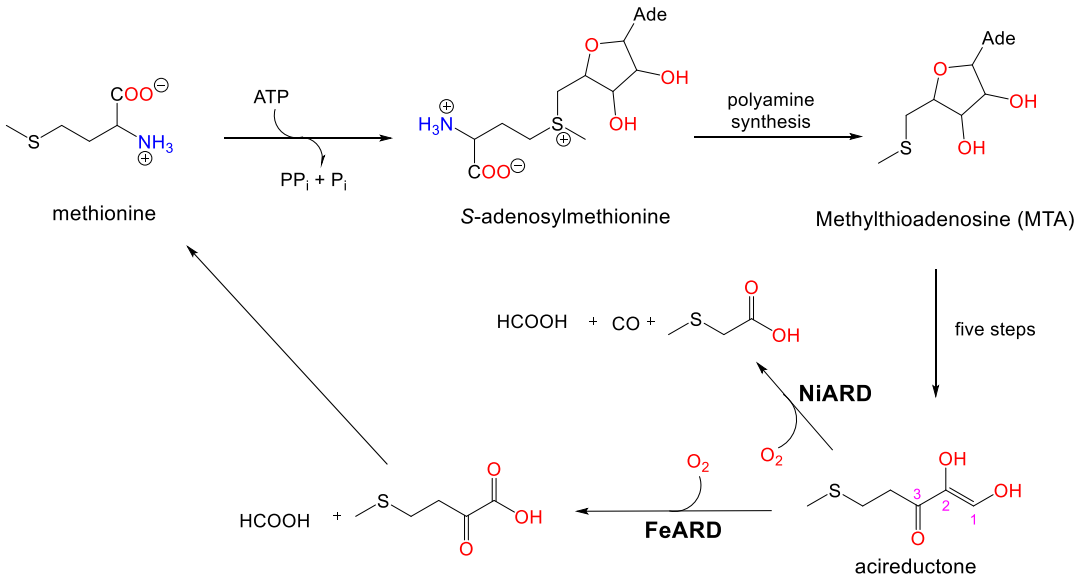

Since O_2 is required for catalysis, NiARD is predominantly found in aerobes or facultative aerobes, which include some proteobacteria and some Gram-positive aerobes such as *Nocardia* and *Frankia*.[18] NiARD is the only known nickel-containing dioxygenase that is also a member of the cupin super family. The first structure of NiARD was obtained from NMR spectra of *K. oxytoca* (also known as *Klebsiella* ATCC 8724), that was later refined using residual dipolar couplings.[40,41] The monomeric NiARD is comprised of a single 179-residue polypeptide that contains two β-sheets that hinge together to form a β-sandwich, which is also known as "jellyroll" fold (Figure 1.3).[40] Similar to other non-S-coordinated Ni enzyme, NiARD utilizes Ni^{2+} as a Lewis acid to

catalyze the oxygenation of acireductone with the via the following proposed mechanism:[42] (i) deprotonation of the monoanionic substrate to form a dianion that coordinates to the Ni center, displacing two water ligands; (ii) the C1 peroxide forms via a series of radical side reactions; (iii) the C1 peroxide attacks the C3 position to form a five-member ring intermediate that undergoes spontaneous decomposition to yield 3-(methylthio)propionate, CO, and formate (Scheme 1.6).

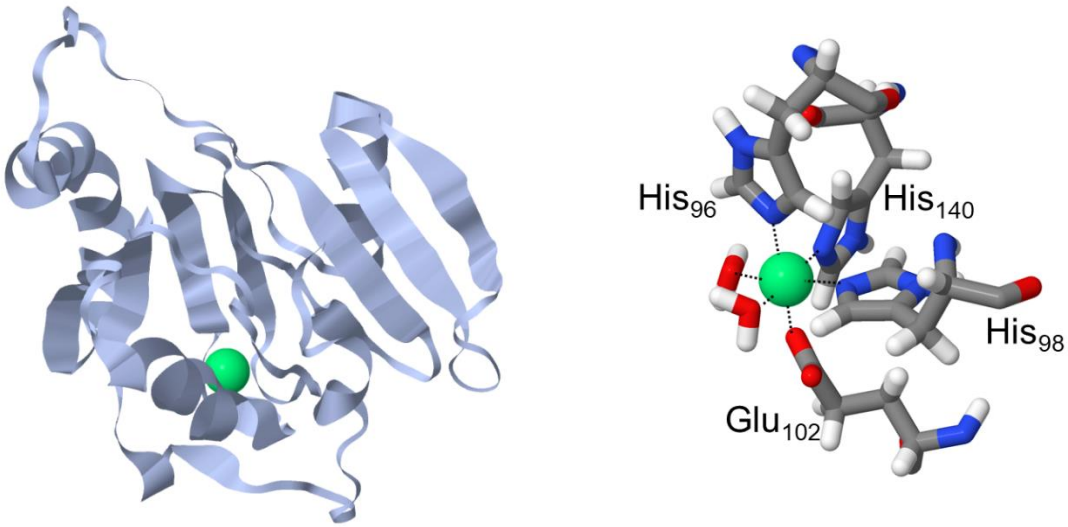

Figure 1.3 (*Left*) The structure of monomeric NiARD from *Klebsiella* ATCC 8724 (PDB: 1ZRR). (*Right*) Ni active site of NiARD. Images were prepared with Jmol.[22] Atom colors: green (nickel), blue (nitrogen), red (oxygen), gray (carbon), white (hydrogen).

Scheme 1.6 Proposed mechanism for NiARD

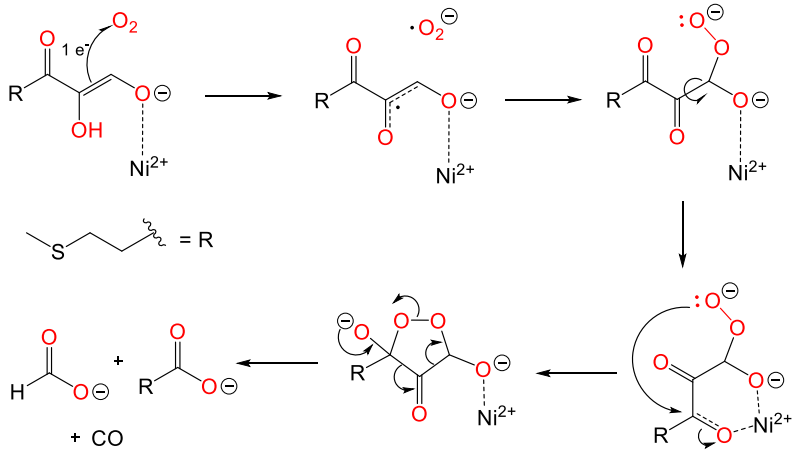

1.2.2 S-coordinated Ni enzymes

Lactate Racemase

Lactate racemase (Lar) catalyzes the isomerization between L- and D-lactate via a proposed hydride transfer mechanism (Scheme 1.7). Lactate isomerization was first reported in *Clostridium acetobutylicum* and *Clostridium beijerinckii* (also known as *C. butylicum*)[43] and subsequently found in several *Lactobacillus* species,[44] rumen bacteria *Megasphaera elsdenii* and *Selenomonas ruminantium*,[45,46] and halophilic archaea.[47] In 2014, LarA from *Lactobacillus plantarum* was identified as the ninth Ni-containing enzyme.[15] In *L. plantarum*, two gene clusters associated with Lar activity, *larABCDE* and *larR(MN)QO*, are transcribed in the opposite direction, inducible by L-lactate. While *larD* is not required for Lar activity, the gene encodes for an aquaglyceroporin, a transporter responsible for channeling both the D- and L- isomer of lactic acid through the membrane.[48] The *lar(MN)QO* gene encodes for an ATP-binding cassette (ABC) transporter system for high-affinity Ni uptake that is homologous to the high-affinity Ni transporters that are associated with Ni-dependent enzymes.[49] *larR* is a transcriptional regulator of the cyclic AMP receptor protein fumarate and nitrate reductase (Crp-Fnr) family, which encodes for a repressor that responds to L-lactate to regulate the transcription of the *larABCDE* operon.

Scheme 1.7 Hypothetical mechanism of Lar.

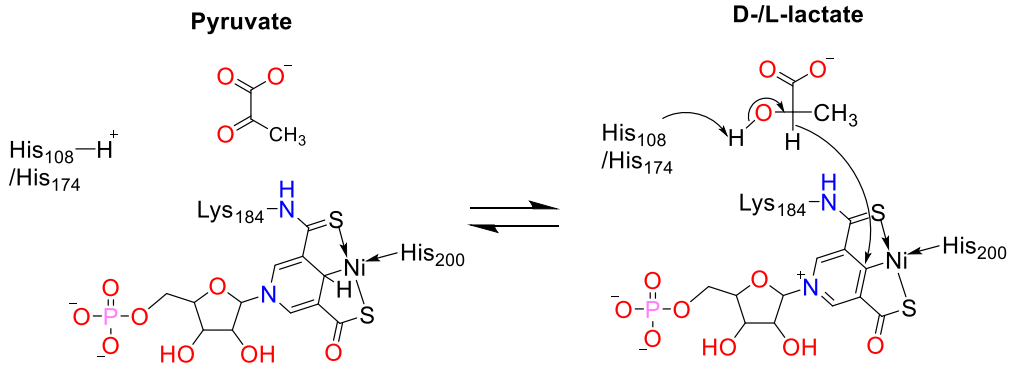

While Ni(SCS) pincer complexes that are widely used in organic synthesis and organometallic catalysis,[50,51] the metallocentre of LarA was the first Ni pincer observed in a biology. The formal name for this Ni chelate is pyridinium-3-thioamide-5-thiocarboxylic acid mononucleotide (PTTMN) Ni pincer. Lar activity depends on the maturation of LarA in the presence of LarB, LarC, and LarE,[15] all of which play an important role in the biosynthetic pathway of PTTMN Ni pincer. The first step in this pathway is LarB, which is a carboxylase/hydrolase of nicotinic acid adenine dinucleotide (NAD). In the presence of bicarbonate (HCO_3^-) and Mg^{2+}, LarB catalyzes the carboxylation of NAD followed by the hydrolysis of the phosphoanhydride linkage to yield the corresponding pyridinium-3,5-dicarboxylic acid mononucleotide (P2CMN) and adenosine monophosphate (AMP) (Figure 1.4).[52] Addition of sulfur into the cofactor requires LarE, which activates the carboxylic acid of P2CMN followed by sacrificial S-atom insertion. After activation of P2CMN by AMPylation, Cys176 of LarE attacks the activated P2CMN forming a thioether via Cys176.[52] Subsequent elimination of a proton on the α-C of Cys176 resulted in the formation of pyridinium-3-carboxylic acid-5-thiocarboxylic acid mononucleotide (PCTMN) and a dehydroalanine residue at position 176 of LarE. This process is repeated a second time with another LarE to yield the corresponding pyridinium-3,5-dithiocarboxylic acid mononucleotide (P2TMN). It has been shown that LarC is capable of inserting nickel into P2TMN to yield the PTTMN Ni pincer cofactor that remains bound to LarE.[52] Lastly, PTTMN Ni pincer is attached to Lys184 via the thioamide linkage. It is still unclear whether this last step happens spontaneously or if additional activation by maturation enzyme is required.

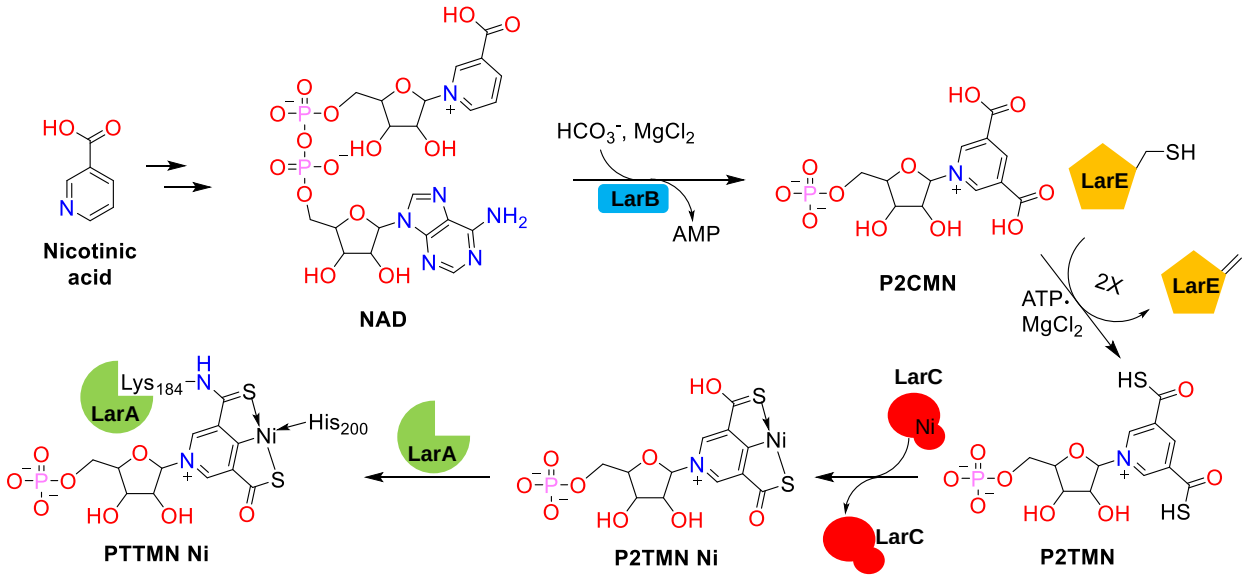

Figure 1.4 The biosynthetic pathway of PTTMN Ni pincer cofactor. NAD: nicotinic acid adenine dinucleotide, AMP: adenosine monophosphate, P2CMN: pyridinium-3,5-dicarboxylic acid mononucleotide, P2TMN: pyridinium-3,5-dithiocarboxylic acid mononucleotide, and PTTMN Ni: pyridinium-3-thioamide-5-thiocarboxylic acid mononucleotide nickel pincer. LarB: NAD hydrolase/carboxylase, LarE: ATP-dependent sacrificial sulfur transferase, and LarC: a nickel chelatase.

The structure of LarA from *L. plantarum* (PDB: 5HUQ) was obtained when LarA was purified in the presence of sulfate, which was shown to protect LarA from oxidation.[53] LarA is a homodimeric enzyme comprised of two 46.2-kDa monomers (Figure 1.5). In the active site, Ni is coordinated by a thioamide S-atom, the pyridinium C4, and the thioacid S-atom to generate a Ni(SCS) pincer complex with Nε-His200 as the fourth ligand to form a near planar coordination environment. The co-crystalized sulfate in the active site of LarA showed that Gln295 and Lys298 can provide H-bonding interactions to provide stability while His108/His174 function as general acid/base during catalysis.

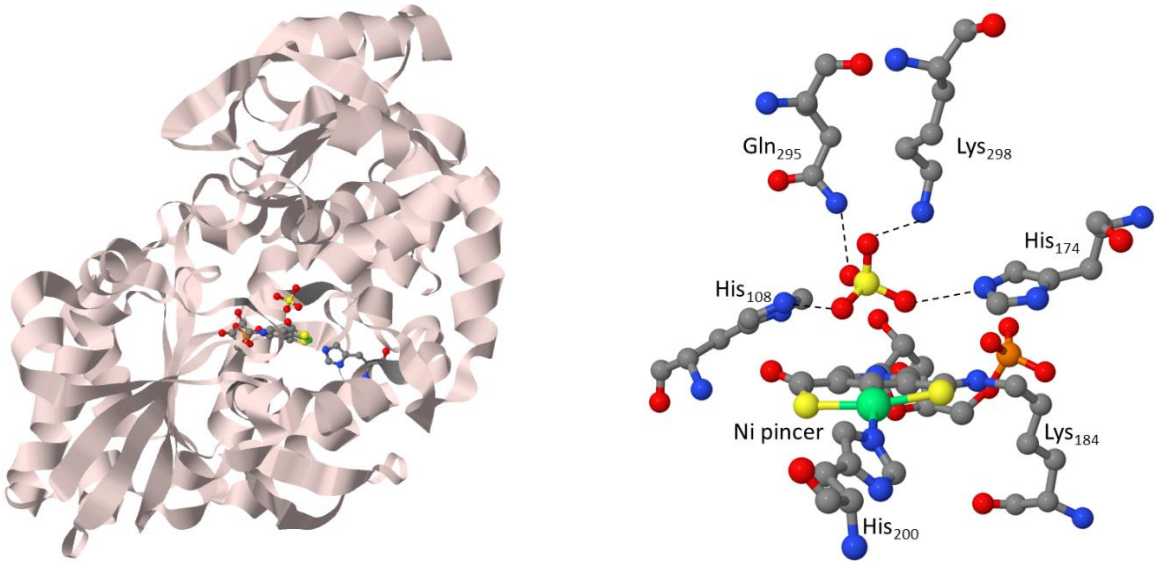

Figure 1.5 (*Left*) Structure of the monomeric LarA from *L. plantarum* (PDB: 5HUQ) with PTTMN Ni cofactor and sulfate in the active site. (*Right*) The active site of LarA with dash lines showing H-bonding interactions. H atoms are omitted for clarity. Images prepared by Jmol.[22] Atom colors: green (nickel), brown (phosphorous), yellow (sulfur), red (oxygen), blue (nitrogen), and gray (carbon).

It is proposed that LarA catalyzes the isomerization of lactate via a hydride transfer mechanism facilitated by the general acid/base from His108 and His174 in the active site (Scheme 1.7). However, the exact mechanism of LarA is still contentious. Synthetic models of PTTMN Ni pincer was reported by Hu and coworkers[54] and catalyze one cycle of benzoic acid dehydrogenation accompanied by loss of Ni. Theoretical studies conducted by Zhang and Chung on various truncated models of the LarA PTTMN Ni cofactor showed there was significant backdonation from the Ni(3d) to pyridinium(π^*) orbital that causes a decrease in electrophilicity of C4.[55] In this proposed mechanism, Ni remains in the 2+ oxidation state to facilitate the isomerization of lactate. Without the coordination of Ni, the NADH-like intermediate that formed after hydride transfer is in equilibrium with the starting pincer compound (Scheme 1.8). With the

coordination of Ni, the resulting metastable NADH-like intermediate (8-10 kcal/mol less stable than the reactant complex) will drive the equilibrium toward the reformation of the stable lactate isomer (Scheme 1.8). Although other electrophilic carbons (C7 and C8 of thioamide and thiocarboxylic acid, respectively) can be potential hydride acceptors, theoretical results show that hydride transfer to C7 and C8 are thermodynamically and kinetically unfavorable with the corresponding energetic barriers of 42-45 kcal/mol and 32-39 kcal/mol, respectively.

Scheme 1.8 Proposed mechanism for LarA that involves a metastable NADH-like intermediate. Adapted from ref 55.

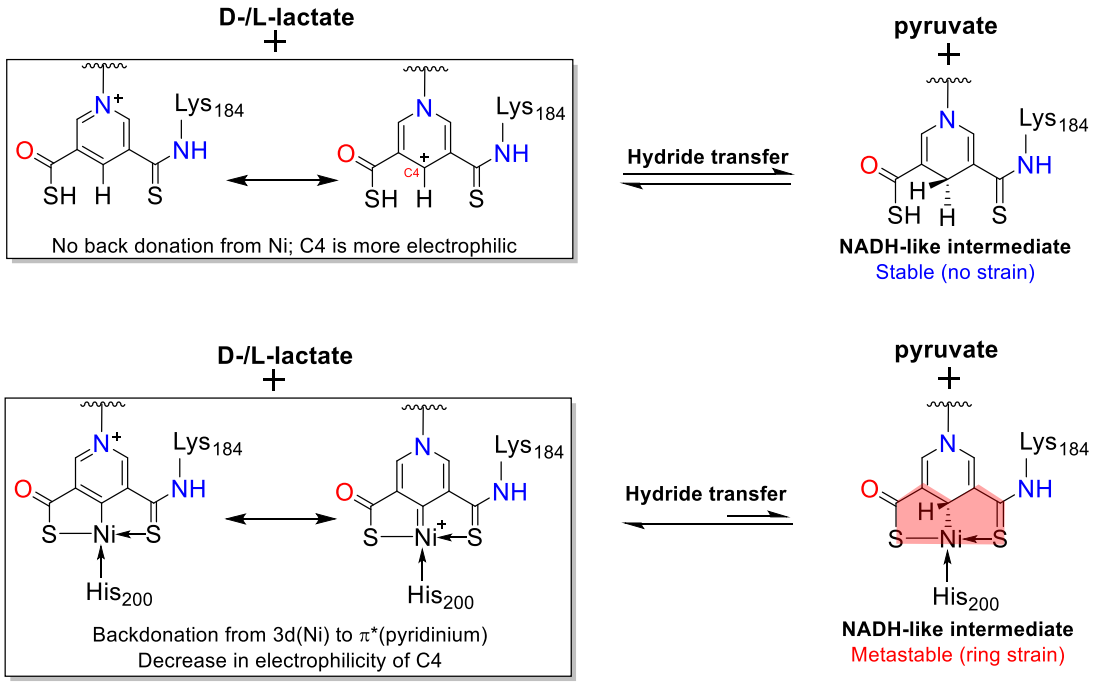

Alternatively, the isomerization of lactate can be mediated by a proton-coupled electron transfer (PCET) mechanism.[56] In the proposed mechanism, PTTMN Ni cofactor acts as a redox center that cycles between Ni^{3+} and Ni^{2+} oxidation state while His108/His174 facilitates the H^+

transfer. In the first step, deprotonation of lactate followed by electron transfer to PTTMN Ni pincer yields an elongated C1–C2 bond in the resulting pyruvate intermediate that can be seen as an acetaldehyde-like intermediate and a $CO_2^{\bullet-}$ anion radical (Scheme 1.9). Rotation about the C1–C2 bond followed by a PCET process from PTTMN Ni cofactor yields L-lactate. Experimental verifications of the intermediates proposed in these mechanisms are much needed to settle the debate on the mechanism of action of LarA.

Scheme 1.9 Proposed PCET-mediated mechanism for LarA. Adapted from ref 56.

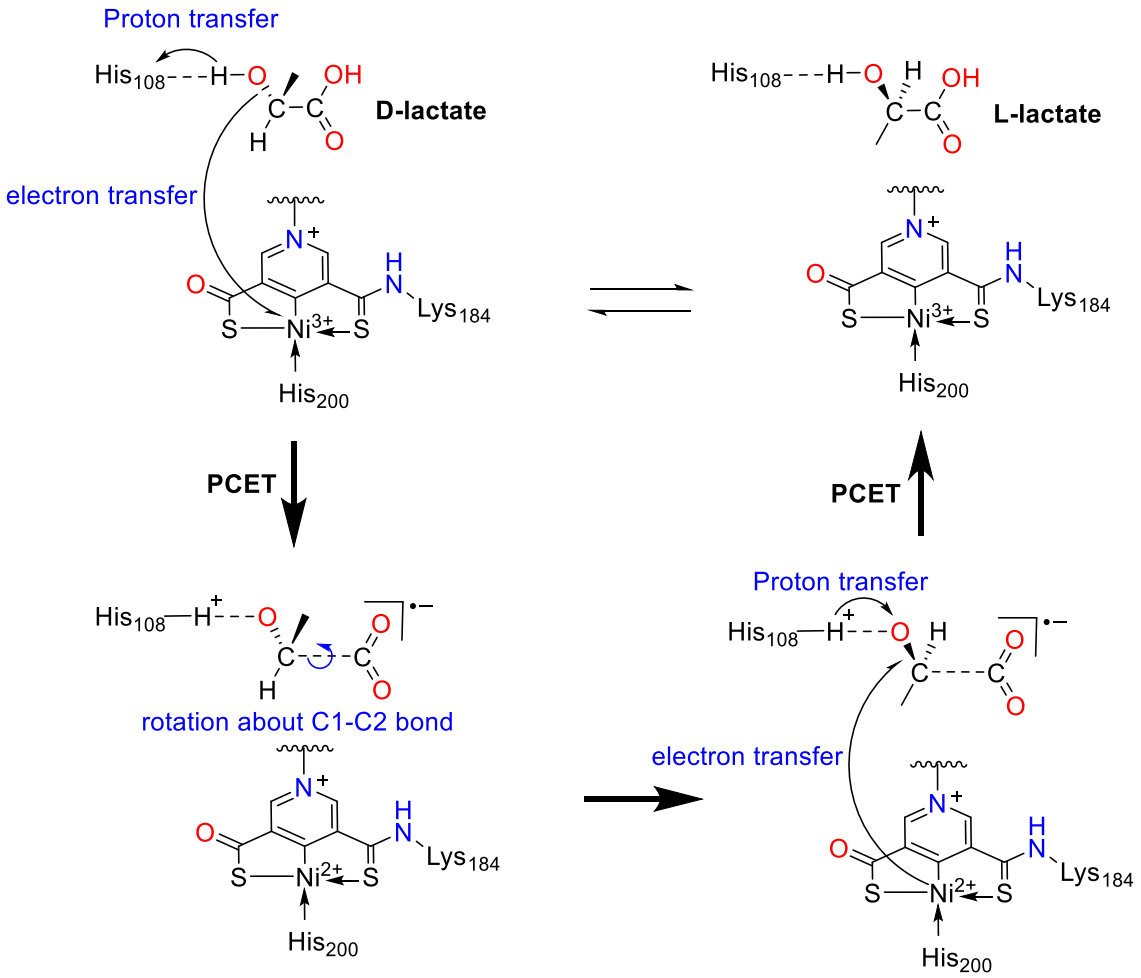

Methyl Coenzyme M Reductase

Methyl-coenzyme M reductase (MCR) catalyzes the formation of methane from methylated coenzyme M (CoM-S-CH_3) to yield a heterodisulfide of coenzyme M and B (CoM-SS-CoB). Unlike the other Ni-containing enzymes described so far, MCR is found exclusive in obligate anaerobes, methanogens bacteria, that belong to the Euryoarchaeota phylum.[18,57] Several crystal structures of MCR were obtained from *Methanobacterium thermoautotrophicum*,[58] *Methanosarcina barkeri*,[59] and *Methanopyrus kandleri*.[59] The structures revealed MCR as a heterohexamer with $(\alpha\beta\gamma)_2$ subunits and two catalytic centers. Each catalytic center contains one noncovalently attached nickel hydrocorphin called coenzyme F_{430} in the α-subunit (Figure 1.6). The as-isolated MCR is inactive with Ni in the 2+ oxidation state. A 50 Å substrate channel extending from the protein surface into the cavity that hosts the binding site for methylated CoM and coenzyme F430. The binding of CoB in the narrow entrance of the substrate channel completely seals off the active site from bulk solvent during catalysis.

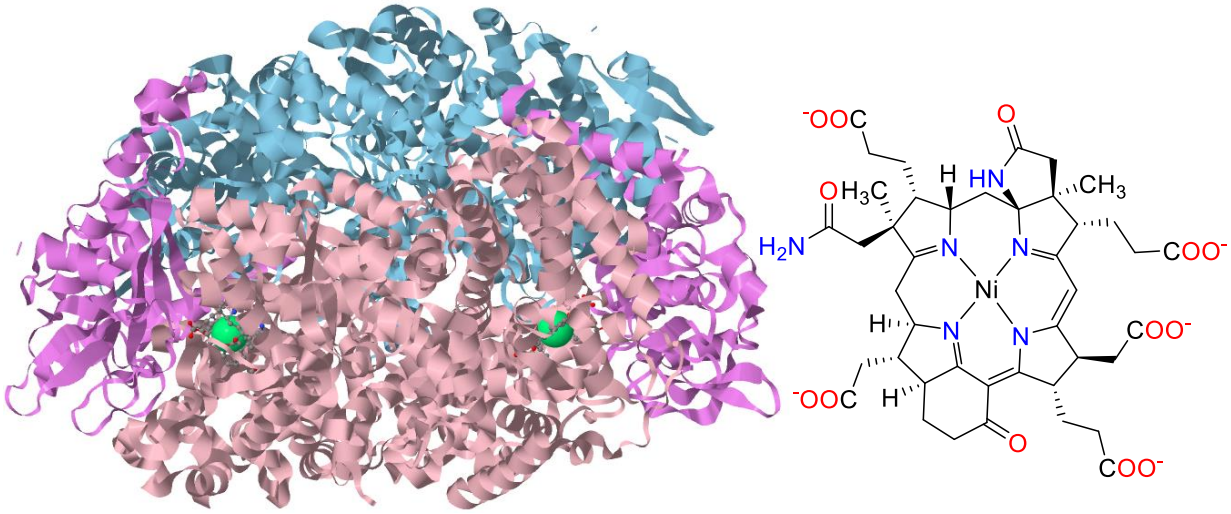

Figure 1.6 (*Left*) The overall structure of the heterohexamer MRD from *M. thermoautotrophicum* at 1.16 Å resolution (PDB: 1HBN). Green spheres indicate the Ni active site. Image prepared with Jmol.[22] (*Right*) ChemDraw depiction of F430 cofactor.

Two different mechanisms have been proposed for MCR based on structural data,[58,60-62] spectroscopy,[63-65] and computational studies.[66-68] The distinction between them is in the proposed intermediate in the first step (Scheme 1.10). The first mechanism proposed an organometallic methyl-nickel intermediate, while the second mechanism calls for a methyl radical. For mechanism I, Ni^{+} attacks the CH_3 of CoM-S-CH_3 to form an organometallic Ni^{3+}-CH_3 via oxidative addition. The resulting CoM reduces the Ni^{3+}-CH_3 to Ni^{2+}-CH_3 with the formation of a CoM radical. The CoM radical then reacts with CoB to form a disulfide anion radical as a proton is transferred from CoM to Ni^{2+}-CH_3 to form CH_4. The reduction of the Ni^{2+} active site by disulfide anion radical of CoM and CoB regenerates the Ni^{+} active site. For mechanism II, Ni^{+} reacts with CoM-S-CH_3 at the S atom to yield a methyl radical and Ni^{2+}-thiolate adduct via hemolytic cleavage of the CoM-S-CH_3 bond. The resulting methyl radical abstracts a H-atom from CoB to yield methane and a thiyl radical on CoB, which reacts with Ni^{2+}-S-CoM to yield Ni^{2+} and a disulfide anion radical of CoM and CoB. The reduction of Ni^{2+} to Ni^{+} by the disulfide anion radical regenerates the active site as proposed in mechanism I.

Scheme 1.10 The proposed mechanisms for MCR.

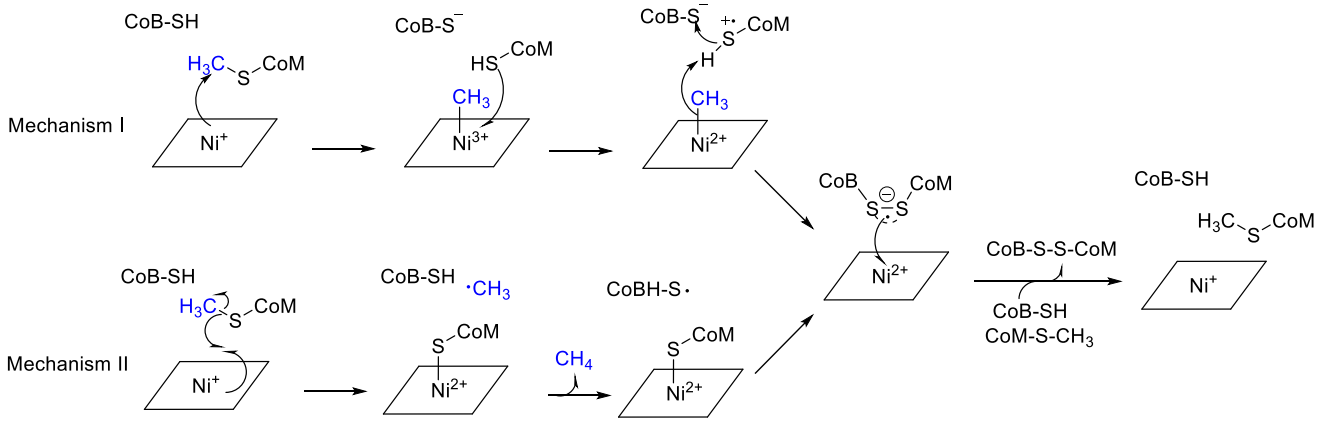

Carbon Monoxide Dehydrogenase

Carbon monoxide dehydrogenase (CODH) catalyzes the reversible oxidation of CO to CO_2. Ni-containing CODH is either found on its own or in complex with acetyl-CoA synthase (ACS), which are both important to the Wood-Ljungdahl Pathway that allows anaerobes to utilize CO or CO_2 as a C source.[69] Ni-CODH is most prevalent in sulfate reducing deltaproteobacteria, gram-positive acetogens, and archaeal methanogens.[18] Ni-CODH is a mushroom shape homodimer containing five metal clusters: two Ni-Fe-S clusters (C clusters), one $[Fe_4S_4]$ D-cluster, and two $[Fe_4S_4]$ B-clusters (Figure 1.7).[70-73] The D-cluster is found bridging the two subunits, where the C-cluster of one is closer to the B-cluster of another than from those in the same subunits. While C-cluster is buried 18 Å below the protein surface, the B- and D-clusters act as conduit to transfer electrons from the C-cluster to external redox proteins such as ferredoxin (Fd; $Fd_{red} = Fe^{2+}$; $Fd_{ox} = Fe^{3+}$).

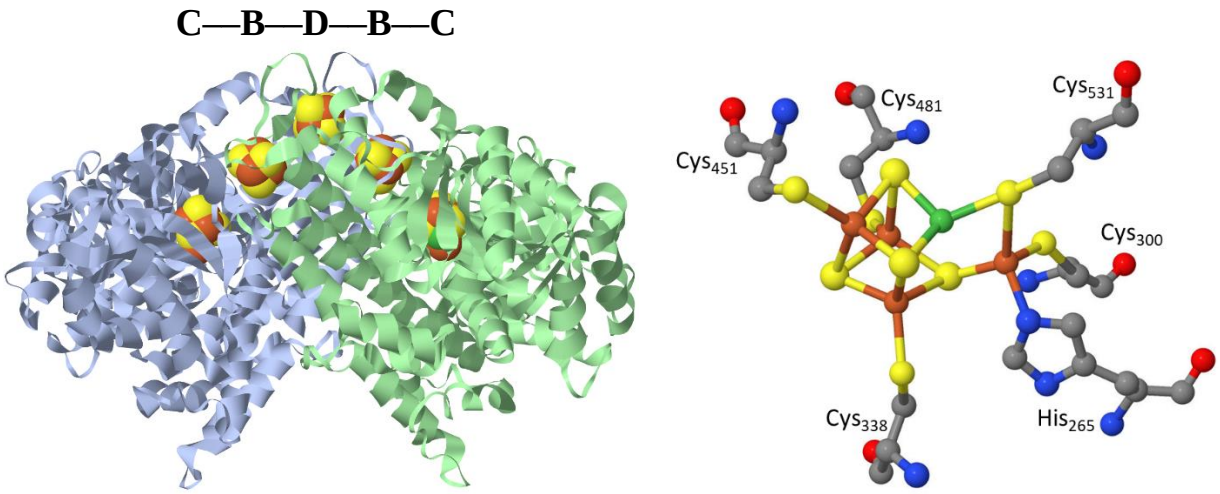

Figure 1.7 (*Left*) The structure of CODH from *Rhodospirillum rubrum* at 2.8 Å resolution (PDB: 1JQK) with five metal clusters (C-clusters, two B-clusters, and one D-cluster as labeled in black). (*Right*) The structure of the C-cluster. H atoms are omitted for clarity. Images generated by Jmol.[22] Atom colors: green (nickel), brown (iron), red (oxygen), blue (nitrogen), yellow (sulfur), and gray (carbon).

In the C-cluster, a $[Fe_3S_4]^{2+/1+}$ coordinates to both Ni and Fe, where Cys531 and one S-sulfide bridge the NiFe dimer. In addition, the Fe^{2+} center is also coordinated by His265 and Cys300 (Figure 1.7). Throughout catalysis the Fe center in the C-cluster remains in the 2+ oxidation state. The proposed mechanism of CO oxidation to CO_2 begins with the CO binding to Ni^{2+} and H_2O to Fe in the binuclear component of the C-cluster that results in the cleavage of the Cys-S bridge, followed by the immediate deprotonation of the bound H_2O to yield an Fe bound hydroxide (Scheme 1.11). The OH group attacks the metal bound CO to form a carboxylate that bridges Ni and Fe in the C-cluster as shown by X-ray crystallography.[74] The formation of CO_2 involves the transfer of two e^- to the C-cluster, which is subsequently transferred to B- and D-clusters in the redox chain to two Fd's or other external redox proteins.

Scheme 1.11 Proposed mechanism of CODH.

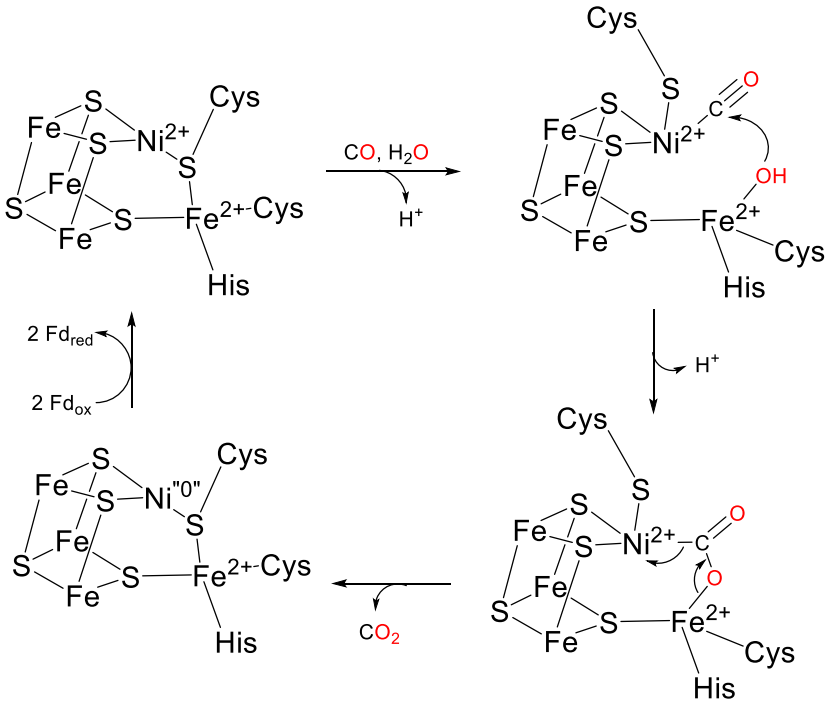

Acetyl-CoA Synthase

Acetyl-CoA synthase (ACS) is part of a bifunctional enzyme with CODH to form a tetrameric super protein (ACS/CODH) that catalyzes acetyl-CoA synthesis. ACS utilizes the product of CODH from CO_2 reduction (CO), a methyl group (provided by a methylated CFeSP, a corrinoid Fe-S protein), and one CoA to generate acetyl-CoA.[71,75,76] The gene *acsB* encoding for ACS was recognized as a marker for the Wood-Ljungdahl pathway because it is found in clusters with other enzymes in the pathway.[77] ACS is found in acetate-utilizing methanogens (e.g., *Methanosarcina barkeri, Methanosarcina thermophila*),[73] homoacetogenic bacteria, and green non-sulfur bacteria.[18] Interestingly, ACS/CODH was also found to catalyze the decomposition of acetyl-CoA to form CoA, a methylated CFeSP, and CO, which demonstrate that ACS/CODH can catalyze the reaction reversibly.[78,79]

The crystal structure of ACS/CODH from *M. thermophila* showed a $\alpha_2\beta_2$ tetrameric structure (Figure 1.8).[73] The overall structure of the β subunit is similar to that reported for CODH, which contains the C-clusters, where reversible CO oxidation takes place. The α subunits are found in either a closed or open conformation. In the open conformation, the A-cluster has a larger exposed surface that allows for solvent access and/or binding of CFeSP. The crystallized structure of ACS/CODH with Xe revealed a 140 Å long hydrophobic channel that allows CO to travel from the C-cluster in CODH to the A-cluster in ACS for acetyl-CoA synthesis.[80]

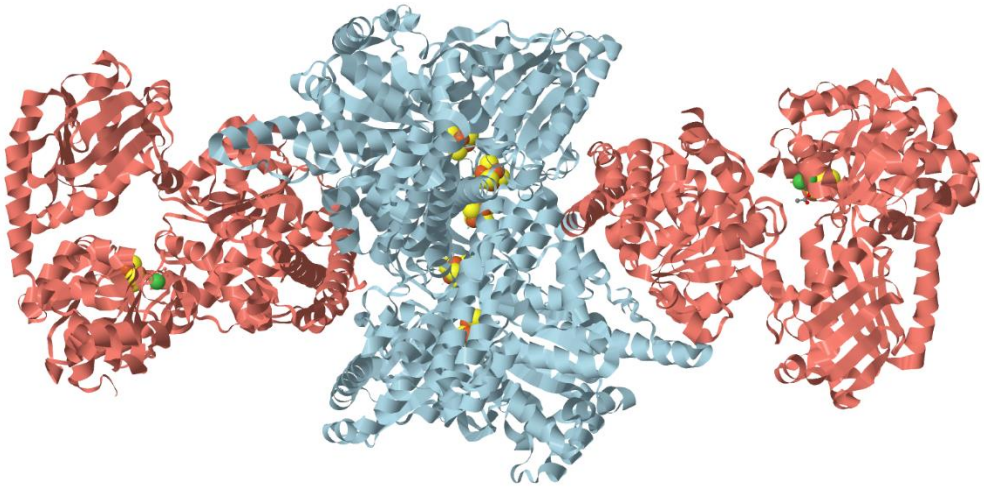

Figure 1.8 Structure of CODH/ACS from *M. thermophila* at 1.9 Å resolution (PDB: 1OAO). The blue units in the center are the two CODH homodimers. The magenta units are ACS containing the A-clusters in the open conformation (left) and the closed conformation (right). Image generated with Jmol.[22]

In the A-cluster, a [Fe_4S_4] cluster is bridged via Cys509 to the proximal nickel site (Ni_p), that is also bridged to the distal nickel site (Ni_d), which is situated in a N_2S_2 coordination environment comprised of two backbone carboxamide-N ligands and two thiolate-S ligands provided by the tripeptide Cys595-Gly596-Cys597 (Figure 1.9). The Ni in Ni_p is coordinated by three S-thiolates from Cys509, Cys595, and Cys597 to form a T-shape coordination environment. However, coordination of Ni_p with acetate[73] to form a distorted square planar coordination was reported (Figure 1.9). The labile nickel in Ni_p was replaced by zinc or copper in early structures of ACS/CODH, which led to the assignment of copper as an important component of the active cluster. However, it was later found that copper was not only not responsible for ACS activity, but it was found to inhibit enzyme activity.[81]

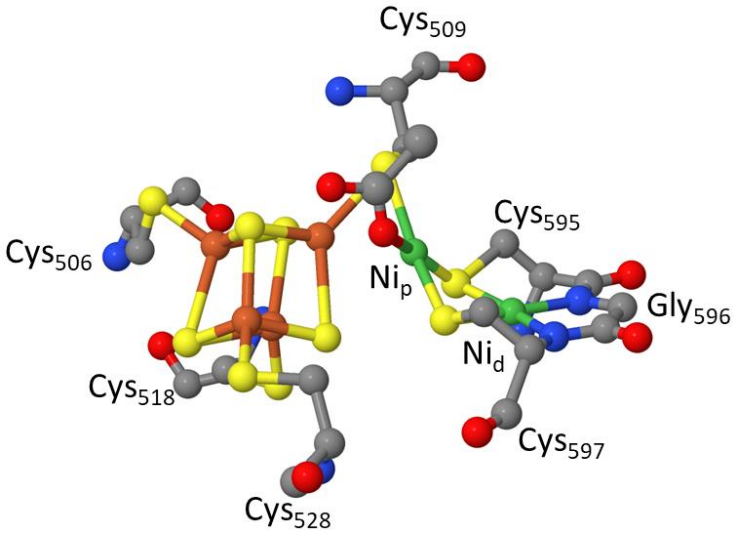

Figure 1.9 The A-cluster in ACS/CODH from *M. thermophila* at 1.9 Å resolution (PDB: 1OAO). Ni_p is coordinated to an acetate and three S-thiolates to form a distorted square-planar geometry. Ni_d is coordinated by Cys595-Gly596-Cys597 in a square-planar NiN_2S_2 coordination environment. H atoms are omitted for clarity. Images generated by Jmol.[22] Atom colors: green (nickel), brown (iron), red (oxygen), blue (nitrogen), yellow (sulfur), and gray (carbon).

While the A-cluster contains six different redox-active atoms, substrate only binds to the Ni_p site. Two competing mechanisms are proposed for ACS: (i) paramagnetic mechanism[82] and (ii) diamagnetic mechanism.[83] A detailed review of these two proposed mechanisms is reported elsewhere.[69] Although the diamagnetic mechanism[83] proposes the formation of a Ni^0 intermediate based on a square planar Ni^0-phospine complex's ability to accept CH_3 group from Co^{3+}–CH_3 complex,[84] Ni^0 intermediate has not been observed or reported. Moreover, the presence of the Ni^0 species adjacent to the Ni_d^{2+} site and $[Fe_4S_4]^{2+}$ cluster seems unlikely. Therefore, the paramagnetic mechanism, which proposes the formation of Ni^{1+}–CO and Ni^{2+}–acetyl intermediates, is presented here (Scheme 1.12). The as-isolated oxidized A-cluster with the configuration of $[Fe_4S_4]^{2+}Ni_p^{2+}Ni_d^{2+}$ was not able to accept methyl group from CFeSP[85,86] or to bind to CO.[87] Therefore, activation via reduction by Fd_{red} or other external electron donor to yield Ni_p^+ is needed for catalysis. Ni_p^+ binds to CO to form a Ni_p^+–CO species (Scheme 1.12) that is characterized by

IR (ν_{CO} = 1995 cm^{-1}),[88,89] and EPR signal ($g_{\perp}$ = 2.074 and $g_{\parallel}$ = 2.028).[90] At this point, ACS is most likely in the open conformation which allows the binding of CFeSP. Second, Ni_p^{+} attacks the methyl group on CFeSP in an S_N2 fashion to yield a Ni_p^{3+} bound to CH_3 and CO,[91-93] which is reduced to Ni_p^{2+} via an internal electron transfer mechanism that has not yet been identified. Lastly, the carbonyl insertion of the methyl group yields an acetyl-Ni complex,[94] which reacts with CoA to generate acetyl-CoA and one electron donated to the internal electron transfer mechanism.

Scheme 1.12 Proposed paramagnetic mechanism of acetyl-CoA synthase catalyzed by the A-cluster.

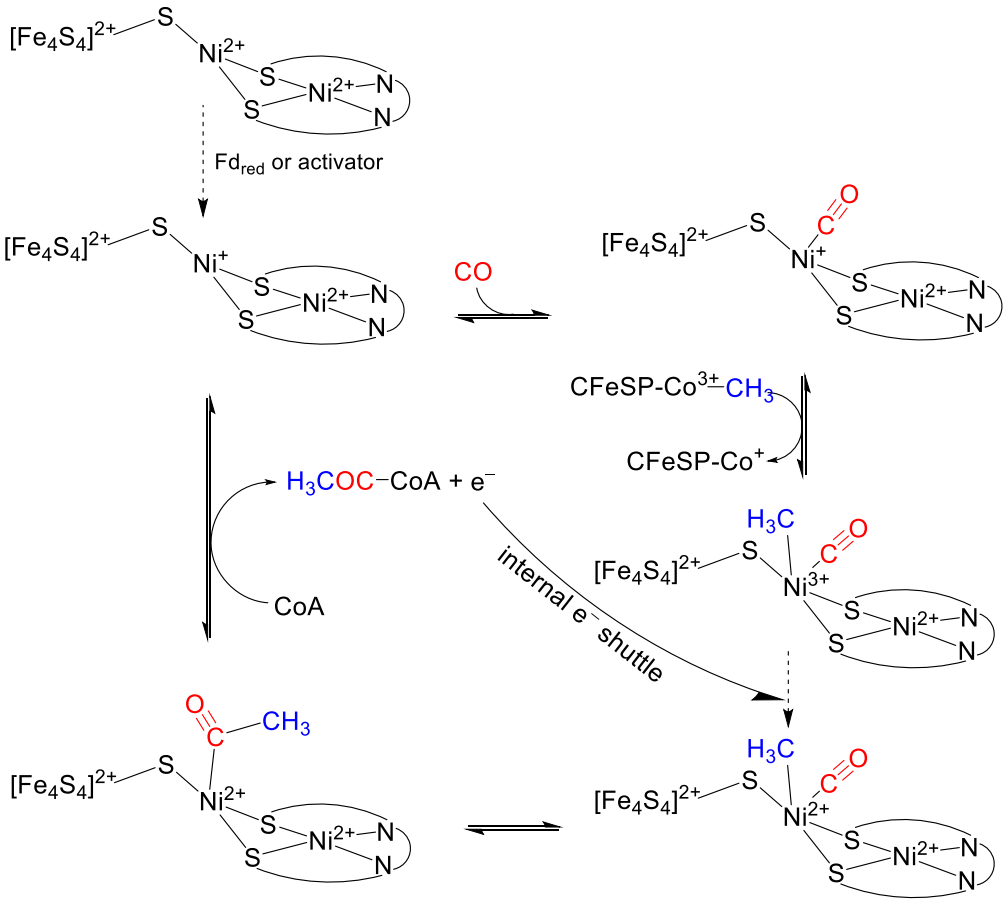

NiFe-hydrogenase

Hydrogenases (H_2ases) catalyze the reversible interconversion of H_2 and H^+. H_2ases belong to one of the following three classes: (i) [NiFe]-H_2ase with a subclass [NiFeSe]-H_2ase, (ii) [FeFe]-H_2ase, and (iii) [Fe]-H_2ase. H_2ases are well distributed throughout bacteria and archaea with the exception of *Theromodesulfobacteria*.[18] While the activity of the standard (O_2-sensitive) [NiFe]-H_2ase diminishes quickly under aerobic conditions, a group of O_2-tolerant [NiFe]-H_2ases that retain their catalytic activity in the presence of O_2 were identified and characterized in *Hydrogenovibrio marinus,*[95] *Ralstonia eutropha,*[96,97] *Escherichia coli,*[98,99] *Citrobacter* sp. S-77,[100-102] and *Pyrococcus furiosus*.[103] The crystal structure of [NiFe] H_2ase from *Desulfovibrio vulgaris* Miyazaki F (*Dv*MF) at 0.89 Å resolution (a periplasmic membrane attached enzyme) reveals a 91 kDa heterodimeric protein comprised of small (29 kDa) and large (62 kDa) subunits (Figure 1.10).[104-108] Three iron-sulfur clusters (proximal $[Fe_4S_4]_p^{2+/1+}$, medial $[Fe_3S_4]_m^{+/0}$, and distal $[Fe_4S_4]_d^{2+/1+}$cluster) are located ~13 Å apart and arranged in an almost linear fashion. These iron-sulfur clusters function as an electron transfer pathway from the active site to external electron acceptors, such as cytochrome c_3.[109] The C-terminus of the large subunit contains a Mg^{2+} coordinated by His552, Glu62, Leu62 and three water molecules in a distorted octahedral geometry that was proposed to stabilize the structure and acts as the H^+ transfer pathway as it is located ~13 Å away from the active site.

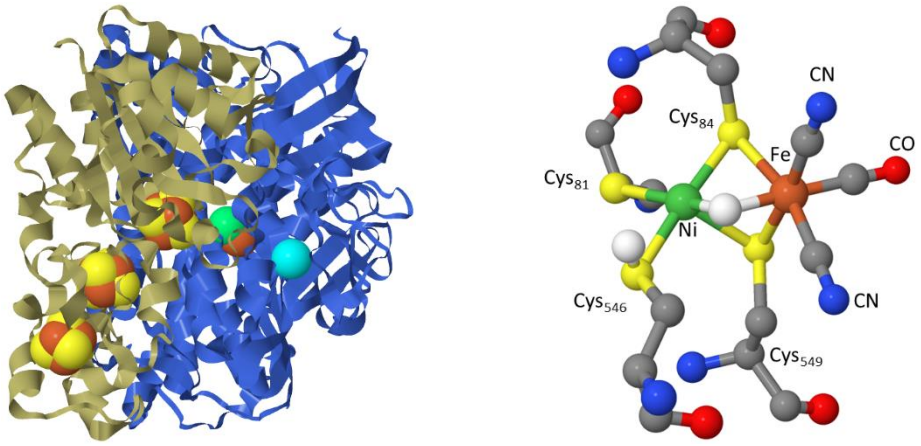

Figure 1.10 (*Left*) The structure of heterodimer of [NiFe] H_2ase from *Dv*MF at 0.89 Å resolution (PDB: 4U9H) with three iron-sulfur clusters, the [NiFe] site, and Mg^{2+} ion. (*Right*) The structure of the **Ni-R** state with a bridging H^- and protonation at the Cys546 position. Images generated with Jmol.[22] H atoms omitted for clarity except the bridging H^- and H^+ on Cys546. Atom colors: green (nickel), brown (iron), cyan (magnesium), red (oxygen), blue (nitrogen), yellow (sulfur), and gray (carbon).

The heteronuclear active site resides in the large subunit, featuring a $Ni(S\text{-}Cys)_4$ center, bridged by two Cys-S^- to an Fe-$(CN)_2(CO)$ fragment. A closer look at the active site of [NiFe] H_2ase revealed that $Ni(S\text{-}Cys)_4$ adopts a seesaw geometry, while the $(Cys\text{-}S)_2Fe(CN)_2(CO)$ is in a distorted square pyramidal geometry (Figure 1.10). Throughout catalysis, the Fe^{2+} is redox inactive while Ni cycles between Ni^{3+}, Ni^{2+}, and Ni^{1+} states. Various spectroscopic and X-ray crystallographic studies led to the identification of many [NiFe] H_2ase intermediate states for *Dv*MF [NiFe] H_2ase. These intermediate states are characterized by EPR that fall under two categories: EPR-active (paramagnetic, i.e. Ni^+ and Ni^{3+} in the active site) and EPR-silent (Ni^{2+} in the active site) (Scheme 1.13).

Scheme 1.13 The intermediate states of [NiFe] H_2ase with the oxidation state of Ni in the [NiFe] site indicated. Intermediate states in blue are important intermediates during catalysis.

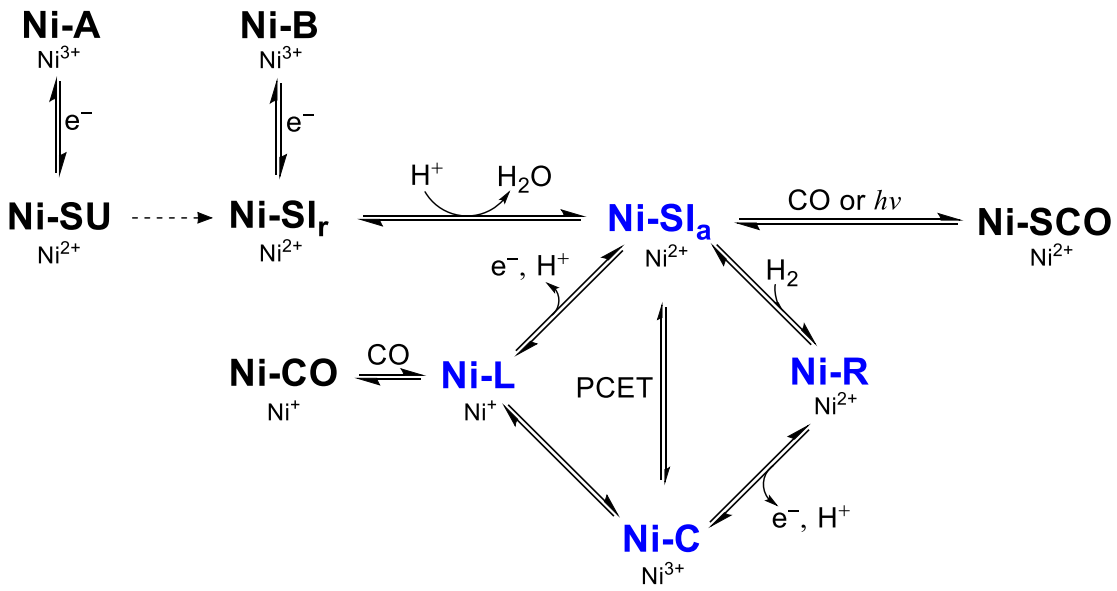

Aerobically isolated *Dv*MF [NiFe] H_2ase is a mixture of **Ni-B** (ready state; fast activation), **Ni-A** (unready state; slow activation), and some EPR-silent Ni^{2+} states with **Ni-B** as the major component. Both **Ni-B** and **Ni-A** contain Ni^{3+}, which can be activated in the presence of H_2 or under electrochemically reducing condition for catalysis. While **Ni-B** is activated within minutes, **Ni-A** may takes up to hours.[110-112] The difference in activation kinetics between **Ni-A** and **Ni-B** can be a result of O2 inactivation and the generation of Cys-sulfoxide (S=O) or Cys-sulfenic acid (SOH) as a ligand in **Ni-A**.[107,112-114] The bridging X ligand in **Ni-B** has been assigned to a bridging hydroxo (μ-OH^-) ligand,[115,116] however, the bridging ligand in **Ni-A** remains a matter of debate. While **Ni-A** and **Ni-B** are the most oxidized states found in standard [NiFe] H_2ase, O_2-tolerant [NiFe] H_2ases employ a unique proximal iron-sulfur cluster ($[Fe_3S_4]_p^{5+/4+/3+}$), in which six Cys residues are coordinated to the cluster (Figure 1.11). In the presence of O_2, $[Fe_4S_3]_p^{3+}$ is oxidized

to $[Fe_4S_3]_p^{5+}$, the super-oxidized cluster, in which the peptido-N of Cys20 coordinates to Fe with OH^- adduct in *R. eutropha* [NiFe] H_2ase (Figure 1.11). Both $[Fe_4S_3]_p^{5+/4+/3+}$ and the $[Fe_3S_4]_m^{0/+}$ are critical to the O_2 to H_2O reduction at the [NiFe] site to prevent the formation of the **Ni-A** state, in which O_2 is reduced to 2 H_2O using four electrons donated by $[Fe_4S_3]_p^{3+}$ (two electrons), $[Fe_3S_4]_m^0$ (one electron), and Ni (one electron) in the [NiFe] site (Figure 1.11).[96-99,117-121]

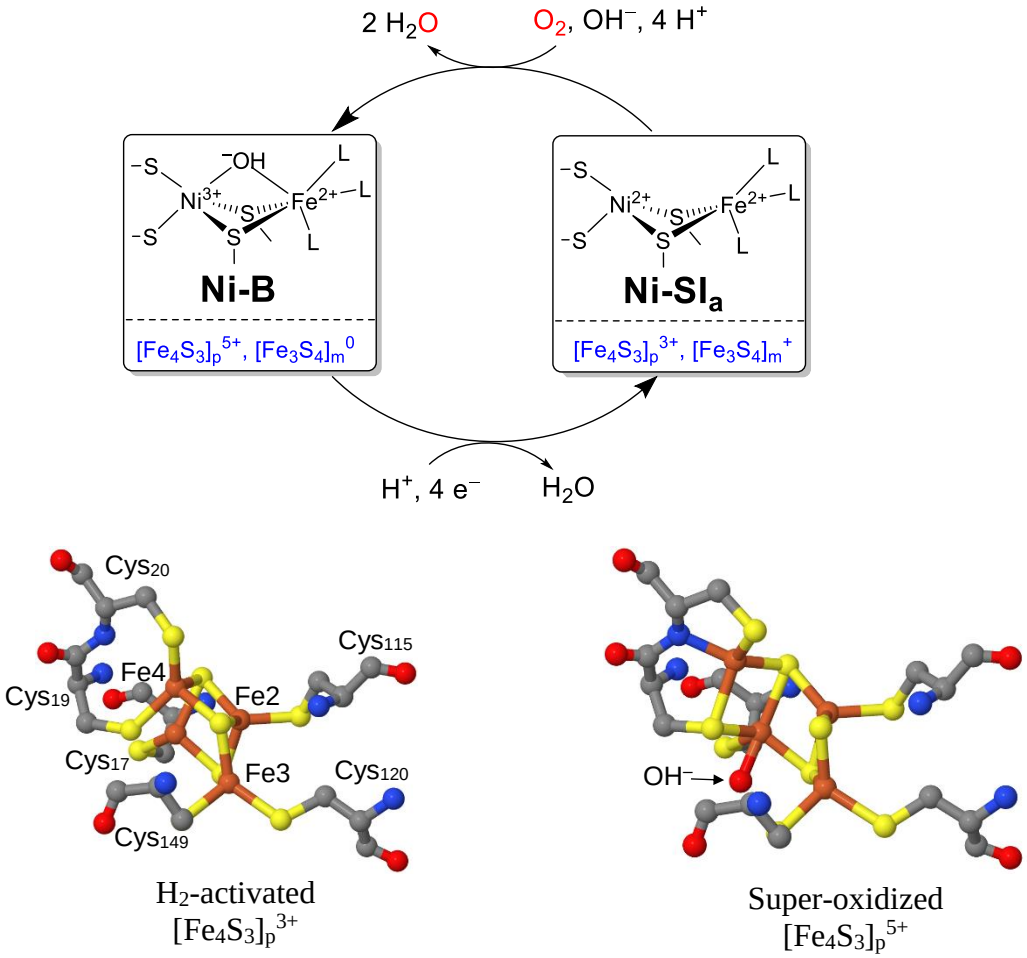

Figure 1.11 *Top*: The proposed mechanism of O_2-inactivation and rapid activation for membrane-bound O_2-tolerant [NiFe] H_2ase. *Bottom*: The structure the proximal $[Fe_4S_3]$-6Cys cluster in the H_2-activated (left, PDB: 3RGW) and super-oxidized (right, PDB: 4IUB) states of O_2-tolerant *R. eutropha* [NiFe] H_2ase. Images generated by Jmol.[22] H atoms omitted for clarity. Atom colors: brown (iron), red (oxygen), blue (nitrogen), yellow (sulfur), and gray (carbon).

Ni-SU (EPR-silent unready state) and **Ni-SI$_r$** (EPR-silent inactive ready state) are one-electron reduced states of **Ni-A** and **Ni-B**, respectively. Since **Ni-A** cannot react with H_2 directly for activation, conversion to **Ni-SU** is a prerequisite for activation by H_2. The key mechanism of activation-inactivation of [NiFe] H_2ase has been identified as the acid-base equilibrium between **Ni-SI$_r$** and **Ni-SI$_a$** with a pK_a value of ~8 (Scheme 1.13).[122-124] Two mechanisms have been proposed: (i) the bridging μ-OH^- ligand in the **Ni-SI$_r$** state is protonated and leaves as H_2O to yield **Ni-SI$_a$**, and (ii) the Ni-coordinating Cys residue is protonated with the bridging X ligand still a mystery. The kinetic isotope effect from a study that monitor the conversion of **Ni-SI$_a$** (obtained by irradiation of **Ni-SI$_r$** with Ar^+ laser) to **Ni-SI$_r$** supports the first mechanism, in which the conversion between **Ni-SI$_a$** to **Ni-SI$_r$** includes the insertion of a bridging μ-OH^- ligand.[125]

The three confirmed intermediate states observed in the catalytic cycle of [NiFe] H_2ase are: **Ni-SI$_a$**, **Ni-R**, and **Ni-C**.[123,124] However, computational studies as well as some experimental studies showed the involvement of **Ni-L** during catalysis (Scheme 1.14).[126-128] In the first step of the proposed H_2 oxidation catalytic cycle of [NiFe] H_2ase,[129] H_2 is cleaved heterolytically by **Ni-SI$_a$** of [NiFe] H_2ase resulting in the fully reduced **Ni-R** (Ni^{2+}) state with a bridging H^- ligand at the [NiFe] site (Scheme 1.14).[111,130-133] The remaining H^+ is either be bound to a Ni-coordinated Cys546 in *Dv*MF [NiFe] H_2ase or Arg509 in *E. coli* [NiFe] H_2ase.[108,134] One-electron oxidation of **Ni-R** yields the paramagnetic **Ni-C** (Ni^{3+}) where the bridging H^- ligand remains coordinated to the [NiFe] site. The final step involves the oxidation and deprotonation of **Ni-C** to yield **Ni-SI$_a$**. While conversion from **Ni-C** to **Ni-SI$_a$** can occur via a concerted proton-coupled electron transfer (PCET) reaction, computational studies support the involvement of **Ni-L** states during transition from **Ni-C** to **Ni-SIa**, in which the $[Fe_4S_4]_p$ is the electron pathway. Upon irradiation, **Ni-C** is converted to **Ni-L2**, in which the bridging H^- ligand migrates to a nearby Cys-S via reductive elimination to

yield a vacant [NiFe] site. The Ni^{+} in **Ni-L2** state is oxidized by $[Fe_4S_4]_p^{2+}$ to yield **Ni-SI$_a$** and $[Fe_4S_4]_p^{+}$. The involvement of the **Ni-L** state in the catalytic cycle is still a matter of debate.

Scheme 1.14 Proposed catalytic cycle of [NiFe] H_2ase. Adapted from ref 129.

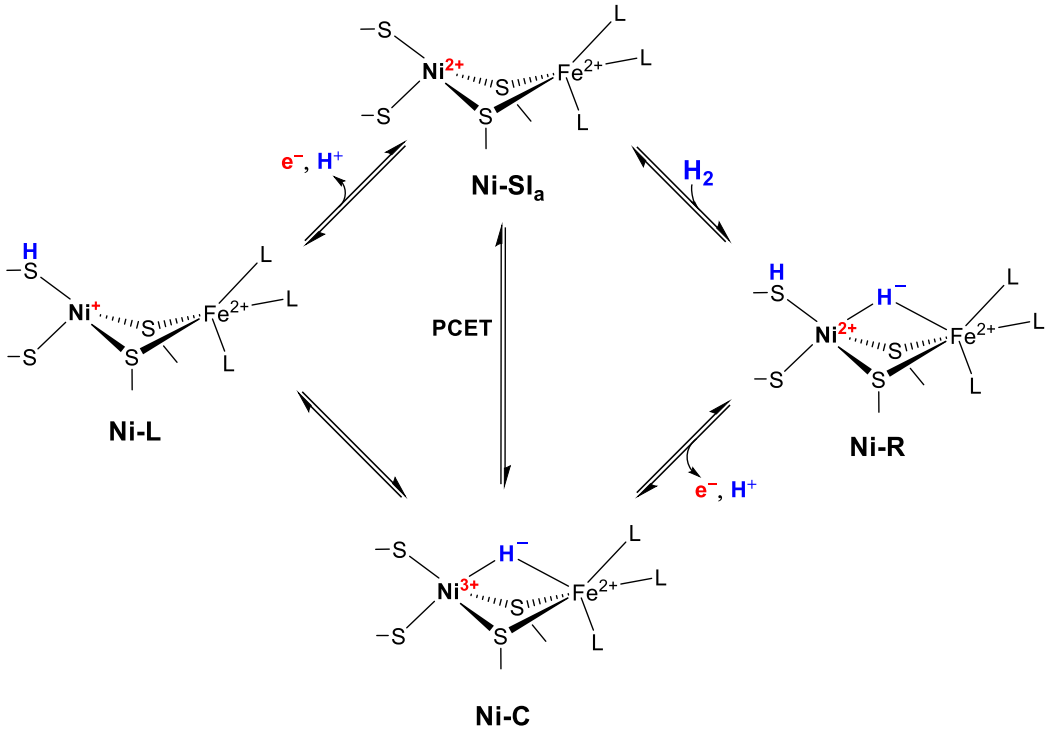

Nickel Superoxide Dismutase

Ni-containing superoxide dismutase (NiSOD) is a member of superoxide dismutases (SODs), a family of metalloenzymes that catalyze the disproportionation of superoxide ($O_2^{\bullet -}$) at the diffusion-controlled rate. Unlike other SODs, NiSOD is isolated as a homohexamer with six-interlocking subunits (Figure 1.12). The Ni active site is found in the N-terminus of each subunit (also known as the Ni-hook motif) (Figure 1.12).[135,136] The structural and spectroscopic properties,

along with computational studies of NiSOD up to 2013, is discussed in Ch. 2. Herein is discussed studies by Maroney and coworkers on the alteration of the peptide-N ligand in NiSOD[137] as well as proposed structural and functional role of His-1 and its H-bonding network.[138]

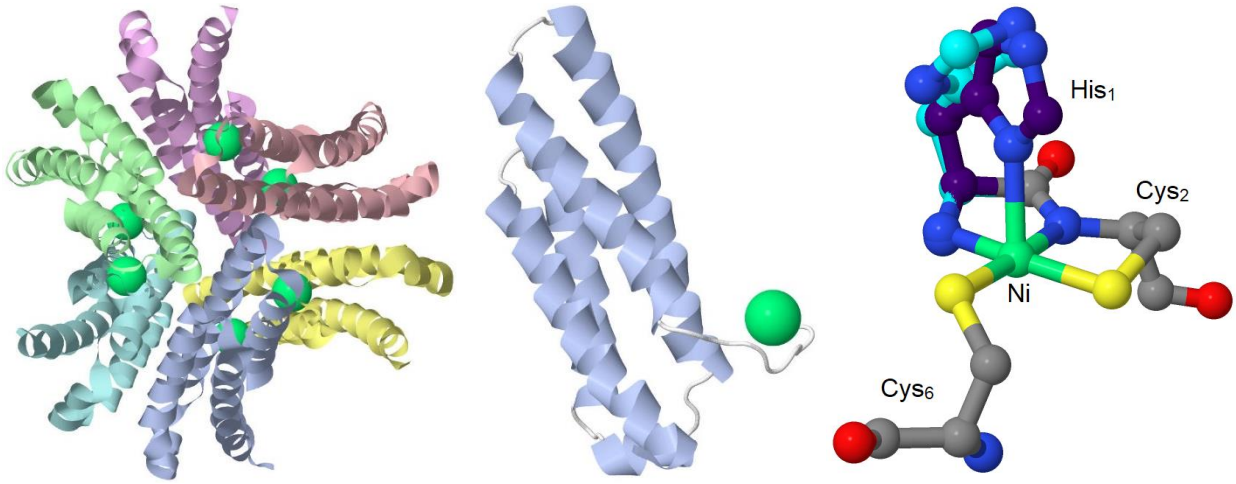

Figure 1.12 (*Left*) The structure of homohexameric NiSOD from *S. ceolicolor* at 1.6 Å resolution (PDB: 1T6U). (*Middle*) Subunit of NiSOD with Ni-hook motif at the N-terminus with green sphere representing nickel ion. (*Right*) Active site of NiSOD. His1 residue depicted in cyan represents the reduced state of NiSOD when His1 is not coordinated. His1 residue depicted in violet represents the oxidized state of NiSOD. Images prepared by Jmol.[22] Atom colors: green (nickel), red (oxygen), blue (nitrogen), yellow (sulfur), and gray (carbon).

In 2015, Maroney utilized the semisynthetic strategy to alter the peptide ligand at the NiSOD active site to an amine to study the role of peptide-N ligand in stabilizing Ni-based redox in NiSOD. Recombinant NiSOD enzyme from *S. ceolicolor* lacking the first five amino acid residues, NΔ5-NiSOD, was combined with either HCDLP pentapeptide or H1*-CDLP to yield wild-type (WT) NiSOD or H1*-NiSOD, respectively. The WT-NiSOD generated by this method exhibited characteristic spectroscopic properties consistent with as-isolated NiSOD. In contrast,

alteration of the peptide ligand to a secondary amine in H1*-NiSOD resulted in a higher E^0 (~0.35 V vs. NHE in comparison to 0.29 V vs. NHE for WT-NiSOD). The increased redox potential also resulted in a lower Ni^{3+} content (11%) in H1*-NiSOD compared to WT-NiSOD (50%). This mutation also significantly affected the catalytic activity of H1*-NiSOD with an observed activity of only 1% of WT-NiSOD. Overall, this study shows that the peptide-N ligand is critical in tuning the redox of NiSOD to allow for facile access to Ni^{3+}.

Maroney also utilized site-directed mutagenesis to obtain four *S. ceolicolor* NiSOD mutants to study the function of His1–Glu17–Arg47 H-bonding network using a variety of structural and spectroscopic techniques in combination with DFT calculations.[138] As proposed by DFT, the His1–Glu17–Arg47 H-bonding network is important in modulating the Ni–Nδ-His1 distance, which is critical in tuning the redox potential of the Ni.[139] As shown with the H1A mutant, His1 is critical to form the "Ni-hook" motif by providing the axial ligand to Ni. In addition, the His1---Glu17 H-bond is also important to the stability of the "Ni-hook" motif. While R47A and R47A/E17A mutants retained more activity compared to H1A mutant, the disruption of the H-bonding between Glu17 and Arg47 resulted in a less stable enzyme with a melting temperature 10-20°C lower than in WT-NiSOD. Overall, this study shows that that His1, Glu17, and Arg47 all play critical roles in stabilizing the NiSOD active site by maintaining inter-subunit interactions via H-bonding.

1.3 Synthetic Analogue Approach

As discussed in previous sections, nature has utilized Ni to catalyze a wide variety of reactions that are important to the global C, H, and N cycles. These enzymes have evolved with a

very specific structure and coordination environment for Ni. For the non-S-coordinated enzymes (i.e., urease, NiARD, and GlxI), Ni is found in a N/O rich coordination environment that utilizes Ni^{2+} as a Lewis acid to activate the substrate. The remaining Ni enzymes contain electronically tuned active sites with Ni situated in a coordination environment rich in Cys-S ligands (except for the PTTMN Ni pincer in LarA), a redox non-innocent ligand, to access the various oxidation states of Ni (Ni^{3+}, Ni^{2+}, and Ni^{1+}) for catalysis. Except for NiSOD and O_2-tolerant [NiFe] H_2ase, many Ni redox-active enzymes found in anaerobes are deactivated in the presence of O_2, which is expected due to oxidation to CysS–SCys disulfide or S-oxygenation of CysS to Cys-SO_x (X = 1-3). Since the structure of NiSOD was solved in 2004, it has generated much interest in the bioinorganic community due to its ability to catalyze the disproportionation of $O_2^{\bullet-}$ to H_2O_2 and O_2 at diffusion-controlled rates. While this role was reserved for Cu/Zn-, Fe-, and Mn-SODs, the discovery of NiSOD introduced a new role of Ni in biology. Although valuable spectroscopic information obtained with the native enzymes,[139] much insight, specifically electronic structure, can be gained from the structure, spectroscopy, and reactivities of simpler low-molecular weight (LMW) biomimetic models. Detailed reviews biomimetic models of NiSOD from have been reported elsewhere.[140,141] Herein, the latest developments in the synthetic modeling of NiSOD since 2013 are reported and are separated into two different categories: peptide maquettes[142-145] and LMW models.[146-151]

1.3.1 Peptide maquettes

The 136 amino-acid residues polypeptide, ACS-α_{15}, was an ACS analogue that contains the Ni_d site, where Ni is coordinated by two peptide-N and two thiolato-S donors in a square-planar geometry (Figure 1.13). Tan and coworkers reported the F598H mutant of ACS-α_{15}, in which

Phe598 is replaced with a His residue to provide His-N as potential fifth ligand in the axial position, as a NiSOD mimic.[142] In ACS-α_{15} polypeptide, Ni coordination yielded the NiN_2S_2 coordination sphere, where Ni is coordinated by two peptido-N and two Cys thiolates-S. Even with excess imidazole (Im) in solution, ACS-α_{15} did not exhibit any SOD activity. As-isolated F598H mutant is coordinated with a Ni^{2+} ion and exhibits two ligand-field transitions at 425 nm (1492 M^{-1} cm^{-1}) and 582 nm (752 M^{-1} cm^{-1}) in the UV-vis spectrum. Oxidation of F598H by KO_2 yields an EPR active Ni^{3+} species with a rhombic EPR signal (S = 1/2) (g_x = 2.276, g_y =2.056, g_z = 2.003). The CV of F598H showed a reversible Ni(III/II) redox couple at 570 mV vs. NHE that is ~ 280 mV more positive than that of NiSOD. The more positive Ni(III/II) couple observed for F598H mutant correlates to a more anionic bisamide/dithiolate donor set compared to amine/amide/dithiolate donor set found in NiSOD. As a result, the SOD activity of F598H is 16-fold lower than that of native NiSOD (*S. ceolicolor*). The moderate activity observed in F598H mutant compared to no activity in ACS-α_{15} highlights the important of His1-N in promoting Ni-based redox for $O_2^{\bullet-}$ disproportionation. Furthermore, this study shows that the mixed amine/amide/dithiolate donor in NiSOD is tuned perfectly to promote Ni-based redox for $O_2^{\bullet-}$ disproportionation in NiSOD.

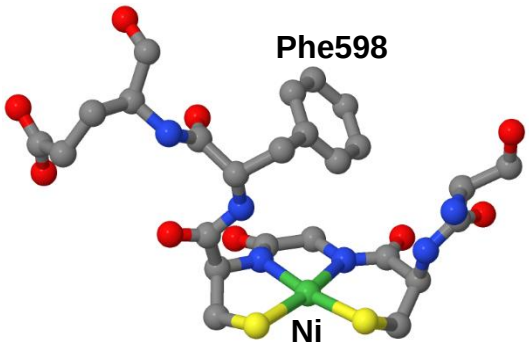

Figure 1.13 Structure of ACS-α_{15} (PDB: 3S2X). Image generated by Jmol.[22] H atoms are omitted for clarity. Atom colors: brown (iron), green (nickel), red (oxygen), blue (nitrogen), yellow (sulfur), and gray (carbon).

Shearer and coworkers have established a peptide maquette system derived from the first 12 amino-acid residues from *S. ceolicolor*, **{Ni(SOD^{m1})}** (SOD^{m1} = H_2N-HCDLPCGVYDPA-COOH), as a biomimetic that replicates the spectroscopy, coordination sphere, and electronic properties of NiSOD and is discussed in detail in Ch. 2. In 2013, Shearer reported the reactivity of **{Ni(SOD^{m1}-Ac)}** (SOD^{m1}-Ac = AcHN-HCDLPCGVYDPA-COOH),[152] in which Ni is in a bisamide coordination, toward O_2 and $O_2^{\bullet-}$ (Figure 1.14).[143] The general spectroscopic, structural, electrochemical, and SOD activity kinetic data for **{Ni(SOD^{m1}-Ac)}** are reported in Table 1.2. Upon exposure to O_2, the cysteine in **{Ni(SOD^{m1}-Ac)}** was oxidized to a sulfinate ligated species (Cys-SO_2^-). In addition, exposure of $O_2^{\bullet-}$ resulted in formation of sulfinate-ligated species (Cys-SO_2^-) along with **{Ni(SOD^{m1}-Ac)}** with multiple O atom insertions as observed by ESI-MS. These results demonstrate again that the mixed amine/amidate dithiolate donor combination in Ni^{2+}-N_2S_2 complexes protected the thiolate from oxidative damage as suggested by DFT.[153] In the same year, Shearer also reported the modified **{Ni(SOD^{m1})}** maquette, {Ni(SOD^{M1}H(1)H^{Me})} (**Ni^{M1}**; SOD^{M1}H(1)H^{Me} = H_2N-H^{Me}CDLPCGVYDPA; HMe = $^{\varepsilon}$*N*-methylhistidine), that is isolable and air-stable at room temperature in both the oxidized and reduced state (Figure 1.14).[144] **Ni^{M1}** exhibits a large deuterium kinetic isotope effect (KIE) of ~20, which suggests that **Ni^{M1}** catalyzes the $O_2^{\bullet-}$ dismutation via a PCET mechanism. S-K edge XAS studies reveal that **Ni(II)^{M1}** is protonated at either Cys-S donor or both while **Ni(III)^{M1}** is not protonated at pH 7.4. At pH 9.5, **Ni(II)^{M1}** is deprotonated with similar XAS spectrum to that of **Ni(III)^{M1}**. Overall, this study shows that at pH 7.4 metallopeptide **Ni(II)^{M1}** is protonated while **Ni(III)^{M1}** is deprotonated, which was shown to catalyze the disproportionation of $O_2^{\bullet-}$ with a PCET mechanism. These results prompted Shearer and coworkers to examine the outersphere $O_2^{\bullet-}$ reduction mechanism of **{Ni(SOD^{m1})}** and **{Ni(SOD^{m1}C(6)C^{Me})}** (SOD^{m1}C(6)C^{Me} = H_2N-HCDLP-C^{Me}GVYDPA-COOH), in which Ni is in

a mixed thioether/thiolate coordinate environment (Table 1.2).[145] While the computationally derived mechanism showed the reduction of $O_2^{\bullet-}$ proceeds via an H-atom transfer (HAT) in **{Ni(SOD^{m1})}**, this mechanism is not representative of NiSOD due to structural differences between **{Ni(SOD^{m1})}** and NiSOD. In addition, this study shows that **{Ni(SOD^{m1})}** and its derivatives operate via a different mechanism for $O_2^{\bullet-}$ disproportionation than NiSOD. These highlight the importance of critical secondary and tertiary interactions in tuning the redox properties of the NiSOD site through H-bonding interactions.

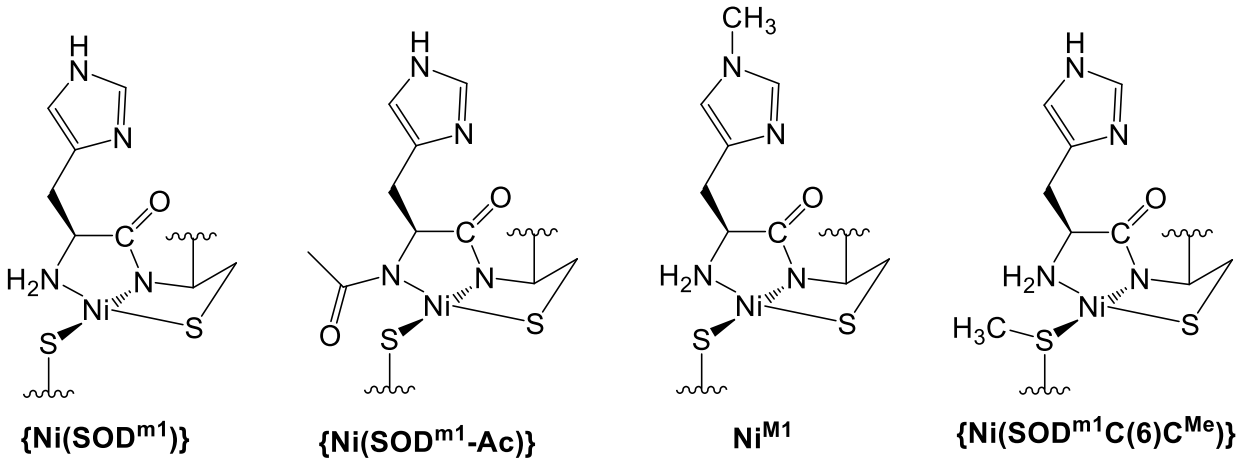

Figure 1.14 Structures of NiSOD maquette models of **{Ni(SOD^{m1})}** (SOD^{M1} = H′CDLPCGVYDPA, H′ = H (**{Ni(SOD^{m1})}**), AcHN-H (**{Ni(SOD^{m1}-Ac)}**), and $^{\varepsilon}N$-methylhistidine (**Ni^{M1}**)) and **{Ni(SOD^{m1}C(6)C^{Me})}** (SOD^{m1}C(6)C^{Me} = H_2N-HCDLP-C^{Me}GVYDPA-COOH).

Table 1.2 Spectroscopic, Structural, Electrochemical, and SOD activity Kinetic Data for NiSOD Maquette Models

Complex	λ_{max} (nm) [ε ($M^{-1}cm^{-1}$)]	$E_{1/2}$ (V)[a]	Ni–N, Ni–S (Å)[b]	SOD activity	refs
{Ni(SOD^{m1}-Ac)}	535 (512), 694 (110)[c]	0.49 V	1.864, 2.174	IC_{50} = 3 × 10^{-5} M[d]	152
{Ni(SOD^{m1}C(6)C^{Me})}	455 (250), 526 (150)[e]	N/A[f]	1.913, 2.194	N/A	145

[a]Data represent the $E_{1/2}$ value for the Ni(III/II) redox couple normalized to the Ag/AgCl reference electrode [*E* vs. NHE = *E* vs. Ag/AgCl(saturated KCl) + 0.199 V] based on information found in ref 154 and 155.[154,155] [b]Ni–S and Ni–N bond distances were obtained by EXAFS. [c]UV-vis collected at pH 7.5. [d]Xanthine/xanthine oxidase assay was used to determine the reactivity of **{Ni(SOD^{m1}-Ac)}** in comparison to **{Ni(SOD^{m1})}** (2 × 10^{-7} M) at pH 7.5. [e]UV-vis collected at pH 7.4. [f]**{Ni(SOD^{m1}C(6)C^{Me})}** exhibits no observable redox activity over the range of -0.2 to 1.0 V vs. SHE.

1.3.2 LMW analogues

In the synthetic analogue community, researchers utilize two separate approaches to model NiSOD: (i) construct models that approximate the primary coordination of NiSOD and aim to mimic its function (Figure 1.15 and Table 1.3), and (ii) to synthesize four-coordinate (4C) N_2S_2 or five-coordinate (5C) N_3S_2 coordination spheres that replicate the structural disposition and electronic nature of the NiSOD active site and to ultimately obtain functional NiSOD models (Figure 1.16 and Table 1.3).

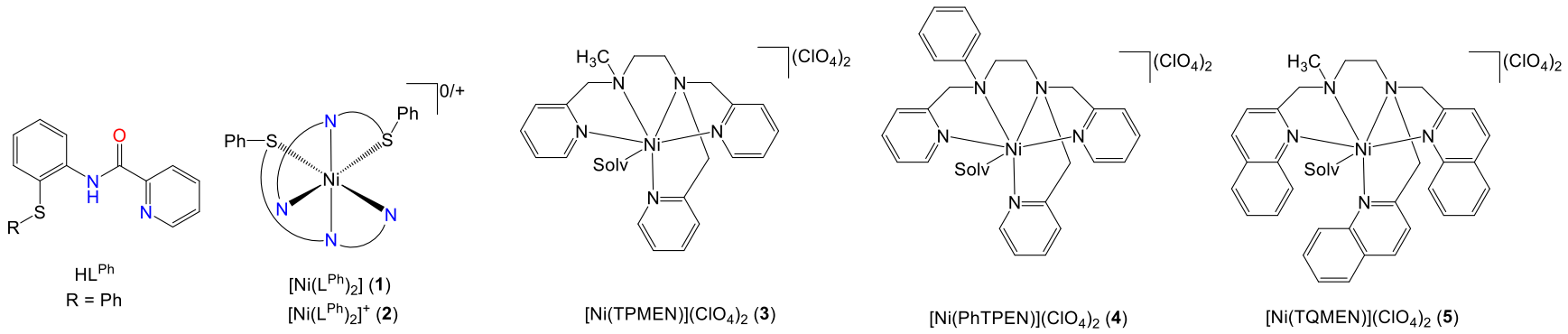

Figure 1.15 Structures of NiSOD approximate model complexes. From left to right: depictions of HLPh ligand, depiction of $[Ni(L^{Ph})_2]$ (**1**) and the cation of $[Ni(L^{Ph})_2](ClO_4)$ (**2**), $[Ni(TPMEN)](ClO_4)_2$ (**3**), $[Ni(PhTPEN)](ClO_4)_2$ (**4**), and $[Ni(TPMEN)](ClO_4)_2$ (**5**).

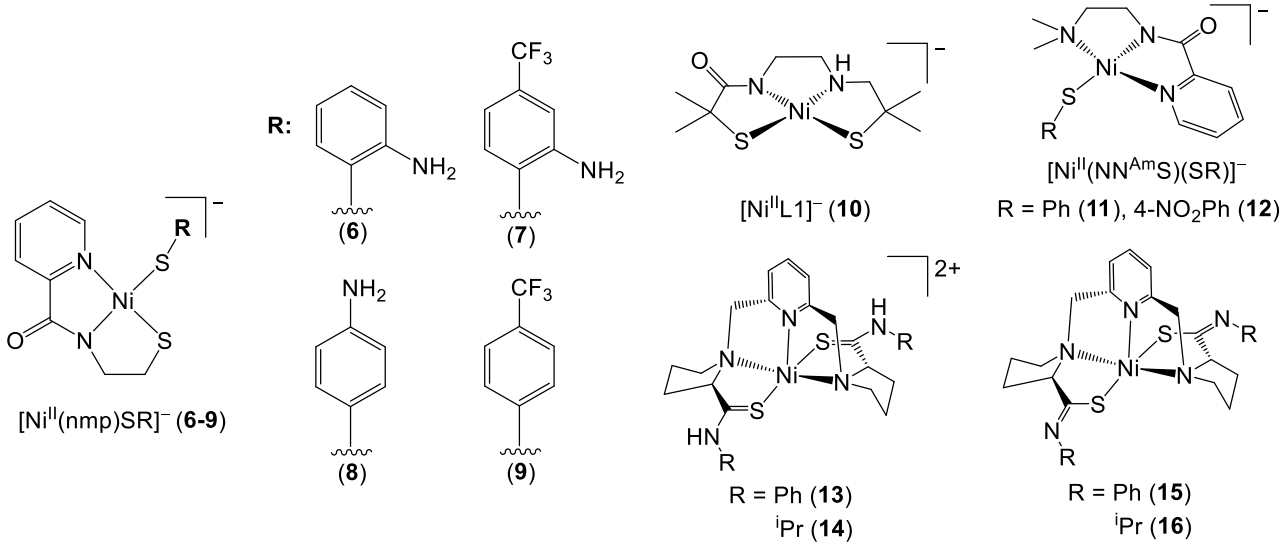

Figure 1.16 Structures of 4C NiSOD model complexes by Harrop (**6-9**),[148] Masuda (**10**),[149] and Eichhorn (**11-12**).[150] Structure of 5C NiSOD model complexes by Lee (**13-16**).[151]

Table 1.3 Spectroscopic, Structural, and Electrochemical Data of NiSOD Synthetic Analogues

Complex	λ_{max} (nm) [ε ($M^{-1}cm^{-1}$)]	E_{ox} (V)[a]	Ni–$N_{peptide}$, Ni–N_{amine} (Å)	Ni–$S_{trans\text{-}peptide}$, $S_{trans\text{-}amine}$ (Å)	S ligand	KO_2 Reactivity (Y/N)	refs
$[Ni(L^{Ph})_2]$ (**1**)	560 (sh, 25), 867 (66)[k]	0.45 V[b,c,k]	2.0258, 2.0566[f]	2.4700[f]	Thioether	Y	146
$[Ni(L^{Ph})_2](ClO_4)$ (**2**)	445 (4500), 775 (200)[k]	N/A	1.905, 2.009[f]	2.3556[f]	Thioether	Y	146
$Ni(TPMEN)](ClO_4)_2$ (**3**)	522 (12), 862 (11)[k]	-0.75[d,l]	2.09[e]	N/A	N/A	Y[h]	147
$[Ni(PhTPEN)](ClO_4)_2$ (**4**)	532 (31), 822 (19)[k]	-0.75[d,l]	2.07[e]	N/A	N/A	Y[h]	147
$[Ni(TPMEN)](ClO_4)_2$ (**5**)	417 (sh), 465 (sh), 712 (7)[k]	-0.77[d,l]	2.09[e]	N/A	N/A	Y[h]	147
$Et_4N[Ni(nmp)(SPh\text{-}o\text{-}NH_2)]$ (**6**)	453 (7200)[k]	-0.69[c,l]	1.8750, 1.9418	2.2173, 2.1386	Thiolate	N/A	148
$Et_4N[Ni(nmp)(SPh\text{-}o\text{-}NH_2\text{-}p\text{-}CF_3)]$ (**7**)	448 (3800)[k]	-0.43[c,l]	N/A	N/A	Thiolate	Y[j]	148
$Et_4N[Ni(nmp)(SPh\text{-}p\text{-}NH_2)]$ (**8**)	458 (6100)[k]	-0.50[l]	1.8698, 1.9450	2.2160, 2.1474	Thiolate	N/A	148
$Et_4N[Ni(nmp)(SPh\text{-}p\text{-}CF_3)]$ (**9**)	432 (4600)[k]	-0.19[l]	N/A	N/A	Thiolate	N/A	148
Na[Ni(L1)] (**10**)	449 (343)[l]	-0.593[c,l]	1.865, 1.923	2.1702, 2.1450	Thiolate	Y[g]	149
$(Ph_4As)[Ni(NN^{AM}S)(SPh)]$ (**11**)	461 (84)[k]	0.047, 0.453, 0.770[k]	1.896, 2.017	2.243, 2.126	Thiolate	N/A	150
$(Ph_4As)[Ni(NN^{AM}S)(4\text{-}NO_2PhS)]$ (**12**)	452 (149)[k]	-0.013, 0.619, 0.881[k]	1.889, 1.998	2.2278, 2.1261	Thiolate	N/A	150
$[Ni(H_2BA^{Ph}TPP)](ClO_4)_2$ (**13**)	355 (9220), 470 (sh, 520), 645 (200)[k]	0.837[c,m]	Ni–N_{avg}: 2.16; Ni–N_{axial}: 1.949	Ni–S_{avg}: 2.3184	Thioamide	Y[i]	151
$[Ni(H_2BA^{Pr}TPP)](ClO_4)_2$ (**14**)	360 (3600), 460 (90), 655 (120)[k]	0.836[c,m]	Ni–N_{avg}: 2.151; Ni–N_{axial}: 1.953	Ni–S_{avg}: 2.329	Thioamide	Y[i]	151
$[Ni(BA^{Ph}TPP)]$ (**15**)	405 (5620), 710 (95)[k]	0.352, 0.630[m]	N/A	N/A	Thiolate	N/A	151
$[Ni(BA^{Pr}TPP)]$ (**16**)	340 (3780), 410 (9230), 720 (70)[k]	0.334, 0.637[m]	N/A	N/A	Thiolate	N/A	151

[a]Data represent the E_{ox} value reported as V vs. Fc^+/Fc. [b]Redox couple normalized to Fc^+/Fc reference electrode based on information found in ref 154.[154] [c]$E_{1/2}$ for Ni(III/II) redox. [d]V vs. Ag/AgCl. [e]Ni–N bond distances were obtained by EXAFS. [f]Averages of Ni–N_{amide}, Ni–N_{amine}, and Ni–$S_{thioether}$ are reported. [g]In the presence of excess Me-Im (10 mol-equiv). [h] Reactivity based on NaI assay in which complexes react with KO_2 and 4 mol-equiv of $HClO_4$. [i]Complexes **13** and **14** reacted with KO2 to yield **15** and **16**, respectively. [j]Oxidized with CAN (1 mol-equiv) then reacted with stoichiometric KO_2. [k]MeCN. [l]DMF. [m]CH_2Cl_2

For the approximate models, Patra reported the hexa-coordinated $[Ni(L^{Ph})_2]^{0/+}$ ($(L^{Ph})^-$ = deprotonated form of *N*-2-phenylthiophenyl-2′-pyridinecarboxamide; **1**) that mimics the full catalytic cycle of NiSOD.[146] The crystal structure of the high-spin (S = 1) complex **1** contains Ni coordinated by two L^{Ph} ligands in a meridional fashion (Figure 1.15). The UV-vis of the yellow solution of **1** in MeCN features two d–d transitions at 560 nm (sh, ε = 25 M^{-1} cm^{-1}) and 867 nm (ε = 66 M^{-1} cm^{-1}). In addition, the CV of **1** in MeCN reveals a reversible Ni(III/II) couple at $E_{1/2}$ = 0.85 V vs. SCE (0.45 V vs. Fc^+/Fc).[154] Oxidation of **1** by ammonium cerium(IV) nitrate (CAN) afforded $[Ni(L^{Ph})_2](ClO_4)$ (**2**) in quantitative yield. Complex **2** exhibits an anisotropic EPR signal center at g = 2.09 with a five-line hyperfine splitting feature ($A_{\|}^N$ = 12 G) that is consistent with a Ni^{3+} (S = 1/2) spin coupled to the nuclear spin of two trans carboxamide-N donors (I = 1). Complex **2** can oxidize $O_2^{\bullet-}$ to yield **1** and O_2 as confirmed by UV-vis and CV. The *in situ* generated **1** from reaction of **2** with $O_2^{\bullet-}$ can react with $O_2^{\bullet-}$ in the presence of $HClO_4$ to yield H_2O_2. However, only 75% of **2** was observed as a result of a side-reaction between **2** and H_2O_2 to yield **1** and $HOO^{\bullet}$ and H^+. The Ni centers in **1** and **2** are coordinately saturated and are coordinated by a mixed amide/amine/thioether donor set that are structurally and electronically different from the mixed amine/amide/thiolate N_3S_2 donor set found in NiSOD. Even though **1** can catalyze both half-reactions of NiSOD via outer-sphere mechanism, NiSOD most likely operates with a different mechanism given the differences in electronic and structural properties between **1** and NiSOD.

In another approach, Mukherjee reported a series of nickel complexes, namely $[Ni(TPMEN)](ClO_4)_2$ (TPMEN = *N*,*N*,*N*′-tris(2-pyridylmethyl)-*N*′-methylethylenediamine; **3**), $[Ni(PhTPEN)](ClO_4)_2$ (PhTPEN = *N*′-phenyl-*N*,*N*,*N*′-tris(2-pyridinylmethyl)-1,2-ethanediamine; **4**), and $[Ni(TQMEN)](ClO_4)_2$ (TQMEN = *N*,*N*,*N*′-tris(2-quinolinemethyl)-*N*′-methylethylene-diamine; **5**), in neutral amine/pyridine ligand frameworks that do not approximate the coordination

of NiSOD.[147] Complexes **3-5** are most likely octahedral complexes with a coordinated solvent molecule with the average Ni–N/O distances of 2.07-2.9 Å from XAS studies (Figure 1.15). Chemical oxidation of **3-5** by $FcPF_6$ revealed new UV-vis bands at 380 and 450 nm, assigned to a putative Ni^{3+} species that was not isolated nor further characterized. UV-vis monitor of reactions between **3-5** and excess KO_2 (10 mol-equiv) indicated the formation of a Ni^{2+}-superoxo species with new absorptions at 370-425 nm, 550-670 nm, and a broad peak in the 1000 nm range; however, the Ni^{2+}-superoxo intermediate was not isolated nor further characterized. The NaI assay showed that **3-5** can catalyze H_2O_2 production (15-20% compared to control) from KO_2 (10 mol-equiv) in the presence of $HClO_4$. This highlights the importance of the anionic donors in the NiSOD active site (peptide-N and thiolate-S) to support a metastable Ni(III/II) redox couple for catalysis. Without the anionic amide and thiolate donors, the redox potential of Ni is not sufficiently suppressed to be within in the redox window dictated by the two half-reaction of SOD.

Since 2013, several 4C Ni complexes that aim to replicate NiSOD's structure and/or functions were also reported by Harrop,[148] Masuda,[149] and Eichhorn (Figure 1.16).[150] In 2014, Harrop reported the synthesis, characterization, and properties of four NiSOD model complexes with the general formula of (Et_4N)[Ni(nmp)(SR)] (nmp^{2-} = dianion of *N*-(2-mercapethyl)-picolinamide) with various substitutions on the exogenous benzenethiolate (S_{exo}) that mimic the NiSOD active site coordination environment (complexes **6-9**, Figure 1.16 and Table 1.3).[148] While structurally **6** and **8** were comparable to other Ni-nmp complexes, the long Ni---NH_2 distances of 4.4 Å excludes the possibility of a 5C Ni-nmp complex. The CVs of **8** and **9** showed irreversible waves consistent with oxidation of S_{exo} to disulfide, however, the CVs of **6** and **7** showed quasi-reversible waves at $E_{1/2}$ = -0.69 V and -0.43 V (vs. Fc^+/Fc), respectively, which were assigned as Ni(III/II) redox couple. Oxidized species $\mathbf{6^{ox}}$ and $\mathbf{7^{ox}}$ obtained by oxidation with CAN or

ferrocenium hexafluorophosphate ($FcPF_6$) are best described as a resonance hybrid between Ni(III)-thiolate and Ni(II)-thiyl radical based on MCD, UV-vis, EPR, and DFT. These results show that incorporation of H-bonding can significant reduce the S-character in the Ni–S bond to promote Ni-based redox. These results suggest that a Ni(III)-thiolate ↔ Ni(II)-thiyl resonance may be an intermediate in the transition between $NiSOD_{red}$ and $NiSOD_{ox}$-His_{off}.

In the same year, Masuda reported the synthesis and characterization of a 4C NiSOD model, namely $[NiL_1]^{2-}$ (L_1 = deprotonated form of *N*-(2-benzylmercapto-2-methylpronaoyl)-1,2-diaminoethane), **10**), which features a mixed amine/carboxamide/dithiolate N_2S_2 ligand that replicates the coordination sphere of $NiSOD_{red}$ (Figure 1.16). While the CV of **10** is reversible in many polar aprotic solvents (i.e., acetone, DMSO, DMF, MeCN, and DMA) with $E_{1/2}$ of Ni(III/II) ranging from -0.53 to -0.72 V vs. Fc^+/Fc, the CV of **10** is irreversible in many polar protic solvents (i.e., EtOH, MeOH, and H_2O) suggesting interactions between solvent and the Ni complex. While 1-methylimidazole (Me-Im) does not coordinate to Ni^{2+} of **10**, the EPR spectrum of one-electron oxidized species of **10**, $\mathbf{10^{ox}}$, exhibited a rhombic EPR signal (g_x = 2.31, g_y = 2.26, g_z = 2.01) with a triplet hyperfine splitting observed at g_z (A_{zz} = 25 G) indicative of a coordination of an axial N-ligand to the Ni^{3+} center similar that of $NiSOD_{ox}$. Complex **10** can catalyze the reduction of $O_2^{\bullet-}$ only with the presence of 10 mol-equiv of Me-Im via a proposed Ni(II)-superoxo species. In addition, $\mathbf{10^{ox}}$ can oxidize $O_2^{\bullet-}$, also in the presence of 10 mol-equiv of Me-Im. Taken together, **10** and $\mathbf{10^{ox}}$ show that NiSOD may operate via a similar mechanism: (i) innersphere for $O_2^{\bullet-}$ reduction to H_2O_2 and (ii) outersphere for $O_2^{\bullet-}$ oxidation to O_2. Furthermore, the requirement of Me-Im for reactivities observed in **10** and $\mathbf{10^{ox}}$ demonstrates the importance of axial N-ligand in promoting Ni-based redox. In 2018, Eichhorn reported the synthesis and characterization of two additional 4C NiN_2S_2 model complexes of NiSOD with the general formula $[Ni(NN^{Am}S)(SR)]^-$ ($NN^{Am}S$ = 2-

(*N*-(dimethylaminoethyl)aminocarbonyl)benzene-thiolate; R = phenyl (complex **11**), 4-nitrophenyl (complex **12**)) (Figure 1.16). The structural and spectroscopic properties of **11** and **12** are consistent with Ni in a square-planar N_2S_2 geometry (Table 1.3). CV of **11** and **12** exhibited multiple irreversible oxidations which were difficult to assign. Chemical oxidation and reactivity with $O_2^{\bullet-}$ were not explored.

Among NiSOD models, very few 5C complexes are isolated, and 5C complexes that accurately replicates the coordination sphere and donor type in NiSOD are even fewer. Taking inspiration from a 5C Ni complex in an N_3O_2 coordination environment (NiBDPP),[156] Lee reported the synthesis and characterization of two 5C models, namely $[Ni(H_2BA^RTPP)](ClO_4)_2$ (R = Ph for **13**, Pr for **14**), that feature N_3S_2 dithioamides coordination environments that somewhat mimic NiSOD with pyridine-N as the axial ligand (Figure 1.16).[151] X-ray structure of **13** and **14** showed distorted square-pyramidal geometry both complexes with S and N donors *trans* to each other (Table 1.3). The CVs of **13** and **14** indicated reversible Ni(III/II) with $E_{1/2}$ = 0.837 V and 0.836 V vs. Fc^+/Fc, respectively. Oxidation of **14** with CAN resulted in formation of a metastable Ni^{3+} species that exhibited a rhombic EPR signal (g_x = 2.15, g_y = 2.12, g_z = 2.01). While **13** and **14** are good structural analogues of NiSOD, no SOD activity was observed. For example, mixing $O_2^{\bullet-}$ with **13** and **14** resulted in ligand deprotonation to yield dithiolates complexes **15** and **16**, which was also obtained independently by reacting **13** and **14** with NaH (Figure 1.16).

1.4 Research Objectives and Purpose

Redox-active Ni enzymes are biocatalysts that can catalyze reactions with energetic (H_2 and CH_4), physiological ($O_2^{\bullet-}$), and environmental (CH_4, CO, CO_2) significance. As such, understanding the requirement for catalysis of these enzymes have great implications toward

alternative fuel production as well as toward CH_4 and CO_2 sequestration. Central to the function of these redox-active Ni enzymes is the presence of Ni-SCys coordination units at their active site. The primary goal of this research is to create fundamental design principles and new synthetic strategies to access N/S-containing ligand frames and their corresponding Ni(III/II) complexes that faithfully model the structure and properties of NiSOD to understand its mechanism, which also further our understanding of other redox-active Ni-enzymes.

Previously, our lab reported the design and synthesis of the 1st generation five-coordinate (5C) NiSOD analogue that features a mixed amine/carboxamide N_3S_2 ligand framework, namely K[Ni(N_3S_2)] (where $[N_3S_2]^{2-}$ = deprotonated form of *N*-(2-mercaptoethyl)-2-((2-mercaptoethyl)(pyridine-2-ylmethyl)amino)acetamide)), containing a pendant pyridine (py) as the potential fifth axial ligand. Oxidation of K[Ni(N_3S_2)] by Fc^+ resulted in the formation of a disulfide bridged dimer that formed via a transient a Ni(III) species characterized by EPR. This result leads to the development of the 2nd generation 5C NiSOD model complex, namely Na[Ni($N_3S_2^{Me2}$)] (where $[N_3S_2^{Me2}]^{2-}$ = deprotonated form of 2-((2-mercapto-2-methylpropyl)(pyridin-2-ylmethyl)-amino)-*N*-(2-mercaptoethyl)acetamide), which contains a *gem*-$(CH_3)_2$ moiety on the α-C adjacent to the S *trans* to carboxamide. The hypothesis is that the steric bulk provided by *gem*-$(CH_3)_2$ moiety will prevent disulfide formation and promote Ni-based redox (Ch. 3). As a result of the steric enforcement by *gem*-$(CH_3)_2$, oxidation of Na[Ni($N_3S_2^{Me2}$)] yielded a thiazolidine rearrangement product (characterized by X-ray crystallography) in addition to the disulfide-bridged complex. Reaction of Na[Ni($N_3S_2^{Me2}$)] with stoichiometric of excess KO_2 also resulted in the formation of the thiazolidine ring rearrangement product as observed by ESI-MS, which supported the formation of the thiazolidine ring under dilute conditions. DFT computations were utilized to probe the electronic structure of K[Ni(N_3S_2)] and Na[Ni($N_3S_2^{Me2}$)], in addition to the effect of

adding electron withdrawing groups (EWGs) (*in silico*) on α-C adjacent to S-ligands via F atoms substitution on the ligand framework. Through this work, we have shown that providing N-py as the potential fifth ligand and addition of steric bulk to alkylthiolate turns on a different oxidation pathway but are still not sufficient to affect purely Ni-based redox.

As an improvement to the 2nd generation 5C NiSOD analogue, the 5C model complex Na[Ni($N_3S_2^{NEM}$)] (where $(N_3S_2^{NEM})^{2-}$ = deprotonated form of *N*-(2-mercaptoethyl)-2-((2-mercaptoethyl)(2-morpholinoethyl)amino)acetamide), which features the superior N-NEM base (pK_a = 7.4)[157] as a potential axial fifth ligand compared to N-py (pK_a = 5.94).[158] The more basic N-NEM moiety is hypothesized to bind to Ni in both oxidation states (Ni^{2+} and Ni^{3+}) more readily than previous models and facilitate Ni-based electrochemical events (Ch. 4). Structural characterization of Na[Ni($N_3S_2^{NEM}$)] revealed Ni in a square-planar N_2S_2 coordination environment with N-NEM pointing away from the Ni center. However, UV-vis of Na[Ni($N_3S_2^{NEM}$)] in MeOH upon air exposure (1 min) is consistent with the formation of a new species in the solution with charge transfer bands at λ_{max} = 448 nm, 550 nm, and 688 nm, assigned as a potential Ni^{3+} species. Stoichiometric oxidation of Na[Ni($N_3S_2^{NEM}$)] by $FcPF_6$ in DMF yielded black precipitates that exhibited similar features to the products observed when Na[Ni($N_3S_2^{NEM}$)] reacted with air and KO_2. X-ray structure of the black precipitates reveals a stair-step trimetallic species, {Ni[Ni($N_3S_2^{NEM}$)]$_2$}, in which the bridging Ni^{2+} is coordinated by two monomeric [Ni($N_3S_2^{NEM}$)]$^-$ complexes. The trimetallic features a terminal Ni site where Ni---N-NEM distance is 2.59 Å, which correlates well to the Ni---His1-N distance between 2.3-2.6 Å.[135,136] Analysis of the chemical oxidation reaction showed that disulfide species formed via intra- or inter-molecular disulfide bond formation resulted in Ni loss in the reaction that yielded the trimetallic species observed. While the CVs of [Ni($N_3S_2^{NEM}$)]$^-$ features irreversible redox events, the CVs of

{Ni[Ni($N_3S_2^{NEM}$)]$_2$} in CH_2Cl_2 exhibit two reversible and one quasi-reversible redox couples. Since {Ni[Ni($N_3S_2^{NEM}$)]$_2$} contains three redox active centers, the exact assignment of redox events proves to be difficult. It is hypothesized that reaction between Na[Ni($N_3S_2^{NEM}$)] with another Lewis acid, $B(C_6F_5)_3$ (BCF), is expected to yield a discrete trimetallic species with no bridging Ni at the thiolates, which will help with assignment of redox events observed in CV of {Ni[Ni($N_3S_2^{NEM}$)]$_2$}. However, a new trimetallic species, {Ni[Ni($N_3S_2^{NEM}$)]$_2$}•2BCF, was identified which contains both the bridging Ni center and a BCF interacting strongly with carbonyl-O resulted in a shorter Ni---N-NEM distance of 2.49 Å. CVs of {Ni[Ni($N_3S_2^{NEM}$)]$_2$}•2BCF in CH2Cl2 showed two reversible redox couple and one quasi-reversible redox couple all shift by +0.13-0.21 V compared to those observed in {Ni[Ni($N_3S_2^{NEM}$)]}, which suggests that all redox events observed in CV of {Ni[Ni($N_3S_2^{NEM}$)]$_2$ occurred at the terminal NiN_3S_2 center. Through this work, we have shown that the incorporation of a more superior N-NEM base did not ensure coordination of N-NEM to Ni in both oxidation states. However, the reactivity of Na[Ni($N_3S_2^{NEM}$)] toward oxidants (i.e., $FcPF_6$, O_2, and KO_2) to yield trimetallic species is unique compared to previous 5C N_3S_2 model complexes of NiSOD. While Na[Ni($N_3S_2^{NEM}$)] can replicate electronically and structurally NiSOD active site, the sequestration of electron density on S-thiolates by Lewis acid (i.e., Ni^{2+}) is reminiscence of the H-bonding interactions in NiSOD active site that fine-tune the electronic properties of the active site for $O_2^{\bullet-}$ disproportionation.

Together, these model complexes will provide the synthetic bioinorganic community valuable insight on the requirements to achieve facile Ni-based redox while preventing S-oxidation. Herein is presented the synthesis, characterization, and analysis of two Ni complexes in mixed N/S environments: (i) 5C NiSOD model complex with steric enforcement adjacent to S-

ligand that opens up new oxidation pathway (Ch. 3), and (ii) 5C NiSOD model with N-NEM as potential fifth ligand in the axial position that yielded stair-step trimetallic complex upon one-electron oxidation (Ch. 4).

1.5 References

(1) Bakırdere, S.; Bölücek, C.; Yaman, M. Determination of contamination levels of Pb, Cd, Cu, Ni, and Mn caused by former lead mining gallery. *Environ. Monit. Assess.* **2016**, *188*, 132.

(2) Grandjean, P. Human exposure to nickel. *IARC Sci. Publ.* **1984**, *53*, 469-485.

(3) Cempel, G. N. M. Nickel: A Review of Its Sources and Environmental Toxicology. *Pol. J. Environ. Stud.* **2006**, *15*, 375-382.

(4) Konhauser, K. O.; Pecoits, E.; Lalonde, S. V.; Papineau, D.; Nisbet, E. G.; Barley, M. E.; Arndt, N. T.; Zahnle, K.; Kamber, B. S. Oceanic nickel depletion and a methanogen famine before the Great Oxidation Event. *Nature* **2009**, *458*, 750-753.

(5) Weiss, M. C.; Sousa, F. L.; Mrnjavac, N.; Neukirchen, S.; Roettger, M.; Nelson-Sathi, S.; Martin, W. F. The physiology and habitat of the last universal common ancestor. *Nat. Microbiol.* **2016**, *1*, 116.

(6) Phipps, T.; Tank, S. L.; Wirtz, J.; Brewer, L.; Coyner, A.; Ortego, L. S.; Fairbrother, A. Essentiality of nickel and homeostatic mechanisms for its regulation in terrestrial organisms. *Environ. Rev.* **2002**, *10*, 209-261.

(7) Pizzutelli, S. Systemic nickel hypersensitivity and diet: myth or reality? *Eur. Ann. Allergy. Clin. Immunol.* **2011**, *43*, 5-18.

(8) Jones, B. D.; Lockatell, C. V.; Johnson, D. E.; Warren, J. W.; Mobley, H. L. Construction of a urease-negative mutant of *Proteus mirabilis*: analysis of virulence in a mouse model of ascending urinary tract infection. *Infect. Immun.* **1990**, *58*, 1120-1123.

(9) Montecucco, C.; Rappuoli, R. Living dangerously: how *Helicobacter pylori* survives in the human stomach. *Nat. Rev. Mol. Cell. Biol.* **2001**, *2*, 457-466.

(10) Lin, W.; Mathys, V.; Ang, E. L. Y.; Koh, V. H. Q.; Martínez Gómez, J. M.; Ang, M. L. T.; Zainul Rahim, S. Z.; Tan, M. P.; Pethe, K.; Alonso, S. Urease Activity Represents an Alternative Pathway for *Mycobacterium tuberculosis* Nitrogen Metabolism. *Infect. Immun.* **2012**, *80*, 2771-2779.

(11) Young, G. M.; Amid, D.; Miller, V. L. A bifunctional urease enhances survival of pathogenic *Yersinia enterocolitica* and *Morganella morganii* at low pH. *J. Bacteriol.* **1996**, *178*, 6487-6495.

(12) Cox, G. M.; Mukherjee, J.; Cole, G. T.; Casadevall, A.; Perfect, J. R. Urease as a Virulence Factor in Experimental Cryptococcosis. *Infect. Immun.* **2000**, *68*, 443-448.

(13) Ragsdale, S. W. Nickel-based Enzyme Systems. *J. Biol. Chem.* **2009**, *284*, 18571-18575.

(14) Boer, J. L.; Mulrooney, S. B.; Hausinger, R. P. Nickel-dependent metalloenzymes. *Arch. Biochem. Biophys.* **2014**, *544*, 142-152.

(15) Desguin, B.; Goffin, P.; Viaene, E.; Kleerebezem, M.; Martin-Diaconescu, V.; Maroney, M. J.; Declercq, J.-P.; Soumillion, P.; Hols, P. Lactate racemase is a nickel-dependent enzyme activated by a widespread maturation system. *Nat. Commun.* **2014**, *5*, 3615.

(16) Hausinger, R. P. Nickel Utilization by Microorganisms. *Microbiol. Rev.* **1987**, *51*, 22-42.

(17) Mobley, H. L. T.; Hausinger, R. P. Microbial Ureases - Significance, Regulation, and Molecular Characterization. *Microbiol. Rev.* **1989**, *53*, 85-108.

(18) Sawers, R. G. Nickel in Bacteria and Archaea. In *Encyclopedia of Metalloproteins*, Kretsinger, R. H.; Uversky, V. N.; Permyakov, E. A., Eds. Springer: Heidelberg, 2013.

(19) Balasubramanian, A.; Ponnuraj, K. Crystal Structure of the First Plant Urease from Jack Bean: 83 Years of Journey from Its First Crystal to Molecular Structure. *J. Mol. Biol.* **2010**, *400*, 274-283.

(20) Jabri, E.; Carr, M.; Hausinger, R.; Karplus, P. The crystal structure of urease from *Klebsiella aerogenes*. *Science* **1995**, *268*, 998-1004.

(21) Benini, S.; Rypniewski, W. R.; Wilson, K. S.; Miletti, S.; Ciurli, S.; Mangani, S. A new proposal for urease mechanism based on the crystal structures of the native and inhibited enzyme from *Bacillus pasteurii*: why urea hydrolysis costs two nickels. *Structure* **1999**, *7*, 205-216.

(22) *Jmol: an open source Java viewer for chemical structures in 3D.* http://www.jmol.org/.

(23) Musiani, F.; Arnofi, E.; Casadio, R.; Ciurli, S. Structure-based computational study of the catalytic and inhibition mechanisms of urease. *J. Biol. Inorg. Chem.* **2001**, *6*, 300-314.

(24) Benini, S.; Kosikowska, P.; Cianci, M.; Mazzei, L.; Vara, A. G.; Berlicki, Ł.; Ciurli, S. The crystal structure of *Sporosarcina pasteurii* urease in a complex with citrate provides new hints for inhibitor design. *J. Biol. Inorg. Chem.* **2013**, *18*, 391-399.

(25) Benini, S.; Rypniewski, W. R.; Wilson, K. S.; Mangani, S.; Ciurli, S. Molecular Details of Urease Inhibition by Boric Acid: Insights into the Catalytic Mechanism. *J. Am. Chem. Soc.* **2004**, *126*, 3714-3715.

(26) Iyengar, R.; Rose, I. A. Concentration of activated intermediates of the fructose-1,6-bisphosphate aldolase and triosephosphate isomerase reactions. *Biochemistry* **1981**, *20*, 1223-1229.

(27) Hopper, D. J.; Cooper, R. A. The regulation of *Escherichia coli* methylglyoxal synthase; a new control site in glycolysis? *FEBS Lett.* **1971**, *13*, 213-216.

(28) Lyles, G. A.; Chalmers, J. Aminoacetone metabolism by semicarbazide-sensitive amine oxidase in rat aorta. *Biochem. Pharmacol.* **1995**, *49*, 416-419.

(29) Maroney, M. J.; Ciurli, S. Nonredox Nickel Enzymes. *Chem. Rev.* **2014**, *114*, 4206-4228.

(30) He, M. M.; Clugston, S. L.; Honek, J. F.; Matthews, B. W. Determination of the Structure of *Escherichia coli* Glyoxalase I Suggests a Structural Basis for Differential Metal Activation. *Biochemistry* **2000**, *39*, 8719-8727.

(31) Davidson, G.; Clugston, S. L.; Honek, J. F.; Maroney, M. J. An XAS Investigation of Product and Inhibitor Complexes of Ni-Containing GlxI from *Escherichia coli*: Mechanistic Implications. *Biochemistry* **2001**, *40*, 4569-4582.

(32) Cameron, A. D.; Ridderström, M.; Olin, B.; Kavarana, M. J.; Creighton, D. J.; Mannervik, B. Reaction Mechanism of Glyoxalase I Explored by an X-ray Crystallographic Analysis of the Human Enzyme in Complex with a Transition State Analogue. *Biochemistry* **1999**, *38*, 13480-13490.

(33) Luk, G. D.; Baylin, S. B. Polyamines in biology and medicine. *West. J. Med.* **1985**, *142*, 88-90.

(34) Yang, S. F.; Hoffman, N. E. Ethylene Biosynthesis and its Regulation in Higher Plants. *Ann. Rev. Plant Physiol.* **1984**, *35*, 155-189.

(35) Schlenk, F. Methylthioadenosine. *Adv. Enzymol. Relat. Areas. Mol. Biol.* **1983**, *54*, 195-265.

(36) Balakrishnan, R.; Frohlich, M.; Rahaim, P. T.; Backman, K.; Yocum, R. R. Appendix - Cloning and Sequence of the Gene Encoding Enzyme *E*-1 from the Methionine Salvage Pathway of *Klebsiella oxytoca*. *J. Biol. Chem.* **1993**, *268*, 24792-24795.

(37) Myers, R. W.; Wray, J. W.; Fish, S.; Abeles, R. H. Purification and Characterization of an Enzyme Involved in Oxidative Carbon-Carbon Bond Cleavage Reactions in the Methionine Salvage Pathway of *Klebsiella pneumoniae*. *J. Biol. Chem.* **1993**, *268*, 24785-24791.

(38) Dai, Y.; Wensink, P. C.; Abeles, R. H. One protein, two enzymes. *J. Biol. Chem.* **1999**, *274*, 1193-1195.

(39) Wray, J. W.; Abeles, R. H. The methionine salvage pathway in *Klebsiella pneumoniae* and rat liver. Identification and characterization of two novel dioxygenases. *J. Biol. Chem.* **1995**, *270*, 3147-3153.

(40) Pochapsky, T. C.; Pochapsky, S. S.; Ju, T.; Hoefler, C.; Liang, J. A refined model for the structure of acireductone dioxygenase from *Klebsiella* ATCC 8724 incorporating residual dipolar couplings. *J. Biomol. NMR* **2006**, *34*, 117-127.

(41) Pochapsky, T. C.; Pochapsky, S. S.; Ju, T. T.; Mo, H. P.; Al-Mjeni, F.; Maroney, M. J. Modeling and experiment yields the structure of acireductone dioxygenase from *Klebsiella pneumoniae*. *Nat. Struct. Biol.* **2002**, *9*, 966-972.

(42) Ju, T.; Goldsmith, R. B.; Chai, S. C.; Maroney, M. J.; Pochapsky, S. S.; Pochapsky, T. C. One protein, two enzymes revisited: a structural entropy switch interconverts the two isoforms of acireductone dioxygenase. *J. Mol. Biol.* **2006**, *363*, 823-834.

(43) Tatum, E. L.; Peterson, W. H.; Fred, E. B. Enzymic racemization of optically active lactic acid. *Biochem. J.* **1936**, *30*, 1892-1897.

(44) Stetter, K. O.; Kandler, O. Formation of DL-Lactic Acid by *Lactobacilli* and Characterization of a Lactic-Acid Racemase from Several Streptobacteria. *Archiv. Fur Mikrobiologie* **1973**, *94*, 221-247.

(45) Melville, S. B.; Michel, T. A.; Macy, J. M. Pathway and Sites for Energy Conservation in the Metabolism of Glucose by *Selenomonas ruminantium*. *J. Bacteriol.* **1988**, *170*, 5298-5304.

(46) Hino, T.; Kuroda, S. Presence of Lactate Dehydrogenase and Lactate Racemase in *Megasphaera elsdenii* Grown on Glucose or Lactate. *Appl. Environ. Microbiol.* **1993**, *59*, 255-259.

(47) Oren, A.; Gurevich, P. Diversity of lactate metabolism in halophilic archaea. *Can. J. Microbiol.* **1995**, *41*, 302-307.

(48) Bienert, G. P.; Desguin, B.; Chaumont, F.; Hols, P. Channel-mediated lactic acid transport: a novel function for aquaglyceroporins in bacteria. *Biochem. J.* **2013**, *454*, 559-570.

(49) Zhang, Y.; Rodionov, D. A.; Gelfand, M. S.; Gladyshev, V. N. Comparative genomic analyses of nickel, cobalt and vitamin B12 utilization. *BMC Genomics* **2009**, *10*, 1-26.

(50) Singleton, J. T. The uses of pincer complexes in organic synthesis. *Tetrahedron* **2003**, *59*, 1837-1857.

(51) van Koten, G.; Milstein, D., *Organometallic Pincer Chemistry*. 1st ed.; Springer-Verlag Berlin Heidelberg: 2013; p 356.

(52) Desguin, B.; Soumillion, P.; Hols, P.; Hausinger, R. P. Nickel-pincer cofactor biosynthesis involves LarB-catalyzed pyridinium carboxylation and LarE-dependent sacrificial sulfur insertion. *Proc. Natl. Acad. Sci. U. S. A.* **2016**, *113*, 5598-5603.

(53) Desguin, B.; Zhang, T.; Soumillion, P.; Hols, P.; Hu, J.; Hausinger, R. P. A tethered niacin-derived pincer complex with a nickel-carbon bond in lactate racemase. *Science* **2015**, *349*, 66-69.

(54) Xu, T.; Wodrich, M. D.; Scopelliti, R.; Corminboeuf, C.; Hu, X. Nickel pincer model of the active site of lactate racemase involves ligand participation in hydride transfer. *Proc. Natl. Acad. Sci. U. S. A.* **2017**, *114*, 1242-1245.

(55) Zhang, X.; Chung, L. W. Alternative Mechanistic Strategy for Enzyme Catalysis in a Ni-Dependent Lactate Racemase (LarA): Intermediate Destabilization by the Cofactor. *Chem. - Eur. J.* **2017**, *23*, 3623-3630.

(56) Wang, B. J.; Shaik, S. The Nickel-Pincer Complex in Lactate Racemase Is an Electron Relay and Sink that acts through Proton-Coupled Electron Transfer. *Angew. Chem., Int. Ed.* **2017**, *56*, 10098-10102.

(57) Thauer, R. K.; Kaster, A. K.; Goenrich, M.; Schick, M.; Hiromoto, T.; Shima, S. Hydrogenases from methanogenic archaea, nickel, a novel cofactor, and H_2 storage. *Annu. Rev. Biochem.* **2010**, *79*, 507-536.

(58) Ermler, U.; Grabarse, W.; Shima, S.; Goubeaud, M.; Thauer, R. K. Crystal structure of methyl-coenzyme M reductase: the key enzyme of biological methane formation. *Science* **1997**, *278*, 1457-1462.

(59) Grabarse, W.; Mahlert, F.; Duin, E. C.; Goubeaud, M.; Shima, S.; Thauer, R. K.; Lamzin, V.; Ermler, U. On the Mechanism of Biological Methane Formation: Structural Evidence for Conformational Changes in Methyl-coenzyme M Reductase upon Substrate Binding. *J. Mol. Biol.* **2001**, *309*, 315-330.

(60) Goenrich, M.; Mahlert, F.; Duin, E. C.; Bauer, C.; Jaun, B.; Thauer, R. K. Probing the reactivity of Ni in the active site of methyl-coenzyme M reductase with substrate analogues. *J. Biol. Inorg. Chem.* **2004**, *9*, 691-705.

(61) Li, X.; Telser, J.; Kunz, R. C.; Hoffman, B. M.; Gerfen, G.; Ragsdale, S. W. Observation of organometallic and radical intermediates formed during the reaction of methyl-coenzyme M reductase with bromoethanesulfonate. *Biochemistry* **2010**, *49*, 6866-6876.

(62) Cedervall, P. E.; Dey, M.; Li, X.; Sarangi, R.; Hedman, B.; Ragsdale, S. W.; Wilmot, C. M. Structural analysis of a Ni-methyl species in methyl-coenzyme M reductase from *Methanothermobacter marburgensis*. *J. Am. Chem. Soc.* **2011**, *133*, 5626-5628.

(63) Dey, M.; Telser, J.; Kunz, R. C.; Lees, N. S.; Ragsdale, S. W.; Hoffman, B. M. Biochemical and spectroscopic studies of the electronic structure and reactivity of a methyl-Ni species formed on methyl-coenzyme M reductase. *J. Am. Chem. Soc.* **2007**, *129*, 11030-11032.

(64) Yang, N.; Reiher, M.; Wang, M.; Harmer, J.; Duin, E. C. Formation of a Nickel-Methyl species in Methyl-Coenzyme M Reductase, an Enzyme Catalyzing Methane Formation. *J. Am. Chem. Soc.* **2007**, *129*, 11028-11029.

(65) Scheller, S.; Goenrich, M.; Thauer, R. K.; Jaun, B. Methyl-coenzyme M reductase from methanogenic archaea: isotope effects on label exchange and ethane formation with the homologous substrate ethyl-coenzyme M. *J. Am. Chem. Soc.* **2013**, *135*, 14985-14995.

(66) Chen, S.-L.; Blomberg, M. R. A.; Siegbahn, P. E. M. How Is Methane Formed and Oxidized Reversibly When Catalyzed by Ni-Containing Methyl-Coenzyme M Reductase? *Chem. - Eur. J.* **2012**, *18*, 6309-6315.

(67) Pelmenschikov, V.; Siegbahn, P. E. Catalysis by methyl-coenzyme M reductase: a theoretical study for heterodisulfide product formation. *J. Biol. Inorg. Chem.* **2003**, *8*, 653-662.

(68) Pelmenschikov, V.; Blomberg, M. R. A.; Siegbahn, P. E. M.; Crabtree, R. H. A Mechanism from Quantum Chemical Studies for Methane Formation in Methanogenesis. *J. Am. Chem. Soc.* **2002**, *124*, 4039-4049.

(69) Can, M.; Armstrong, F. A.; Ragsdale, S. W. Structure, Function, and Mechanism of the Nickel Metalloenzymes, CO Dehydrogenase, and Acetyl-CoA Synthase. *Chem. Rev.* **2014**, *114*, 4149-4174.

(70) Drennan, C. L.; Heo, J.; Sintchak, M. D.; Schreiter, E.; Ludden, P. W. Life on carbon monoxide: X-ray structure of *Rhodospirillum rubrum* Ni-Fe-S carbon monoxide dehydrogenase. *Proc. Natl. Acad. Sci. U. S. A.* **2001**, *98*, 11973-11978.

(71) Dobbek, H.; Svetlitchnyi, V.; Gremer, L.; Huber, R.; Meyer, O. Crystal structure of a carbon monoxide dehydrogenase reveals a [Ni-4Fe-5S] cluster. *Science* **2001**, *293*, 1281-1285.

(72) Doukov, T. I.; Iverson, T. M.; Seravalli, J.; Ragsdale, S. W.; Drennan, C. L. A Ni-Fe-Cu center in a bifunctional carbon monoxide dehydrogenase/acetyl-CoA synthase. *Science* **2002**, *298*, 567-572.

(73) Darnault, C.; Volbeda, A.; Kim, E. J.; Legrand, P.; Vernede, X.; Lindahl, P. A.; Fontecilla-Camps, J. C. Ni-Zn-[Fe_4-S_4] and Ni-Ni-[Fe_4-S_4] clusters in closed and open α subunits of acetyl-CoA synthase/carbon monoxide dehydrogenase. *Nat. Struct. Biol.* **2003**, *10*, 271-279.

(74) Jeoung, J. H.; Dobbek, H. Carbon dioxide activation at the Ni,Fe-cluster of anaerobic carbon monoxide dehydrogenase. *Science* **2007**, *318*, 1461-1464.

(75) Kumar, M.; Lu, W. P.; Liu, L. F.; Ragsdale, S. W. Kinetic Evidence That Carbon Monoxide Dehydrogenase Catalyzes the Oxidation of Carbon Monoxide and the Synthesis of Acetyl-CoA at Separate Metal Centers. *J. Am. Chem. Soc.* **1993**, *115*, 11646-11647.

(76) Ragsdale, S. W.; Wood, H. G. Acetate Biosynthesis by Acetogenic Bacteria - Evidence That Carbon-Monoxide Dehydrogenase Is the Condensing Enzyme That Catalyzes the Final Steps of the Synthesis. *J. Biol. Chem.* **1985**, *260*, 3970-3977.

(77) Pierce, E.; Xie, G.; Barabote, R. D.; Saunders, E.; Han, C. S.; Detter, J. C.; Richardson, P.; Brettin, T. S.; Das, A.; Ljungdahl, L. G.; Ragsdale, S. W. The complete genome sequence of *Moorella thermoacetica* (f. *Clostridium thermoaceticum*). *Environ. Microbiol.* **2008**, *10*, 2550-2573.

(78) Grahame, D. A. Catalysis of acetyl-CoA cleavage and tetrahydrosarcinapterin methylation by a carbon monoxide dehydrogenase-corrinoid enzyme complex. *J. Biol. Chem.* **1991**, *266*, 22227-22233.

(79) Terlesky, K. C.; Nelson, M. J.; Ferry, J. G. Isolation of an Enzyme Complex with Carbon Monoxide Dehydrogenase Activity Containing Corrinoid and Nickel from Acetate-Grown *Methanosarcina thermophila*. *J. Bacteriol.* **1986**, *168*, 1053-1058.

(80) Doukov, T. I.; Blasiak, L. C.; Seravalli, J.; Ragsdale, S. W.; Drennan, C. L. Xenon in and at the End of the Tunnel of Bifunctional Carbon Monoxide Dehydrogenase/Acetyl-CoA Synthase. *Biochemistry* **2008**, *47*, 3474-3483.

(81) Bramlett, M. R.; Tan, X.; Lindahl, P. A. Inactivation of Acetyl-CoA Synthase/Carbon Monoxide Dehydrogenase by Copper. *J. Am. Chem. Soc.* **2003**, *125*, 9316-9317.

(82) Ragsdale, S. W. Metals and their scaffolds to promote difficult enzymatic reactions. *Chem. Rev.* **2006**, *106*, 3317-3337.

(83) Lindahl, P. A. Acetyl-coenzyme A synthase: the case for a Ni_p^0-based mechanism of catalysis. *J. Biol. Inorg. Chem.* **2004**, *9*, 516-524.

(84) Hsiao, Y. M.; Chojnacki, S. S.; Hinton, P.; Reibenspies, J. H.; Darensbourg, M. Y. Organometallic Chemistry of Sulfur Phosphorus Donor Ligand Complexes of Nickel(II) and Nickel(0). *Organometallics* **1993**, *12*, 870-875.

(85) Tan, X.; Sewell, C.; Yang, Q.; Lindahl, P. A. Reduction and Methyl Transfer Kinetics of the α Subunit from Acetyl Coenzyme A Synthase. *J. Am. Chem. Soc.* **2003**, *125*, 318-319.

(86) Bramlett, M. R.; Stubna, A.; Tan, X.; Surovtsev, I. V.; Münck, E.; Lindahl, P. A. Mössbauer and EPR Study of Recombinant Acetyl-CoA Synthase from *Moorella thermoacetica*. *Biochemistry* **2006**, *45*, 8674-8685.

(87) Seravalli, J.; Kumar, M.; Ragsdale, S. W. Rapid Kinetic Studies of Acetyl-CoA Synthesis: Evidence Supporting the Catalytic Intermediacy of a Paramagnetic NiFeC Species in the Autotrophic Wood−Ljungdahl Pathway. *Biochemistry* **2002**, *41*, 1807-1819.

(88) Kumar, M.; Ragsdale, S. W. Characterization of the CO Binding Site of Carbon Monoxide Dehydrogenase from *Clostridium thermoaceticum* by Infrared Spectroscopy. *J. Am. Chem. Soc.* **1992**, *114*, 8713-8715.

(89) George, S. J.; Seravalli, J.; Ragsdale, S. W. EPR and Infrared Spectroscopic Evidence That a Kinetically Competent Paramagnetic Intermediate is Formed When Acetyl-Coenzyme A Synthase Reacts with CO. *J. Am. Chem. Soc.* **2005**, *127*, 13500-13501.

(90) Ragsdale, S. W.; Wood, H. G.; Antholine, W. E. Evidence that an iron-nickel-carbon complex is formed by reaction of CO with the CO dehydrogenase from *Clostridium thermoaceticum*. *Proc. Natl. Acad. Sci. U. S. A.* **1985**, *82*, 6811-6814.

(91) Barondeau, D. P.; Lindahl, P. A. Methylation of Carbon Monoxide Dehydrogenase from *Clostridium thermoaceticum* and Mechanism of Acetyl Coenzyme A Synthesis. *J. Am. Chem. Soc.* **1997**, *119*, 3959-3970.

(92) Seravalli, J.; Xiao, Y.; Gu, W.; Cramer, S. P.; Antholine, W. E.; Krymov, V.; Gerfen, G. J.; Ragsdale, S. W. Evidence That NiNi Acetyl-CoA Synthase Is Active and That the CuNi Enzyme Is Not. *Biochemistry* **2004**, *43*, 3944-3955.

(93) Shin, W.; Anderson, M. E.; Lindahl, P. A. Heterogeneous Nickel Environments in Carbon Monoxide Dehydrogenase from *Clostridium thermoaceticum*. *J. Am. Chem. Soc.* **1993**, *115*, 5522-5526.

(94) Volbeda, A.; Darnault, C.; Tan, X.; Lindahl, P. A.; Fontecilla-Camps, J. C. Novel Domain Arrangement in the Crystal Structure of a Truncated Acetyl-CoA Synthase from *Moorella thermoacetica*. *Biochemistry* **2009**, *48*, 7916-7926.

(95) Shomura, Y.; Yoon, K. S.; Nishihara, H.; Higuchi, Y. Structural basis for a [4Fe-3S] cluster in the oxygen-tolerant membrane-bound [NiFe]-hydrogenase. *Nature* **2011**, *479*, 253-256.

(96) Fritsch, J.; Scheerer, P.; Frielingsdorf, S.; Kroschinsky, S.; Friedrich, B.; Lenz, O.; Spahn, C. M. The crystal structure of an oxygen-tolerant hydrogenase uncovers a novel iron-sulphur centre. *Nature* **2011**, *479*, 249-252.

(97) Frielingsdorf, S.; Fritsch, J.; Schmidt, A.; Hammer, M.; Lowenstein, J.; Siebert, E.; Pelmenschikov, V.; Jaenicke, T.; Kalms, J.; Rippers, Y.; Lendzian, F.; Zebger, I.; Teutloff, C.; Kaupp, M.; Bittl, R.; Hildebrandt, P.; Friedrich, B.; Lenz, O.; Scheerer, P. Reversible [4Fe-3S] cluster morphing in an O_2-tolerant [NiFe] hydrogenase. *Nat. Chem. Biol.* **2014**, *10*, 378-385.

(98) Volbeda, A.; Amara, P.; Darnault, C.; Mouesca, J. M.; Parkin, A.; Roessler, M. M.; Armstrong, F. A.; Fontecilla-Camps, J. C. X-ray crystallographic and computational studies of the O_2-tolerant [NiFe]-hydrogenase 1 from *Escherichia coli*. *Proc. Natl. Acad. Sci. U. S. A.* **2012**, *109*, 5305-5310.

(99) Volbeda, A.; Darnault, C.; Parkin, A.; Sargent, F.; Armstrong, F. A.; Fontecilla-Camps, J. C. Crystal Structure of the O_2-Tolerant Membrane-Bound Hydrogenase 1 from *Escherichia coli* in Complex with Its Cognate Cytochrome b. *Structure* **2013**, *21*, 184-190.

(100) Eguchi, S.; Yoon, K. S.; Ogo, S. O2-stable membrane-bound [NiFe]hydrogenase from a newly isolated *Citrobacter* sp. S-77. *J. Biosci. Bioeng.* **2012**, *114*, 479-484.

(101) Nguyen, N. T.; Yatabe, T.; Yoon, K. S.; Ogo, S. Molybdenum-containing membrane-bound formate dehydrogenase isolated from Citrobacter sp. S-77 having high stability against oxygen, pH, and temperature. *J. Biosci. Bioeng.* **2014**, *118*, 386-391.

(102) Matsumoto, T.; Eguchi, S.; Nakai, H.; Hibino, T.; Yoon, K. S.; Ogo, S. [NiFe]Hydrogenase from *Citrobacter* sp. S-77 Surpasses Platinum as an Electrode for H_2 Oxidation Reaction. *Angew. Chem., Int. Ed. Engl.* **2014**, *53*, 8895-8898.

(103) Kwan, P.; McIntosh, C. L.; Jennings, D. P.; Hopkins, R. C.; Chandrayan, S. K.; Wu, C.-H.; Adams, M. W. W.; Jones, A. K. The [NiFe]-Hydrogenase of *Pyrococcus furiosus* Exhibits a New Type of Oxygen Tolerance. *J. Am. Chem. Soc.* **2015**, *137*, 13556-13565.

(104) Higuchi, Y.; Yagi, T.; Yasuoka, N. Unusual ligand structure in Ni-Fe active center and an additional Mg site in hydrogenase revealed by high resolution X-ray structure analysis. *Structure* **1997**, *5*, 1671-1680.

(105) Higuchi, Y.; Ogata, H.; Miki, K.; Yasuoka, N.; Yagi, T. Removal of the bridging ligand atom at the Ni-Fe active site of [NiFe] hydrogenase upon reduction with H_2, as revealed by X-ray structure analysis at 1.4 A resolution. *Structure* **1999**, *7*, 549-556.

(106) Ogata, H.; Mizoguchi, Y.; Mizuno, N.; Miki, K.; Adachi, S.-i.; Yasuoka, N.; Yagi, T.; Yamauchi, O.; Hirota, S.; Higuchi, Y. Structural Studies of the Carbon Monoxide Complex of [NiFe]hydrogenase from Desulfovibrio vulgaris Miyazaki F: Suggestion for the Initial Activation Site for Dihydrogen. *J. Am. Chem. Soc.* **2002**, *124*, 11628-11635.

(107) Ogata, H.; Hirota, S.; Nakahara, A.; Komori, H.; Shibata, N.; Kato, T.; Kano, K.; Higuchi, Y. Activation Process of [NiFe] Hydrogenase Elucidated by High-Resolution X-Ray Analyses: Conversion of the Ready to the Unready state. *Structure* **2005**, *13*, 1635-1642.

(108) Ogata, H.; Nishikawa, K.; Lubitz, W. Hydrogens detected by subatomic resolution protein crystallography in a [NiFe] hydrogenase. *Nature* **2015**, *520*, 571-574.

(109) Yahata, N.; Saitoh, T.; Takayama, Y.; Ozawa, K.; Ogata, H.; Higuchi, Y.; Akutsu, H. Redox Interaction of Cytochrome c_3 with [NiFe] Hydrogenase from *Desulfovibrio vulgaris* Miyazaki F. *Biochemistry* **2006**, *45*, 1653-1662.

(110) Fernandez, V. M.; Hatchikian, E. C.; Cammack, R. Properties and reactivation of two different deactivated forms of *Desulfovibrio gigas* hydrogenase. *Biochim. Biophys. Acta* **1985**, *832*, 69-79.

(111) Kurkin, S.; George, S. J.; Thorneley, R. N. F.; Albracht, S. P. J. Hydrogen-Induced Activation of the [NiFe]-Hydrogenase from *Allochromatium vinosum* as Studied by Stopped-Flow Infrared Spectroscopy. *Biochemistry* **2004**, *43*, 6820-6831.

(112) Lamle, S. E.; Albracht, S. P. J.; Armstrong, F. A. Electrochemical Potential-Step Investigations of the Aerobic Interconversions of [NiFe]-Hydrogenase from *Allochromatium vinosum*: Insights into the Puzzling Difference between Unready and Ready Oxidized Inactive States. *J. Am. Chem. Soc.* **2004**, *126*, 14899-14909.

(113) Pardo, A.; De Lacey, A. L.; Fernández, V. M.; Fan, Y.; Hall, M. B. Characterization of the active site of catalytically inactive forms of [NiFe] hydrogenases by density functional theory. *J. Biol. Inorg. Chem.* **2007**, *12*, 751-760.

(114) Barilone, J. L.; Ogata, H.; Lubitz, W.; van Gastel, M. Structural differences between the active sites of the Ni-A and Ni-B states of the [NiFe] hydrogenase: an approach by quantum chemistry and single crystal ENDOR spectroscopy. *Phys. Chem. Chem. Phys.* **2015**, *17*, 16204-16212.

(115) van Gastel, M.; Fichtner, C.; Neese, F.; Lubitz, W. EPR experiments to elucidate the structure of the ready and unready states of the [NiFe] hydrogenase of *Desulfovibrio vulgaris* Miyazaki F. *Biochem. Soc. Trans.* **2005**, *33*, 7-11.

(116) van Gastel, M.; Stein, M.; Brecht, M.; Schröder, O.; Lendzian, F.; Bittl, R.; Ogata, H.; Higuchi, Y.; Lubitz, W. A single-crystal ENDOR and density functional theory study of the oxidized states of the [NiFe] hydrogenase from *Desulfovibrio vulgaris* Miyazaki F. *J. Biol. Inorg. Chem.* **2006**, *11*, 41-51.

(117) Roessler, M. M.; Evans, R. M.; Davies, R. A.; Harmer, J.; Armstrong, F. A. EPR Spectroscopic Studies of the Fe–S Clusters in the O_2-Tolerant [NiFe]-Hydrogenase Hyd-1 from *Escherichia coli* and Characterization of the Unique [4Fe–3S] Cluster by HYSCORE. *J. Am. Chem. Soc.* **2012**, *134*, 15581-15594.

(118) Wulff, P.; Day, C. C.; Sargent, F.; Armstrong, F. A. How oxygen reacts with oxygen-tolerant respiratory [NiFe]-hydrogenases. *Proc. Natl. Acad. Sci. U. S. A.* **2014**, *111*, 6606-6611.

(119) Goris, T.; Wait, A. F.; Saggu, M.; Fritsch, J.; Heidary, N.; Stein, M.; Zebger, I.; Lendzian, F.; Armstrong, F. A.; Friedrich, B.; Lenz, O. A unique iron-sulfur cluster is crucial for oxygen tolerance of a [NiFe]-hydrogenase. *Nat. Chem. Biol.* **2011**, *7*, 310-318.

(120) Pandelia, M.-E.; Bykov, D.; Izsak, R.; Infossi, P.; Giudici-Orticoni, M.-T.; Bill, E.; Neese, F.; Lubitz, W. Electronic structure of the unique [4Fe-3S] cluster in O_2-tolerant hydrogenases characterized by ^{57}Fe Mössbauer and EPR spectroscopy. *Proc. Natl. Acad. Sci. U. S. A.* **2013**, *110*, 483-488.

(121) Evans, R. M.; Parkin, A.; Roessler, M. M.; Murphy, B. J.; Adamson, H.; Lukey, M. J.; Sargent, F.; Volbeda, A.; Fontecilla-Camps, J. C.; Armstrong, F. A. Principles of Sustained Enzymatic Hydrogen Oxidation in the Presence of Oxygen – The Crucial Influence of High Potential Fe–S Clusters in the Electron Relay of [NiFe]-Hydrogenases. *J. Am. Chem. Soc.* **2013**, *135*, 2694-2707.

(122) Fichtner, C.; Laurich, C.; Bothe, E.; Lubitz, W. Spectroelectrochemical Characterizationt of the [NiFe] Hydrogenase of *Desulfovibrio vulgaris* Miyazaki F. *Biochemistry* **2006**, *45*, 9706-9716.

(123) de Lacey, A. L.; Hatchikian, E. C.; Volbeda, A.; Frey, M.; Fontecilla-Camps, J. C.; Fernandez, V. M. Infrared-Spectroelectrochemical Characterization of the [NiFe] Hydrogenase of *Desulfovibrio gigas*. *J. Am. Chem. Soc.* **1997**, *119*, 7181-7189.

(124) Bleijlevens, B.; van Broekhuizen, F. A.; De Lacey, A. L.; Roseboom, W.; Fernandez, V. M.; Albracht, S. P. J. The activation of the [NiFe]-hydrogenase from *Allochromatium vinosum*. An infrared spectro-electrochemical study. *J. Biol. Inorg. Chem.* **2004**, *9*, 743-752.

(125) Tai, H.; Xu, L.; Inoue, S.; Nishikawa, K.; Higuchi, Y.; Hirota, S. Photoactivation of the Ni-SI_r state to the Ni-SI_a state in [NiFe] hydrogenase: FT-IR study on the light reactivity of the ready Ni-SI_r state and as-isolated enzyme revisited. *Phys. Chem. Chem. Phys.* **2016**, *18*, 22025-22030.

(126) Hulin, T.; Koji, N.; Masayuki, S.; Yoshiki, H.; Shun, H. Control of the Transition between Ni-C and Ni-SI_a States by the Redox State of the Proximal Fe-S Cluster in the Catalytic Cycle of [NiFe] Hydrogenase. *Angew. Chem., Int. Ed.* **2014**, *53*, 13817-13820.

(127) Hidalgo, R.; Ash, P. A.; Healy, A. J.; Vincent, K. A. Infrared Spectroscopy During Electrocatalytic Turnover Reveals the Ni-L Active Site State During H_2 Oxidation by a NiFe Hydrogenase. *Angewandte Chemie (International Ed. in English)* **2015**, *54*, 7110-7113.

(128) Murphy, B. J.; Hidalgo, R.; Roessler, M. M.; Evans, R. M.; Ash, P. A.; Myers, W. K.; Vincent, K. A.; Armstrong, F. A. Discovery of Dark pH-Dependent H^+ Migration in a [NiFe]-Hydrogenase and Its Mechanistic Relevance: Mobilizing the Hydrido Ligand of the Ni-C Intermediate. *J. Am. Chem. Soc.* **2015**, *137*, 8484-8489.

(129) Tai, H.; Higuchi, Y.; Hirota, S. Comprehensive reaction mechanisms at and near the Ni-Fe active sites of [NiFe] hydrogenases. *Dalton Trans.* **2018**, *47*, 4408-4423.

(130) Siegbahn, P. E. M.; Tye, J. W.; Hall, M. B. Computational Studies of [NiFe] and [FeFe] Hydrogenases. *Chem. Rev.* **2007**, *107*, 4414-4435.

(131) George, S. J.; Kurkin, S.; Thorneley, R. N. F.; Albracht, S. P. J. Reactions of H_2, CO, and O_2 with Active [NiFe]-Hydrogenase from *Allochromatium vinosum*. A Stopped-Flow Infrared Study. *Biochemistry* **2004**, *43*, 6808-6819.

(132) Roberts, L. M.; Lindahl, P. A. Stoichiometric Reductive Titrations of *Desulfovibrio gigas* Hydrogenase. *J. Am. Chem. Soc.* **1995**, *117*, 2565-2572.

(133) Ogo, S.; Ichikawa, K.; Kishima, T.; Matsumoto, T.; Nakai, H.; Kusaka, K.; Ohhara, T. A Functional [NiFe]Hydrogenase Mimic That Catalyzes Electron and Hydride Transfer from H_2. *Science* **2013**, *339*, 682-684.

(134) Evans, R. M.; Brooke, E. J.; Wehlin, S. A. M.; Nomerotskaia, E.; Sargent, F.; Carr, S. B.; Phillips, S. E. V.; Armstrong, F. A. Mechanism of hydrogen activation by [NiFe] hydrogenases. *Nat. Chem. Biol.* **2015**, *12*, 46-52.

(135) Barondeau, D. P.; Kassmann, C. J.; Bruns, C. K.; Tainer, J. A.; Getzoff, E. D. Nickel Superoxide Dismutase Structure and Mechanism. *Biochemistry* **2004**, *43*, 8038-8047.

(136) Wuerges, J.; Lee, J.-W.; Yim, Y.-I.; Yim, H.-S.; Kang, S.-O.; Carugo, K. D. Crystal structure of nickel-containing superoxide dismutase reveals another type of active site. *Proc. Natl. Acad. Sci. U. S. A.* **2004**, *101*, 8569-8574.

(137) Campeciño, J. O.; Dudycz, L. W.; Tumelty, D.; Berg, V.; Cabelli, D. E.; Maroney, M. J. A Semisynthetic Strategy Leads to Alteration of the Backbone Amidate Ligand in the NiSOD Active Site. *J. Am. Chem. Soc.* **2015**, *137*, 9044-9052.

(138) Ryan, K. C.; Guce, A. I.; Johnson, O. E.; Brunold, T. C.; Cabelli, D. E.; Garman, S. C.; Maroney, M. J. Nickel Superoxide Dismutase: Structural and Functional Roles of His1 and Its H-Bonding Network. *Biochemistry* **2015**, *54*, 1016-1027.

(139) Fiedler, A. T.; Bryngelson, P. A.; Maroney, M. J.; Brunold, T. C. Spectroscopic and Computational Studies of Ni Superoxide Dismutase: Electronic Structure Contributions to Enzymatic Function. *J. Am. Chem. Soc.* **2005**, *127*, 5449-5462.

(140) Broering, E. P.; Truong, P. T.; Gale, E. M.; Harrop, T. C. Synthetic Analogues of Nickel Superoxide Dismutase: A New Role for Nickel in Biology. *Biochemistry* **2013**, *52*, 4-18.

(141) Shearer, J. Insight into the Structure and Mechanism of Nickel-Containing Superoxide Dismutase Derived from Peptide-Based Mimics. *Acc. Chem. Res.* **2014**, *47*, 2332-2341.

(142) Liu, Y.; Wang, Q. L.; Wei, Y. Z.; Lin, Y. W.; Li, W.; Su, J. H.; Wang, Z.; Tian, Y.; Huang, Z. X.; Tan, X. S. Functional conversion of nickel-containing metalloproteins via molecular design: from a truncated acetyl-coenzyme A synthase to a nickel superoxide dismutase. *Chem. Commun.* **2013**, *49*, 1452-1454.

(143) Shearer, J. Dioxygen and superoxide stability of metallopeptide based mimics of nickel containing superoxide dismutase: The influence of amine/amidate vs. bis-amidate ligation. *J. Inorg. Biochem.* **2013**, *129*, 145-149.

(144) Shearer, J. Use of a Metallopeptide-Based Mimic Provides Evidence for a Proton-Coupled Electron-Transfer Mechanism for Superoxide Reduction by Nickel-Containing Superoxide Dismutase. *Angew. Chem., Int. Ed.* **2013**, *52*, 2569-2572.

(145) Shearer, J.; Peck, K. L.; Schmitt, J. C.; Neupane, K. P. Cysteinate Protonation and Water Hydrogen Bonding at the Active-Site of a Nickel Superoxide Dismutase Metallopeptide-Based Mimic: Implications for the Mechanism of Superoxide Reduction. *J. Am. Chem. Soc.* **2014**, *136*, 16009-16022.

(146) Chatterjee, S. K.; Maji, R. C.; Barman, S. K.; Olmstead, M. M.; Patra, A. K. Hexacoordinate Nickel(II)/(III) Complexes that Mimic the Catalytic Cycle of Nickel Superoxide Dismutase. *Angew. Chem., Int. Ed.* **2014**, *53*, 10184-10189.

(147) Snider, V. G.; Farquhar, E. R.; Allen, M.; Abu-Spetani, A.; Mukherjee, A. Design and reactivity of Ni-complexes using pentadentate neutral-polypyridyl ligands: Possible mimics of NiSOD. *J. Inorg. Biochem.* **2017**, *175*, 110-117.

(148) Broering, E. P.; Dillon, S.; Gale, E. M.; Steiner, R. A.; Telser, J.; Brunold, T. C.; Harrop, T. C. Accessing Ni(III)-Thiolate Versus Ni(II)-Thiyl Bonding in a Family of Ni–N_2S_2 Synthetic Models of NiSOD. *Inorg. Chem.* **2015**, *54*, 3815-3828.

(149) Nakane, D.; Wasada-Tsutsui, Y.; Funahashi, Y.; Hatanaka, T.; Ozawa, T.; Masuda, H. A Novel Square-Planar Ni(II) Complex with an Amino–Carboxamido–Dithiolato-Type Ligand as an Active-Site Model of NiSOD. *Inorg. Chem.* **2014**, *53*, 6512-6523.

(150) Senaratne, N. K.; Mwania, T. M.; Moore, C. E.; Eichhorn, D. M. Ni complexes of N_2S ligands with amine/imine and amine/amide donors with relevance to the active site of Ni superoxide dismutase. *Inorg. Chim. Acta* **2018**, *476*, 27-37.

(151) Chiang, C.-W.; Chu, Y.-L.; Chen, H.-L.; Kuo, T.-S.; Lee, W.-Z. Synthesis and Characterization of Ni^{III}N3S2 Complexes as Active Site Models for the Oxidized Form of Nickel Superoxide Dismutase. *Chem. - Eur. J.* **2014**, *20*, 6283-6286.

(152) Neupane, K. P.; Shearer, J. The Influence of Amine/Amide versus Bisamide Coordination in Nickel Superoxide Dismutase. *Inorg. Chem.* **2006**, *45*, 10552-10566.

(153) Mullins, C. S.; Grapperhaus, C. A.; Kozlowski, P. M. Density functional theory investigations of NiN_2S_2 reactivity as a function of nitrogen donor type and N–H···S hydrogen bonding inspired by nickel-containing superoxide dismutase. *JBIC, J. Biol. Inorg. Chem.* **2006**, *11*, 617-625.

(154) Connelly, N. G.; Geiger, W. E. Chemical Redox Agents for Organometallic Chemistry. *Chem. Rev.* **1996**, *96*, 877-910.

(155) Bard, A. J. a. F., L. R., *Electrochemical Methods : Fundamentals and Applications*. 2nd ed. ed.; New York: Wiley, 2000.

(156) Lee, W.-Z.; Chiang, C.-W.; Lin, T.-H.; Kuo, T.-S. A Discrete Five-Coordinate Ni^{III} Complex Resembling the Active Site of the Oxidized Form of Nickel Superoxide Dismutase. *Chem. - Eur. J.* **2012**, *18*, 50-53.

(157) Rayer, A. V.; Sumon, K. Z.; Jaffari, L.; Henni, A. Dissociation Constants (pK_a) of Tertiary and Cyclic Amines: Structural and Temperature Dependences. *J. Chem. Eng. Data* **2014**, *59*, 3805-3813.

(158) Linnell, R. Notes- Dissociation Constants of 2-Substituted Pyridines. *J. Org. Chem.* **1960**, *25*, 290-290.

CHAPTER 2

LITERATURE REVIEW

SYNTHETIC ANALOGUES OF NICKEL SUPEROXIDE DISMUTASE (NISOD): A NEW ROLE FOR NICKEL IN BIOLOGY[1]

---

[1] Truong, P. T.;* Broering, E. P.;* Gale, E. M.; Harrop, T. C. Synthetic Analogues of Nickel Superoxide Dismutase (NiSOD): A New Role for Nickel in Biology. *Biochemistry* **2013**, 52, 4-18.

* Both authors contributed equally to this work.

2.1 Abstract

Nickel-containing superoxide dismutases (NiSODs) represent a novel approach to the detoxification of superoxide in biology and thus contribute to the biodiversity of mechanisms for the removal of reactive oxygen species (ROS). While Ni ions play critical roles in anaerobic microbial redox (hydrogenases and CO dehydrogenase/acetyl coenzyme A synthase), they have never been associated with oxygen metabolism. Several SODs have been characterized from numerous sources and are classified by their catalytic metal as Cu/ZnSOD, MnSOD, or FeSOD. Whereas aqueous solutions of Cu(II), Mn(II), and Fe(II) ions are capable of catalyzing the dismutation of superoxide, solutions of Ni(II) are not. Nonetheless, NiSOD catalyzes the reaction at the diffusion-controlled limit ($\sim 10^9$ M^{-1} s^{-1}). To do this, nature has created a Ni coordination unit with the appropriate Ni(III/II) redox potential (~0.090 V vs Ag/AgCl). This potential is achieved by a unique ligand set comprised of residues from the N-terminus of the protein: Cys2 and Cys6 thiolates, the amino terminus and imidazole side chain of His1, and a peptide N-donor from Cys2. Over the past several years, synthetic modeling efforts by several groups have provided insight into understanding the intrinsic properties of this unusual Ni coordination site. Such analogues have revealed information regarding the (i) electrochemical properties that support Ni-based redox, (ii) oxidative protection and/or stability of the coordinated CysS ligands, (iii) probable H^+ sources for H_2O_2 formation, and (iv) nature of the Ni coordination geometry throughout catalysis. This review includes the results and implications of such biomimetic work as it pertains to the structure and function of NiSOD.

2.2 Introduction

The anionic superoxide radical ($O_2^{\bullet-}$) is an inevitable byproduct of aerobic respiration formed primarily in the mitochondrial matrix upon O_2 reduction along the electron transport chain.[1] If this reactive oxygen species (ROS) is not eliminated, significant damage to surrounding cells will occur, leading to a variety of disease states.[1,2] For example, the formation of ROS such as superoxide has been implicated in diseases such as diabetes,[3] neurological disorders like Parkinson's[4] and Alzheimer's,[5] and the cell death and tissue damage that occur following stroke or heart attack (post-ischemic tissue injury).[6] To combat oxidative stress, all aerobic organisms possess metalloenzyme defense systems known as superoxide dismutases (SODs, EC 1.15.1.1) that catalyze the disproportionation of superoxide to hydrogen peroxide (H_2O_2) and molecular oxygen (O_2) through alternate oxidation and reduction of their respective catalytic metal centers (eqs 2.1–2.3).[1,7,8] Several distinct types of SODs are known, and each is classified by the first-row transition metal utilized to conduct the chemistry.[7] The more widely studied SODs include the dinuclear Cu/ZnSOD[9] and the mononuclear MnSOD[10-12] and FeSOD,[11-14] which have been characterized by numerous biochemical, structural, and theoretical techniques. For instance, point mutations in the gene that encodes the mammalian Cu/ZnSOD have been linked with the progression of the neurodegenerative disease Amyotrophic Lateral Sclerosis (ALS or Lou Gehrig's disease).[15] Several features common to these SODs include (i) a positively charged Lys amino acid channel that guides the anionic substrate toward the active site, (ii) utilization of a metal ion that disproportionates $O_2^{\bullet-}$ even in the free $[M(H_2O)_6]^{n+}$ aquated state, (iii) similarity among the primary coordination spheres of the redox-active metal ion (supported mainly by His-N ligation), and (iv) anion binding affinity at the M^{ox} center supportive of an inner-sphere electron-transfer (eT) mechanism for one of the two SOD half-reactions (eq 2.1, oxidative half-reaction with respect

to substrate).[8] Recently, a new and distinct class of SOD has been discovered from *Streptomyces* soil bacteria[16] and found in the genome of cyanobacteria[17] that contain Ni at the active site. These SODs show no sequence homology with other SODs, have different and unusual primary coordination spheres, and utilize an active site metal ion not normally associated with oxygen binding or activation. NiSOD thus represents a new role for Ni in a biological context.

$$M^{ox} + O_2^{\bullet -} \rightarrow M^{red} + O_2 \qquad (2.1)$$

$$M^{red} + O_2^{\bullet -} + 2H^+ \rightarrow M^{ox} + H_2O_2 \qquad (2.2)$$

$$\textit{Overall}: 2\ O_2^{\bullet -} + 2\ H^+ \rightarrow O_2 + H_2O_2 \qquad (2.3)$$

2.2.1 Structural and Spectroscopic Properties of NiSOD

The structure of NiSOD has been determined by independent groups on two separate *Streptomyces* strains at high resolution (1.30 Å for *Streptomyces coelicolor*[18] and 1.68 Å for *Streptomyces seoulensis*[19]). The separate crystallographic investigations yield nearly identical structures, which is not surprising considering their amino acid sequences are ~90% homologous. NiSOD is a homohexamer (total molecular mass of 78 kDa) comprised of six interlocked four-helix bundle subunits arranged in the right-handed turn up–down–up–down topology with each subunit housing one solvent inaccessible Ni(III/II) ion (Figure 2.1).

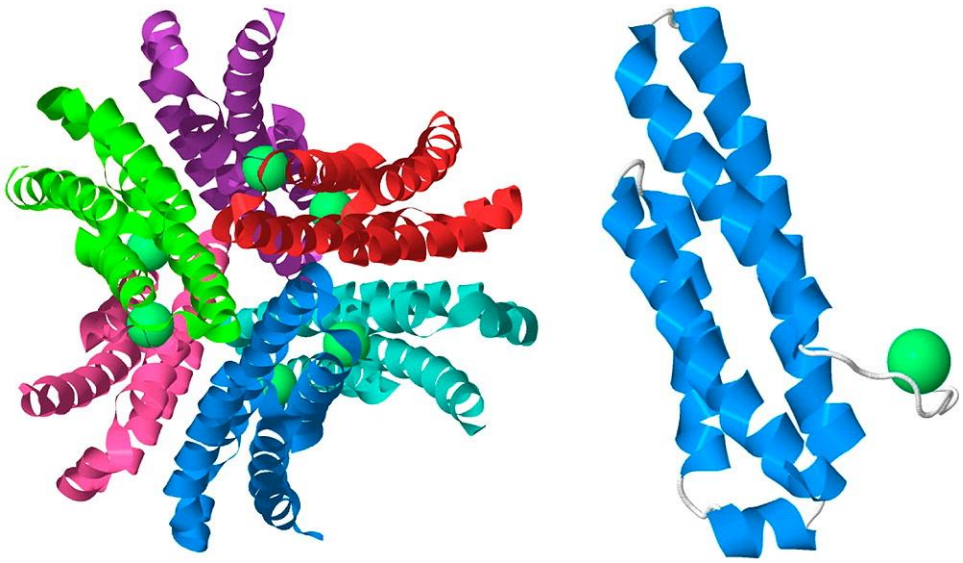

Figure 2.1 X-ray crystal structure of NiSOD from *S. coelicolor* (1.30 Å resolution, Protein Data Bank entry 1T6U). At the left is the NiSOD biological unit as a hexameric assembly of four-helix bundles. Ni centers are shown as green spheres; subunits are shown in different colors. At the right is the NiSOD subunit with nickel binding hook. This image was generated with Jmol.

The overall protein shape is globular with a hollow inner cavity, which is proposed to be a solvent channel. Depending on the strain, the outer diameter spans 60–72 Å with an interior cavity volume of ~8800 $Å^3$ that is 20–23 Å in diameter. The global protein structure and solvent-filled interior are somewhat reminiscent of the ferritin cavity for iron storage. Close examination of the subunits reveals that they are mostly stabilized by hydrophobic intersubunit interactions and salt bridges. The residues primarily responsible for chelating Ni comprise the first nine amino acids from the N-terminus with a recognizable Cys-X-X-X-Cys metal binding motif, i.e., His-Cys-X-X-Pro-Cys-Gly-X-Tyr. It has been proposed that this sequence may be an identifier for NiSOD or a means for detecting NiSOD in future protein isolations from other species. These residues form a hook-like shape and have thus been called the "Ni-hook" region of the protein (Figure 2.1). Unlike four-helix bundles in other metalloproteins, the Ni-hook protrudes out of the bundle in NiSOD, a

novel mode for metal binding among this structural motif. While arguments exist for a positively charged substrate guide by a series of Lys residues that line the active site pocket, calculations reveal no significant positively charged surface residues, which argue against an electrostatic guide. This result is in agreement with the weak ionic strength dependence of the catalytic rate constant (k) for NiSOD.[20]

In both crystal structures of NiSOD, the active site Ni is found in two separate coordination geometries that are dependent on the metal oxidation state (Figure 2.2). The mononuclear Ni sites of each subunit appear to operate independently of each other as the shortest Ni–Ni separation is ~25 Å. Several intersubunit connections, however, could serve as another means of active site communication during catalysis and have been advocated on the basis of mutagenesis studies.[20] As isolated, half of the Ni ions are in the +2 oxidation state and the other half are in the +3 state, highlighting the stability of both states in as-isolated protein. In stark contrast to other known SODs, the reduced form of NiSOD ($NiSOD_{red}$) contains a square-planar Ni(II) ion ligated in an N_2S_2 environment consisting of one deprotonated peptido-N from Cys2, one primary amine-N from the N-terminal His1 residue, and two *cis*-coordinated thiolates from Cys2 and Cys6 (Figure 2.2). During turnover, superoxide oxidizes the Ni(II)–N_2S_2 site, forming a five-coordinate (5C) square-pyramidal Ni(III)–N_3S_2 species ($NiSOD_{ox}$) via coordination of His1-N_δ (Figure 2.2). The Ni–N (1.9–2.1 Å) and Ni–S (2.2–2.3 Å) distances in the basal coordination plane appear to be consistent with other known Ni-metalloenzymes with the same donors as well as small molecule complexes.[21] However, the Ni–HisN distance in $NiSOD_{ox}$ is relatively long (2.3–2.6 Å), which may be explained by the heterogeneity in the crystal structure, i.e., the presence of both Ni(II) and Ni(III) centers. Additionally, a long X-ray exposure time appears to reduce the Ni(III) center in $NiSOD_{ox}$, yielding a $NiSOD_{red}$ structure in which the deligation and C_β–C_γ rotation of the His1

imidazole plane away from the Ni center by ~3–4 Å can be visualized. On this basis, the structure of NiSOD is very different from its Cu/Zn and Fe, Mn congeners.

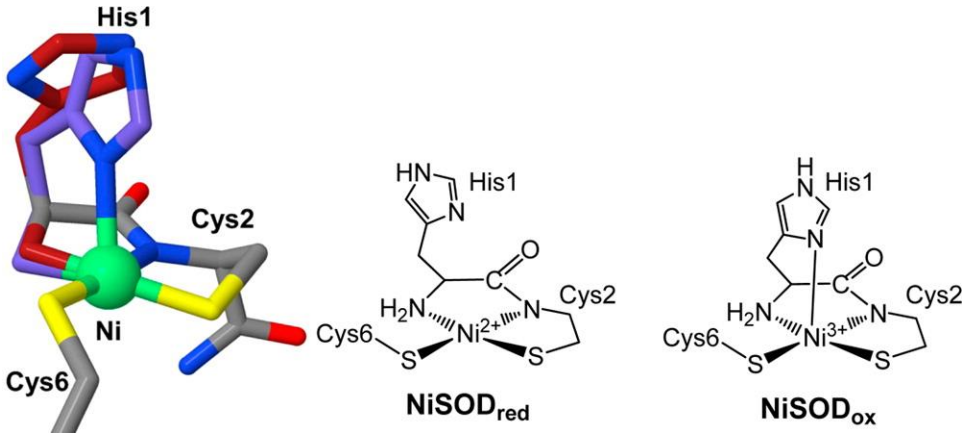

Figure 2.2 Active site of NiSOD from *S. coelicolor* showing the active site residues involved as ligands to the Ni center (left). The violet depiction of His1 represents the $NiSOD_{ox}$ state, whereas the dark red depiction of His1 represents the $NiSOD_{red}$ state where His1 is noncoordinated. This image was generated with Jmol. At the right is a ChemDraw depiction of the Ni(II) and Ni(III) active site geometries in NiSOD.

NiSOD has unique spectroscopic properties that mainly arise from the high-valent Ni(III) oxidation state.[20,22,23] The low-spin ($S = {}^1/_2$) Ni(III) center in $NiSOD_{ox}$ displays a rhombic EPR spectrum with principal g values of 2.30, 2.24, and 2.01 with a distinct triplet superhyperfine splitting pattern ($A_{zz} =$ 24.9 G) in the g_z component consistent with axial N-ligation ($I = 1$) (Figure 2.3).[18,22]

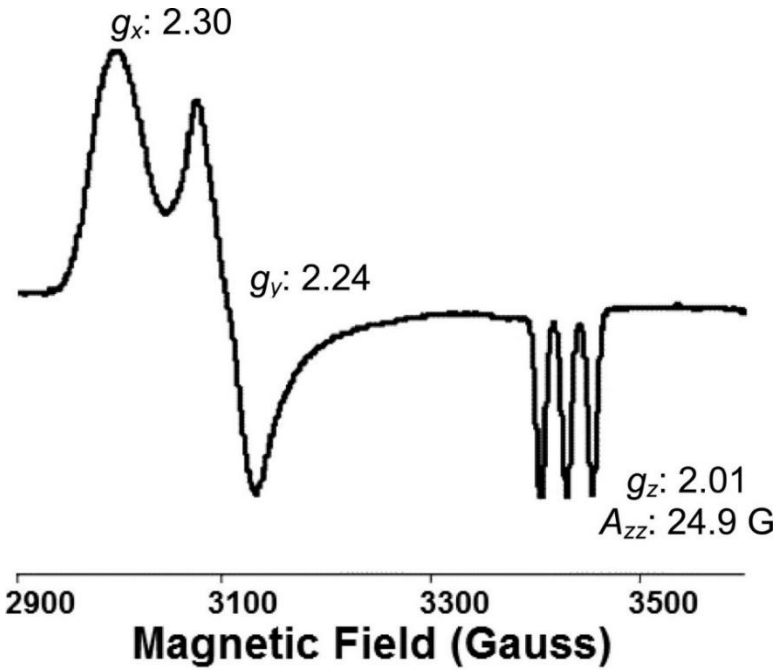

Figure 2.3 EPR spectrum of as-isolated NiSOD from *S. coelicolor* with the selected *g*-values. Sample was prepared in 50 mM HEPES buffer, pH 8.0. EPR collected at 55 K using a microwave frequency of 9.678 GHz, microwave power of 10 mW, and modulation amplitude of 5 G. Adapted from ref. 18.

As isolated, the enzyme contains an equal distribution of Ni(II) and Ni(III) centers that is reflected in the electronic absorption spectrum of the wild-type (WT) holoenzyme.[23] Because the overall UV–vis spectrum represents a mixture of these oxidation states, researchers have attempted to isolate the pure reduced or oxidized enzyme. The fully reduced enzyme was obtained by chemical reduction with dithionite, which resulted in very weak bands in the UV–vis spectrum. The main features in the visible region in the room-temperature (RT) spectrum are a shoulder at 362 nm (ε = 880 M^{-1} cm^{-1}) and two peaks at 450 nm (ε = 480 M^{-1} cm^{-1}) and 543 nm (ε = 150 M^{-1} cm^{-1}).[23]These features are hallmarks of square-planar Ni(II)–N_2S_2 coordination complexes,[24] where the λ_{max} peaks have been assigned as ligand-field bands originating from electronic transitions in the d-manifold (d-to-d transitions) of the Ni(II) ion. Subtracting this

spectrum from the as-isolated NiSOD spectrum resulted in the UV–vis contributions of $NiSOD_{ox}$. Incidentally, fully oxidized NiSOD could not be obtained even with strong oxidants such as ferricyanide, highlighting the instability of six Ni(III) centers in the protein matrix. The high intensity of the main bands at 372 nm (ε = 6800 M^{-1} cm^{-1}) and 502 nm (ε = 1510 M^{-1} cm^{-1}) are due to sulfur-to-nickel charge-transfer (S-to-Ni CT) bands that are σ and π (i.e., S-pσ to Ni-dσ and S-pπ to Ni-dπ) in origin, respectively.[23]

The presence of the intense CT band in $NiSOD_{ox}$ allowed for a further probe of the nature of this transition from resonance Raman (rR) experiments.[23] Excitation into the S–Ni(III) CT at 413.1 nm resulted in three enhanced vibrational modes at 349, 365, and 391 cm^{-1}. From normal coordinate analysis, the 349 and 365 cm^{-1} peaks are more intense than the third and were assigned as $\nu_{Ni–S}$ stretching modes of the coordinated sulfur atoms of Cys2 and Cys6. The peak at 391 cm^{-1} was attributed to either a combined Ni–S stretching and S–C_β–C_α–N bending mode of the Cys2 or perhaps to the $\nu_{Ni–N(Cys2)}$ stretching mode. Force constants of the Ni–S bonds were also calculated, resulting in a value of 1.68–1.79 mdyn $Å^{-1}$ for the Ni–S bonds in $NiSOD_{ox}$.[23,25] This value is characteristic of a high degree of covalency in the Ni–S coordination bond. The covalent nature of the Ni–S bonds in NiSOD has also been supported by further theoretical studies. [23,25] For comparison, the M–S force constants in NiSOD are on par with those of other classic electron-transfer metalloproteins such as Fe–S clusters (1.2–1.4 mdyn $Å^{-1}$)[26,27] and blue-copper proteins (∼1.9 mdyn $Å^{-1}$).[28,29] Hence, metallosulfur systems involved in biological electron transfer and/or redox catalysis contain M–S bonds that exhibit a high degree of metal–sulfur covalency.

Analogous to other SODs, NiSOD catalyzes the dismutation reaction near the diffusion-controlled limit with a k of 1.3×10^9 M^{-1} s^{-1}.[22] Furthermore, site-directed mutagenesis studies of the protein have revealed that the axial His1-N ligand is crucial for catalysis.[30] This result was

further supported by a rigorous DFT study.[23] Other mutagenesis studies that reveal the significance of the Cys2 and Cys6 S-ligands[31,32] and secondary-sphere residues vital for catalysis have also been performed.[20] For example, a combined structural and biochemical study has demonstrated the importance of Tyr9 as a "gatekeeper" residue to allow the $O_2^{\bullet-}$ substrate access to the active site.[20] Similar to those of other SODs,[33,34] the redox potential of NiSOD is 0.090 V (vs Ag/AgCl, pH 7.4 phosphate buffer),[20] between the corresponding oxidation and reduction potentials for superoxide [$E^{\circ\prime}$ ($O_2/O_2^{\bullet-}$) = −0.360 V, and $E^{\circ\prime}$ ($O_2^{\bullet-}/H_2O_2$) = 0.690 V, respectively (both vs Ag/AgCl, pH 7)].[35] Thus, the novel mixed N/S coordination unit in NiSOD has produced a Ni center that is electrochemically poised to conduct the disproportionation reaction.

2.2.2 NiSOD Questions and Analogue Approach

The atypical coordination sphere and spectroscopy of the redox-active Ni center in NiSOD have generated many questions regarding the structure/function relationship in this enzyme. It is the only SOD that uses a metal whose corresponding aquated species, $[Ni(H_2O)_6]^{2+}$, does not react with $O_2^{\bullet-}$ because its redox potential is >2 V[36] and well beyond the required potential for SOD chemistry. It is recognized that the unusual set of donor atoms imparts a high degree of covalency to the Ni–L bonds and thus aids in depressing this potential substantially to be within the dismutation window.[12,23,37] Unlike the other SODs, which consist primarily of His-N ligation around the catalytic metal, NiSOD contains two CysS residues that are themselves susceptible to ROS.[38] It has been suggested from DFT studies that the inclusion of the deprotonated peptide in combination with the CysS donors, all relatively strong-field ligands, aids in promoting primarily Ni-based redox by destabilizing the Ni(dπ) set of orbitals via strong Ni–ligand−π–antibonding

interactions [dπ–pπ repulsions (see Summary and Outlook)].[23,39-41] In this regard, CysS ligation is a logical choice because it appears to promote redox-driven reactions at other biological Ni centers and is a prerequisite for redox-active Ni metalloenzymes; NiFe-hydrogenase, the Ni_pNi_d site of the A-cluster, and the NiFe-cubane of the C-cluster of acetyl-CoA synthase/CO dehydrogenase are relevant examples.[21,42-45] Another distinction from other SODs is the low affinity of the Ni center for anions like azide (N_3^-), a common substitute for $O_2^{\bullet-}$, as other SODs bind this anion in their oxidized form, suggestive of an outer-sphere mechanism for NiSOD. Lastly, the identity of potential H^+-donors for the reductive half-reaction (eq 2.2) to form H_2O_2 is unknown. Several possible donors have been suggested, including a nearby tyrosine residue (Tyr9), the protonated imidazole-N_ε of His1, and Cys2 or Cys6 in the form of a coordinated thiol.[40,46,47]

NiSODs are certainly outliers in the SOD family. They contain a different overall protein fold, metal center, ligand environment and geometry, and spectroscopic properties. The $N_{2/3}S_2$ environment is rather unusual for a metal center that involves interaction with and conversion of ROS because the CysS resides are themselves quite susceptible to the formation of S-oxygenates (SO_x) or disulfides.[38] The unusual chemical nature of the N-ligands should also be noted as N-terminal amine coordination has been observed only in the CO sensor CooA,[48] and deprotonated peptido-N ligation is present in only three other metalloenzymes (nitrile hydratase,[49] the Ni_d site of acetyl-coenzyme A synthase/CO dehydrogenase,[50] and the oxidized P-cluster of nitrogenase[51]).

In summary, the presence of the unique primary coordination sphere in NiSOD has led the bioinorganic community to pose several fundamental questions regarding this enzyme. (i) What intrinsic properties do the coordinated amino acid ligands, which include two CysS residues, a primary amine-N, and a deprotonated peptido-N, impart on the Ni center? (ii) How does such a

coordination sphere modulate the redox properties of the Ni center allowing the substrate ($O_2^{\bullet-}$) to preferentially react with Ni to undergo facile one-electron oxidation and reduction and not react with the coordinated CysS residues? (iii) How does nature utilize Ni, typically not considered an O_2 derivative activator/regulator, to react with and disproportionate $O_2^{\bullet-}$; i.e., what is the catalytic mechanism? The fundamental biochemistry that governs the dismutation reaction at the Ni site has initiated the construction of low-molecular weight (MW) complexes (also termed "synthetic models/analogues" or "biomimetics") that reproduce the primary coordination environment observed in the enzyme. This method has been labeled as the synthetic analogue approach,[52] a paradigm in bioinorganic chemistry that has provided valuable information about the structure and mechanism of numerous metalloenzymes. The objective of such an approach is to gain fundamental insight into the structural and electronic properties of the metal active site germane to catalysis through simpler, low-MW constructs. For NiSOD, some of the important criteria for the design and synthesis of suitable models are as follows:

(i) First, the ligand frame must contain a mixed nitrogen/sulfur (N/S) donor set to mimic the primary coordination sphere observed in the enzyme. Indeed, the prerequisite for redox-active Ni in biology is coordination of CysS ligands.

(ii) Second, and beyond a mere stoichiometric replication of the donor atoms, is the electronic nature of the N/S frame and spatial disposition of the donor atoms. The ligand construct must contain one deprotonatable peptide-N (carboxamide-N is the more general terminology), one primary amine-N, and two *cis*-thiolates situated in a planar N_2S_2 arrangement. An additional neutral N-donor ligand (an imidazole-N is preferable) would be required to replicate the low-spin 4C-to-5C Ni(II/III)SOD redox conversion.

(iii) Third, the ligand construct should be amenable to a variety of straightforward modifications much like the environment in the protein matrix of NiSOD. For example, secondary structure, H-bonding, or electrostatic interactions should be considered in construction of the model. This important last requirement will allow for electronic and structural "fine-tuning" of the biomimetic for its desirable function of superoxide dismutation.

Several groups have employed some or all of these criteria by utilizing (i) small peptides or peptide maquettes typically 3–12 amino acids long that mimic the NiSOD primary sequence,[53-62] (ii) mixed N/S or N/O ligand frames that approximate some aspect of the electronic or structural nature of the NiSOD donors,[63-66] (iii) electronically accurate N_2S_2 or N_3S_2 frames,[67-69] (iv) asymmetric N_2S ligands that approximate the Ni active site with an open coordination site where exogenous N-donors bind (NiN_3S),[70-72] and (v) asymmetric N_2S ligands with NiSOD accurate donors containing an open coordination site where exogenous S-ligands bind to afford NiN_2S_2 species.[73-75] In this review, we describe these approaches and their relationship to the active site properties and function in NiSOD. We also propose, at the end, a mechanistic possibility and our current understanding of this unusual metalloenzyme based on the collection of synthetic modeling work in combination with the structural, spectroscopic, and theoretical results for the protein.

2.3 Synthetic Analogues of NiSOD

This novel SOD class has provided the bioinorganic community with a new system for testing the essential features required for SOD's crucial biological function in ROS regulation. To date (2012), several model systems employing short peptides or longer peptide maquettes (3–12 amino acid residues in length) and low-MW (non-maquette) coordination complexes have been

constructed. Synthetic endeavors in low-MW analogues have been split between complexes that replicate some aspect of the NiSOD structure or function yet are not entirely parallel to the electronic properties of the His1, Cys2, and Cys6 ligands in the enzyme. These latter systems are designated as approximate models. Other models that replicate the structural disposition and electronic donor type of that found in NiSOD are labeled as accurate models. Research in the maquette area has been especially active as these molecules replicate some aspect of their biological inspiration, taking advantage of secondary and tertiary structural features offered by the biological peptide scaffold. While the construction of low-MW models that accurately reproduce the primary coordination sphere of NiSOD is not as widespread, synthetic endeavors aimed at these model systems are slowly becoming more prevalent. The knowledge gained from both approaches and the structural, electronic, and mechanistic relevance to NiSOD are presented below.

2.3.1. NiSOD Peptide Analogues: Synthetic Models based on Peptide Maquettes

The first NiSOD maquette model was synthesized by Shearer and co-workers, which was designated [Ni(SOD^{M1})] [**1**, where SOD^{M1} is HCDLPCGVYDPA (Figure 2.4)].[53] Several derivatives of **1** were also constructed to electronically modify the His1 ligand, namely, [Ni(SOD^{M1}-Im-X)] where X = Me ($\mathbf{1^{MeIm}}$), 2,4-dinitrophenyl ($\mathbf{1^{DNP}}$), and tosyl ($\mathbf{1^{Tos}}$) (Figure 2.4).[55]

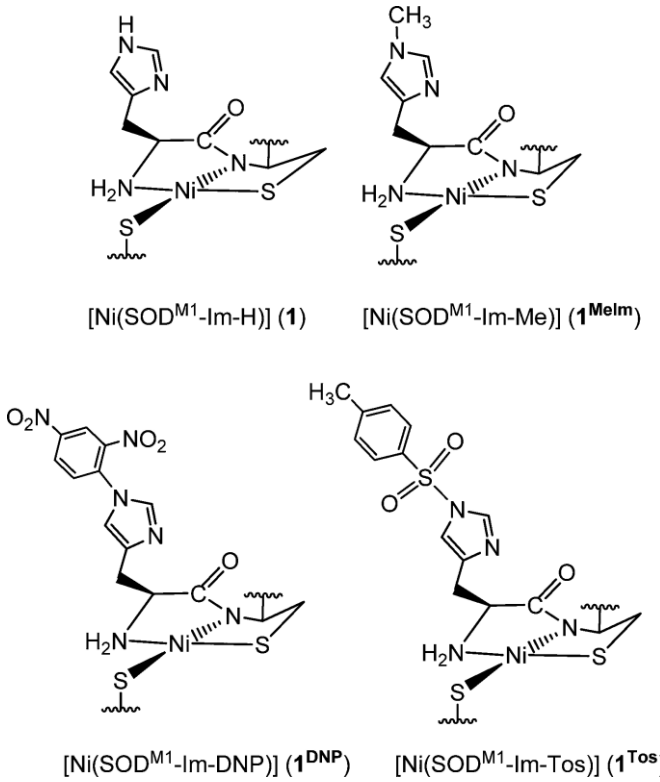

Figure 2.4 Structures of the NiSOD maquette models based on [Ni(SOD^{M1})] (SOD^{M1} = H′CDLPCGVYDPA, H′ = H (**1**), Me (**1^{MeIm}**), 2,4-dinirophenyl (**1^{DNP}**), and tosyl (**1^{Tos}**).

This base maquette is comprised of the first 12 residues from the *S. coelicolor* primary sequence and was shown to coordinate Ni(II) in a 1:1 Ni:peptide ratio under slightly basic conditions. Neutral to slightly acidic conditions did not afford the Ni-coordinated maquettes likely because of protonation of the CysS and peptide-N ligands at these pH values. Additionally, the Ni systems are unstable to air over the course of hours and yield intractable high-MW polymeric species upon exposure. Yields for **1** and **1^{MeIm}** were stoichiometric; however, yields of **1^{DNP}** and **1^{Tos}** were low (14–21%) because of the sensitivity of the tosyl and 2,4-dinitrophenyl functional groups to workup conditions. All of the Ni peptides were characterized by UV–vis, X-ray absorption spectroscopy (XAS), and electrochemistry (results listed in Table 2.1). For example, **1** and its derivatives afforded light beige-pink-colored solutions originating from the

low-intensity ligand-field band at λ_{avg} = 461 nm (ε_{avg} = 420 M^{-1} cm^{-1}) with a shoulder at λ_{avg} = 553 nm (ε_{avg} = 180 M^{-1} cm^{-1}) in pH 7.4 NEM buffer. These electronic transitions are typical of Ni(II) housed in a planar N_2S_2 coordination sphere.[21,25] XAS further supported the UV–vis data with metric parameters (Ni–N_{avg}, 1.90 Å; Ni–S_{avg}, 2.179 Å) and edge transitions consistent with a square-planar Ni(II)–N_2S_2 metal site in all maquettes.[76] The electrochemistry revealed quasi-reversible $E_{1/2}$ values in the cyclic voltammograms (CVs) with the Ni(III/II) couple ranging from 0.280 to 0.600 V (vs Ag/AgCl, pH 7.4 NEM buffer), which trend with the electron-withdrawing (for $\mathbf{1}^{\mathbf{DNP}}$, $E_{1/2}$ = 0.470 V; for $\mathbf{1}^{\mathbf{Tos}}$, $E_{1/2}$ = 0.598 V) and electron-donating (for $\mathbf{1}^{\mathbf{MeIm}}$, $E_{1/2}$ = 0.282 V) nature of the groups attached to the His1-N_ε imidazole atom (Table 2.1). All values are within the superoxide disproportionation window, suggesting that these NiSOD maquette models can perform SOD redox chemistry (vide infra). Collectively, the structural and spectroscopic features of maquettes based on **1** are nearly identical and resemble those obtained for $NiSOD_{red}$.

Table 2.1 Spectroscopic, Structural, Electrochemical, and SOD Activity Kinetic Data for NiSOD and NiSOD Maquette Models.

Complex	λ_{max} [nm] (ε[M^{-1} cm^{-1}])	$E_{1/2}$ (V)[a]	Ni–N, Ni–S (Å)[b]	k (M^{-1} s^{-1})	Refs.
$NiSOD_{red}$ (*S. coelicolor*)	450 (480), 543 (150)[c]	0.090 [d]	1.89, 2.18	7×10^8	18, 20, 23
$NiSOD_{red}$ (*S. seoulensis*)	N/A	N/A	2.01, 2.21	1.3×10^9	19
[Ni(SOD^{M1}-Im-H)] (**1**)	458 (510), 552 (240) [e]	0.434 [e]	1.93, 2.180	$4(3) \times 10^7$	53
[Ni(SOD^{M1}-Im-Me)] ($\mathbf{1^{MeIm}}$)	461 (360), 554 (160 sh) [e]	0.282 [e]	1.91, 2.182	$6(1) \times 10^6$	55
[Ni(SOD^{M1}-Im-DNP)] ($\mathbf{1^{DNP}}$)	464 (410 sh), 552 (150 sh) [e]	0.470 [e]	1.89, 2.179	$3(2) \times 10^8$	55
[Ni(SOD^{M1}-Im-Tos)] ($\mathbf{1^{Tos}}$)	460 (405 sh), 552 (180 sh) [e]	0.598 [e]	1.87, 2.174	$6(2) \times 10^8$	55
[Ni(SOD^{M2})] (**2**)	457 (345), 548 (130 sh) [e]	0.520 [e]	1.875, 2.176	$1(1) \times 10^{-6}$ M (IC_{50})[f]	54
[Ni(mSOD)] (**3**)	454 (432)[g]	N/A	N/A	830 U/μmol [h]	56, 57

[a]Data represents the $E_{1/2}$ value for the Ni(III/II) redox couple normalized to the Ag/AgCl reference electrode based on information found in ref 77-78.[77,78] [b]Ni–S and Ni–N bond distances represent the averages of the two distinct sets of CysS-donors and N-donors from the X-ray crystal structure of NiSOD; metric parameters for the maquette systems were obtained by EXAFS, which cannot distinguish between these sets of atoms. [c]Tris buffer (pH 8.5). [d]Potassium phosphate buffer/pH 7.5. [e]NEM buffer (pH 7.4). [f]Only IC_{50} value measured for **2** where IC_{50} is the concentration of SOD mimic required to effect a 50% reduction in the rate of formazan formation; IC_{50} for Cu/ZnSOD is 4×10^{-8} M. [g]Nonbuffered, deionized H_2O/NaOH mixture measured at pH 7.8. [h]The 1:1 Ni/peptide activity provided (see the text). The activity is defined as the half-limited reduction of NBT by superoxide where 1 unit = $2(Abs_{NBT\text{-}control}\text{-}Abs_{NBT\text{-}maquette})/Abs_{NBT\text{-}control}$); the activity of NiSOD (*S. coelicolor*) is ~ 45,000 units/μmol per subunit (see ref. 56).

Despite the structural and electronic similarity of the maquettes to $NiSOD_{red}$, accessing Ni(III) was problematic. Achieving this oxidation state (at least transiently) is a requirement to realize functionality in these systems. Indeed, the isolation and characterization of Ni(III) complexes with thiolate ligands is difficult and rare; only one such Ni(III)–thiolate complex has ever been crystallized.[79] Initial attempts to chemically oxidize **1** resulted in decomposition and formation of high-MW polymers. However, utilizing a mild oxidant (I_2) afforded Ni(III) maquettes that could be trapped in situ at low temperatures. The resulting X-band EPR spectra of all Ni(III)-bound peptides are similar [g_{avg} values for g_x (2.34), g_y (2.26), and g_z (2.01) at 77 K] and resemble the rhombic $S = {}^1/_2$ EPR spectrum of as-isolated NiSOD (see Figure 2.3).[18] The superhyperfine coupling in the g_z component (A_{zz}) is also observed in all Ni(III)-bound peptides, which ranges from 18.3 to 26.4 G compared to the A_{zz} value of 24.9 G for NiSOD. Interestingly, the A_{zz} values for $\mathbf{1}^{\mathbf{Tos}}$ and $\mathbf{1}^{\mathbf{DNP}}$are the closest to that of the enzyme. This value is reflective of the strength of the interaction between the unpaired spin on Ni(III) and the His1 Nδ ligand, and the relatively long Ni(III)–NIm bond distance in $NiSOD_{ox}$ defines the extent of this coupling in the enzyme. Thus, the Ni maquettes with the electron-withdrawing groups on Nε (i.e., the weaker Lewis base) better resemble A_{zz} in $NiSOD_{ox}$ because they contained the longer Ni–NIm bond. Moreover, this electronic modification should correlate with superoxide reaction kinetics. Indeed, **1** and its derivatives are able to catalytically disproportionate superoxide as monitored by stopped-flow kinetics [$k \sim 10^6$–10^8 M^{-1} s^{-1} (Table 2.1)]. As expected from EPR, complexes $\mathbf{1}^{\mathbf{DNP}}$ and $\mathbf{1}^{\mathbf{Tos}}$ are the most active NiSOD mimetics with k values of $3(2) \times 10^8$ M^{-1} s^{-1} for $\mathbf{1}^{\mathbf{DNP}}$ and $6(2) \times 10^8$ M^{-1} s^{-1} for $\mathbf{1}^{\mathbf{Tos}}$. These k values are only 1 order of magnitude lower than the diffusion-controlled rate observed for all SODs ($k \sim 10^9$ M^{-1} s^{-1}). Accordingly, the nature of the long axial Ni(III)–NIm

bond in $NiSOD_{ox}$ is modeled nicely with the SOD^{M1} maquettes with electronic modifications on the His1 residue.

In a second-generation system, Shearer reported the synthesis and properties of the Ni maquette complex with the heptapeptide SOD^{M2}, namely [Ni(SOD^{M2})] (**2**, where SOD^{M2} = HCDLPCG, a Ni coordination sphere similar to that depicted for **1** in Figure 2.4).[54] Analogous to SOD^{M1}, $SOD^{M2}$and its derivatives coordinated Ni(II) in a 1:1 ratio under slightly basic conditions affording light beige-pink solutions of **2** with similar UV–vis profiles (Table 2.1). Complex **2** has an appropriate redox potential to act as an SOD [$E_{1/2}$ = 0.520 V vs Ag/AgCl, pH 7.4 NEM (see footnote [a] of Table 2.1 for conversion to NHE)], contains a Ni(II) center in an N_2S_2 environment (XAS), does not bind anions such as N_3^-, and catalytically disproportionates superoxide. Thus, the removal of the last five residues outside of the Ni-hook of native NiSOD does not compromise the Ni affinity or electronic structure with the smaller peptide in **2**. The CV displays quasi-reversible behavior with an $E_{ox} - E_{red}$ peak-to-peak separation (ΔE_p) of 0.240 V, which is suggestive of substantial structural rearrangement taking place about the Ni center during redox. The Ni(III)-bound peptides cannot be obtained or isolated in pure form upon chemical oxidation or bulk electrolysis, suggesting, as with **1**, the relative instability of Ni(III) in this environment. However, the Ni(III)-bound peptide was obtained in situ following substoichiometric addition of KO_2 to afford a rhombic EPR spectrum similar to that of $NiSOD_{ox}$.[54] Activities were measured using a modified xanthine/xanthine oxidase assay and afforded an IC_{50} value (where IC_{50} is the concentration of SOD mimic to effect a 50% reduction in the rate of formazan formation) of 1×10^{-6} M for **2**, 2 orders of magnitude higher than the IC_{50} value of Cu/ZnSOD (4×10^{-8} M). Replacing His1 in **2**with Ala (**2^{Ala}**) completely shut off activity, comparable to the H1A mutation in NiSOD.[30] Additional insight from DFT and eT rate calculations at overpotential confirmed that

the Ni center in **2** remains 5C when cycling through the Ni(III/II) states. Taken together, maquettes **1** and **2**afford excellent structural and functional models of NiSOD, advocating for a 5C Ni center and outer-sphere eT as probable mechanistic features of this enzyme.

At approximately the same time, the groups of Weston and Buntkowsky reported an extensive study on the properties of a Ni(II) nonapeptide maquette that they label as [Ni(mSOD)] (**3**, where mSOD = HCDLPCGVY) (see Figure 2.4 for the analogous Ni coordination structure).[56-59] Similar to the aforementioned NiSOD maquette studies of **1** and **2**, Ni coordinated to mSOD in a mostly 1:1 Ni:peptide ratio in **3** (other ratios were observed on the basis of ESI-MS and UV–vis titrations), affording pink-colored solutions.[56,57] Although XAS was not performed to define the Ni coordination sphere in this model, solution NMR, UV–vis, and DFT studies were indicative of an N_2S_2 square-planar environment about the Ni(II) ion. The theoretically estimated Ni–N and Ni–S distances are on par with those experimentally observed in maquettes **1** and **2**, suggesting similar Ni coordination environments (Table 2.1). In contrast to **1** and **2**, an enhanced stability to ambient lab conditions was noted for **3**. The Ni(III) version of this maquette was not isolated; however, DFT computations predict that the ground state of Ni(III)-mSOD is a triplet and thus high-spin. This result is opposite to what is found with **1**, **2**, and the native enzyme. The $S = 1$ state for Ni(III)-mSOD is supposedly due to the fifth axial ligand arising from the neutral carbonyl-O of the Leu4-Pro5 peptide backbone, rather than axial binding of His1 as seen in **1**, **2**, and $NiSOD_{ox}$. This dissimilar coordination environment is due to a conformational difference with respect to Pro5: in NiSOD, Pro5 is in a *cis* conformation, whereas in **3**, Pro5 is orientated in a *trans* configuration because of H-bonding interactions of the peptide. It was suggested that the Pro5 *trans*arrangement prevents His1-N_δ from binding, and it was also proposed to prevent the binding of superoxide opposite to His1. The activity of maquette **3** is thus considerably lower than that of native NiSOD

(vide infra). As such, a new maquette was constructed to enforce the *cis*conformation observed in the enzyme.[58] However, this maquette did not affect the reactivity, suggesting that this structural perturbation is not responsible for the low activity of these maquettes.

Reactivity studies were conducted with **3** in the presence of KO_2 using the nitroblue tetrazolium (NBT) assay, and it was shown to be stable for 60–90 s.[56] In attempts to account for both 1:1 and 2:1 stoichiometries for the Ni–peptide complexes in solution, the xanthine/xanthine oxidase assay was run to establish lower and upper limits of $O_2^{\bullet-}$ activity. The 1:1 complex produced an activity value of 830 units μmol^{-1} [activity defined as the half-limited reduction of NBT by superoxide where 1 unit = $2(Abs_{NBT\text{-}control} - Abs_{NBT\text{-}maquette})/Abs_{NBT\text{-}control}$]; the 2:1 ratio resulted in an activity of 1250 units μmol^{-1}, demonstrating that the nine-residue peptide can serve as a functional NiSOD mimic. Activity studies were repeated with a mutated peptide for which His1 was replaced with Ala to yield a negligible decrease in activity, disputing the essentiality of His1 for catalytic activity. It was proposed instead that Pro5 is responsible for tuning the oxidation state of the biomimetic, as the *trans*-Pro5 residue prevents an axial histidine nitrogen atom from binding to Ni(III) in this maquette.

Further reactivity of **3** was performed using cyanide anion (CN^-) as a substrate analogue.[57] Complexes **1** and **2** show no evidence of binding anions such as azide, and CN^- strips the Ni(II) center from the peptide, all pointing toward an outer-sphere mechanism for NiSOD (vide supra). Upon addition of 1 equiv of CN^- to **3**, the pink solution turned yellow, consistent with a change in the Ni coordination environment. Indeed, MS experiments confirmed the presence of the mono-CN^- adduct of the Ni maquette, [Ni(mSOD)(CN)] (**4**). The UV–vis spectrum of **4** in a pH 7.8 H_2O/NaOH nonbuffered medium revealed mostly UV transitions (λ = 252 nm, ε = 12000 M^{-1} cm^{-1}, and λ_{sh} = 282 nm) and one visible band at 410 nm (ε = 180 M^{-1} cm^{-1}). The resulting electronic

transitions of **4** all blue-shift from the parent Ni(II) square-planar species **3** (see Table 2.1). The formation of **4** was further confirmed by ^{13}C and ^{15}N NMR and FTIR spectroscopy, which revealed one strong and single ν_{CN} peak at 2108 cm^{-1} (KBr).

Collectively, the properties and reaction chemistry of peptide maquettes **1–3** provide a somewhat unifying picture of Ni in the SOD coordination sphere. The Ni(II)–N_2S_2 square-planar coordination environment is maintained throughout and affords similar metric parameters and electronic absorption profiles (see Table 2.1). Maquettes **1** and **2** break down and form intractable polymeric species upon being exposed to air within hours, whereas maquette **3** was stable for days at RT and weeks at 4 °C. The defining feature of the oxidative stability is unknown at present. All of the Ni maquettes disproportionate $O_2^{\bullet-}$ at rates higher than the spontaneous rate but significantly lower than the rate of NiSOD. Ni(III) forms of the maquettes are difficult to obtain; however, in situ EPR isolation of Ni(III) maquettes **1** and **2** has been successful, and in one case, a Ni(III) species has been confirmed by XAS (**1**$^{\mathbf{MeIm}}$). One defining feature of maquette **3** is the stoichiometric binding of CN^-, a property that supports inner-sphere coordination and eT to $O_2^{\bullet-}$ in NiSOD. Furthermore, replacement of His with Ala does not significantly change the rate in **3**. This result is quite in contrast to the same modification in the enzyme and in maquette **2**. Perhaps the carbonyl-O ligand from Pro5 in **3** supports the SOD reaction, albeit through a mechanism different from that in NiSOD. It is difficult to delineate the variances between the system of Shearer and the system of Weston and Buntkowsky. Perhaps the noted differences lie in the relative instability of some of the maquettes. For example, the nonapeptide Ni maquette **3** is shown to exist in equilibrium with 2:1 and 1:1 Ni–peptide species in solution. This observation alone warrants the need for more definitive structural information on **3** or more discrete and crystallizable small molecule analogues. The work on maquette **3** is also controversial as a separate publication from

the same group states that only a 1:1 species exists.[57,59] Additionally, the electronic similarity of $O_2^{\bullet-}$ and CN^- is a bit of a stretch, and one would expect Ni (or any transition metal) to bind the strong-field CN^- ligand. The CN^- binding results are also contradictory to those of the anion binding studies performed on the enzyme and in the maquettes of Shearer. Their experiments reveal that CN^-, rather than binding, strips the Ni from the model to form $[Ni(CN)_4]^{2-}$, which may be explained by the use of excess CN^-.[54] In contrast, Buntkowsky proposed that by limiting the stoichiometry to 1 equiv, CN^- can bind to the metal center without disrupting the coordination sphere and that this binding capability should translate to the native enzyme. As of 2012, binding of an anion to the Ni center in NiSOD (ox or red) has yet to be established. Taken together, it appears that the minimal requirement to achieve functionality in these maquettes is the first seven amino acid residues of the Ni-hook as this length appears to bind Ni with high affinity and provides suitable aqueous stability. Additionally, special attention must be given to the positioning of the His1-Im in these maquettes for proper binding to the Ni center so that Ni(III/II) redox cycling is facile and turnover is fast.

2.3.2. NiSOD Low-MW Analogues: NiSOD Approximate Models

The work on approximate models of NiSOD has utilized a variety of different ligand platforms that incorporate some but not all features of the biological coordination unit. The first low-MW NiSOD model complex that demonstrated SOD activity was synthesized by Darensbourg and co-workers in 2009.[70] They employed the ligand 1-(2-mercapto-2-methylpropyl)methyl-1,4-diazacycloheptane (mmp-dachH, where H is a dissociable proton) as an amine-thiol N_2S chelate for Ni (Figure 2.5).

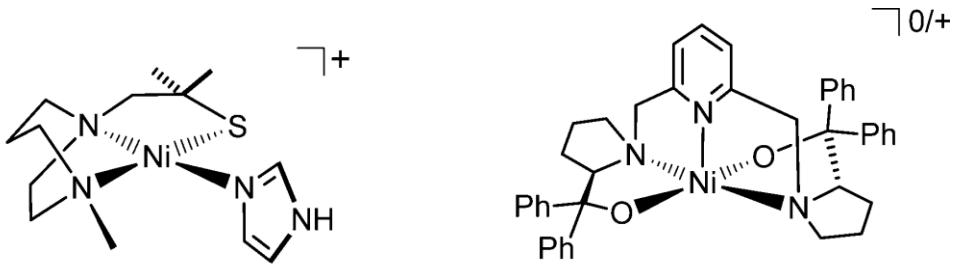

[Ni(mmp-mdach)(Im)]$^+$ (cation of **5**)

[Ni(BDPP)] (**6**)
[Ni(BDPP)]$^+$ (cation of **6^{ox}**)

Figure 2.5 Structures of the NiSOD approximate model complexes [Ni(mmp-mdach)Im]Cl (cation of **5**, left) and [Ni(BDPP)] (**6**, right)/[Ni(BDPP)]PF_6 (cation **6^{ox}**, right) SOD^{M1}). Ph is for phenyl or C_6H_5 for the structures of **6** and **6^{ox}**, respectively.

Reaction of the deprotonated ligand with Ni(II) salts resulted in a dimeric Ni(II) complex with bridging alkyl thiolates (S,S-bridged or μ-thiolato bridge) that approximated the N_2S_2coordination sphere of $NiSOD_{red}$. Because the active sites of NiSOD function as discrete monomeric species, attempts were made to cleave the μ-thiolato core with biologically relevant ligands. Although this reaction appears feasible, it has not been widely adopted as a successful approach to accessing monomeric Ni–thiolato complexes. Bridge splitting of the dimer with imidazole (Im) afforded the monomeric Ni(II) complex [Ni(mmp-mdach)(Im)]Cl (**5**) (Figure 2.5). The geometry about the Ni(II) center in **5** is square-planar arising from the N_2S ligand and the monodentate Im to afford an N_3S chromophore. The Ni–S distance (2.149 Å) is typical for planar Ni–thiolate complexes and similar to that of NiSOD, but the Ni–N_{Im} distance is short (1.888 Å) and unlike the enzyme value (~2.3–2.5 Å) because of its location in the equatorial plane. This complex was the first structurally characterized Ni(II) species containing both thiolate and imidazole donors, both of which are key ligands in NiSOD albeit in different positions in the

coordination sphere (see Figure 2.5). This orange complex displayed one d–d band in the visible region at 467 nm (ε = 500 M^{-1} cm^{-1}), which is different from Ni(II)–N_2S_2 complexes and $NiSOD_{red}$. The CV of **5** exhibited an irreversible oxidation wave (E_{ox}) at 0.43 V in DMF (vs Ag/AgCl), which has been attributed to thiolate oxidation of the mmp-mdach ligand. This property would suggest that **5** would not be a functional SOD mimic. However, an aqueous solution of **5** (61 μM) provided protection against 100 equiv of $O_2^{\bullet-}$ to NBT (61 μM), preventing formazan formation by ~40% in pH 7.4 phosphate buffer. Furthermore, this complex is stable to O_2 and affords S-oxygenated species when reacted with H_2O_2. Thus, this model implies that the mixed N/S-donors of NiSOD provide O_2-stability to the coordination unit. The exact role of the Ni center in the SOD chemistry was not defined; however, **5** was the first example of a NiSOD functional model.

The first 5C analogue of NiSOD was described in late 2011 by Kuo and co-workers utilizing an N_3O_2 chelate.[65] The pentadentate ligand, 2,6-bis{[(*S*)-2-(diphenylhydroxymethyl)-1-pyrrolidinyl]methyl}pyridine (H_2BDPP, where H represents dissociable protons), employed nonbiological donor atoms that included one pyridine-N, two tertiary pyrrolidine-N atoms, and two alcohol-O donors. Because of the steric restrictions imposed by the ligand frame, the pyridine-N was forced into an axial position upon coordination to Ni regardless of the oxidation state, a clever design strategy to impose a 5C geometry. The resulting Ni(II) complex [Ni(BDPP)] (**6**) contained a Ni(II) center in a distorted square-pyramidal N_3O_2 environment that structurally replicated the 5C geometry of $NiSOD_{ox}$ (Figure 2.5). The X-ray structure of **6** revealed a Ni–N_{py} distance of 1.969 Å with two longer Ni–N_{avg} distances (2.149 Å) from the pyrrolidines and two short Ni–O_{avg} bonds (1.930 Å) from the tertiary O-donors in a *trans* configuration (Figure 2.5). The bond distances in **6**advocate for a diamagnetic low-spin (S = 0) 5C Ni(II) center,

although no other evidence was presented to support this electronic configuration. The pale green complex exhibited a quasi-reversible CV with an $E_{1/2}$ of 0.308 V (vs Ag/AgCl in CH_2Cl_2), suggesting that the $BDPP^{2-}$ ligand could support Ni(III) with minimal structural rearrangement. Indeed, chemical oxidation of **6** cleanly yielded the Ni(III) complex [Ni(BDPP)](PF_6) (**6^{ox}**) that was structurally characterized by X-ray crystallography. As expected, the Ni–L distances in **6^{ox}** contracted (~0.1 Å for equatorial ligands; ~0.02 Å for the axial Ni–N_{py} distance) from the parent Ni(II) complex **6** because of decreased Ni–ligand electron repulsion (Ni–N_{py}, 1.947 Å; Ni–$N_{pyrrolidine}$, 2.045 Å; Ni–O, 1.844 Å). In contrast to that of $NiSOD_{ox}$, the X-band EPR spectrum of **6^{ox}** afforded an axial signal because of the high degree of symmetry and electronic equivalency of the *trans*-N_2O_2 donors in the basal plane ($g_x = g_y = 2.18$ and $g_z = 2.04$ in CH_2Cl_2 at 77 K) (see Figure 2.3 for $NiSOD_{ox}$). The hyperfine coupling in the g_z component in **6^{ox}** (A_{zz} = 25.0 G), however, is identical to the coupling in the enzyme. Both of these hyperfine patterns are due to the axial N-ligand. In fact, DFT studies confirm that the majority of the spin density in **6^{ox}** resides in an MO with significant Ni d_z^2 character much like that of $NiSOD_{ox}$.[23] Taken together, the data suggest that **6** or **6^{ox}** should be capable of $O_2^{\bullet-}$disproportionation. Indeed, **6^{ox}** was shown to react with excess KO_2 in MeCN to produce O_2 and Ni(II) complex **6** in stoichiometric yields. Interestingly, Ni(II) complex **6** did not react with KO_2 to produce H_2O_2. Despite the presence of the RO^- ligands, the spin-state of the Ni center appears to remain low-spin in both Ni oxidation states. This spin-state appears to be a requisite for catalysis as high-spin Ni(III/II) has never been found in enzyme preparations, nor would it be of the appropriate redox potential. Additionally, this model appears to be at odds with data from Cys-to-Ser mutations in the enzyme. This mutation resulted in high-spin Ni(II) centers that could not access the high-valent Ni(III) state.[31,32] Ultimately, this mutation afforded inactive NiSOD. It appears that careful construction

of the ligand frame to house 5C and low-spin Ni(II) could be an additional requirement for a functional NiSOD model.

2.3.3. NiSOD Low-MW Analogues: Accurate Models

The first low-MW analogue that accurately reproduced the NiSOD primary coordination sphere was the square-planar Ni(II)–N_2S_2 complex, (Me_4N)[Ni(BEAAM)] [**7** (Figure 2.6)].[67] This orange-colored complex was structurally characterized by X-ray crystallography and consists of an $N_{amine}N_{carboxamide}S_2$ chromophore with asymmetric Ni–N bonds because of the electronic differences in the N-donors. The spectroscopic and structural properties are summarized in Table 2.2. For example, the Ni–N_{amine} bond is notably longer (1.989 Å) than the Ni–$N_{carboxamide}$ bond (1.858 Å). The high resolution of small molecule crystallography has provided the electronic discrepancy in these two Ni–N bonds that is absent in the EXAFS data of maquette systems **1** and **2**. The variance in the Ni–N bond lengths is due to the good σ-donating ability of the carboxamido-N, which provides for more covalency in this bond. These effects are also manifested in the Ni–S bond which it is *trans* to. The Ni–S bond *trans* to the carboxamido-N is significantly elongated (2.177 Å) with respect to the Ni–S bond *trans* to the amine (2.137 Å). A similar difference is observed in the Ni–S distances of $NiSOD_{red}$ (*S. coelicolor*).[18] Analogous to those of the maquette systems and the enzyme, a double-humped UV–vis spectrum is observed with ligand-field transitions at 461 nm ($\varepsilon = 290\ M^{-1}\ cm^{-1}$) and 556 nm ($\varepsilon = 70\ M^{-1}\ cm^{-1}$) in MeCN underscoring the electronic equivalence of this model and $NiSOD_{red}$. The quasi-reversible Ni(III/II) couple observed for **7** at 0.120 V (vs Ag/AgCl in MeCN) is also within the potential window for SOD chemistry, but the complex does not react with $O_2^{\bullet-}$. Additionally, bulk oxidation studies at low temperature resulted in the formation of a short-lived purple/blue species that is

nonisolable, and no other spectroscopic evidence was provided for this oxidized species. The axial N-ligand, which is notably absent from this complex, may be necessary for the stabilization of Ni(III) in these models and in NiSOD.

In a follow-up to this communication, Shearer and Hegg reported the NiSOD model, K[Ni(HL2)] [**8** (Figure 2.6)], with a similar N_2S_2 ligand frame as in **7** but with the absence of the *gem*-dimethyl groups on the carbon atoms α to sulfur.[68] The metric parameters and electronic absorption spectrum are very similar between the two complexes (Table 2.2), suggesting analogous structural and electronic properties. One noted difference, however, is in the CV data, which displayed an irreversible oxidation for **8** at 0.065 V (vs Ag/AgCl in DMF) indicative of ligand-based redox. Additionally, attempts to chemically oxidize **8** at low temperatures resulted in an EPR-inactive species that supports S-oxidation to disulfide. The difference in CV data between otherwise structurally (and presumably electronically) equivalent Ni(II) centers was puzzling. The DFT-generated redox-active MOs in **7** and **8** revealed a significant change in the amounts of S-pπ and Ni-dπ character in these complexes. For example, the Ni-character in **8** (32% Ni-dπ, 68% S-pπ) is much lower (and S-character higher) than in **7** (56% Ni-dπ, 32% S-pπ). While the ligand frames are similar, it appears that the methyl substituents on the ligand in **7** clearly aid in stabilizing and supporting Ni-based redox and access to the Ni(III) oxidation state. Even though both complexes do not react with superoxide, the clear differences in the CVs reveal key factors for obtaining at least Ni(III) in this asymmetric N/S coordination environment by providing steric bulk and enhanced Lewis basicity at the S-donor. Taken together, the results for complexes **7** and **8** propose that well-defined and controlled modifications at or near the S-ligands in Ni-N_2S_2 coordination units can significantly alter the nature of the frontier MOs that ultimately dictate redox behavior in these systems and presumably in the enzyme.

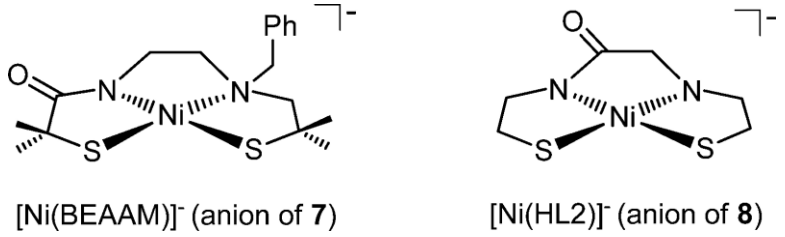

Figure 2.6 Structures of the NiSOD model complexes (Me_4N)[Ni(BEAAM)] (anion of **7,** left) and K[Ni(H2L)] (anion of **8**, right). Ph is phenyl or C_6H_5 for the structure of **7**.

As a means of realizing selective S-modifications in NiSOD models, Harrop and co-workers developed a coordinatively unsaturated N_2S ligand that would allow for unconstrained modeling of a second S-ligand (S′) to complete the N_2SS' coordination sphere.[73] Reaction of the deprotonated form of the ligand nmp^{2-} [dianion of *N*-(2-mercaptoethyl)picolinamide] with Ni(II) ultimately led to an intractable *S*,*S*-bridged dimeric species, $[Ni_2(nmp)_2]$ (**9**). Complex **9** was initially thought to be an unusable precursor because of its poor solubility and the kinetic inertness of *S*,*S*-bridged square-planar Ni(II) complexes. However, reaction of **9** with different exogenous thiolates afforded the red-colored mononuclear square-planar Ni(II)–N_2S_2 species, (Et_4N)[Ni(nmp)(SR)] (where R represents various alkyl and aromatic thiolate ligands), in very good yields (Figure 2.7). The nmp^{2-} ligand replicates the two five-membered chelate rings formed by His1 and Cys2 in NiSOD, while the exogenous thiolate allows for unconstrained modeling of Cys6. Single-crystal X-ray analysis in combination with UV–vis, FTIR, ^{1}H NMR, CV, and ESI-MS of these complexes revealed a distorted planar coordination sphere with spectroscopic and electrochemical features similar to those of $NiSOD_{red}$.

Table 2.2. Spectroscopic, Structural, and Electrochemical Data of NiSOD Low MW Synthetic Analogues.

Complex	λ_{max} [nm] (ε[M^{-1} cm^{-1}])	E_{ox} (V)[a]	Ni–$N_{peptide}$, Ni–N_{amine} (Å)	Ni–$S_{trans\text{-}peptide}$, Ni–$S_{trans\text{-}amine}$ (Å)	Refs.
$NiSOD_{red}$ (*S. coelicolor*)	450 (480), 543 (150)[b]	0.090[c]	1.91, 1.87	2.19, 2.16	18, 20, 23
$NiSOD_{red}$ (*S. seoulensis*)	N/A	N/A	1.94, 2.07	2.18, 2.24	19
(Me_4N)[Ni(BEAAM)] (**7**)	461 (290), 556 (70)[d]	0.120[d]	1.858, 1.989	2.177, 2.137	67
K[Ni(H2L)] (**8**)	449 (340), 570 (70 sh)[e]	0.065[f]	1.862, 1.937	2.1711, 2.1671	68
(Et_4N)[Ni(nmp)(SC_6H_4-*p*-Cl)] (**10**)	450 (5450)[d]	0.236 [d]	1.8638, 1.9470	2.2139, 2.1492	73
(Et_4N)[Ni(nmp)(S^tBu)] (**11**)	464 (4540) [d]	0.075 [d]	1.882, 1.9635	2.1938, 2.1629	73
(Et_4N)[Ni(nmp)(S-*o*-babt)] (**12**)	450 (3500) [d]	0.276 [d]	1.877, 1.947	2.1939, 2.1518	74
(Et_4N)[Ni(nmp)(S-meb)] (**13**)	449 (3900) [d]	0.214 [d]	1.863, 1.944	2.172, 2.156	74
K[Ni(GC-OMe)(SC_6H_4-*p*-Cl)] (**15**)	481 (390), 560 (230) [f]	0.220 [f]	1.83, 1.99[g]	2.16 (avg.) [g]	75
K[Ni(GC-OMe)(SNAc)] (**17**)	463 (350), 545 (160)[f]	0.310 [f]	1.83, 1.99 [g]	2.17 (avg.) [g]	75
K[Ni(N_3S_2)] (**19**)	449 (320), 570 (90) [e]	-0.125 [f]	1.8575, 1.954	2.1805, 2.1739	69

[a]Data represent the E_{ox} value normalized to the Ag/AgCl reference electrode [E vs NHE = E vs Ag/AgCl(saturated KCl) + 0.199 V] based on information found in ref 77-78; the quasi-reversible $E_{1/2}$ is reported for **7**, and a reversible $E_{1/2}$ is reported for NiSOD, which represent the Ni(III/II) redox couple. [b]Tris buffer (pH 8.5). [c]Potassium phosphate buffer (pH 7.5). [d]MeCN. [e]MeOH. [f]DMF. [g]Metric parameters from EXAFS. The reported Ni–S bond distance represents the average from two separate S scattering atoms.

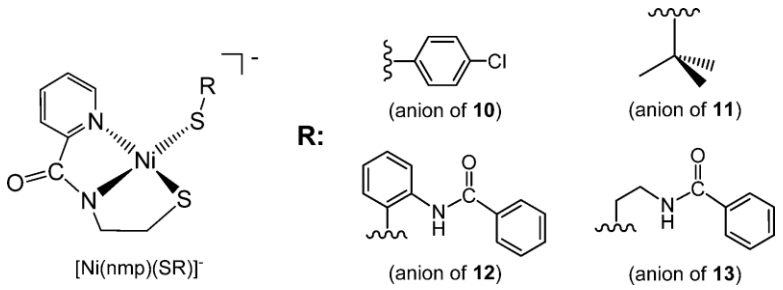

Figure 2.7 Structures of the anionic portion of NiSOD model complexes of general formula (Et_4N)[Ni(nmp)(SR)] [where R = C_6H_4-*p*-Cl in **10**, ^{t}Bu in **11**, *ortho*-benzoylaminobenzene or *o*-babt in **12**, and *N*-(2-mercaptoethyl)benzamide or meb in **13**]. The skewed line represents the point of attachment to the monodentate thiolate ligand.

For example, the metric parameters for **10–13** [Ni–N_{amine}, 1.950 Å; Ni–$N_{carboxamide}$, 1.871 Å; Ni–$S_{trans\text{-}carboxamide}$, 2.193 Å; Ni–$S_{trans\text{-}amine}$, 2.155 Å (average values)][70,71] are consistent with square-planar Ni(II)–N_2S_2 coordination (see **7** and **8**). In complexes **10–13**, the dominant electronic transition at ~450 nm masks the d–d bands due to the pyridine–N/Ni(II) CT (see Table 2.2). These complexes also displayed irreversible CVs consistent with ligand-based redox processes. Bulk oxidation studies revealed this to be the case with the oxidation occurring at the monodentate S-ligand to form disulfide and the insoluble *S*,*S*-bridged dimer **9**. Regardless, the Ni–nmp constructs afforded suitable structural models of $NiSOD_{red}$ that could be modified at one specific coordination position.

To demonstrate the utility of this synthetic route, modifications such as appended H-bonding moieties were incorporated into the monodentate S-ligand [see complexes **10** and **12** (Figure 2.8)].[74] These modifications are significant because NiSOD contains two key H-bonds to the coordinated cysteine thiolate *trans* to the peptide-N (Cys6).[18,38] The H-bonds in **12** and **13** were shown to be both intra- and intermolecular in nature. In both cases, the H-bond is bifurcated between both S-ligands in the basal plane, but more so with the monodentate

thiolate (Figure 2.8). An interesting feature is that H-bonding to sulfur resulted in a decrease in the Ni–S bond distance from the simple alkyl or aryl analogues (compare values of 2.2139 Å in **10** and 2.1939 Å in **12**; 0.02 Å bond contraction). At first glance, this result is opposite to what one would predict on the basis of a decrease in the Lewis basicity of the H-bonded thiolate ligand. However, examination of the frontier MOs that govern this interaction in **10–13**, as well as $NiSOD_{red}$, reveals that the HOMO is antibonding in nature with large and nearly equal contributions from both Ni-dπ AOs and S-pπ ligand orbitals, a so-called dπ–pπ repulsion (filled–filled interaction or four-electron repulsion). The Ni–S bond contraction in **12** and **13** is thus the result of stabilization of S-based ligand orbitals upon H-bonding, which results in a decrease in the filled–filled Ni dπ–S pπ antibonding interaction. Theoretical studies of truncated versions of $NiSOD_{red}$ reveal a similar contraction of 0.03 Å when the CysS ligands become fully protonated CysSH thiols.[23] DFT calculations on **10–13** also show a decrease in the level of S-character in the HOMO (S-based MOs lower in energy) and an increase in the level of Ni-character upon incorporation of the H-bond to support more of a metal-based redox-active MO. The H-bonding interaction also resulted in an S-ligand that is less susceptible to reactions with electrophiles and/or oxidants such as O_2 with an overall stability gain of 15 kcal/mol at the S-atom with the H-bond. Thus, synthetically enforcing H-bond donors in these model complexes (also present at the NiSOD active site) decreases the nucleophilicity of a coordinated S-donor, stabilizes the Ni–S bond via relief of the dπ–pπ interaction, and serves as one potential mechanism that nature has incorporated to protect the CysS donors of NiSOD from oxidative modification and/or degradation during turnover.

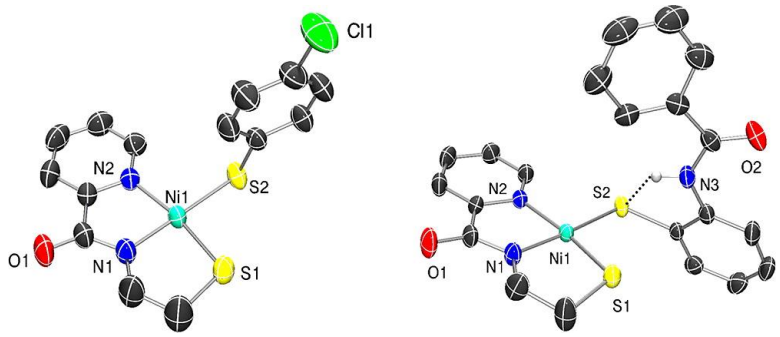

Figure 2.8 X-ray crystal structures of the anions of $NiSOD_{red}$ models $(Et_4N)[Ni(nmp)(SC_6H_4$-*p*-Cl)] (**10**, left) and (Et_4N)[Ni(nmp)(S-*o*-babt)] (**12**, right) highlighting intramolecular H-bonding between the carboxamide NH group (N3) and the monodentate thiolate (S2) in complex **12**.

Models **10–13** certainly afforded suitable structural analogues of NiSOD with variable synthetic manipulation at one S coordination position. The tunability of one S-ligand allowed this group to probe secondary-sphere interactions with coordinated S-ligands such as H-bonding, which proved to protect the sulfur from oxidation and promote more Ni-based redox. These models suffered, however, from a lack of water stability and solubility, thus limiting these studies to organic solvents. To achieve aqueous solubility and stability and ultimately superoxide chemistry, a new N_2S ligand utilizing a peptide backbone consisting of glycine and cysteine (denoted as GC-OMeH_2) was synthesized.[75] Analogous to the previous Ni–nmp systems (**10–13**), reaction of GC-OMe^{2-} with Ni(II) led to the expected *S*,*S*-bridged dimeric species $[Ni_2(GC\text{-}OMe)_2]$ (**14**) that was used in the construction of monomeric Ni(II) complexes with variability at the fourth coordination position. Reaction of **14** with numerous exogenous thiolates afforded a variety of red/violet-colored mononuclear square-planar Ni(II)–N_2S_2 species of the general formula [Ni(GC-OMe)(SR)] (where R represents various alkyl and aromatic thiolate ligands) in good yields [**15–18** (Figure 2.9)]. EXAFS, in combination with UV–vis, FTIR, ^{1}H NMR, CV, and ESI-MS, of **15** and **17** revealed a distorted square-planar coordination (Ni–$N_{amine\text{-}avg}$, 1.99 Å; Ni–$N_{peptide\text{-}avg}$,

1.83 Å; Ni–S_{avg}, 2.17 Å) with spectroscopic and electrochemical features similar to those of $NiSOD_{red}$ and previous models [average λ_{max} = 480 nm (ε = 420 M^{-1} cm^{-1}) and 560 nm (ε = 200 M^{-1} cm^{-1}) in DMF] and an irreversible E_{ox} of ~0.200 V (vs Ag/AgCl in DMF) (Table 2.2). Importantly, all of these measurements have been performed in organic solvents such as MeCN and a buffered (pH 7.4) aqueous medium, representing some of the first low-MW models to be probed under pseudophysiological conditions. These structurally characterized peptide-based Ni(II) complexes simulate many of the electronic features of $NiSOD_{red}$; however, they do not afford isolable Ni(III) species or superoxide-reactive systems, suggesting again the significance of the fifth His-N ligand in the enzyme. In fact, saturating solutions of these complexes with excess *N*-methylimidazole do not impart any electrochemical reversibility or other spectroscopic changes. Interestingly, the ^{1}H NMR spectra of **15–18** in D_2O or any protic solvent provide broad, ill-resolved signals that may correspond to variable solution speciation. It was hypothesized that these species could be solvent-bound or S-bridged oligomers because of the lability of the monodentate thiolate ligand. Addition of excess thiolate ligand afforded well-resolved spectra with a splitting pattern consistent with a monomeric, diamagnetic square-planar Ni(II) complex. In contrast, dissolution of as-isolated **15–18** (from the synthesis) in aprotic solvents such as CD_3CN afforded neat, readily discernible ^{1}H NMR spectra consistent with one discrete species. These models suggest that the active site fragment of NiSOD may be rather dynamic with a propensity to oligomerize outside of the protein matrix (see the results from maquette system **3** described above). Thus, the surrounding environment and the N_3S_2 chelate may be crucial for maintaining coordinative integrity. In fact, mutagenesis of just one CysS to SerO (Cys6Ser or Cys2Ser) resulted in inactive enzyme with the addition of two new water ligands.[31,32] The absence of one cysteine thiolate promotes a high-spin (S = 1) aquated Ni(II) center at the NiSOD active site with no

evidence of the remaining Ni–CysS bond in the mutants. This finding, coupled with the results for **15–18**, suggests more than redox-modulation and/or H^+-storage roles for cysteine in NiSOD. It is likely that the presence of both the Cys6 and Cys2 ligands in NiSOD is crucial for proper active site assembly and stabilization.

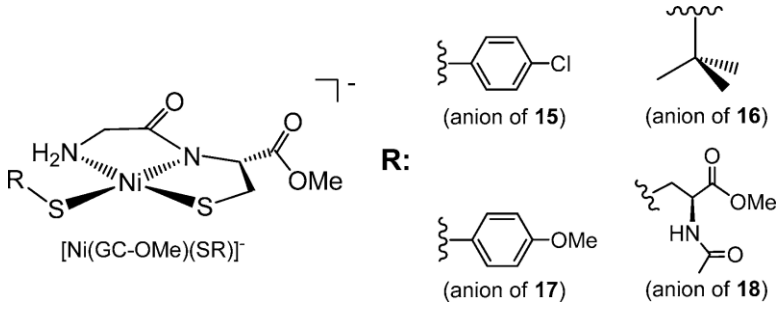

Figure 2.9 Structures of the anionic portion of NiSOD model complexes of general formula K[Ni(GC-OMe)(SR)] (where R = C_6H_4-*p*-Cl in **15**, ^{t}Bu in **16**, C_6H_4-*p*-OMe in **17**, and N-acetyl-L-cysteine or NAc in **18**). The skewed line represents the point of attachment to the monodentate thiolate ligand.

In an effort to obtain functional NiSOD complexes and to assess the role of the axial N-donor, Harrop's group designed and synthesized a 5C N_3S_2 ligand frame.[52] This ligand contained the appropriate donor atoms, in an electronic sense, that are situated in a spatial fashion exactly analogous to the active site of NiSOD. In fact, the presence of the axial N-donor ligand is hypothesized to stabilize, at least to some extent, the high-valent Ni(III) oxidation state (vide supra). If this hypothesis were correct, then an appropriately disposed Ni–N_3S_2 complex would be a significant step toward realizing catalytic function in NiSOD small molecule analogues and would explain the lack of reactivity of models **7–18**. The corresponding Ni(II) complex with this

N_3S_2ligand, namely K[Ni(N_3S_2)] [**19** (Figure 2.10)], was prepared by reacting the ligand with $Ni(OAc)_2 \cdot 4H_2O$ and NaOAc in MeOH to afford **19** in high yield.[67]

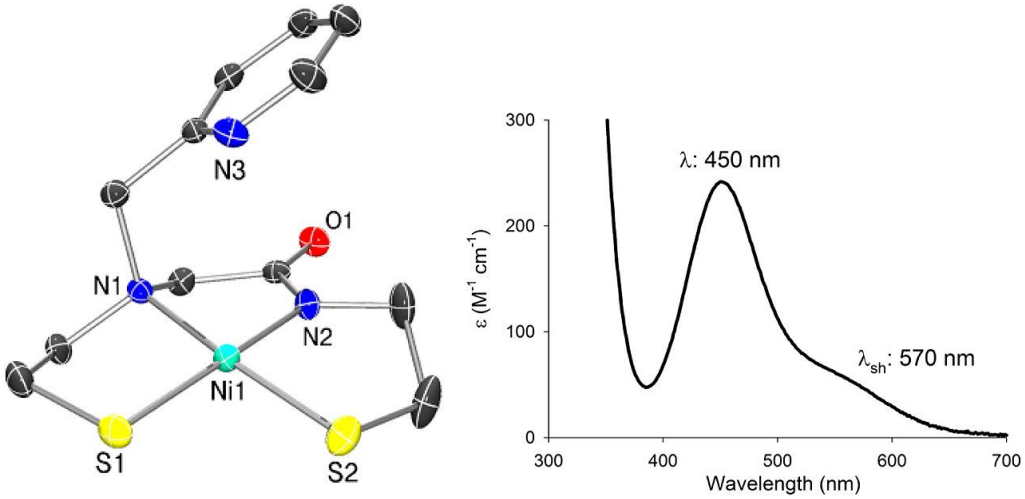

Figure 2.10 X-ray crystal structure of the anion of K[Ni(N_3S_2)] (**19**) (left). The electronic absorption spectrum of **19** in pH 7.5 PIPES buffer at 25 °C (right).

Complex **19** has been characterized by X-ray crystallography, UV–vis, FTIR, ^{1}H NMR, CV, and ESI-MS. Much like peptide models **15–18** described above, **19** also demonstrated excellent water solubility. Additionally, **19** is very stable in buffered media; no multiple speciation was observed as monitored by ^{1}H NMR and UV–vis spectroscopies. This stability is likely due to the chelate effect of the N_3S_2ligand. The UV–vis spectrum of **19** in pH 7.5 PIPES buffer resembled the maquette and $NiSOD_{red}$ spectrum with double-humped ligand-field bands at 449 nm (ε = 230 M^{-1} cm^{-1}) and 570 nm (ε = 50 M^{-1} cm^{-1}) (Figure 2.10). The structural features are comparable to prior models (see Table 2.2) featuring a 4C Ni(II)–N_2S_2 planar complex with the only exception of the noncoordinated pyridine-N situated ~3.2 Å and tilted away from the metal. The Ni–

N_{py} distance of this potential fifth ligand and the tilt of the pyridine plane are structurally analogous to the values observed for $NiSOD_{red}$. The electrochemistry of **19** displayed the typical irreversible behavior even with a potential N-donor in the ligand frame with an E_{ox} of −0.125 V (DMF vs Ag/AgCl). However, a new reduction wave was found at E_{red} = −1.44 V, which only appeared when the oxidized species was traversed. The large ΔE_p (∼1.2 V) suggested that a significant structural rearrangement occurred during the redox process. To identify the site of the redox process, bulk oxidation was performed with Fc^+, which resulted in dinuclear disulfide-linked species **20** that formed from a transient 5C Ni(III) intermediate (Scheme 2.1). Interestingly, the S atoms in the disulfide linkage of **20** originate from the S-donor *trans* to the carboxamide-N in **19**, highlighting the lability of this particular ligand and potentially Cys6 in NiSOD. This conversion mimics the same redox and coordination geometry change as observed in NiSOD. While the results suggested that the axial His1-Im ligand in NiSOD is not entirely responsible for Ni-based redox, it still appears to be critical for keeping the coordination sphere intact to prevent polymeric RSSR formation. Thus, His1-N binding in combination with the protein structure is primarily responsible for Ni(III/II) cycling in NiSOD. Further support for this hypothesis comes from theoretical studies of the enzyme, which suggest a primarily S-based HOMO in $NiSOD_{red}$[23] along with the long Ni(III)–$N_{imidazole}$ distance (∼2.5 Å) observed in $NiSOD_{ox}$.[18]

Scheme 2.1 Proposed mechanism of the oxidative conversion of the $NiSOD_{red}$ model complex **19** to the disulfide linked complex **20**.[a]

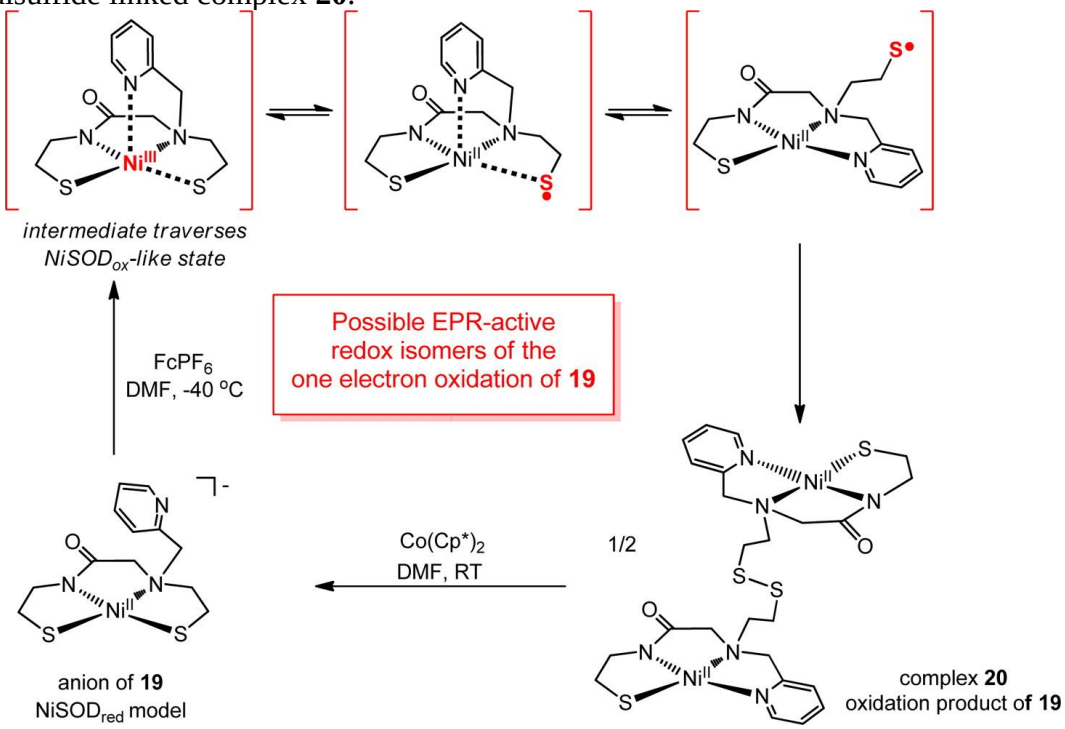

[a]Hypothesized intermediates are shown in red brackets, with paramagnetic atoms shown in bold and colored red. $FcPF_6$ is the chemical oxidant ferrocenium hexafluorophosphate; $CoCp^*_2$ is the chemical reductant decamethylcobaltocene. This scheme was adapted from ref. 69.

2.4 Summary and Outlook

NiSOD presents numerous structural and spectroscopic characteristics that distinguish it from other members of the SOD family; however, it is certainly representative of redox-active Ni metalloenzymes. As such, the results of synthetic modeling work have revealed valuable information regarding the properties of this unique Ni coordination environment. It is evident that the mixed amine/peptide-N ligands assist in the stabilization of high-valent Ni(III) as well as the low-spin electronic configuration of the metal. It is believed that the unique asymmetric N-donor set, in combination with the two CysS-donors, sufficiently depresses the Ni(III/II) redox couple so that it is physiologically accessible and within the window of the superoxide redox potentials. All

of the models report redox potentials in this range (see Tables 2.1 and 2.2). The $N_{amine}N_{carboxamide}S_2$coordination environment also provides kinetic stability against O_2 and H_2O_2 (the products of SOD) under turnover conditions as noted in several analogues. Some of the model systems demonstrate SOD functionality albeit at rates significantly lower than that of the enzyme. Of these functional models, most contain an axial N-ligand. Indeed, NiSOD His1 mutants and certain maquette models that do not have this ligand demonstrate low activity. We suspect that this ligand is crucial in NiSOD. While approximate models such as **5** highlight the potential for functionality even in the absence of a fifth ligand, it appears that the basic requisite for SOD activity is a low-spin Ni center with the correct redox potential (see complex **6** that contains biologically irrelevant alkoxy ligands). To underscore the importance of His1 in terms of NiSOD function, the Ni(III) state is only achieved, at least transiently, in low-MW accurate models that contain this or a similar type of ligand (e.g., py-N).

With regard to the NiSOD catalytic mechanism, the synthetic analogue, biochemical, and theoretical data have led to the following postulates. The 4C square-planar $NiSOD_{red}$ site observed in the crystal structure is likely a resting state of the enzyme that is not catalytically active. Indeed, models such as **7–18** that accurately reproduce the structure and electronic spectrum of $NiSOD_{red}$ but lack a fifth axial N-ligand exhibit mostly irreversible redox potentials (ligand-based redox processes, disulfide formation) and no SOD activity. The one system that displays quasi-reversible redox behavior (**7**) has never been isolated or proven to be Ni(III). This result can be explained by the electronic structure that defines the nature of the frontier MO involved in this redox process. This MO has significant contributions of both S-pπ and Ni-dπ character, which are symptomatic of a highly covalent Ni–S bond (Figure 2.11).

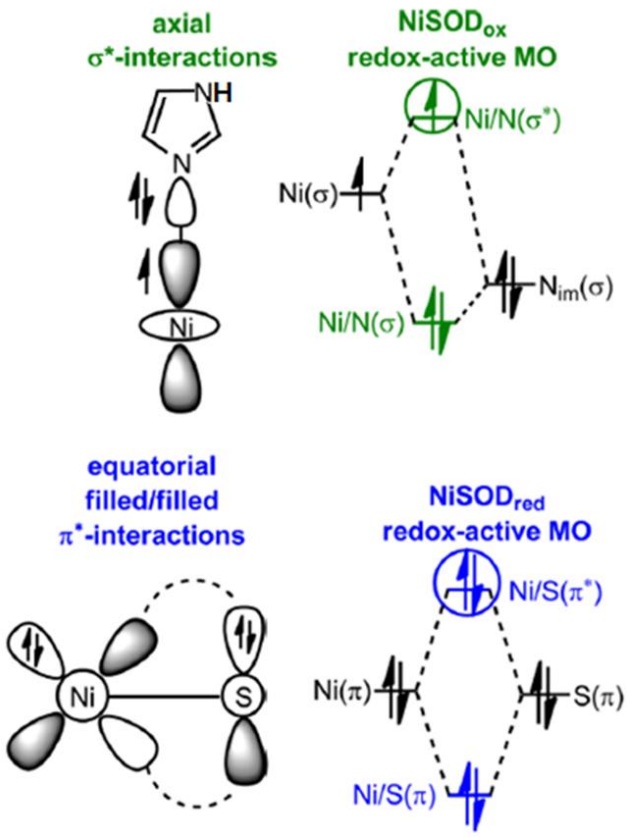

Figure 2.11 Frontier MOs and illustration of the dominant bonding interactions in $NiSOD_{ox}$ (top) and $NiSOD_{red}$ (bottom). This figure was adapted from ref 23.

In theoretical studies of NiSOD, this MO exhibits predominantly S-pπ character as well (HOMO, 26% Ni-dπ and 66% S-pπ; HOMO-1, 36% Ni-dπ and 45% S-pπ).[23] This result is not at all unique to $NiSOD_{red}$ and has been demonstrated in all accurate Ni(II)–N_2S_2 models (**7–19**), which display significant contributions from both Ni and S in this redox-active MO. This begs the question of what prevents S-oxidation in the enzyme. One possibility is that NiSOD has evolved to prevent S-oxidation by destabilizing the Ni-based AOs or by stabilizing the S-based ligand group orbitals by some mechanism that cannot be modeled accurately by DFT. Either change will yield a redox-active MO with more Ni-character. Stabilization of S-based orbitals has been demonstrated through H-bonding interactions both computationally[39,40,46] and experimentally[74] to

increase the level of Ni character and decrease the nucleophilicity (viz. oxygen reactivity) of the H-bonded sulfur. In addition to S-protection from ROS, full protonation of the coordinated cysteinates to cysteine thiols could serve as a reservoir for H^+ in the formation of H_2O_2 (eq 2.2). This proposal has been advocated by separate DFT studies.[40,46] Another postulate is that the Ni center remains 5C throughout catalysis.[40,54] Examination of the electronic structure of $NiSOD_{ox}$ reveals a redox-active MO with predominantly Ni-dσ character that is antibonding with respect to the Ni-d_z^2(dσ) AO and N-pσ orbital of the axial His ligand (Figure 2.11).[23] This electronic structure explains the hyperfine feature in the EPR as well as the relatively long Ni–HisN bond in the NiSOD structures. If this orbital was the redox-active MO during catalysis, then one would expect the Ni–HisN distance to vary during turnover, which would result in the atypical Ni–Im distance. This analysis excludes the effects imparted by the H-bonding network, His1-Glu17-Arg47. A 5C active species would also minimize the reorganizational energy (λ) that occurs during eT, which has been suggested for functional maquette system **2**.[54] This explanation makes intuitive sense as eT rates are inherently faster than bond-forming and/or -breaking rates. Additionally, all model systems that have been isolated in the Ni(III) form contain the Im axial ligand. We thus propose the mechanism as highlighted in Scheme 2.2. The debate over outer-sphere versus inner-sphere redox still remains, and we will not attempt to elect one in the present account, although their differences are noted in Scheme 2.2. Most of the biochemical evidence points toward an outer-sphere mechanism that includes (i) the lack of rate dependence on the ionic strength of the medium, (ii) no evidence of small anions such as N_3^-, even in large excess, binding to Ni, and (iii) the presence of a noncoordinated Cl^- ligand in the X-ray structure of the NiSOD Tyr9Phe mutant positioned ~3.5 Å from the Ni center (a suggested superoxide binding site). An outer-sphere mechanism would also keep ROS away from and protect the CysS-ligands from S-oxidation and/or

oxygenation. To date, most of the model work is supportive of this proposal. However, evidence of CN^- binding in some maquette models and theoretical studies of substrate coordination suggest otherwise. We anticipate that the bioinorganic synthetic modeling community will have a significant role in addressing these outlying issues in future NiSOD analogue systems.

Scheme 2.2 Proposed Active Forms of NiSOD during Outer-Sphere Turnover (black) and Potential Inner-Sphere Intermediates (gray, I and II)[a]

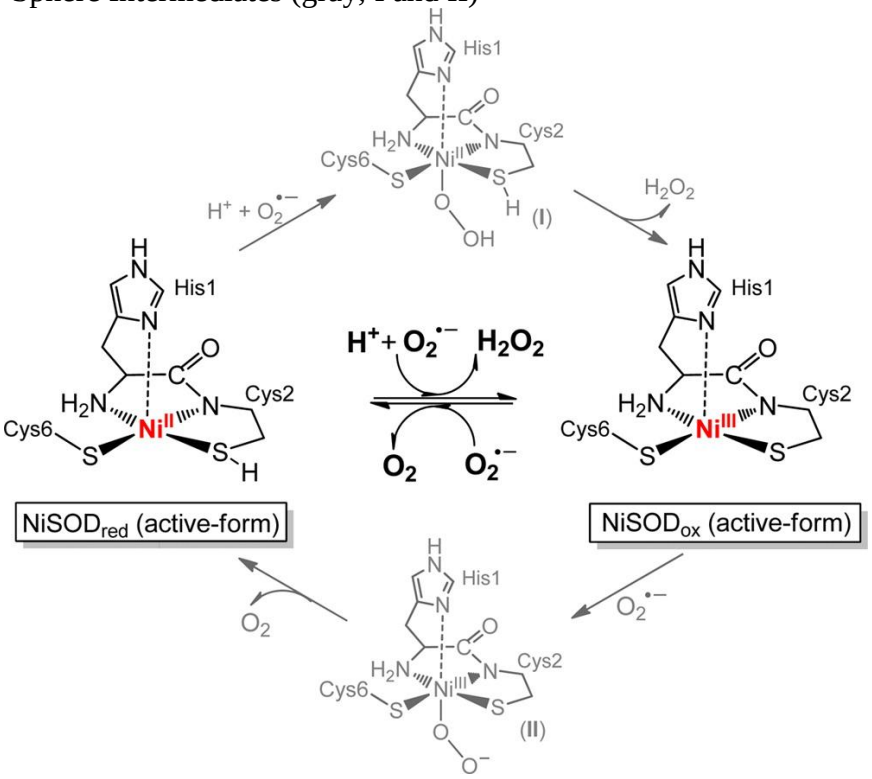

[a]Intermediate I may also be viewed as a Ni(III)−hydroperoxo species after internal transfer of an electron from Ni(II) to the coordinated hydrosuperoxo. The dashed line from HisN to Ni implies a relatively long bond as observed in the X-ray crystal structures of NiSOD (see refs 18 and 19). The protonation of both cysteinates has not been widely established; however, either cysteine is a likely candidate, and we have chosen Cys2 in this depiction for the sake of clarity. If only one CysSH is present, a protonated hydrosuperoxo radical (HOO•) has been proposed to enter the active site (see ref 40) despite the known superoxide pK_a of 4.8.

2.5 References

(1) Valentine, J. S.; Wertz, D. L.; Lyons, T. J.; Liou, L.-L.; Goto, J. J.; Gralla, E. B. The dark side of dioxygen biochemistry. *Curr. Opin. Chem. Biol.* **1998**, *2*, 253-262.

(2) McCord, J. M. Oxidative stress related diseases—overview. In *Critical Reviews of Oxidative Stress and Aging: Advances in Basic Science, Diagnostics, and Intervention*, Rodriguez, H.; Cutler, R., Eds. World Scientific Publishing Co. Pte. Ltd.: Singapore, 2003; Vol. 2, pp 883-895.

(3) Maritim, A. C.; Sanders, R. A.; Watkins, J. B., III Diabetes, Oxidative Stress, and Antioxidants: A Review. *J. Biochem. Mol. Toxicol.* **2003**, *17*, 24-38.

(4) Kocatürk, P. A.; Akbostanci, M. C.; Tan, F.; Kavas, G. Ö. Superoxide dismutase activity and zinc and copper concentrations in Parkinson's disease. *Pathophysiology* **2000**, *7*, 63-67.

(5) De Leo, M. E.; Borrello, S.; Passantino, M.; Palazzotti, B.; Mordente, A.; Daniele, A.; Filippini, V.; Galeotti, T.; Masullo, C. Oxidative stress and overexpression of manganese superoxide dismutase in patients with Alzheimer's disease. *Neurosci. Lett.* **1998**, *250*, 173-176.

(6) Fortunato, G.; Pastinese, A.; Intrieri, M.; Lofrano, M. M.; Gaeta, G.; Censi, M. B.; Boccalatte, A.; Salvatore, F.; Sacchetti, L. Serum Mn-Superoxide Dismutase in Acute Myocardial Infarction. *Clin. Biochem.* **1997**, *30*, 569-571.

(7) Miller, A.-F. Superoxide dismutases: active sites that save, but a protein that kills. *Curr. Opin. Chem. Biol.* **2004**, *8*, 162-168.

(8) Fridovich, I. Superoxide Dismutase. In *Encyclopedia of Biological Chemistry*, 1st ed.; Lennarz, W. J.; Lane, M. D., Eds. Elsevier: New York, 2004; Vol. 4, pp 135-138.

(9) Tainer, J. A.; Getzoff, E. D.; Richardson, J. S.; Richardson, D. C. Structure and mechanism of copper, zinc superoxide dismutase. *Nature* **1983**, *306*, 284-287.

(10) Borgstahl, G. E. O.; Parge, H. E.; Hickey, M. J.; Beyer, W. F., Jr.; Hallewell, R. A.; Tainer, J. A. The structure of human mitochondrial manganese superoxide dismutase reveals a novel tetrameric interface of two 4-helix bundles. *Cell* **1992**, *71*, 107-118.

(11) Grove, L. E.; Brunold, T. C. Second-Sphere Tuning of the Metal Ion Reduction Potentials in Iron and Manganese Superoxide Dismutases. *Comments Inorg. Chem.* **2008**, *29*, 134-168.

(12) Miller, A.-F. Redox Tuning over Almost 1 V in a Structurally Conserved Active Site: Lessons from Fe-Containing Superoxide Dismutase. *Acc. Chem. Res.* **2008**, *41*, 501-510.

(13) Tierney, D. L.; Fee, J. A.; Ludwig, M. L.; Penner-Hahn, J. E. X-ray Absorption Spectroscopy of the Iron Site in *Escherichia coli* Fe(III) Superoxide Dismutase. *Biochemistry* **1995**, *34*, 1661-1668.

(14) Grove, L. E.; Xie, J.; Yikilmaz, E.; Karapetyan, A.; Miller, A.-F.; Brunold, T. C. Spectroscopic and Computational Insights into Second-Sphere Amino-Acid Tuning of Substrate Analogue/Active-Site Interactions in Iron(III) Superoxide Dismutase. *Inorg. Chem.* **2008**, *47*, 3993-4004.

(15) Brown, R. H., Jr. SOD1 aggregates in ALS: Cause, correlate or consequence? *Nature Med.* **1998**, *4*, 1362-1364.

(16) Youn, H.-D.; Youn, H.; Lee, J.-W.; Yim, Y.-I.; Lee, J. K.; Hah, Y. C.; Kang, S.-O. Unique Isozymes of Superoxide Dismutase in *Streptomyces griseus*. *Arch. Biochem. Biophys.* **1996**, *334*, 341-348.

(17) Palenik, B.; Brahamsha, B.; Larimer, F. W.; Land, M.; Hauser, L.; Chain, P.; Lamerdin, J.; Regala, W.; Allen, E. E.; McCarren, J.; Paulsen, I.; Dufresne, A.; Partensky, F.; Webb, E. A.; Waterbury, J. The genome of a motile marine *Synechococcus*. *Nature* **2003**, *424*, 1037-1042.

(18) Barondeau, D. P.; Kassmann, C. J.; Bruns, C. K.; Tainer, J. A.; Getzoff, E. D. Nickel Superoxide Dismutase Structure and Mechanism. *Biochemistry* **2004**, *43*, 8038-8047.

(19) Wuerges, J.; Lee, J.-W.; Yim, Y.-I.; Yim, H.-S.; Kang, S.-O.; Carugo, K. D. Crystal structure of nickel-containing superoxide dismutase reveals another type of active site. *Proc. Natl. Acad. Sci. U. S. A.* **2004**, *101*, 8569-8574.

(20) Herbst, R. W.; Guce, A.; Bryngelson, P. A.; Higgins, K. A.; Ryan, K. C.; Cabelli, D. E.; Garman, S. C.; Maroney, M. J. Role of Conserved Tyrosine Residues in NiSOD Catalysis: A Case of Convergent Evolution. *Biochemistry* **2009**, *48*, 3354-69.

(21) Harrop, T. C.; Mascharak, P. K. Model Complexes of Ni-Containing Enzymes. In *Concepts and Models in Bioinorganic Chemistry*, Kraatz, H.-B.; Metzler-Nolte, N., Eds. Wiley-VCH: Weinheim, Germany, 2006; pp 309-329.

(22) Choudhury, S. B.; Lee, J.-W.; Davidson, G.; Yim, Y.-I.; Bose, K.; Sharma, M. L.; Kang, S.-O.; Cabelli, D. E.; Maroney, M. J. Examination of the Nickel Site Structure and Reaction Mechanism in *Streptomyces seoulensis* Superoxide Dismutase. *Biochemistry* **1999**, *38*, 3744-3752.

(23) Fiedler, A. T.; Bryngelson, P. A.; Maroney, M. J.; Brunold, T. C. Spectroscopic and Computational Studies of Ni Superoxide Dismutase: Electronic Structure Contributions to Enzymatic Function. *J. Am. Chem. Soc.* **2005**, *127*, 5449-5462.

(24) Krüger, H.-J.; Peng, G.; Holm, R. H. Low-Potential Nickel(III,II) Complexes: New Systems Based on Tetradentate Amidate–Thiolate Ligands and the Influence of Ligand Structure on Potentials in Relation to the Nickel Site in [NiFe]-Hydrogenases. *Inorg. Chem.* **1991**, *30*, 734-742.

(25) Fiedler, A. T.; Brunold, T. C. Spectroscopic and Computational Studies of Ni^{3+} Complexes with Mixed S/N Ligation: Implications for the Active Site of Nickel Superoxide Dismutase. *Inorg. Chem.* **2007**, *46*, 8511-8523.

(26) Xiao, Y.; Wang, H.; George, S. J.; Smith, M. C.; Adams, M. W.; Jenney, F. E., Jr.; Sturhahn, W.; Alp, E. E.; Zhao, J.; Yoda, Y.; Dey, A.; Solomon, E. I.; Cramer, S. P. Normal mode analysis of *Pyrococcus furiosus* Rubredoxin via nuclear resonance vibrational spectroscopy (NRVS) and resonance raman spectroscopy. *J. Am. Chem. Soc.* **2005**, *127*, 14596-606.

(27) Han, S.; Czernuszewicz, R. S.; Kimura, T.; Adams, M. W. W.; Spiro, T. G., Fe_2S_2 Protein Resonance Raman Spectra Revisited: Structural Variations among Adrenodoxin, Ferredoxin, and Red Paramagnetic Protein. In *J. Am. Chem. Soc.*, American Chemical Society: 1989; Vol. 111, pp 3505-3511.

(28) Qiu, D.; Kilpatrick, L.; Kitajima, N.; Spiro, T. G. Modeling blue copper protein resonance Raman spectra with thiolate-CuII complexes of a sterically hindered tris(pyrazolyl)borate. *J. Am. Chem. Soc.* **1994**, *116*, 2585-2590.

(29) Qiu, D.; Dasgupta, S.; Kozlowski, P. M.; Goddard, W. A.; Spiro, T. G. Chromophore-in-Protein Modeling of the Structures and Resonance Raman Spectra for Type 1 Copper Proteins. *J. Am. Chem. Soc.* **1998**, *120*, 12791-12797.

(30) Bryngelson, P. A.; Arobo, S. E.; Pinkham, J. L.; Cabelli, D. E.; Maroney, M. J. Expression, Reconstitution, and Mutation of Recombinant *Streptomyces coelicolor* NiSOD. *J. Am. Chem. Soc.* **2004**, *126*, 460-461.

(31) Ryan, K. C.; Johnson, O. E.; Cabelli, D. E.; Brunold, T. C.; Maroney, M. J. Nickel superoxide dismutase: structural and functional roles of Cys2 and Cys6. *JBIC, J. Biol. Inorg. Chem.* **2010**, *15*, 795-807.

(32) Johnson, O. E.; Ryan, K. C.; Maroney, M. J.; Brunold, T. C. Spectroscopic and computational investigation of three Cys-to-Ser mutants of nickel superoxide dismutase: insight into the roles played by the Cys2 and Cys6 active-site residues. *JBIC, J. Biol. Inorg. Chem.* **2010**, *15*, 777-793.

(33) Lawrence, G. D.; Sawyer, D. T. Potentiometric titrations and oxidation-reduction potentials of manganese and copper-zinc superoxide dismutases. *Biochemistry* **1979**, *18*, 3045-50.

(34) Barrette, W. C., Jr.; Sawyer, D. T.; Fee, J. A.; Asada, K. Potentiometric titrations and oxidation--reduction potentials of several iron superoxide dismutases. *Biochemistry* **1983**, *22*, 624-627.

(35) Sawyer, D. T.; Valentine, J. S. How Super Is Superoxide? *Acc. Chem. Res.* **1981**, *14*, 393-400.

(36) Uudsemaa, M.; Tamm, T. Density-functional theory calculations of aqueous redox potentials of fourth-period transition metals. *J. Phys. Chem. A* **2003**, *107*, 9997-10003.

(37) Shearer, J.; Dehestani, A.; Abanda, F. Probing Variable Amine/Amide Ligation in $Ni^{II}N_2S_2$ Complexes Using Sulfur K-Edge and Nickel L-Edge X-ray Absorption Spectroscopies: Implications for the Active Site of Nickel Superoxide Dismutase. *Inorg. Chem.* **2008**, *47*, 2649-2660.

(38) Grapperhaus, C. A.; Darensbourg, M. Y. Oxygen Capture by Sulfur in Nickel Thiolates. *Acc. Chem. Res.* **1998**, *31*, 451-459.

(39) Mullins, C. S.; Grapperhaus, C. A.; Kozlowski, P. M. Density functional theory investigations of NiN_2S_2 reactivity as a function of nitrogen donor type and N–H···S hydrogen bonding inspired by nickel-containing superoxide dismutase. *JBIC, J. Biol. Inorg. Chem.* **2006**, *11*, 617-625.

(40) Pelmenschikov, V.; Siegbahn, P. E. M. Nickel Superoxide Dismutase Reaction Mechanism Studied by Hybrid Density Functional Methods. *J. Am. Chem. Soc.* **2006**, *128*, 7466-7475.

(41) Neupane, K. P.; Shearer, J. The Influence of Amine/Amide versus Bisamide Coordination in Nickel Superoxide Dismutase. *Inorg. Chem.* **2006**, *45*, 10552-10566.

(42) Zilbermann, I.; Maimon, E.; Cohen, H.; Meyerstein, D. Redox Chemistry of Nickel Complexes in Aqueous Solutions. *Chem. Rev.* **2005**, *105*, 2609-2625.

(43) Halcrow, M. A.; Christou, G. Biomimetic Chemistry of Nickel. *Chem. Rev.* **1994**, *94*, 2421-2481.

(44) Ragsdale, S. W. Nickel biochemistry. *Curr. Opin. Chem. Biol.* **1998**, *2*, 208-215.

(45) Ragsdale, S. W. Nickel-based Enzyme Systems. *J. Biol. Chem.* **2009**, *284*, 18571-18575.

(46) Prabhakar, R.; Morokuma, K.; Musaev, D. G. A DFT Study of the Mechanism of Ni Superoxide Dismutase (NiSOD): Role of the Active Site Cysteine-6 Residue in the Oxidative Half-Reaction. *J. Comput. Chem.* **2006**, *27*, 1438-1445.

(47) Szilagyi, R. K.; Bryngelson, P. A.; Maroney, M. J.; Hedman, B.; Hodgson, K. O.; Solomon, E. I. S K-edge X-ray Absorption Spectroscopic Investigation of the Ni-Containing Superoxide Dismutase Active Site: New Structural Insight into the Mechanism. *J. Am. Chem. Soc.* **2004**, *126*, 3018-3019.

(48) Lanzilotta, W. N.; Schuller, D. J.; Thorsteinsson, M. V.; Kerby, R. L.; Roberts, G. P.; Poulos, T. L. Structure of the CO sensing transcription activator CooA. *Nat. Struct. Mol. Biol.* **2000**, *7*, 876-880.

(49) Nagashima, S.; Nakasako, M.; Dohmae, N.; Tsujimura, M.; Takio, K.; Odaka, M.; Yohda, M.; Kamiya, N.; Endo, I. Novel non-heme iron center of nitrile hydratase with a claw setting of oxygen atoms. *Nat. Struct. Mol. Biol.* **1998**, *5*, 347-351.

(50) Darnault, C.; Volbeda, A.; Kim, E. J.; Legrand, P.; Vernede, X.; Lindahl, P. A.; Fontecilla-Camps, J. C. Ni-Zn-[Fe_4-S_4] and Ni-Ni-[Fe_4-S_4] clusters in closed and open α subunits of acetyl-CoA synthase/carbon monoxide dehydrogenase. *Nature Structural Biology* **2003**, *10*, 271-279.

(51) Peters, J. W.; Stowell, M. H. B.; Soltis, S. M.; Finnegan, M. G.; Johnson, M. K.; Rees, D. C. Redox-dependent structural changes in the nitrogenase P-cluster. *Biochemistry* **1997**, *36*, 1181-1187.

(52) Ibers, J. A.; Holm, R. H. Modeling Coordination Sites in Metallobiomolecules. *Science* **1980**, *209*, 223-235.

(53) Shearer, J.; Long, L. M. A Nickel Superoxide Dismutase Maquette That Reproduces the Spectroscopic and Functional Properties of the Metalloenzyme. *Inorg. Chem.* **2006**, *45*, 2358-2360.

(54) Neupane, K. P.; Gearty, K.; Francis, A.; Shearer, J. Probing Variable Axial Ligation in Nickel Superoxide Dismutase Utilizing Metallopeptide-Based Models: Insight into the Superoxide Disproportionation Mechanism. *J. Am. Chem. Soc.* **2007**, *129*, 14605-14618.

(55) Shearer, J.; Neupane, K. P.; Callan, P. E. Metallopeptide Based Mimics with Substituted Histidines Approximate a Key Hydrogen Bonding Network in the Metalloenzyme Nickel Superoxide Dismutase. *Inorg. Chem.* **2009**, *48*, 10560-10571.

(56) Schmidt, M.; Zahn, S.; Carella, M.; Ohlenschläger, O.; Görlach, M.; Kothe, E.; Weston, J. Solution Structure of a Functional Biomimetic and Mechanistic Implications for Nickel Superoxide Dismutases. *ChemBioChem* **2008**, *9*, 2135-2146.

(57) Tietze, D.; Breitzke, H.; Imhof, D.; Kothe, E.; Weston, J.; Buntkowsky, G. New Insight into the Mode of Action of Nickel Superoxide Dismutase by Investigating Metallopeptide Substrate Models. *Chem. - Eur. J.* **2009**, *15*, 517-523.

(58) Tietze, D.; Tischler, M.; Voigt, S.; Imhof, D.; Ohlenschläger, O.; Görlach, M.; Buntkowsky, G. Development of a Functional *cis*-Prolyl Bond Biomimetic and Mechanistic Implications for Nickel Superoxide Dismutase. *Chem. - Eur. J.* **2010**, *16*, 7572-7578.

(59) Tietze, D.; Voigt, S.; Mollenhauer, D.; Tischler, M.; Imhof, D.; Gutmann, T.; González, L.; Ohlenschläger, O.; Breitzke, H.; Görlach, M.; Buntkowsky, G. Revealing the Position of the Substrate in Nickel Superoxide Dismutase: A Model Study. *Angew. Chem., Int. Ed.* **2011**, *50*, 2946-2950.

(60) Krause, M. E.; Glass, A. M.; Jackson, T. A.; Laurence, J. S. Novel Tripeptide Model of Nickel Superoxide Dismutase. *Inorg. Chem.* **2010**, *49*, 362-364.

(61) Krause, M. E.; Glass, A. M.; Jackson, T. A.; Laurence, J. S. MAPping the Chiral Inversion and Structural Transformation of a Metal-Tripeptide Complex Having Ni-Superoxide Dismutase Activity. *Inorg. Chem.* **2011**, *50*, 2479-2487.

(62) Glass, A. M.; Krause, M. E.; Laurence, J. S.; Jackson, T. A. Controlling the Chiral Inversion Reaction of the Metallopeptide Ni-Asparagine-Cysteine-Cysteine with Dioxygen. *Inorg. Chem.* **2012**, *51*, 10055-10063.

(63) Ma, H.; Chattopadhyay, S.; Petersen, J. L.; Jensen, M. P. Harnessing Scorpionate Ligand Equilibria for Modeling Reduced Nickel Superoxide Dismutase Intermediates. *Inorg. Chem.* **2008**, *47*, 7966-7968.

(64) Ma, H.; Wang, G.; Yee, G. T.; Petersen, J. L.; Jensen, M. P. Scorpionate-supported models of nickel-dependent superoxide dismutase. *Inorg. Chim. Acta* **2009**, *362*, 4563-4569.

(65) Lee, W.-Z.; Chiang, C.-W.; Lin, T.-H.; Kuo, T.-S. A Discrete Five-Coordinate Ni^{III} Complex Resembling the Active Site of the Oxidized Form of Nickel Superoxide Dismutase. *Chem. - Eur. J.* **2012**, *18*, 50-53.

(66) Nakane, D.; Funahashi, Y.; Ozawa, T.; Masuda, H. A Square-planar Ni(II) Complex with an Asymmetric N_2S_2 Donor Set as a Model for the Active Site of Nickel-containing SOD: Structural Conversion Driven by Addition of a Strong Donor Ligand in the High Oxidation State. *Chem. Lett.* **2010**, *39*, 344-346.

(67) Shearer, J.; Zhao, N. $[Me_4N](Ni^{II}(BEAAM))$: A Synthetic Model for Nickel Superoxide Dismutase That Contains Ni in a Mixed Amine/Amide Coordination Environment. *Inorg. Chem.* **2006**, *45*, 9637-9639.

(68) Mathrubootham, V.; Thomas, J.; Staples, R.; McCraken, J.; Shearer, J.; Hegg, E. L. Bisamidate and Mixed Amine/Amidate NiN_2S_2 Complexes as Models for Nickel-Containing Acetyl Coenzyme A Synthase and Superoxide Dismutase: An Experimental and Computational Study. *Inorg. Chem.* **2010**, *49*, 5393-5406.

(69) Gale, E. M.; Simmonett, A. C.; Telser, J.; Schaefer, H. F., III; Harrop, T. C. Toward Functional Ni-SOD Biomimetics: Achieving a Structural/Electronic Correlation with Redox Dynamics. *Inorg. Chem.* **2011**, *50*, 9216-9218.

(70) Jenkins, R. M.; Singleton, M. L.; Almaraz, E.; Reibenspies, J. H.; Darensbourg, M. Y. Imidazole-Containing (N_3S)-Ni^{II} Complexes Relating to Nickel Containing Biomolecules. *Inorg. Chem.* **2009**, *48*, 7280-7293.

(71) Mullins, C. S.; Grapperhaus, C. A.; Frye, B. C.; Wood, L. H.; Hay, A. J.; Buchanan, R. M.; Mashuta, M. S. Synthesis and Sulfur Oxygenation of a (N_3S)Ni Complex Related to Nickel-Containing Superoxide Dismutase. *Inorg. Chem.* **2009**, *48*, 9974-9976.

(72) Herdt, D. R.; Grapperhaus, C. A. Kinetic study of nickel-thiolate oxygenation by hydrogen peroxide. Implications for nickel-containing superoxide dismutase. *Dalton Trans.* **2012**, *41*, 364-366.

(73) Gale, E. M.; Patra, A. K.; Harrop, T. C. Versatile Methodology Toward NiN_2S_2 Complexes as Nickel Superoxide Dismutase Models: Structure and Proton Affinity. *Inorg. Chem.* **2009**, *48*, 5620-5622.

(74) Gale, E. M.; Narendrapurapu, B. S.; Simmonett, A. C.; Schaefer, H. F., III; Harrop, T. C. Exploring the Effects of H-Bonding in Synthetic Analogues of Nickel Superoxide Dismutase (Ni-SOD): Experimental and Theoretical Implications for Protection of the Ni–SCys Bond. *Inorg. Chem.* **2010**, *49*, 7080-7096.

(75) Gale, E. M.; Cowart, D. M.; Scott, R. A.; Harrop, T. C. Dipeptide-Based Models of Nickel Superoxide Dismutase: Solvent Effects Highlight a Critical Role to Ni–S Bonding and Active Site Stabilization. *Inorg. Chem.* **2011**, *50*, 10460-10471.

(76) Colpas, G. J.; Maroney, M. J.; Bagyinka, C.; Kumar, M.; Willis, W. S.; Suib, S. L.; Baidya, N.; Mascharak, P. K. X-ray Spectroscopic Studies of Nickel Complexes, with Application to the Structure of Nickel Sites in Hydrogenases. *Inorg. Chem.* **1991**, *30*, 920-928.

(77) Connelly, N. G.; Geiger, W. E. Chemical Redox Agents for Organometallic Chemistry. *Chem. Rev.* **1996**, *96*, 877-910.

(78) Bard, A. J. a. F., L. R., *Electrochemical Methods : Fundamentals and Applications*. 2nd ed. ed.; New York: Wiley, 2000.

(79) Hanss, J.; Krüger, H.-J. First Isolation and Structural Characterization of a Nickel(III) Complex Containing Aliphatic Thiolate Donors. *Angew. Chem., Int. Ed.* **1998**, *37*, 360-363.

CHAPTER 3

STERIC ENFORCEMENT ABOUT ONE THIOLATE DONOR LEADS TO NEW OXIDATION CHEMISTRY IN A NISOD MODEL COMPLEX[1]

[1] Truong, P. T.; Gale, E. M.; Dzul, S. P.; Stemmler, T. L.; Harrop, T. C. *Inorg. Chem.* **2017**, 56, 7761-7780.

3.1 Abstract

Ni-containing superoxide dismutase (NiSOD) represents an unusual member of the SOD family due to the presence of oxygen-sensitive Ni–SCys bonds at its active site. Reported in this account is the synthesis and properties of the Ni^{II} complex of the N_3S_2 ligand $[N_3S_2^{Me2}]^{3-}$ ($[N_3S_2^{Me2}]^{3-}$ = deprotonated form of 2-((2-mercapto-2-methylpropyl)(pyridin-2-ylmethyl)amino)-*N*-(2-mercaptoethyl)acetamide), namely $Na[Ni(N_3S_2^{Me2})]$ (**2**), as a NiSOD model that features sterically robust *gem*-$(CH_3)_2$ groups on the thiolate α-C positioned trans to the carboxamide. The crystal structure of **2**, coupled with spectroscopic measurements from ^{1}H NMR, X-ray absorption, IR, UV–vis, and mass spectrometry (MS), reveal a planar Ni^{II} (S = 0) ion coordinated by only the N_2S_2 basal donors of the N_3S_2 ligand. While the structure and spectroscopic properties of **2** resemble those of $NiSOD_{red}$ and other models, the asymmetric S ligands open up new reaction paths upon chemical oxidation. One unusual oxidation product is the planar Ni^{II}–N_3S complex $[Ni(L^{ox})]$ (**5**; L^{ox} = 2-(5,5-dimethyl-2-(pyridin-2-yl)thiazolidin-3-yl)-*N*-(2-mercaptoethyl)acetamide), where two-electron oxidation takes place at the substituted thiolate and py-CH_2 carbon to generate a thiazolidine heterocycle. Electrochemical measurements of **2** reveal irreversible events wholly consistent with thiolate redox, which were identified by comparison to the Zn^{II} complex $Na[Zn(N_3S_2^{Me2})]$ (**3**). Although no reaction is observed between **2** and azide, reaction of **2** with superoxide produces multiple products on the basis of UV–vis and MS data, one of which is **5**. Density functional theory (DFT) computations suggest that the HOMO in **2** is π* with primary contributions from Ni-dπ/S-pπ orbitals. These contributions can be modulated and biased toward Ni when electron-withdrawing groups are placed on the thiolate α-C. Analysis of the oxidized five-coordinate species $\mathbf{2^{ox*}}$ by DFT reveal a singly occupied spin-up (α) MO that is

largely thiolate based, which supports the proposed Ni^{III}-thiolate/Ni^{II}-thiyl radical intermediates that ultimately yield **5** and other products.

3.2 Introduction

Superoxide dismutases (SODs) represent a family of enzymes that regulate superoxide ($O_2^{\bullet-}$) concentrations in cells, as well as control levels of other reactive oxygen species (ROS) derived from $O_2^{\bullet-}$, through a redox-active metal center.[1] Among this enzyme class, the Ni-containing SOD (NiSOD), found in soil microbes[2,3] and cyanobacteria,[4] is the outlier. Unlike other SODs, NiSOD employs cysteine sulfur (CysS) ligands that are susceptible to potentially damaging reactions with ROS to generate RSO_x^- (x = 1–3) or RS$^{\bullet}$/RSSR.[5-9] Structural analysis of NiSOD crystals from different *Streptomyces* strains demonstrate different coordination geometries in the Ni^{II} and Ni^{III} states, as displayed in Figure 3.1.[10,11] Reduced enzyme ($NiSOD_{red}$) consists of a square-planar Ni^{II}-N_2S_2 site from His1-NH_2, the Cys2-peptido-N, and the two S-thiolates of Cys2 and Cys6. Spectroscopic studies of $NiSOD_{red}$,[12-14] along with a peptide maquette model utilizing the first 12 residues of the enzyme with supporting theoretical analyses,[15,16] suggest that one of the CysS groups (likely Cys6) is a coordinated thiol. The active site of oxidized enzyme ($NiSOD_{ox}$) has an N_3S_2 square-pyramidal geometry, the main difference from $NiSOD_{red}$ being the addition of a His1-Nδ-Ni^{III} bond resulting in a low-spin (S = 1/2) rhombic EPR spectrum as a benchmark of this state.[10,17,18] Site-directed mutants,[19] especially those of His1-N[17,20] and the Cys2-peptide-N,[21] indicate that these residues are critical for function, due primarily to an inability of the mutants to achieve the high-valent Ni^{III} state. Further NiSOD variants, e.g., CysS-to-SerO (single and double mutants), result in inactive high-spin (S = 1) octahedral Ni^{II} centers.[22,23] Taken together,

this particular combination of N/S donors and their spatial disposition is critical for NiSOD function.

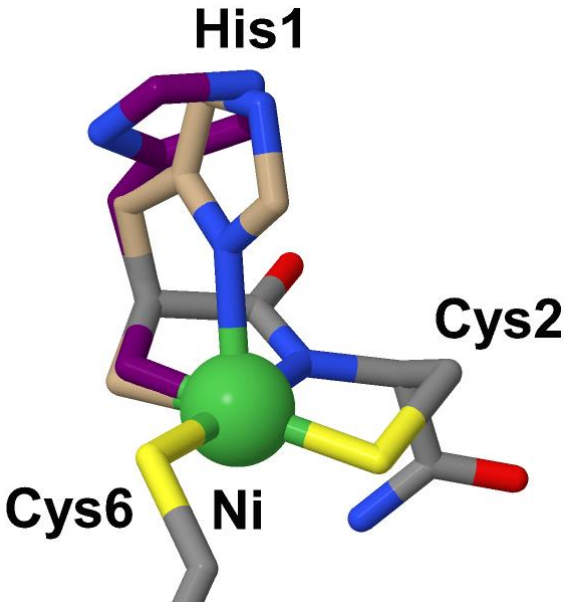

Figure 3.1 Jmol image of the active site of NiSOD from X-ray diffraction (*S. coelicolor*; PDB: 1T6U) showing primary coordinating ligands. The beige depiction of His1 represents $NiSOD_{ox}$, whereas the violet depiction of His1 represents $NiSOD_{red}$ (His1-Nδ not coordinated).

This unprecedented donor set has inspired synthetic inorganic chemists to generate discrete models of the enzyme active site in order to better understand its electronic structure and implications on NiSOD function.[24,25] Models of NiSOD range from peptide maquettes[15,16,26-34] and tripeptides[35-37] to low-molecular-weight (LMW) synthetic systems.[38-54] In particular, Shearer's maquettes provide the best NiSOD mimic from a structural and functional standpoint.[27,29] However, the functional maquette {$Ni(SOD^{m1})$} (SOD^{m1} = HCDLPCGVYDPA) goes through a mechanism that is proposed to be different from native NiSOD due to geometric

constraints in the maquette that are not present in the enzyme.[15,16] LMW analogues that approximate NiSOD indicate paths to Ni^{III} (without thiolate donors),[48] and even a planar Ni^{II}–N_3S complex displays some degree of SOD function.[43] In contrast, models more in-line with the N/S active site are relatively scarce (see Chart 3.1). Synthetic efforts by Shearer,[52] Hegg,[53] Masuda,[54] and our laboratory[51] have resulted in reasonable Ni^{II}–N_2S_2 complexes that are faithful mimics of the active site of $NiSOD_{red}$.

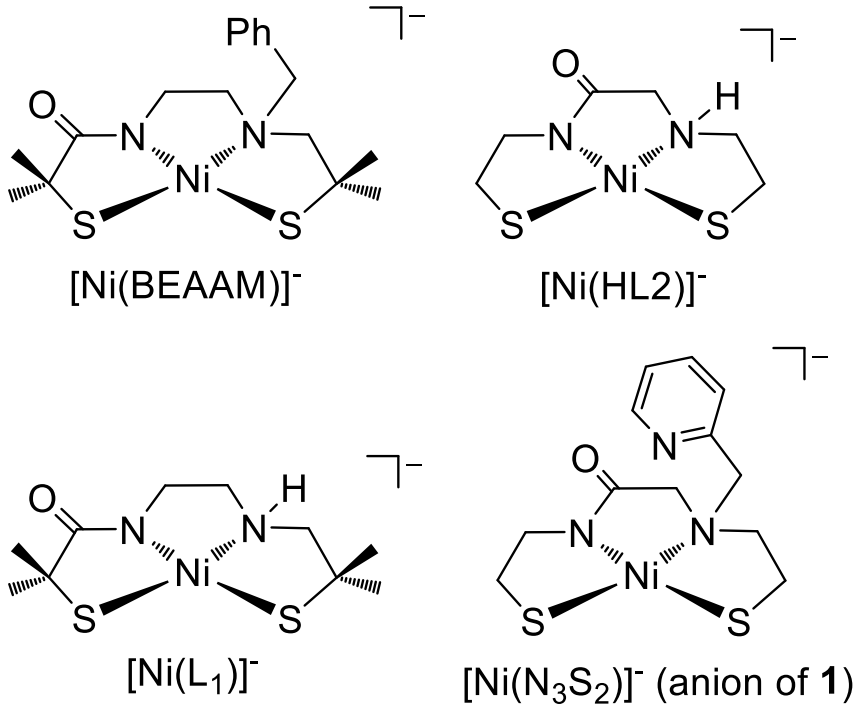

Chart 3.1 Structures of the anions of LMW NiSOD model complexes with the minimal $N_{carboxamide}N_{amine}S_2$ coordination sphere (counterions not shown).

In 2011, our laboratory described the synthesis, properties, and redox chemistry of the first model (nonmaquette) with all relevant donors that most closely mimic the NiSOD active site:

namely, K[Ni(N_3S_2)] (**1**) (where $[N_3S_2]^{3-}$ = deprotonated form of *N*-(2-mercaptoethyl)-2-((2-mercaptoethyl)(pyridin-2-ylmethyl)amino)acetamide).[51] Chemical oxidation of **1** results in a disulfide-linked Ni^{II}-N_3S complex (**1^{ox}**) where the previously unbound py-N takes the place of the thiolate-S positioned trans to the carboxamido-N (Scheme 3.1). The oxidation product **1^{ox}** was isolated and characterized by X-ray diffraction and other spectroscopic measurements. Low-temperature monitoring of the reaction in Scheme 3.1 revealed that Ni^{III} is traversed, on the basis of EPR, on the way to **1^{ox}**. At that time, the **1** to **1^{ox}** transformation represented the only NiSOD LMW model system where Ni^{III} was visualized and the corresponding oxidation product isolated and subsequently characterized. In 2014, Masuda reported the Ni^{II}-N_2S_2 complex Na[Ni(L_1)] (Chart 3.1; L_1 = deprotonated form of 2-mercapto-*N*-(2-((2-mercapto-2-methylpropyl)amino)ethyl)-2-methylpropanamide), which resulted in putative Ni^{III}-N_2S_2 and N_2S_2-Ni^{II}-superoxo complexes detected by spectroscopy.[54] With the exception of **1**, NiSOD models with sterically enhanced thiolates, namely $[Ni(L_1)]^-$ and $[Ni(BEAAM)]^-$ (BEAAM = deprotonated form of *N*-(2-(benzyl(2-mercapto-2-methylpropyl)amino)ethyl)-2-mercapto-2-methylpropanamide;[52] Chart 3.1), yield Ni^{III} complexes on the basis of EPR or qualitative solution color changes. However, neither the oxidized intermediates nor the ultimate end product(s) were isolated. With the objective of preventing S-oxidation/disulfide formation and isolating/characterizing a Ni^{III} model of $NiSOD_{ox}$, we designed and constructed a new N,S-containing ligand with additional steric bulk on the thiolate α-carbon (α-C) situated trans to the carboxamide-N: namely, $H_3N_3S_2^{Me2}$ ($H_3N_3S_2^{Me2}$ = 2-((2-mercapto-2-methylpropyl)(pyridin-2-ylmethyl)amino)-*N*-(2-mercaptoethyl)acetamide; H represents dissociable protons). The synthesis of this ligand and its corresponding Ni^{II} (Na[Ni($N_3S_2^{Me2}$)] (**2**) and Zn^{II}(Na[Zn($N_3S_2^{Me2}$)] (**3**) complexes are reported in this account (Chart 3.2). Complexes **2** and **3** were both characterized by

X-ray crystallography, numerous spectroscopic techniques, and electrochemistry. While Ni complex **2**, much like the analogues listed in Chart 3.1, represents a reasonable structural and spectroscopic model of $NiSOD_{red}$, chemical oxidation still yields disulfide-bridged species under concentrated solutions, whereas under the dilute conditions used for crystallization a new ligand-oxidized product results. Mechanistic considerations for this product, along with a density functional theory (DFT) study of **2** and computational derivatives thereof, are also presented.

Scheme 3.1 Redox conversions of NiSOD model complex **1**. Major changes highlighted in color.

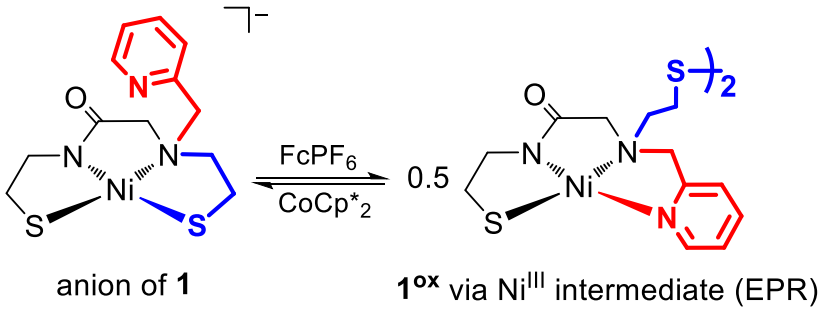

Chart 3.2 Anion of the NiSOD model complex **2** and Zn analogue **3** reported in this work.

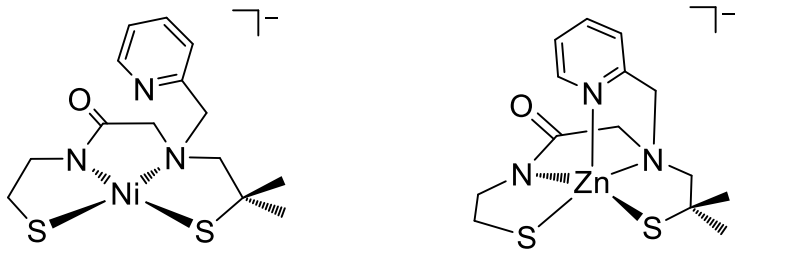

3.3 Results and Discussion

3.3.1 Synthesis and Properties of N_3S_2 Ligand

The synthesis of the potentially pentadentate ligand $H_3N_3S_2^{Me2}$ comprises several steps, with the most salient ones depicted in Scheme 3.2. The two compounds 2-bromo-*N*-(2-(tritylthio)ethyl)acetamide[51] (**I**) and (2-methyl-2-triphenylsulfanylpropyl)pyridine-2-ylmethylamine[55,56] (**II**) were prepared as described previously. Mixing stoichiometric amounts of **I** and **II** for 1 week provided the trityl (Tr = CPh_3) protected precursor (Tr-$N_3S_2^{Me2}$) in 39% yield. Attempts to optimize the yield of this reaction by refluxing the solvent ultimately led to decomposition products. Finally, deprotection of the Tr groups using Et_3SiH in TFA afforded $H_3N_3S_2^{Me2}$ as a yellow oil in 94% yield. Some notable spectroscopic features of $H_3N_3S_2^{Me2}$ (Figures 3.S4–3.S6 in the Supporting Information) include the different ^{1}H NMR chemical shifts of the thiol protons $-CH_2SH$ (D_2O-exchangeable triplet at 1.66 ppm) versus the $-C(Me)_2SH$ (D_2O-exchangeable singlet at 1.77 ppm), highlighting the asymmetry in the ligand. Strong bands in the IR spectrum indicate the presence of the carboxamide C═O (ν_{CO}: 1655 cm^{-1}) and N–H (ν_{NH}: 3274 cm^{-1}) stretches, which are common IR bands to monitor after metal coordination (vide infra).[57]

Scheme 3.2 Synthesis of $H_3N_3S_2^{Me2}$ and Ni^{II} Complex **2**[a]

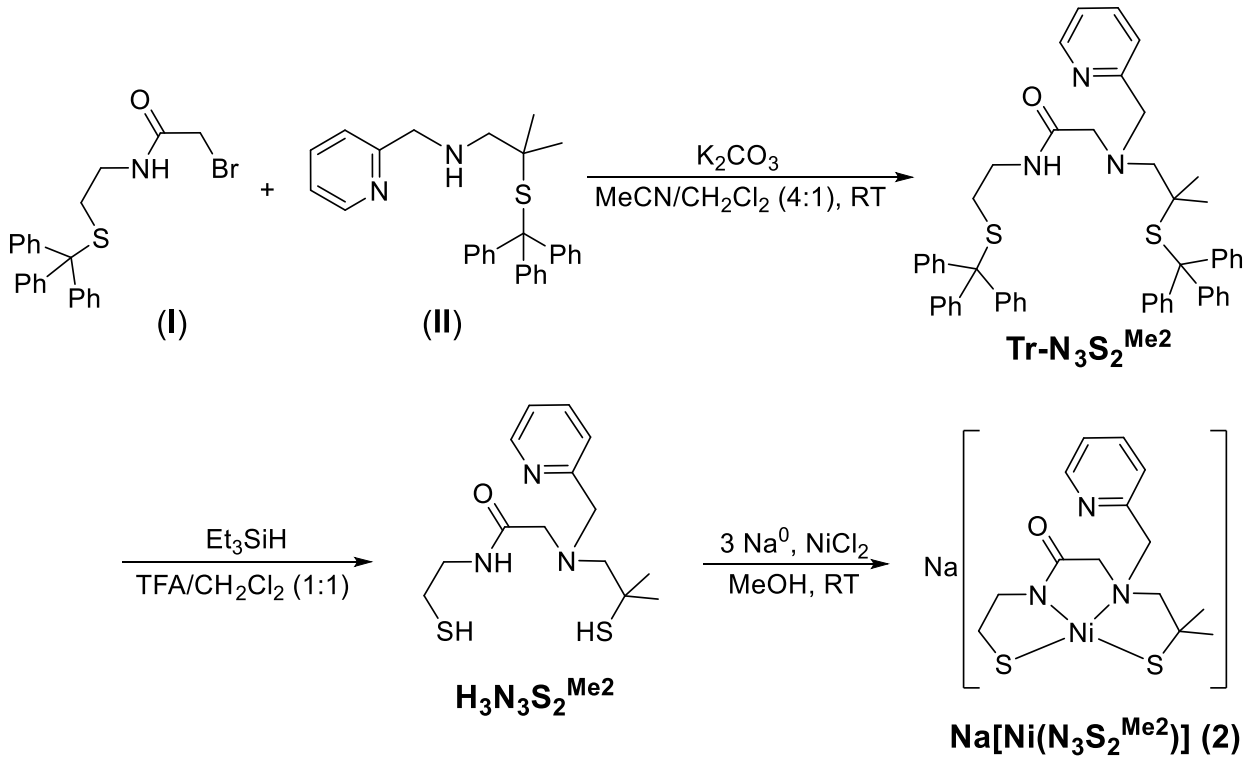

[a] Tr: trityl or triphenylmethyl (CPh_3) groups.

3.3.2 Synthesis of Ni^{II} and Zn^{II} Complexes

To examine the impact of selectively modifying one thiolate donor on the properties of isostructural NiSOD models, we synthesized the Ni^{II} complex $Na[Ni(N_3S_2^{Me2})]$ (**2**). The corresponding Zn^{II} complex $Na[Zn(N_3S_2^{Me2})]$ (**3**) was also prepared as a control for differentiating metal thiolate versus pure thiolate-centered electrochemical events (vide infra). Complex **2** was generated by reacting the deprotonated ligand with anhydrous $NiCl_2$ in MeOH (56% yield) (Scheme 3.2). The red-orange complex exhibits high solubility in polar solvents (MeOH, H_2O, DMSO) with no solubility in nonpolar solvents such as CH_2Cl_2; however, partial solubility exists

in other solvents such as THF and MeCN. Complex **3** was isolated as a yellow powder by employing conditions similar to those for **2**, with the exception of using $ZnCl_2$ as the metal salt, and exhibits a similar solubility profile.

3.3.3 Spectroscopic Properties

All complexes were characterized by numerous spectroscopic measurements including FTIR, ^{1}H NMR (vide infra), UV–vis, and electrospray ionization mass spectrometry (ESI-MS). FTIR is especially useful for metal carboxamido systems, as the ligand ν_{CO} and ν_{NH} frequencies indicate coordination.[57] For complexes **2** and **3**, the ν_{CO} value shifts $\sim$−50 cm^{-1} from that of $H_3N_3S_2^{Me2}$ upon coordination to Ni^{II} and Zn^{II} (Figures 3.S10 and 3.S12 in the Supporting Information). Additionally, the ligand ν_{NH} band is absent in the IR of the complexes, consistent with the coordination of a deprotonated carboxamido-N. High-resolution ESI-MS is also confirmatory of **2** and **3**, indicating molecular ion peaks with the appropriate isotope distribution (Figures 3.S13 and 3.S14 in the Supporting Information). Solutions of **1** are red-orange, typical for square-planar Ni^{II}-N_2S_2 complexes.[5,51-54,58] The UV–vis spectrum of **2** in MeOH reveals two closely spaced features at 459 nm (ε = 250 M^{-1} cm^{-1}) with a shoulder at 557 nm (ε = 75 $M^{-1}cm^{-1}$), characteristic of d–d electronic transitions (Table 3.1 and Figure 3.2). A near-identical UV–vis spectrum of **2** is also observed in pH 7.4 HEPES buffer (Figure 3.2). Similarly positioned ligand field bands are noted in other NiSOD models such as **1** and in $NiSOD_{red}$ (Table 3.1), further suggestive of a square-planar solution structure for **2**. Because these transitions are of d–d parentage; their positions have typically served as a measure of the ligand field strength in otherwise isostructural planar Ni^{II}–N_2S_2 complexes. However, examination of electronic

absorption spectra (in MeOH) of other NiSOD models reveals bands that are too close to distinguish with λ: 441–459 nm and are difficult to compare with the second band being a shoulder (λ_{sh}: 550–570 nm).[51-54]

Table 3.1 UV–vis and Electrochemical Data of NiSOD and Select Models[a]

NiSOD Model	**λ (nm) (ε (M^{-1} cm^{-1}))[b]**	***E*** **(V vs Fc/Fc^{+})[c]**	**Ref.**
$NiSOD_{red}$	450 (480), 543 (150)[d]	$E_{½}$: 0.290 V (vs NHE), 0.046 V (vs SCE)[d]	13, 19
K[Ni(N_3S_2)] (**1**)	449 (320), 570 sh (90)	E_{ox}: –0.620, E_{red}: –1.84	51
Na[Ni($N_3S_2^{Me}$)] (**2**)	459 (250), 557 sh (75)	E_{ox}: –0.670, E_{red}: –1.98	TW
Me_4N[Ni(BEAAM)]	461 (290), 556 sh (70)[e]	$E_{½}$: –0.330[e]	52
K[Ni(HL2)]	449 (340), 570 sh (~70)	E_{ox}: –0.458	53
Na[Ni(L_1)]	441 (258)	$E_{½}$: –0.593; $E_{½}$: –0.570[e]	54

[a] Abbreviations: sh = shoulder; TW = this work. [b] UV–vis spectra reported for MeOH solutions unless otherwise stated. [c] Data represents the redox potential as reported versus the ferrocene/ferrocenium (Fc/Fc^{+}) couple in DMF unless otherwise stated. [d] Aqueous buffer; pH 7.4 phosphate buffer for the $E_{½}$ measurement. [e] MeCN.

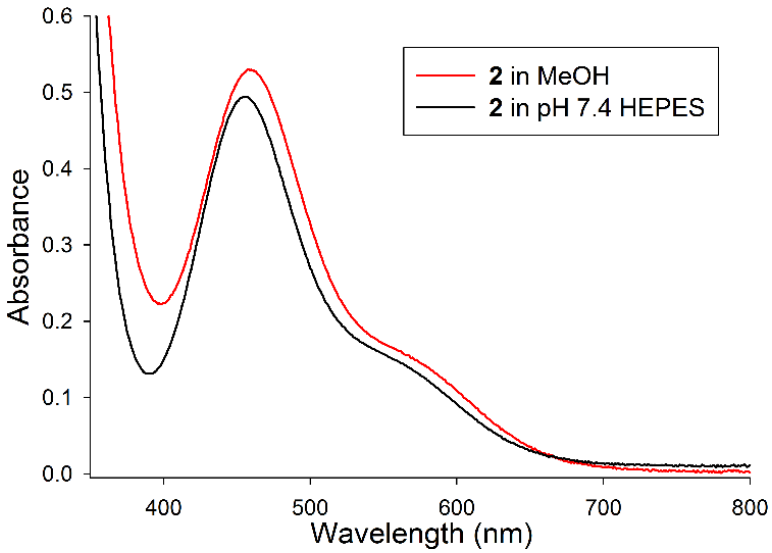

Figure 3.2 UV–vis spectra of Na[Ni($N_3S_2^{Me2}$)] (**2**) in MeOH (red, 2.2 mM) and in pH 7.4 HEPES buffer (black, 2.5 mM). Both spectra recorded at 25 °C.

3.3.4 X-ray Structures of Metal Complexes

Crystals of **2**·MeCN were grown by slowly cooling a saturated MeCN solution of **2** from room-temperature (RT) to −20 °C. The structure of the potassium salt of **2**, namely K[Ni($N_3S_2^{Me2}$)] (**2^{K}**; Figure 3.S15 in the Supporting Information), was also obtained and exhibits similar parameters (Table 3.2). Much like **1** and other NiSOD models bearing the $N_{carboxamide}N_{amine}S_2$ coordination sphere (five in total), the structure of **2** reveals a planar Ni^{II} ion coordinated by the two N and S donors of $H_3N_3S_2^{Me2}$ (Figure 3.3). Despite the pentadentate nature of the ligand, the py-N does not bind to Ni in **2**·MeCN or **2^{K}** (Ni---N_{py} ≈ 3.2 Å). Indeed, the py plane in **2** is rotated ~45° away from the Ni-N_2S_2 plane, with the py-N lone pair engaged in an interaction with the Na^+ counterion (Figure 3.S16 in the Supporting Information). To differentiate the degree of planarity in these and other four-coordinate (4C) complexes, Houser developed the

4C distortion parameter τ_4.[59] Analogous to the trigonal distortion parameter (τ_5) developed by Addison and Reedijk that assigns values for 5C complexes to distinguish between square-pyramidal ($\tau_5 = 0$) and trigonal-bipyramidal (tbp; $\tau_5 = 1$) geometries,[60] the τ_4 parameter allows one to describe the degree of planarity ($\tau_4 = 0$ for square-planar; $\tau_4 = 1$ for tetrahedral) in 4C complexes. An optional version of this parameter, denoted as τ_4',[61] has also been reported, although τ_4' does not reveal any further geometric information from τ_4 in the complexes reported here and thus is not included. While this metric has not been as widely adopted as τ_5, it will be useful for more quantitative descriptions of the geometry of 4C complexes in the future. An examination of τ_4 values in **2**, other NiSOD models, and the reduced enzyme reveals geometries closer to square-planar. This geometry is expected on the basis of the tetradentate nature and tight bite angle (exclusively five-membered chelate rings) of the ligand frames in Table 3.2.

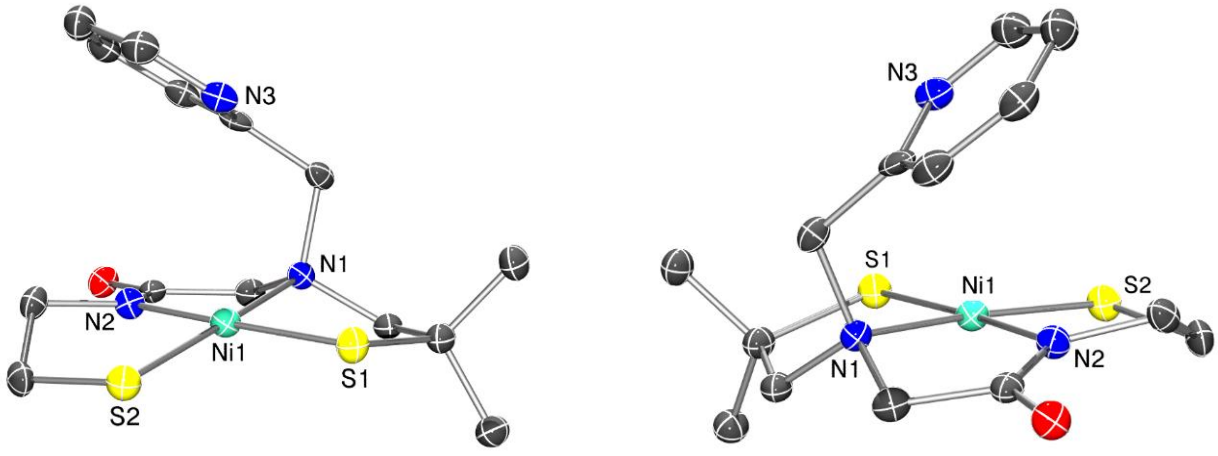

Figure 3.3 Separate depictions of the X-ray structure of the anion of Na[Ni($N_3S_2^{Me2}$)]·MeCN (**2**·MeCN) showing 50% thermal probability ellipsoids with the atom labeling scheme. H atoms and MeCN solvent of crystallization omitted for clarity.

Table 3.2 Select Metric Parameters for NiSOD and Its Model Complexes[a]

NiSOD Model	Ni–N_{amide} (Å)	Ni–N (Å)	Ni–S (Å)	Ni–S (Å)	Ni---N_{axial} (Å)	τ_4	Ref.
$NiSOD_{red}$	1.91	1.87	2.19	2.16	NA	0.09	10
K[Ni(N_3S_2)] (**1**)	1.8565	1.954	2.181	2.174	~3.21	0.09	51
Na[Ni($N_3S_2^{Me2}$)] (**2**)	1.856	1.937	2.1819	2.1582	~3.23	0.08	TW
K[Ni($N_3S_2^{Me2}$)] (**2^K**)	1.859	1.943	2.170	2.165	~3.20	0.07	TW
Me_4N[Ni(BEAAM)]	1.858	1.989	2.177	2.137	NA	0.16	52
K[Ni(HL2)]	1.862	1.937	2.1711	2.1671	NA	0.09	53
Na[Ni(L_1)]	1.865	1.923	2.1702	2.1450	NA	0.07	54
av (all)	**1.859(4)**	**1.947(23)**	**2.175(5)**	**2.158(14)**			
av (Na^+, Me_4N^+ salts)	**1.860(5)**	**1.950(35)**	**2.176(6)**	**2.147(11)**			

[a] Abbreviation: TW = this work.

Other metrics in the structure of **2**·MeCN that deserve mention are the bond distances, a reflection of the differing electronic nature of the N and S donors in $[N_3S_2^{Me2}]^{3-}$. For example, the shortest bond in **2**·MeCN is the Ni–$N_{carboxamide}$ bond (1.856(4) Å), which tracks with other NiSOD models[51-54] (Table 3.2). This short bond is attributed to the σ-donating nature of the carboxamide, which also exerts a structural effect on the trans Ni–S bond (Ni–S1 in Figure 3.3). This electronic trans influence is certainly observed in the structure of **2**·MeCN, i.e., Ni–S1 = 2.1819 Å and Ni–

S2 = 2.1582 Å, a difference of nearly 0.025 Å. Comparing these values to other models reveals the same trend, but the extent of carboxamido-N-influenced elongation is different and appears to be dependent on counterion–thiolate interactions. For instance, the structures of NiSOD models that contain Na^+ or Me_4N^+ counterions display the largest difference (average 0.029 Å) in the two Ni–SR bonds as in **2**·MeCN. This list includes Me_4N[Ni(BEAAM)][52] and Na[Ni(L_1)],[54] both of which do not contain a potential fifth ligand (see Chart 3.1 and Table 3.2). Further insight into what causes this structural deviation is found in the extended lattice structure of **2**·MeCN and $\mathbf{2^K}$ (Figure 3.S16 in the Supporting Information). In both structures, Na^+ and K^+ ions interact with the Ni-bound thiolates and carbonyl-O of $[N_3S_2{}^{Me2}]^{3-}$ to generate coordination polymers. The same interaction between K^+ and the Ni-thiolate is also observed in the extended structure of **1**.[51] The stronger soft–soft K–S interaction in $\mathbf{2^K}$ ($K–S_{avg}$ = 3.33 Å), **1** ($K–S_{avg}$ = 3.34 Å), and K[Ni(HL2)] ($K–S_{avg}$ = 3.33 Å)[53] engages the S(π) lone pair in an ionic bond with K^+ that results in a shorter than expected $Ni–SR_{\textit{trans}\text{-carboxamide}}$ bond due to alleviation of the Ni(dπ)–S(pπ) repulsion (vide infra). These K- - -S interactions are more electrostatic in nature, as structurally characterized potassium thiolate complexes with aromatic thiolates exhibit average K–SR distances of 3.165 ± 0.074 Å.[62] However, it is unlikely that these structural deviations exist in solution, as the solid-state extended structure is a result of crystal packing and is doubtful to persist under dilute conditions.

X-ray-quality crystals of the Zn^{II} complex with a MeOH solvent of crystallization (**3**·MeOH) were grown by slow diffusion of Et_2O into a saturated MeOH/MeCN (1:1) solution of **3** at −20 °C (Figure 3.4). In contrast to **2**, the Zn^{II} center coordinates *all* donor atoms to afford a 5C geometry that is slightly more disposed toward tbp (τ_5 = 0.58) with the N1–Zn–S2 atoms (162.28°) comprising the pseudo-axial *z* axis. Not surprisingly, the lack of any ligand field

stabilization results in a higher coordination number between $[N_3S_2^{Me2}]^{3-}$ and Zn^{II}. The Zn–L bond distances are unremarkable (Figure 3.4) and are on-par with other 5C Zn^{II} compounds in a mixed N/S ligand frame.[63,64] For example, the large Zn–S distances in **2**, which are greater than 2.3 Å, reflect the higher coordination number for this and other 5C Zn^{II}-N/S complexes,[56,63,65-68] whereas 4C Zn^{II}-N/S complexes generally have Zn–S bond lengths less than 2.3 Å.[69,70] Importantly, the structure of **3** provides insight into how $[N_3S_2^{Me2}]^{3-}$ may coordinate Ni to generate a 5C species that mimics $NiSOD_{ox}$. Indeed, DFT computations predict a geometry more square-pyramidal in nature for the computed Ni^{III} analogues of **1**[51] ($\tau_5 = 0.33$)[71] and **2** ($\tau_5 = 0.15$) (vide infra).

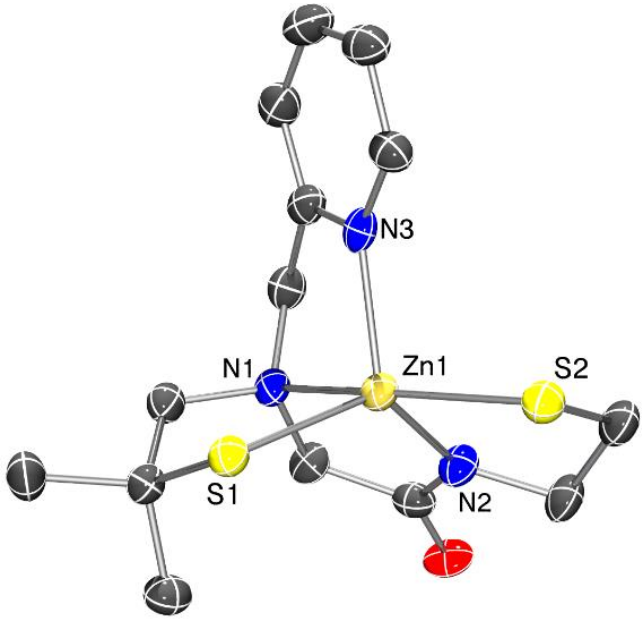

Figure 3.4 X-ray structure of the anion of $Na[Zn(N_3S_2^{Me2})]\cdot MeOH$ (**3**·MeOH) showing 50% thermal probability ellipsoids along with the atom labeling scheme. H atoms are omitted for clarity. Selected bond distances (Å) and angles (deg): Zn–S1 = 2.3242(12), Zn–S2 = 2.4153(13), Zn–N1 = 2.332(4), Zn–N2 = 2.008(3), Zn–N3 = 2.106(4), N1–Zn–S2 = 162.28(9), N2–Zn–N3 = 114.94(14), N3–Zn–S1 = 108.57(10), N3–Zn–N1 = 77.25(13).

3.3.5 X-ray Absorption Spectroscopy (XAS) of Ni^{II} Complexes 1 and 2

X-ray absorption near-edge spectra (XANES) collected on **1** (Figure 3.S17 in the Supporting Information) and **2** (Figure 3.5) are very similar, with the first inflection point of the edge energies measured at 8335.5 eV for solid samples of **1** and **2** (diluted with boron nitride (BN)) and 8335.1 eV for samples of **1** and **2** in a MeOH glass, and are suggestive of a Ni^{II} oxidation state.[72] Pre-edge analysis of features in the spectra of **1** and **2** are consistent with Ni existing in a structurally constrained but identical coordination geometry in both solid and MeOH samples (Figure 3.5 and Figure 3.S17). All samples contain two distinct pre-edge features corresponding to a 1s → 3d transition at 8332 eV and a 1s → 4p transition at 8337 eV. The small area of the 1s → 3d features (dimensionless values: 0.032 for **1**, 0.015 for **1** in MeOH; 0.030 for **2**, 0.011 for **2** in MeOH) suggest that Ni^{II} is held in a square-planar geometry.[72,73] This geometry is also consistent with the presence of a prominent 1s → 4p feature (dimensionless values: 1.08 for **1**, 0.83 for **1** in MeOH; 1.27 for **2**, 0.95 for **2** in MeOH), which indicates that tetrahedral, octahedral, and tbp geometries are not likely for Ni in any sample. The prominent 1s → 4p feature (area ∼1) in the presence of a small 1s → 3d feature (area <0.05) suggests square-planar coordination.[72,73] Collectively, these data indicate that Ni, in both solid and MeOH samples of **1** and **2**, is held in the Ni^{II} oxidation state and constrained in a square-planar coordination sphere.

The averaged XAS spectra for all samples demonstrate both N and S scattering in the nearest-neighbor environment, with additional long-range C scattering also present. Simulation best-fit results are provided in Table S2 in the Supporting Information. Both samples were fit using a three-, four-, or five-ligand model. Average Ni–N (1.91 Å for solid **2**) and Ni–S (2.17 Å for solid **2**) distances are in agreement with crystallographically characterized distances for

Ni^{II} compounds in a square-planar geometry (Table 3.2).[51] Lower than expected coordination numbers in the MeOH sample of **1** can likely be attributed to destructive interference between neighboring S atoms, as has been observed in zinc-binding sites.[74]

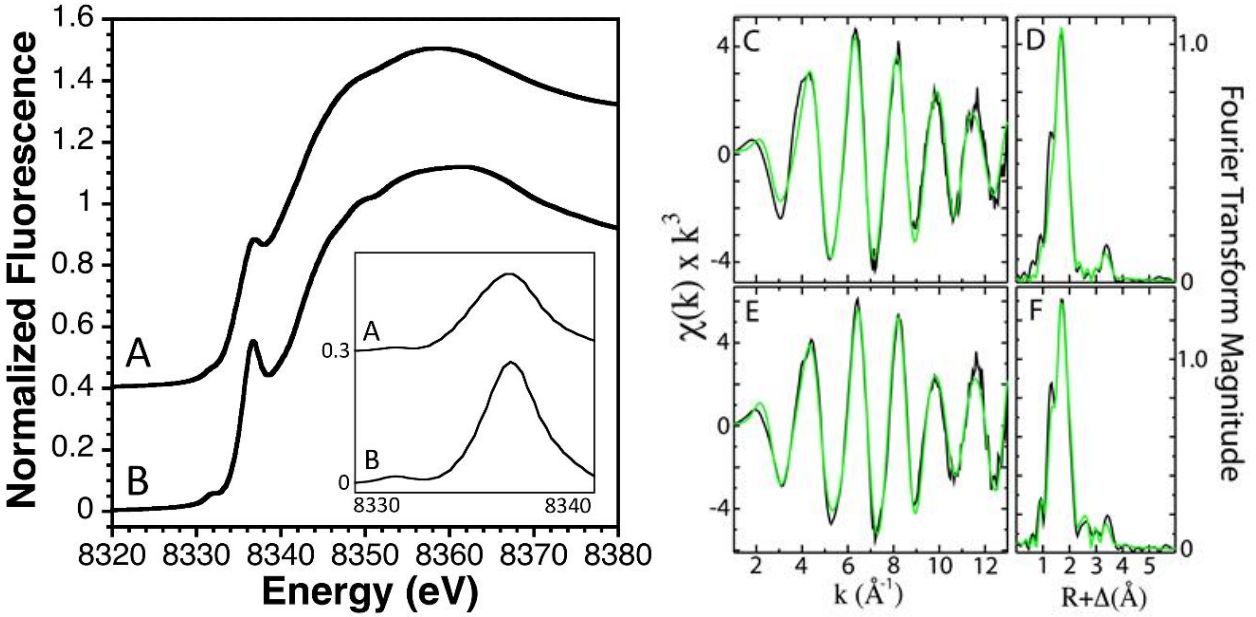

Figure 3.5 *Left*: Ni K-edge XANES spectra for **2** in MeOH (A) and solid **2** diluted with BN (B) offset for clarity. Inset: expansion of the pre-edge region, background subtracted for normalization and offset for clarity. *Right*: EXAFS (C, E) and Fourier-transform simulations (D, F), comparing raw data (black) to best-fit model (green) for **2** in MeOH (C, D), and solid **2** (E, F).

3.3.6 ^{1}H NMR Spectroscopy

To determine whether the planar coordination sphere of **2** is retained in RT solutions, we measured the ^{1}H NMR spectrum of **2** in a variety of solvents. The spectrum of **2** in $(CD_3)_2SO$ (Figure 3.6 and Figure 3.S7 in the Supporting Information) reveals sharp resonances for all chemically distinct protons in the 1–9 ppm region, consistent with a planar (S = 0) Ni^{II} complex. As expected, the H atoms in the chelate portion of the ligand are diastereotopic and, as such, afford

distinct chemical shift values for H atoms above and below the Ni-N_2S_2 square-plane. A similar pattern is observed in the ^{1}H NMR spectrum of **1**.[51] The spectrum of **2** changes, however, in protic solvents such as CD_3OD and D_2O (Figure 3.6 and Figures 3.S8 and 3.S9 in the Supporting Information). For instance, the ^{1}H NMR spectrum of **2** in CD_3OD exhibits broad features over a wide chemical shift range (2–12 ppm), reminiscent of the type of signals expected for exchangeable protons (Figure 3.6 and Figure 3.S8). Because all H atoms are attached to C, this broadening is not a result of exchange. One explanation is the coordination number of **2** increases (binding of py-N, solvent, or both), causing a small degree of paramagnetism (S = 1 for octahedral Ni^{II}) to result in the broad spectrum. However, UV–vis of **2** in different solvents and XAS of **2** in the solid-state and in frozen MeOH (vide supra) support identical coordination geometries regardless of medium. Even a small amount of a 5C or 6C Ni^{II} may cause a detectable amount of paramagnetic behavior in NMR, but not significant enough to result in any perturbation in the UV–vis or XAS. Indeed, the effective magnetic moment (μ_{eff}) of a CD_3OD solution of **2** was 0.81 μ_B and the observed shift of the ^{t}BuOH indicator ($\Delta\nu$ = 5 Hz, $\chi_M = 56 \times 10^{-6}$ emu/mol (before diamagnetic correction), 500 MHz spectrometer, 21 °C) only corresponds to ~2% of that expected for a pure S = 1 system ($\Delta\nu \approx 300$ Hz, $\chi_M \approx 3400 \times 10^{-6}$ emu/mol (before diamagnetic correction), under identical conditions). A more probable reason behind the broadened NMR peaks is tetrahedral twisting of the ligand due to H-bonds between S donors and solvent that perturb the square-planar ligand field. Similar solvent effects have been observed in other square-planar Ni^{II} systems. For example, the X-ray structure and solid-state magnetic measurements of a Ni^{II}-N_2S_2 complex with imine-N and thiolato-S donors suggest square-planar Ni; however, RT measurements from ^{1}H NMR (broad) and magnetism (μ_{eff} = 3.21 μ_B) are more consistent with

high-spin Ni^{II}.[75] Analogous results were also found in a structurally characterized Ni^{II}-S_4 complex.[76]

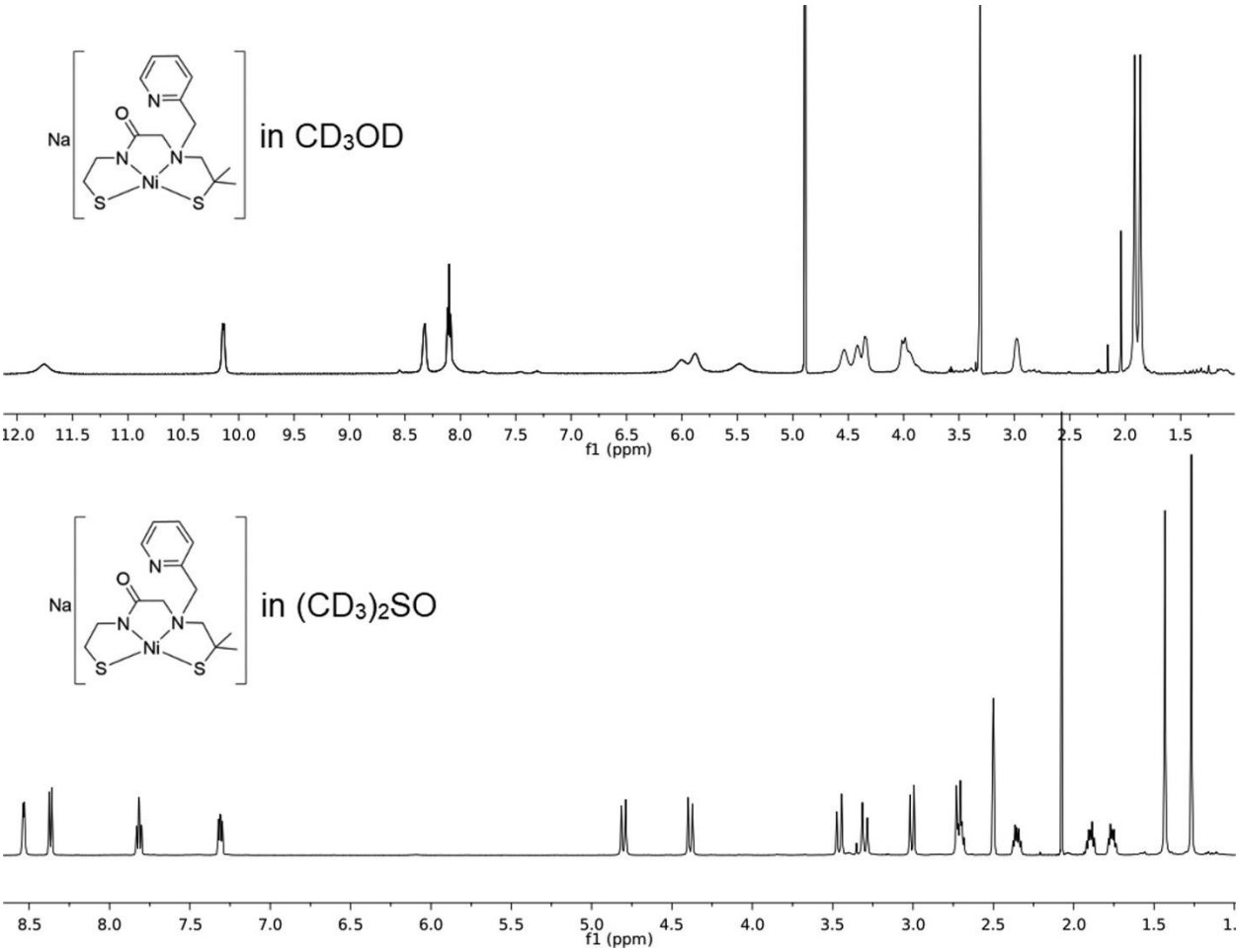

Figure 3.6 ^{1}H NMR spectra of Na[Ni($N_3S_2^{Me2}$)] (**2**) in CD_3OD (top) and $(CD_3)_2SO$ (bottom) at RT: (top) peaks at 3.31 and 4.89 ppm represent residual protio solvent and water, respectively; (bottom) peaks at 2.50 and 2.08 ppm represent residual protio solvent and MeCN, respectively. Full peak assignment is provided in the Supporting Information for the $(CD_3)_2SO$ spectrum.

To observe any through-space ^1H–^1H interactions between py-H and ligand-H in the N_2S_2 plane, we obtained two-dimensional (2D) rotating-frame Overhauser effect spectroscopic

(ROESY) measurements of **1** and **2** in $(CD_3)_2SO$. This measurement would indicate the potential for the py-N to coordinate to the Ni^{II} center. For **1**, the ROESY demonstrated interactions of the py-CH_2 protons (H5 in Figure 3.S18 in the Supporting Information) with methylene protons H1 and H2, protons attached to C atoms bonded to the amine-N ligand. Additional interactions are observed between these protons with py-H4 and collectively indicate free rotation of the pendant py unit of **1** in solution. In contrast, the ROESY of **2** does not show any through-space ^1H–^1H interactions among similar protons (Figure 3.S19 in the Supporting Information). The lack of through-space interactions of the py-H with other protons in the aliphatic region in **2** is most consistent with restricted rotation of the py-CH_2 unit due to steric constraints of the *gem*-$(CH_3)_2$ substitution on the S1 α-C (thiolate *trans* to the carboxamide). The diamagnetic nature of the ^1H NMR spectrum and the freely rotating py moiety in **1** show that N-py is most likely not coordinating to the Ni center in **1**. Even when the free rotation of py is restricted, as observed in **2**, the ^1H NMR remains sharp and is most consistent with a noncoordinated py-N. Collectively, the ROESY experiments show that **1** and **2** are diamagnetic Ni^{II} complexes in a square-planar coordination environment, consistent with X-ray diffraction, XAS, and UV–vis measurements.

3.3.7 Electrochemistry

The cyclic voltammograms (CVs) of **2** and **3** were measured in DMF (0.1 M ^{n}Bu$_4$NPF$_6$ electrolyte), and potentials are reported versus an internal ferrocene/ferrocenium (Fc/Fc^+) standard. On scanning in the positive direction, the full CV of **2** exhibits four discernible oxidation waves between −0.80 and 0.50 V with several ill-defined reduction waves around −2.0 V (Figure 3.S20 in the Supporting Information). To discriminate primarily ligand based, i.e., thiolate, redox

events from those with potential Ni contributions, the CV of the Zn^{II} complex **3** was also recorded (Figure 3.S21 in the Supporting Information). Indeed, L-based events, assigned as thiolate to thiyl oxidation in **3**, nearly superimpose onto electrochemical events observed between −0.30 and 0.50 V in **2** (Figure 3.7). This result suggests that the irreversible oxidation event (E_{ox}) at −0.67 V is Ni-thiolate based. The E_{ox} value of **1** at −0.62 V is comparable to that of **2**, which has been attributed to Ni^{III}-thiolate/Ni^{II}-thiyl (from EPR) to form the disulfide-linked complex (vide supra, Scheme 3.1). As expected, the oxidation in **2** is more facile (−0.05 V shift in E_{ox} from **1**) due to the electron-donating nature of the *gem*-$(CH_3)_2$ groups. Isolating E_{ox} by scanning in the positive direction and then switching to negative potentials revealed an irreversible reduction event (E_{red}) at −1.98 V, assigned as disulfide to thiolate conversion. As observed for **1**, E_{red} and E_{ox} of **2** are coupled, as E_{red} is only observed after traversing E_{ox} and not the reverse (Figure 3.S22 in the Supporting Information). Again, the inductive effects of the *gem*-$(CH_3)_2$ group in **2** result in a more negative E_{red} value in comparison to **1** (E_{red} = −1.84 V), i.e., reduction is more difficult. While free alkyl thiolates are typically oxidized at more negative potentials (E_{ox} = −0.68 V for $^tBuS^-$ in DMA vs Fc/Fc^+),[77] the shift observed in **2** and **3** is due to coordination to the M^{II}centers. In fact, E_{ox} can be altered by nearly 1 V by simple substitution of an electron-withdrawing NO_2 group for an electron-donating NH_2 group in para-substituted benzenethiol in DMF.[78] Overall, the irreversible E_{ox} in **2** is similar to those found in other NiSOD models that lack steric protection at the thiolate (Table 3.1). However, the NiSOD models with methyl substitution on both thiolate α-C atoms generally result in reversible $Ni^{III/II}$ couples ($E_{1/2}$ = −0.57 and −0.33 V in MeCN vs Fc/Fc^+, Table 3.1), which are appropriately shifted in the positive direction from dicarboxamido Ni-N_2S_2 complexes with alkyl thiolate ligands ($E_{1/2}$ = −0.90 to −0.72 V in DMF vs Fc/Fc^+[79,80]). Interestingly, the Ni-based couple in $Na[Ni(L_1)]$ becomes

irreversible in protic solvents (and to a lesser extent in MeCN) and resembles the CVs of **1** and **2**. The identity of this event was assigned as $Ni^{III/II}$ redox, but it is more likely due to the thiolates, as indirectly confirmed by isolation and characterization of the oxidation products of **1** and **2** (vide infra).

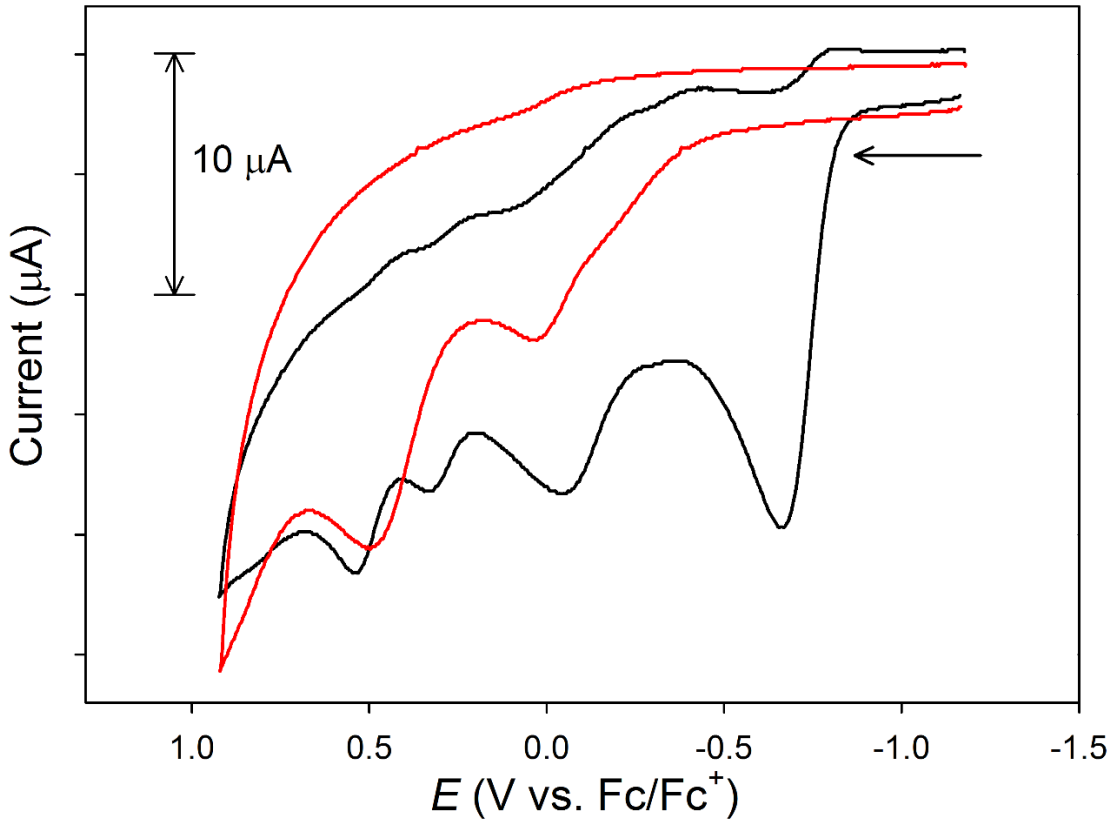

Figure 3.7 CV of **2** (2.9 mM, black) and **3** (2.7 mM, red) in DMF at RT (0.1 M $^{n}Bu_4NPF_6$ supporting electrolyte, glassy carbon working electrode, 100 mV/s scan rate). Arrow displays scan direction.

3.3.8 Oxidation of Ni^{II} Complex 2

In order to determine the origin of the waves in the CV, chemical oxidation of **2** was performed with ferrocenium hexafluorophosphate ($FcPF_6$; 1:1) in DMF. Addition of Fc^+ to **2** resulted in a red-brown solution that became slightly darker over time. Initial characterization of the isolated tan solid by ESI-MS(+) revealed a singly charged intense peak at *m*/*z* 739.1, which matches the mass and isotope pattern of that calculated for the disulfide-linked Ni^{II}-N_3S dimer **4** ($[2M + H]^+$; Figure 3.S24 in the Supporting Information). In this case, the proposal is that oxidation occurs at the Me-substituted thiolate to form a transient thiyl, and the py-N takes the coordination position vacated by that thiolate. Formation of **4** may occur through a path similar to that for $\mathbf{1^{ox}}$, where a transient Ni^{III}-thiolate intermediate is observed by in situ EPR measurements (Scheme 3.1).[51] Although no EPR signal was found in the case of **2**, this observation is likely due to the electron-rich and more reactive nature of the thiyl despite the increased steric restriction. Additional evidence from the negative shift in E_{ox} of **2** from **1** further points to the substituted thiolate as the probable site of redox. UV–vis provides additional proof of the N_3S chromophore (Figure 3.S25 in the Supporting Information) in **4**, with similar profiles observed in other planar Ni^{II}-N_3S complexes.[41,51] However, the ^1H NMR (Figure 3.S26 in the Supporting Information) is not entirely conclusive and advocates for other oxidation products that are not easily distinguished by UV–vis or ESI-MS. Overall, under bulk synthesis conditions, the principal product of chemical oxidation is a disulfide-linked dimer regardless of the thiolate α-C substitution.

Interestingly, an unusual oxidation product was unexpectedly isolated under crystallization conditions by slow (3 weeks) air exposure of a THF/MeOH (1:1) solution of **2** diffused with Et_2O. Small red crystals suitable for X-ray diffraction were mounted, and the resulting structure indicated

the formation of the new square-planar Ni^{II}-N_3S product [Ni(L^{ox})] (**5**; L^{ox} = 2-(5,5-dimethyl-2-(pyridin-2-yl)thiazolidin-3-yl)-*N*-(2-mercaptoethyl)acetamide), where analogous to disulfide formation via Fc^+ oxidation the py-N takes the place of the α-C-substituted alkyl thiolate. However, the nature of the oxidation is different. Instead of disulfide, a five-membered N,S-heterocycle (thiazolidine) forms through the alkyl-S and the py-CH (Figure 3.8). Attempts to synthesize this complex in bulk have not been successful, and thus **5** likely represents a minor product of oxidation. In general, the metric parameters of **5** (see the caption of Figure 3.8) match those in other structurally characterized planar Ni^{II}–N_{py}/S complexes,[47,51] complexes with thiazolidines as part of the ligand frame,[81,82] and other organic thiazolidines.[83,84]

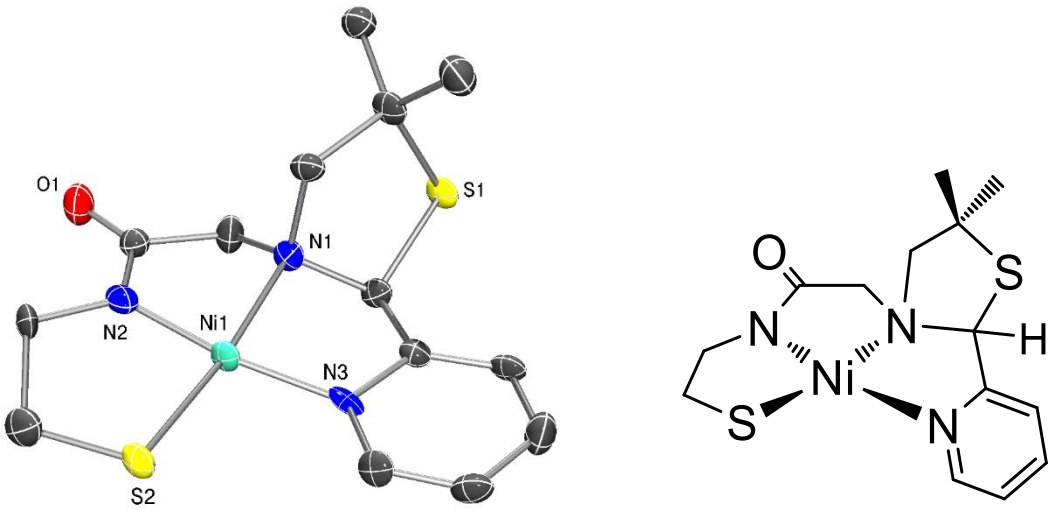

Figure 3.8 X-ray structure of [Ni(L^{ox})] (**5**) showing 50% thermal probability ellipsoids with the atom labeling scheme (*left*) and ChemDraw depiction of **5** (*right*). H atoms omitted for clarity. Selected bond distances (Å) and angles (°): Ni–S2: 2.148(3), Ni–N1: 1.929(7), Ni–N2: 1.832(9), Ni–N3: 1.875(8), N1–Ni–S2: 172.4(2), N2–Ni–N3: 170.5(3), N2–Ni–N1: 85.4(3), N3–Ni–N1: 85.2(3), N2–Ni–S2: 89.8(3), N3–Ni–S2: 99.7(2).

The formation of **5** represents the net loss of two electrons and one proton (or one electron and one H atom). Two major paths can be envisioned for the formation of **5**. The first path initiates by H atom transfer of a Ni-coordinated thiol to generate the thiyl. Analogous to the {Ni(SOD^{m1})} maquette,[15,16] **2** may contain a protonated thiol-S donor in protic solvents. However, the EXAFS of **2** in MeOH shows a 0.01 Å lengthening of the Ni–S distance (Table 3.S2 in the Supporting Information) and not the anticipated contraction of Ni–S after protonation (up to 0.03 Å by DFT[13]) as observed in {Ni(SOD^{m1})}.[16] Perhaps this increase is due to the steric constraints of the Me groups and thus the anticipated contraction is not manifested in the EXAFS of **2**. Regardless, the H atom abstraction capacity of O_2 is much weaker (bond dissociation free energy (BDFE) of O_2/$^{\bullet}$OO-H ~58 kcal/mol in DMSO[85]) than the estimated S–H BDFE (79 kcal/mol) of the coordinated thiol in {Ni(SOD^{m1})}[15] and, by analogy, **2**. The more likely path involves the following steps (Scheme 3.3): (i) one-electron oxidation of **2** to generate the thiyl followed by Ni–S_{thiyl} bond dissociation and Ni–N_{py} bond formation, akin to Fc^+ oxidation and (ii) H atom abstraction from the py-CH_2– group by HOO$^{\bullet}$ (superoxide protonation from MeOH[86,87]), which has a BDFE of 91 kcal/mol in H_2O (formed after step i to yield H_2O_2 and py-C$^{\bullet}$H); the radical would be in proximity to the thiyl so that (iii) the thiazolidine ring forms to yield **5**. Generally, O_2 is a poor one-electron oxidant (E = −0.18 V vs NHE[88] and −1.29 V vs Fc/Fc^+ in DMF[89]); however, O_2 is a better one-electron oxidant in the presence of protons (E = 0.12 V vs NHE[89] and −0.57 V vs Fc/Fc^+ in DMF[89]), which is probable under the conditions employed and reported elsewhere.[86,87] Because the E_{ox} value of **2** is −0.68 V, it is thermodynamically favorable for the oxidation in step i to occur. The estimated C–H BDFE of a coordinated py-CH_2 is 83.5 kcal/mol,[85,90-92] lower than the HOO$^{\bullet}$ BDFE, [85] suggesting that H atom abstraction by HOO$^{\bullet}$ is indeed feasible. Additionally, metal-coordinated py-CH_2-NR_2groups are susceptible to oxidation

with air as observed in Fe^{III},[93] Co^{III},[93] Ir^{I},[94] and Rh^{I} complexes[95] to afford, in most cases, the corresponding pyridine-2-carboxamide, i.e., py-(C═O)-NR_2. Similar activation of sp^3 C–H bonds is also observed in $[RuCl_2(LH)(PPh_3)_2]$ (LH = 4,5-diazafluorene), where O_2 oxidation results in the formation of the ketone to yield $[RuCl_2L'(PPh_3)_2]$ (L′ = 4,5-diazafluoren-9-one).[96] While this result does not necessarily correlate to bulk oxidation, i.e., disulfide complex **4**, it does establish that imparting steric demands on coordinated thiolates can prevent disulfide bond formation as well as open up new reaction paths to other species.

Scheme 3.3 Proposed reaction path to disulfide complex **4** or thiazolidine **5**. Complexes in brackets are proposed intermediates not isolated or characterized by spectroscopy.

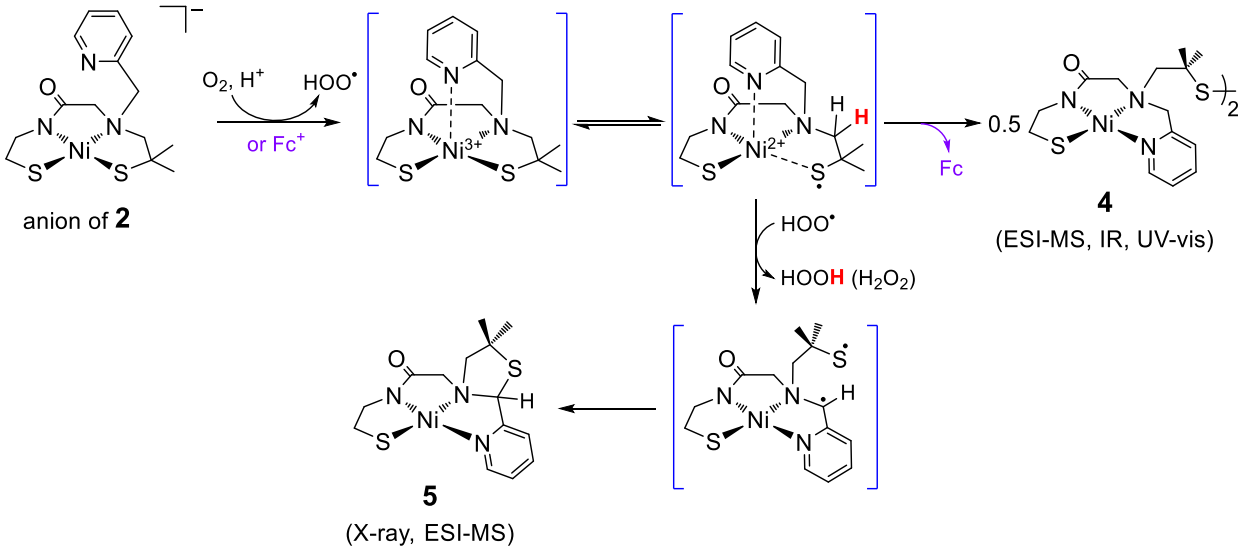

3.3.9 Reactivity with Superoxide ($O_2^{\bullet-}$) and azide (N_3^-)

To test the capability of **2** as an SOD, in addition to gaining insight into any interactions with superoxide, we performed spectroscopic measurements (ESI-MS, UV–vis) of the reactions

of **2** with excess KO_2 (solubilized with 18-crown-6 ether for nonaqueous measurements) and NaN_3, a commonly employed electronic analogue of superoxide. Mixing 10 equiv of N_3^- with **2** in pH 7.4 HEPES buffer resulted in minor changes to the UV–vis of **2** over 17 h (Figure 3.S27 in the Supporting Information). Performing this same reaction in MeOH confirmed that **2** is still present on the basis of UV–vis and ESI-MS(−) (*m*/*z*: 368) with no indication of a Ni^{II}-azido species, even after 17 h (Figures 3.S28 and 3.S29 in the Supporting Information). Thus, N_3^- does not bind to the Ni center in **2**. In contrast, mixing 10 equiv of $O_2^{\bullet-}$ with **2** in pH 7.4 HEPES resulted in significant changes to the UV–vis with decreases in the d–d bands of **2** and the appearance of an intense peak in the UV region (~270 nm) that slowly decreases over 15 h (Figure 3.S30 in the Supporting Information). Performing the same reaction in MeOH revealed a somewhat different appearance to the UV–vis with the bands of **2** absent and the emergence of a peak at 350 nm (Figure 3.S31 in the Supporting Information). The ESI-MS of this solution revealed several peaks. Notably, the peak associated with **2** disappears and the one identifiable intense peak corresponds to a singly charged species with *m*/*z*: 405.9 that matches to $[\mathbf{2} - H + K]^+$: i.e., thiazolidine complex **5** + K^+ (Figure 3.S32 in the Supporting Information). As expected, reacting $O_2^{\bullet-}$ (excess or stoichiometric) in aprotic solvents such as DMF produced no UV–vis changes owing to the instability of O_2^{2-}. Remarkably, there is no indication of the disulfide complex **4**, as seen in the oxidation of **2** with Fc^+, or S-oxygenation. These results support the formation of **5** under the dilute conditions employed for the spectroscopic measurements and observed under crystallization conditions (vide supra).

To gauge the activity of **2** as an SOD, we utilized the nitroblue tetrazolium (NBT) assay, a common test for SOD activity where NBT reacts with $O_2^{\bullet-}$ to yield the intensely colored blue formazan (λ_{max} = 530 nm, ε_{530} = 12800 M^{-1} cm^{-1} in pH 5.7–6.7 phosphate buffer).[97] SODs

disproportionate $O_2^{\bullet-}$ and prevent the formation of the formazan, as H_2O_2 and O_2 do not react with NBT. Thus, an active SOD, or a good model thereof, should not yield formazan from NBT.[98] Unexpectedly, control reactions of **1** or **2** with NBT *in the absence of* $O_2^{\bullet-}$ resulted in formazan. For example, addition of a stoichiometric amount of **2** to a colorless pH 7.4 solution of NBT immediately generated formazan, as indicated by the resulting dark blue solution and the UV–vis spectral monitor (Figure 3.S33 in the Supporting Information). Given the comparable CVs of **1** and **2**, a similar reaction was observed between NBT and **1**. The NBT/formazan assay is thus not suitable for these NiSOD models, and it would not be surprising if other reports of NBT reacting with similar Ni-N/S complexes will soon emerge.

In an effort to circumvent the shortcomings of the NBT/formazan assay, and realizing that **2** is not capable of superoxide oxidation based on electrochemistry, we utilized the Amplex Red (AR) assay to evaluate the superoxide reducing capability of **2**. This test has been successfully used in models of the nonheme enzyme superoxide reductase.[99] In this assay, AR is converted to resorufin (λ_{max} = 572 nm, ε = 54000 M^{-1} cm^{-1}; λ_{em} = 587 nm, in pH 7.4 Tris–HCl buffer;[100] λ_{max} = 572 nm, ε = 56000 M^{-1} cm^{-1}; λ_{em} = 585 nm; Φ = 0.74 in water at pH 9.5[101]) by the Fe^{IV}═O intermediates (compounds I and II) of horseradish peroxidase (HRP) that form when HRP reacts with H_2O_2.[100] The accepted mechanism of AR with H_2O_2 is depicted in Scheme 3.S1 in the Supporting Information, the H_2O_2 response of which relies on the autodisproportionation of the radical of AR ($AR^{\bullet}$). Reactions of AR in the presence of KO_2 were monitored by both UV–vis and fluorescence in the presence and absence of NiSOD model **2** in pH 7.4 HEPES buffer. After 30 min of incubation at RT, the reaction mixture containing **2** and KO_2 (1:1), along with AR and HRP, showed a ~60% decrease in integrated fluorescence intensity in comparison to control (Figure 3.9). This result is opposite to the *expected increase* in fluorescence due to H_2O_2-induced

formation (via HRP) of resorufin, where complex **2** is responsible for H_2O_2 generation, viz. Ni^{II}-L + $O_2^{\bullet-}$ + $2H^+ \rightarrow Ni^{III}$-L (or 0.5 Ni^{II}-L_{thiyl}; see above) + H_2O_2. While not anticipated, several possibilities explain the decreased fluorescence response. First, H_2O_2 (from oxidation of **2** or spontaneous disproportionation) can be depleted by its reaction with the thiolate(s) of the ligand to result in S-oxidation to disulfide or S-oxygenation to RSO_x^- (x = 1–3). However, given that H_2O_2 and HRP react with a rate constant (k) of 1.7×10^7 M^{-1} s^{-1},[102] and k = 0.47 M^{-1} s^{-1} for H_2O_2 S-oxygenation of a square-planar Ni^{II}-N_3S complex,[42] it is unlikely for H_2O_2 to react with **2** before HRP. Second, the AR$^\bullet$ intermediate could react directly with **2**, instead of its autodisproportionation to resorufin, indicating that **2** does not generate H_2O_2 but instead interferes with the formation of the fluorescent product. This proposal is also doubtful because the rate of the autodisproportionation of AR is likely faster than its reaction with the S = 0 Ni^{II} complex **2**, and the phenol radical is not a strong enough oxidant (E(α-tocopherol) = −0.87 V in DMSO vs Fc/Fc^+[85]). The third and more likely path involves the oxidized intermediate of **2**, a thiyl radical (vide supra) with a new Ni–N_{py} bond, interfering with the assay by direct reaction with AR$^\bullet$. The oxidation of **2** by $O_2^{\bullet-}$ will result in disulfide product **4** or thiazolidine **5**, the latter of which is more likely under the dilute conditions of the AR assay (Scheme 3.S2 in the Supporting Information). With AR$^\bullet$ being consumed by the oxidized intermediate, resorufin production will decrease to result in the quenched fluorescence observed (Figure 3.9). Theoretically, this reaction diminishes the resorufin signal by 50%, a value in close agreement with the experimental decrease of ∼60%.

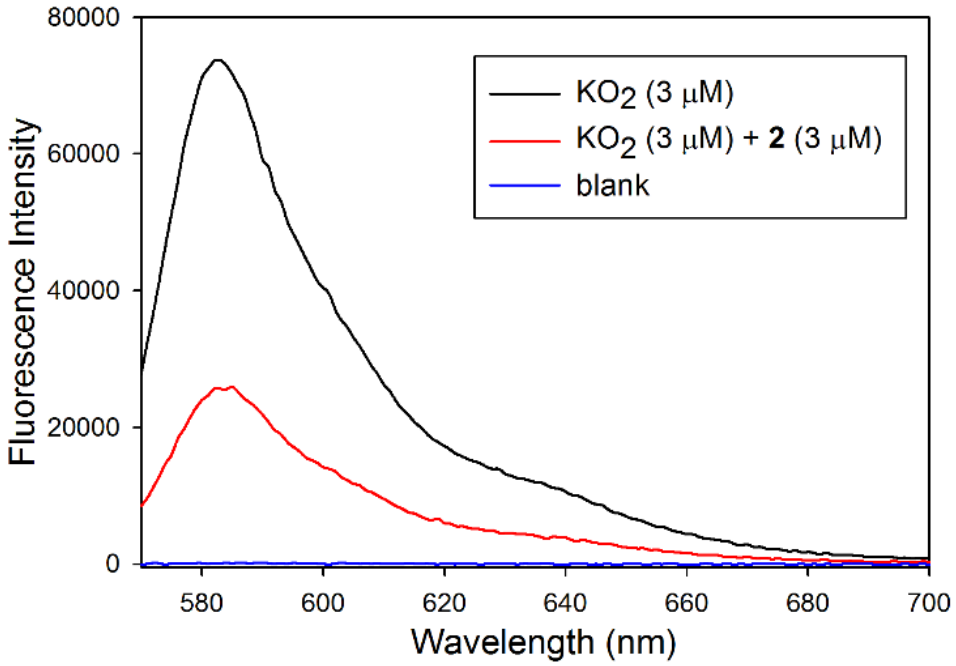

Figure 4.9 Fluorescence spectra (λ_{ex}: 563 nm) of a 10 μM HEPES buffer solution (pH 7.4) of Amplex Red and 1 U/mL of HRP (blue) and its response to KO_2 (black) and KO_2/complex **2** (1:1) (red) at 25 °C.

3.3.10 Electronic Structure Calculations

Several theoretical studies on NiSOD[13,103,104] and its models[46,51-53,105,106] have revealed valuable information on the electronic structure of this unique active site. DFT computations, primarily using the hybrid B3LYP functional, suggest that the highest occupied MO (HOMO) in $NiSOD_{red}$ and planar Ni^{II}-N_2S_2 models is antibonding in nature and highly covalent, with significant contributions from Ni-dπ atomic and S-pπ group orbitals. Furthermore, the extent of these individual contributions renders the HOMO more Ni based to support the $Ni^{III/II}$ redox conversion during turnover. For example, DFT studies on planar Ni^{II}-N_2S_2complexes with variable N ligation,[53,105-107] i.e., diamine to amine/carboxamide to dicarboxamide, reveal that sequential addition of negatively charged, σ-donating carboxamides not only increases the Ni character in the

HOMO but also "activates" the thiolate lone pairs toward electrophilic attack. Hence, the mixed amine-N/carboxamide-N combination is sufficient to promote Ni redox without significantly activating the thiolates. Regardless, there is still significant S-pπ character in the computed HOMO of truncated versions of $NiSOD_{red}$.[13] While many of the DFT analyses have concentrated on the electronic structural effects of the N ligands, few have focused on the thiolates. Most S-based modifications have included H-bonding[13,46,105] to or protonation[13,15,16] of the thiolates. Indeed, these in silico (and in some cases coupled with experimental) modifications have resulted in contracted Ni–thiolate bonds by upward of 0.03 Å with the modified S-pπ contribution to the HOMO decreasing by 12%. Thus, peptide H-bonding and/or protonation may be one method to protect CysS during turnover. To provide additional insight into how modifications to the N/S ligand alter the electronic structure in NiSOD models, we employed DFT at the OLYP/def2-TZVPP level of theory with solvent effects accounted for by utilizing the conductor-like screening model (COSMO) with a dielectric constant (ε) of 38.3 for DMF. Computations in the gas phase and other solvents (MeOH, H_2O) yielded similar results (data not shown). Specifically compared are geometry-optimized structures and MO contributions of **1*** and **2*** (***** indicates DFT-optimized complexes using input coordinates from the X-ray crystal structures of **1** and **2**) with in silico generated complexes $[Ni(N_3S_2^{F2})]^-$ (**6***) and $[Ni(N_3S_2^{F4})]^-$ (**7***) containing F-substitution on the S α-C (**6*** and **7*** input structures were obtained using coordinates from the structure of **1** after substituting F on the S α-C atom) (Figure 3.10).

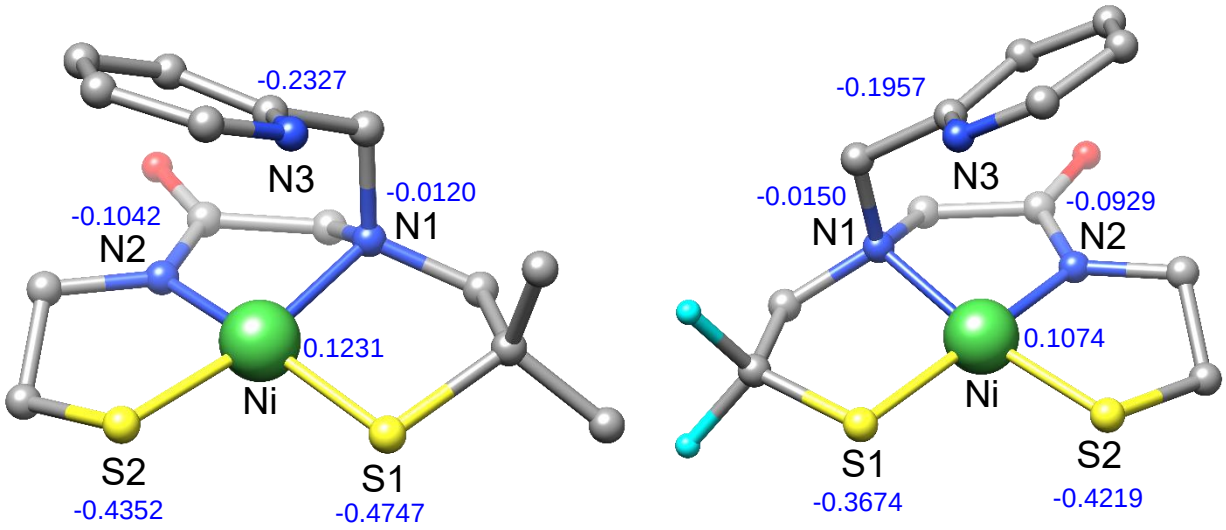

Figure 3.10 Geometry-optimized structure of **2*** (left) and **6*** (right) with Mulliken atomic charges on Ni, S, and N atoms in blue. Green = Ni; yellow = S; blue = N; red = O; cyan = F; gray = C. H atoms are omitted for clarity.

The geometry-optimized structures of **1*** and **2*** (Table 3.3) are in close agreement with those determined from crystallography (Table 3.2) and are well within the error of the DFT method. That is, Ni–$N_{carboxamide}$ (Ni–N2 in Figure 3.10) and Ni–$S1_{trans\text{-}carboxamide}$ are the shortest and longest bonds, respectively. These metric trends are also observed in the in silico generated complexes **6*** and **7***. Not surprisingly, the first F substitution lengthens Ni–S1 by ~0.03 Å, likely caused by the diminished Lewis basicity from the electron-withdrawing group and confirmed by the decreased Mulliken charge on this atom (Figure 3.10). However, the second F substitution (**7***) does not result in any significant Ni–L changes from **6***. Overall, the metric parameters of **1*** and **2*** largely reproduce what is observed experimentally. Furthermore, the fact that F-substituted versions **6*** and **7*** are nearly isostructural with **1*** and **2*** suggest that, barring difficult synthetic steps, these complexes should be isolable.

Table 3.3 Selected Bond Distances and Bond Angles of the DFT-Optimized Structures of **1***, **2***, **6***, and **7***[a]

Compound	1*	2*	6*	7*
	Bond Distances (Å)			
Ni–N1	1.987	1.987	1.977	1.971
Ni–N2	1.881	1.883	1.873	1.872
Ni–S1	2.180	2.169	2.193	2.192
Ni–S2	2.167	2.165	2.166	2.167
Ni - - - N3	3.347	3.296	3.351	3.292
	Bond Angles (°)			
N1–Ni–N2	84.88	84.87	85.44	85.52
N2–Ni–S2	91.51	88.97	88.99	90.6
N1–Ni–S1	89.17	92.04	90.68	89.21
S1–Ni–S2	95.69	95.81	95.55	95.25
S1–Ni–N2	169.38	167.15	172.45	172.92
S2–Ni–N1	170.11	169.42	171.54	171.88
τ_4	0.15	0.17	0.11	0.11

[a] Definitions: N1 = amino-N; N2 = carboxamido-N; N3 = pyridine-N; S1 = $S_{trans\text{-carboxamide}}$; S2 = $S_{trans\text{-amine}}$.

The longer Ni–N1 bonds compared to Ni–N2 bonds for **1***, **2***, **6***, and **7*** are consistent with a more negatively charged carboxamido-N ligand, as suggested by the computed Mulliken charge for N2 (Figure 3.10 and Figure 3.S34 in the Supporting Information). While the Ni–S2 bond remains relatively constant in **1***, **2***, **6***, and **7***, variations at the S1 α-C have a significant effect on the Ni–S1 bond (Table 3.3). Due to the established nature of the HOMO in planar Ni^{II}-N_2S_2 systems, the S α-C substituents vary the S-contribution and affect the Ni–S bond. However, the expected trend is not observed because the Lewis basicity factor outweighs the MO composition changes. For example, F-substitution in **6*** and **7*** lowers the S-contribution in the HOMO (vide infra) and should result in a shorter Ni–S1 bond because of the diminished Ni(dπ)–S(pπ) interaction. In comparison to **1*** and **2***, however, the Ni–S1 bond is elongated by upward of 0.024 Å, and Ni–N1 and Ni–N2 contract by ~0.01 Å in **6*** and **7*** (Table 3.3) due to decreased S-basicity, as reflected in the Mulliken charge. Further support for the basicity argument is

observed in the Ni–S1 bond of **2***, which contains the most negatively charged S ligand among the complexes in Table 3.3 and, as a result, the shortest Ni–S1 bond. On the basis of the τ_4 values (τ_4 = 0.11–0.17),[59] the coordination geometry is more square-planar, but with slightly more tetrahedral distortion in comparison to the X-ray structures of **1**, **2**, and $NiSOD_{red}$ (τ_4 = 0.07–0.09) (Table 3.2). This deviation from planarity in the DFT-optimized structures is attributed to the restriction applied to the neutral N-donor (N1). From the optimized structures, the lone pair of the tertiary-N points toward the Ni^{II} ion in a classic trigonal-pyramidal geometry about N1 (sp^3-hybridized) that is somewhat relaxed in the X-ray structures of **1** and **2** likely due to crystal packing and interactions with counterions that are absent in the computations.

MO plots reveal the major contributions to the frontier MOs (FMOs) of these complexes (Figure 3.11 and Table 3.4 for **2***; Figures 3.S36–3.S38 and Tables 3.S3–3.S5 in the Supporting Information for **1***, **6***, and **7***). As with $NiSOD_{red}$[13] and other models,[46,51,53,105-107] the FMOs are comparable with slightly more Ni-dπ versus S-pπ contribution to the HOMO. Going across the series of α-C substitutions (H_2 (**1***) → Me_2 (**2***) → F_2 (**6***) → F_4 (**7***)), one notices several trends with respect to orbital energies (Figure 3.S35 in the Supporting Information). First, the FMOs are slightly destabilized in the Me_2 derivative **2*** but then are stabilized upon the addition of the F substituents in **6*** and **7***. Indeed, the complex with F substitution on both S α-C atoms (**7***) contains the most stabilized FMOs. One notable feature is that the singly F modified α-C derivative (**6***) yields a HOMO and HOMO-1 that are nearly degenerate, likely arising from the stabilization of ligand group orbitals associated with S1 (trans to the carboxamide), which then shifts the S-based contribution in this MO to unsubstituted S2 (trans to the amine).[105] Basically, the decreased basicity of S1 is compensated for by shifting the HOMO contribution over to S2 (Table 3.S4 in the Supporting Information). This result leads to the general conclusion that, regardless of what

alterations are made to noncoordinating atoms on the ligand, the HOMO of NiSOD models such as **2** will still contain large S-pπ character (vide infra). Indeed, analysis of the FMOs of **1***, **2***, **6***, and **7*** reveal the same basic electronic structure (Figure 3.11 and Figures 3.S36–3.S38 in the Supporting Information) and the Löwdin population analysis for selected MOs are compiled in Table 3.4 and Tables 3.S3–3.S5 in the Supporting Information. The LUMO is σ* with primary contributions from Ni $d_{x^2-y^2}$ and pσ orbitals of all equatorial N/S donors of the ligand. As stated earlier, the HOMO is π* with principal contributions from Ni-dπ and S-pπ orbitals and is in-line with previous computations on **1**[51] and other Ni^{II}-N_2S_2 NiSOD models.[53,105-107] The increased Lewis basicity of S1 on going from **1*** to **2*** results in less Ni-dπ character (62.7 to 61.9%) and a small increase in S-pπ (24.6 to 25.9% total S) with the major contribution from S1 (20.4% in **2***; S trans to carboxamide) in the HOMO. However, as F is substituted onto the S α-C, the Ni-dπ contributions are highest (68.3% in **6***, 67.3% in **7***) and the S-pπ contributions are the smallest (13.5% in **6***, 13.1% in **7***). It is important to note that in **6*** the true nature of the HOMO is difficult to identify because HOMO-1 is only 0.002 eV away (Figure 3.S37 and Table 3.S4). Intuitively, HOMO-1 may represent the true HOMO in **6*** with the primary S contribution from S2 (trans to the amine) due to the single F substitution on the S1 α-C rendering it less basic. Regardless, these calculations demonstrate that the HOMO in $NiSOD_{red}$ models is still covalent, although trending toward more Ni, with respect to Ni and S contributions. However, the MO contributions are tunable by ligand modification that should lead to primarily Ni-based versus thiolate-based electrochemical events, albeit sacrificing a positive shift in the $Ni^{III/II}$ redox potential.

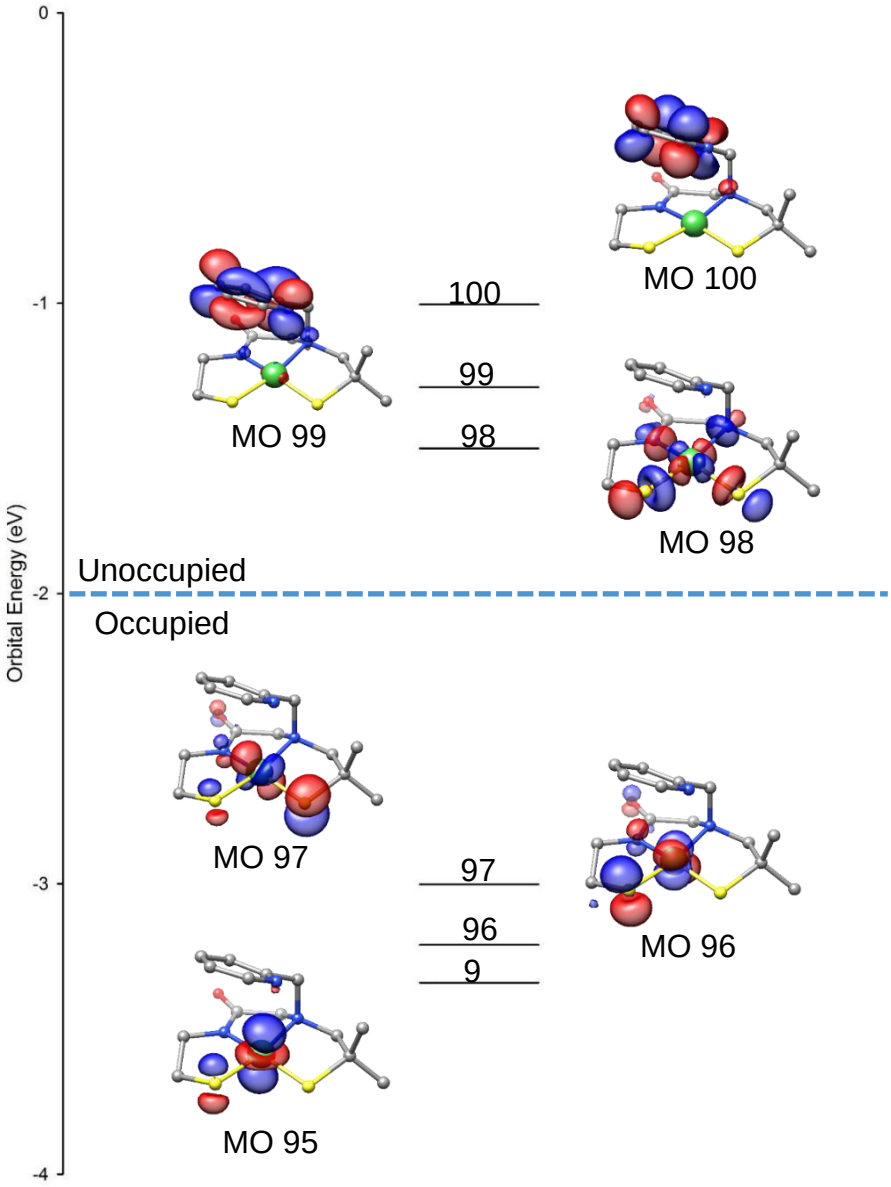

Figure 3.11 DFT-generated isosurface plots of the frontier MOs of **2***. The orbitals descend in the order LUMO+2, LUMO+1, LUMO, HOMO, HOMO-1, and HOMO-2.

Table 3.4 Löwdin Population Analysis Derived from the DFT Calculations for Selected MOs of **2*** from OLYP/def2-TZVPP with COSMO(DMF)[a]

	MO#	Energy (eV)	%Ni	%S1	%S2	%N1	%N2	Type of Interactions
LUMO+2	100	-1.0041	1.2	0	0	1	0.1	pyridine(π*)
LUMO+1	99	-1.2893	2.5	0.3	0.3	1.2	0.9	pyridine(π*)
LUMO	98	-1.5003	48.9	9.8	13.5	5.4	5	Ni(d_σ)–S1(σ)–S2(σ)–N1(σ)–N2(σ)
HOMO	97	-3.0017	61.9	20.4	5.5	0	2.1	Ni(d_π)–S1(π)–S2(π)–N2(π)
HOMO-1	96	-3.2099	68.4	0.7	17.2	0.4	2.9	Ni(d_π)–S2(π)–N2(π)
HOMO-2	95	-3.3406	83.2	1.2	8.4	0.2	0.6	Ni(d_σ)–S2(π)

[a] Only s and p contributions were tabulated for N and S atoms. Bonding interactions are represented with a +, and antibonding interactions are denoted with a −. Definitions: N1 = amino-N; N2 = carboxamido-N; S1 = $S_{trans\text{-carboxamide}}$; S2 = $S_{trans\text{-amine}}$.

To assess the electronic structure of oxidized analogues, the hypothetical complexes **2^{ox}*** and **6^{ox}*** were generated by removing one electron from the geometry-optimized Ni^{II} complexes **2*** and **6***, reoptimizing for the doublet ($S = 1/2$), and performing single-point energy calculations to obtain the corresponding MOs (OLYP/def2-TZVPP). Interestingly, the spin-unrestricted calculation did not converge for **2^{ox}*** unless the py-N was forced to coordinate to Ni as the input structure (Figure 3.12). In contrast, **6^{ox}*** converged to the same structure, i.e., the 5C complex, regardless of whether the py-N was left unbound, as in the structure of Ni^{II} complex **6***, or forced to bind. Theoretical generation of both oxidized complexes afford similar 5C structures and FMOs, and thus most of the discussion is dedicated to **2^{ox}***. The computational details of **6^{ox}*** are provided in Figures 3.S39 and 3.S41 and Table 3.S7 in the Supporting Information.

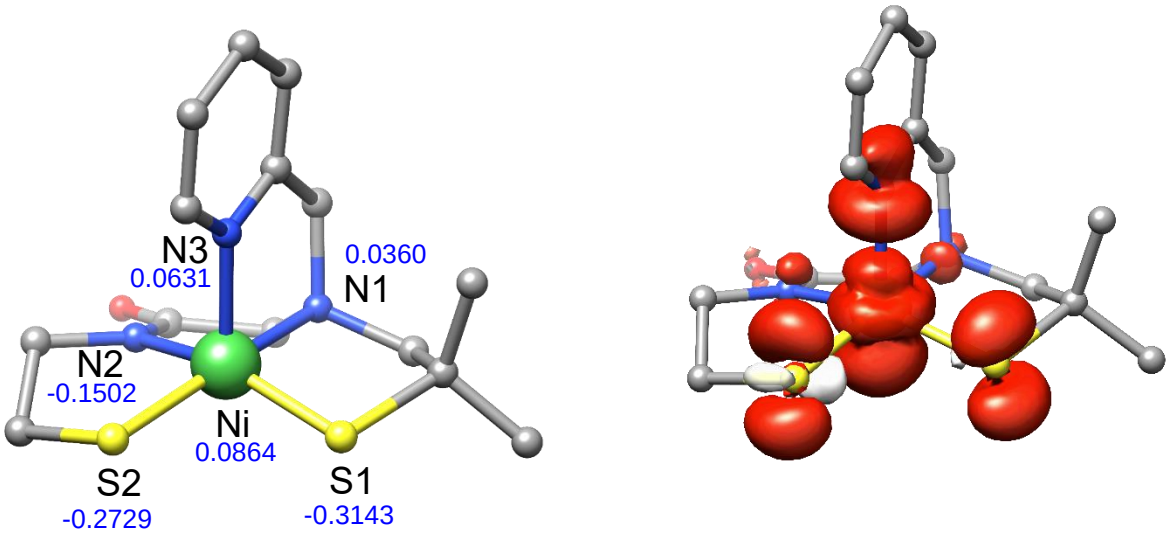

Figure 3.12 Geometry optimized structure of **2^{ox}*** with Mulliken atomic charges on Ni, S, and N atoms in blue (left) and spin-density plot (right; red denotes positive spin density and white denotes negative spin density). H atoms are omitted for clarity. Atom coloring is the same as in Figure 3.10. Selected bond lengths (Å) and angles (deg): Ni–N1 = 2.038; Ni–N2 = 1.895; Ni–N3 = 2.003; Ni–S1 = 2.181; Ni–S2 = 2.191; N1–Ni–S2 = 169.04; N2–Ni–S1 = 159.83; N1–Ni–N2 = 83.43; N2–Ni–S2 = 88.34; S2–Ni–S1 = 93.52; S1–Ni–N1 = 91.76; S2–Ni–N3 = 103.34; N2–Ni–N3 = 96.76; S1–Ni–N3 = 102.32; N1–Ni–N3 = 84.87.

The optimized structure of **2^{ox}*** indicates a 5C square-pyramidal (τ_5 = 0.15) complex with two different Ni–thiolate distances that are ~0.02 Å longer than in **2*** (Figure 3.12). The Ni–$N_{carboxamide}$distance remains the shortest, with the Ni–N_{py} and Ni–N_{amine} distances hovering around 2 Å. Collectively, the Ni–L distances are longer than in **2*** because of increased electron–electron repulsion upon going from 4C **2*** to 5C **2^{ox}***. In contrast, DFT analysis on other oxidized models of NiSOD result in a collective contraction of all Ni–L distances by ~0.03–0.10 Å;[53] however, these computations were performed on 4C square-planar Ni^{III}-N_2S_2 systems lacking additional donors. Overall, there is a preference for the py-N to bind in **2^{ox}*** and **6^{ox}***. In comparison, the coordination sphere about Ni^{III} in $NiSOD_{ox}$ remains largely unchanged, with the exception of the long Ni–N_{His} bond of ~2.3 Å. However, this distance is skewed due to the presence of Ni^{II} (His-

off) and Ni^{III} (His-on) active sites in the crystal. Indeed, data from DFT on truncated forms of the NiSOD active site,[13,16] as well as X-ray structures of Ni–N_{py} (or Ni–N_{Im}) complexes,[108] reveal that typical Ni–N bonds are 2.0–2.2 Å, a distance supported by the calculations here.

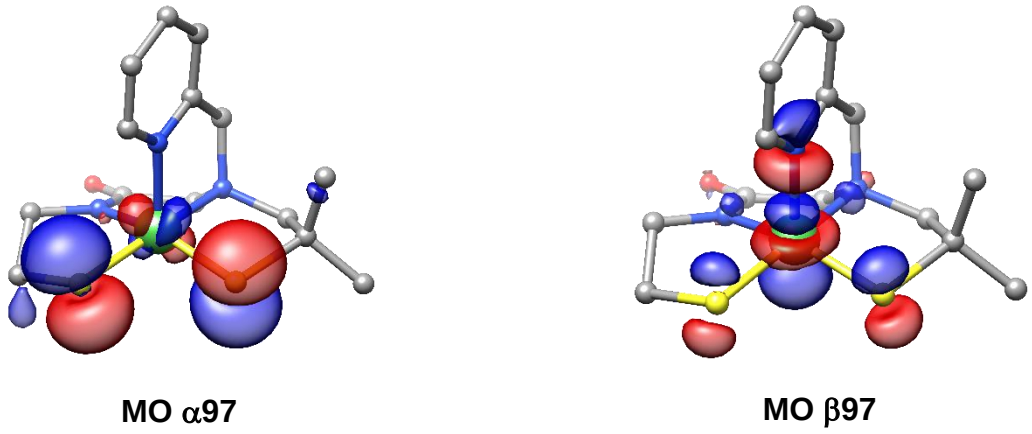

Figure 3.13 DFT-generated isosurface plots of the frontier MOs of **2^{ox}*:** MO α97 (*left*) and MO β97 (*right)*. H atoms omitted for clarity.

The MO diagram reveals a LUMO, the redox-active MO (β97), that is primarily σ* in character with major contributions from Ni-d_z^2 (61%) and N-pσ (10%) of the axial py-N (Figure 3.13 and Figure 3.S40 and Table 3.S6 in the Supporting Information), similar to that computed for $NiSOD_{ox}$.[13] In contrast, the singly-occupied MO (SOMO, defined as the spin-up αMO97) is primarily comprised of S-pπ contributions (36% S1, 33% S2; total S = 69%) with a small degree of Ni-dπ character (18%). There is minimal overlap between the Ni and S orbitals in the SOMO, essentially making this MO nonbonding with minor π* character. Thus, upon oxidation of **2*** to generate **2^{ox}***, the unpaired electron primarily resides on S to generate a thiyl. The electronic nature of the SOMO is responsible for the formation of the disulfide and thiazolidine

complexes reported above. Analogous to the case for $NiSOD_{ox}$, a Mulliken spin population analysis of $\mathbf{2^{ox*}}$shows the majority of the spin density on Ni (70%) with minor amounts on N3 (14%), S1 (8%), and S2 (5%) (Figure 3.12).

3.4 Conclusions

This work demonstrates that square-planar NiSOD models, even with the correct in-plane ligand field and potential axial N donor, exhibit ligand-based (primarily thiolate) reactions upon oxidation to afford disulfide and thiazolidine compounds. These observations lead to several postulates as to how this reactivity is deterred in the enzyme. For example: (i) structural restrictions imposed by the macromolecule may prevent disulfide as well as other ligand oxidized species, (ii) protonation of Cys2 and/or Cys6 will decrease the S nucleophilicity and diminish S-character in the HOMO, and (iii) the catalytic cycle could involve 5C Ni(III/II); this geometry would alter the electronic structure such that the HOMO is primarily Ni-based.[13] Indeed, the degree of covalency in the Ni–SCys bonds of SOD rival those found in Fe/S clusters and blue-copper proteins.[13] The NiSOD electronic structure thus presents challenges to the synthetic modeling chemist, where strategies must be employed to prevent autoreduction reactions in addition to formation of S-bridged oligomers of uncontrollable nuclearity. Autoredox is especially difficult to overcome with high-valent metals (Ni^{III}, Fe^{III}) because of the low oxidation potential of alkyl thiolates, i.e., M^{II}-SR + ox → [M^{III}-SR] → M^{II} + 1/2 RSSR.[109,110] Collectively, the additional reactions associated with metal thiolates introduce further complications in modeling such active sites. While steric enforcement of the thiolate α-C presents a reasonable modification to prevent undesired chemistry, Ni^{III}-SR complexes are still very much transiently characterized, and despite interest in this

particular species in NiSOD and [NiFe]-hydrogenases,[111] the only structurally characterized monomeric Ni^{III}-SR complex was published ~20 years ago in 1998.[80] In fact, complexes **1** and **2** represent the only LMW NiSOD models comprising the "NiSOD-accurate" $N_{carboxamide}N_{amine}S_2$ in-plane coordination sphere where isolation and characterization of oxidation products has been accomplished. Furthermore, it is quite common to read the phrase, "oxidation of M-SR results in intractable species" in the synthetic metal thiolate literature. The isolation and crystallization of oxidation products such as thiazolidine complex **5** reflect the reactive nature of the Ni^{II}-N_2S_2 coordination sphere of **2**, and by analogy NiSOD, an oxidation path likely turned on, yet never observed before, by incorporation of the *gem*-$(CH_3)_2$ groups on the S α-C. Another common decomposition for Ni^{III}-peptido complexes involves H atoms in positions that neighbor the peptide functionality. Indeed, methylation of the methylene groups of the tripeptide Ni-GGG results in a Ni^{III} complex stable for days even in the presence of 5 M $HClO_4$.[112] While this decomposition reaction is not observed here, its description is warranted for future modeling efforts. As Maroney stated some 30 years ago, "*Ni^{III} has no real existence with simple alkyl thiolates*".[113] This statement has some truth, as even "complicated" thiolates in the Ni^{II} complexes **2**, $[Ni(BEAAM)]^-$, $[Ni(L1)]^-$, and the sterically demanding $[Ni(nbdt)_2]^-$ (nbdt = bicyclo[2.2.1]heptane-*exo*-*cis*-2,3-dithiolate or norbornanedithiolate)[114] do not result in isolable Ni^{III} complexes. Enforcing a five-coordinate pyramidal geometry about the Ni^{II} center may be the only way to change the electronic structure to yield a primarily Ni centered redox-active MO to achieve catalysis. Overall, future ligand constructs must consider the aforementioned points and, in particular, the highly covalent nature (Ni-dπ/S-pπ) of the $NiSOD_{red}$ HOMO.

3.5 Materials and Methods

3.5.1 General Information

All reagents were purchased from commercial suppliers and used as received unless otherwise noted. Acetonitrile (MeCN), methylene chloride (CH_2Cl_2), tetrahydrofuran (THF), diethyl ether (Et_2O), and pentane were purified by passage through activated alumina columns using an MBraun MB-SPS solvent purification system and stored over 4 Å molecular sieves under an N_2atmosphere before use. *N*,*N*-Dimethylformamide (DMF) was purified with a VAC Solvent Purifier containing 4 Å molecular sieves and stored under similar conditions. Methanol (MeOH) was stored over 3 Å molecular sieves for at least 1 week before using. The compounds *S*-tritylcysteamine,[44] 2-bromo-*N*-(2-(tritylthio)ethyl)acetamide (I),[51] isobutylene sulfide,[115] 2-methyl-1-[(pyridin-2-ylmethyl)amino]propane-2-thiol,[55] (2-methyl-2-triphenylsulfanylpropyl)pyridine-2-ylmethylamine (II),[55] $H_3N_3S_2$ ligand,[51] and $K[Ni(N_3S_2)]$[51] (1) were prepared and checked according to the published procedures. Amplex Red (AR) reagent was obtained from ThermoFisher Scientific and used as received. Horseradish peroxidase (HRP) type VI (250–330 U/mg; U = amount of peroxidase that will form 1.0 mg of purpurogallin from pyrogallol in 20 s at pH 6.0 and 20 °C; the purpurogallin (20 s) unit is equivalent to ∼18 μM units/min at 25 °C) was used as received from Sigma and stored at −5 °C prior to use. 18-crown-6 ether (18C6) was obtained from Aldrich and used as received. All reactions were performed under an inert atmosphere of N_2 using standard Schlenk techniques or in an MBraun Unilab glovebox under an atmosphere of purified N_2.

3.5.2 Physical Methods

FTIR spectra were collected on a ThermoNicolet 6700 spectrophotometer running the OMNIC software, where samples were prepared either as pressed KBr pellets or as a neat oil on a diamond window using attenuated total reflectance (ATR). Electronic absorption spectra were recorded at 25 °C using a Cary-50 spectrophotometer containing a Quantum Northwest TC 125 temperature control unit. Fluorescence measurements were obtained on a FluoroMax-3 spectrofluorometer equipped with a Lauda Ecoline RE 106 refrigerated circulating water bath to maintain the temperature at 25 °C and controlled by DataMax version 2.20 spectroscopy software. All UV–vis and fluorescence samples were prepared in gastight Teflon-lined screw-cap quartz cells with an optical pathlength of 1 cm. Cyclic voltammetry (CV) measurements were performed with a PAR Model 273A potentiostat using a nonaqueous Ag/Ag^+ (0.01 M $AgNO_3$/0.1 M $^n Bu_4NPF_6$ in MeCN) reference electrode, Pt wire counter electrode, and a glassy-carbon working milli-electrode (2 mm diameter). Measurements were performed at ambient temperature using 3–5 mM analyte in the appropriate solvent under Ar containing 0.1 M $^n Bu_4NPF_6$ as the supporting electrolyte. The "Maximize Stability" mode was utilized in the PAR PowerCV software utilizing a low-pass 5.3 Hz filter. Analyte potentials were referenced against a 0.5 mM ferrocene internal standard under identical conditions, where $E_{1/2}$ = 0.073 V in DMF vs the reported nonaqueous Ag/Ag^+ electrode. Low-resolution electrospray ionization mass spectrometry (LR-ESI-MS) data were collected using a PerkinElmer Sciex API I Plus quadrupole mass spectrometer or a Bruker Esquire 3000 plus ion trap mass spectrometer. High-resolution electrospray ionization mass spectrometry (HR-ESI-MS) data were collected using an Orbitrap Elite system with precision to the third decimal place. Elemental microanalysis for C, H, and N was performed by QTI-Intertek in Whitehouse, NJ, or ALS Environmental (formerly Columbia Analytical) in Tucson, AZ.

1D NMR spectra were recorded in the listed deuterated solvent on either a 400 MHz Bruker BZH 400/52 NMR spectrometer at RT or a 500 MHz Varian Unity INOVA NMR spectrometer at RT with chemical shifts referenced to tetramethylsilane (TMS) or the residual protio signal of the deuterated solvent.[116] 2D NMR spectra (HSQC, HMBC, and ROESY) of **1** and **2** were performed on the 500 MHz NMR spectrometer at RT. For complex **1**, HSQC acquisition was performed with a relaxation delay of 1 s and 64 scans per t_1 increment for a total of 128 $t_1$increments. The *g*HMBC acquisition was performed with a relaxation delay of 1 s and 64 scans per t_1 increment for a total of 200 t_1 increments and a multiple-bond coupling constant of 8 Hz. The ROESY acquisition was performed with 32 scans per t_1 increments for a total of 200 $t_1$increments, 200 ms mixing time, and a relaxation delay of 1 s. For complex **2**, HSQC acquisition was performed with a relaxation delay of 1 s and 32 scans per t_1 increment for a total of 128 $t_1$increments. HMBC acquisition was performed with a relaxation delay of 1 s and 32 scans per $t_1$increment for a total of 256 t_1 increments and a multiple-bond coupling constant of 8 Hz. The ROESY acquisition was performed with 32 scans per

t_1 increment for a total of 200 $t_1$increments, 200 ms mixing time, and a relaxation delay of 1 s. The magnetic susceptibility measurement of **2**·0.33MeCN (43 mM in CD_3OD containing 2% of ^{t}BuOH as indicator) was performed in CD_3OD at 21 °C using the Evans method on a 500 MHz NMR spectrometer (details above).[117] Pascal's constants for diamagnetic corrections are taken from the literature.[118]

3.5.3 Synthesis of Compounds

The synthesis of the ligand 2-((2-mercapto-2-methylpropyl)(pyridin-2-ylmethyl)amino)-*N*-(2-mercaptoethyl)acetamide ($H_3N_3S_2^{Me2}$) was comprised of the following steps.

*Step 1, 2-((2-methyl-2-(tritylthio)propyl)(pyridin-2-ylmethyl)amino)-N-(2-(tritylthio)ethyl)-acetamide (**Tr-$N_3S_2^{Me2}$**)*

A batch of 2-bromo-*N*-(2-(tritylthio)ethyl)acetamide (1.1882 g, 2.6980 mmol) and 2-methyl-*N*-(pyridin-2-ylmethyl)-2-(tritylthio)propan-1-amine (1.1748 g, 2.6783 mmol) was mixed in 8 mL of CH_2Cl_2 to afford a homogeneous yellow-brown solution. To this solution was added a homogeneous solution of NaI (0.3947 g, 2.633 mmol) in 32 mL of MeCN, and the mixture was stirred at RT. After the mixture was stirred for 5 min, white insolubles formed. To the reaction mixture was next added a solid batch of K_2CO_3 (3.4521 g, 24.979 mmol), which was stirred at RT for 1 week. The resulting pale insolubles were filtered from the solution over Celite and washed with MeCN. The combined yellow-orange filtrate was then concentrated to a yellow oil and purified on basic Al_2O_3 with 3:1 hexanes/ethyl acetate as eluent. The desired product fraction (R_f = 0.21) was collected, concentrated, and dried under high vacuum to yield a yellow foamlike solid (0.8390 g, 1.051 mmol, 39%). mp 59 °C dec. ^{1}H NMR (500 MHz, $CDCl_3$ with 0.05% v/v TMS, δ from TMS): 8.57 (t, 1H, N*H*, confirmed by D_2O exchange, *J* = 5.4 Hz), 8.36 (m, 1H), 7.53 (m, 7H), 7.38 (d, 7H, *J* = 7.3 Hz), 7.20 (m, 20H, integrates higher than expected due to overlap with residual $CHCl_3$), 7.08 (m, 2H), 3.56 (s, 2H), 3.12 (m, 4H), 2.36 (t, 2H, *J* = 6.8 Hz), 2.32 (s, 2H), 0.73 (s, 6H, C*H*$_3$). ^{13}C NMR (125 MHz, $CDCl_3$ with 0.05% v/v TMS, δ from solvent signal): 171.41 (*C*═O), 158.35, 149.61, 145.46, 144.91, 136.43, 130.17, 129.69, 128.02, 127.70, 126.77, 126.57, 123.53, 122.45, 67.67, 67.63, 66.70, 63.46, 62.14, 53.38, 38.14, 32.05, 27.54. FTIR (KBr pellet) ν_{max} (cm^{-1}): 3276 (br w, ν_{NH}), 3054 (w), 3029 (w), 2959 (w), 2923 (w), 2865 (w), 1667 (s, ν_{CO}), 1592 (m), 1571 (w), 1518 (m), 1488 (s), 1444 (s), 1317 (w), 1240 (w), 1183 (w), 1148 (w), 1114 (m), 1083 (m), 1033 (m), 1001 (w), 973 (w), 908 (w), 884 (w), 844 (w), 765 (m), 742 (vs), 700 (vs), 675 (m), 629 (w), 620 (m), 504 (w). LR-ESI-MS (*m*/*z*): [M + H]$^+$calcd for

$C_{52}H_{52}N_3OS_2$ (relative abundance), 798.4 (100.0), 799.4 (58.9), 800.4 (24.5), 801.4 (7.9); found, 798.3 (100.0), 799.2 (57.9), 800.2 (25.5), 801.2 (8.2).

*Step 2, 2-((2-mercapto-2-methylpropyl)(pyridin-2-ylmethyl)amino)-N-(2-mercaptoethyl)-acetamide (**$H_3N_3S_2^{Me2}$**)*

A batch of Tr-$N_3S_2^{Me2}$ (0.3538 g, 0.4433 mmol) was dissolved in 12 mL of CH_2Cl_2/TFA (1:1) to yield a red-brown solution with a yellow tint. The reaction mixture was stirred at RT for 15 min. To this solution was then added Et_3SiH (0.294 mL, 1.84 mmol), which caused the solution to immediately lose its color intensity and become a pale red-brown. After 30 min of stirring at RT, the mixture was concentrated via short-path vacuum distillation to yield a red-pink oil with white solids. The oil was triturated with pentane (4 × 5 mL) to remove Ph_3CH. The resulting oil was then dissolved in 12 mL of CH_2Cl_2, and to it was added solid $NaHCO_3$ until no more effervescence was observed. After 2 h of stirring, the solution turned from brown to yellow. The insolubles were filtered off through Celite and washed with CH_2Cl_2. The filtrate was then collected and concentrated to a yellow oil (0.1309 g, 0.4176 mmol, 94%). ^{1}H NMR (500 MHz, $CDCl_3$ with 0.05% v/v TMS, δ from protio solvent): 8.94 (br s, 1H, N*H*, confirmed by D_2O exchange), 8.61 (d, 1H, *J* = 4.6 Hz), 7.65 (m, 1H), 7.21 (m, 2H), 3.83 (s, 2H), 3.55 (q, 2H, *J* = 6.2 Hz), 3.51 (s, 2H), 2.78 (s, 2H), 2.74 (q, 2H, *J* = 7.0 Hz), 1.77 (s, 1H, S*H*, confirmed by D_2O exchange), 1.66 (t, 1H, S*H*, confirmed by D_2O exchange, *J* = 8.5 Hz), 1.14 (s, 6H). ^{13}C NMR (125 MHz, $CDCl_3$, δ from solvent signal): 171.73 (*C*═O), 158.36, 149.81, 136.83, 123.67, 122.84, 69.73, 63.56, 62.36, 46.09, 42.47, 30.80, 24.86. FTIR (neat oil, ATR diamond window), ν_{max} (cm^{-1}): 3274 (br w, ν_{NH}), 3051 (vw), 3009 (w), 2959 (w), 2926 (w), 2861 (w), 2533 (br w, ν_{SH}), 1746 (w), 1655 (s, ν_{CO}), 1591 (m), 1570 (w), 1518 (m), 1462 (w), 1435 (m), 1387 (w), 1361 (w), 1302 (w), 1258 (w), 1235

(w), 1197 (w), 1148 (w), 1122 (m), 1108 (m), 1092 (m), 1048 (w), 1018 (w), 998 (w), 984 (w), 911 (w), 842 (w), 803 (w), 760 (m), 729 (m), 680 (w), 669 (w), 657 (w), 639 (w), 622 (w), 580 (w), 545 (w), 533 (w), 518 (w), 506 (w), 467 (w), 464 (w). LR-ESI-MS (*m*/*z*): $[M - H]^-$ calcd for $C_{14}H_{22}N_3OS_2$ (relative abundance), 312.1 (100.0), 313.1 (17.8), 314.1 (10.1); found, 311.9 (100.0), 312.9 (16.9), 313.9 (10.8).

*Na[Ni($N_3S_2^{Me2}$)] (**2**)*

To 6 mL of MeOH were added solid pieces of sodium metal (0.0951 g, 4.14 mmol), which resulted in vigorous effervescence of H_2 to generate NaOMe in situ. The NaOMe solution was added to 4 mL of a light yellow MeOH solution of $H_3N_3S_2^{Me2}$ (0.3315 g, 1.057 mmol) to yield a dark yellow solution after 1 h of stirring at RT. A 2 mL MeOH solution of $NiCl_2$ (0.1361 g, 1.050 mmol) was then added to the reaction mixture, which immediately became dark red. The red solution was stirred at RT for 18 h. After it was stirred, the solution was filtered over Celite to remove any insolubles and concentrated to a dark solid. This solid was then dissolved in 50 mL of THF and stirred at RT for 1 h. The resulting dark red THF solution was filtered over Celite to remove NaCl. Finally, the filtrate was concentrated to a dark residue, to which a minimal amount of MeCN was added to triturate the solid, and the orange-brown product was collected via vacuum filtration (0.2288 g, 0.5835 mmol, 56%). ^{1}H NMR (500 MHz, $(CD_3)_2SO$, δ from protio solvent): 8.54 (d, 1H, *J* = 4.3 Hz), 8.37 (d, 1H, *J* = 7.8 Hz), 7.82 (td, 1H, *J* = 7.7 Hz, 1.5 Hz), 7.31 (dd, 1H, *J* = 6.9 Hz, 5.1 Hz), 4.80 (d, 1H, *J* = 13.5 Hz), 4.39 (d, 1H, *J* = 13.4 Hz), 3.46 (d, 1H, *J* = 15.1 Hz), 3.30 (d, 1H, *J* = 15.1 Hz), 3.01 (d, 1H, *J* = 12.1 Hz), 2.71 (m, 2H), 2.35 (m, 1H), 1.90 (m, 1H), 1.76 (m, 1H), 1.43 (s, 3H), 1.27 (s, 3H). ^{1}H NMR (500 MHz, CD_3OD, δ from protio solvent): 11.76 (broad s, 1H), 10.14 (d, 1H, *J* = 6.9 Hz), 8.32 (s, 1H), 8.10 (t, 2H, *J* = 7.5 Hz), 6.01 (s, 1H),

5.88 (s, 1H), 5.49 (s, 1H), 4.54 (s, 1H), 4.42 (s, 1H), 4.35 (s, 1H), 3.99 (m, 2H), 2.98 (s, 1H), 1.91 (s, 3H), 1.86 (s, 3H). ^{1}H NMR (500 MHz, D_2O, δ from protio solvent): 10.45 (broad s, 1H), 9.92 (d, 1H, *J* = 6.4 Hz), 8.11 (t, 1H, *J* = 7.6 Hz), 8.04 (s, 1H), 7.29 (broad s, 1H), 5.34 (s, 1H), 5.15 (s, 1H), 4.06 (d, 1H, *J* = 14.3 Hz), 3.80 (d, 1H, *J* = 7.9 Hz), 3.71 (s, 1H), 3.63 (s, 2H), 3.40 (s, 1H), 2.54 (s, 1H), 1.77 (s, 3H), 1.61 (s, 3H). FTIR (KBr pellet), ν_{max} (cm^{-1}): 3390 (br w, ν_{OH} from H_2O), 3058 (vw), 2987 (w), 2952 (w), 2919 (m), 2843 (m), 2252 (w, ν_{CN} from MeCN of crystallization), 1606 (vs, ν_{CO}), 1471 (w), 1479 (w), 1438 (m), 1414 (m), 1372 (vw), 1361 (w), 1325 (w), 1314 (w), 1256 (w), 1204 (w), 1162 (w), 1150 (m), 1135 (w), 1095 (m), 1076 (w), 1062 (w), 1018 (vw), 1003 (m), 968 (vw), 957 (vw), 947 (vw), 927 (vw), 883 (m), 848 (vw), 821 (w), 769 (s), 696 (w), 665 (vw), 625 (w), 587 (vw), 574 (vw), 535 (vw), 521 (vw), 492 (w), 476 (w), 444 (w), 430 (w), 413 (w). UV–vis (MeOH, 25 °C), λ_{max}, nm (ε, M^{-1} cm^{-1}): 459 (250), 557 (75). UV–vis (HEPES buffer pH 7.4, 25 °C), λ_{max}, nm (ε, M^{-1} cm^{-1}): 455 (200), 571 (60). HR-ESI-MS (*m*/*z*): $[M - Na]^-$ calcd for $C_{14}H_{20}N_3NiOS_2$ (relative abundance), 368.040 (100.0), 369.043 (17.8), 370.036 (48.6), 371.039 (8.9), 372.033 (8.8), 374.033 (1.4); found, 368.041 (100.0), 369.044 (15.9), 370.036 (49.8), 371.039 (8.5), 372.033 (9.5), 374.033 (1.2). μ_{eff} (solution, 21 °C): 0.81 μ_B in CD_3OD. Anal. Calcd for $C_{14}H_{20}N_3NiOS_2Na \cdot 0.8MeCN \cdot 2.7MeOH$: C, 42.97; H, 6.54; N, 10.41. Found: C, 42.63; H, 6.90; N 10.74. An elemental analysis consistent with full (or without) solvent occupancy has not been obtained.

*K[Ni($N_3S_2^{Me2}$)] (**2^K**)*

A batch of 0.102 g (2.54 mmol) of KH was added to 3 mL of MeOH to generate KOMe. To this solution was then added 0.228 g (0.727 mmol) of $H_3N_3S_2^{Me2}$ in 4 mL of MeOH. After the

mixture was stirred at RT for 30 min, a solid batch of $Ni(OAc)_2 \cdot 4H_2O$ (0.160 g, 0.643 mmol) was added that generated a deep red-brown solution within seconds. After 2 h of stirring at RT, the reaction mixture was filtered to remove any insolubles and concentrated to dryness. The resultant brown residue was taken up in 4 mL of a MeOH/MeCN (1:1) solution, and 10 mL of Et_2O was slowly added to result in the precipitation of 0.271 g of solid (0.664 mmol, >100%, byproducts such as KOAc present in the isolated product). Lustrous red, microcrystalline solids deposited from the mother liquor over 48 h; the FTIR spectrum of the bulk and microcrystalline products indicate the same product. Recrystallization of these solids by slow diffusion of Et_2O into a MeOH/MeCN (1:1) saturated solution of the product afforded small red-orange crystals suitable for X-ray diffraction. The spectroscopic properties of this compound were nearly identical with those of **2**.

*$Na[Zn(N_3S_2^{Me2})]$ (**3**)*

A yellow MeOH solution (3 mL) containing $H_3N_3S_2^{Me2}$ (0.1657 g, 0.5286 mmol) was mixed with sodium metal (0.0429 g, 1.87 mmol) to result in vigorous bubbling and a dark yellow homogeneous solution. After 20 min of stirring at RT, a 1 mL MeOH solution containing $ZnCl_2$(0.0719 g, 0.528 mmol) was added, resulting in immediate precipitation of white solids. After it was stirred at RT for 90 min, the reaction mixture was filtered over Celite to remove the white (NaCl) solid, and the filtrate was stripped to dryness to yield a yellow solid. The yellow solid was dissolved in 30 mL of THF and stirred at RT for 6 h. The light yellow insoluble solid was collected and washed with copious amounts of THF and then stirred in 25 mL of MeCN at RT for 3 h. The light yellow insolubles were collected by vacuum filtration and washed with MeCN to yield 0.1995 g (0.5002 mmol, 95%) of product. ^1H NMR (500 MHz, CD_3OD, δ from protio

solvent): 8.88 (d, 1H, *J* = 4.8 Hz), 7.94 (t, 1H, *J* = 7.2 Hz), 7.50 (t, 1H, *J* = 6.3 Hz), 7.41 (d, 1H, *J* = 7.8 Hz), 4.17 (d, 1H, *J* = 16.0 Hz), 3.83 (d, 1H, *J* = 15.9 Hz), 3.46 (d, 2H, *J* = 16.5 Hz), 3.23 (d, 1H, *J* = 17.2 Hz), 3.16 (m, 1H), 2.86 (d, 1H, *J* = 12.9 Hz), 2.78 (m, 1H), 2.53 (m, 1H), 2.25 (dd, 2H (integrates high due to unidentified impurity), *J* = 16.6, 9.5 Hz), 1.39 (s, 3H), 1.15 (s, 3H). FTIR (KBr pellet), ν_{max} (cm^{-1}): 3396 (br w, ν_{OH} from H_2O), 2951 (w), 2897 (m), 2873 (w), 2848 (w), 2827 (w), 1661 (w sh), 1604 (vs, ν_{CO}), 1589 (vs, ν_{CO}), 1478 (w), 1436 (m), 1403 (s), 1356 (w), 1325 (m), 1290 (m), 1271 (m), 1210 (w), 1176 (w), 1138 (w), 1124 (w), 1091 (m), 1050 (w), 1022 (w), 987 (w), 963 (w), 906 (w), 887 (w), 823 (w), 760 (w), 728 (w), 686 (w), 659 (w), 642 (w), 602 (w), 543 (w), 487 (w), 477 (w), 444 (w). LR-ESI-MS (*m*/*z*): $[M - Na]^-$ calcd for $C_{14}H_{20}N_3OS_2Zn$ (relative abundance), 374.0 (100.0), 375.0 (17.8), 376.0 (67.5), 377.0 (17.1), 378.0 (45.1); found, 374.0 (100.0), 374.9 (15.5), 375.9 (65.4), 376.9 (18.6), 377.8 (47.2). HR-ESI-MS (*m*/*z*): $[M - Na]^-$ calcd for $C_{14}H_{20}N_3OS_2Zn$ (relative abundance), 374.034 (100.0), 375.037 (17.8), 376.031 (67.5), 377.034 (17.1), 378.030 (45.1), 379.033 (5.8), 380.025 (4.8); found, 374.035 (100.0), 375.038 (16.4), 376.032 (64.7), 377.034 (18.4), 378.030 (41.7), 379.033 (5.2), 380.026 (3.0). Anal. Calcd for $C_{14}H_{20}N_3ZnOS_2Na \cdot 2NaCl \cdot 0.3MeOH$: C, 32.70; H, 4.07; N, 8.00. Found: C, 32.96; H, 3.54; N, 7.49. Despite several attempts, no satisfactory elemental analysis results could be obtained.

3.5.4 Bulk oxidation of 2

To a 2 mL DMF solution of **2** (0.0767 g, 0.196 mmol) was added a 3 mL DMF solution of $FcPF_6$(0.0647 g, 0.195 mmol) to yield a dark brown solution. After 1 h of stirring at RT, the DMF was removed via short-path vacuum distillation to yield a dark residue. This material was triturated

with Et_2O (3 × 5 mL), and the combined yellow Et_2O-soluble component was identified as Fc (0.0312 g, 0.168 mmol, 86%). The Et_2O insolubles were dissolved in 10 mL of MeCN to afford a dark brown solution with some black insolubles. The MeCN-soluble component (0.0822 g, 0.0973 mmol, 115%; the yield is greater due to the presence of $NaPF_6$ (based on IR); a similar scenario is reported for the oxidation of **1** with $FcPF_6$(51)) was collected by filtration and dried under high vacuum overnight. LR-ESI-MS (*m*/*z*): $[2M + H]^+$ calcd for $C_{28}H_{41}N_6Ni_2O_2S_4$ (relative abundance), 737.1 (100), 738.1 (35.7), 739.1 (99.5), 740.1 (36.4), 741.1(43.9), 742.1 (10.3), 743.1 (9.7), 744.1 (1.2); found, 737.1 (99.3), 738.1 (29.0), 739.1 (100), 740.0 (36.7), 741.0 (46.4), 742.0 (17.6), 743.0 (15.3), 744.0 (5.8); $[2M + Na]^+$ calcd for $C_{28}H_{40}N_6Ni_2O_2S_4Na$ (relative abundance), 759.1 (100), 760.1 (35.7), 761.1 (99.5), 762.1 (36.3), 763.1 (45.0), 764.1 (13.2) 765.1 (11.4), 766.1 (1.2), 7671 (1.0); found, 759.0 (100), 759.9 (34.7), 761.0 (95.4), 761.9 (35.1), 763.0 (47.0), 764.0 (19.1) 765.0 (15.2); $[M – Na]^-$ (very minor) calcd for $C_{14}H_{20}N_3NiOS_2$ (relative abundance), 368.0 (100), 369.0 (17.8), 370.0 (48.6), 371.0 (8.9), 372.0 (8.8); found, 368.0 (100.0), 369.0 (20.3), 370.0 (45.4), 371.0 (13.0), 372.0 (13.3). FTIR (KBr pellet), ν_{max} (cm^{-1}): 1668 (s, ν_{CO}, DMF), 1594 (s, ν_{CO}), 845 (vs, ν_{PF}).

3.5.5 General Reaction of 2 with N_3^- and $O_2^{\bullet-}$

All reactions of **2** with NaN_3 or KO_2 (solubilized with 18C6 in some cases) were performed in quartz UV–vis cuvettes and monitored by UV–vis spectroscopy and/or LR-ESI-MS under anaerobic conditions in 50 mM HEPES (pH 7.4) buffer or MeOH at 25 °C.

Reaction of 2 and NaN_3 in pH 7.4 HEPES

A 120 μL aliquot (10 mol equiv) of a 327 mM buffer solution of NaN_3 was placed in a cuvette containing **2** (2.380 mL, 1.63 mM) in buffer to yield final concentrations of 1.55 and 15.7 mM for **2** and NaN_3, respectively (total volume 2.500 mL). The UV–vis spectrum was recorded immediately and monitored at 5 min intervals over 5 h. After 5 h, UV–vis was recorded at 1 h intervals for 20 h.

Reaction of 2 and NaN_3 in MeOH

A 332 μL aliquot (10 mol equiv) of a 120 mM MeOH solution of NaN_3 was placed in a cuvette containing **2** (2.168 mL, 1.84 mM) in MeOH to yield a final concentration of 1.60 and 15.9 mM for **2** and NaN_3, respectively (total volume 2.500 mL). The UV–vis spectrum was recorded immediately and monitored at 5 min intervals for 17 h. LR-ESI-MS was recorded after ~30 h.

Reaction of 2 with KO_2 in pH 7.4 HEPES

A 158 mM stock solution of KO_2 was prepared in DMSO containing 2 mol equiv of 18C6. A 200 μL aliquot (10 mol equiv) of the KO_2 stock was placed in a cuvette containing **2** (3.100 mL, 1.02 mM) in buffer to yield final concentrations of 0.958 and 9.58 mM for **2** and KO_2, respectively (total volume 3.300 mL). The UV–vis spectrum was recorded immediately and monitored at 15 min intervals for 15 h.

Reaction of 2 with KO_2 in MeOH

A 383 μL aliquot (10 mol equiv) of a 104 mM MeOH solution of KO_2 was placed in a cuvette containing **2** (2.117 mL, 1.88 mM) in MeOH to yield final concentrations of 1.59 and 15.9

mM for **2** and KO_2, respectively (total volume 2.500 mL). The UV–vis spectrum was recorded immediately and monitored at 5 min intervals for 17 h. LR-ESI-MS was recorded after 17 h.

3.5.6 NBT Assay

The NBT assay of **1** and **2** was performed in quartz UV–vis cuvettes and monitored by UV–vis spectroscopy under anaerobic conditions in 50 mM HEPES (pH 7.4) buffer at 25 °C. Using **2** as a general representative, a 59 μL aliquot of a 5 mM buffer solution of **2** was placed in a cuvette containing NBT (3.000 mL, 98 μM) in buffer to yield a final concentration of 97 μM for both **2** and NBT (total volume 3.059 mL). The UV–vis spectrum was recorded immediately and monitored at 1 min intervals for 30 min. After 30 min, UV–vis was recorded at 30 min intervals for 17 h.

3.5.7 AR-HRP Assay for H_2O_2 Detection

The AR-HRP assay was prepared using the protocol described by Haugland and co-workers.[100] Milli-Q grade water (18.0 MΩ cm) was used to prepare 50 mM HEPES (pH 7.4) buffer, which was treated with Chelex 100 for 18 h to remove trace metals. The excitation wavelength (λ_{ex}) was set at 563 nm unless stated otherwise. The slit widths for both excitation and emission were set at 1 nm. The fluorescence signals were collected from 570 to 700 nm, and the integrated fluorescence intensity was calculated using SigmaPlot. All measurements were performed in triplicate, and we report the average. Solid samples of **2** and **3** were dissolved in DMF to yield 180 μM stock solutions of the complexes.

As AR and HRP are stable to air, all solutions for the standard curve were prepared under aerobic conditions. A 100 μM solution of AR was prepared by diluting aliquots of a 10 mM stock of AR in DMSO (stored at −20 °C) with HEPES. A stock solution of HRP was prepared by dissolving the powdered HRP into HEPES to yield a 10 U/mL HRP stock solution. A 100 μM stock solution of H_2O_2 was prepared by diluting the 30% H_2O_2 solution with HEPES. The standard curve was obtained by adding known concentrations of H_2O_2 into a mixture of 10 μM AR and 1 U/mL of HRP with a final volume of 3.000 mL. The UV–vis and fluorescence spectra were collected 30 min after addition of H_2O_2 to allow for complete reaction. The blank consisted of a 3.000 mL solution of 10 μM AR and 1 U/mL HRP in HEPES. Due to the air sensitivity of **2**, all solutions were prepared with degassed solvents. The reaction mixture contained a total volume of 3.000 mL with 10 μM of AR, 1 U/mL of HRP, 3 μM of KO_2/18C6 (1:1), and 3 μM of **2**. The fluorescence intensity of the aforementioned mixture was compared to a control sample with no complex: i.e., 3 μM KO_2/18C6 (1:1) with 10 μM of AR and 1 U/mL of HRP.

3.5.8 Computational Details

Density functional theory (DFT) calculations were performed with the ORCA electronic structure package, version 3.0.3.[119] Geometry optimization and frequency analysis of all models were performed using the BP86 functional[120,121] along with resolution of the identity (RI) approximation[122] and Grimme's D3(BJ) dispersion correction[123,124] with coordinates from the crystal structures of **1** and **2**. The triple-ζ basis set def2-TZVPP[125,126] was used for geometry optimization and frequency analysis with an automatically constructed auxiliary basis set on all atoms. No imaginary frequencies were found.

Single-point energy (SPE) calculations were performed on the optimized structures using the OLYP functional (OPTX exchange functional of Cohen and Handy[127] coupled with Lee, Yang, and Parr's correlation functional[128]) with RI approximation.[122] The triple-ζ basis set def2-TZVPP[125,126] was used for all atoms with the matching auxiliary basis set def2-TZVPP/J. The conductor-like screening model (COSMO)[129] was utilized to model solvent environments of DMF (ε = 38.3, n = 1.430). UCSF Chimera[130] was used to generate model structures and to visualize isosurface plots of MOs and spin-density plots with isodensity values of 0.05 and 0.002 a.u., respectively.

3.5.9 X-ray Crystallographic Data Collection and Structure Solution and Refinement

Red rectangular crystals of **2** were obtained from a saturated solution of **2** in CD_3CN stored in a −20 °C freezer. Slow diffusion of Et_2O into a saturated MeOH/MeCN (1:1) solution of $\mathbf{2^K}$ yielded red-orange crystals of $\mathbf{2^K}$. Colorless crystals of **3** were grown by slow diffusion of Et_2O into a saturated MeOH solution of **3** at −20 °C. Crystals of the ligand-oxidized product of **2**, namely **5**, were obtained by slow diffusion of Et_2O into a saturated MeOH/THF (1:1) solution of $\mathbf{2^K}$ stored under atmospheric conditions at RT for 3 weeks. Suitable crystals were mounted on a glass fiber. The X-ray intensity data were measured at 100 K on a Bruker SMART APEX II X-ray diffractometer system with graphite-monochromated Mo Kα radiation (λ = 0.71073 Å) using the ω-scan technique controlled by the SMART software package.[131] The data were collected in 1464 frames with 10 s exposure times. The data were corrected for Lorentz and polarization effects[132] and integrated with the manufacturer's SAINT software. Absorption corrections were applied with the program SADABS.[133] Subsequent structure refinement was performed using the

SHELXTL 6.1 solution package operating on a Pentium computer. The structure was solved by direct methods using the SHELXTL 6.1 software package.[134,135] All non-hydrogen atoms were refined anisotropically[136] and were located from successive difference Fourier map calculations. For **5**, a twinning feature was detected and the reflections were indexed in two domains using PLATON. The HKLF 4 file was used for structure solution, while the HKLF 5 file was used for structure refinement. Although the twinning processing helps significantly reduce the remaining electron density around the heavy atoms of Ni(1) and Ni(2), they are still large with alerts at level B. Peaks and holes around the heavy atoms (Ni(1) and Ni(2) with distances of 0.95 and 0.85 Å, respectively) on the final difference map ranging from 3.339 to −1.533 e/Å^{3}were of no chemical significance. The current level B alerts were thus associated with poor quality of data that might be caused by a phase transition in low-temperature data collection. Selected data and metric parameters for these complexes are summarized in Table 3.2 or Table 3.S1 in the Supporting Information.

3.5.10 X-ray absorption spectroscopy (XAS)

Nickel XAS data were collected on four samples: **1** and **2** in solid form and **1** and **2** dissolved in MeOH. All samples are oxygen-sensitive and were prepared in an anaerobic glovebox immediately prior to data collection. Complexes **1** and **2** were dissolved in MeOH to a concentration of 3 mM Ni. Solid samples of **1** and **2** were diluted with inert BN at a 4:1 BN/sample ratio (w/w). XAS data were collected at the Stanford Synchrotron Radiation Lightsource (SSRL) on beamline 7-3, which utilizes a Si[220] double-crystal monochromator with an inline mirror for X-ray focusing and for harmonic rejection. During data collection, samples

were maintained at 12 K using a liquid He continuous flow cryostat. Fluorescence XAS spectra were collected for solution samples, while transmittance spectra were collected for the solid compound. Protein fluorescence excitation spectra were collected using a 30-element Ge solid-state detector, and a Co fluorescence filter (0.6 μM in width) was placed between the cryostat and detector to filter out lower energy photons. All spectra were measured in 5 eV increments in the pre-edge region (8265–8325 eV), 0.25 eV increments in the edge region (8325–8405 eV), and 0.05 $Å^{-1}$ increments in the extended X-ray absorption fine structure (EXAFS) region (out to $k = 14$ $Å^{-1}$), integrating from 1 to 25 s in a k^3-weighted manner for a total scan length of approximately 50 min. X-ray energies were individually calibrated by collecting Ni-foil absorption spectra simultaneously with the compound spectra; the first inflection point of the Ni-foil spectrum was assigned at 8333 eV. Data represent the average of four to six scans. All spectra were collected on independent duplicate samples to ensure spectral reproducibility.

XAS spectra were processed using the Macintosh OS X version of the EXAFSPAK program suite[137] integrated with the Feff v8 software[138] for theoretical model generation. Data reduction utilized a Gaussian spline for background removal in the pre-edge region and a three-region cubic spline throughout the EXAFS. Data were converted to k space using a Ni E_0 value of 8333 eV. The k^3-weighted EXAFS was truncated between 1.0 and 13.0 $Å^{-1}$ for filtering purposes. This k range corresponds to a spectral resolution of ca. 0.12 Å for all Ni–ligand interactions; therefore, only independent scattering environments outside 0.12 Å were considered resolvable in the EXAFS fitting analysis.[139] EXAFS fitting analysis was performed first on filtered data and then verified on the raw unfiltered data. EXAFS data were fit using both single- and multiple-scattering amplitude and phase functions calculated with the program Feff v8. Single-scattering theoretical models were calculated for carbon, nitrogen, and sulfur coordination to simulate Ni nearest-

neighbor ligand environments. Scale factor (Sc) and E_0values, used in a static manner during the simulations, were calibrated by fitting crystallographically characterized Ni models; specific values include a scale factor of 0.9 and E_0values of −10.55 eV for N/C and −12.22 eV for S. Criteria for judging the best-fit simulation utilized both the lowest mean square deviation between data and fit (F'), corrected for the number of degrees of freedom, and a reasonable Debye–Waller factor.[140,141] Pre-edge analysis was done using EDG_FIT software. A spline function was best-fit between 8328 and 8342 eV, and a two-peak model was applied to accommodate the 1s → 3d and 1s → 4p pre-edge features.

3.6 Supporting Information

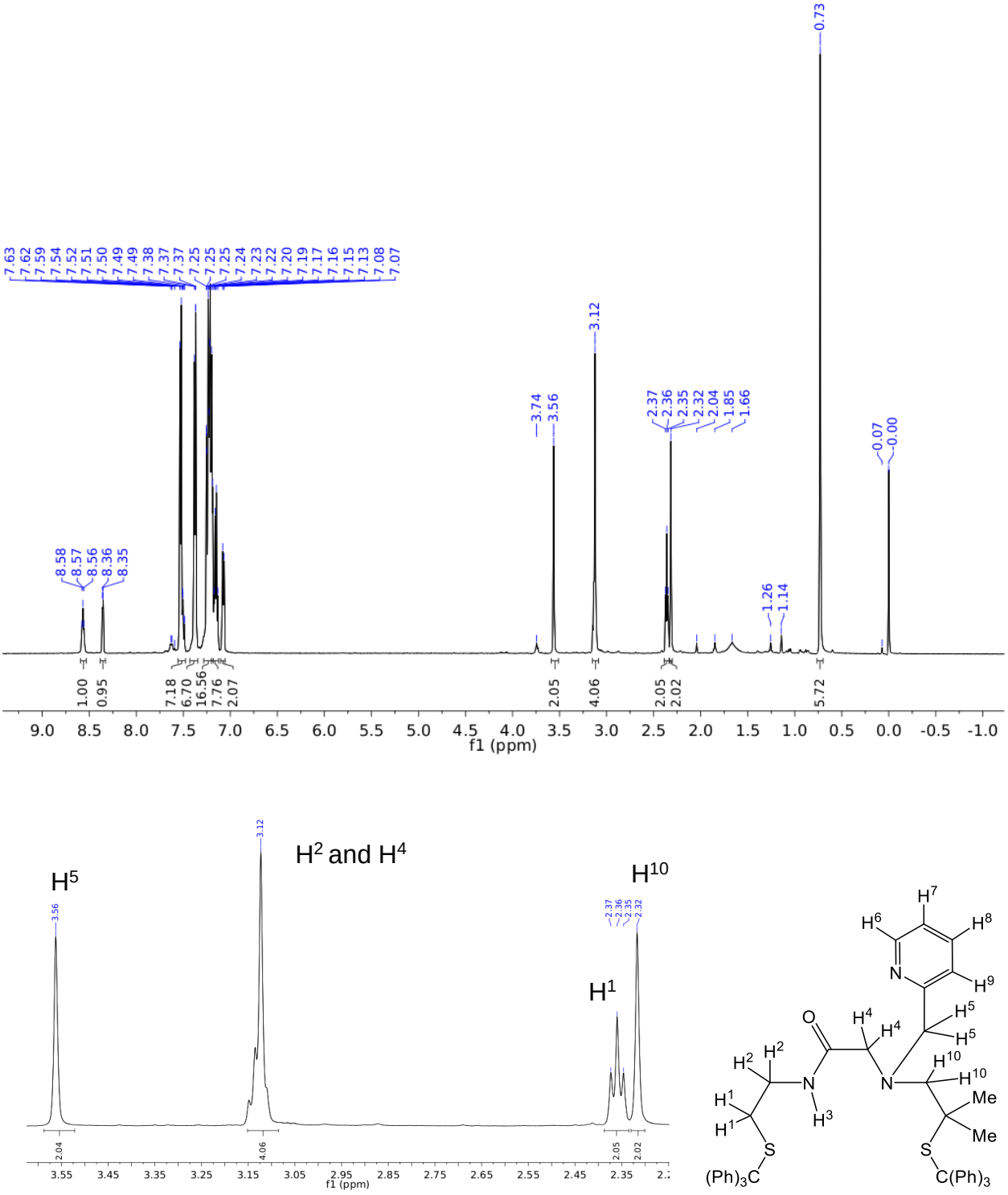

Figure 3.S1 *Top:* ^{1}H NMR spectrum of **Tr-N$_3$S$_2^{Me2}$** in $CDCl_3$ containing 0.05% v/v TMS at RT (δ vs. residual protio solvent signal). The peaks at 7.26 and 1.66 ppm are from protio solvent and water, respectively. *Bottom:* Expansion of the aliphatic regions.

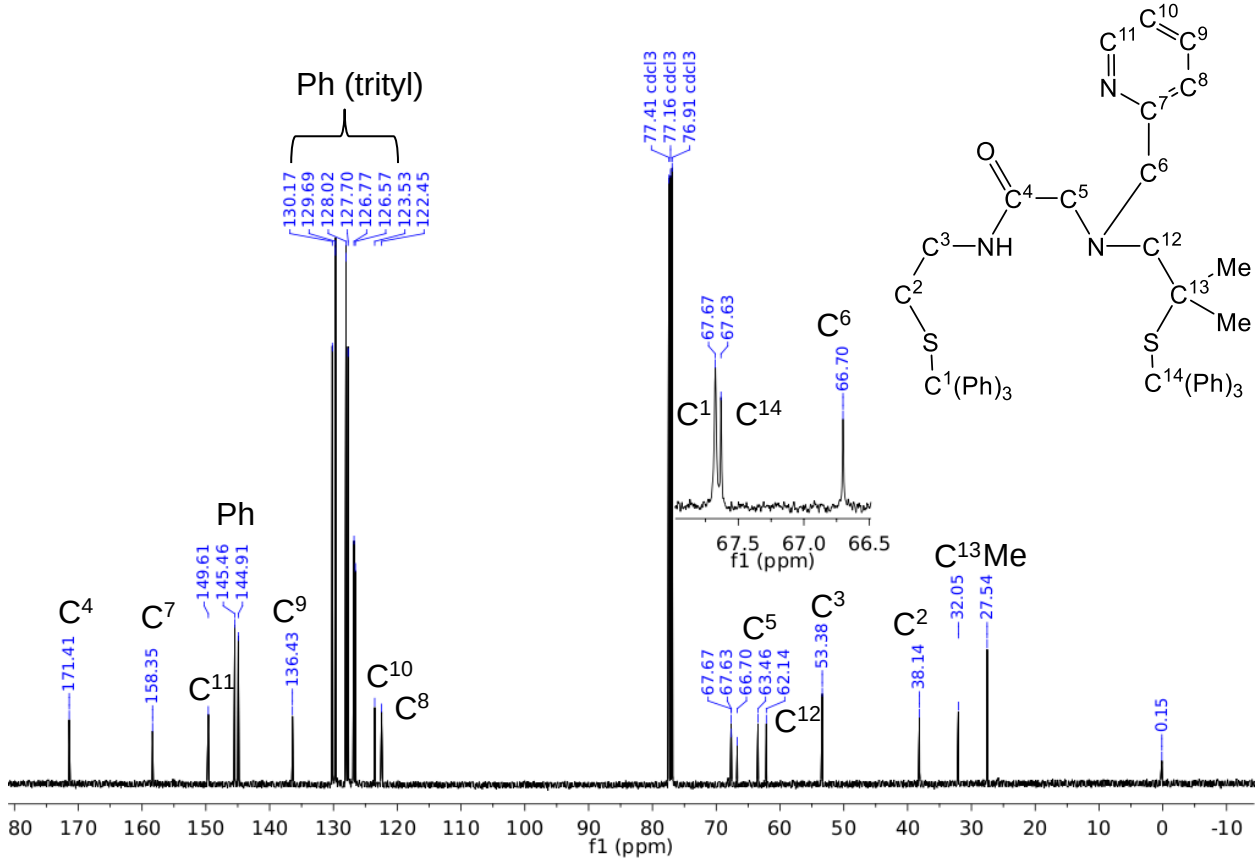

Figure 3.S2 ^{13}C NMR spectrum of **Tr-N$_3$S$_2^{Me2}$** in $CDCl_3$ containing 0.05% v/v TMS at RT. *Inset*: zoom-in of 66-68 ppm region. Solvent signal at 77.16 ppm is indicated.

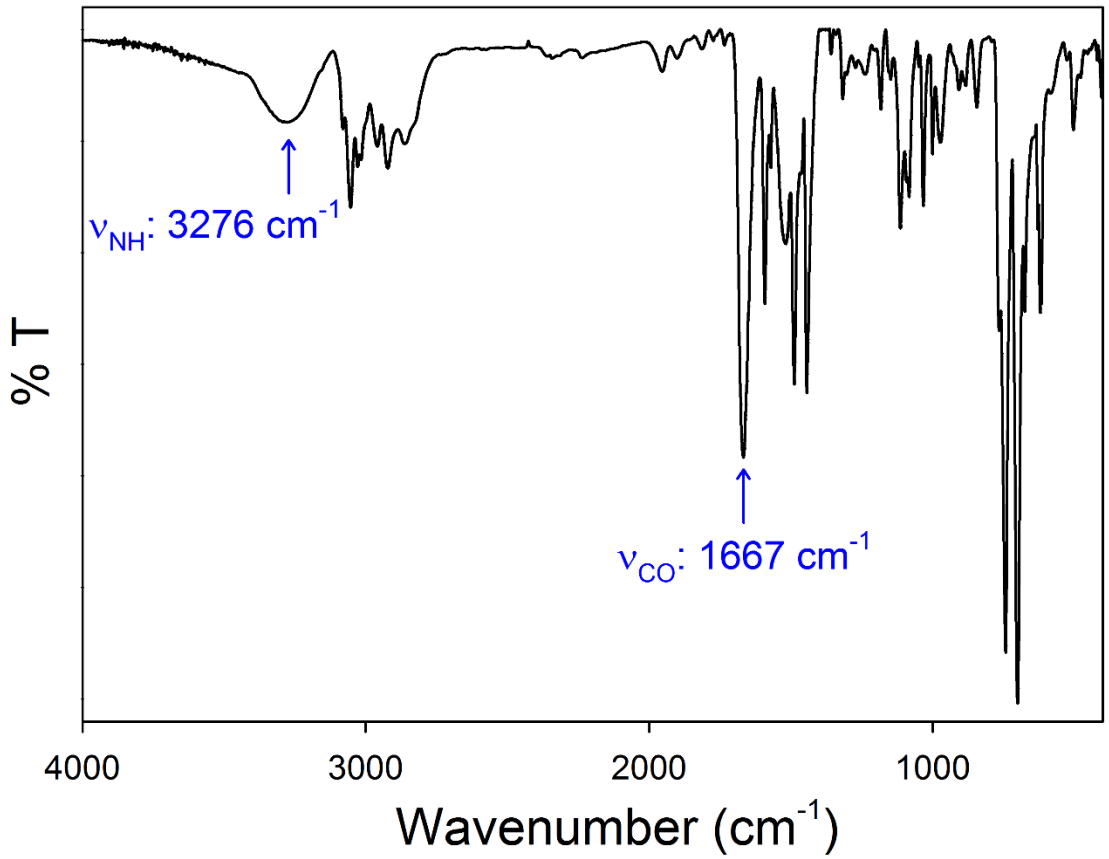

Figure 3.S3 Solid-state FTIR spectrum of **Tr-N$_3$S$_2^{Me2}$** in a KBr matrix at RT.

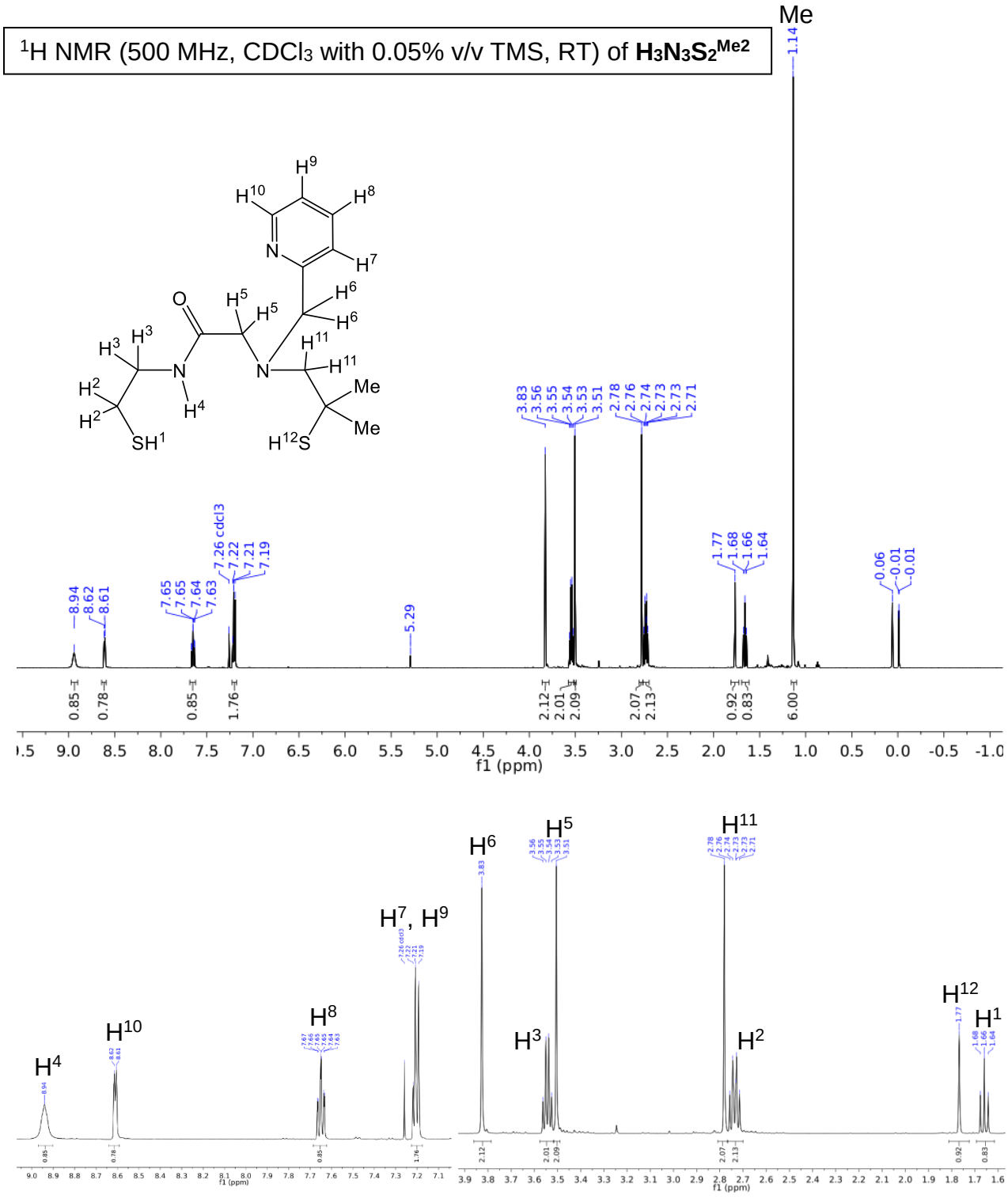

Figure 3.S4 *Top*: ^{1}H NMR spectrum of $\mathbf{H_3N_3S_2^{Me2}}$ in $CDCl_3$ containing 0.05% v/v TMS at RT (δ vs. residual protio solvent signal). The peak at 7.26 ppm is from protio solvent. Minor amounts of grease (0.06 ppm) and CH_2Cl_2 (5.29 ppm) are present from workup. *Bottom*: expansion of the aromatic and aliphatic regions.

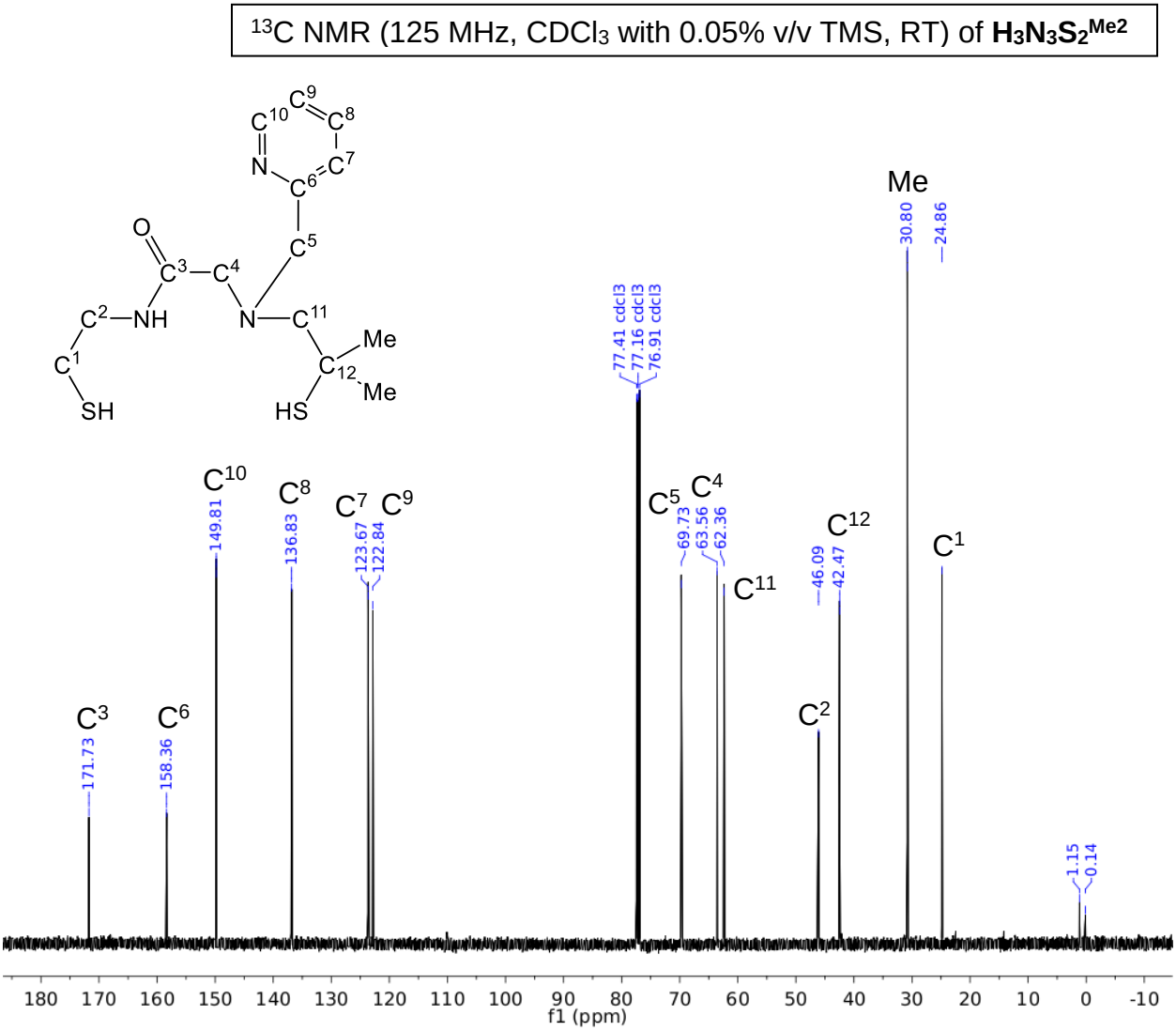

Figure 3.S5 ^{13}C NMR spectrum of **$H_3N_3S_2^{Me2}$** in $CDCl_3$ containing 0.05% v/v TMS at RT. Solvent signal at 77.16 ppm is indicated.

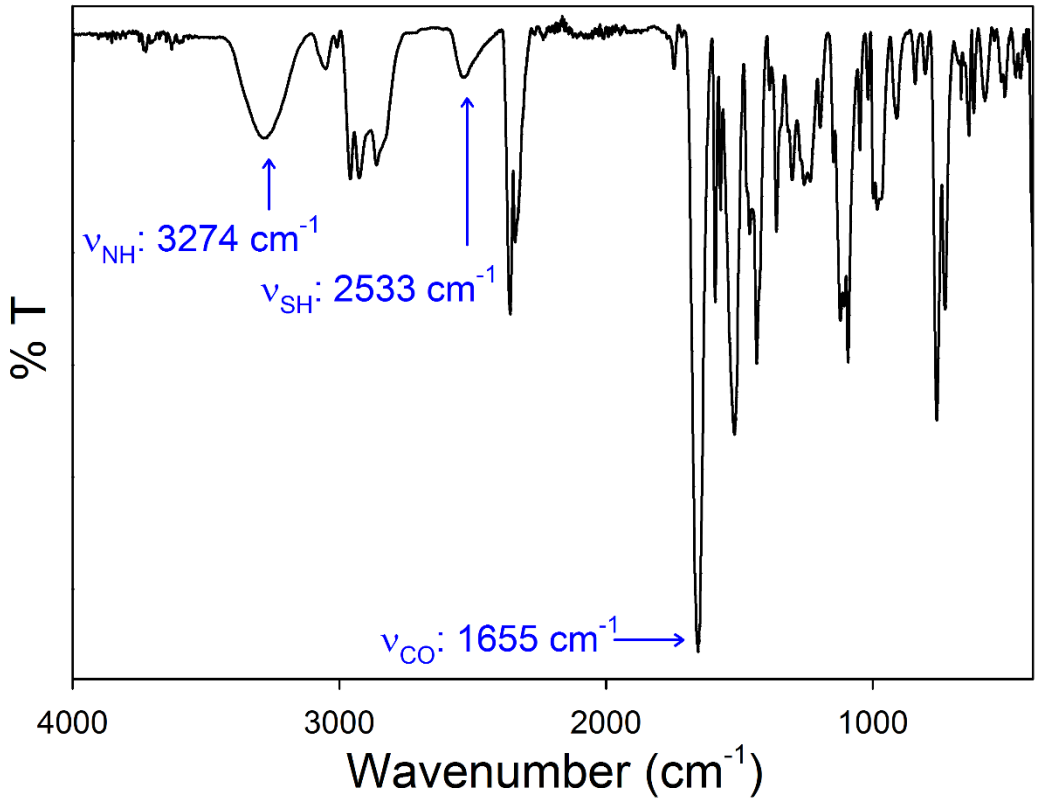

Figure 3.S6 FTIR spectrum of **$H_3N_3S_2^{Me2}$** as a neat oil at RT (ATR diamond).

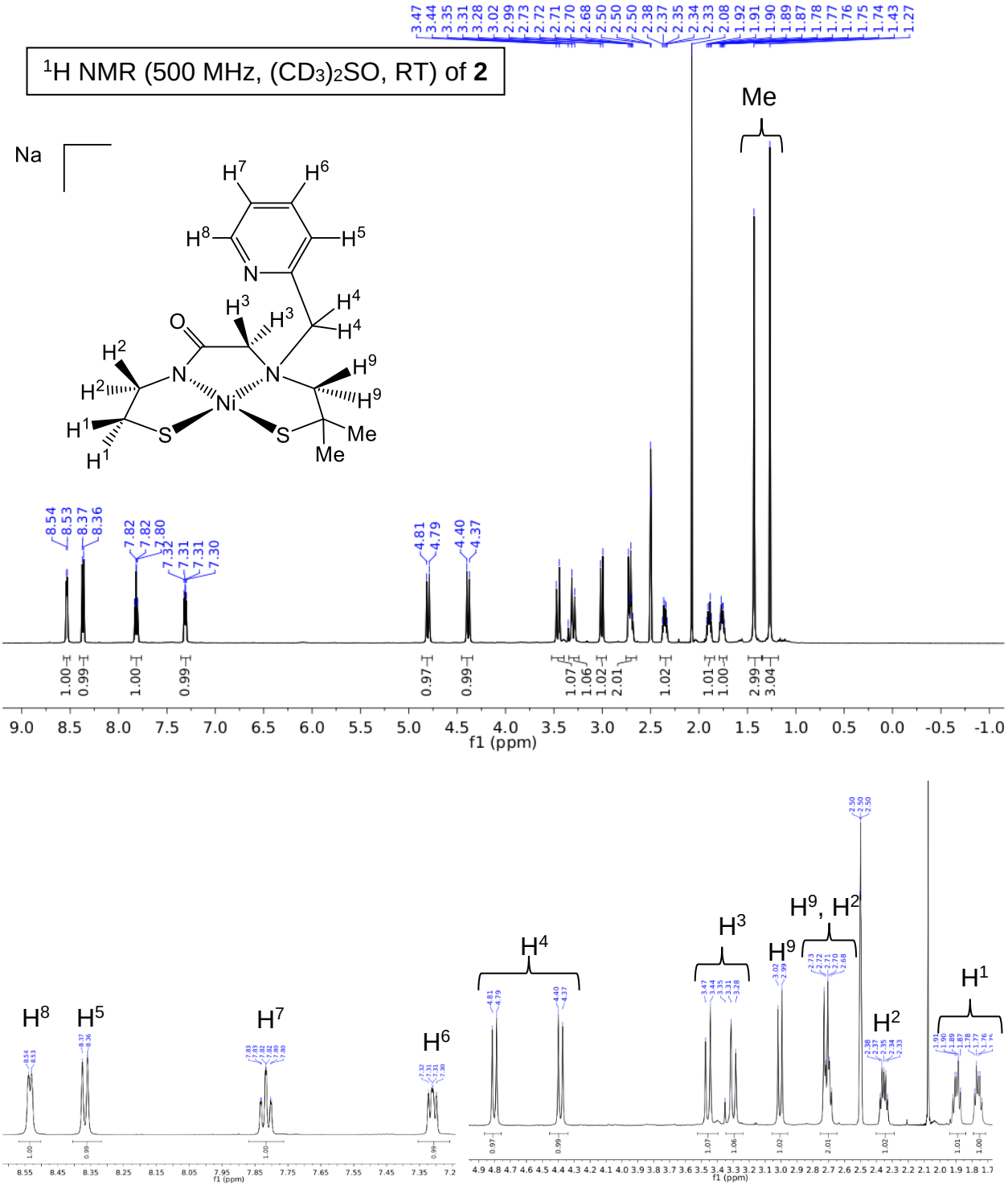

Figure 3.S7 *Top*: ^{1}H NMR spectrum of **2** in $(CD_3)_2SO$ at RT (δ vs. residual protio solvent signal). Peaks at 2.50 and 3.35 ppm are from protio solvent and water, respectively. The peak at 2.08 ppm is from MeCN solvent of crystallization. *Bottom*: expansion of aromatic and aliphatic regions.

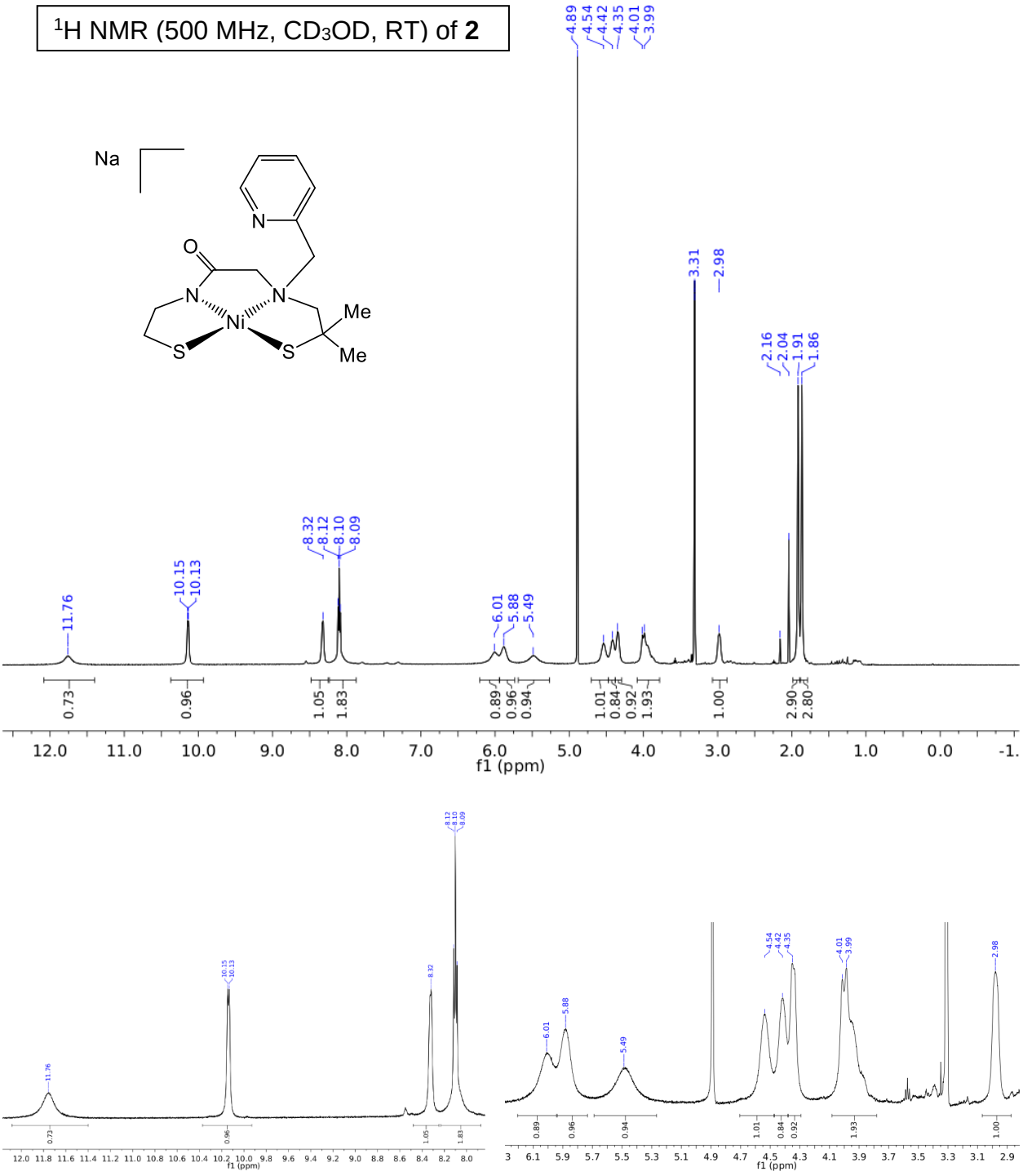

Figure 3.S8 *Top*: ^{1}H NMR spectrum of **2** in CD_3OD at RT (δ vs. residual protio solvent signal). Peaks at 3.31 and 4.89 ppm are from residual protio solvent and water, respectively. MeCN solvent of crystallization is present at 2.04 ppm. *Bottom*: expansion of aromatic and aliphatic regions.

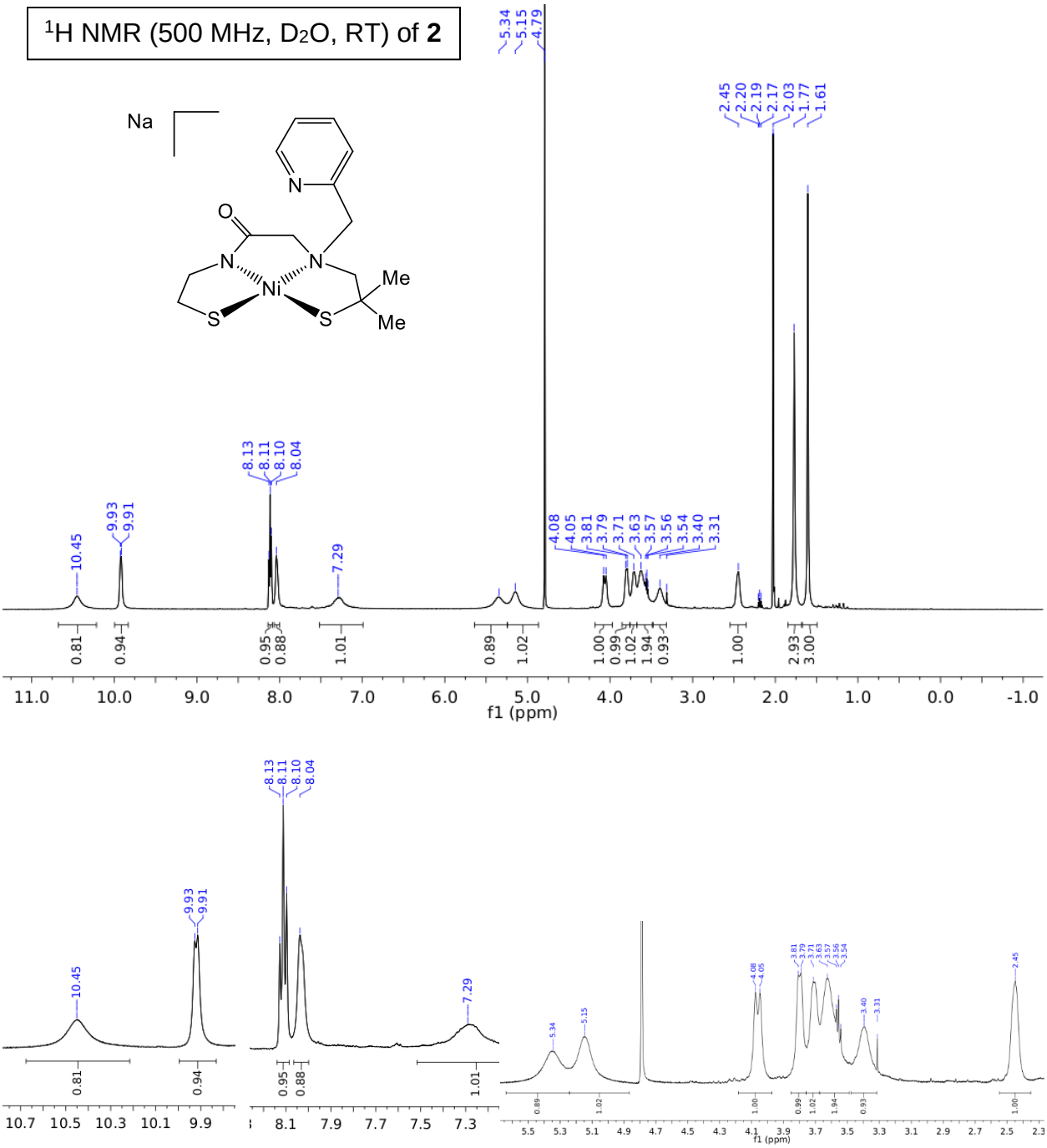

Figure 3.S9 *Top*: ^{1}H NMR spectrum of **2** in D_2O at RT (δ vs. residual protio solvent signal). Solvent residual and MeCN solvent of crystallization at 4.89 and 2.03 ppm, respectively, are present. Minor amounts of Et_2O (1.17, 3.56 ppm), acetone (2.19 pm), and MeOH (3.31 ppm) are also present. *Bottom*: expansion of aromatic and aliphatic regions.

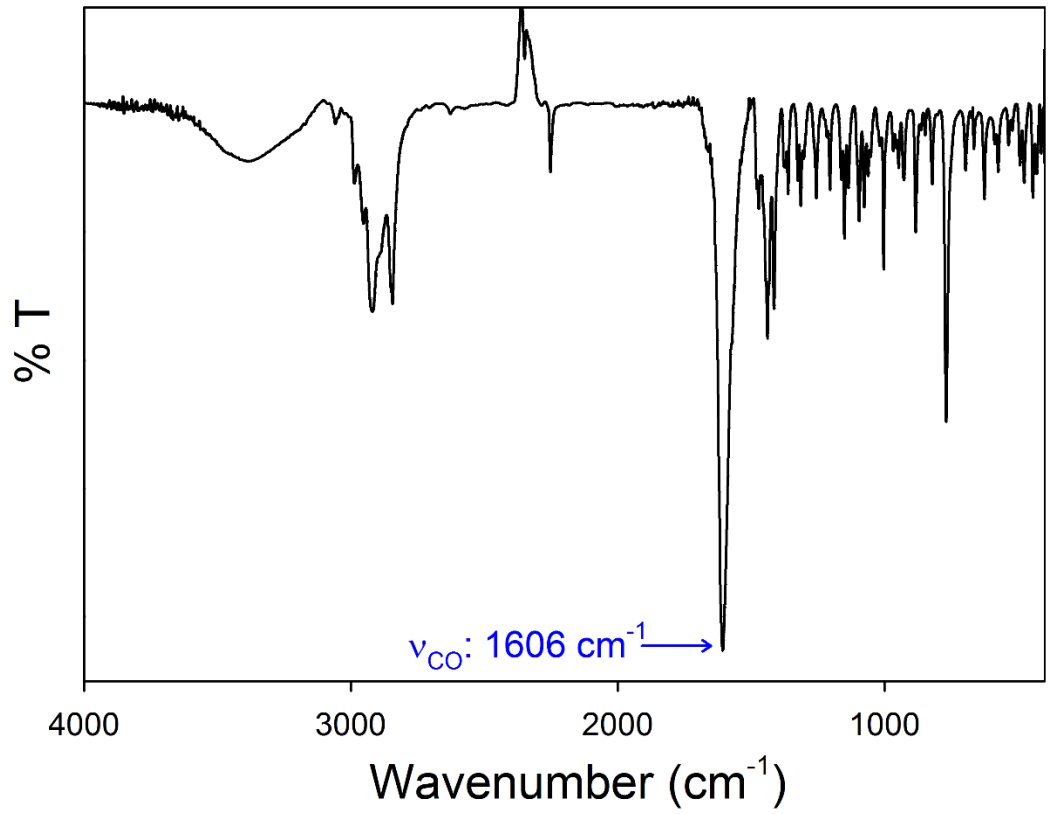

Figure 3.S10 Solid-state FTIR spectrum of **2** in a KBr matrix at RT.

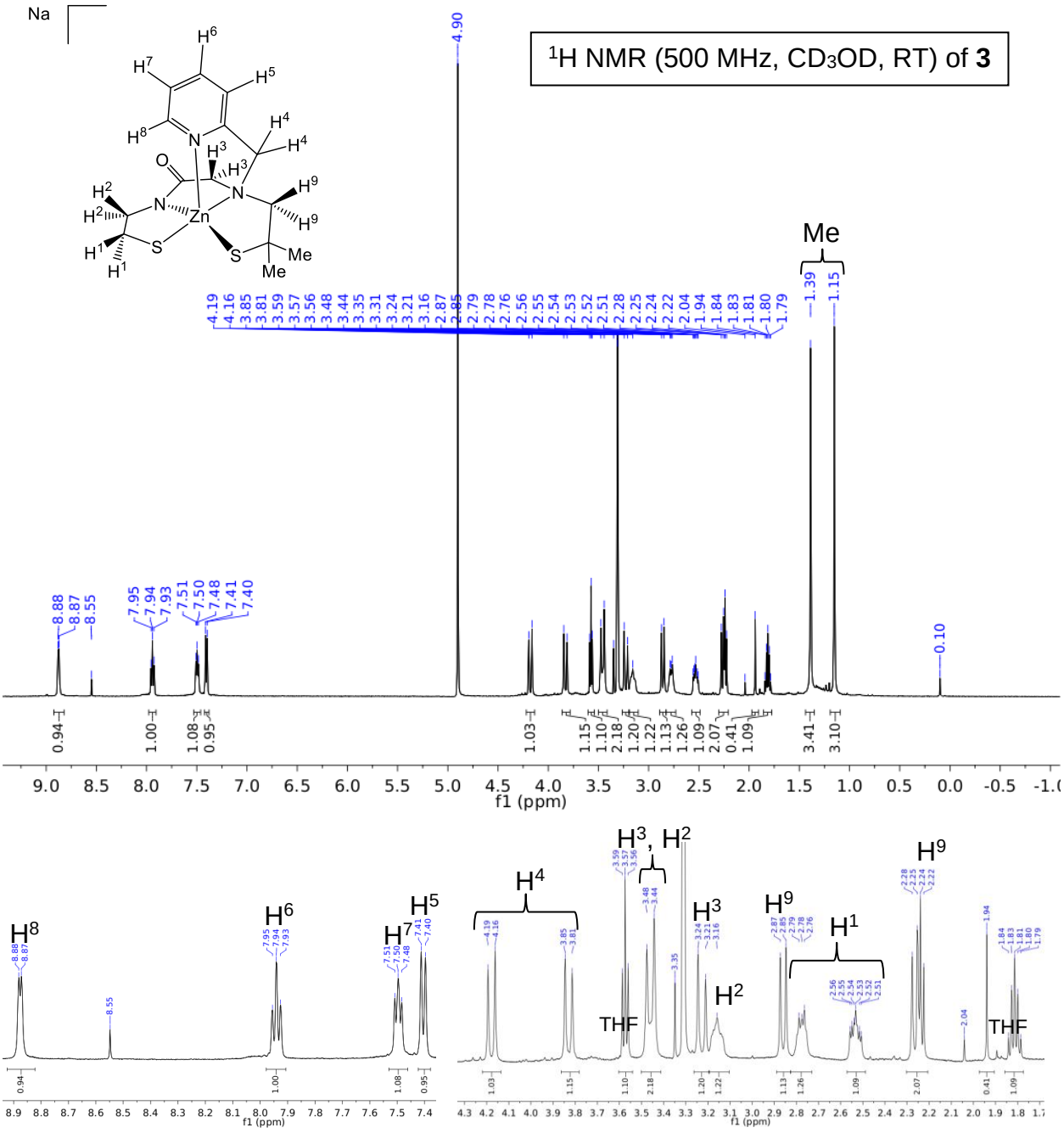

Figure 3.S11 *Top*: ^{1}H NMR spectrum of **3** in CD_3OD at RT (δ vs. residual protio solvent signal). Peaks at 3.31 and 4.90 ppm are from residual protio solvent and water, respectively. MeOH solvent of crystallization is present at 3.35 ppm. A minor amount of THF (1.81 and 3.57 ppm) is also present. The peaks at 8.55, 2.25, and 1.94 ppm are minor impurities that have not been identified. *Bottom*: expansion of aromatic and aliphatic regions.

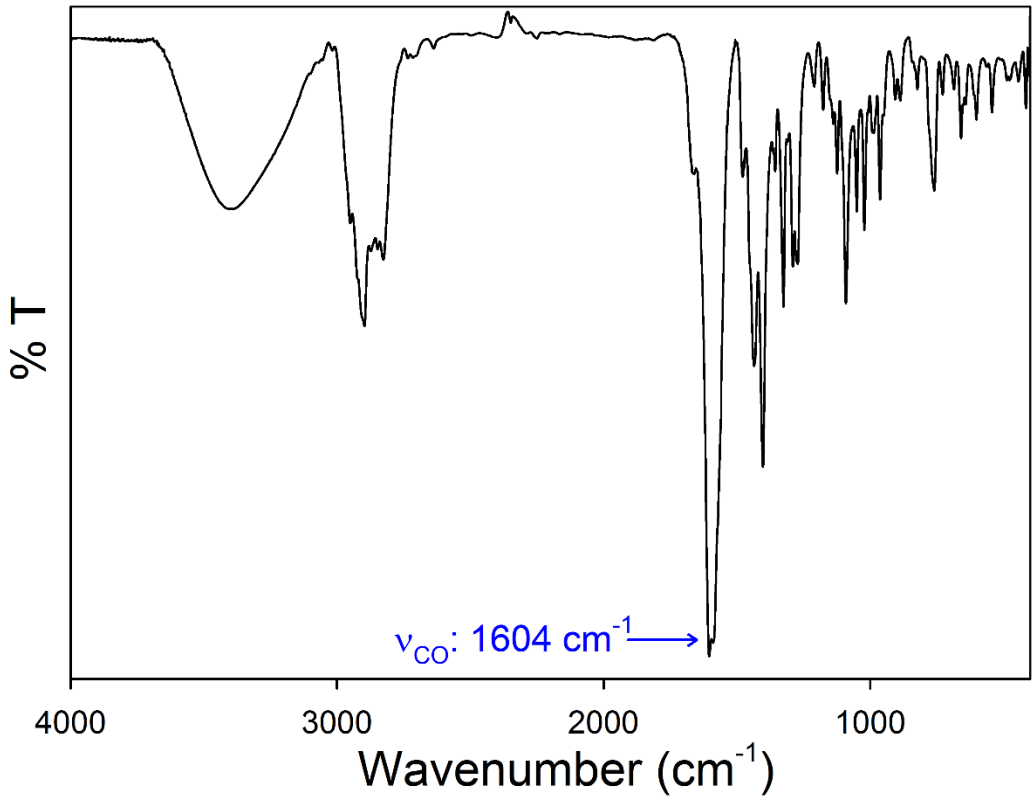

Figure 3.S12 Solid-state FTIR spectrum of **3** in a KBr matrix at RT.

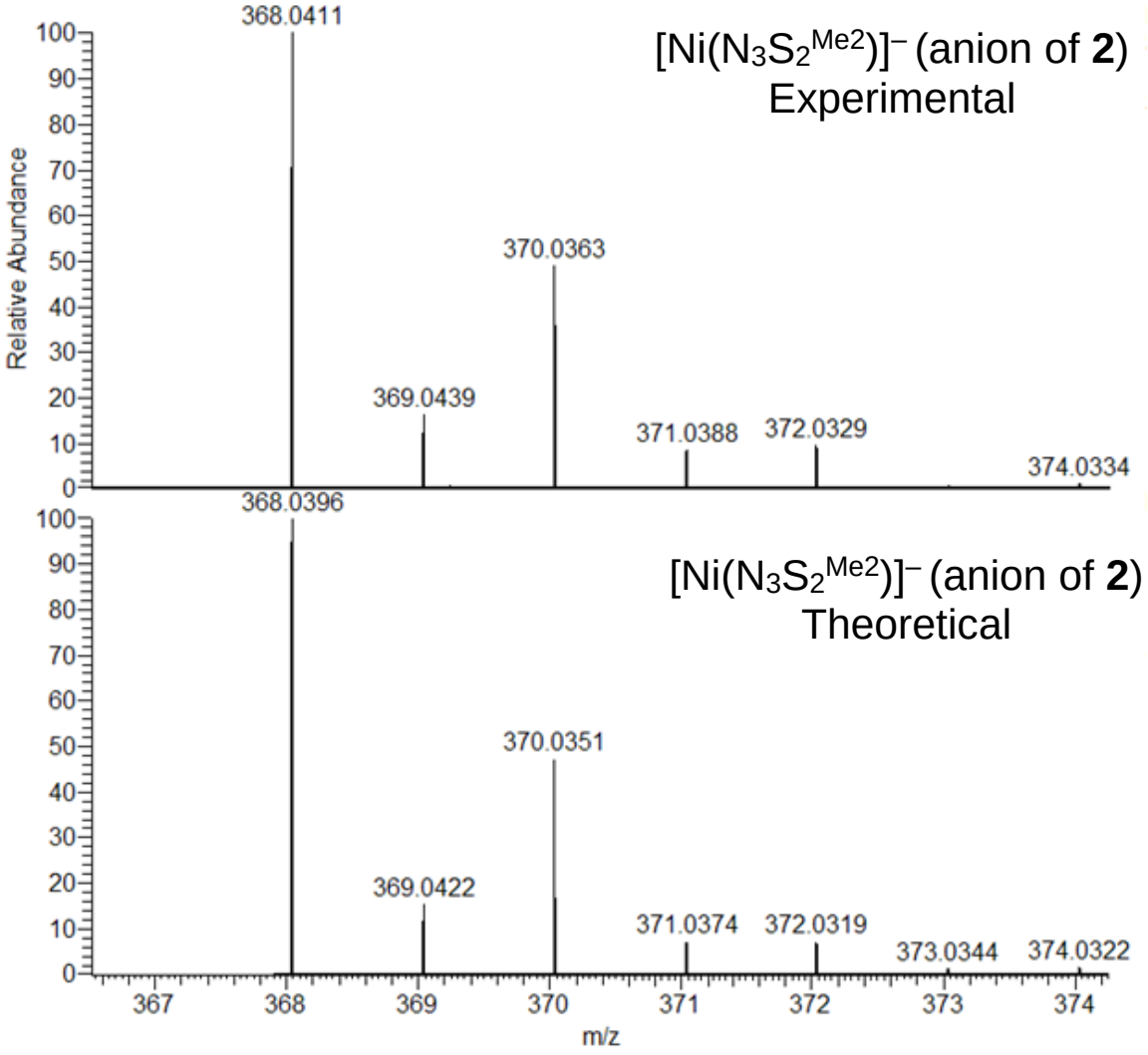

Figure 3.S13 *Top*: High-resolution ESI-MS (negative mode) of the anion of Na[Ni($N_3S_2^{Me2}$)] (**2**) [M-Na]$^-$. *Bottom*: Theoretical isotopic distribution.

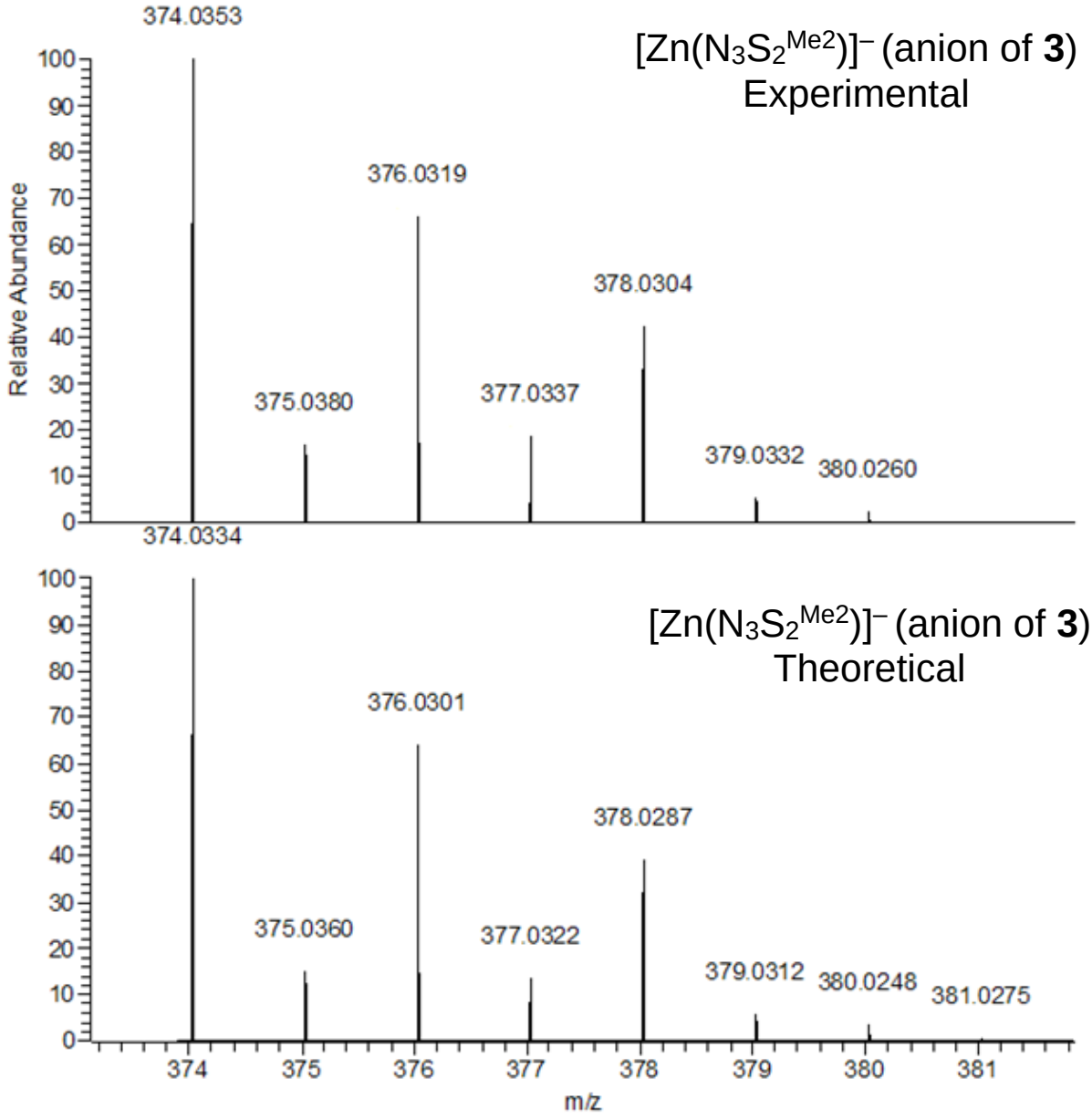

Figure 3.S14 *Top*: High-resolution ESI-MS (negative mode) of the anion of Na[Zn($N_3S_2^{Me2}$)] (**3**) [M-Na]$^-$. *Bottom*: Theoretical isotopic distribution.

Table 3.S1 Summary of Crystal Data and Intensity Collection and Structure Refinement Parameters for Na[Ni($N_3S_2^{Me2}$)]•MeCN (**2**•MeCN), K[Ni($N_3S_2^{Me2}$)] (**2^{K}**), Na[Zn($N_3S_2^{Me2}$)]•MeOH (**3**•MeOH), and [Ni(L^{ox})] (**5**).

Parameters	**2•MeCN**	**2^{K}**	**3•MeOH**	**5**
Formula	$C_{16}H_{23}N_4NaNiOS_2$	$C_{14}H_{22}KN_3NiO_2S_2$	$C_{16}H_{28}N_3NaO_3S_2Zn$	$C_{14}H_{19}N_3NiOS_2$
Formula weight	433.20	426.28	462.89	368.15
Crystal system	Monoclinic	Monoclinic	Triclinic	Triclinic
Space group	*P*2(1)/c	*C*2/c	*P*-1	*P*-1
Crystal color, habit	red crystal	red-orange crystal	colorless crystal	red crystal
a, Å	10.646(3)	18.565(7)	7.8111(10)	10.950(7)
b, Å	11.978(3)	11.991(4)	9.5183(12)	12.603(8)
c, Å	15.107(4)	16.388(6)	15.2826(19)	13.560(8)
α, deg	90	90	75.969(5)	65.451(7)
β, deg	94.404(4)	98.339(5)	77.444(5)	67.752(8)
γ, deg	90	90	78.348(5)	89.678(9)
V, Å^3	1920.6(8)	3610(2)	1062.5(2)	1549.7(16)
Z	4	8	2	4
$\rho_{calcd,}$ g/cm^3	1.498	1.569	1.447	1.578
T, K	100(2)	100(2)	100(2)	100(2)
abs coeff, μ (Mo Kα), mm^{-1}	1.262	1.548	1.392	1.522
θ limits, deg	2.17-25.00	2.03-25.00	2.233-26.021	1.90-25.00
total no. of data	19817	13717	11599	5425
no. of unique data	3376	3173	4198	5425
no. of parameters	227	208	244	380
GOF of F^2	1.072	1.180	1.011	1.048
R_1,[a] %	0.0487	0.0853	0.0504	0.0862
wR_2,[b] %	0.0940	0.2249	0.1093	0.2503
max, min peaks, e/Å^3	0.524, -0.425	1.088, -0.982	0.515, -0.823	3.339, -1.533

[a]$R_1 = \Sigma| |F_o| - |F_c| | / \Sigma |F_o|$; [b]$wR_2 = \{\Sigma[w(F_o^2 - F_c^2)^2]/\Sigma[w(F_o^2)^2]\}^{1/2}$

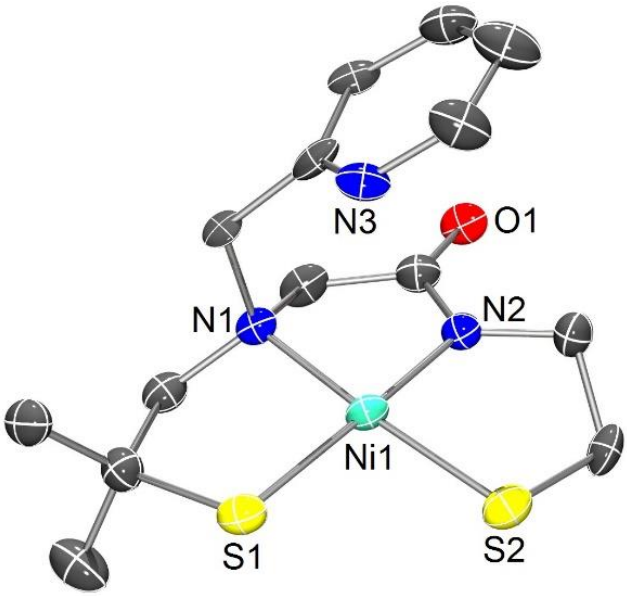

Figure 3.S15 ORTEP diagram of the anion of $\mathbf{2^K}$ at 50% thermal probability ellipsoids. H atoms and counterions are omitted for clarity.

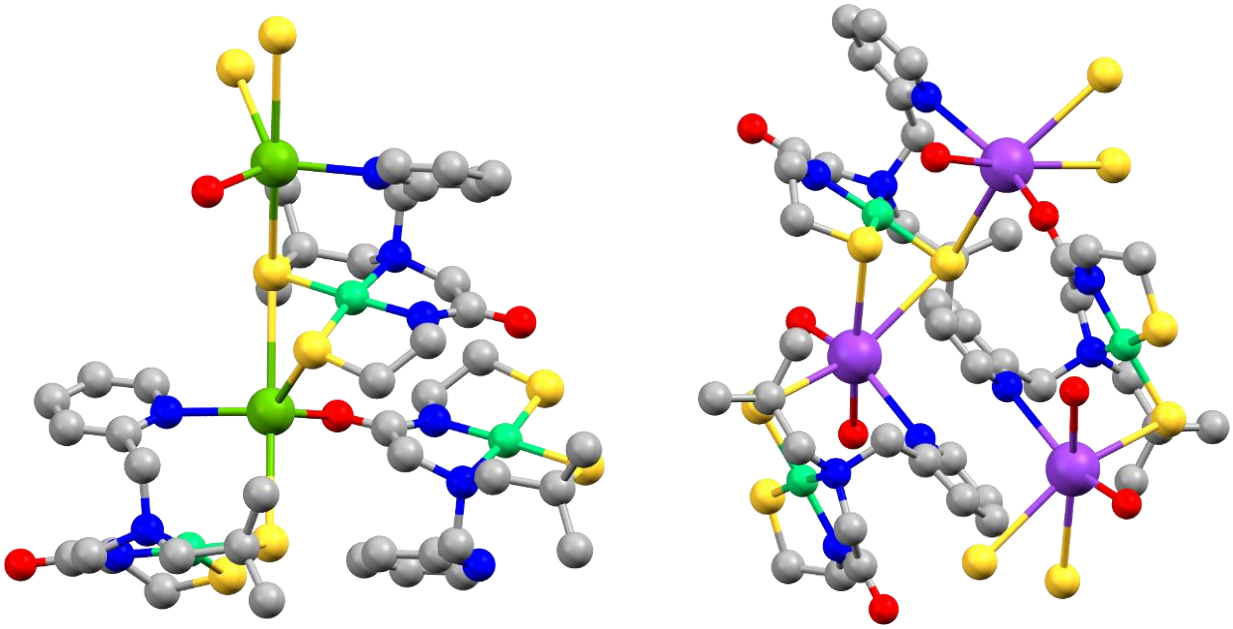

Figure 3.S16 Extended lattice of **2**•MeCN (*left*) and $\mathbf{2^K}$ (*right*). H atoms omitted. C = gray; Ni = aquamarine; S = yellow; N = blue; O = red; K = purple; Na = green.

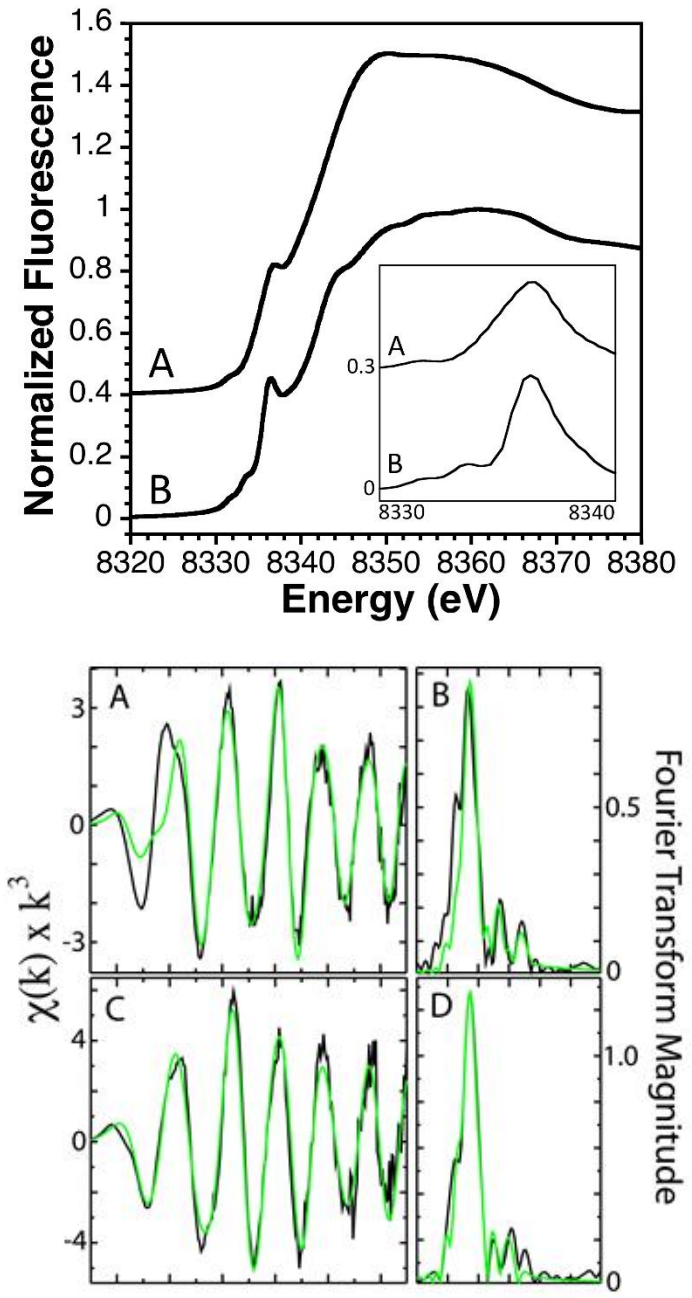

Figure 3.S17 *Top:* Ni K-edge XANES spectra for **1** in MeOH (A) and as a solid diluted in BN (B) offset for clarity. *Inset*: expansion of the pre-edge region, background subtracted for normalization and offset for clarity. *Bottom*: EXAFS (A, C) and Fourier-transform simulations (B, D) comparing raw data (black) to best-fit model (green) for **1** in MeOH (A, B), and as a solid (C, D).

Table 3.S2 Summary of best fit simulations to EXAFS[a] of **1** and **2** in MeOH and as solids.

Sample	Nearest Neighbor Ligand Environment[b]				Long Range Ligand Environment[b]				*F'*[g]
	Atom[c]	R(A)[d]	CN[e]	σ^{2}[f]	Atom[c]	R(A)[d]	CN[e]	σ^{2}[f]	
1 in MeOH	N	1.98	1.0	2.78	C	3.12	1.5	2.07	0.35
	S	2.19	1.0	2.23	C	3.85	1.5	1.75	
1 (solid)	N	1.93	1.5	3.75	C	2.83	1.5	5.46	0.43
	S	2.17	1.5	1.46	C	3.39	1.5	1.45	
					C	3.79	1.0	4.71	
2 in MeOH	N	1.95	1.5	5.46	C	3.82	2.0	3.33	0.20
	S	2.18	1.5	3.52					
2 (solid)	N	1.91	2.0	4.26	C	2.79	1.5	0.15	0.22
	S	2.17	1.5	1.12	C	3.81	3.0	5.94	

[a]Data were fit over a *k* range of 1 to 13.0 $Å^{-1}$
[b]Independent metal-ligand scattering environment
[c]Scattering atoms: N (nitrogen), S (Sulfur) and C (carbon)
[d]Average metal-ligand bond length from two scans
[e]Average metal-ligand coordination number from two scans
[f]Average Debye-Waller factor in $Å^2 \times 10^3$ from two scans
[g]Number of degrees of freedom weighted mean square deviation between data and fit

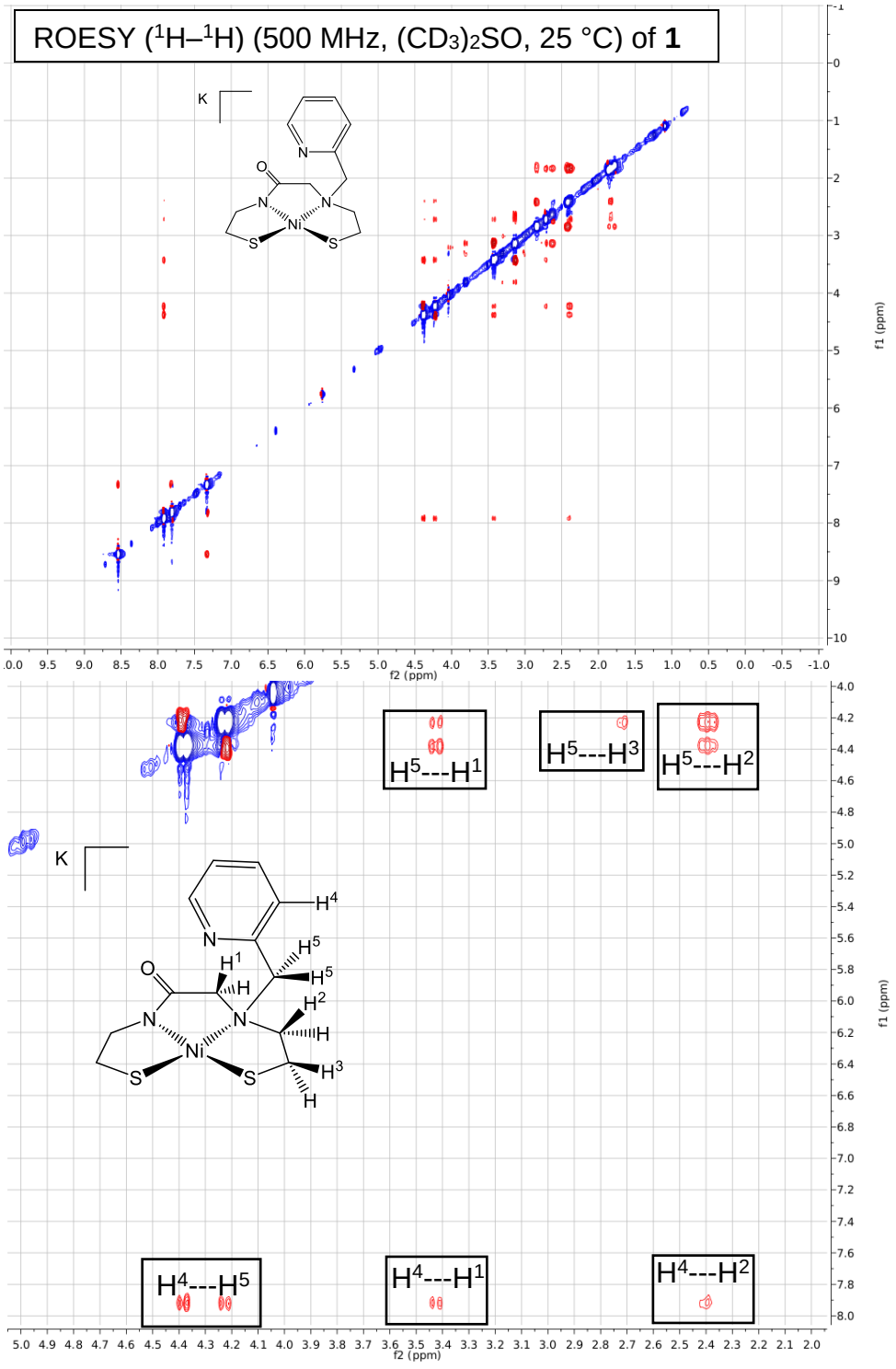

Figure 3.S18 *Top*: Full ROESY spectrum of **1** in $(CD_3)_2SO$ at 25 °C. The pre-saturation method was utilized to suppress the solvent signal. *Bottom*: Zoom-in of the 2-5 ppm × 4-8 ppm window to show the interactions of the protons indicated.

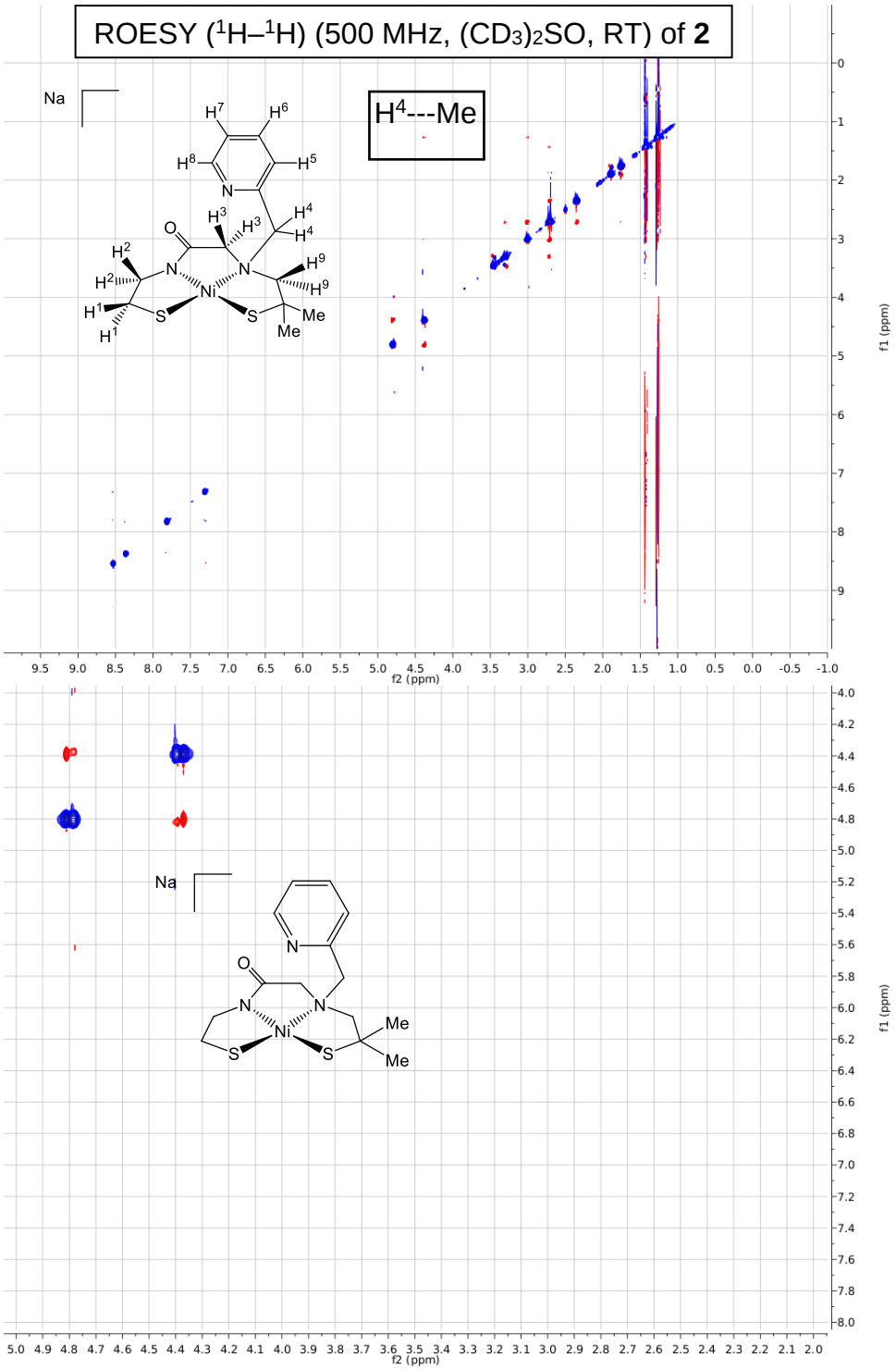

Figure 3.S19 *Top*: Full ROESY spectrum of **2** in $(CD_3)_2SO$ at RT. The pre-saturation method was utilized to suppress the solvent signal. Black box indicates the interaction between the H4 and Me group. *Bottom*: Zoom-in of the 2-5 ppm × 4-8 ppm window.

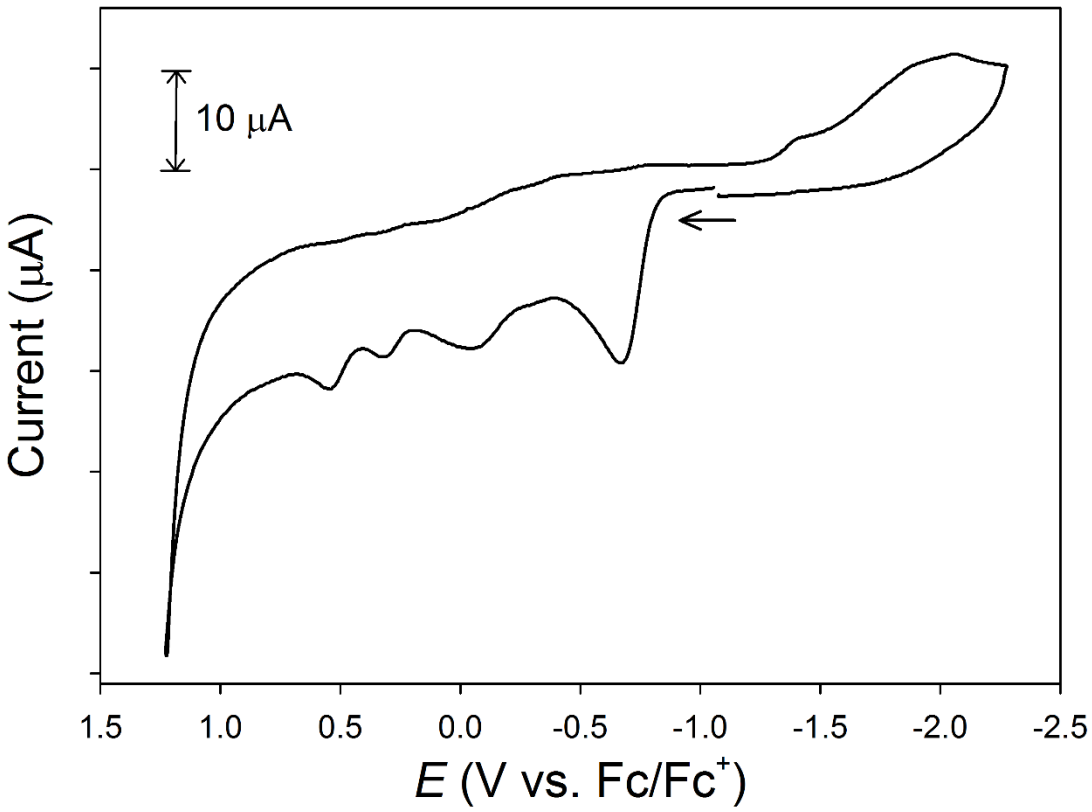

Figure 3.S20 Full CV of **2** in DMF at RT (0.1 M $^{n}Bu_4NPF_6$ supporting electrolyte, glassy carbon working electrode, 100 mV/s scan rate). Arrow shows the direction of the scan.

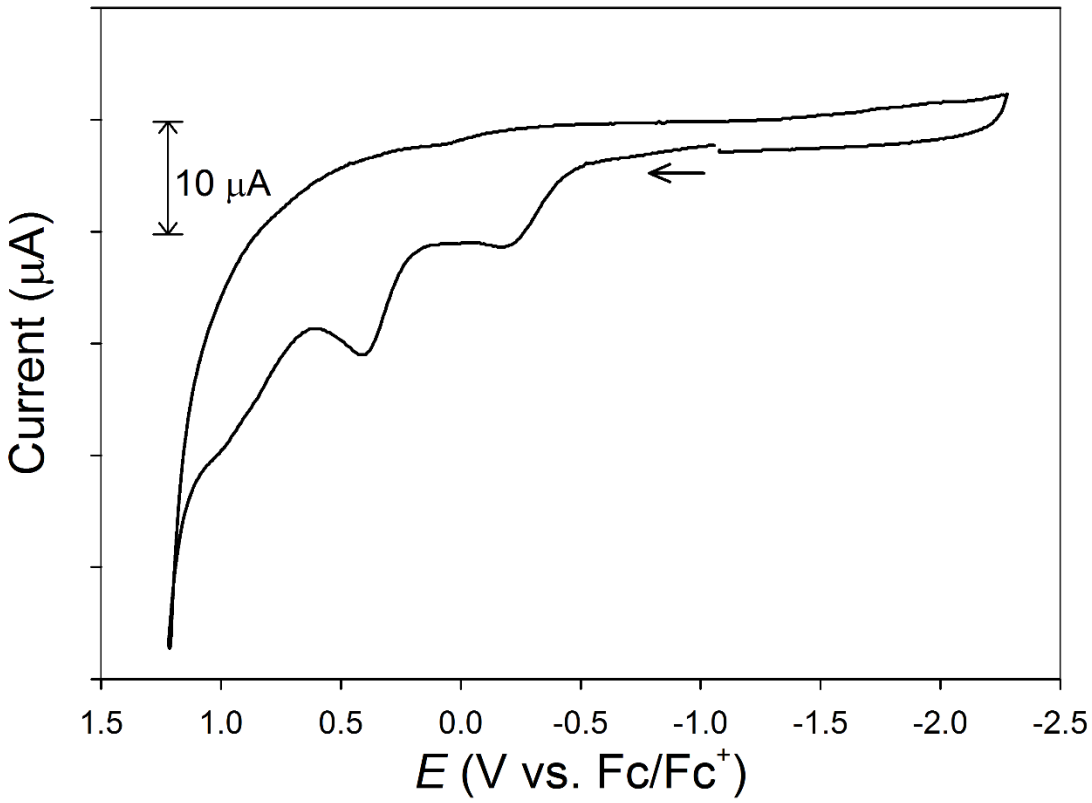

Figure 3.S21 Full CV of **3** in DMF at RT (0.1 M $^{n}Bu_4NPF_6$ supporting electrolyte, glassy carbon working electrode, 100 mV/s scan rate). Arrow shows the direction of the scan.

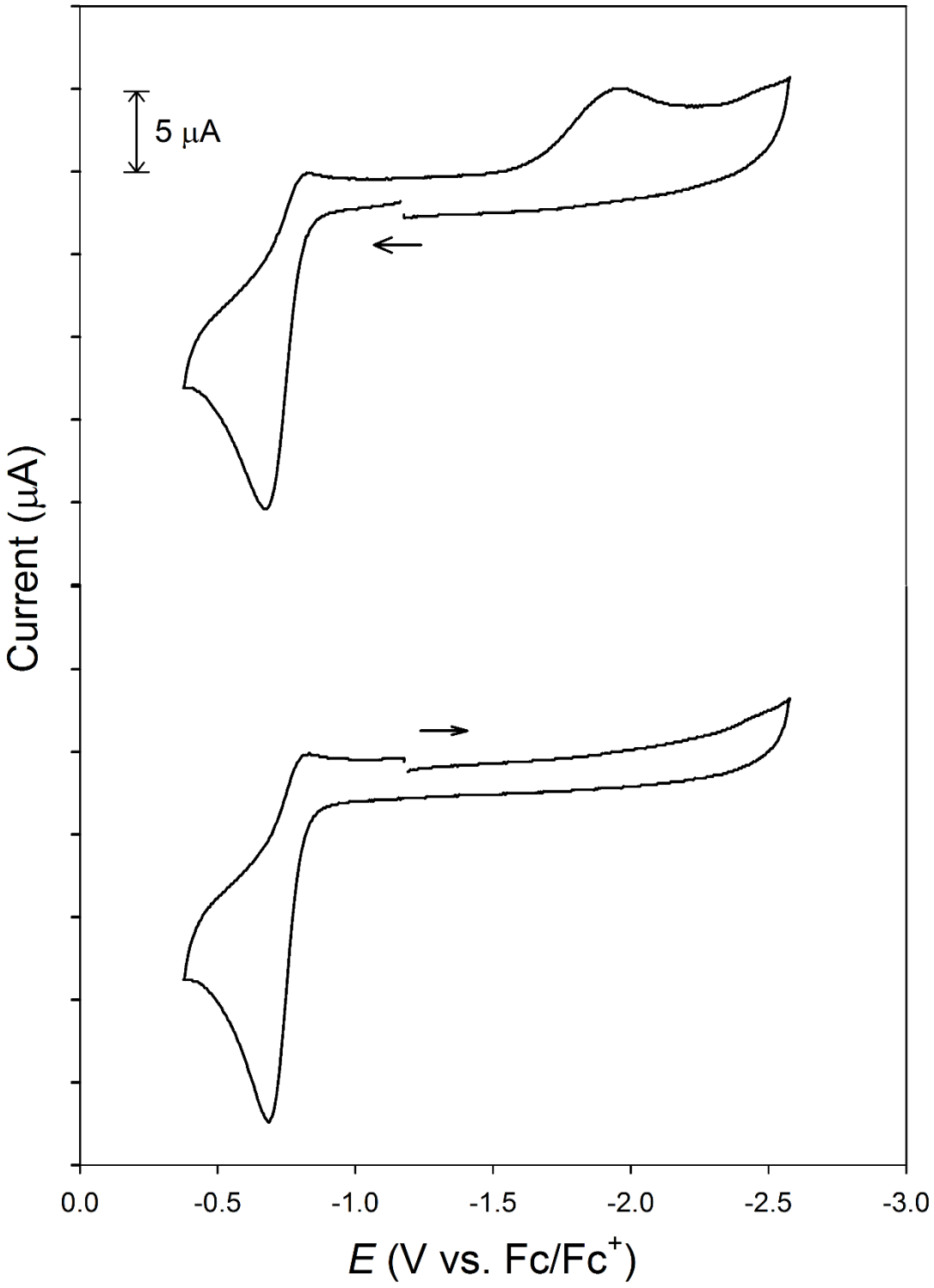

Figure 3.S22 CV of **2** in DMF at RT initiated from different scan directions (0.1 M $^{n}Bu_4NPF_6$ supporting electrolyte, glassy carbon working electrode, 100 mV/s scan rate). Arrow shows the direction of the scan.

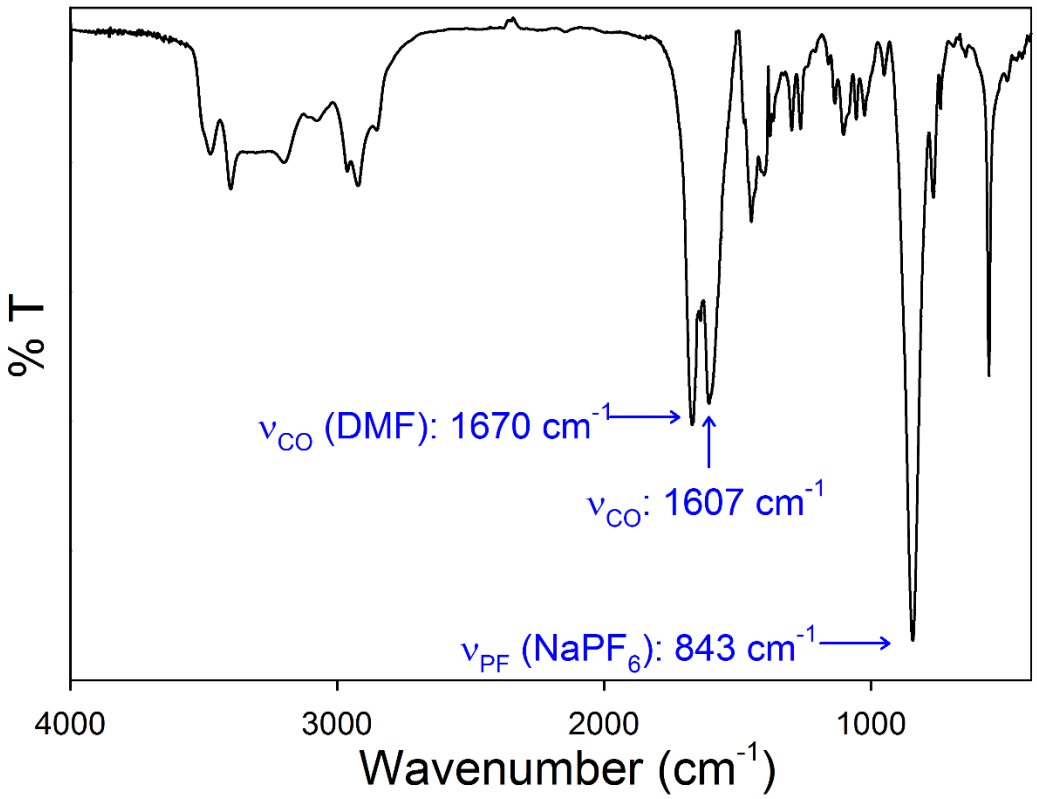

Figure 3.S23 FTIR spectrum (KBr pellet) of the worked-up reaction mixture (MeCN-soluble/Et_2O-insoluble portion) of the reaction of complex **2** with $FcPF_6$ (1:1) in DMF.

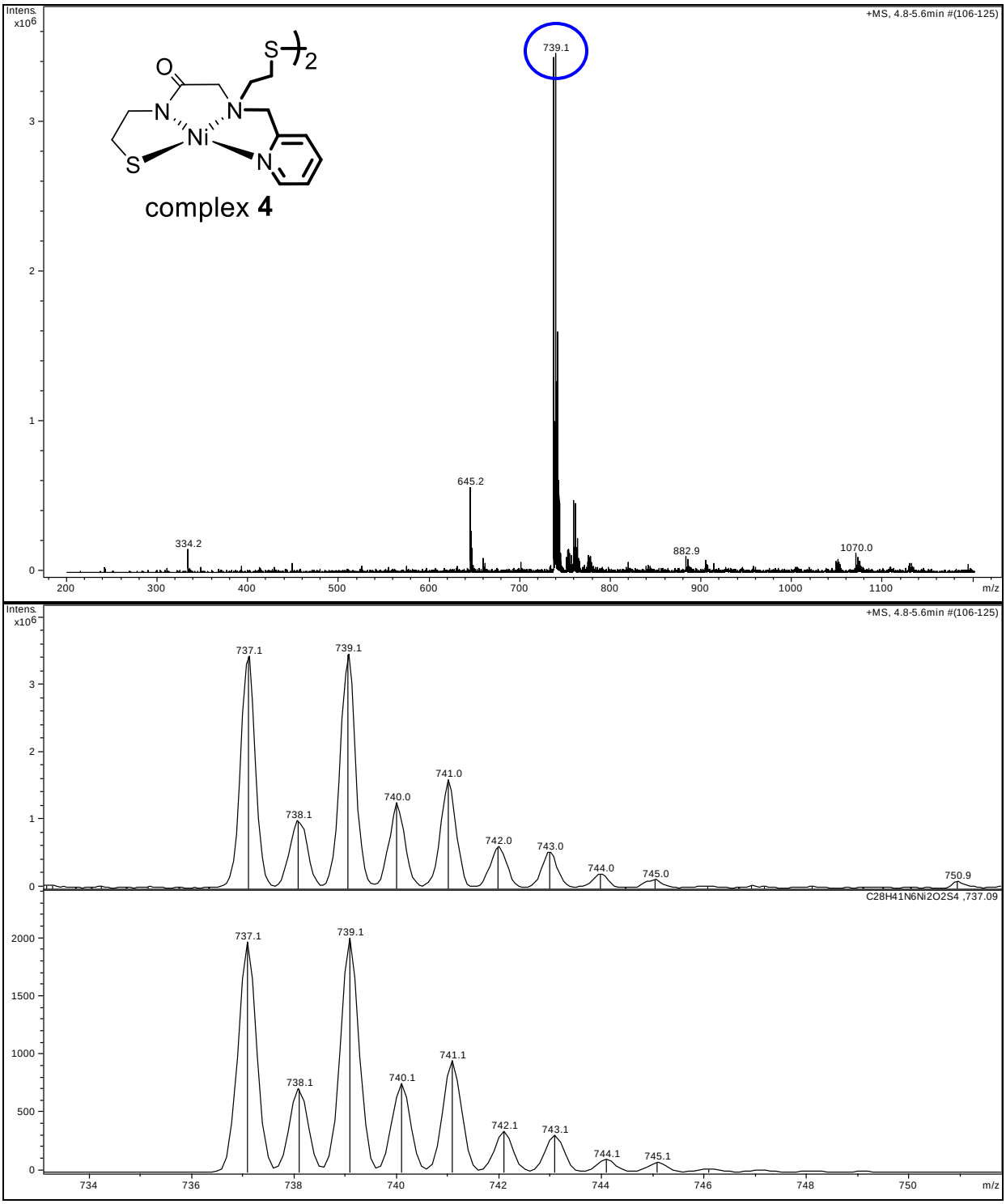

Figure 3.S24 *Top*: Low-resolution ESI-MS(+) of the worked-up reaction mixture (MeCN-soluble/Et_2O-insoluble portion) of the reaction of complex **2** with $FcPF_6$ (1:1) in DMF. *Bottom*: comparison of the isotopic distribution of peak at *m/z*: 739.1 with theoretical isotopic distribution of $[2M+H]^+$. This result suggests the formation of the disulfide-linked complex **4** (see inset for structure).

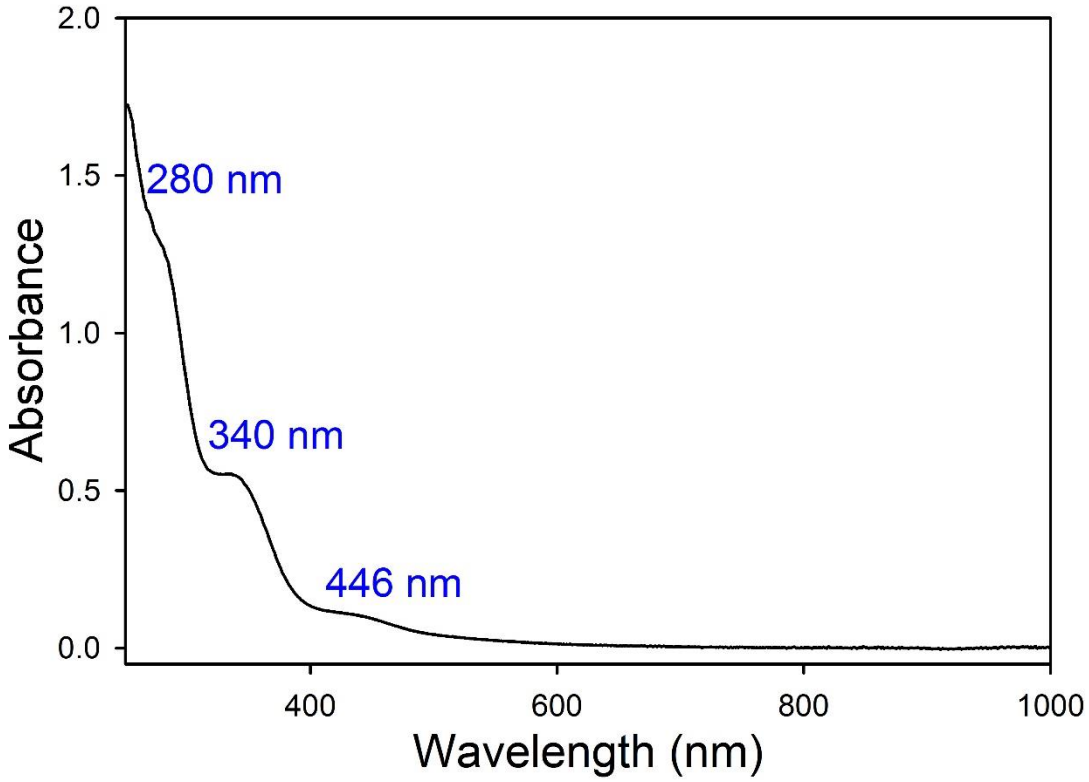

Figure 3.S25 UV-vis spectrum of the worked-up reaction mixture (MeCN-soluble/Et_2O-insoluble portion) of the reaction of complex **2** with $FcPF_6$ (1:1) in MeOH at RT.

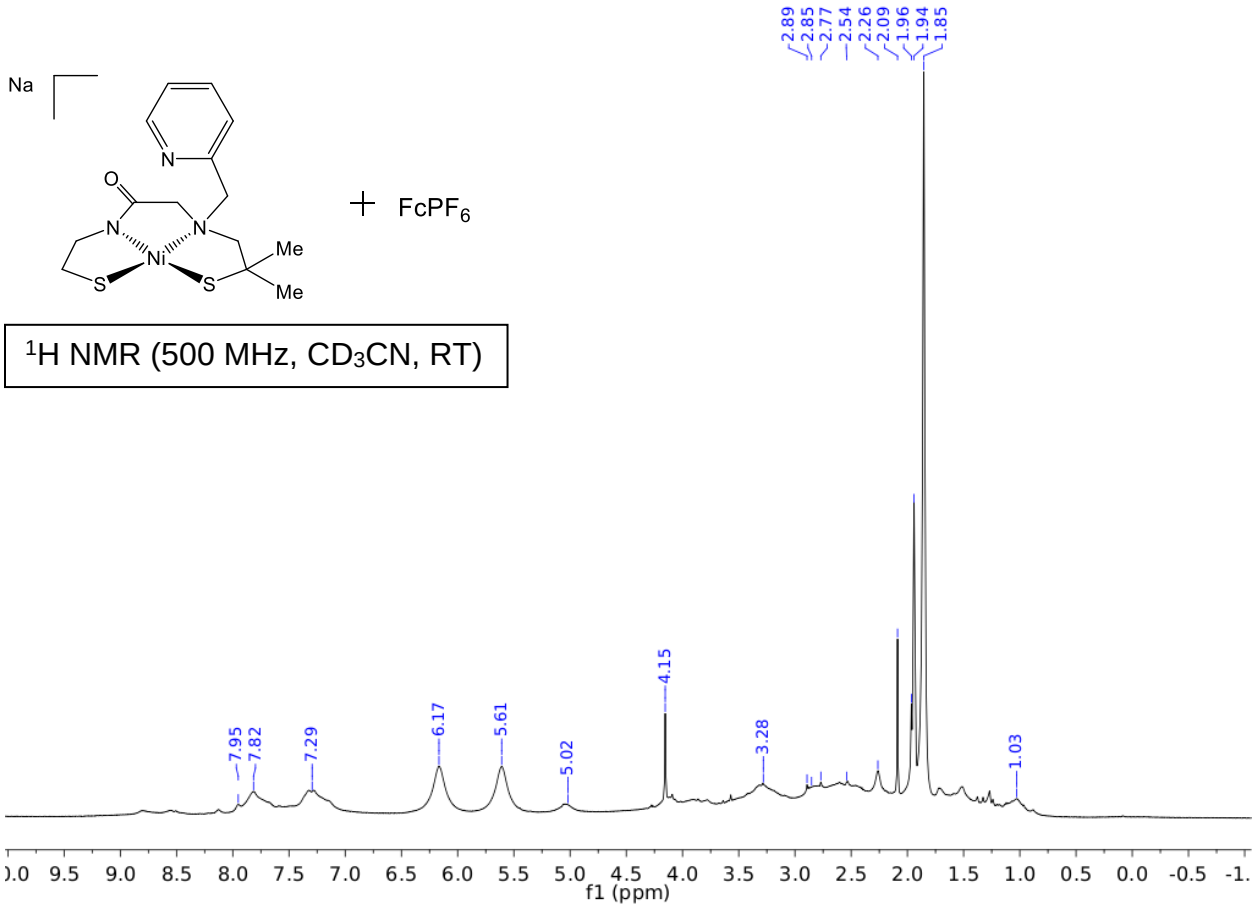

Figure 3.S26 ^{1}H NMR spectrum of the worked-up reaction mixture (MeCN-soluble/Et_2O-insoluble portion) of the reaction of complex **2** with $FcPF_6$ (1:1) in CD_3CN at RT (δ vs. residual protio solvent signal). Protio solvent (1.94 ppm) and residual MeCN (1.96 ppm), respectively, are present. A minor amount of acetone (2.09 ppm), DMF (2.77, 2.89, and 7.95 ppm), and Fc (4.15 ppm) are also present.

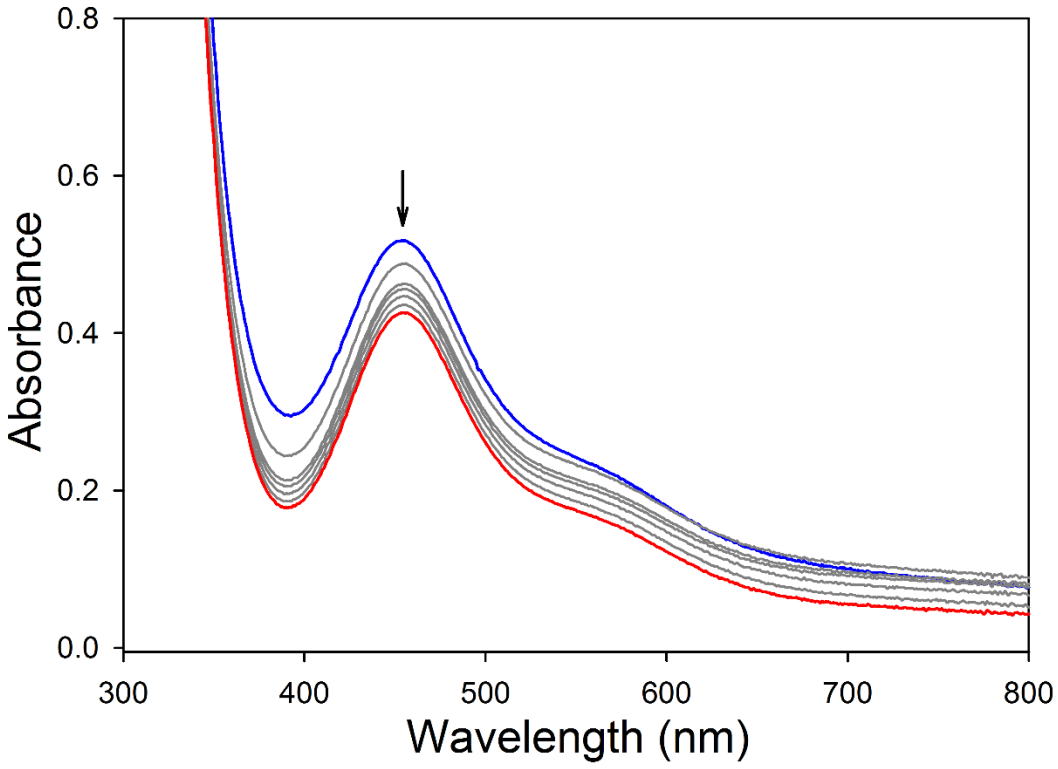

Figure 3.S27 UV-vis spectral monitor of a 1.55 mM HEPES buffer solution (pH 7.4) of Na[Ni($N_3S_2^{Me2}$)] (**2**) (blue trace) and after the addition of 10 mol-equiv NaN_3 (dark gray traces at 1, 3, 5, and 10 h; arrow shows direction of change) at 25 °C. Final trace in red (15 h).

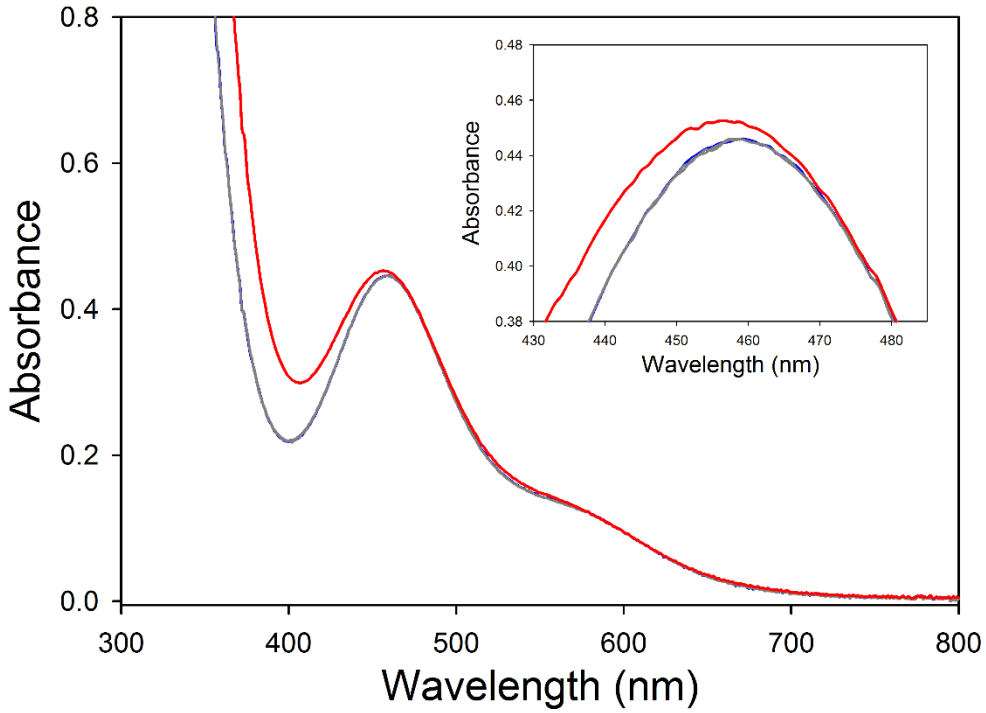

Figure 3.S28 UV-vis spectral monitor of a 1.59 mM MeOH solution of Na[Ni($N_3S_2^{Me2}$)] (**2**) (blue trace) and after the addition of 10 mol-equiv NaN_3 (dark gray traces at 1 and 3 h) at 25 °C. Final trace in red (17 h). *Inset*: expansion to show that traces superimpose on one another.

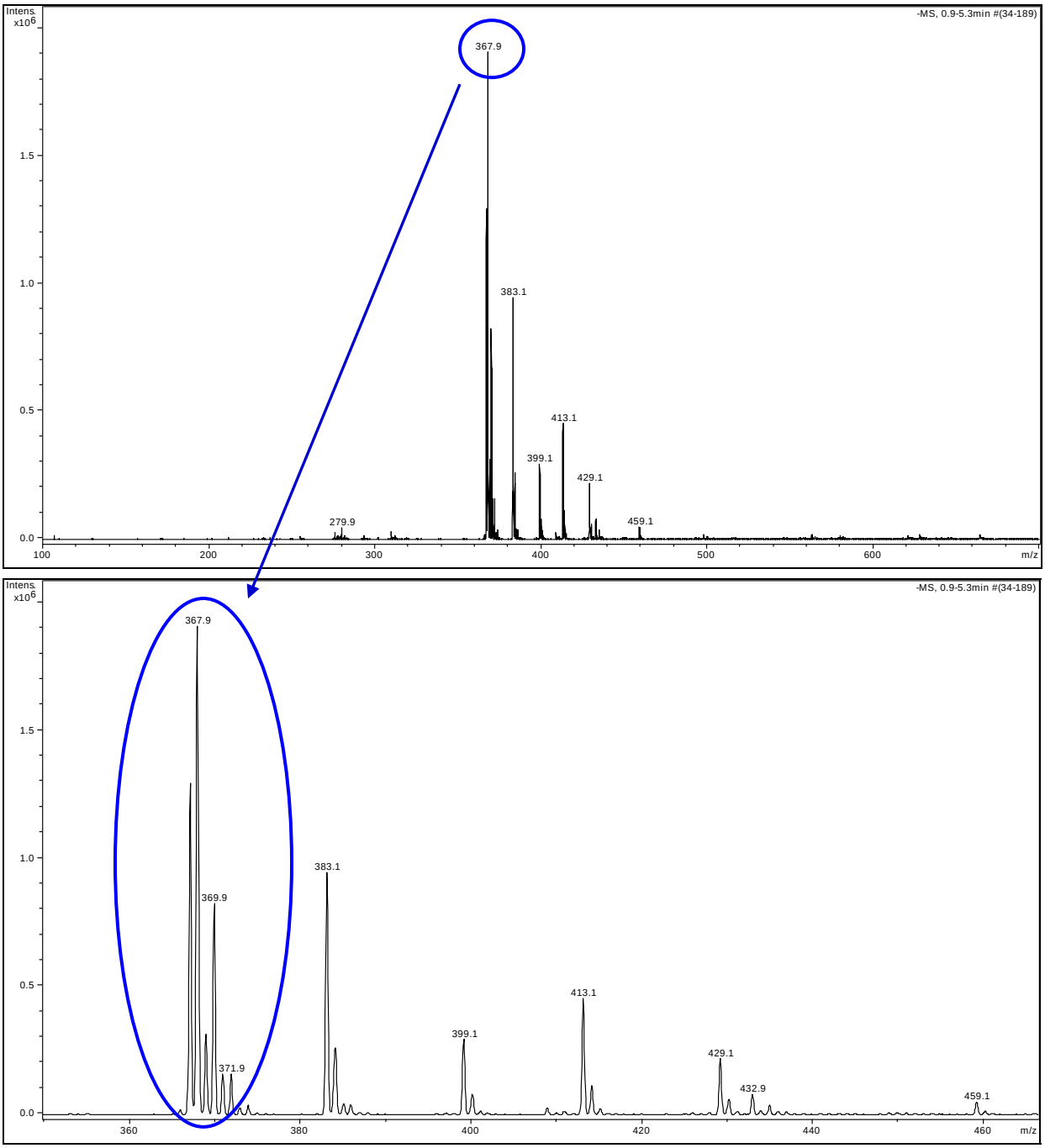

Figure 3.S29 *Top*: Low-resolution ESI-MS(-) of the reaction of a 1.59 mM MeOH solution of Na[Ni($N_3S_2^{Me2}$)] (**2**) and 10 mol-equiv NaN_3 after 17 h (taken from UV-vis sample). Highlighted peak in blue is due to unreacted **2**. *Bottom*: expansion of 350–470 *m/z* region. Other peaks are present in blank solvent and are not due to the reaction mixture.

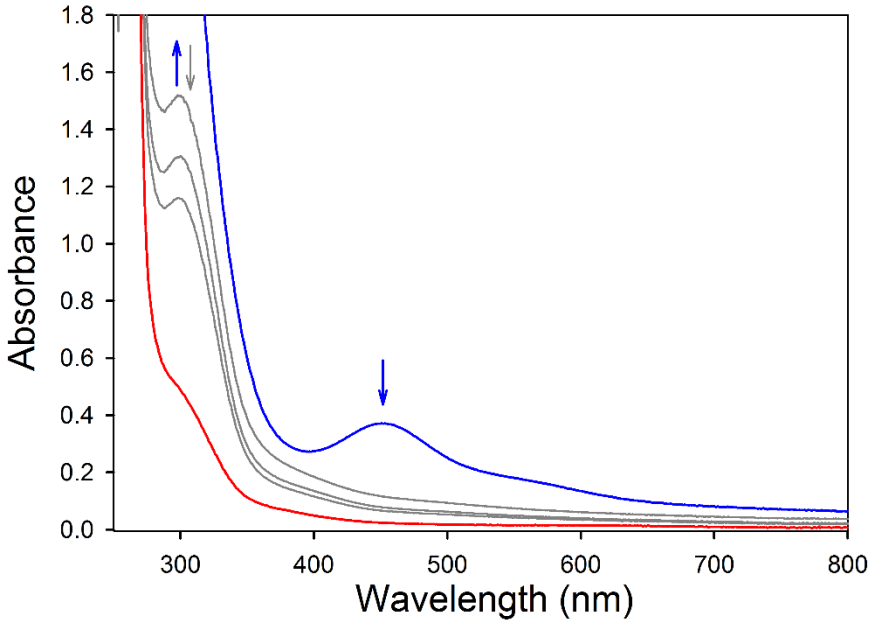

Figure 3.S30 UV-vis spectral monitor of a 0.96 mM HEPES buffer solution (pH 7.4) of Na[Ni($N_3S_2^{Me2}$)] (**2**) (blue trace) and after the addition of 10 mol-equiv KO_2 (dark gray traces at 0 (after addition), 1, and 2 h; arrow shows direction of change from the initial blue trace and the dark gray trace immediately after addition of KO_2) at 25 °C. Final trace in red (15 h).

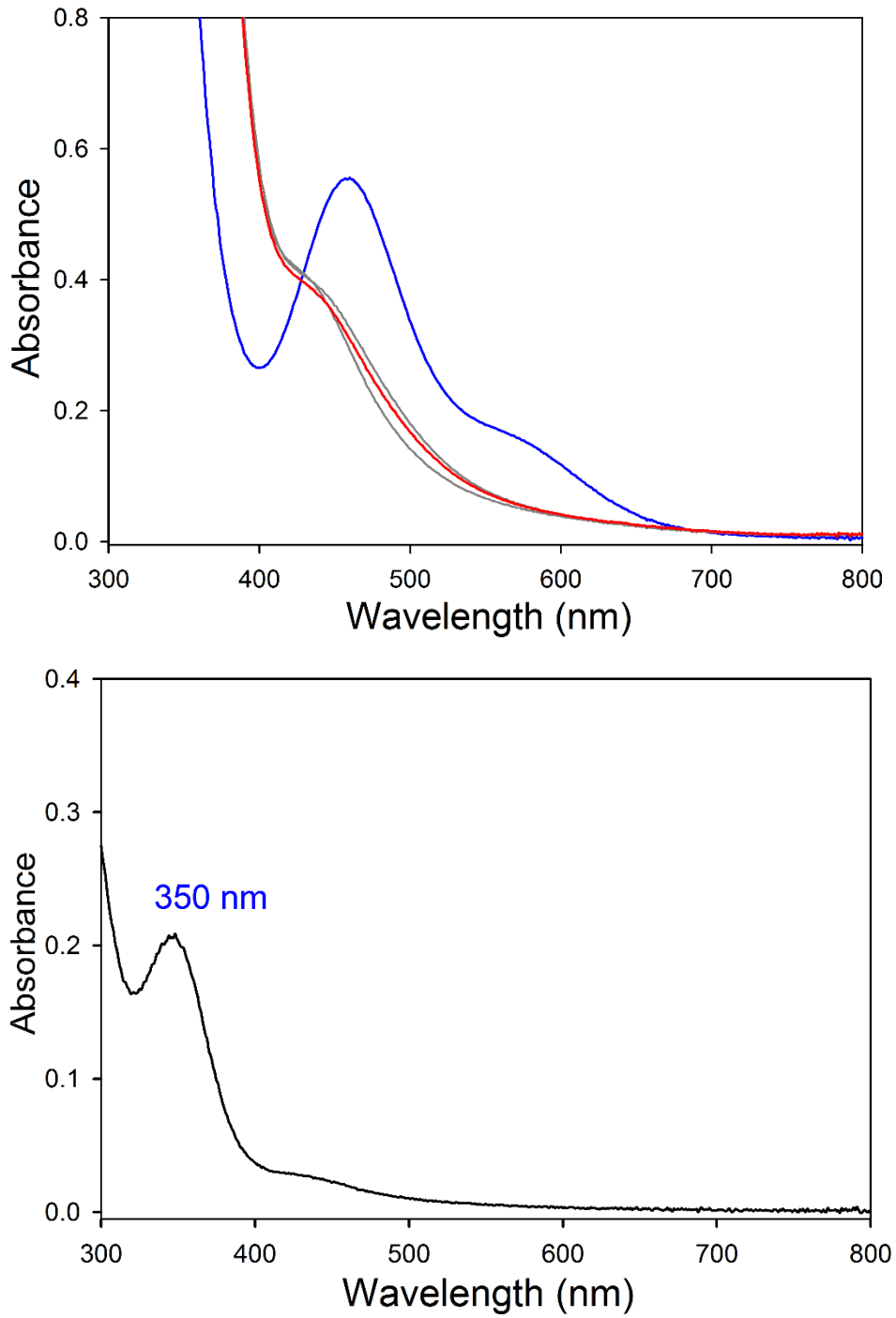

Figure 3.S31 *Top*: UV-vis spectral monitor of a 1.59 mM MeOH solution of Na[Ni($N_3S_2^{Me2}$)] (**2**) (blue trace) and after the addition of 10 mol-equiv KO_2 (dark gray traces immediately after addition and at 1 h) at 25 °C. Final trace in red (17 h). *Bottom*: 16-fold dilution of the 17 h spectrum.

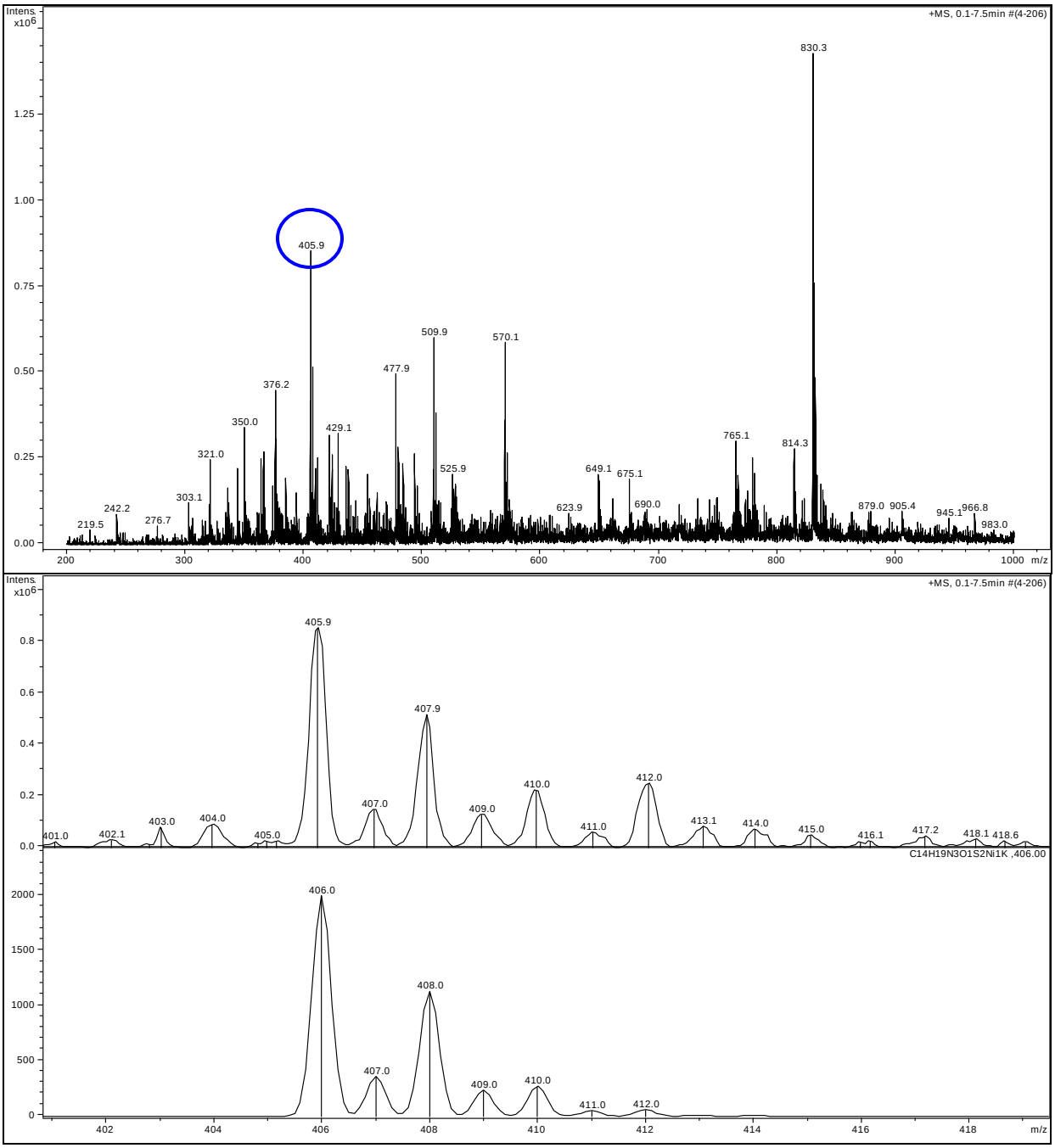

Figure 3.S32 *Top*: Low-resolution ESI-MS(+) of the reaction mixture of a 1.59 mM MeOH solution of Na[Ni($N_3S_2^{Me2}$)] (**2**) and 10 mol-equiv KO_2 after 17 h (taken from UV-vis sample). *Bottom*: comparison of the isotopic distribution of the highlighted peak at *m/z*: 405.9 with theoretical isotopic distribution that matches to [Ni(L^{ox})] (**5**) + K. i.e., $[M–H+K]^+$. Other peaks have not been identified as reaction products.

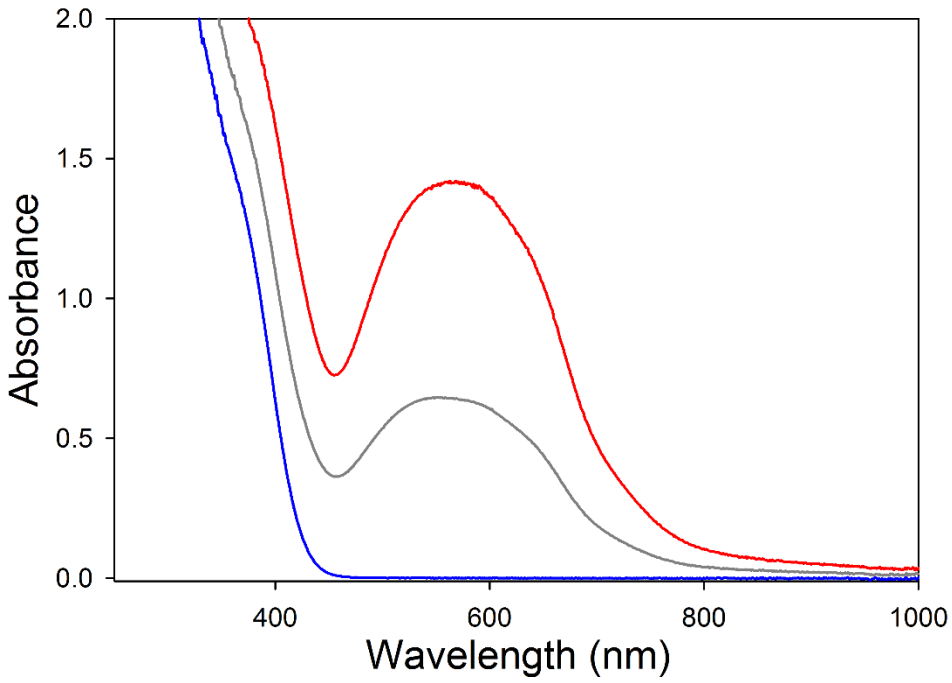

Figure 3.S33 UV-vis spectral monitor of a 97 μM HEPES buffer solution (pH 7.4) of NBT (blue trace) after the addition of one-equiv of Na[Ni($N_3S_2^{Me2}$)] (**2**) (dark gray = 1 min; red trace = 17 h) at 25 °C.

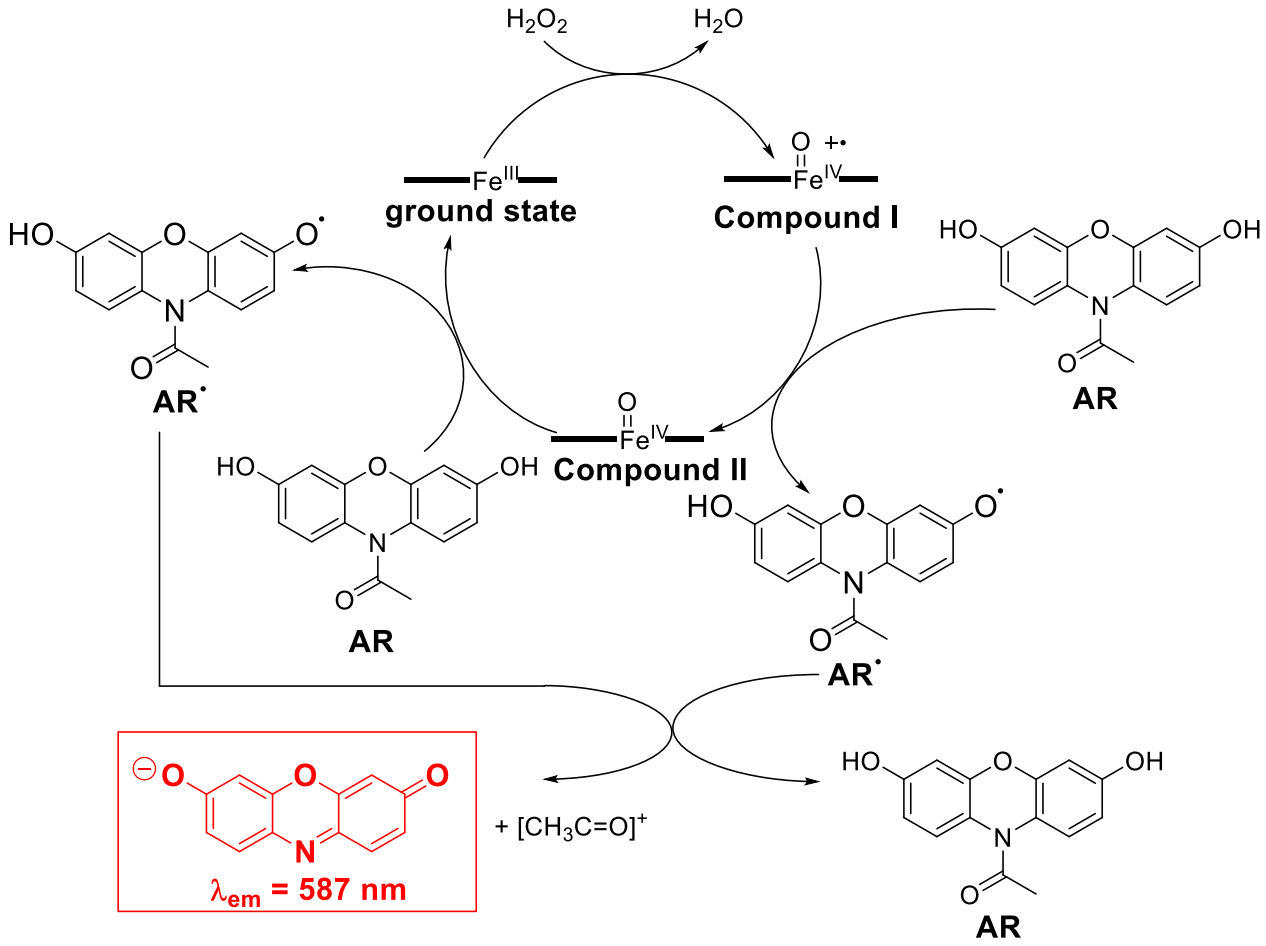

Scheme 3.S1 Mechanism of action for the Amplex Red (AR) assay for fluorescence-based H_2O_2 detection. This scheme is a modified version of that reported in Ehrl, B. N.; Liebherr, R. B.; Gorris, H. H. Single molecule kinetics of horseradish peroxidase exposed in large arrays of femtoliter-sized fused silica chambers. *Analyst* **2013**, *138*, 4260-4265.

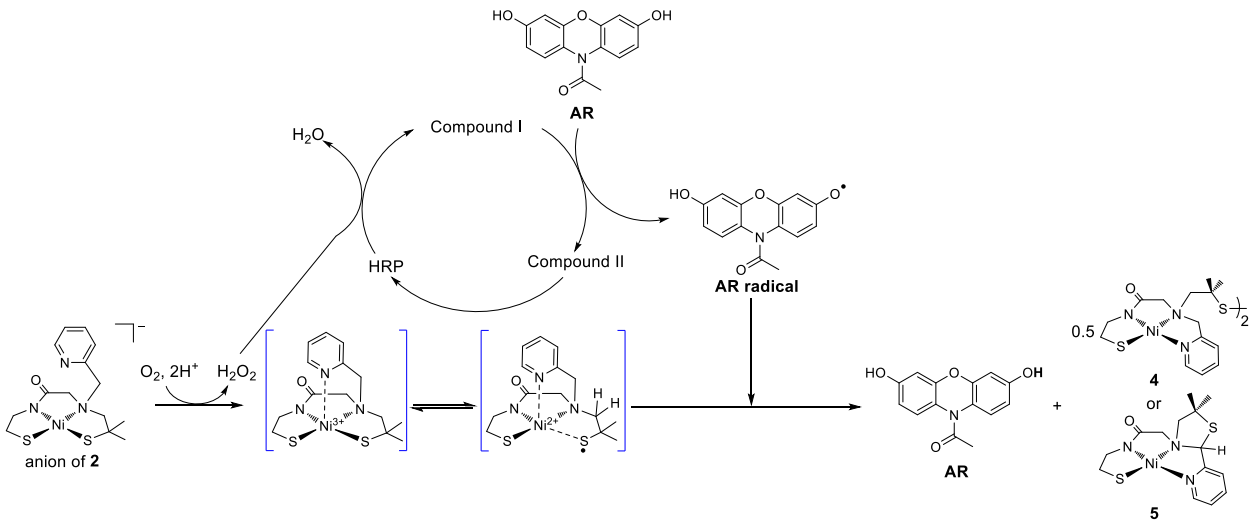

Scheme 3.S2 Proposed reaction of complex 2 with Amplex Red (AR).

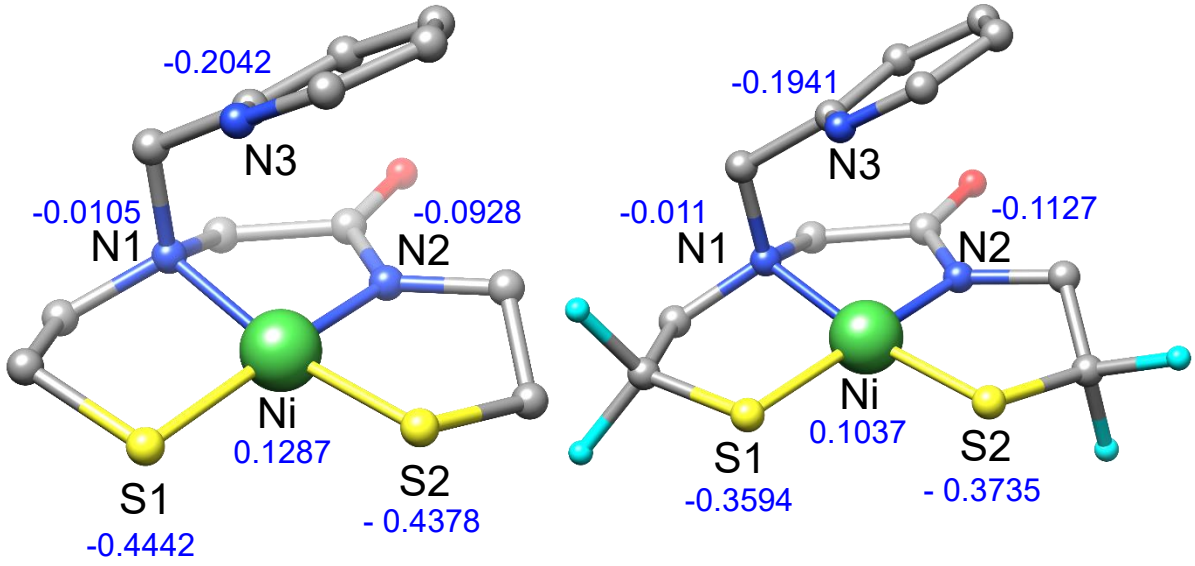

Figure 3.S34 Geometry-optimized structures of **1*** (*left*) and **7*** (*right*) with Mulliken atomic charges on Ni, S, and N atoms in blue. Green = Ni; yellow = S; blue = N; red = O; cyan = F; gray = C.

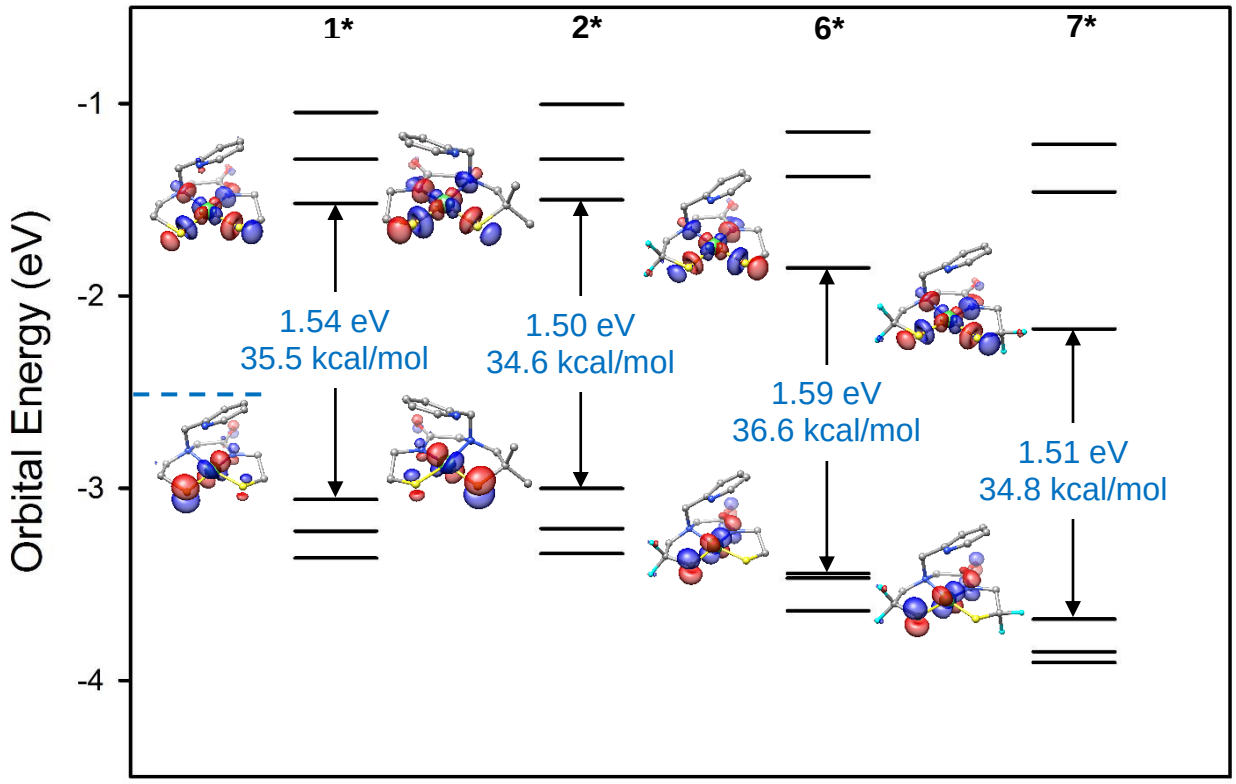

Figure 3.S35 Orbital energy diagram of **1***, **2***, **6***, and **7*** (left to right) with HOMO-LUMO gap in blue. In each column, the MOs descend in the order LUMO+2, LUMO+1, LUMO, HOMO, HOMO-1, and HOMO-2. Dashed line indicates the level blow which MOs are occupied.

Table 3.S3 Löwdin population analysis derived from the DFT calculations for selected MOs of **1*** from OLYP/def2-TZVPP with COSMO(DMF). Only s and p contributions were tabulated for N and S atoms. Bonding interactions are represented with a + and antibonding interactions are denoted with a –. N1 = amino-N; N2 = carboxamido-N; N3 = pyridine-N; S1 = $S_{trans\text{-carboxamide}}$; S2 = $S_{trans\text{-amine}}$.

	MO#	Energy (eV)	%Ni	%S1	%S2	%N1	%N2	Type of Interaction
LUMO+2	92	-1.0	1.3	0.1	0.0	0.9	0.3	pyridine(π*)
LUMO+1	91	-1.3	3.0	0.4	0.5	1.0	0.9	pyridine(π*)
LUMO	90	-1.5	48.3	9.9	13.2	5.4	5.0	$Ni(d_\sigma)$–S1(σ)–S2(σ)–N1(σ)–N2(σ)
HOMO	89	-3.1	62.7	20	4.6	0.0	2.3	$Ni(d_\pi)$–S1(π)–S2(π)–N1(σ)
HOMO-1	88	-3.2	67.8	0.4	19.1	0.3	2.7	$Ni(d_\pi)$–S2(π)–N2(π)
HOMO-2	87	-3.4	85.0	1.0	7.2	0.4	0.7	$Ni(d_\sigma)$–S2(π)

Table 3.S4 Löwdin population analysis derived from the DFT calculations for selected MOs of **6*** from OLYP/def2-TZVPP with COSMO(DMF). Only s and p contributions were tabulated for N and S atoms. Bonding interactions are represented with a + and antibonding interactions are denoted with a –. N1 = amino-N; N2 = carboxamido-N; N3 = pyridine-N; S1 = $S_{trans\text{-carboxamide}}$; S2 = $S_{trans\text{-amine}}$.

	MO#	Energy (eV)	%Ni	%S1	%S2	%N1	%N2	Type of Interaction
LUMO+2	100	-1.1475	1.6	0.2	0.0	0.9	0.4	pyridine(π*)
LUMO+1	99	-1.3795	1.5	0.2	0.3	1.0	0.7	pyridine(π*)
LUMO	98	-1.8546	49.6	7.5	13.7	5.4	5.9	$Ni(d_\sigma)$–S1(σ)–S2(σ)–N1(σ)–N2(σ)
HOMO	97	-3.443	68.3	11.6	1.9	0.0	4.7	$Ni(d_\pi)$–S1(π)–N2(π)
HOMO-1	96	-3.4673	59.9	0.2	28.9	0.3	1.8	$Ni(d_\pi)$–S2(π)–N2(π)
HOMO-2	95	-3.6373	88.8	1.1	3.6	0.5	0.9	$Ni(d_\sigma)$

Table 3.S5 Löwdin population analysis derived from the DFT calculations for selected MOs of **7*** from OLYP/def2-TZVPP with COSMO(DMF). Only s and p contributions were tabulated for N and S atoms. Bonding interactions are represented with a + and antibonding interactions are denoted with a –. N1 = amino-N; N2 = carboxamido-N; N3 = pyridine-N; S1 = $S_{trans\text{-carboxamide}}$; S2 = $S_{trans\text{-amine}}$.

	MO#	Energy (eV)	%Ni	%S1	%S2	%N1	%N2	Type of Interaction
LUMO+2	108	-1.2129	1.6	0.2	0.0	0.9	0.4	pyridine(π^*)
LUMO+1	107	-1.4599	0.7	0.1	0.1	1.1	0.7	pyridine(π^*)
LUMO	106	-2.1717	50.5	8.3	11.6	5.9	6.0	Ni(d_σ)–S1(σ)–S2(σ)–N1(σ)–N2(σ)
HOMO	105	-3.6806	67.3	12.6	0.5	0.0	5.3	Ni(d_π)–S1(π)–N2(π)
HOMO-1	104	-3.8506	81.5	1.4	8.9	0.6	1.4	Ni(d_π)–S2(π)
HOMO-2	103	-3.906	77.9	0.4	14.8	0.2	0.6	Ni(d_σ)–S2(π)

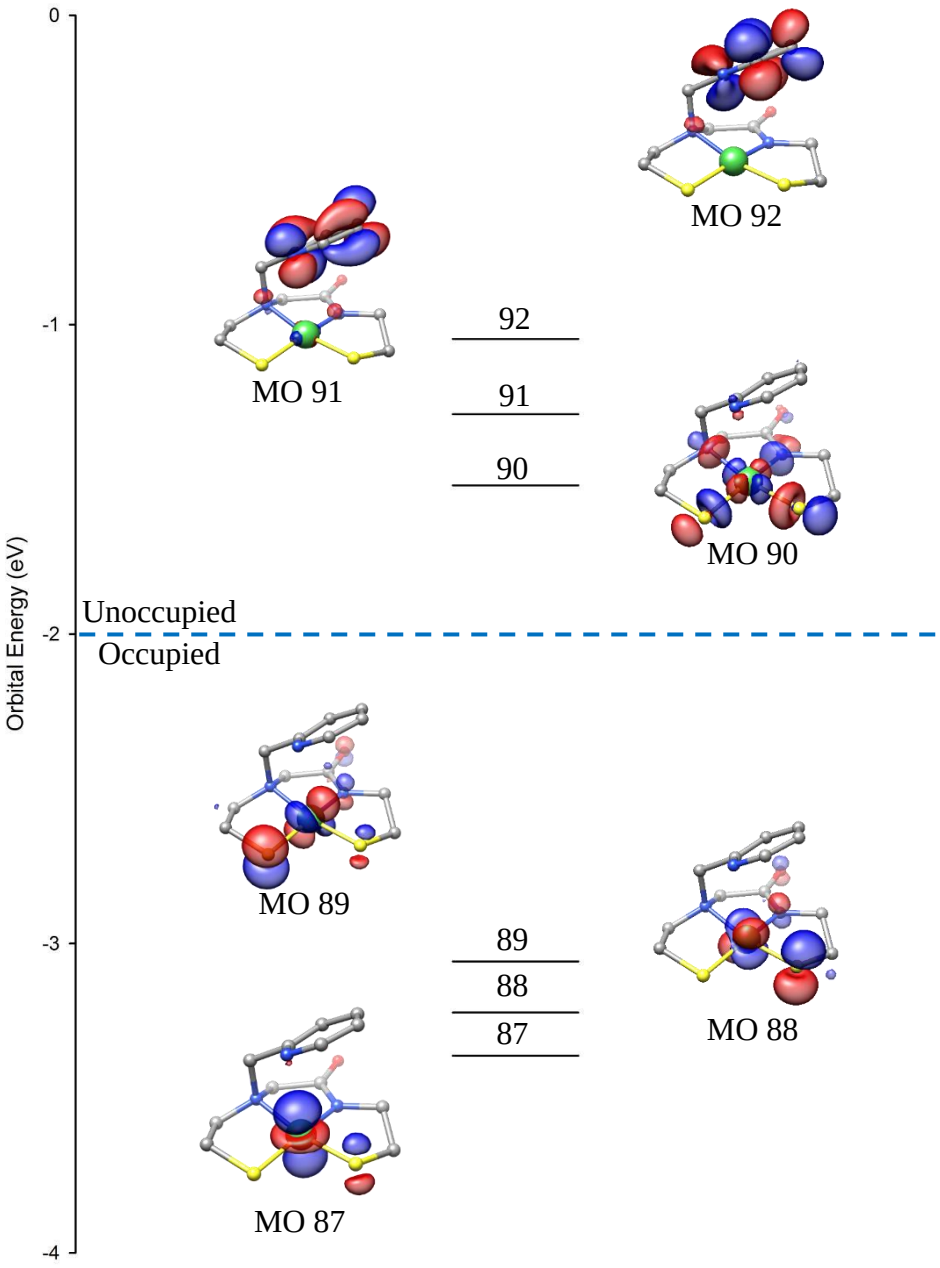

Figure 3.S36 DFT-generated isosurface plots (OLYP/def2-TZVPP) of the frontier MOs of **1***. The MOs descend in the order of LUMO+2, LUMO+1, LUMO, HOMO, HOMO-1, HOMO-2.

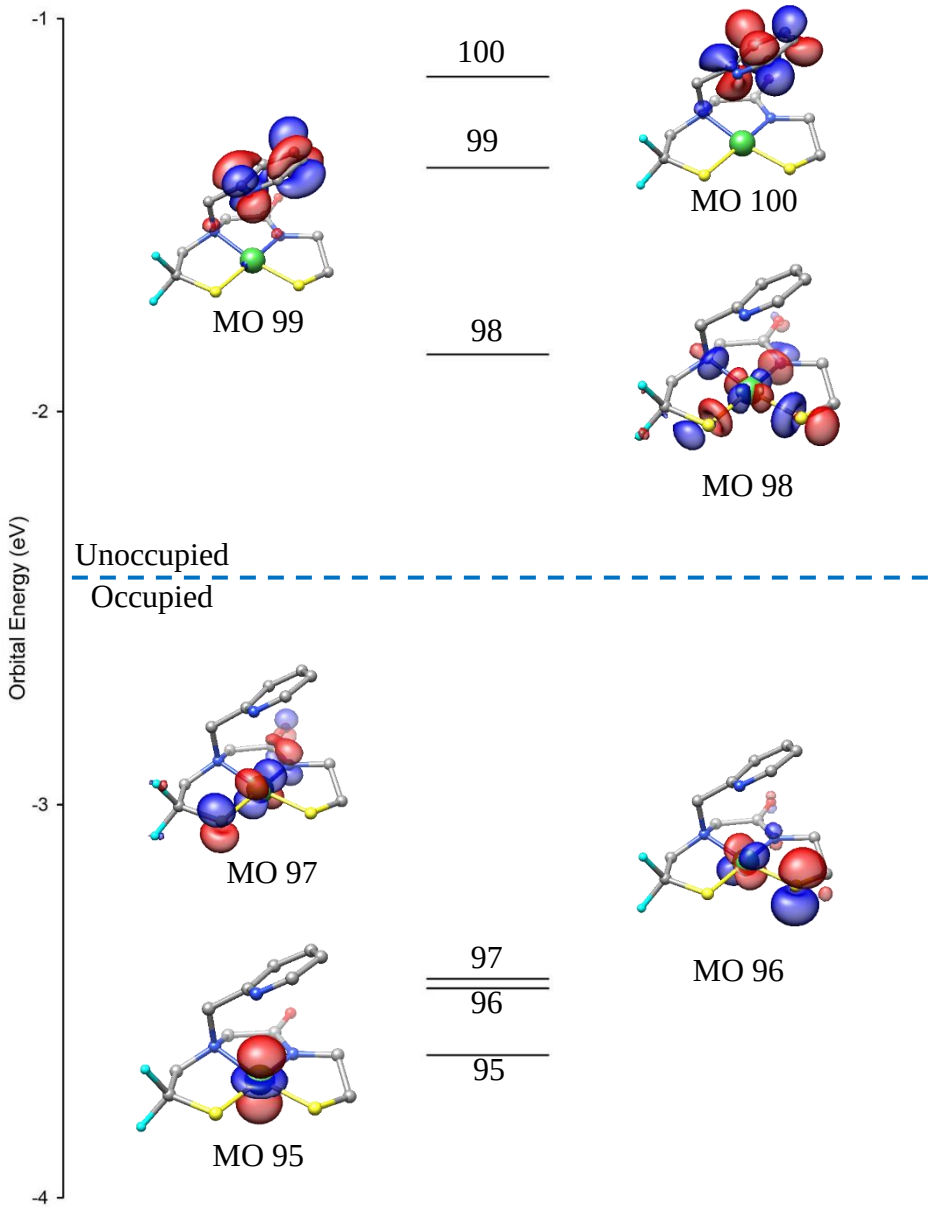

Figure 3.S37 DFT-generated isosurface plots (OLYP/def2-TZVPP) of the frontier MOs of **6***. The MOs descend in the order of LUMO+2, LUMO+1, LUMO, HOMO, HOMO-1, HOMO-2.

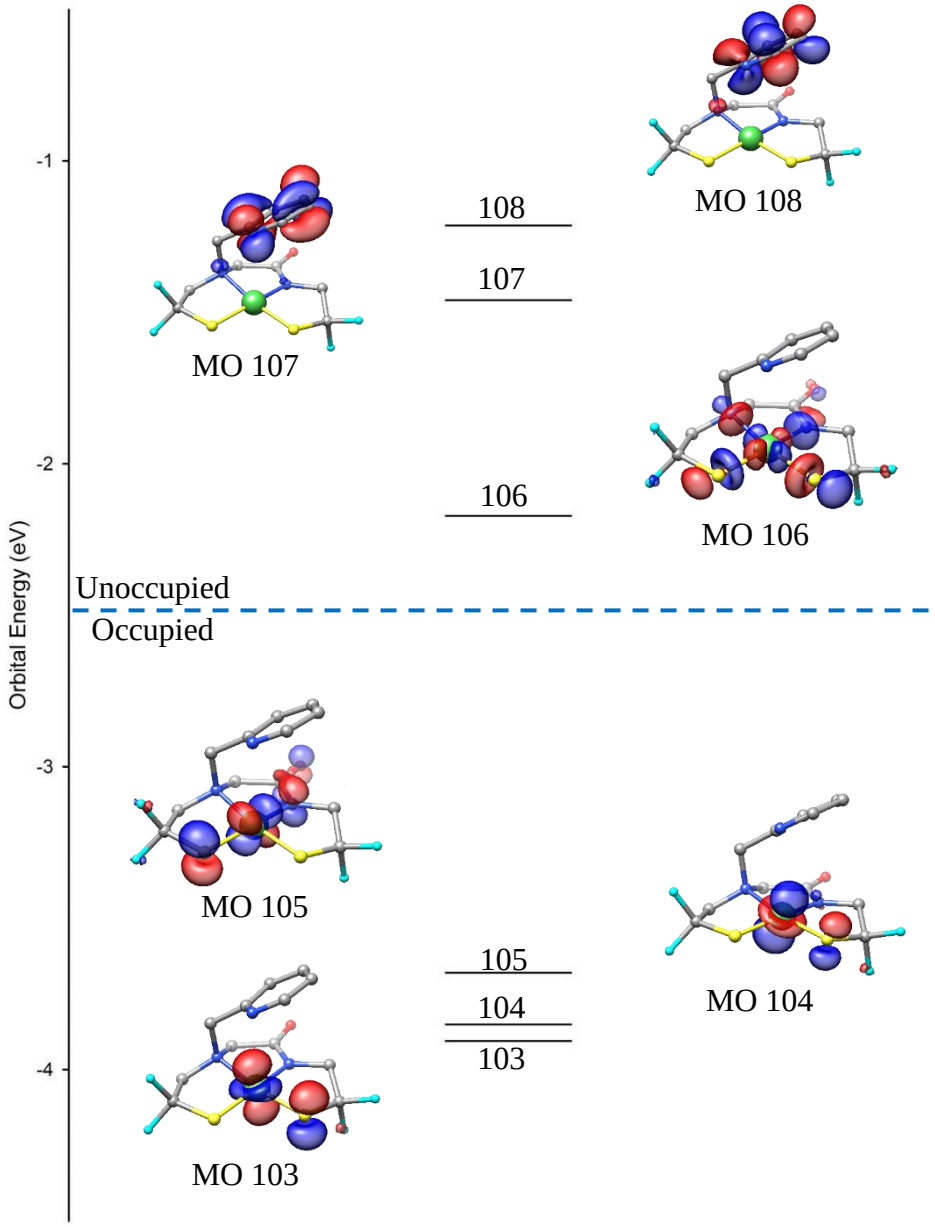

Figure 3.S38 DFT-generated isosurface plots (OLYP/def2-TZVPP) of the frontier MOs of **7***. The MOs descend in the order of LUMO+2, LUMO+1, LUMO, HOMO, HOMO-1, HOMO-2.

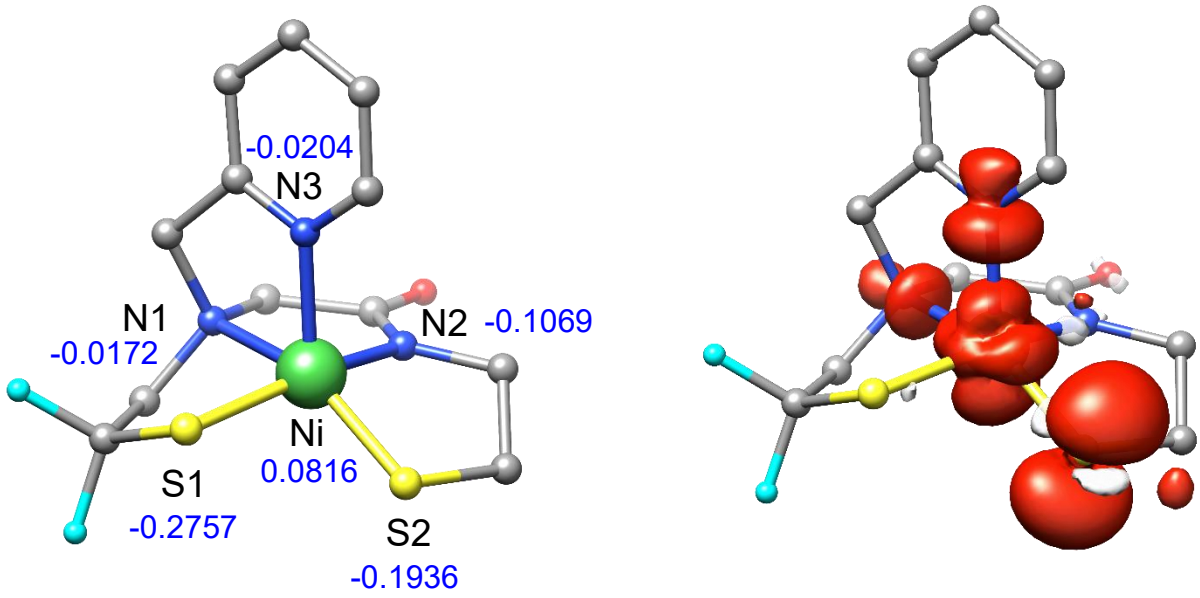

Figure 3.S39 Geometry-optimized structure of **6^{ox}*** with Mulliken atomic charges on Ni, S, and N atoms in blue (*left*) and spin density plot (red = positive spin density; white = negative spin density) (*right*). H atoms are omitted. Green = Ni; yellow = S; blue = N; red = O; cyan = F; gray = C. Selected bond lengths (Å) and angles (°): Ni–N1 = 2.071; Ni–N2 = 1.887; Ni–N3 = 2.068; Ni–S1 = 2.252; Ni–S2 = 2.140; N1–Ni–S2 = 152.38; N2–Ni–S1 = 166.74; N1–Ni–N2 = 85.73; N2–Ni–S2 = 88.03; S2–Ni–S1 = 92.56; S1–Ni–N1 = 87.64; S2–Ni–N3 = 125.73; N2–Ni–N3 = 93.82; S1–Ni–N3 = 96.56; N1–Ni–N3 = 81.58.

Table 3.S6 Löwdin population analysis derived from the DFT calculations for selected MOs of **2^{ox*}** from OLYP/def2-TZVPP with COSMO(DMF). Only s and p contributions were tabulated for N and S atoms. Bonding interactions are represented with a + and antibonding interactions are denoted with a –. N1 = amino-N; N2 = carboxamido-N; N3 = pyridine-N; S1 = $S_{trans\text{-carboxamide}}$; S2 = $S_{trans\text{-amine}}$.

	MO #	**Energy (eV)**	**%Ni**	**%S1**	**%S2**	**%N1**	**%N2**	**%N3**	**Type of Interaction**
α									
LUMO+1	99	-2.0892	1.4	0.4	0.0	0.0	0.2	18.5	pyridine(π*)
LUMO	98	-3.102	39.8	13.5	17.8	6.0	7.7	0.1	Ni(d_σ)–S1(σ)–S2(σ)–N1(σ)–N2(σ)
HOMO	97	-4.6005	18.3	35.7	33.1	0.0	0.7	0.0	Ni(d_π)–S1(π)–S2(π)
HOMO-1	96	-4.6704	29.1	18.8	29.1	1.4	0.7	7.1	Ni(d_σ)–S1(π)–S2(π)–N3(σ)
HOMO-2	95	-4.8782	30.1	4.4	6.9	0.3	21.2	4.1	Ni(d_π)–S1(σ)–S2(σ)–N2(π)–N3(σ)
β									
LUMO+2	99	-2.033	2.0	0.4	0.0	0.0	0.2	18.9	pyridine(π*)
LUMO+1	98	-2.7384	45.4	11.9	14.9	5.8	7.2	0.1	Ni(d_σ)–S1(σ)–S2(σ)–N1(σ)–N2(σ)
LUMO	97	-3.636	60.9	8.2	7.0	1.5	1.2	9.7	Ni(d_σ)–S1(π)–S2(π)–N3(σ)
HOMO	96	-4.4141	26.2	33.1	27.4	0.0	1.2	0.1	Ni(d_π)–S1(π)–S2(π)
HOMO-1	95	-4.6482	31.4	4.6	26.1	0.0	13.2	0.1	Ni(d_π)–S1(π)–S2(π)–N2(π)

Table 3.S7 Löwdin population analysis derived from the DFT calculations for selected MOs of **6^{ox*}** from OLYP/def2-TZVPP with COSMO(DMF). Only s and p contributions were tabulated for N and S atoms. Bonding interactions are represented with a + and antibonding interactions are denoted with a –. N1 = amino-N; N2 = carboxamido-N; N3 = pyridine-N; S1 = $S_{trans\text{-carboxamide}}$; S2 = $S_{trans\text{-amine}}$.

	MO#	Energy (eV)	%Ni	%S1	%S2	%N1	%N2	%N3	Type of Interaction
α									
LUMO+1	99	-2.1589	1.1	0.2	0.0	0.3	0.3	19.2	pyridine(π*)
LUMO	98	-3.4294	40.1	13.0	16.3	4.6	9.3	0.9	Ni(d_σ)–S1(σ)–S2(σ)–N1(σ)–N2(σ)
HOMO	97	-4.9676	30.2	3.0	42.8	4.7	0.2	4.4	Ni(d_π)–N1(σ)–S2(π)–N3(σ)
HOMO-1	96	-5.0809	27.1	23.8	2.3	0.0	17.6	0.1	Ni(d_π)–S1(π)–N2(π)
HOMO-2	95	-5.1629	23.6	28.3	8.1	0.1	10.9	6.5	Ni(d_σ)–S1(π)–S2(σ)–N2(π)–N3(σ)
β									
LUMO+2	99	-2.1162	1.4	0.2	0.0	0.3	0.3	19.5	pyridine(π*)
LUMO+1	98	-3.0785	45.6	11.3	13.7	4.5	8.5	0.9	Ni(d_σ)–S1(σ)–S2(σ)–N1(σ)–N2(σ)
LUMO	97	-3.952	57.4	0.4	20.2	3.5	0.5	6.9	Ni(d_σ)–N1(σ)–S2(π)–N3(σ)
HOMO	96	-4.8977	35.3	4.4	8.9	0.0	20.7	0.6	Ni(d_π)–S1(π)–S2(π)–N2(π)
HOMO-1	95	-4.9212	30.8	36.1	18.8	0.3	0.5	1.8	Ni(d_π)–S1(π)–S2(π)–N3(σ)

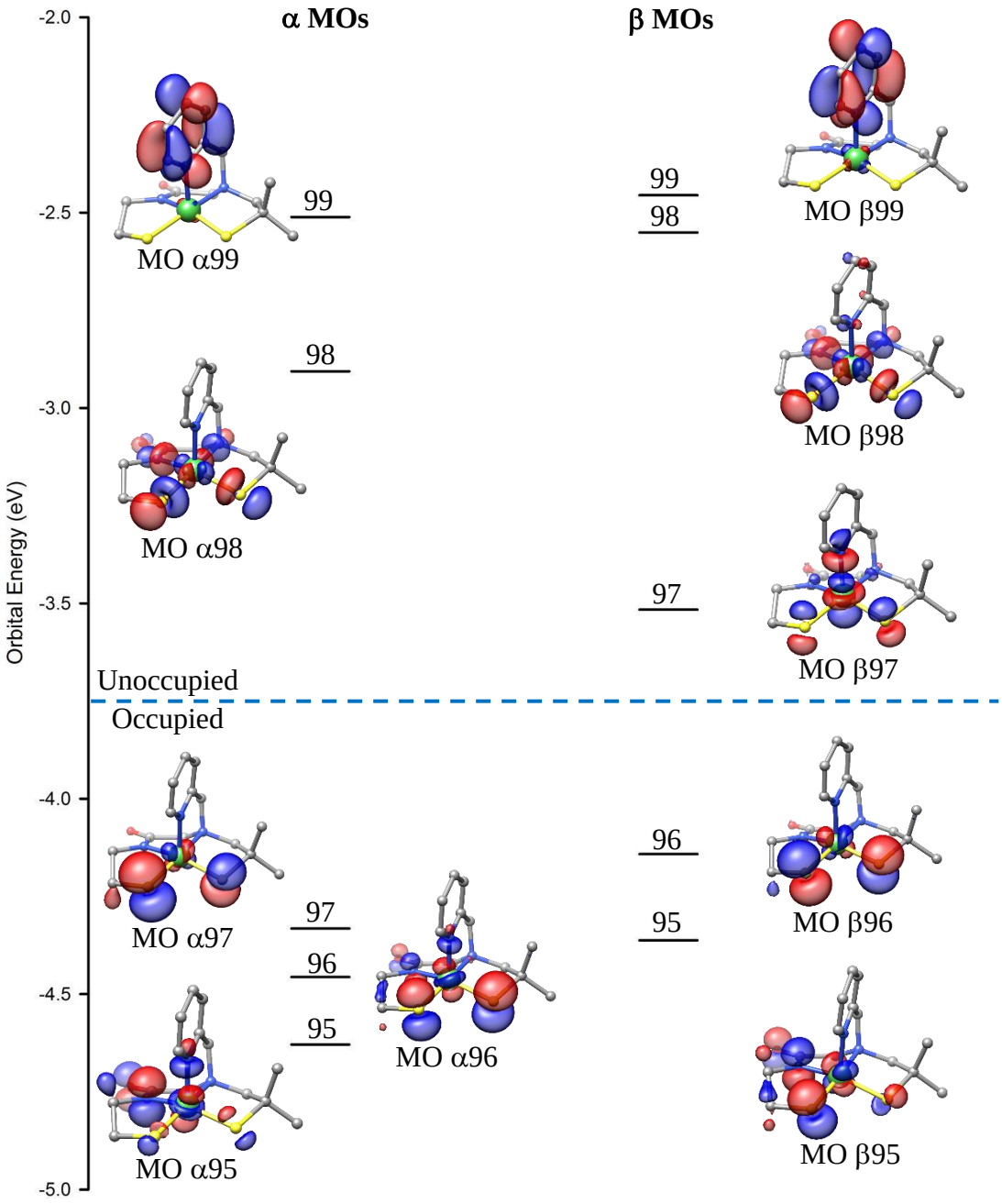

Figure 3.S40 DFT-generated isosurface plots (OLYP/def2-TZVPP) of the frontier MOs of **2^{ox*}**. Spin-up (α) MOs (*left*); spin-down (β) MOs (*right*).

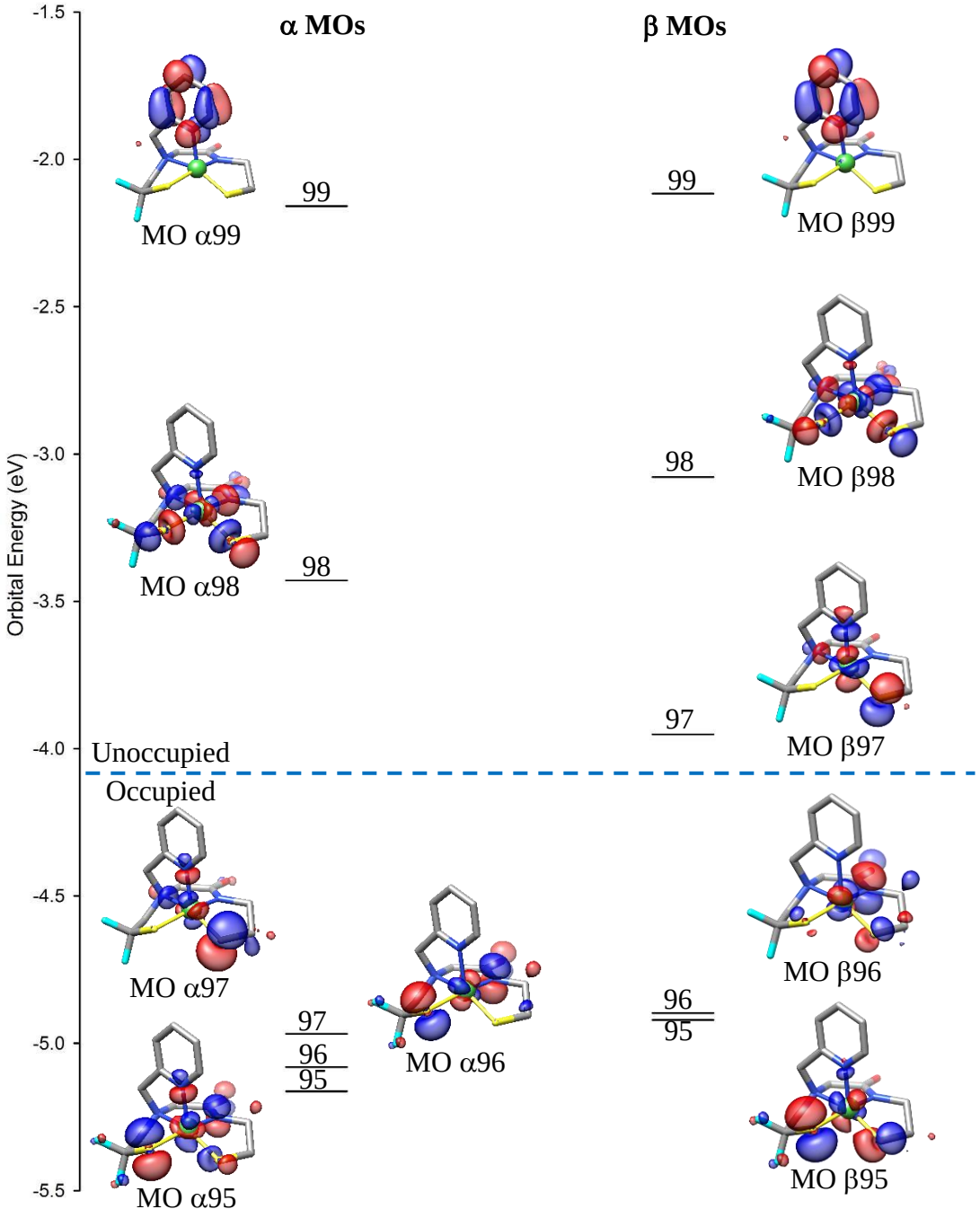

Figure 3.S41 DFT-generated isosurface plots (OLYP/def2-TZVPP) of the frontier MOs of **6^{ox*}**. Spin-up (α) MOs (*left*); spin-down (β) MOs (*right*).

Table 3.S8 Optimized BP86/def2-TZVPP Cartesian coordinates (Å) for **1***.

Ni	5.84498360873948	9.93816652267030	-0.54572675723694
S	4.01210387334390	9.45442429266023	0.53030799548669
S	4.86972358585446	10.45358977044556	-2.41052717644341
N	6.96363713230997	9.29868069788340	0.96632741429699
N	7.46076915108487	10.60825800865562	-1.23717131212638
N	6.45174739472619	6.71045421767317	-1.19312712790364
O	9.69843122187514	11.01413525943157	-0.69130807823012
C	4.80084322819464	8.74074218642747	2.02986067388894
H	4.17583516936458	8.95885788025460	2.90967452971059
H	4.87013475242895	7.64349834015942	1.94951122844204
C	6.17348335199459	9.36027184137369	2.23137320961486
H	6.05375916841130	10.42587746152992	2.46654678598299
H	6.74317333720176	8.87369630759303	3.05171709736281
C	8.14478258435821	10.20219165897805	0.98811795958171
H	9.00962021247050	9.72202081523655	1.47839499045449
H	7.87525930133282	11.09624558202036	1.56940854202389
C	8.52645380119956	10.65410781754045	-0.43175539150319
C	7.55881944602763	10.98685444169331	-2.63811030907557
H	7.77864892820695	10.08682224796524	-3.24452995820895
H	8.38561359150597	11.70316341900404	-2.78239127878959
C	6.20788361610344	11.55006162720895	-3.05449677856860
H	6.11697530885086	11.61047565630297	-4.15029575553768
H	6.08124198068733	12.56297997479270	-2.64139621050860
C	7.37944645317806	7.87876868812611	0.70591395049489
H	6.62397884229801	7.22530490312047	1.15229762479799
H	8.34590435510944	7.70365945195635	1.21433969389815
C	7.45940691869827	7.48802217016946	-0.75155367353309
C	8.54858392814216	7.84284750303258	-1.56366429730372
H	9.37386949747501	8.43157802459879	-1.16387552568658
C	8.52184550580797	7.48772109250476	-2.90898658374059
H	9.33508469562141	7.78787030266273	-3.57073098258626
C	7.43465617952373	6.75650669827366	-3.39345266329061
H	7.35950989609826	6.47984926025498	-4.44535075436543
C	6.44371878573727	6.37332604423286	-2.48821287704444
H	5.59391419603729	5.76937083386660	-2.81858220425364

Table 3.S9 Optimized BP86/def2-TZVPP Cartesian coordinates (Å) for **2***.

Ni	5.70245201012747	10.19522499154148	1.73296524112100
S	4.22198942457605	10.12848734522884	3.31652296264824
S	7.40251229845909	10.51391318440739	3.03563610484459
N	4.36332281753078	9.66873473612172	0.36210817402752
N	6.79655300014853	10.61544614343023	0.25857534110293
N	5.74294877194099	6.90152547052204	1.62596382496908
O	6.73927162651505	10.89672803792824	-2.06244009326842
C	2.77498115268011	9.48337717755397	2.34251816137041
C	2.98429569281600	9.89704121701121	0.87795174944426
H	2.24942089006647	9.40115964120135	0.20974027321663
H	2.82142751276151	10.98084804569786	0.82108142662070
C	4.68856660057519	10.55449702654262	-0.79206463706079
H	4.27217926450571	11.54914037791602	-0.57925584513370
H	4.24334776696663	10.17799249974927	-1.72908183116047
C	6.21419519940058	10.69902552419544	-0.94230470583134
C	8.23080846287314	10.77961145651397	0.42516460606697
H	8.64046050437051	11.39585887777218	-0.39344750122419
H	8.72756935221660	9.79124618484236	0.38517753561970
C	8.45817404803987	11.39143039348854	1.80065796269375
H	8.18990855343778	12.45911536251991	1.78435376961797
H	9.51059842272085	11.30417296387721	2.11279920843891
C	4.57686086587684	8.22917149457044	-0.03942525980482
H	3.73845532731755	7.64204922235044	0.34403671545669
H	4.56066024084415	8.17662516802782	-1.13992570042365
C	5.85255238256795	7.61124268372788	0.48609292719424
C	7.05451196886861	7.69215269597069	-0.23523807956089
H	7.09164423495073	8.23377612298223	-1.18018577082533
C	8.20202701877886	7.12933713668063	0.31259787651192
H	9.15602819744808	7.20900601039431	-0.20983160990957
C	8.11351777213914	6.48137034020728	1.54740880556336
H	8.99325525329137	6.05590607964033	2.03019094519873
C	6.85759761963627	6.37564052265565	2.14606778493021
H	6.73707688580517	5.84307559807596	3.09353984589331
C	2.61951452068737	7.96977058910434	2.55797875580561
H	1.82657732842959	7.54743702448603	1.91072032678802
H	2.33308242712779	7.78880851317635	3.60364287263126
H	3.55992121096215	7.43344442175483	2.38356902145686
C	1.50270281590617	10.18667114139908	2.84035931736075
H	0.60700253613415	9.82815832943808	2.30211341580520
H	1.58463775590291	11.27500463856649	2.71530101854791
H	1.36121126459617	9.98013660872928	3.91019306325648

Table 3.S10 Optimized BP86/def2-TZVPP Cartesian coordinates (Å) for **6***.

Ni	5.78103321942440	9.93662701683601	-0.52173349674796
S	3.99149995007506	9.36258846265687	0.60786604274907
S	4.71552458326001	10.54718578144734	-2.30626475858910
N	6.94251009983588	9.25211976852059	0.92484355922530
N	7.36650771463878	10.56805325347973	-1.29253619200048
N	6.46079715493056	6.77099873159295	-1.38639688884264
O	9.63861777627350	10.91660228489837	-0.87481952668240
C	4.78435237047909	8.97063315367558	2.15597582357998
F	4.14359565420801	9.57335680824119	3.25671598459946
F	4.70161897410469	7.59232259676263	2.49005353333269
C	6.24912502523032	9.41016951055593	2.22374284901924
H	6.24091929134219	10.47917027456865	2.46028182108337
H	6.77146615056144	8.86301404562024	3.03069339044360
C	8.19363531402017	10.06147681428700	0.86865349547443
H	9.05557809297596	9.48745927655025	1.24844423859061
H	8.06329401149775	10.93933033853768	1.51625288121910
C	8.48111025392076	10.56414377444493	-0.55484398663767
C	7.40311776564385	10.96601795081925	-2.69326376389643
H	7.55698386709368	10.06718565741534	-3.31998417833736
H	8.24853900298871	11.65220736895185	-2.86928558486447
C	6.05713504584698	11.59016243278547	-3.02519655238092
H	5.90101187547784	11.66229179325089	-4.11242338174365
H	5.99856740398898	12.60354812047869	-2.59931111068822
C	7.21156217958855	7.79600227567633	0.66734117743009
H	6.32264141991719	7.24185308339934	0.97912236493357
H	8.07168514689878	7.49332457467716	1.29608311266923
C	7.45668181290440	7.44618447656038	-0.78275540053844
C	8.65531367381069	7.76101315422527	-1.44082732293062
H	9.46101468284122	8.27923231535623	-0.92243765266244
C	8.77665660676009	7.46278879470555	-2.79545759818270
H	9.67994012956020	7.74413933590250	-3.33740335030880
C	7.72046421921258	6.81791341430895	-3.44106463365462
H	7.76404031732378	6.58100190600402	-4.50449729997071
C	6.59815971758489	6.47517886555500	-2.68389302942591
H	5.75914249577901	5.94510358755182	-3.14312856516421

Table 3.S11 Optimized BP86/def2-TZVPP Cartesian coordinates (Å) for **7***.

Ni	5.78039734477591	9.92717358790330	-0.49164928152448
S	3.99777965931795	9.34638281852698	0.64363951128193
S	4.69492240446687	10.54873840615618	-2.26113277936342
N	6.94373064021117	9.23610280927326	0.94137520911026
N	7.36301356247302	10.54768617704484	-1.27611193537954
N	6.43753720768727	6.83323417561621	-1.40549923491252
O	9.63742579871316	10.87240726660243	-0.88164389472762
C	4.79757307982902	8.95260789126984	2.18964376262568
F	4.16086249368463	9.55245950529810	3.29038682285090
F	4.71756417867090	7.57479509504443	2.51757718208205
C	6.26142671367523	9.39411032771675	2.24693167265777
H	6.25437798482144	10.46303974201347	2.48366705868313
H	6.79155995585080	8.84684735908785	3.04809474693259
C	8.19825232638965	10.03936746801666	0.88036491487269
H	9.05770166478155	9.46358210526158	1.26113691162596
H	8.07138692887126	10.92192173104178	1.52183269738047
C	8.48355750359606	10.53366434105035	-0.54593627125643
C	7.40958419290743	10.95085055990061	-2.66388062758126
H	7.61957664567385	10.08386173318246	-3.31431278417868
H	8.18328463686924	11.71375624517421	-2.83734552305073
C	6.03460692807895	11.48242145664993	-3.04330244240842
F	5.89477116024745	11.46365299421701	-4.43443406277967
C	7.20879213904306	7.77816759302816	0.67831135600856
H	6.31623189151499	7.22688489659627	0.98447593576694
H	8.06555416034513	7.47188477599957	1.30838777264969
C	7.45789420657941	7.44234942692549	-0.77399711264661
C	8.67473361040606	7.72345136517615	-1.41154008995294
H	9.49571458699156	8.19176551162639	-0.87030968746551
C	8.79568507705161	7.46140285162378	-2.77430709896718
H	9.71471776889776	7.71929113506920	-3.30100868538461
C	7.71737559045906	6.88598053142934	-3.44736570832058
H	7.75905532690101	6.68265433640364	-4.51757002153873
C	6.57320412773819	6.57103605212250	-2.71035021733269
H	5.71530559690846	6.09506326227616	-3.19265342656831
F	5.97121484397086	12.84796362237515	-2.72362107508869

Table 3.S12 Optimized BP86/def2-TZVPP Cartesian coordinates (Å) for **2^{ox}***.

Ni	5.870350	10.141865	1.745110
S	4.355701	9.864448	3.290322
S	7.386877	10.834756	3.166220
N	4.502517	9.849747	0.263491
N	6.869966	10.964788	0.361755
N	6.430522	8.259483	1.352964
O	6.675176	11.930305	-1.742671
C	3.013157	9.154581	2.216099
C	3.123572	9.821861	0.841362
H	2.433241	9.354376	0.114047
H	2.828015	10.870294	0.962984
C	4.714668	11.019011	-0.640947
H	4.214045	11.888666	-0.195718
H	4.283615	10.842515	-1.637884
C	6.216439	11.343759	-0.752635
C	8.276532	11.255878	0.592419
H	8.647489	11.941863	-0.184612
H	8.864591	10.322957	0.539773
C	8.384576	11.850823	1.989217
H	7.993598	12.877051	1.998195
H	9.420503	11.863432	2.355372
C	4.872317	8.602779	-0.467933
H	3.963882	8.045150	-0.741402
H	5.366828	8.894644	-1.406057
C	5.819024	7.710022	0.291228
C	6.072686	6.391830	-0.090830
H	5.559821	5.967142	-0.953606
C	6.976885	5.636586	0.653977
H	7.188357	4.603848	0.378152
C	7.598160	6.218130	1.761686
H	8.304025	5.659226	2.373623
C	7.298055	7.537603	2.084322
H	7.744317	8.066311	2.926678
C	3.084321	7.622507	2.171922
H	2.302639	7.214518	1.509277
H	2.922337	7.218885	3.179094
H	4.055952	7.252380	1.832530
C	1.670613	9.570767	2.837310
H	0.828095	9.182416	2.243147
H	1.585875	10.663152	2.901263
H	1.584482	9.163003	3.852582

Table 3.S13 Optimized BP86/def2-TZVPP Cartesian coordinates (Å) for **6^{ox}***.

Ni	5.916281	9.534588	-0.894163
S	4.337752	8.359342	0.201552
S	4.459428	10.617452	-2.028388
N	7.133659	9.279875	0.761608
N	7.202702	10.788561	-1.471537
N	7.001141	7.906392	-1.563414
O	9.167860	11.871037	-0.899575
C	4.930560	8.756129	1.861905
F	3.995148	9.461999	2.605351
F	5.109342	7.573944	2.603268
C	6.233195	9.573090	1.904829
H	5.955293	10.631089	1.834361
H	6.732825	9.400397	2.874298
C	8.250901	10.271099	0.643570
H	9.218684	9.761269	0.744472
H	8.187438	10.998852	1.464281
C	8.257173	11.061894	-0.678713
C	6.978553	11.504739	-2.723616
H	7.172611	10.833380	-3.578478
H	7.678379	12.351342	-2.795097
C	5.523106	11.951251	-2.743192
H	5.165095	12.172918	-3.757870
H	5.373681	12.843774	-2.119242
C	7.624078	7.875729	0.763150
H	6.856615	7.248370	1.238107
H	8.549469	7.783344	1.354086
C	7.817189	7.363223	-0.640805
C	8.713141	6.343277	-0.968165
H	9.370875	5.930305	-0.203282
C	8.745291	5.867426	-2.278573
H	9.435884	5.072051	-2.558510
C	7.884189	6.426368	-3.224934
H	7.876032	6.082919	-4.258207
C	7.029181	7.451379	-2.827364
H	6.341091	7.931597	-3.523166

3.7 References

(1) Sheng, Y.; Abreu, I. A.; Cabelli, D. E.; Maroney, M. J.; Miller, A.-F.; Teixeira, M.; Valentine, J. S. Superoxide Dismutases and Superoxide Reductases. *Chem. Rev.* **2014**, *114*, 3854-3918.

(2) Youn, H.-D.; Kim, E.-J.; Roe, J.-H.; Hah, Y. C.; Kang, S.-O. A novel nickel-containing superoxide dismutase from *Streptomyces* spp. *Biochem. J.* **1996**, *318*, 889-896.

(3) Youn, H.-D.; Youn, H.; Lee, J.-W.; Yim, Y.-I.; Lee, J. K.; Hah, Y. C.; Kang, S.-O. Unique Isozymes of Superoxide Dismutase in *Streptomyces griseus*. *Arch. Biochem. Biophys.* **1996**, *334*, 341-348.

(4) Palenik, B.; Brahamsha, B.; Larimer, F. W.; Land, M.; Hauser, L.; Chain, P.; Lamerdin, J.; Regala, W.; Allen, E. E.; McCarren, J.; Paulsen, I.; Dufresne, A.; Partensky, F.; Webb, E. A.; Waterbury, J. The genome of a motile marine *Synechococcus*. *Nature* **2003**, *424*, 1037-1042.

(5) Grapperhaus, C. A.; Darensbourg, M. Y. Oxygen Capture by Sulfur in Nickel Thiolates. *Acc. Chem. Res.* **1998**, *31*, 451-459.

(6) Kumar, M.; Colpas, G. J.; Day, R. O.; Maroney, M. J. Ligand Oxidation in a Nickel Thiolate Complex: A Model for the Deactivation of Hydrogenase by O_2. *J. Am. Chem. Soc.* **1989**, *111*, 8323-8325.

(7) Mirza, S. A.; Pressler, M. A.; Kumar, M.; Day, R. O.; Maroney, M. J. Oxidation of Nickel Thiolate Ligands by Dioxygen. *Inorg. Chem.* **1993**, *32*, 977-987.

(8) Mirza, S. A.; Day, R. O.; Maroney, M. J. Oxidation of a Dimeric Nickel Thiolate Complex with O_2. *Inorg. Chem.* **1996**, *35*, 1992-1995.

(9) Maroney, M. J.; Choudhury, S. B.; Bryngelson, P. A.; Mirza, S. A.; Sherrod, M. J. Theoretical Study of the Oxidation of Nickel Thiolate Complexes by O_2. *Inorg. Chem.* **1996**, *35*, 1073-1076.

(10) Barondeau, D. P.; Kassmann, C. J.; Bruns, C. K.; Tainer, J. A.; Getzoff, E. D. Nickel Superoxide Dismutase Structure and Mechanism. *Biochemistry* **2004**, *43*, 8038-8047.

(11) Wuerges, J.; Lee, J.-W.; Yim, Y.-I.; Yim, H.-S.; Kang, S.-O.; Carugo, K. D. Crystal structure of nickel-containing superoxide dismutase reveals another type of active site. *Proc. Natl. Acad. Sci. U. S. A.* **2004**, *101*, 8569-8574.

(12) Choudhury, S. B.; Lee, J.-W.; Davidson, G.; Yim, Y.-I.; Bose, K.; Sharma, M. L.; Kang, S.-O.; Cabelli, D. E.; Maroney, M. J. Examination of the Nickel Site Structure and Reaction Mechanism in *Streptomyces seoulensis* Superoxide Dismutase. *Biochemistry* **1999**, *38*, 3744-3752.

(13) Fiedler, A. T.; Bryngelson, P. A.; Maroney, M. J.; Brunold, T. C. Spectroscopic and Computational Studies of Ni Superoxide Dismutase: Electronic Structure Contributions to Enzymatic Function. *J. Am. Chem. Soc.* **2005**, *127*, 5449-5462.

(14) Szilagyi, R. K.; Bryngelson, P. A.; Maroney, M. J.; Hedman, B.; Hodgson, K. O.; Solomon, E. I. S K-edge X-ray Absorption Spectroscopic Investigation of the Ni-Containing Superoxide Dismutase Active Site: New Structural Insight into the Mechanism. *J. Am. Chem. Soc.* **2004**, *126*, 3018-3019.

(15) Shearer, J. Use of a Metallopeptide-Based Mimic Provides Evidence for a Proton-Coupled Electron-Transfer Mechanism for Superoxide Reduction by Nickel-Containing Superoxide Dismutase. *Angew. Chem., Int. Ed.* **2013**, *52*, 2569-2572.

(16) Shearer, J.; Peck, K. L.; Schmitt, J. C.; Neupane, K. P. Cysteinate Protonation and Water Hydrogen Bonding at the Active-Site of a Nickel Superoxide Dismutase Metallopeptide-Based Mimic: Implications for the Mechanism of Superoxide Reduction. *J. Am. Chem. Soc.* **2014**, *136*, 16009-16022.

(17) Bryngelson, P. A.; Arobo, S. E.; Pinkham, J. L.; Cabelli, D. E.; Maroney, M. J. Expression, Reconstitution, and Mutation of Recombinant *Streptomyces coelicolor* NiSOD. *J. Am. Chem. Soc.* **2004**, *126*, 460-461.

(18) Lee, H.-I.; Lee, J.-W.; Yang, T.-C.; Kang, S.-O.; Hoffman, B. M. ENDOR and ESEEM investigation of the Ni-containing superoxide dismutase. *JBIC, J. Biol. Inorg. Chem.* **2010**, *15*, 175-182.

(19) Herbst, R. W.; Guce, A.; Bryngelson, P. A.; Higgins, K. A.; Ryan, K. C.; Cabelli, D. E.; Garman, S. C.; Maroney, M. J. Role of Conserved Tyrosine Residues in NiSOD Catalysis: A Case of Convergent Evolution. *Biochemistry* **2009**, *48*, 3354-69.

(20) Ryan, K. C.; Guce, A. I.; Johnson, O. E.; Brunold, T. C.; Cabelli, D. E.; Garman, S. C.; Maroney, M. J. Nickel Superoxide Dismutase: Structural and Functional Roles of His1 and Its H-Bonding Network. *Biochemistry* **2015**, *54*, 1016-1027.

(21) Campeciño, J. O.; Dudycz, L. W.; Tumelty, D.; Berg, V.; Cabelli, D. E.; Maroney, M. J. A Semisynthetic Strategy Leads to Alteration of the Backbone Amidate Ligand in the NiSOD Active Site. *J. Am. Chem. Soc.* **2015**, *137*, 9044-9052.

(22) Johnson, O. E.; Ryan, K. C.; Maroney, M. J.; Brunold, T. C. Spectroscopic and computational investigation of three Cys-to-Ser mutants of nickel superoxide dismutase: insight into the roles played by the Cys2 and Cys6 active-site residues. *JBIC, J. Biol. Inorg. Chem.* **2010**, *15*, 777-793.

(23) Ryan, K. C.; Johnson, O. E.; Cabelli, D. E.; Brunold, T. C.; Maroney, M. J. Nickel superoxide dismutase: structural and functional roles of Cys2 and Cys6. *JBIC, J. Biol. Inorg. Chem.* **2010**, *15*, 795-807.

(24) Broering, E. P.; Truong, P. T.; Gale, E. M.; Harrop, T. C. Synthetic Analogues of Nickel Superoxide Dismutase: A New Role for Nickel in Biology. *Biochemistry* **2013**, *52*, 4-18.

(25) Shearer, J. Insight into the Structure and Mechanism of Nickel-Containing Superoxide Dismutase Derived from Peptide-Based Mimics. *Acc. Chem. Res.* **2014**, *47*, 2332-2341.

(26) Shearer, J.; Long, L. M. A Nickel Superoxide Dismutase Maquette That Reproduces the Spectroscopic and Functional Properties of the Metalloenzyme. *Inorg. Chem.* **2006**, *45*, 2358-2360.

(27) Neupane, K. P.; Shearer, J. The Influence of Amine/Amide versus Bisamide Coordination in Nickel Superoxide Dismutase. *Inorg. Chem.* **2006**, *45*, 10552-10566.

(28) Neupane, K. P.; Gearty, K.; Francis, A.; Shearer, J. Probing Variable Axial Ligation in Nickel Superoxide Dismutase Utilizing Metallopeptide-Based Models: Insight into the Superoxide Disproportionation Mechanism. *J. Am. Chem. Soc.* **2007**, *129*, 14605-14618.

(29) Shearer, J.; Neupane, K. P.; Callan, P. E. Metallopeptide Based Mimics with Substituted Histidines Approximate a Key Hydrogen Bonding Network in the Metalloenzyme Nickel Superoxide Dismutase. *Inorg. Chem.* **2009**, *48*, 10560-10571.

(30) Shearer, J. Dioxygen and superoxide stability of metallopeptide based mimics of nickel containing superoxide dismutase: The influence of amine/amidate vs. bis-amidate ligation. *J. Inorg. Biochem.* **2013**, *129*, 145-149.

(31) Schmidt, M.; Zahn, S.; Carella, M.; Ohlenschläger, O.; Görlach, M.; Kothe, E.; Weston, J. Solution Structure of a Functional Biomimetic and Mechanistic Implications for Nickel Superoxide Dismutases. *ChemBioChem* **2008**, *9*, 2135-2146.

(32) Tietze, D.; Breitzke, H.; Imhof, D.; Kothe, E.; Weston, J.; Buntkowsky, G. New Insight into the Mode of Action of Nickel Superoxide Dismutase by Investigating Metallopeptide Substrate Models. *Chem. - Eur. J.* **2009**, *15*, 517-523.

(33) Tietze, D.; Tischler, M.; Voigt, S.; Imhof, D.; Ohlenschläger, O.; Görlach, M.; Buntkowsky, G. Development of a Functional *cis*-Prolyl Bond Biomimetic and Mechanistic Implications for Nickel Superoxide Dismutase. *Chem. - Eur. J.* **2010**, *16*, 7572-7578.

(34) Tietze, D.; Voigt, S.; Mollenhauer, D.; Tischler, M.; Imhof, D.; Gutmann, T.; González, L.; Ohlenschläger, O.; Breitzke, H.; Görlach, M.; Buntkowsky, G. Revealing the Position of the Substrate in Nickel Superoxide Dismutase: A Model Study. *Angew. Chem., Int. Ed.* **2011**, *50*, 2946-2950.

(35) Krause, M. E.; Glass, A. M.; Jackson, T. A.; Laurence, J. S. Novel Tripeptide Model of Nickel Superoxide Dismutase. *Inorg. Chem.* **2010**, *49*, 362-364.

(36) Krause, M. E.; Glass, A. M.; Jackson, T. A.; Laurence, J. S. MAPping the Chiral Inversion and Structural Transformation of a Metal-Tripeptide Complex Having Ni-Superoxide Dismutase Activity. *Inorg. Chem.* **2011**, *50*, 2479-2487.

(37) Glass, A. M.; Krause, M. E.; Laurence, J. S.; Jackson, T. A. Controlling the Chiral Inversion Reaction of the Metallopeptide Ni-Asparagine-Cysteine-Cysteine with Dioxygen. *Inorg. Chem.* **2012**, *51*, 10055-10063.

(38) Ma, H.; Chattopadhyay, S.; Petersen, J. L.; Jensen, M. P. Harnessing Scorpionate Ligand Equilibria for Modeling Reduced Nickel Superoxide Dismutase Intermediates. *Inorg. Chem.* **2008**, *47*, 7966-7968.

(39) Ma, H.; Wang, G.; Yee, G. T.; Petersen, J. L.; Jensen, M. P. Scorpionate-supported models of nickel-dependent superoxide dismutase. *Inorg. Chim. Acta* **2009**, *362*, 4563-4569.

(40) Ma, H.; Petersen, J. L.; Young, V. G., Jr.; Yee, G. T.; Jensen, M. P. Solid-State Spin Crossover of Ni(II) in a Bioinspired N_3S_2 Ligand Field. *J. Am. Chem. Soc.* **2011**, *133*, 5644-5647.

(41) Mullins, C. S.; Grapperhaus, C. A.; Frye, B. C.; Wood, L. H.; Hay, A. J.; Buchanan, R. M.; Mashuta, M. S. Synthesis and Sulfur Oxygenation of a (N_3S)Ni Complex Related to Nickel-Containing Superoxide Dismutase. *Inorg. Chem.* **2009**, *48*, 9974-9976.

(42) Herdt, D. R.; Grapperhaus, C. A. Kinetic study of nickel-thiolate oxygenation by hydrogen peroxide. Implications for nickel-containing superoxide dismutase. *Dalton Trans.* **2012**, *41*, 364-366.

(43) Jenkins, R. M.; Singleton, M. L.; Almaraz, E.; Reibenspies, J. H.; Darensbourg, M. Y. Imidazole-Containing (N_3S)-Ni^{II} Complexes Relating to Nickel Containing Biomolecules. *Inorg. Chem.* **2009**, *48*, 7280-7293.

(44) Gale, E. M.; Patra, A. K.; Harrop, T. C. Versatile Methodology Toward NiN_2S_2 Complexes as Nickel Superoxide Dismutase Models: Structure and Proton Affinity. *Inorg. Chem.* **2009**, *48*, 5620-5622.

(45) Gale, E. M.; Cowart, D. M.; Scott, R. A.; Harrop, T. C. Dipeptide-Based Models of Nickel Superoxide Dismutase: Solvent Effects Highlight a Critical Role to Ni–S Bonding and Active Site Stabilization. *Inorg. Chem.* **2011**, *50*, 10460-10471.

(46) Gale, E. M.; Narendrapurapu, B. S.; Simmonett, A. C.; Schaefer, H. F., III; Harrop, T. C. Exploring the Effects of H-Bonding in Synthetic Analogues of Nickel Superoxide Dismutase (Ni-SOD): Experimental and Theoretical Implications for Protection of the Ni–SCys Bond. *Inorg. Chem.* **2010**, *49*, 7080-7096.

(47) Broering, E. P.; Dillon, S.; Gale, E. M.; Steiner, R. A.; Telser, J.; Brunold, T. C.; Harrop, T. C. Accessing Ni(III)-Thiolate Versus Ni(II)-Thiyl Bonding in a Family of Ni–N_2S_2 Synthetic Models of NiSOD. *Inorg. Chem.* **2015**, *54*, 3815-3828.

(48) Lee, W.-Z.; Chiang, C.-W.; Lin, T.-H.; Kuo, T.-S. A Discrete Five-Coordinate Ni^{III} Complex Resembling the Active Site of the Oxidized Form of Nickel Superoxide Dismutase. *Chem. - Eur. J.* **2012**, *18*, 50-53.

(49) Chiang, C.-W.; Chu, Y.-L.; Chen, H.-L.; Kuo, T.-S.; Lee, W.-Z. Synthesis and Characterization of $Ni^{III}N3S2$ Complexes as Active Site Models for the Oxidized Form of Nickel Superoxide Dismutase. *Chem. - Eur. J.* **2014**, *20*, 6283-6286.

(50) Nakane, D.; Funahashi, Y.; Ozawa, T.; Masuda, H. A Square-planar Ni(II) Complex with an Asymmetric N_2S_2 Donor Set as a Model for the Active Site of Nickel-containing SOD: Structural Conversion Driven by Addition of a Strong Donor Ligand in the High Oxidation State. *Chem. Lett.* **2010**, *39*, 344-346.

(51) Gale, E. M.; Simmonett, A. C.; Telser, J.; Schaefer, H. F., III; Harrop, T. C. Toward Functional Ni-SOD Biomimetics: Achieving a Structural/Electronic Correlation with Redox Dynamics. *Inorg. Chem.* **2011**, *50*, 9216-9218.

(52) Shearer, J.; Zhao, N. $[Me_4N](Ni^{II}(BEAAM))$: A Synthetic Model for Nickel Superoxide Dismutase That Contains Ni in a Mixed Amine/Amide Coordination Environment. *Inorg. Chem.* **2006**, *45*, 9637-9639.

(53) Mathrubootham, V.; Thomas, J.; Staples, R.; McCraken, J.; Shearer, J.; Hegg, E. L. Bisamidate and Mixed Amine/Amidate NiN_2S_2 Complexes as Models for Nickel-Containing Acetyl Coenzyme A Synthase and Superoxide Dismutase: An Experimental and Computational Study. *Inorg. Chem.* **2010**, *49*, 5393-5406.

(54) Nakane, D.; Wasada-Tsutsui, Y.; Funahashi, Y.; Hatanaka, T.; Ozawa, T.; Masuda, H. A Novel Square-Planar Ni(II) Complex with an Amino–Carboxamido–Dithiolato-Type Ligand as an Active-Site Model of NiSOD. *Inorg. Chem.* **2014**, *53*, 6512-6523.

(55) Nolan, E. M.; Racine, M. E.; Lippard, S. J. Selective Hg(II) Detection in Aqueous Solution with Thiol Derivatized Fluoresceins. *Inorg. Chem.* **2006**, *45*, 2742-2749.

(56) Brand, U.; Vahrenkamp, H. Zinc complexes of the new *N,N,S* ligand *N*-(2-mercaptoisobutyl)(picolyl)amine. *Inorg. Chim. Acta* **2000**, *308*, 97-102.

(57) Marlin, D. S.; Mascharak, P. K. Coordination of carboxamido nitrogen to tervalent iron: insight into a new chapter of iron chemistry. *Chem. Soc. Rev.* **2000**, *29*, 69-74.

(58) Harrop, T. C.; Mascharak, P. K. Structural and spectroscopic models of the A-cluster of acetyl coenzyme a synthase/carbon monoxide dehydrogenase: Nature's Monsanto acetic acid catalyst. *Coord. Chem. Rev.* **2005**, *249*, 3007-3024.

(59) Yang, L.; Powell, D. R.; Houser, R. P. Structural variation in copper(I) complexes with pyridylmethylamide ligands: structural analysis with a new four-coordinate geometry index, τ_4. *Dalton Trans.* **2007**, 955-964.

(60) Addison, A. W.; Rao, T. N.; Reedijk, J.; van Rijn, J.; Verschoor, G. C. Synthesis, Structure, and Spectroscopic Properties of Copper(II) Compounds containing Nitrogen–Sulphur Donor Ligands: the Crystal and Molecular Structure of Aqua[1,7-bis(*N*-methylbenzimidazol-2'-yl)-2,6-dithiaheptane]copper(II) Perchlorate. *J. Chem. Soc., Dalton Trans.* **1984**, 1349-1356.

(61) Okuniewski, A.; Rosiak, D.; Chojnacki, J.; Becker, B. Coordination polymers and molecular structures among complexes of mercury(II) halides with selected 1-benzoylthioureas. *Polyhedron* **2015**, *90*, 47-57.

(62) Englich, U.; Chadwick, S.; Ruhlandt-Senge, K. Sodium and Potassium Triisopropylbenzenethiolates: Influence on Solid-State Structure by Metal and Donor. *Inorg. Chem.* **1998**, *37*, 283-293.

(63) Brines, L. M.; Shearer, J.; Fender, J. K.; Schweitzer, D.; Shoner, S. C.; Barnhart, D.; Kaminsky, W.; Lovell, S.; Kovacs, J. A. Periodic Trends within a Series of Five-Coordinate Thiolate-Ligated $[M^{II}(S^{Me2}N_4(tren))]^+$ (M = Mn, Fe, Co, Ni, Cu, Zn) Complexes, Including a Rare Example of a Stable Cu^{II}–Thiolate. *Inorg. Chem.* **2007**, *46*, 9267-9277.

(64) Zheng, A.-X.; Si, J.; Tang, X.-Y.; Miao, L.-L.; Yu, M.; Hou, K.-P.; Wang, F.; Li, H.-X.; Lang, J.-P. Reactions of the Cationic Zinc Thiolate Model Complex $[Zn(Tab)_4](PF_6)_2$ with N-Donor Ligands and Cobalt Dichloride. *Inorg. Chem.* **2012**, *51*, 10262-10273.

(65) Jiang, Y.; Widger, L. R.; Kasper, G. D.; Siegler, M. A.; Goldberg, D. P. Iron(II)-Thiolate *S*-Oxygenation by O_2: Synthetic Models of Cysteine Dioxygenase. *J. Am. Chem. Soc.* **2010**, *132*, 12214-12215.

(66) Shoner, S. C.; Humphreys, K. J.; Barnhart, D.; Kovacs, J. A. A Model for the Interaction of Alcohol with the Zinc Thiolate Site of Alcohol Dehydrogenase. *Inorg. Chem.* **1995**, *34*, 5933-5934.

(67) Brand, U.; Burth, R.; Vahrenkamp, H. Design of Trigonal-Bipyramidal ZnN_3S_2 Complexes. *Inorg. Chem.* **1996**, *35*, 1083-1086.

(68) Brand, U.; Vahrenkamp, H. A New Tridentate N,N,S Ligand and Its Zinc Complexes. *Inorg. Chem.* **1995**, *34*, 3285-3293.

(69) Chang, S.; Karambelkar, V. V.; diTargiani, R. C.; Goldberg, D. P. Model Complexes of the Active Site in Peptide Deformylase: A New Family of Mononuclear N_2S–M(II) Complexes. *Inorg. Chem.* **2001**, *40*, 194-195.

(70) Yam, V. W.-W.; Pui, Y.-L.; Cheung, K.-K.; Zhu, N. Synthesis, photophysics, electrochemistry and binding studies of zinc(II) dithiolate crown complexes. *New J. Chem.* **2002**, *26*, 536-542.

(71) The τ_5 value for **1** was previously calculated to be 0.51 with no dispersion correction factor applied. In this work, Grimme's DFT-D3 (D3BJ) dispersion correction factor was applied to the geometry optimization of both **1** and **2** to yield the values reported.

(72) Colpas, G. J.; Maroney, M. J.; Bagyinka, C.; Kumar, M.; Willis, W. S.; Suib, S. L.; Baidya, N.; Mascharak, P. K. X-ray Spectroscopic Studies of Nickel Complexes, with Application to the Structure of Nickel Sites in Hydrogenases. *Inorg. Chem.* **1991**, *30*, 920-928.

(73) Higgins, K. A.; Chivers, P. T.; Maroney, M. J. Role of the N-terminus in Determining Metal-Specific Responses in the *E. coli* Ni- and Co-Responsive Metalloregulator, RcnR. *J. Am. Chem. Soc.* **2012**, *134*, 7081-7093.

(74) Clark-Baldwin, K.; Tierney, D. L.; Govindaswamy, N.; Gruff, E. S.; Kim, C.; Berg, J.; Koch, S. A.; Penner-Hahn, J. E. The Limitations of X-ray Absorption Spectroscopy for Determining the Structure of Zinc Sites in Proteins. When Is a Tetrathiolate Not a Tetrathiolate? *J. Am. Chem. Soc.* **1998**, *120*, 8401-8409.

(75) Toftlund, H.; Nivorozhkin, A. L.; la Cour, A.; Adhikary, B.; Murray, K. S.; Fallon, G. D.; Nivorozhkin, L. E. Bis[4-(2,6-dimethylphenyliminomethyl)-5-pyrazolethiolato]nickel(II) complexes with an unusual *trans*-planar structure. *Inorg. Chim. Acta* **1995**, *228*, 237-241.

(76) Weber, K.; Heise, I.; Weyhermüller, T.; Lubitz, W. Synthesis and Characterization of Nickel Compounds with Tetradentate Thiolate–Thioether Ligands as Precursors for [NiFe]–Hydrogenase Models. *Eur. J. Inorg. Chem.* **2014**, *2014*, 148-155.

(77) Bosser, G.; Anouti, M.; Paris, J. Formation and scission of the sulfur–sulfur bond: a new approach to reactions between sulfur/polysulfide ions and thiolate ions/disulfides in *N,N*-dimethylacetamide. *J. Chem. Soc., Perkin Trans. 2* **1996**, 1993-1999.

(78) Antonello, S.; Daasbjerg, K.; Jensen, H.; Taddei, F.; Maran, F. Formation and Cleavage of Aromatic Disulfide Radical Anions. *J. Am. Chem. Soc.* **2003**, *125*, 14905-14916.

(79) Krüger, H.-J.; Peng, G.; Holm, R. H. Low-Potential Nickel(III,II) Complexes: New Systems Based on Tetradentate Amidate–Thiolate Ligands and the Influence of Ligand Structure on Potentials in Relation to the Nickel Site in [NiFe]-Hydrogenases. *Inorg. Chem.* **1991**, *30*, 734-742.

(80) Hanss, J.; Krüger, H.-J. First Isolation and Structural Characterization of a Nickel(III) Complex Containing Aliphatic Thiolate Donors. *Angew. Chem., Int. Ed.* **1998**, *37*, 360-363.

(81) Shafaatian, B.; Hashemibagha, M.; Notash, B.; Rezvani, S. A. Synthesis, characterization, X-ray crystal structure, luminescence, electrochemical and solvatochromism studies of new dimer of nickel and palladium complexes containing ferrocenyl imine ligand. *J. Organomet. Chem.* **2015**, *791*, 51-57.

(82) Warner, D. S.; Limberg, C.; Mebs, S. Synthesis of a Chiral, Polydentate Ligand System Setting Out from L-Cysteine and First Nickel Complexes Thereof. *Z. Anorg. Allg. Chem.* **2013**, *639*, 1577-1583.

(83) Loscalzo, J.; Kallen, R. G.; Voet, D. The X Ray Structure of Thiazolidine-4-carboxylic Acid. *Arch. Biochem. Biophys.* **1973**, *157*, 426-430.

(84) Domagała, M.; Grabowski, S. J.; Urbaniak, K.; Mlostoń, G. Role of C−H···S and C−H···N Hydrogen Bonds in Organic Crystal Structures − The Crystal and Molecular Structure of 3-Methyl-2,4-diphenyl-(1,3)-thiazolidine-5-spiro-2′-adamantane and 3-Methyl-2,4,5,5-tetraphenyl-(1,3)-thiazolidine. *J. Phys. Chem. A* **2003**, *107*, 2730-2736.

(85) Warren, J. J.; Tronic, T. A.; Mayer, J. M. Thermochemistry of Proton-Coupled Electron Transfer Reagents and Its Implications. *Chem. Rev.* **2010**, *110*, 6961-7001.

(86) Theisen, R. M.; Kovacs, J. A. Role of Protons in Superoxide Reduction by a Superoxide Reductase Analogue. *Inorg. Chem.* **2005**, *44*, 1169-1171.

(87) Nam, E.; Alokolaro, P. E.; Swartz, R. D.; Gleaves, M. C.; Pikul, J.; Kovacs, J. A. Investigation of the Mechanism of Formation of a Thiolate-Ligated Fe(III)-OOH. *Inorg. Chem.* **2011**, *50*, 1592-1602.

(88) Koppenol, W. H.; Stanbury, D. M.; Bounds, P. L. Electrode potentials of partially reduced oxygen species, from dioxygen to water. *Free Radical Biol. Med.* **2010**, *49*, 317-322.

(89) Sawyer, D. T.; Valentine, J. S. How Super Is Superoxide? *Acc. Chem. Res.* **1981**, *14*, 393-400.

(90) Kotani, H.; Sugiyama, T.; Ishizuka, T.; Shiota, Y.; Yoshizawa, K.; Kojima, T. Redox-Noninnocent Behavior of Tris(2-pyridylmethyl)amine Bound to a Lewis Acidic Rh(III) Ion Induced by C–H Deprotonation. *J. Am. Chem. Soc.* **2015**, *137*, 11222-11225.

(91) Connelly, N. G.; Geiger, W. E. Chemical Redox Agents for Organometallic Chemistry. *Chem. Rev.* **1996**, *96*, 877-910.

(92) The BDFE value was calculated using the pK_a and redox potential of [Rh(Cl)$_2$(L$_2$-H6)](Cl) (L$_2$-H6: TPACOOMe = tris(5-methoxycarbonyl-2-pyridylmethyl)amine) reported in ref 90 The $E_{1/2}$ was converted to V vs. Fc/Fc$^+$ using the equation E vs. Fc/Fc$^+$ = E vs. SCE - 0.40 V in MeCN with ^{n}Bu$_4$NPF$_6$ as electrolyte based on the information provided in ref 91. The BDFE calculation was performed using the following equation: BDFE = 1.37•pK_a + 23.06•$E_{1/2}$ + $C_{G,sol}$ (from ref 85), where $C_{G,sol}$ = 54.9 for MeCN.

(93) Rowland, J. M.; Olmstead, M. M.; Mascharak, P. K. Unusual Reactivity of Methylene Group Adjacent to Pyridine-2-Carboxamido Moiety in Iron(III) and Cobalt(III) Complexes. *Inorg. Chem.* **2002**, *41*, 2754-2760.

(94) Tejel, C.; del Río, M. P.; Ciriano, M. A.; Reijerse, E. J.; Hartl, F.; Záliš, S.; Hetterscheid, D. G. H.; Tsichlis i Spithas, N.; de Bruin, B. Ligand-Centred Reactivity of Bis(picolyl)amine Iridium: Sequential Deprotonation, Oxidation and Oxygenation of a "Non-Innocent" Ligand. *Chem. - Eur. J.* **2009**, *15*, 11878-11889.

(95) Tejel, C.; Ciriano, M. A.; del Río, M. P.; van den Bruele, F. J.; Hetterscheid, D. G. H.; Tsichlis i Spithas, N.; de Bruin, B. Deprotonation Induced Ligand-to-Metal Electron Transfer: Synthesis of a Mixed-Valence Rh(−I,I) Dinuclear Compound and Its Reaction with Dioxygen. *J. Am. Chem. Soc.* **2008**, *130*, 5844-5845.

(96) Jiang, H.; Stepowska, E.; Song, D. Aerobic oxidation of C(sp^3)–H bonds of 4,5-diazafluorene promoted by coordination. *Dalton Trans.* **2008**, 5879-5881.

(97) Bielski, B. H. J.; Shiue, G. G.; Bajuk, S. Reduction of Nitro Blue Tetrazolium by CO_2^- and O_2^- Radicals. *J. Phys. Chem.* **1980**, *84*, 830-833.

(98) Tabbì, G.; Driessen, W. L.; Reedijk, J.; Bonomo, R. P.; Veldman, N.; Spek, A. L. High Superoxide Dismutase Activity of a Novel, Intramolecularly Imidazolato-Bridged Asymmetric Dicopper(II) Species. Design, Synthesis, Structure, and Magnetism of Copper(II) Complexes with a Mixed Pyrazole–Imidazole Donor Set. *Inorg. Chem.* **1997**, *36*, 1168-1175.

(99) Kitagawa, T.; Dey, A.; Lugo-Mas, P.; Benedict, J. B.; Kaminsky, W.; Solomon, E.; Kovacs, J. A. A Functional Model for the Cysteinate-Ligated Non-Heme Iron Enzyme Superoxide Reductase (SOR). *J. Am. Chem. Soc.* **2006**, *128*, 14448-14449.

(100) Zhou, M.; Diwu, Z.; Panchuk-Voloshina, N.; Haugland, R. P. A Stable Nonfluorescent Derivative of Resorufin for the Fluorometric Determination of Trace Hydrogen Peroxide: Applications in Detecting the Activity of Phagocyte NADPH Oxidase and Other Oxidases. *Anal. Biochem.* **1997**, *253*, 162-168.

(101) Bueno, C.; Villegas, M. L.; Bertolotti, S. G.; Previtali, C. M.; Neumann, M. G.; Encinas, M. V. The Excited-State Interaction of Resazurin and Resorufin with Amines in Aqueous Solutions. Photophysics and Photochemical Reaction. *Photochem. Photobiol.* **2002**, *76*, 385-390.

(102) Dolman, D.; Newell, G. A.; Thurlow, M. D.; Dunford, H. B. A Kinetic Study of the Reaction of Horseradish Peroxidase with Hydrogen Peroxide. *Can. J. Biochem.* **1975**, *53*, 495-501.

(103) Pelmenschikov, V.; Siegbahn, P. E. M. Nickel Superoxide Dismutase Reaction Mechanism Studied by Hybrid Density Functional Methods. *J. Am. Chem. Soc.* **2006**, *128*, 7466-7475.

(104) Prabhakar, R.; Morokuma, K.; Musaev, D. G. A DFT Study of the Mechanism of Ni Superoxide Dismutase (NiSOD): Role of the Active Site Cysteine-6 Residue in the Oxidative Half-Reaction. *J. Comput. Chem.* **2006**, *27*, 1438-1445.

(105) Mullins, C. S.; Grapperhaus, C. A.; Kozlowski, P. M. Density functional theory investigations of NiN_2S_2 reactivity as a function of nitrogen donor type and N–H···S hydrogen bonding inspired by nickel-containing superoxide dismutase. *JBIC, J. Biol. Inorg. Chem.* **2006**, *11*, 617-625.

(106) Shearer, J.; Dehestani, A.; Abanda, F. Probing Variable Amine/Amide Ligation in $Ni^{II}N_2S_2$ Complexes Using Sulfur K-Edge and Nickel L-Edge X-ray Absorption Spectroscopies: Implications for the Active Site of Nickel Superoxide Dismutase. *Inorg. Chem.* **2008**, *47*, 2649-2660.

(107) Fiedler, A. T.; Brunold, T. C. Spectroscopic and Computational Studies of Ni^{3+} Complexes with Mixed S/N Ligation: Implications for the Active Site of Nickel Superoxide Dismutase. *Inorg. Chem.* **2007**, *46*, 8511-8523.

(108) See, R. F.; Kruse, R. A.; Strub, W. M. Metal–Ligand Bond Distances in First-Row Transition Metal Coordination Compounds: Coordination Number, Oxidation State, and Specific Ligand Effects. *Inorg. Chem.* **1998**, *37*, 5369-5375.

(109) Maelia, L. E.; Millar, M.; Koch, S. A. General Synthesis of Iron(III) Tetrathiolate Complexes. Structural and Spectroscopic Models for the [Fe(Cys-*S*)$_4$] Center in Oxidized Rubredoxin. *Inorg. Chem.* **1992**, *31*, 4594-4600.

(110) Millar, M.; Lee, J. F.; O'Sullivan, T.; Koch, S. A.; Fikar, R. Models for the iron-sulfur protein rubredoxin: the use of sterically hindered thiolate ligands to stabilize [Fe(SR)$_4$]$^{1-}$ complexes; some considerations of the structure of the [Fe(S-Cys)$_4$] centers in oxidized rubredoxins. *Inorg. Chim. Acta* **1996**, *243*, 333-343.

(111) Schilter, D.; Camara, J. M.; Huynh, M. T.; Hammes-Schiffer, S.; Rauchfuss, T. B. Hydrogenase Enzymes and Their Synthetic Models: The Role of Metal Hydrides. *Chem. Rev.* **2016**, *116*, 8693-8749.

(112) Kirksey, S. T., Jr.; Neubecker, T. A.; Margerum, D. W. Thermally Stable Copper(III)- and Nickel(III)-Tripeptide Complexes and Their Photochemical Decomposition in Acid Solution. *J. Am. Chem. Soc.* **1979**, *101*, 1631-1633.

(113) Kumar, M.; Day, R. O.; Colpas, G. J.; Maroney, M. J. Ligand Oxidation in a Nickel Thiolate Complex. *J. Am. Chem. Soc.* **1989**, *111*, 5974-5976.

(114) Fox, S.; Wang, Y.; Silver, A.; Millar, M. Viability of the [Ni^{III}(SR)$_4$]$^-$ Unit in Classical Coordination Compounds and in the Nickel-Sulfur Center of Hydrogenases. *J. Am. Chem. Soc.* **1990**, *112*, 3218-3220.

(115) Snyder, H. R.; Stewart, J. M.; Ziegler, J. B. The Synthesis of Amino Mercaptans from Olefin Sulfides. *J. Am. Chem. Soc.* **1947**, *69*, 2672-2674.

(116) Fulmer, G. R.; Miller, A. J. M.; Sherden, N. H.; Gottlieb, H. E.; Nudelman, A.; Stoltz, B. M.; Bercaw, J. E.; Goldberg, K. I. NMR Chemical Shifts of Trace Impurities: Common Laboratory Solvents, Organics, and Gases in Deuterated Solvents Relevant to the Organometallic Chemist. *Organometallics* **2010**, *29*, 2176-2179.

(117) Löliger, J.; Scheffold, R. Paramagnetic Moment Measurements by NMR. A micro technique. *J. Chem. Educ.* **1972**, *49*, 646-647.

(118) Bain, G. A.; Berry, J. F. Diamagnetic Corrections and Pascal's Constants. *J. Chem. Educ.* **2008**, *85*, 532-536.

(119) Neese, F. The ORCA program system. *WIREs Comput. Mol. Sci.* **2012**, *2*, 73-78.

(120) Becke, A. D. Density functional calculations of molecular bond energies. *J. Chem. Phys.* **1986**, *84*, 4524-4529.

(121) Perdew, J. P. Density-functional approximation for the correlation energy of the inhomogeneous electron gas. *Phys. Rev. B: Condens. Matter Mater. Phys* **1986**, *33*, 8822-8824.

(122) Neese, F. An Improvement of the Resolution of the Identity Approximation for the Formation of the Coulomb Matrix. *J. Comput. Chem.* **2003**, *24*, 1740-1747.

(123) Grimme, S.; Antony, J.; Ehrlich, S.; Krieg, H. A consistent and accurate *ab initio* parametrization of density functional dispersion correction (DFT-D) for the 94 elements H-Pu. *J. Chem. Phys.* **2010**, *132*, 154104.

(124) Grimme, S.; Ehrlich, S.; Goerigk, L. Effect of the Damping Function in Dispersion Corrected Density Functional Theory. *J. Comput. Chem.* **2011**, *32*, 1456-1465.

(125) Weigend, F.; Ahlrichs, R. Balanced basis sets of split valence, triple zeta valence and quadruple zeta valence quality for H to Rn: Design and assessment of accuracy. *Phys. Chem. Chem. Phys.* **2005**, *7*, 3297-3305.

(126) Schäfer, A.; Horn, H.; Ahlrichs, R. Fully optimized contracted Gaussian basis sets for atoms Li to Kr. *J. Chem. Phys.* **1992**, *97*, 2571-2577.

(127) Cohen, A. J.; Handy, N. C. Dynamic correlation. *Mol. Phys.* **2001**, *99*, 607-615.

(128) Lee, C.; Yang, W.; Parr, R. G. Development of the Colle-Salvetti correlation-energy formula into a functional of the electron density. *Phys. Rev. B: Condens. Matter Mater. Phys* **1988**, *37*, 785-789.

(129) Klamt, A.; Schüürmann, G. COSMO: A New Approach to Dielectric Screening in Solvents with Explicit Expressions for the Screening Energy and its Gradient. *J. Chem. Soc., Perkin Trans. 2* **1993**, 799-805.

(130) Pettersen, E. F.; Goddard, T. D.; Huang, C. C.; Couch, G. S.; Greenblatt, D. M.; Meng, E. C.; Ferrin, T. E. UCSF Chimera—A Visualization System for Exploratory Research and Analysis. *J. Comput. Chem.* **2004**, *25*, 1605-1612.

(131) *SMART v5.626: Software for the CCD Detector System*; Bruker AXS: Madison, WI, 2000.

(132) Walker, N.; Stuart, D. An empirical method for correcting diffractometer data for absorption effects. *Acta Crystallogr., Sect. A: Found. Crystallogr.* **1983**, *39*, 158-166.

(133) Sheldrick, G. M. *SADABS, Area Detector Absorption Correction*; University of Göttingen: Göttingen, Germany, 2001.

(134) Sheldrick, G. M. *SHELX-97, Program for Refinemen of Crystal Structures*; University of Göttingen: Göttingen, Germany, 1997.

(135) Sheldrick, G. M. A Short History of SHELX. *Acta Crystallogr., Sect. A: Found. Crystallogr.* **2008**, *64*, 112-122.

(136) Sheldrick, G. M. *SHELXTL 6.1, Crytallographic Computing System*; Siemens Analytical X-Ray Instruments: Madison, WI, 2000.

(137) George, G. N.; George, S. J.; Pickering, I. J. *EXAFSPAK*; Stanford Synchotron Radiation Lightsource: Menlo Park, CA, 2001. http://www-ssrl.slac.stanford.edu/~george/exafspak/exafs.htm.

(138) Rehr, J. J.; Ankudinov, A. L. Progress and challenges in the theory and interpretation of X-ray spectra. *J. Synchrotron Radiat.* **2001**, *8*, 61-65.

(139) Riggs-Gelasco, P. J.; Stemmler, T. L.; Penner-Hahn, J. E. XAFS of dinuclear metal sites in proteins and model compounds. *Coord. Chem. Rev.* **1995**, *144*, 245-286.

(140) Bencze, K. Z.; Kondapalli, K. C.; Stemmler, T. L. X-Ray Absorption Spectroscopy. In *Applications of Physical Methods in Inorganic and Bioinorganic Chemistry: Handbook, Encyclopedia of Inorganic Chemistry*, 2nd ed.; Wiley: Chichester, U.K., 2007.

(141) Cotelesage, J. J. H.; Pushie, M. J.; Grochulski, P.; Pickering, I. J.; George, G. N. Metalloprotein active site structure determination: Synergy between X-ray absorption spectroscopy and X-ray crystallography. *J. Inorg. Biochem.* **2012**, *115*, 127-137.

CHAPTER 4

REACTIVITIES OF N3S2 NISOD ANALOGUES WITH OXIDANTS AND LEWIS ACIDS: PATHWAY TO REVERSIBLE NI REDOX [1]

[1] Truong, P. T.; Harrop, T. C. To be submitted to Inorganic Chemistry.

4.1 Abstract

Herein, we report the synthesis and properties of Na[Ni($N_3S_2^{NEM}$)] (**4**) with the N_3S_2 ligand $[N_3S_2^{NEM}]^{3-}$ ($[N_3S_2^{NEM}]^{3-}$ = deprotonated form of 2-((2-mercapto-2-methylpropyl)(pyridin-2-ylmethyl)-amino)-*N*-(2-mercaptoethyl)-acetamide), which features an axial N-ligand from *N*-ethyl morpholine poised to coordinate to the Ni center. Structural and spectroscopic characterization of **4** by X-ray crystallography, ^{1}H NMR, IR, UV–vis, and mass spectrometry (MS), reveal a square-planar Ni^{2+} (S = 0) complex coordinated by $N_{carboxamide}N_{amine}S_2$ donors from the $N_3S_2^{NEM}$ ligand framework. Chemical oxidation of **4** with air or ferrocenium hexafluorophosphate ($FcPF_6$) yielded a blue-black stair-step trimetallic species, {Ni[Ni($N_3S_2^{NEM}$)]$_2$} (**6**) (80% yield) via oxidation of the ligand and release of Ni^{2+}. This type of oxidation product has not been observed in other N_3S_2 NiSOD models from our laboratory. Electrochemical measurements of **4** in CH_2Cl_2 reveal irreversible events consistent with thiolate ligand redox, while the cyclic voltammogram (CV) of **6** reveals two reversible redox couples ($E_{1/2}$ = -1.62 V and -0.13 V vs. Fc^+/Fc) and one quasi-reversible redox couple (E_{pa} = 0.23 V and E_{pc}= 0.02 V vs. Fc^+/Fc). These electrochemical events were assigned as Ni(II/I), Ni(III/II), and Ni(IV/III) redox states at the terminal Ni of **6** for -1.62 V, -0.13 V and E_{pa} = 0.23 V, respectively. Density functional theory (DFT) analysis of the electronic properties of **4** and **6** reveal a HOMO in **4** consisting primarily of Ni(dπ)/S(pπ) antibonding orbitals while the HOMO of **6** is primarily Ni(d_z^2)/N3(σ) antibonding in nature, which suggests that oxidation of **6** will primarily be Ni-based. Results from Amplex Red (AR) assay indicate that **4** and **6** was not able **c**atalyze the reduction of superoxide ($O_2^{\bullet-}$) to H_2O_2 in buffer.

4.2 Introduction

The latest addition to the family of superoxide dismutases (SODs), a family of metalloenzymes that catalyze the disproportionation of superoxide ($O_2^{\bullet-}$) to O_2 and H_2O_2 at diffusion controlled rate, is the nickel-containing enzyme (NiSOD).[1] NiSOD is unique because Ni is coordinated by CysS residues, which are susceptible to oxidation and S-oxygenation in the presence of reactive oxygen species (ROS) (e.g., $O_2^{\bullet-}$ and H_2O_2). The structure of NiSOD from *Streptomyces* soil bacteria[2,3] revealed a homohexameric protein with six interlocking subunits, each containing the Ni active site in the "Ni-hook" motif at the N-terminus. In the reduced state ($NiSOD_{red}$), the square planar Ni^{II}-N_2S_2 active site is coordinated by two S-thiolates from Cys2 and Cys6, His-NH_2, and Cys2-peptido-N. In the oxidized state ($NiSOD_{ox}$), His1-Nδ coordinates to Ni^{3+} in the apical position to form a five-coordinate (5C) square pyramidal Ni^{III}-N_3S_2 coordination environment. Mutagenesis[4-6] and theoretical studies[7] of NiSOD suggest that the specific combination of mixed N/S coordination environment of NiSOD, specifically His1-N[8,9] and Cys-S[6] are critical to its function.

The unique NiSOD active site has generated much interest in the synthetic inorganic community,[10,11] which led to the development of NiSOD models ranging from peptide maquettes (including peptide models)[12-26] to low-molecular-weight (LMW) model complexes.[27-45] Among LMW analogues, complexes that feature the $N_{carboxamide}N_{amine}S_2$ coordination environment have been reported by Shearer,[42] Hegg,[43] Masuda,[44] Eichhorn,[45] and our laboratory (Chart 4.1).[33-36,41,46] In 2011, we reported the synthesis and characterization of a first-generation model with a pendant axial N-ligand that closely mimics the NiSOD active site, K[Ni(N_3S_2)] (**1**) (where $[N_3S_2]^{3-}$ = deprotonated form of *N*-(2-mercaptoethyl)-2-((2-mercaptoethyl)(pyridin-2-ylmethyl)amino)-acetamide)[41] (Chart 4.1). Oxidation of **1** by $FcPF_6$ yields a disulfide-bridged Ni^{2+}-N_3S species, in

which the pyridine-N (py-N) displaces the S-thiolate *trans* to the carboxamide. This result prompted the development of new generation ligands and their Ni^{2+} complexes, such as $Na[Ni(N_3S_2^{Me2})]$ (**2**) ($[N_3S_2^{Me2}]^{3-}$ = deprotonated form of 2-((2-mercapto-2-methylpropyl)(pyridin-2-ylmethyl)amino)-*N*-(2-mercaptoethyl)-acetamide) and its Zn^{2+} analogue $Na[Zn(N_3S_2^{Me2})]$ (**3**),[46] that contains *gem*-$(CH_3)_2$ functional groups on the α-carbon (α-C) of the S-thiolate *trans* to the carboxamide as steric enforcement to prevent disulfide formation. The steric enforcement of the *gem*-$(CH_3)_2$ led to a new oxidation pathway for **2** that resulted in a thiazolidine rearrangement product in addition to the Ni^{II}-N_3S disulfide-bridged species (see Ch. 3).

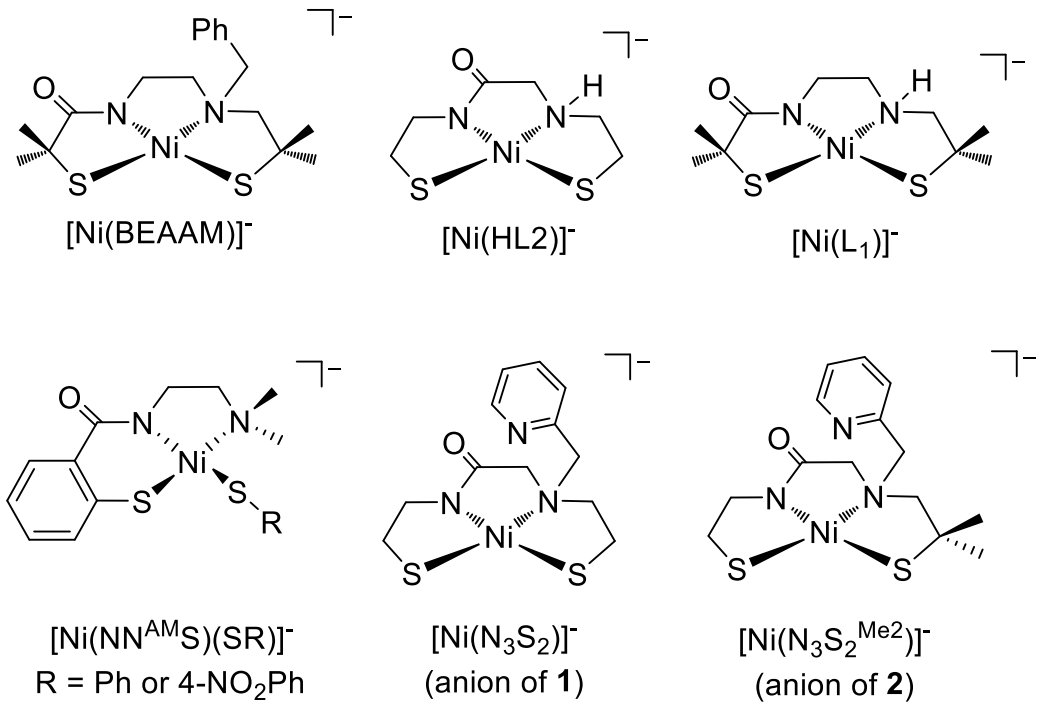

Chart 4.1 Structures of the anions of LMW NiSOD model complexes with the minimal $N_{carboxamide}N_{amine}S_2$ coordination sphere (counterions not shown).

With the overall goal of obtaining a functional model of NiSOD that can support Ni(III/II) oxidation states while preventing S-oxidation/oxygenation, we have designed and synthesized a new ligand construct with the same N/S coordination environment as prior models with the exception of adding *N*-ethyl morpholine (NEM) as the potential axial N-ligand, namely $H_3N_3S_2^{NEM}$ (where $H_3N_3S_2^{NEM}$ = *N*-(2-mercaptoethyl)-2-((2-mercaptoethyl)(2-morpholinoethyl)amino)-acetamide; H represents deprotonatable protons). With a more flexible α-C on the axial N-ligand (sp^3 for N-NEM and sp^2 for N-py) and a more Lewis basic N ligand (pK_a of N-NEM = 7.4[47] vs. pK_a of N-py = 5.94[48]), we expect the axial N-NEM ligand will bind to both oxidation states of the Ni center more readily than **1** and **2**. This binding of the axial N-ligand, i.e., generation of a 5C Ni complex, should result in reversible Ni electrochemical events. The synthesis and properties of the ligand and its corresponding Ni^{2+} and Zn^{2+} complexes, Na[Ni($N_3S_2^{NEM}$)] (**4**) and Na[Zn($N_3S_2^{NEM}$)] (**5**), are reported in this account. Unexpectedly, oxidation of **4** by atmospheric O_2 or a one-electron oxidant, such as $FcPF_6$, yields a stair-step trimetallic species, {Ni[Ni($N_3S_2^{NEM}$)]$_2$} (**6**), a product never observed during the oxidation of **1** and **2**. While irreversible electrochemical events were observed for **4** in CH_2Cl_2, CV of **6** shows multiple reversible and quasi-reversible electrochemical events. Taken inspiration from **6**, reaction between **4** and another Lewis acid, tris(pentafluorophenyl) borane (BCF), is hypothesized to generate a 5C Ni complex of **4** with BCF adduct to aid in assignment of electrochemical events observed in the CV of **6**. Interestingly, another stair-step trimetallic species with BCF adduct, {Ni[Ni($N_3S_2^{NEM}$)]$_2$}•2BCF (**7**), was isolated. Comparison between the CVs of **6** and **7** in CH_2Cl_2 shows that all observed electrochemical events originate from the terminal Ni center (Ni_T) of the trimetallic species. Reactivity studies (NBT assay and Amplex Red assay) as well as the electronic structure of these complexes was also reported.

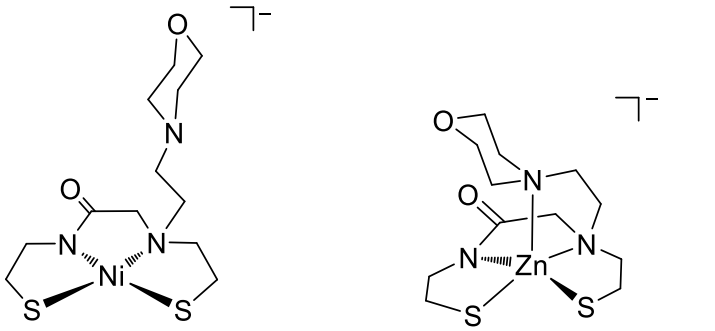

$[Ni(N_3S_2^{NEM})]^-$ (anion of **4**) $[Zn(N_3S_2^{NEM})]^-$ (anion of **5**)

Chart 4.2 Anion of the NiSOD model complex **4** and Zn analogue **5** reported in this work.

4.3 Results and Discussion

4.3.1 Synthesis and Properties of $N_3S_2^{NEM}$ Ligand

Synthesis of the pentadentate ligand ($H_3N_3S_2^{NEM}$•2HCl, H = dissociable hydrogens) follows procedures used for other NiSOD models from our lab (Scheme 4.1).[41,46] For example, starting from the known trityl-protected (Tr = CPh_3) N_2S_2 compound *N*-(2-(tritylthio)ethyl)-2-((2-(tritylthio)ethyl)amino)acetamide ($N_2S_2Tr_2$),[49] the protected ligand ($N_3S_2^{NEM}Tr_2$) was synthesized in 48% yield by mixing this synthon with 4-(2-chloroethyl)morpholine hydrochloride (1:1) under reflux for 24 h. Deprotection of $N_3S_2^{NEM}Tr_2$ with Et_3SiH in CH_2Cl_2/TFA (1:1) followed and the protonated ligand salt ($H_3N_3S_2^{NEM}$•2HCl) was isolated as a yellow solid in 62% yield by stirring in 1 M HCl in Et_2O. The advantage to making this salt is the ease of handling the HCl adduct as a tractable solid. It was difficult to remove TFA from the ligand (gel-like material) after deprotection even when stirring in $NaHCO_3$ (stronger bases run the risk of deprotonating the thiol-SH and carboxamide-NH). While the formation of $H_3N_3S_2^{NEM}$•$(TFA)_X$ adducts was not observed in other N_3S_2 ligands, the enhanced basicity of N-NEM is likely the cause, e.g., pK_a of N-NEM = 7.4[47] vs. pK_a of N-py = 5.94[48]Notable spectroscopic properties of $H_3N_3S_2^{NEM}$•2HCl (Figures 4.S5-4.S10 in

the Supporting Information(SI)) include a very broad peak in the IR spectrum between 3700 cm^{-1} and 2000 cm^{-1} due to ammonium N-H stretches.[50] Other strong bands include the carboxamide C=O (ν_{CO}: 1676 cm^{-1}) and N–H (ν_{NH}: 3212 cm^{-1}) (Figure 4.S9 in the SI). The N*H* peaks in the ^{1}H NMR spectrum of $H_3N_3S_2^{NEM}$•2HCl in CD_3CN present as two broad peaks in the 8-12 ppm region (Figure 4.S6 in the SI), and the S*H* groups show up as two broad triplets at ~2.2 ppm. The absence of these signals in the ^{1}H NMR spectrum recorded in CD_3OD is consistent with the exchangeable nature of these protons (Figure 4.S5).

Scheme 4.1 Synthesis of $H_3N_3S_2^{NEM}$•2HCl ligand and Ni^{2+} Complex **4**

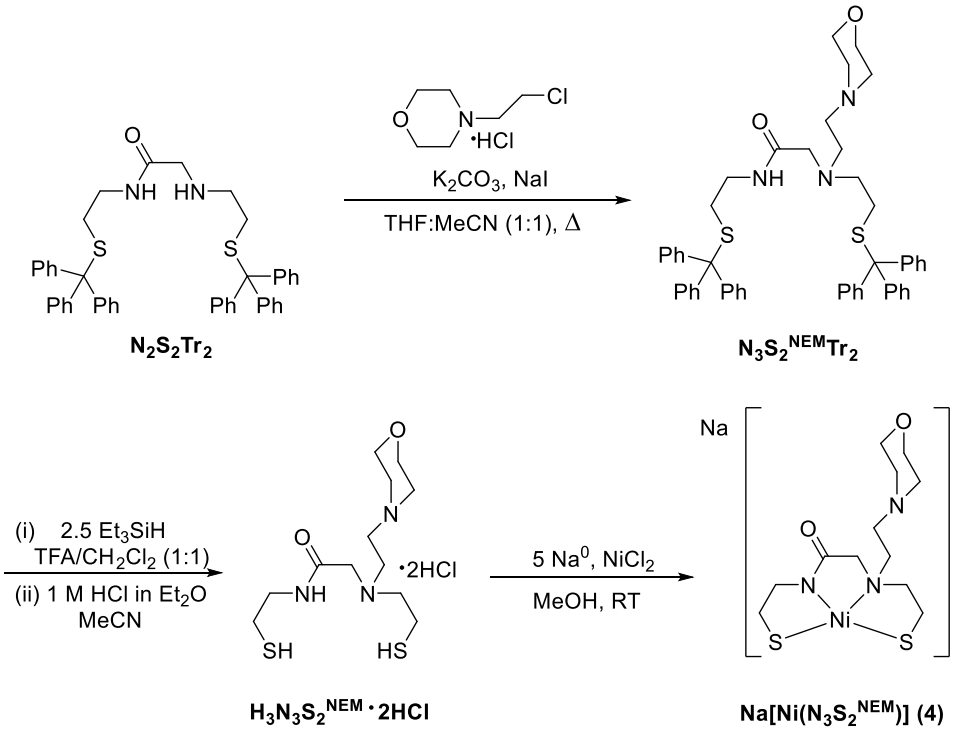

4.3.2 Synthesis of Ni^{2+} and Zn^{2+} complexes

The Ni^{2+} complex Na[Ni($N_3S_2^{NEM}$)] (**4**) was synthesized by reacting the deprotonated ligand with $NiCl_2$ in MeOH to yield the red-brown complex in 80% yield. Complex **4** is soluble in polar solvents (MeOH, H_2O, DMF, and acetone) with slight solubility in MeCN and THF. Using analogous synthetic conditions, the Zn^{2+} analogue Na[Zn($N_3S_2^{NEM}$)] (**5**) was isolated as a white powder in 93% yield when using $ZnCl_2$ in the metalation reaction. The solubility profile of **5** is similar to **4**.

4.3.3 Spectroscopic Properties

Complexes **4** and **5** were characterized by FTIR, ^{1}H NMR (vide infra), UV–vis, electrospray ionization mass spectrometry (ESI-MS), and CHN analysis. The IR spectra of **4** and **5** display the characteristic ν_{CO} downshift (80-90 cm^{-1}) and absent ν_{NH} from the free ligand to indicate carboxamido-N ligation (Figures 4.S13 and 4.S16 in the SI, respectively).[51] High-resolution ESI-MS(-) further confirms the formation of **4** (*m/z*: 362.051) and **5** (*m/z*: 368.043), indicated by the molecular ion peaks with the appropriate isotopic distribution (Figures 4.S14 and 4.S17 in the SI). Typical of square-planar NiSOD models[40-46] and $NiSOD_{red}$,[4,7] the UV-vis spectrum of **4** features two d-d transitions at 455 nm (ε = 240 M^{-1} cm^{-1}) and 575 nm (ε = 60 M^{-1} cm^{-1}) (MeOH, 25 °C; Table 4.1 and Figure 4.1). Unlike previous models from our lab featuring py-N axial ligands,[41,46] the ^{1}H NMR spectrum (CD_3OD) of **4** features sharp resonances for all chemically distinct protons in the 2–4 ppm region (Figures 4.S11 in the SI), supporting a square-planar (S = 0) solution structure for the Ni^{2+} complex. The ^{1}H NMR of **4** does not change in aprotic solvents such as acetone-d_6 (Figure 4.S12 in the SI). As expected, the ^{1}H NMR spectrum of Zn^{2+}

complex **5** in CD_3OD also features sharp peaks including that from the ^{i}PrOH solvent of crystallization also observed in the X-ray structure (vide infra) and CHN analysis (Figure 4.S15 in the SI).

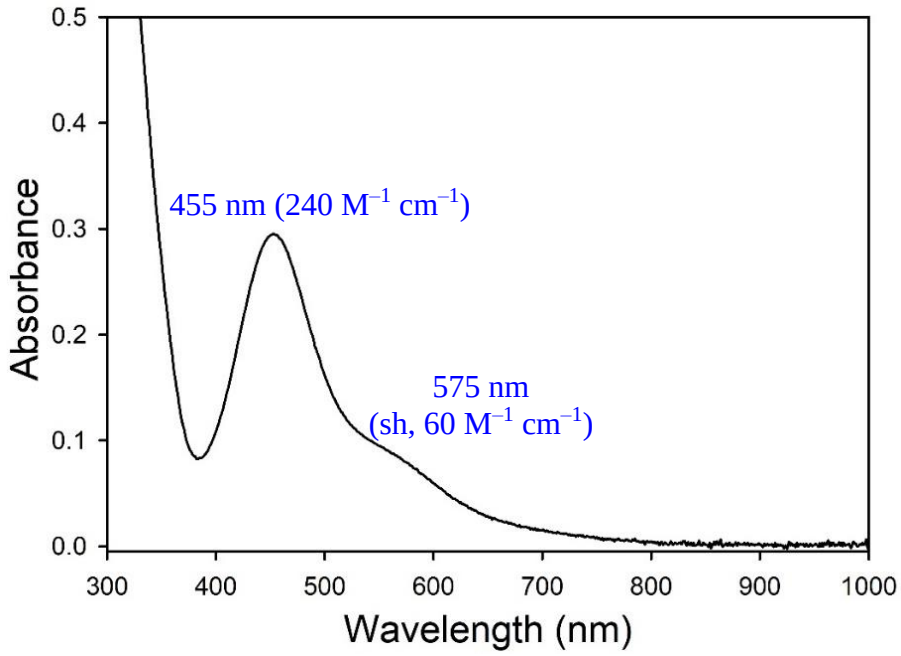

Figure 4.1 UV–vis spectrum of **4** (1.21 mM) in MeOH at 25 °C.

Table 4.1 UV–vis and Electrochemical Data of NiSOD and Select Models[a]

NiSOD Model	**λ (nm) (ε (M^{-1} cm^{-1}))[b]**	***E* (V vs Fc/Fc^{+})[c]**	**Ref.**
$NiSOD_{red}$	450 (480), 543 (150)[d]	$E_{½}$: 0.290 V (vs NHE), 0.046 V (vs SCE)[d]	4, 7
K[Ni(N_3S_2)] (**1**)	449 (320), 570 sh (90)	E_{ox}: –0.620, E_{red}: –1.84	41
Na[Ni($N_3S_2^{Me}$)] (**2**)	459 (250), 557 sh (75)	E_{ox}: –0.670, E_{red}: –1.98	46
Na[Ni($N_3S_2^{NEM}$)] (**4**)	455 (238), 575 sh (64)	E_{ox}: –0.40, E_{red}: –1.49	TW
Me_4N[Ni(BEAAM)]	461 (290), 556 sh (70)[e]	$E_{½}$: –0.330[e]	42
K[Ni(HL2)]	449 (340), 570 sh (~70)	E_{ox}: –0.458	43
Na[Ni(L_1)]	441 (258)	$E_{½}$: –0.593; $E_{½}$: –0.570[e]	44
(Ph_4As)[Ni($NN^{Am}S$)(SPh)]	461 (84)	E_{ox}: 0.047, 0.469, 0.851	45
(Ph_4As)[Ni($NN^{Am}S$)(4-NO_2PhS)]	452 (149)	E_{ox}: -0.013, 0.619, 0.881	45

[a] Abbreviations: sh = shoulder; TW = this work. [b] UV–vis spectra reported for MeOH solutions unless otherwise stated. [c] Data represents the redox potential as reported versus the ferrocene/ferrocenium (Fc/Fc^{+}) couple in DMF unless otherwise stated. [d] Aqueous buffer; pH 7.4 phosphate buffer for the $E_{½}$ measurement. [e] MeCN.

4.3.4 X-ray Structures of Metal Complexes

Red plate crystals of **4**•diacetone alcohol (DAA) as a solvent of crystallization was obtained via slow diffusion of Et_2O into a saturated solution of **4** in acetone with 25% MeOH at -25 °C for two weeks. Although DAA was not used in the synthesis of **4**, its presence in the crystal lattice suggests that it's an impurity in the acetone that was used during workup. The structure of **4** reveals a Ni(II) ion coordinated by the N_2S_2 donors of the $N_3S_2^{NEM}$ ligand to yield a square-planar complex, which replicates the $NiSOD_{red}$[2,3] coordination sphere and other NiSOD model complexes with a mixed amine/carboxamide N_2S_2 coordination sphere.[40-46] Even with a more Lewis basic N donor, the NEM moiety is almost perpendicular to the N_2S_2 plane with N-NEM pointing away from the Ni center (Figure 4.2), which is reminiscent of the pendant py moiety in **1** and **2**. The tetrahedral distortion parameter (τ_4), developed by Houser to differentiate between square-planar ($\tau_4 = 0$) and tetrahedral ($\tau_4 = 1$) geometries,[52] was calculated for **4** ($\tau_4 = 0.13$) indicating a square-planar complex with a slight tetrahedral distortion. Although the τ_4 of **4** indicates more tetrahedral twist in comparison to **1** and **2**, it's still more biased toward square-planar geometry as with other NiSOD models and NiSOD (Table 4.2). Comparable to other NiSOD models, the shortest bond in **4**•DAA is the $Ni\text{-}N_{carboxamide}$ (1.864(2) Å), which is consistent with the strong σ-donating nature of the carboxamide. The *trans* influence is observed in **4**•DAA, which is evident in the bond distances of Ni–S1 and Ni–S2 at 2.1745 Å and 2.1706 Å, respectively. However, the difference between Ni–S1 and Ni–S2 in **4**·DAA is only 0.004 Å compared to those observed in other NiSOD models. This can be the result of the interaction between Na^+ and the S-ligand on S2 in the extended crystal lattice of **4**·DAA, which was observed previously between **2** and $\mathbf{2^K}$ (see Ch. 3).

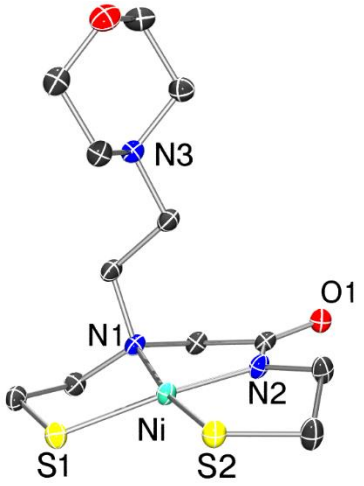

Figure 4.2 ORTEP diagram of the anion of Na[Ni($N_3S_2^{NEM}$)]•DAA (**4**•DAA) showing 50% thermal probability ellipsoids with atom labeling scheme. H atoms and solvent of crystallization are omitted for clarity. Selected bond distances (Å) and angles (deg): Ni–S1 = 2.1745(7), Ni–S2 = 2.1706(6), Ni–N1 = 1.9560(19), Ni–N2 = 1.864(2), N1–Ni–S2 = 170.24(6), N2–Ni–S1 = 171.53(6), S1–Ni–S2 = 96.03(2), N2–Ni–S2 = 88.64(6), N1–Ni–S1 = 91.19(6), N2–Ni–N1 = 85.04(8).

Table 4.2 Select Bond Distances (Å) and τ_4 values for NiSOD and Its Model Complexes[a]

NiSOD Model	Ni–N_{amide}	Ni–N	Ni–S	Ni–S	Ni---N_{axial}	τ_4	ref
$NiSOD_{red}$	1.91	1.87	2.19	2.16	N/A	0.09	2
K[Ni(N_3S_2)] (**1**)	1.8565	1.954	2.181	2.174	~3.21	0.09	41
Na[Ni($N_3S_2^{Me2}$)] (**2**)	1.856	1.937	2.1819	2.1582	~3.23	0.08	46
Na[Ni($N_3S_2^{NEM}$) (**4**)	1.864	1.956	2.1745	2.1706	~4.50	0.14	TW
Me_4N[Ni(BEAAM)]	1.858	1.989	2.177	2.137	N/A	0.16	42
K[Ni(HL2)]	1.862	1.937	2.1711	2.1671	N/A	0.09	43
Na[Ni(L_1)]	1.865	1.923	2.1702	2.1450	N/A	0.07	44
(Ph_4As)[Ni($NN^{Am}S$)(SPh)]	1.896	2.017	2.243	2.126	N/A		45
(Ph_4As)[Ni($NN^{Am}S$)(4-NO_2PhS)]	1.889	1.998	2.2278	2.1261	N/A		45

[a] Abbreviation: TW = this work.

Slow diffusion of Et_2O into a saturated solution of **5** in ^{i}PrOH at -25 °C over three weeks yielded clear prism crystals of **5**•^{i}PrOH. While all ligands coordinate to the Zn center in **3** and **5** to form a 5C complexes, **5** is more disposed toward square pyramidal (τ_5 = 0.40) geometry than **3** which has a τ_5 value of 0.58 (Figure 4.3). From the structure of **5**, the prediction is that coordination of N-NEM to Ni^{2+} in **4** will yield a complex that is more disposed toward square-pyramidal than tbp geometry.

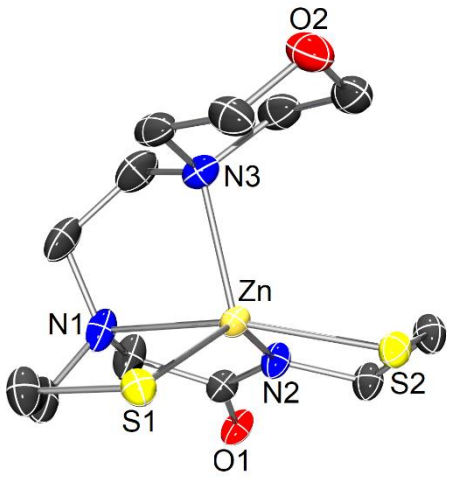

Figure 4.3 ORTEP diagram of the anion of Na[Zn($N_3S_2^{NEM}$)]•^{i}PrOH (**5**•^{i}PrOH) showing 50% thermal probability ellipsoids with atom labeling scheme. H atoms and solvent of crystallization are omitted for clarity. Selected bond distances (Å) and angles (deg): Zn–S1 = 2.3656(9), Zn–S2 = 2.3783(3), Zn–N1 = 2.337(3), Zn–N2 = 2.031(3), Zn–N3 = 2.225(3), N1–Zn–S2 = 161.52(7), N2–Zn–S1 = 137.29(8), N3–Zn–S2 = 112.82(8), N3–Zn–S1 = 107.09(8), N2–Zn–N3 = 106.86(11), S1–Zn–S2 = 103.55 (3), N2–Zn–S2 = 86.21(8), N1–Zn–S1 = 83.82(8), N2–Zn–N1 = 77.20(10), N1–Zn–N3 = 80.2(1).

4.3.5 Reactivity of 4 toward atmospheric O_2

A light yellow-solution of **4** in MeOH in UV-vis cuvette was left in ambient atmosphere overnight resulted in a dark brown/blue solution. This observation inspired the observation of UV-vis of **4** in MeOH after atmospheric O_2 exposure. The UV-vis spectrum was of a light-yellow

solution of **4** (0.987 mM) was monitored for 14 h in MeOH after exposure to atmospheric O_2 for 1 min. Within 30 min, a new species was observed with intense charge transfer transitions at 448 nm, 550 nm, and 688 nm (Figure 4.4 and Figure 4.S18 in the SI). In addition to the change observed in the UV–vis, the cuvette solution changed from light yellow to dark brown/blue. This color change was not observed in **1** or **2**, which typically result in slow bleaching of the solution after O_2 exposure instead of becoming darker.[41,46] This result indicated the formation of a potential Ni^{3+} species in the solution due to the enhanced Lewis basicity of N-axial ligand. Although multiple oxygenated species were observed in the negative mode of LR-ESI-MS (*m/z*: 378 (+1O), 394 (+2O), 410 (+3O), and 426 (+4O)) along with unreacted **4** (*m/z*: 362) (Figure 4.S19 in the SI), the proposed Ni^{3+} species, $\{[Ni(N_3S_2^{NEM})]+H\}^+$ or $\{[Ni(N_3S_2^{NEM})]+Na\}^+$, was not observed by LR-ESI-MS. Although not surprising because of charge neutrality of the proposed Ni^{3+} species. These results prompted us to perform a prep-scale bulk oxidation of **4** with $FcPF_6$ in DMF, which was worked up as depicted in Scheme 4.S1 in the SI.

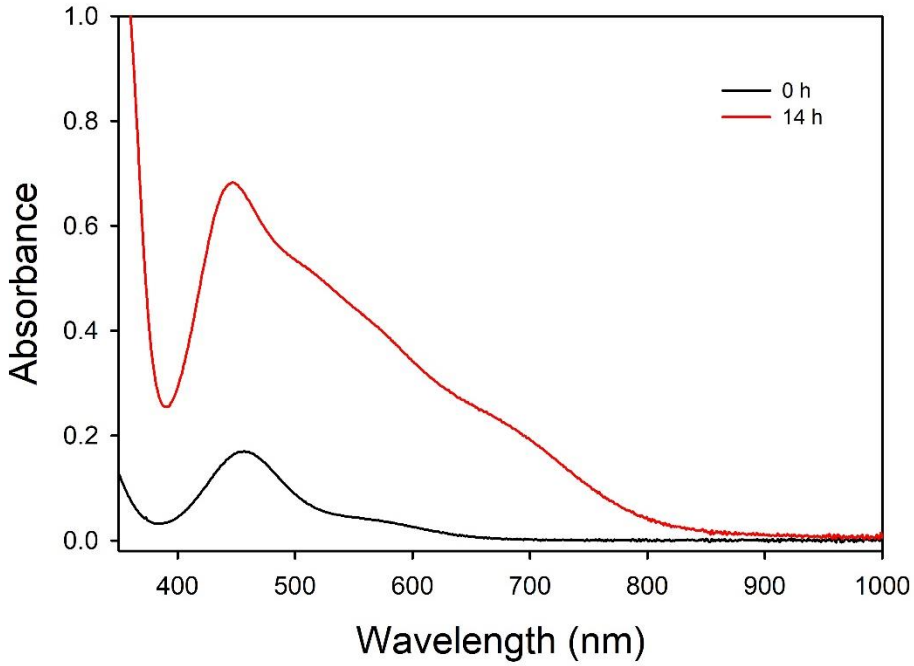

Figure 4.7 UV-vis spectrum of **4** (0.987 mM) after 1 min of exposure to air in MeOH at t = 0 h (black) and t = 14 h (red). Measurements were collected at 25 °C.

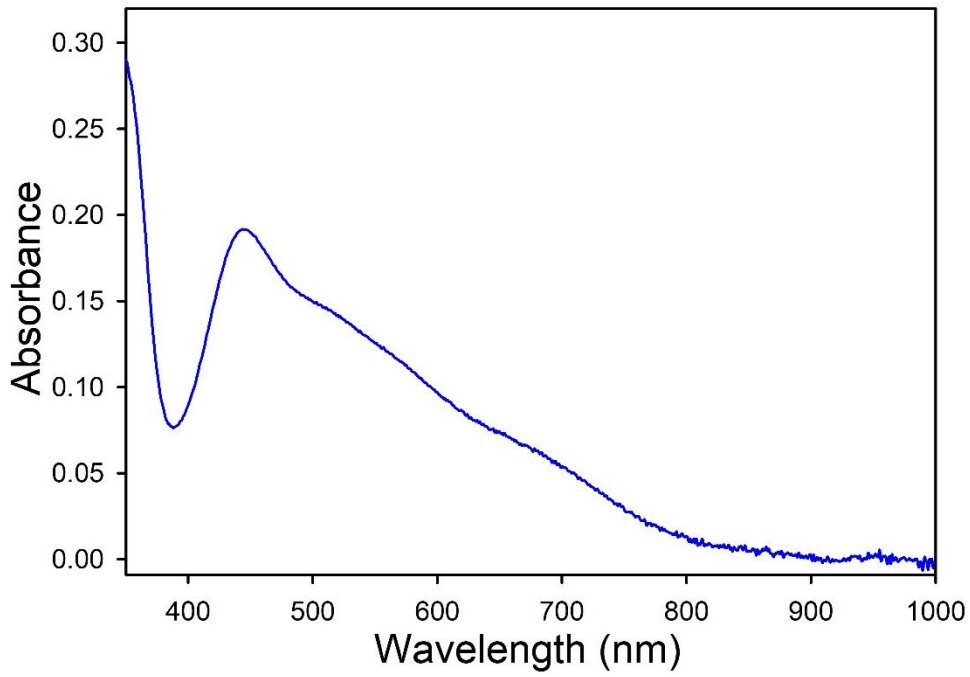

Figure 4.8 Qualitative UV-vis spectrum of **DMF-insoluble** black precipitates from oxidation of **4** by $FcPF_6$ in MeOH.

Upon addition of stoichiometric $FcPF_6$ to the dark red DMF solution of **4**, an immediate color change to turned dark brown that became darker over time and eventually yielded black precipitates. The initial FTIR characterization of the isolated **DMF-insoluble** black solid revealed the formation of a metal complex with ν_{CO} = 1614 cm^{-1} that would be consistent with the formation of a Ni^{3+} species, i.e., favors carboxamide vs. iminol resonance structure (Figure 4.S20 in the SI). In addition, the UV-vis of this complex in MeOH showed multiple new transitions that has striking similarity to that of **4** after exposure to atmospheric O_2 (Figure 4.8), indicating that both oxidation reactions result in the same oxidized Ni species. Additionally, the ^{1}H NMR spectrum of the **DMF-insoluble** black solid indicated a diamagnetic species (Figure 4.S21 in the SI). Additional workup resulted in the identification of Fc (0.0252 g, 0.135 mmol, 72%) in the **DMF-soluble/Et_2O-soluble** (characterized by FTIR and NMR). The **DMF-soluble/Et_2O-insoluble/MeCN-soluble** contained a mixture of ligand disulfides (intra- and inter-molecular) as seen in LR-ESI-MS (*m/z* = 633.2 for $[2M+H]^+$) and ^{1}H NMR (Figures 4.S22-4.S23). Taken together, the net equation for the oxidation reaction is depicted in Scheme 4.2. Based on this equation, the oxidation of **4** by $FcPF_6$ results in the formation of a Ni^{2+}-thiyl radical that undergo RS–SR coupling to yield **6** and the disulfide of $N_3S_2^{NEM}$ ligand, either intramolecularly or intermolecularly. The formation of the disulfides results in the loss of Ni^{2+} to the reaction solution, which captured by the monomeric **4** to ultimately yield **6**.

Scheme 4.2 Net reaction for the oxidation of **4** by $FcPF_6$.

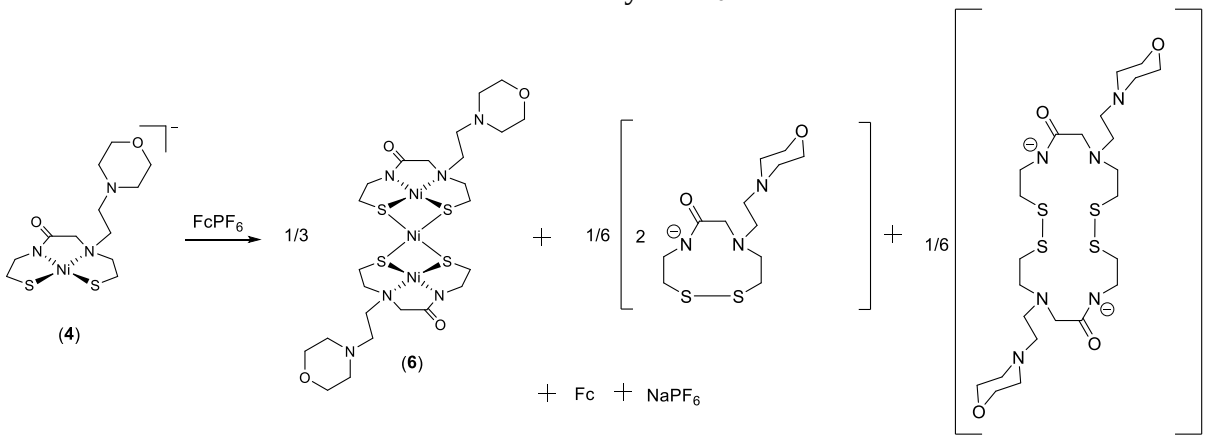

X-ray diffraction of black needle obtained by slow diffusion of Et_2O into a saturated $MeOH/CH_2Cl_2$ solution (1:1 v/v) of the black DMF-insoluble material at -25 °C for 12 days revealed a "stair-step" trimetallic complex, $\{Ni[Ni(N_3S_2^{NEM})]_2\}$•4MeOH (**6**•4MeOH) (Figure 4.9). While **6** is not the first stair-step trimetallic complex that contains a bridging Ni^{2+} ion coordinated by the S-ligands from two monomeric NiN_2S_2 complexes,[43,45,53-67] it is the first trimetallic complex with a pendant axial N-ligand. The structure of **6** reveals two monomers of **4** in the terminal positions (Ni_T) bridged by a Ni^{2+} ion in a square-planar NiS_4 geometry (Ni_C) that constitute the stair-step trimetallic complex (Figure 4.9). The dihedral angle where square planar of Ni_T bisects that of Ni_C is 75.36° for **6**, which is the smallest among all previously reported stair-step trimetallic complexes (101° to 146°).[43,45,53-68] In addition, the Ni1---Ni2 distance of **6** at 2.71943(16) Å is comparable to other Ni---Ni distances from 2.67–3.15 Å,[67] which is larger than the sum of covalent radii of 2.4 Å for a Ni–Ni bond. The coordination of the bridging Ni to the lone pairs on the S-ligands of **4** result in a decrease of 0.01 Å and 0.013 Å for Ni1–S1 and Ni1–S2 bonds, respectively, while the distances of the Ni–N bonds remain essentially the same.

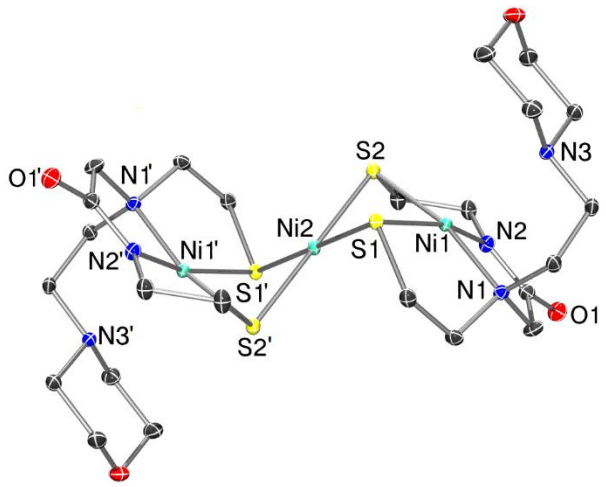

Figure 4.6 ORTEP diagram of {Ni[Ni($N_3S_2^{NEM}$)]$_2$}•4MeOH (**6**•4MeOH) showing 50% thermal probability ellipsoids along with the atom labeling scheme. H atoms and solvent molecules are omitted for clarity. Selected bond distances (Å) and angles (deg): Ni1–N2 = 1.8553(8), Ni1–N1 = 1.9577(8), Ni1–S2 = 2.1570(3), Ni1–S1 = 2.1653(3), Ni1---Ni2 = 2.71943(16), Ni2---Ni1′ = 2.71939(16), Ni2–S1 = 2.2262(2), Ni2–S1′ = 2.2261(2), Ni2–S2 = 2.2288(2), Ni2–S2′ = 2.2288(2), Ni1---N3 = 2.593, N1–Ni1–S2 = 166.29(2), N2–Ni1–S1 = 164.36(3), N1–Ni1–S1 = 92.52(2), N2–Ni1–S2 = 90.18(3), N2–Ni1–N1 = 87.22(3), S2–Ni1–S1 = 86.370(10), S1′–Ni2–S1 = 180.0, S2–Ni2–S2′ = 179.999(11), S1′–Ni2–S2 = 96.792(9), S1–Ni2–S2′ = 97.791(9), S1–Ni2–S2 = 83.209(9), S1′–Ni2– S2′ = 83.208(9).

The formation of Ni_C through coordination of Ni^{2+} by four S-thiolates from the Ni_T sites effectively weakens the N_2S_2 square-planar ligand field to result in a more Lewis acidic Ni_T center. As a result, the pendant N-NEM, which was pointing away from Ni in the X-ray structure of **4** (see Figure 4.2), is now only 2.593 Å away from the Ni in Ni_T, which resembles the long Ni---N-His1 distance of 2.3-2.6 Å in $NiSOD_{ox}$.[2,3] While many of the stair-step trimetallic species with the general formula of {Ni[Ni(N_2S_2)]$_2$} have been reported,[43,45,53-68] many were generated either from addition of Ni^{2+} to monomeric [Ni(N_2S_2)] complexes or as a minor by-product of metallation. One exception is the trimeric complex {Ni[(BME-DACO)Ni]$_2$}$^{2+}$ (BME-DACO = *N,N'*-bis-(mercaptoethy1)-1,5-diazacyclooctanato),[56] which was generated in 10% yield via oxidation of

[(BME-DACO)Ni] under 1 atm of O_2 for 24 h. Overall, 50% of [(BME-DACO)Ni] remained unreacted along with 20% mono-sulfinate ligated species and 5% of bis-sulfinate ligated species were isolated. The formation of $\{Ni[(BME\text{-}DACO)Ni]_2\}^{2+}$ was attributed to the oxidation of [(BME-DACO)Ni] to yield disulfides species by an inter- or intramolecular route results in Ni releases.

4.3.6 Electrochemistry of 4 and 6

The cyclic voltammograms (CVs) of **4** and **6** were measured in MeOH (0.1 M $^{n}Bu_4NPF_6$ electrolyte), and the potentials are reported versus an internal ferrocenium/ferrocene (Fc^{+}/Fc) standard. For **4**, two irreversible E_{ox} at -0.40 V and 0.19 V were observed with one irreversible E_{red} at -1.49 V when scanning in the oxidative direction. The E_{red} at -1.49 V is coupled to the Ni/SR based oxidation event at -0.40 V (Figure 4.7) which is not observable when scanning toward negative potentials. Based on these results, the E_{ox} at -0.40 V and the E_{red} at -1.49 V were assigned as the disulfide/thiolate potentials similar to those observed for **1** and **2**.[41,46] The CV of **6** in MeOH exhibited similar behavior to that of **4**, which showed two irreversible E_{ox} at 0 and 0.17 V and one irreversible E_{red} at -1.55 V (Figure 4.8). These redox events are not dependent upon the scanning direction, which indicates that they are not due to disulfide/thiolate electrochemical event. This observation is consistent with the structure of **6**, in which the S-thiolates are now tightly bound to a Ni^{2+} ion in Ni_C site.

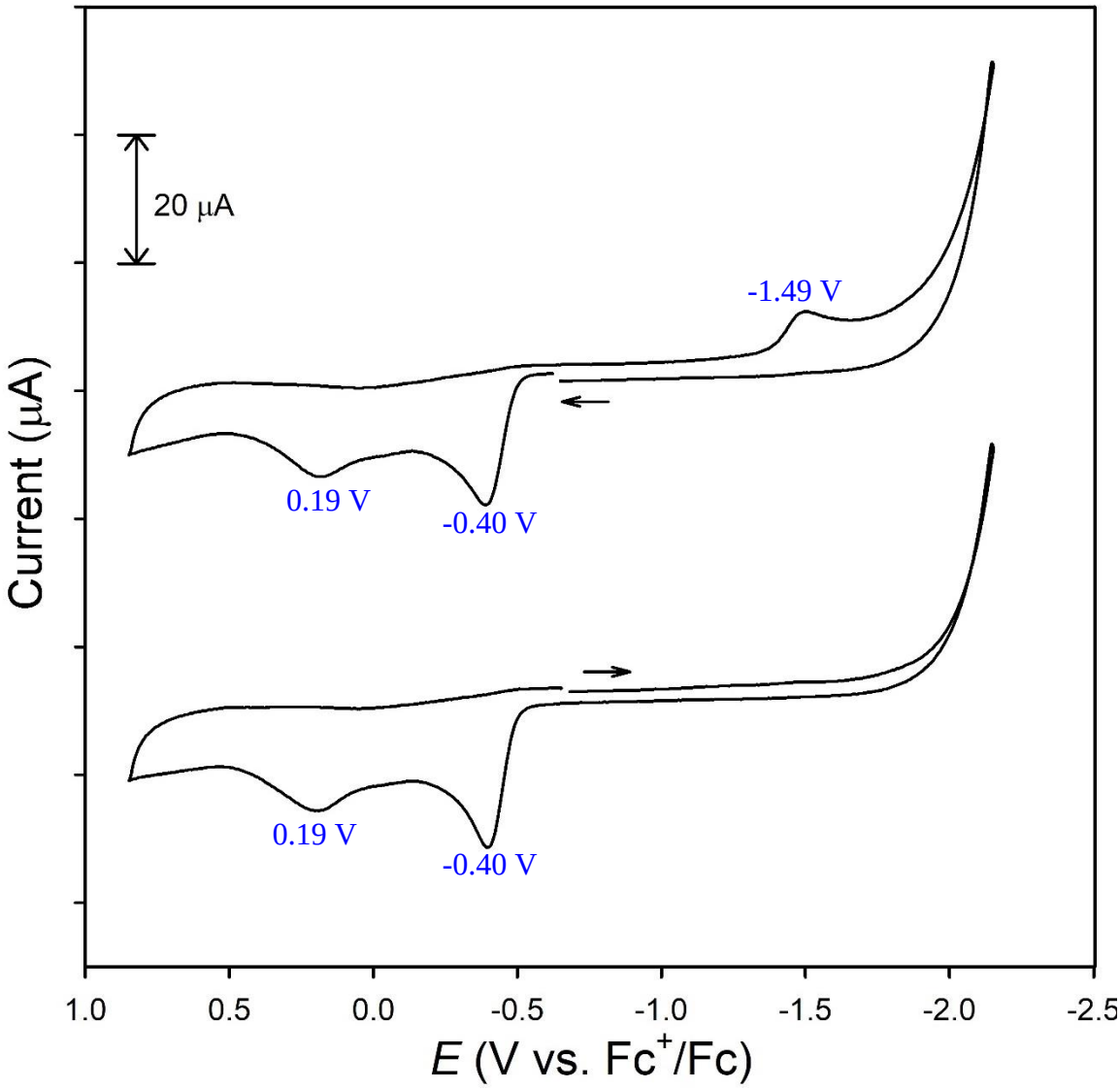

Figure 4.7 CV of **4** (2.5 mM) in MeOH at RT (0.1 M $^{n}Bu_4NPF_6$ supporting electrolyte, glassy carbon working electrode, 100 mV/s scan rate). Arrow displays scan direction.

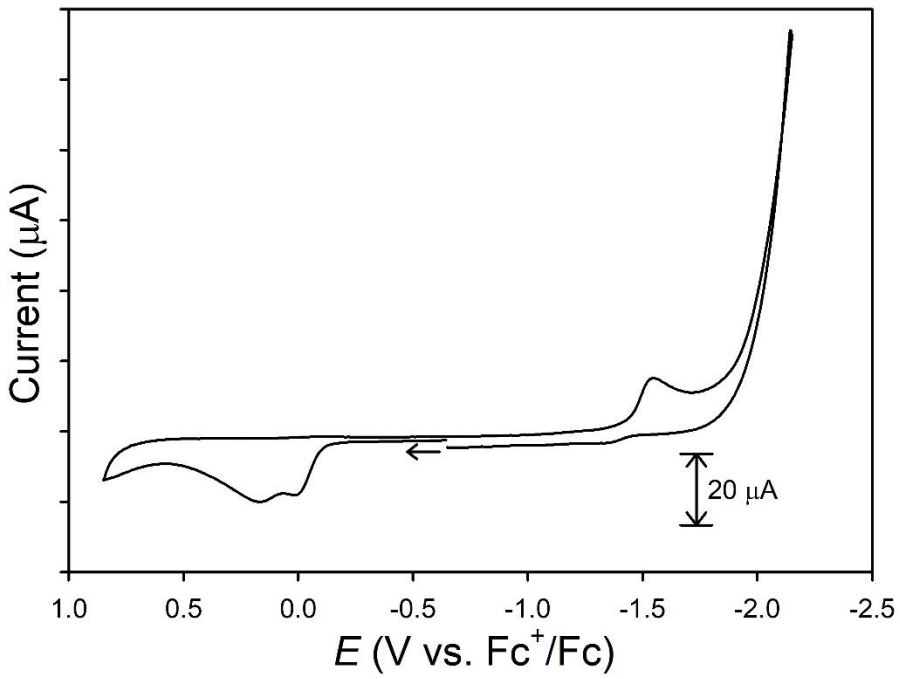

Figure 4.8 CV of **6** (1.3 mM) in MeOH at RT (0.1 M $^{n}Bu_4NPF_6$ supporting electrolyte, glassy carbon working electrode, 100 mV/s scan rate). Arrow displays scan direction.

The CV of **6** was also measured in a non-polar/non-donor solvent such as CH_2Cl_2 where it has good solubility. Interestingly, the full CV of **6** upon scanning toward negative potentials displays a reversible couple at $E_{1/2}$ = -1.51 V followed by two E_{ox} at -0.08 V and 0.21 V (Figure 4.S24). By limiting the potential range between -1.7 and 1.0 V, two reversible redox couples at $E_{1/2}$ = -1.61 V (ΔE_p = 0.10 V) and -0.13 V (ΔE_p = 0.09 V) and one quasi-reversible redox couple at $E_{1/2}$ = 0.13 V (ΔE_p = 0.18 V) were observed (Figure 4.9 and Figures 4.S25-4.S29 in the SI). The differences in the CV of **6** in CH_2Cl_2 in comparison to that in MeOH can be attributed to a solvent effect. Specifically, protic solvents such as MeOH can form H-bonds to the NEM moiety at the N and O positions, which can disrupt the Ni---N-NEM interactions as seen in the crystal structure of

6. In contrast, aprotic non-donor solvents, such as CH_2Cl_2, help maintain and even promote the Ni---N-NEM interactions in solution, to prevent structural rearrangement of **6** in CH_2Cl_2.

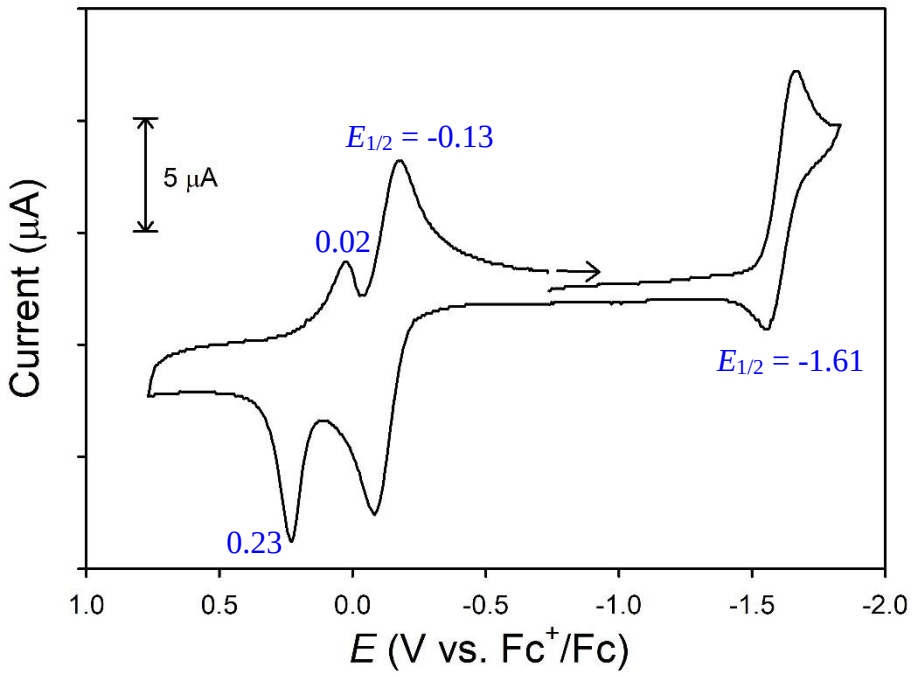

Figure 4.9 CV of **6** (2.9 mM) in CH_2Cl_2 at RT (0.1 M $^nBu_4NPF_6$ supporting electrolyte, glassy carbon working electrode, 100 mV/s scan rate). Arrow displays scan direction.

Differential pulse voltammetry (DPV) of **6** was also measured in CH_2Cl_2 and exhibited three distinct electrochemical responses at -1.61 V, -0.13 V, and 0.21 V (Figure 4.S29 in the SI) consistent with the CV of **6**. The area under the curve of -1.61, -0.13, and 0.21 V were integrated to yield a ratio of 0.6:1:1, respectively. Since **6** can be obtained independently by reacting 0.5 mol-equiv of Ni^{2+} to **4**, it is hypothesized that $\{Ni[Zn(N_3S_2^{NEM})]_2\}$, a Zn–Ni–Zn trimetallic species, can be generated *in situ* by addition of Ni^{2+} to a solution of **5**. CVs of the *in situ* generated

{Ni[Zn($N_3S_2^{NEM}$)]$_2$} can help with the assignment of electrochemical events in **6**, because Zn is redox inert. CV of **5** in CH_2Cl_2 solubilized with 12-crown-4 ether (12C4) exhibits two ligand-based oxidations at E_{ox} = 0.76 V. A batch of 0.5 mol-equiv of $Ni(PPh_3)_2Cl_2$ was added to the solution of **5** to yield a light brown solution that exhibits an oxidation event at 0.88 V, shifted by ~0.12V, which is consistent with the interaction of **5** with a Lewis acid (Figure 4.10). However, limiting the CV window to -2 V to 1 V yielded a similar CV profile with no Ni-based redox events observed (Figure 4.S31 in the SI). The same result was observed when $[Ni(H_2O)_6](BF_4)_2$ was used as the external Ni^{2+} source.

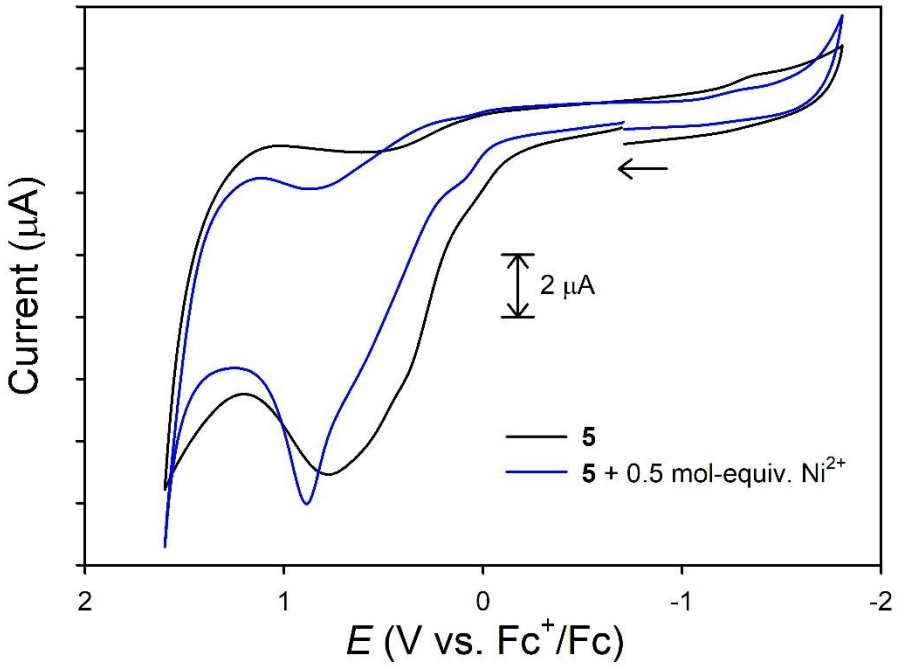

Figure 4.10 CV of **5** (2.8 mM, black) and **5**+$Ni(PPh_3)_2Cl_2$ (0.5 mol-equiv, blue) in CH_2Cl_2 at RT (0.1 M $^nBu_4NPF_6$ supporting electrolyte, glassy carbon working electrode, 100 mV/s scan rate). Arrow displays scan direction.

Influenced by the ability of Lewis acids to essentially eliminate S-based electrochemical events in **6**, we chose to react **4** with BCF to generate an analogue with Ni–S–BR_3 bonds to eliminate S-based electrochemical events and promote Ni-based redox. Addition of stoichiometric BCF to a red-brown slurry of **4** results in immediate color change to a dark brown solution with precipitates. The **CH_2Cl_2-soluble/Et_2O-insoluble** dark brown solid was isolated and characterized by UV-vis, NMR, and FTIR (Figures 4.S31-4.S35 in the SI). Qualitative UV-vis of **CH_2Cl_2-soluble/Et_2O-insoluble** component in CH_2Cl_2 features two electronic transitions reminiscent of the double-hump d–d transitions of **4** at λ_{max} = 440 nm and 542 nm (Figure 4.S31 in the SI and Figure 4.1), but quantitative UV-vis is needed before we can properly assign these electronic transitions. X-ray diffraction of black needles obtained from slow evaporation of a saturated CH_2Cl_2 solution of **CH_2Cl_2-soluble/Et_2O-insoluble** component reveals a stair-step trimetallic species identified as the trimetallic species $\{Ni[Ni(N_3S_2^{NEM})]_2\}$•2(BCF) (**7**) (Figure 4.11). In addition to the bridging Ni_C site similar to that in **6**, **7** contains two BCF molecules that are bonded to carbonyl-O with the B–O bond distance of 1.525(2) Å, which is consistent with B–O bond of 1.52(1) Å found in *N*,*N*-diisopropylbenzamide with BCF adduct.[69] In addition, the NiT site in **7** contains an elongated C=O bond compared to that in **6** (1.30 Å for **7** and 1.271 Å for **6**) and a shortened N–CO bond (1.295 Å for **7** and 1.31 Å for **6**). These results indicate that the carboxamide in **7** favors the iminol resonance structure, which is consistent with the coordination of BCF to carbonyl O. Therefore, the ν_{CO} of **7** is expected to be lower in energy compared ν_{CO} = 1613 cm^{-1} of **6**. The FTIR of **CH_2Cl_2-soluble/Et_2O-insoluble** component exhibits multiple intense stretching frequencies at 1628 cm^{-1}, 1517 cm^{-1}, and 1468 cm^{-1} (Figure 4.S32).

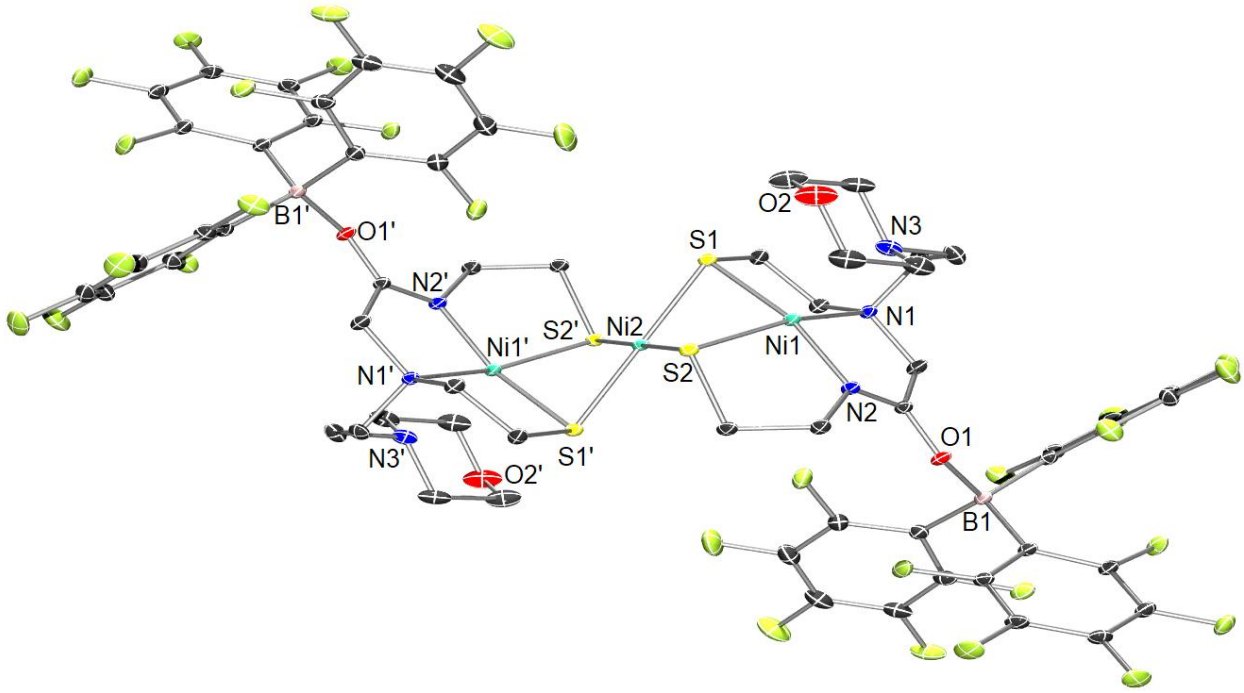

Figure 4.11 ORTEP diagram of {Ni[Ni($N_3S_2^{NEM}$)]$_2$}•2(BCF)•6(CH_2Cl_2) (**7**•6CH_2Cl_2) showing 50% thermal probability ellipsoids along with the atom labeling scheme. H atoms and solvent molecules of crystallization are omitted for clarity. Selected bond distances (Å) and angles (deg): Ni1–N2 = 1.8679(13), Ni1–N1 = 1.9629(13), Ni1–S2 = 2.1689(4), Ni1–S1 = 2.1704(4), Ni1---Ni2 = 2.7269(3), Ni2---Ni1′ = 2.7269(3), Ni2–S1 = 2.2125(4), Ni2–S1′ = 2.2125(4), Ni2–S2 = 2.2185(4), Ni2–S2′ = 2.2185(4), Ni1---N3 = 2.491(2), B1–O1 = 1.525(2), N1–Ni1–S2 = 161.66(4), N2–Ni1–S1 = 163.27(5), N1–Ni1–S1 = 92.10(4), N2–Ni1–S2 = 89.99(4), N2–Ni1–N1 = 86.42(5), S2–Ni1–S1 = 86.189(16), S1′–Ni2–S1 = 180.0, S2–Ni2–S2′ = 180, S1′–Ni2–S2 = 96.012(14), S1–Ni2–S2′ = 96.012(14), S1–Ni2–S2 = 83.989(14), S1′–Ni2– S2′ = 83.989(14).

Solution phase properties of **7** was also characterized by NMR. The broad ^{1}H NMR spectrum of **7** in CD_2Cl_2 indicates the presence of a paramagnetic species (Figure 4.S33), which is consistent with a high-spin Ni^{2+} (S = 1) in a square-pyramidal geometry with Ni---N-NEM bond distance of 2.491 Å. Determination of the magnetic moment of **7** using Evan's method is required before we can confirm the presence of a paramagnetic Ni^{2+} in **7**. Two separate peaks for ^{11}B NMR of **7** indicate some form of dynamic flux where BCF is bound/unbound in solution, which can be

distinguished with low-temperature NMR (Figure 4.S35). Both the solid state and solution phase characterization of **7** are consistent with a stair-step trimetallic species with the coordination of BCF at the carbonyl O.

The coordination of BCF to carbonyl O is expected to remove electronic contribution from the anionic carboxamide-N donor, which we predict will result in a positive shift in the redox processes associated with Ni_T in **7** compared to those in **6**. The CV of **7** in CH_2Cl_2 showed three reversible couples at $E_{1/2}$ = 0.25, 0.00, and -1.32 V (ΔE_p = 0.18 V, 0.06 V, and 0.12 V, respectively) (Figure 4.12), which are shifted by +0.02 V, +0.13 V, and +0.21 V, respectively, compared to those observed in the CV of **6** (Figures 4.8). Similar shift was also observed in the DPV of these two complexes (Figures 4.13). The shift in the redox potential is consistent with the coordination of a Lewis acid (i.e., BCF) to the Ni_T site of the trimetallic species **6**. The coordination of BCF at the carbonyl O effectively remove a significant amount of charge density from the carboxamide-N donor, which manifest in the shortening of all bonds by 0.003-0.01 Å (Figure 4.6 and Figure 4.S32 in the SI). It is more favorable to reduce **7** than **6** due to a decrease in Lewis basicity in the Ni_T as a result of the coordination of BCF. From the CV of **6** and **7** in CH_2Cl_2, we can assign the $E_{1/2}$ at -1.61 V, -0.13 V, and E_{pa} = 0.23 V to be Ni(II/I), Ni(III/II), and potentially Ni(IV/III) redox couples at the Ni_T site of **6**.

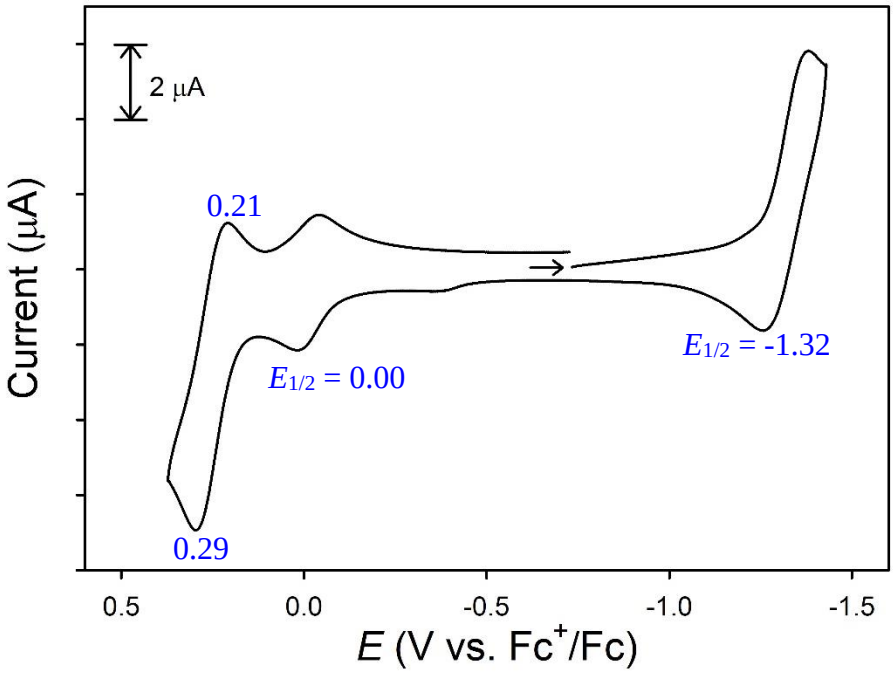

Figure 4.12 CV of **7** (saturated solution filtered through nylon filter) in CH_2Cl_2 at RT (0.1 M $^nBu_4NPF_6$ supporting electrolyte, glassy carbon working electrode, 100 mV/s scan rate). Arrow displays scan direction.

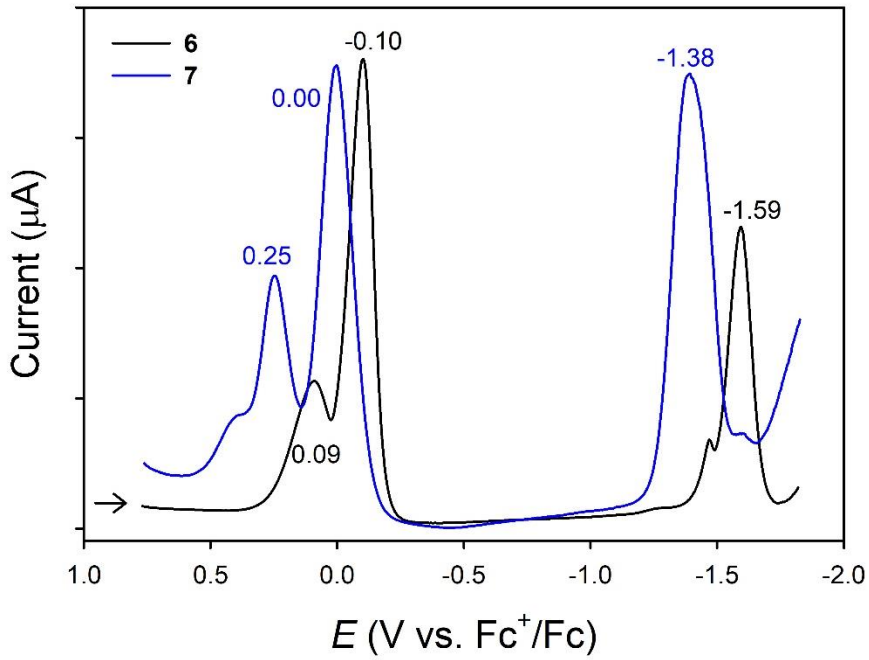

Figure 4.13 DPV of **6** (black) and **7** (blue) (saturated solution filtered through nylon filter) in CH_2Cl_2 at RT (0.1 M $^nBu_4NPF_6$ supporting electrolyte, glassy carbon working electrode, 20 mV/s scan rate, amplitude = 25 mV, frequency = 10 Hz, E_{step} = 2 mV). Arrow displays scan direction.

4.3.7 Reactivity of 4 with azide (N_3^-) and Superoxide ($O_2^{\bullet-}$)

To test the ability of **4** to function as an SOD, we performed spectroscopic measurements (ESI-MS and UV–vis) of the reactions of **4** with NaN_3 and KO_2 (solubilized with 18C6). The reactivity of **4** in the presence of 1 mol-equiv or 10 mol-equiv of N_3^- in MeOH was monitored by UV-vis (Figure 4.14 and Figure 4.S34 in the SI) at 25 °C. The UV-vis of **4** in the presence of excess N_3^- shows an increased in absorbance by ~ 0.07 up to 18 h (Figure 4.11), which eliminates any Ni^{2+}-azido species. This result is similar to previous observations for **1** and **2** (see Ch 3).

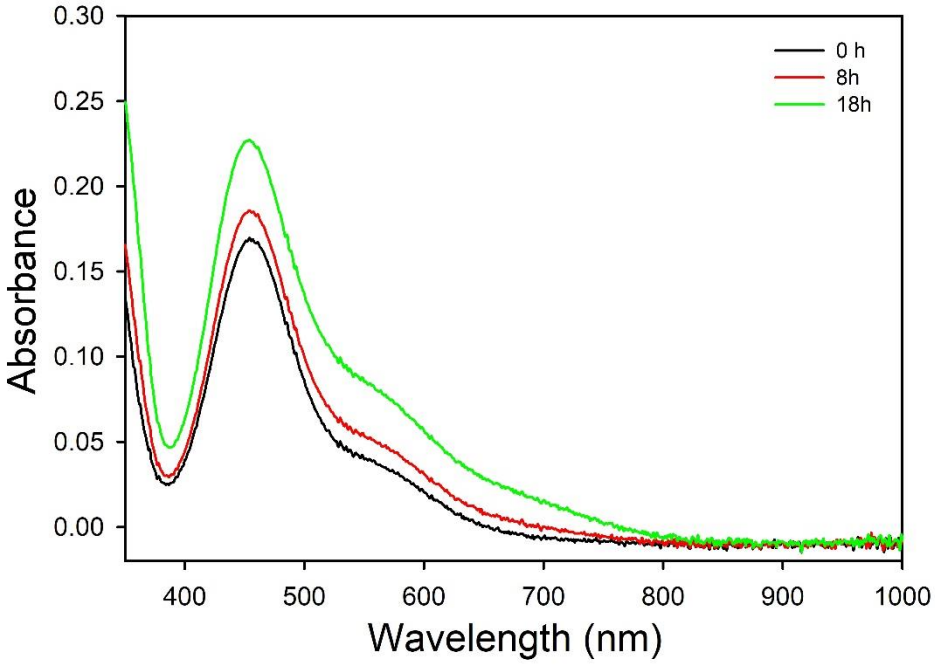

Figure 4.14 UV-vis spectral monitor of **4** (0.850 mM) + NaN_3 (8.50 mM, 10 mol-equiv) in MeOH at 25 °C.

Lastly, the reaction of **4** with 1 mol-equiv or 10 mol-equiv of KO_2 were monitored by UV-vis and characterized by LR-ESI-MS. In the presence of stoichiometric KO_2 in MeOH, **4** reacted slowly with KO_2 to yield a UV-vis profile similar to that of trimetallic **6** after 13 h (Figure 4.15).

However, a LR-ESI-MS(+), the peak at *m/z*: 807 that corresponding to [**6**+Na]$^+$ was not observed, which is not surprising because **6** is a neutral complex, but all the peaks at *m/z*: 378 (+1O), 394 (+2O), 410 (+3O), and 426 (+4O)) along with unreacted **4** (*m/z*: 362) were observed in LR-ESI-MS(–) (Figure 4.S38 in the SI). The formation of oxygenated products is most consistent with reaction between **4** and H_2O_2 that formed from autodisproportionation of $O_2^{\bullet-}$ in the presence of protic solvent (i.e., MeOH), which have been reported for other nickel complexes in mixed N/S ligand frameworks.[31]

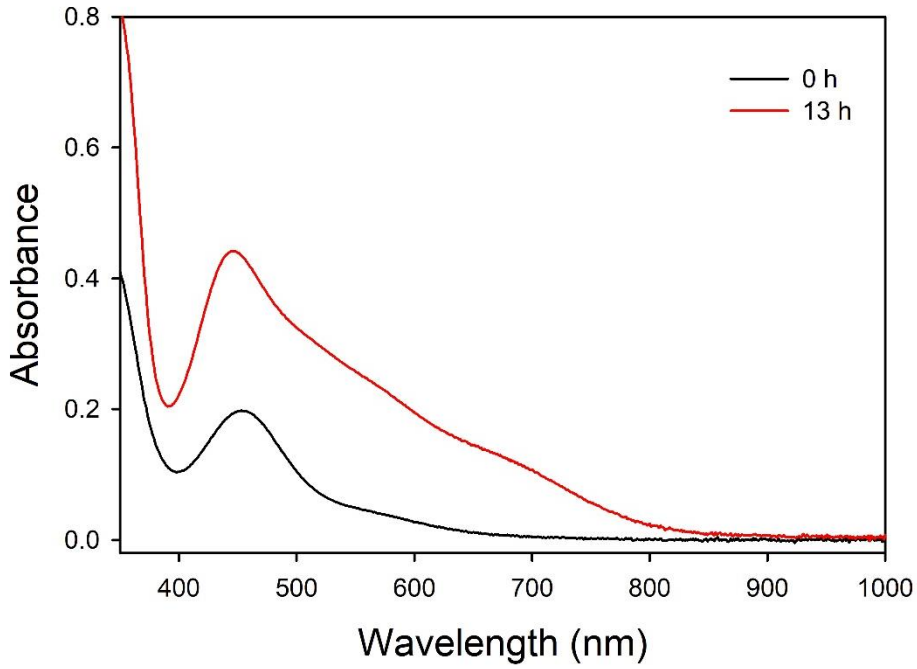

Figure 4.15 UV-vis spectral monitor of **4** (0.971 mM) with stoichiometric KO_2 (1.05 mM, stabilized by 18C6) at 25 °C at t = 0 h (black) and t = 13 h (red).

4.3.8 Amplex Red assay

To assess the ability of **4** and **6** to function as an SOD mimic, the Amplex Red (AR) assay was conducted in 50 mM HEPES buffer at pH 7.4 to evaluate the superoxide reducing capability of **4** and **6**. This test has been successfully used in models of the nonheme enzyme superoxide reductase.[70] In this assay, AR is converted to resorufin by the Fe^{IV}═O intermediates (compounds I and II) of horseradish peroxidase (HRP) that form when HRP reacts with H_2O_2.[71] While AR is colorless, resorufin is red and highly fluorescent (λ_{max} = 572 nm, ε = 54000 M^{-1} cm^{-1}; λ_{em} = 587 nm, in pH 7.4 Tris–HCl buffer;[71] λ_{max} = 572 nm, ε = 56000 M^{-1} cm^{-1}; λ_{em} = 585 nm; Φ = 0.74 in water at pH 9.5[72]). Mixing AR in the presence of KO_2 was monitored by UV–vis with and without NiSOD models **4** and **6** in pH 7.4 HEPES buffer. After an incubation period of 30 min at RT, the reaction mixture containing **4** (or **6**) and KO_2 (1:1), along with AR and HRP, was monitored via UV-vis and showed a ~ 50% decrease in absorbance in comparison to the control (Figure 4.16). These results indicate that **4** and **6** were not able to catalyze the reduction of superoxide to H_2O_2, but instead interfere with the autodisproportionation of the radical of AR ($AR^{\bullet}$) to result in a decrease in amount resorufin produced. This result is not unexpected as this interference is observed for NiSOD models **1** and **2** (Ch 3) with similar electrochemical properties with the same assay.[46]

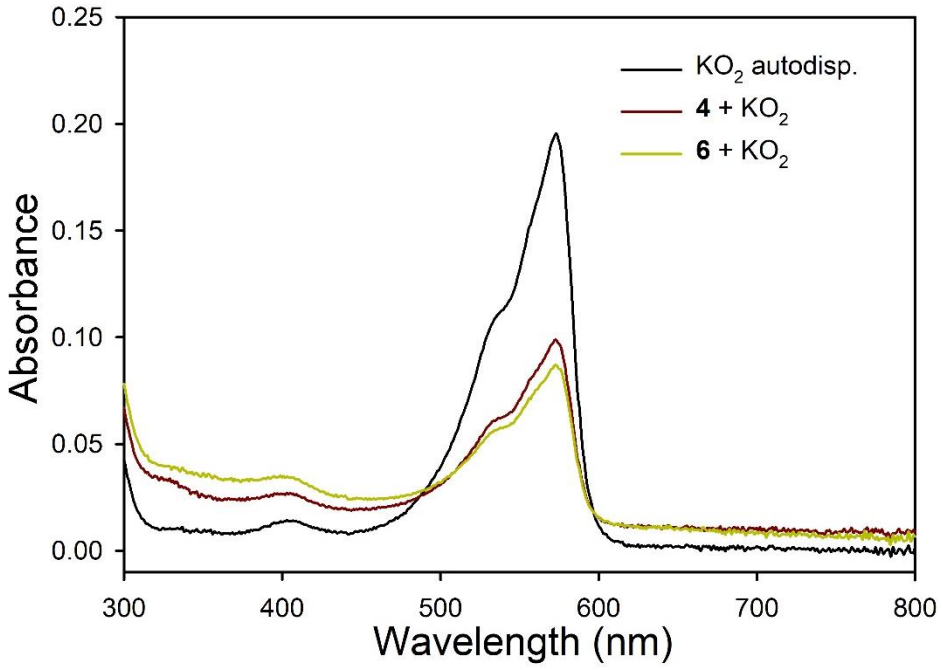

Figure 4.16 The UV-vis spectra of 10 μM HEPES buffer solutions (pH 7.4) of Amplex Red and 1 U/mL of HRP and its response to KO_2 (black), KO_2/complex **4** (1:1) (red), and KO_2/complex **6** (2:1) (gold) at 25 °C.

4.3.9 Electronic Structure Calculations

The ground state electronic structures of **4*** and **6*** (* indicates DFT-optimized complexes using coordinates from the X-ray structures of **4** and **6**) and their one-electron oxidized species $\mathbf{4^{ox}*}$ and $\mathbf{6^{ox}*}$ were examined with DFT at the OLYP/def2-TZVPP level of theory with solvent effects accounted for by utilizing the conductor-like screening model (COSMO) with a dielectric constant (ε) of 38.3 for DMF. Atomic charges were obtained from natural population analysis (NPA). The DFT-optimized structure of **4*** reveals a 4C square planar (τ_4 = 0.11) complex, in which the $Ni–N_{carboxamide}$ (Ni–N2) bond is the shortest and $Ni–S_{trans\text{-}carboxamide}$ (Ni–S1) is the longest bond. While it is not coordinating to the Ni ion, N3 from the NEM moiety is located 3.97 Å away, which is approximately 0.5 Å shorter than the Ni---N3 distance of ~4.50 Å as observed in the

crystal structure of **4**. Overall, the bond distances in **4*** are in good agreement with those in the crystal structure of **4** (Figure 4.17 and Table 4.2).

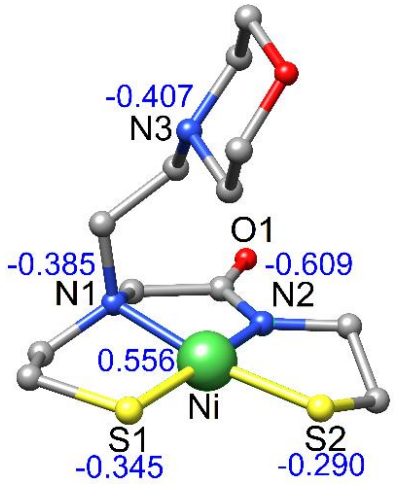

Figure 4.17 Geometry-optimized structure of **4*** with NPA charges on Ni, S, and N atoms in blue. Green = Ni; yellow = S; blue = N; red = O; gray = C. H atoms are omitted for clarity. Selected bond distances (Å) and angles (deg): Ni–S1 = 2.1893, Ni–S2 = 2.1663, Ni–N1 = 1.9815, Ni–N2 = 1.8789, Ni---N3 = 3.973, N1–Ni–S2 = 171.33, N2–Ni–S1 = 173.18, S1–Ni–S2 = 95.89, N2–Ni–S2 = 89.19, N1–Ni–S1 = 90.23, N2–Ni–N1 = 85.22. τ_4: 0.11.

Table 4.3 NPA charges from DFT analysis of **4***, **6***, **4^{ox}***, and **6^{ox}***.[a]

	Ni1	N1	N2	S1	S2	N3	Ni2
4*	0.556	-0.385	-0.609	-0.345	-0.290	-0.407	N/A
4^{ox}*	0.869	-0.395	-0.643	-0.249	-0.095	-0.385	N/A
6*	0.632	-0.395	-0.616	-0.131	-0.114	-0.433	0.380
6^{ox}*	0.753	-0.387	-0.616	-0.094	-0.078	-0.423	0.447

[a] N1 = amino-N; N2 = carboxamido-N; N3 = NEM-N; S1 = S *trans* carboxamide; S2 = S *trans* amine.

An analysis of the frontier MOs (FMOs) of **4*** reveals a highest-occupied molecular orbital (HOMO, MO 96) that is Ni(dπ)/S(π) antibonding MO with 62.9% Ni- and 23.0% S-contributions (Table 4.S2 and Figure 4.S37 in the SI). The LUMO (MO 97) is σ* with primary contributions from Ni $d_{x^2-y^2}$ and the pσ orbitals of all equatorial N/S donors of the ligand. While the Ni contribution in the HOMO of **4*** is very similar to those in **1*** and **2*** (62.7% and 61.9%, respectively), the S contribution in **4*** is smaller than that in **2*** (25.9%), which is expected because of the presence of *gem*-$(CH_3)_2$ in the α-C position of the $S_{trans\text{-}carboxamide}$ of **2***.

The optimized structure of $\mathbf{4^{ox*}}$, the one-electron oxidized species of **4***, indicates a 5C square-pyramidal (τ_5 = 0.04) complex with the coordination of N3 to Ni with a Ni–N3 bond distance of 2.25 Å, which is ~ 0.25 Å longer than the Ni–N3 bonds in $\mathbf{1^{ox*}}$ and $\mathbf{2^{ox*}}$ (Figure 4.17)**.**[46] In $\mathbf{4^{ox*}}$, Ni–S bonds are ~0.01-0.03 Å longer than **4*** (Figure 4.18) with the Ni–S1 (trans carboxamide) bond being the longest. The two Ni–N bonds are also longer than those in **4*** by ~0.03 Å with the Ni-N2 being the shortest. Overall, the bonds in $\mathbf{4^{ox*}}$ are longer than **4*** because of increased electron-electron repulsion upon coordination of N3 to Ni to form 5C $\mathbf{4^{ox*}}$. This result is consistent with the DFT analysis of $\mathbf{1^{ox*}}$ and $\mathbf{2^{ox*}}$.[46] The MO diagram of $\mathbf{4^{ox*}}$ shows that the redox-active MO (RAMO, MO β96) is primarily Ni-dz^2 (55%), with contributions from S-pπ (19%) and N3-σ (11%), similar to that computed for $\mathbf{1^{ox*}}$, $\mathbf{2^{ox*}}$, and $NiSOD_{ox}$ (Figure 4.19 and Table 4.S4 in the SI).[7,46] In contrast, the singly-occupied molecular orbital (SOMO, MO α96) is primarily Ni-dπ/S-pπ antibonding with mostly S-pπ contribution (8% S2, 53% S1; total S = 61%) and a small Ni-dπ contribution (23%) (Table 4.S4 in the SI). Analogous to $\mathbf{1^{ox*}}$ and $\mathbf{2^{ox*}}$, the large S-contribution in the SOMO showed that the unpaired electron primarily resides on S-ligand upon oxidation from **4*** to $\mathbf{4^{ox*}}$, which results in the formation of a thiyl radical. This is also supported by the Mulliken spin density analysis, that shows the majority of the spin in $\mathbf{4^{ox*}}$ resides on the

ligand with minor spin density on Ni. This result explains the reactive nature of **4** toward oxidants such as Fc^{+} and O_2, that yields disulfide species, loss of Ni^{2+}, and the trimetallic complex **6**.

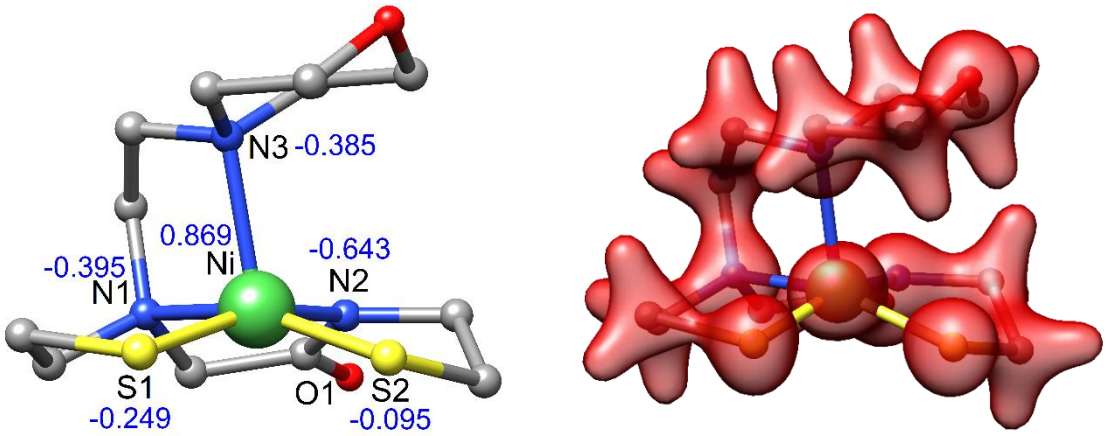

Figure 4.18 Geometry-optimized structure of **4^{ox}*** (*left*) with NPA charges on Ni, S, and N atoms in blue. Spin density plot from the SPE calculation with positive spin density in red and negative spin density in cyan (*right*). H atoms are omitted for clarity. Selected bond distances (Å) and angles (deg): Ni–N1 = 2.0253; Ni–N2 = 1.9077; Ni–N3 = 2.2493; Ni–S1 = 2.2158; Ni–S2 = 2.1499; N1–Ni–S2 = 160.55; N2–Ni–S1 = 163.03; N1–Ni–N2 = 83.20; N2–Ni–S2 = 88.35; S2–Ni–S1 = 92.21; S1–Ni–N1 = 90.89; S2–Ni–N3 = 112.84; N2–Ni–N3 = 99.52; S1–Ni–N3 = 95.88; N1–Ni–N3 = 85.89. τ_5 = 0.04.

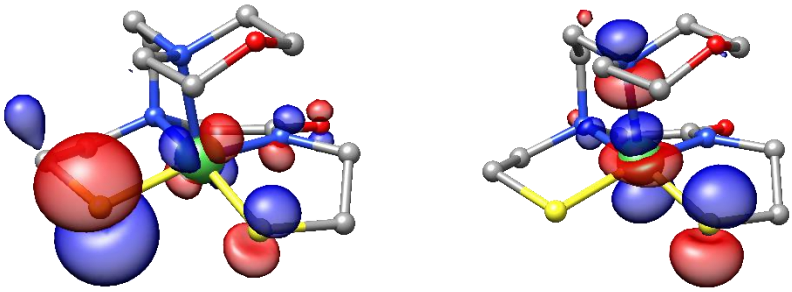

Figure 4.19 DFT-generated isosurface plots of the frontier MOs of **4^{ox}*:** SOMO (MO α96) (*left*) and RAMO (MO β96) (*right)*. H atoms omitted for clarity.

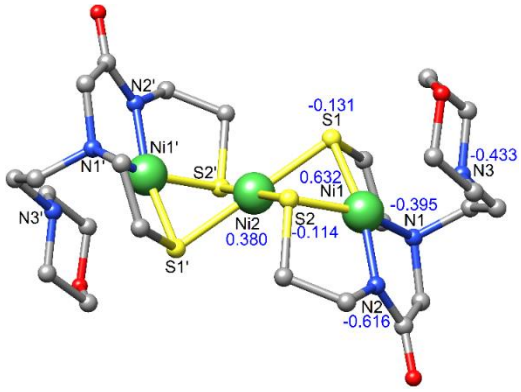

Figure 4.20 Geometry-optimized structure of **6*** with NPA charges on Ni, S, and N atoms. H atoms omitted for clarity. Selected bond distances (Å) and angles (deg): Ni1–N1 = 1.9886, Ni1–N2 = 1.8572, Ni1–S1 = 2.1701, Ni1–S2 = 2.1507, Ni1–Ni2 = 2.6657, Ni2–Ni1′ = 2.6657, Ni2–S1 = 2.2249, Ni2–S1′ = 2.2249, Ni2–S2 = 2.2314, Ni2–S2′ = 2.2314, Ni1---N3 = 2.5686, N1–Ni1–S2 =163.48, N2–Ni1–S1 = 166.08, N1–Ni1–S1 = 92.3, N2–Ni1–S2 = 90.05, N2–Ni1–N1 = 86.57, S2–Ni1–S1 = 87.11, S1′–Ni2–S1 = 179.97, S2–Ni2–S2′ = 179.97, S1′–Ni2–S2 = 96.16, S1–Ni2–S2′ = 96.16, S1–Ni2–S2 = 83.84, S1′–Ni2– S2′ = 83.84. τ_4: 0.22.

The optimized structure **6*** shows a stair-step trimetallic complex with two 4C square planar (τ_4 = 0.22) complexes bridged by a planar Ni^{2+} with four S coordination. The Ni---Ni distance of 2.67 Å and the Ni–S and Ni–N distances of the Ni_T sites are within ~0.2 Å to those found in the crystal structure of **6** (Figure 4.20 and Table 4.2). The Ni---N3 distances remain at 2.57 Å, just larger than 2.0-2.2 Å of reported Ni–N bonds. By occupying the lone pairs on the S-ligands by Lewis acids such as Ni^{2+}, the electron density on S decreases significantly. This effect is seen by analysis the NPA charges. While the NPA charges on the N ligands remain the same compared to **4***, the NPA charges on the S ligands show significant decreases by 0.23 and 0.16 for S1 and S2, respectively (Table 4.3).

FMO analysis of **6*** reveals a HOMO (MO 204) comprised of major contributions from Ni-dz^2 (32%) and N3-σ (6%) with only minor S-contribution (4%) (Figure 4.S40 and Table 4.S3 in the SI). In addition to the Ni-dz^2 (26%) and N3-σ (3%) contributions from the Ni_T site, the LUMO (MO 205) also has contribution from the Ni-dz^2 (27%) from the NiS_4 bridge (Figure 4.S40

in the SI). Based on the MO of **6***, we can expect that upon oxidation, the electron will most likely be taken from Ni-dz^2, which is consistent with DFT results of $NiSOD_{ox}$ site with His_{on}. The analysis of the ground state structure of **6*** shows that occupying the lone pair of the S-ligands significantly lower S-pπ contributions in the HOMO, which will promote Ni-based redox upon oxidation.

The optimized structure of the one-electron oxidized species of **6***, **6^{ox*}**, reveals a trimetallic step-stair complex with two 5C square pyramidal complexes (τ_5 = 0.04) bridged by a Ni^{2+} in NiS_4 square planar geometry (Figure 4.21). As observed in **6^{ox*},** the removal of one electron from the system from **6*** promoted the coordination of N3 to Ni in the Ni_T sites and elongated the other Ni-N/S bonds in the square-plane of the Ni_T sites by ~0.01-0.03 Å (Figure 4.21 and Table 4.2). The RAMO (MO β205) and SOMO (MO α205) of **6^{ox*}** is mostly comprised of Ni-dz^2 and N3-σ contributions, which indicates that either reduction or oxidation of **6^{ox*}** will be Ni-based (Figure 4.22). This is consistent with the spin density plot that shows the majority of the spin resides on Ni-dz^2 and N3-σ that is delocalized over three Ni centers (Figure 4.S42 and Table 4.S5 in the SI).

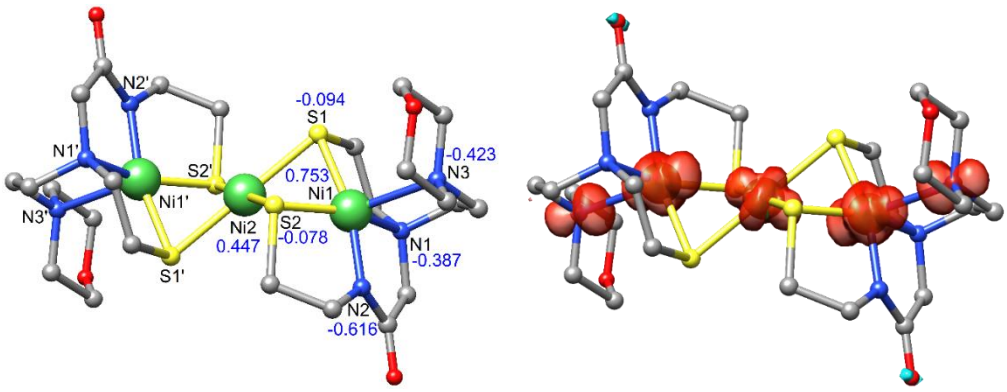

Figure 4.21 DFT-optimized structure of **6^{ox}*** with NPA charges on Ni, S, and N atoms in blue (*top*) and spin density plot from SPE calculation with positive spin density in red and negative spin density in cyan (*bottom*). Green = Ni; yellow = S; blue = N; red = O; gray = C. H atoms are omitted for clarity. Selected bond distances (Å) and angles (deg): Ni1–N1 = 2.0063, Ni1–N2 = 1.8627, Ni1–S1 = 2.1839, Ni1–S2 = 2.1679, Ni1–N3 = 2.3292, Ni1–Ni2 = 2.6217, Ni2–Ni1′ = 2.6217, Ni2–S1 = 2.2254, Ni2–S1′ = 2.2254, Ni2–S2 = 2.2325, Ni2–S2′ = 2.2325, N1–Ni1–S2 =160.6, N2–Ni1–S1 = 163.01, N1–Ni1–S1 = 92.12, N2–Ni1–S2 = 89.29, N2–Ni1–N1 = 86.08, S2–Ni1–S1 = 86.84, N1–Ni1–N3 =84.96, S1–Ni1–N3 = 104.09, S2–Ni1–N3 = 114.10, N2–Ni1–N3 = 92.6, S1′–Ni2–S1 = 179.97, S2–Ni2–S2′ = 179.97, S1′–Ni2–S2 = 95.72, S1–Ni2–S2′ = 95.72, S1–Ni2–S2 = 83.84, S1′–Ni2– S2′ = 83.84. τ_5 = 0.04.

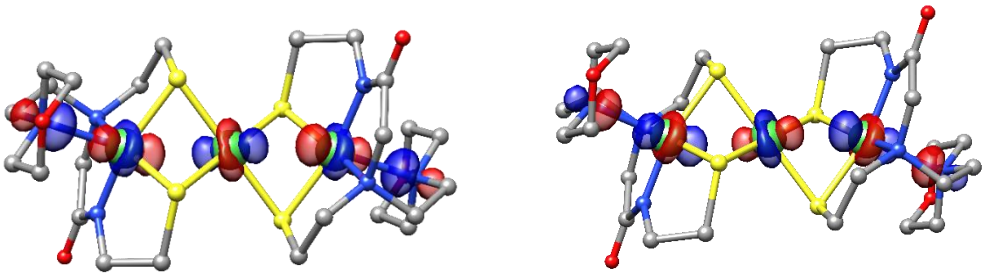

Figure 4.22 DFT-generated isosurface plots of the frontier MOs of **6^{ox}*:** SOMO (MO α205) (*left*) and RAMO (MO β205) (*right).* H atoms omitted for clarity.

4.4 Conclusions

In this work, we have successfully synthesized the 3rd generation NiSOD model with a NEM moiety to provide the potential fifth N-ligand (complex **4**). We have also shown that oxidation of **4** by air (O_2), KO_2, or chemical oxidant resulted in the formation of the stair-step trimetallic species, complex **6**, which is not observed before in **1** and **2**. While the incorporation of

the more basic N-NEM moiety into the ligand did not promote coordination of axial N ligand to Ni^{2+} as observed in solid state structure of **4**, sequestration of electron density from S-thiolates in the square plane ligand sphere by bridging Ni^{2+} ion significantly weakened the N_2S_2 square plane ligand field strength. As a result, N-NEM is poised to coordinate to a more Lewis acidic Ni center in the Ni_T site on **6** at with a Ni---N-NEM distance of 2.593 Å. The electrochemical properties of **4** and **6** were studied by CV. While CV of **4** was similar to those of **1** and **2**, CV of **6** showed two reversible couple at -1.61 V and -0.13 V and one quasi-reversible couple centered at 0.13 V in CH_2Cl_2. With three redox active centers in **6**, the assignment of these redox event proves to be difficult. However, comparing the CV of **6** to **7** showed that all electrochemical processes in **6** were shifted by +0.13 V, which suggests that these redox events originate on the terminal Ni site of **6** since the interaction between BCF and the carbonyl-O significantly lower the basicity of the carboxamide-N ligand in the N_2S_2 square plane. Taken together, these results show that while synthetic analogues can replicate the structure and electronic properties of the primary coordination sphere of NiSOD, they lack the H-bonding interactions afforded by the enzyme's tertiary structure to effectively modulate the electronic property of the active site for catalysis.

4.5 Materials and Methods

4.5.1 General Information

See General Information section in Chapter 3. Acetone was degassed with freeze-pump-thaw method and dried over $CaSO_4$ overnight before using (it was not decanted from $CaSO_4$ before using). Isopropyl alcohol (^{i}PrOH) was stored over 4 Å molecular sieves for at least 48 h and

degassed with freeze-pump-thaw method before using. The compounds *N*-(2-(tritylthio)ethyl)-2-((2-(tritylthio)ethyl)amino)acetamide (S-trityl N_2S_2)[41,49] was prepared according to the published procedures. 1,4,7-Trithiacyclononane ([9]aneS3) and dichlorobis(triphenylphosphine)Ni(II) ($Ni(PPh_3)_2Cl_2$) were obtained from Aldrich and used as received.

4.5.2 Physical Methods.

See Physical Methods section in Chapter 3. Cyclic voltammetry (CV) and differential pulse voltammetry (DPV) measurements were performed with either a PAR Model 273A potentiostat controlled by Princeton Applied Research PowerSuite software or a μAutolab Type III potentiostat/galvonostat controlled by Autolab GPES software. Measurements were performed at ambient temperature using 1-3 mM analyte in the appropriate solvent under Ar containing 0.1 M $^nBu_4NPF_6$ as the supporting electrolyte. The "Maximize Stability" mode was utilized in the PAR PowerCV software utilizing a low-pass 5.3 Hz filter. Analyte potentials were referenced against a 0.5 mM ferrocene internal standard under identical conditions, where $E_{1/2}$ = 0.197 V in CH_2Cl_2, and 0.139 V in MeOH vs. the reported non-aqueous Ag/Ag^+ electrode. ^1H NMR and ^{13}C NMR (125 MHz) spectra were recorded in the listed deuterated solvent on a 500 MHz Varian Unity INOVA NMR spectrometer NMR spectrometer at RT with chemical shifts referenced to tetramethylsilane (TMS) or the residual protio signal of the deuterated solvent.[73] ^1H NMR (400 MHz), ^{19}F NMR (376 MHz), and ^{11}B NMR (128 MHz) spectra were obtained with quartz NMR tubes and recorded in the listed deuterated solvent on a 400 MHz Bruker Advance III HD NMR spectrometer at RT with chemical shifts referenced to TMS or the residual protio signal of the deuterated solvent.[73] ^{19}F NMR spectra are referenced internally or externally to fluorobenzene (-

113.15 ppm vs. $CFCl_3$).[74] ^{11}B NMR spectra are referenced externally to BF_3•Et_2O (0.00 ppm) in the same solvent system. Elemental microanalysis for C, H, and N was performed by ALS Environmental (formerly Columbia Analytical) in Tucson, AZ.

4.5.3 Synthesis of Compounds

*2-((2-morpholinoethyl)(2-(tritylthio)ethyl)amino)-N-(2-(tritylthio)ethyl)acetamide (**$N_3S_2^{NEM}Tr_2$**)*

A round-bottom flask was loaded with $N_2S_2Tr_2$ (0.5922 g, 0.8722 mmol), 4-(2-chloroethyl)morpholine hydrochloride (0.1696 g, 0.9114 mmol), NaI (0.1402 g, 0.9354 mmol), K_2CO_3 (0.3576 g, 2.588 mmol), and 10 mL of THF/MeCN (1:1). This heterogeneous solution was heated to reflux for 24 h. After reflux, white insoluble salts were removed by filtration and the yellow filtrate was concentrated to a yellow solid. The crude material was purified by column chromatography using basic Al_2O_3 and a hexanes/ethyl acetate (1:1) mobile phase. The desired product fractions (R_f = 0.26) were collected, concentrated, and dried on a vacuum line to yield the product as a light-yellow foam-like solid (0.3343 g, 0.4220 mmol, 48%). mp 49-53 °C. ^1H NMR (500 MHz, $CDCl_3$ with 0.05% v/v TMS, δ from TMS): 7.79 (t, 1H, carboxamide-N*H*, confirmed by D_2O exchange, *J* = 6.1 Hz), 7.38 (m, 12H), 7.23 (m, 12H), 7.18 (m, 6H), 3.58 (t, 4H, *J* = 4.6 Hz), 3.06 (q, 2H, *J* = 6.5 Hz), 2.91 (s, 2H), 2.41 (q, 4H, *J* = 6.4 Hz), 2.38 (t, 2H, *J* = 6.8 Hz), 2.29 (m, 6H), 2.24 (t, 2H, *J* = 6.8 Hz). ^{13}C NMR (125 MHz, $CDCl_3$ with 0.05% v/v TMS, δ from solvent signal): 171.54 (*C*=O), 144.81, 144.77, 129.62, 129.61, 128.00, 126.79, 66.98, 66.84, 66.76, 58.51, 56.79, 55.00, 53.84, 51.76, 38.16, 32.08, 30.09. FTIR (KBr pellet) ν_{max} (cm^{-1}): 3448 (br m, ν_{NH}), 3081 (w), 3054 (m), 3029 (w), 2955 (m), 2919 (m), 2850 (m), 2813 (m), 1955 (vw), 1897 (vw), 1812 (vw), 1773 (vw), 1672 (s, ν_{CO}), 1594 (w), 1517 (w), 1489 (m), 1443 (m), 1396 (w), 1358

(w), 1301 (w), 1262 (vw), 1205 (vw), 1183 (w), 1116 (m), 1082 (w), 1070 (vw), 1033 (m), 1009 (vw), 1002 (vw), 924 (w), 885 (vw), 855 (w), 802 (vw), 766 (m), 743 (s), 700 (vs), 675 (w), 628 (w), 621 (w), 581 (vw), 504 (vw). LR-ESI-MS (*m/z*): $[M+H]^+$ calcd for $C_{50}H_{54}N_3O_2S_2$ (relative abundance), 792.4 (100.0), 793.4 (56.8), 794.4 (23.3), 795.4 (6.6); found: 792.3 (100.0), 793.3 (55.1), 794.3 (24.8), 795.2 (7.1).

N-(2-mercaptoethyl)-2-((2-mercaptoethyl)(2-morpholinoethyl)amino)acetamide dihydrochloride ***($H_3N_3S_2^{NEM}$•2HCl)***

A batch of $N_3S_2^{NEM}Tr_2$ (1.3109 g, 1.6549 mmol) was dissolved in 20 mL of TFA/CH_2Cl_2 (1:1) to form a red-orange solution. After 15 min stirring at RT, Et_3SiH (0.4885 g, 4.2011 mmol) was added to the mixture, which resulted in immediate bleaching of the solution to pale-yellow. The solvent was removed via short-path vacuum distillation and the resulting yellow oil with white precipitates was stirred in pentane (7 × 10 mL). The pentane was decanted to remove Ph_3CH and the yellow oil was taken into the glovebox and dissolved in 13 mL of CH_2Cl_2/MeCN (10:3) to afford a yellow solution. Solid $NaHCO_3$ (2.6616 g, 31.682 mmol) was added to neutralize the solution and the mixture was stirred at RT for 18 h. The solution was filtered over Celite, the solid washed with 8 mL of CH_2Cl_2/MeCN (1:1), and the filtrate concentrated to approximately 6 mL. To the yellow filtrate was then added 4 mL of 1 M HCl in Et_2O (4 mmol) to yield a yellow sticky solid. The cloudy solution was decanted and the yellow solid was triturated with 4 mL of Et_2O. The resulting yellow solid was dried on a vacuum line over a 30 °C water bath for 14 h to yield 0.4194 g (1.103 mmol, 67%) of product. ^{1}H NMR (500 MHz, CD_3OD, δ from protio solvent): 4.16 (s, 2H), 4.02 (br s, 4H), 3.80 (t, 2H, J = 6.4 Hz), 3.69 (t, 2H, J = 6.4 Hz), 3.52 (m, 4H), 3.45 (t,

4H, *J* = 6.7 Hz), 2.96 (m, 2H), 2.67 (t, 2H, *J* = 6.7 Hz). ^{13}C NMR (125 MHz, CD_3OD, δ from solvent signal): 166.81 (*C*=O), 65.10, 59.45, 55.80, 53.80, 52.97, 50.67, 44.02, 24.44, 19.35. ^{1}H NMR (500 MHz, CD_3CN, δ from protio solvent): 11.83 (br s, 0.3H), 8.71 (br s, carboxamide-N*H*, 1H), 4.14 (br s, 2H), 3.98 (br s, 4H), 3.73 (br s, 2H), 3.63 (br s, 4H), 3.53 (t, 2H, *J* = 8.0 Hz), 3.41 (q, 2H, *J* = 6.3 Hz, integrates higher than expected due to overlap with Et_2O from workup, value listed is after subtraction of Et_2O CH_2 protons from integration of the CH_3 peak at 1.12 ppm), 3.08 (br s, 2H), 3.01 (m, 2H), 2.66 (q, 2H, *J* = 6.9 Hz), 2.29 (br t, S*H*, 1H), 2.20 (t, S*H*, 1H, *J* = 8.5 Hz). ^{13}C NMR (125 MHz, CD_3CN, δ from solvent signal): 165.73 (*C*=O), 64.58, 58.64, 54.75, 53.20, 52.73, 50.13, 43.59, 30.08, 24.51, 19.48. FTIR (KBr pellet) ν_{max} (cm^{-1}): 3208 (br s, ν_{NH}), 3056 (s), 2976 (vs), 2939 (vs), 2866 (s), 2642 (s), 2530 (vs), 2448 (vs), 1681 (vs, ν_{CO}), 1560 (m), 1447 (m), 1400 (m), 1380 (m), 1304 (w), 1264 (m), 1200 (w), 1137 (m), 1106 (m), 1050 (m), 1018 (w), 983 (w), 909 (w), 872 (w), 856 (w), 815 (vw), 756 (w), 727 (w), 660 (vw), 625 (vw), 600 (vw), 583 (vw), 487 (vw), 460 (vw). LR-ESI-MS (*m/z*): $[M+H]^+$ calcd for $C_{12}H_{26}N_3O_2S_2$ (relative abundance), 308.1 (100.0), 309.1 (15.7), 310.1 (9.0); found: 308.0 (100.0), 309.0 (16.7), 310.0 (10.4).

Na[Ni($N_3S_2^{NEM}$)] (**4**)

To a yellow MeOH solution (6 mL) of $H_3N_3S_2^{NEM}$•2HCl (0.3857 g, 1.014 mmol) was added sodium metal (0.1344 g, 5.844 mmol) to cause rigorous effervescence along with the formation of white precipitates. After stirring this mixture at RT for 10 min, a green 1 mL MeOH solution of $NiCl_2$ (0.1262 g, 0.9738 mmol) was added to yield a red-brown solution with white precipitates. After stirring at RT for 2 h, the MeOH was removed via short-path vacuum distillation and the

resulting brown solid was dissolved in 21 mL of MeCN/MeOH (20:1) and stored at -25 °C for 30 min. The white insoluble materials were removed by filtration over Celite and the brown filtrate was concentrated to a solid via short-path vacuum distillation. The brown residue was then stirred in 8 mL of MeCN for 3 h and the resulting solid was collected by vacuum filtration, washed with 4 mL of MeCN, 2 × 5 mL of pentane, and dried to yield 0.3091 g of product (0.8005 mmol, 82%). ^{1}H NMR (500 MHz, CD_3OD, δ from protio solvent): 3.73 (m, 4H), 3.58 (m, 2H), 3.29 (m, 3H, integrates higher than expected due to overlap with residual protio solvent at 3.31 ppm), 3.11 (m, 1H), 3.05 (m, 2H), 2.93 (m, 1H), 2.77 (m, 2H), 2.61 (m, 4H), 2.35 (m, 1H), 2.18 (m, 1H), 2.09 (m, 2H). ^{1}H NMR (400 MHz, $(CD_3)_2CO$, δ from protio solvent): 3.62 (m, 4H), 3.36 (m, 2H), 3.22 (m, 2H), 3.09 (m, 1H), 2.86 (m, 4H), 2.68 (m, 1H), 2.50 (br s, 4H), 2.21 (m, 1H), 1.95 (m, 3H). UV-vis (MeOH, 25 °C), λ_{max}, nm (ε, M^{-1} cm^{-1}): 455 (240), 575 (60). FTIR (KBr pellet) ν_{max} (cm^{-1}): 3407 (br w), 2920 (m), 2848 (m), 2260 (vw, ν_{CN}), 2246 (vw, ν_{CN}), 1685 (m), 1593 (vs, ν_{CO}), 1448 (m), 1437 (m), 1415 (m), 1322 (vw), 1304 (w), 1265 (w), 1206 (w), 1191 (w), 1145 (m), 1113 (s), 1068 (m), 1034 (w), 1006 (w), 973 (vw), 939 (vw), 920 (vw), 865 (w), 801(w), 729 (vw), 692 (vw), 626 (vw), 585 (vw), 540 (vw), 517 (vw), 462 (m). HR-ESI-MS (*m/z*): $[M\text{-}Na]^-$ calcd for $C_{12}H_{22}N_3NiO_2S_2$ (relative abundance), 362.051 (100.0), 364.046 (47.5), 363.054 (13.0), 366.044 (5.3), 365.049 (5.0); found: 362.051 (100.0), 364.046 (47.0), 363.054 (12.5), 366.043 (7.1) 365.050 (5.2). Anal. Calcd for $C_{12}H_{22}N_3NaNiO_2S_2$: C, 37.33; H, 5.74; N, 10.88. Found: C, 37.06; H, 5.94; N, 10.18.

Na[Zn($N_3S_2^{NEM}$)]•^{i}PrOH (**5**)

To a 16 mL MeOH solution of $H_3N_3S_2^{NEM}$•2HCl (0.3874 g, 1.018 mmol) was added sodium metal (0.1454 g, 6.322 mmol) to cause rigorous effervescence along with the formation of white precipitates. The yellow heterogeneous solution was stirred at RT for 30 min and to this was added a MeOH solution (2 mL) of $ZnCl_2$ (0.1380 g, 1.012 mmol). The resulting yellow solution with white precipitates was stirred for 2 h at RT with no changes. Insoluble white solid was removed by filtering over Celite and the filtrate was concentrated to a light-yellow solid that was dissolved in 12 mL of ^{i}PrOH/MeCN (1:1) and stored at -25 °C for 30 min. The mixture was filtered over Celite to remove any additional precipitates and the yellow filtrate was concentrated to a light yellow solid. An 8 mL portion of Et_2O was added to yield a suspended white powder, which was collected on a sintered glass frit, washed with 2 mL of Et_2O, 2 mL of pentane, and dried on a high vacuum line to afford 0.3737 g of complex (0.8251 mmol, 82%). ^{1}H NMR (500 MHz, CD_3OD, δ from protio solvent): 3.92 (sept, $(H_3C)_2CHOH$, 1H, J = 6.2 Hz), 3.84 (br s, 2H), 3.70 (br s, 1H), 3.35 (m, 2H), 3.12 (m, 2H), 3.07 (d, 2H, J = 7.0 Hz), 2.90 (m, 4H), 2.61 (m, 7H), 2.49 (m, 2H), 1.15 (d, $(H_3C)_2CHOH$, J = 6.2 Hz, 5H). FTIR (KBr pellet) ν_{max} (cm^{-1}): 3421 (br m, ν_{OH} of ^{i}PrOH), 2951 (m), 2915 (m), 2837 (m), 2755 (w), 2708 (w), 2576 (w), 2101 (vw), 1934 (vw), 1653 (sh m), 1593 (vs, ν_{CO}), 1447 (s), 1404 (s), 1352 (m), 1328 (s), 1303 (m), 1284 (m), 1235 (vw), 1210 (vw), 1152 (m), 1112 (s), 1069 (m), 1031 (m), 1004 (m), 972 (s), 950 (m), 935 (m), 919 (s), 885 (vw), 873 (vw), 858 (w), 812 (vw), 792 (m), 767 (w), 745 (w), 689 (vw), 669 (vw), 659 (vw), 613 (w), 497 (m), 460 (w). LR-ESI-MS (*m/z*): $[M–Na]^-$ calcd for $C_{12}H_{22}N_3O_2S_2Zn$ (relative abundance), 368.0 (100.0), 370.0 (66.4), 372.0 (44.9), 371.0 (15.8), 369.0 (15.7), 373.0 (5.0), 374.0 (4.8); found, 367.9 (100.0), 369.9 (62.1), 371.8 (39.5), 370.9 (15.3), 368.9 (13.5), 372.8 (6.4), 373.8 (4.4). HR-ESI-MS (*m/z*): $[M-Na]^-$ calcd for $C_{12}H_{22}N_3O_2S_2Zn$ (relative abundance), 368.044

(100.0), 370.041 (66.4), 372.040 (46.0), 371.042 (15.8), 369.048 (13.0), 373.044 (5.0), 374.036 (3.5); found: 368.043 (100.0), 370.040 (67.7), 372.038 (43.5), 371.042 (14.0), 369.047 (13.1), 373.042 (4.6), 374.034 (3.4). Anal. Calcd for $C_{12}H_{22}N_3NaO_2S_2Zn•C_3H_8O$: C, 39.78; H, 6.68; N, 9.28. Found: C, 39.82; H, 6.88; N, 8.97.

4.5.4 Bulk oxidation of 4

To a dark-brown DMF solution (3 mL) of **4** (0.0734 g, 0.1901 mmol), was added a dark-blue DMF solution (2 mL + 2 mL to wash vial) of $FcPF_6$ (0.0625 g, 0.1888 mmol). After 1 h of stirring, black precipitates formed in the reaction mixture. The reaction was worked-up as depicted in Scheme 4.S1. The black ***DMF-insoluble*** material was identified as the trimetallic compound $[Ni\{Ni(N_3S_2^{NEM}\}_2]$ (**6**) (0.0473 g, 0.0603 mmol, 96% yield based on Scheme 4.2). Characterization: ^{1}H NMR (500 MHz, CD_2Cl_2, δ from protio solvent): 5.14 (br s, 4H), 4.90 (br s, 2H), 4.74 (br m, 2H), 4.12 (br s, 8H), 3.96 (br s, 5H), 3.84 (br s, 3H), 3.63 (m, 4H), 3.32 (br s, 2H), 3.08 (br s, 4H), 2.64 (br s, 4H), 2.43 (br s, 4H), 1.56 (br s, 2H). FTIR (KBr pellet) ν_{max} (cm^{-1}): 3448 (br vw), 2962 (w), 2926 (w), 2855 (w), 1670 (m, ν_{CO} from DMF), 1614 (vs, ν_{CO}), 1458 (w), 1405 (w), 1300 (vw), 1261 (m), 1115 (s), 1036 (m), 937 (vw), 861 (vw), 792 (m), 612 (vw), 587 (vw), 493 (w). UV-vis (CH_2Cl_2, RT, qualitative). Diffraction-quality crystals for **6** were obtained from this reaction (see details in X-ray section). The yellow ***DMF-soluble/Et$_2$O-soluble*** compound was identified as ferrocene (0.0252 g, 0.1355 mmol, 72% based on Scheme 4.2) Characterization: ^{1}H NMR (500 MHz, $CDCl_3$, δ from protio solvent): 4.17. ^{13}C NMR (125 MHz, $CDCl_3$, δ from protio solvent): 68.05. FTIR (KBr pellet) ν_{max} (cm^{-1}): 3439 (br, w), 3103 (vw), 3091 (vw), 3081 (vw), 2962 (w), 2920 (vw), 2849 (vw), 1670 (w), 1407 (m), 1261 (s), 1105 (vs), 1022 (s), 1001 (s), 814

(vs), 491 (s), 475 (s). The remaining products were next extracted with MeCN. The light-brown solid that was ***DMF-soluble/Et$_2$O-insoluble/MeCN-soluble*** was identified as a mixture of ligand disulfide and some unidentified Ni(II) complex with PF_6^- as counterion or $NaPF_6$ (both may also be present) (0.0378 g). Characterization: FTIR (KBr pellet) ν_{max} (cm^{-1}): 1670 (vs, ν_{CO}), 844 (vs, ν_{PF} of PF_6^-). The ^{1}H NMR showed a mixture of species (Figure 4.S23). LR-ESI-MS (*m/z*): cyclic disulfide via intramolecular thiolate oxidation = $[M+Na]^+$ calcd for $C_{12}H_{23}N_3NaO_2S_2$ (relative abundance), 328.1 (100.0), 329.1 (15.7), 330.1 (9.0), 331.1 (1.2). Found: 328.1 (100.0), 329.1 (16.7), 330.1 (10.3), 331.1 (2.4); intermolecular disulfide = $[2M+Na]^+$ calcd for $C_{24}H_{46}N_6NaO_4S_4$ (relative abundance), 633.2 (100.0), 634.2 (31.4), 635.2 (21.3), 636.2 (4.7). Found: 633.2 (100.0), 634.2 (32.5), 635.2 (24.2), 636.2 (7.1); $[2M+2H_2O+H^+]^+$ calcd for $C_{24}H_{51}N_6O_6S_4$ (relative abundance), 647.3 (100.0), 648.3 (31.4), 649.3 (22.5), 650.3 (4.7). Found: 647.2 (100.0), 648.2 (35.3), 649.2 (30.2), 650.2 (11.4). A UV-vis experiment was performed with the crown thioether 1,4,7-trithiacyclononane (9S3) to determine if any free Ni(II) ion was present in this mixture. The ***DMF-soluble/Et$_2$O-insoluble/MeCN-soluble*** brown solid (0.0378 g) was added to 1 mL of MeCN to yield a stock solution. A 500 uL aliquot of this stock was diluted with 2.5 mL of MeCN in a quartz cuvette to yield a final solution volume of 3 mL (0.0189 g of solid in 3 mL). The UV-vis of the solution was recorded at 25 °C and displayed bands consistent with **6** (λ = 447, 574 sh, and 713 nm). A solid batch of 9S3 (0.0088 g, 0.0488 mmol) was added to the cuvette and the UV-vis spectrum was recorded. No change was observed. An additional portion of 9S3 (0.0209 g, 0.1159 mmol) was added to the cuvette with still no change. The light-gray solid from the ***DMF-soluble/Et$_2$O-insoluble/MeCN-insoluble*** portion was identified as mixture of some Ni species and ligand (0.0154 g). Characterization: FTIR (KBr pellet) ν_{max} (cm^{-1}): 1617 (vs, ν_{CO}). The ^{1}H NMR in $CDCl_3$ showed a mixture of species.

{Ni[Ni($N_3S_2^{NEM}$)]$_2$} (**6**)

To a dark-brown DMF solution (2 mL) of **4** (0.0488 g, 0.1264 mmol) was added a 1 mL DMF solution of $[Ni(H_2O)_6](BF_4)_2$ (0.0216 g, 0.0635 mmol) dropwise over 1 min. The solution turned from red-brown to dark-brown and black precipitates appeared over several minutes. After 2 h stirring at RT, the insoluble material was collected via vacuum filtration and dried to yield 0.0423 g of complex **6** (0.0539 mmol, 85%). ^{1}H NMR (500 MHz, CD_2Cl_2, δ from protio solvent): 5.14 (br s, 4H), 4.90 (m, 2H), 4.69 (m, 4H), 4.12 (br s, 8H), 3.96 (br s, 6H), 3.83 (br s, 4H), 3.57 (m, 4H), 3.32 (br s, 2H), 3.08 (m, 2H), 2.59 (m, 4H), 2.37 (m s, 4H). FTIR (KBr pellet) ν_{max} (cm^{-1}): 2961 (w), 2926 (w), 2887 (w), 2855 (w), 2839 (m), 1671 (m, ν_{CO} from DMF), 1612 (vs, ν_{CO}), 1456 (m), 1403 (m), 1379 (vw), 1356 (vw), 1300 (w), 1254 (w), 1209 (vw), 1161 (vw), 1143 (vw), 1115 (s), 1092 (w), 1068 (w), 1047 (w), 1036 (w), 998 (vw), 952 (vw), 937 (w), 915 (vw), 861 (w), 819 (w), 791 (m), 768 (w), 684 (vw), 659 (vw), 612 (vw), 588 (vw), 494 (vw), 455 (w), 417 (vw). LR-ESI-MS (*m/z*): $[M+H]^+$ calcd for $C_{24}H_{45}N_6Ni_3O_4S_4$ (relative abundance), 785.0 (100.0), 783.0 (74.8), 787.0 (64.2), 786.0 (34.3), 789.0 (26.0), 784.0 (23.5), 788.0 (19.7). Found: 784.9 (100.0), 782.8 (66.5), 786.8 (44.0), 785.9 (39.2), 788.8 (31.8), 783.8 (22.2), 787.8 (20.5); $[M+Na]^+$ calcd for $C_{24}H_{44}N_6NaNi_3O_4S_4$ (relative abundance), 807.0 (100.0), 805.0 (73.1), 809.0 (64.1), 808.0 (33.6), 811.0 (26.2), 806.0 (23.0), 810.0 (19.3); found: 806.8 (100.0), 804.8 (80.7), 808.8 (69.8), 807.8 (43.4), 810.8 (23.2), 805.8 (24.2), 809.8 (29.0); $[M+K]^+$ calcd for $C_{24}H_{44}KN_6Ni_3O_4S_4$ (relative abundance), 823.0 (100.0), 821.0 (69.7), 825.0 (66.5), 824.0 (33.4), 827.0 (27.6), 822.0 (21.9), 826.0 (19.9); found: 822.8 (100.0), 820.8 (76.7), 824.8 (90.7), 823.8 (35.6), 826.8 (38.2), 821.8 (27.2), 825.9 (31.8); UV-vis (MeOH, 25 °C), λ_{max}, nm (ε, M^{-1} cm^{-1}): 320 (14000), 358 sh (5100), 448 (3300), 550 sh (2300), 688 sh (1100). Anal. Calcd for $C_{24}H_{44}N_6Ni_3O_4S_4$: C, 36.72; H, 5.65; N, 10.71. Found: C, 36.51; H, 5.70; N, 10.71.

{Ni[Ni($N_3S_2^{NEM}$)]$_2$}•2($B(C_6F_5)_3$) (**7**)

To a light-brown slurry of **4** (0.1098 g, 0.2844 mmol) in 10 mL of CH_2Cl_2, was added a CH_2Cl_2 (2 mL) light-yellow solution of tris(pentafluorophenyl)borane = $B(C_6F_5)_3$ (0.1464 g, 0.2859 mmol) to yield a dark-brown solution within 1 min. After 1 h of stirring at RT, the brown insoluble solid (0.0602 g) was collected via vacuum filtration and washed with CH_2Cl_2 (3 × 2 mL). The black filtrate was concentrated to a solid, to which 5 mL of Et_2O was added to yield a black solution with black precipitates. The Et_2O-insoluble solid (0.0650 g, 0.0359 mmol, 38%) was collected via vacuum filtration and washed with Et_2O (3 × 2 mL) and dried and determined to be the trimetallic compound {Ni[Ni($N_3S_2^{NEM}$)]$_2$}•2$B(C_6F_5)_3$ (**7**). The Et_2O-soluble filtrate was concentrated to a dark brown solid (0.1323 g). The ***CH_2Cl_2-insoluble*** portion is most consistent with unreacted **4** with potential coordinated $B(C_6F_5)_3$ based on the IR signal at 1463 cm^{-1} Characterization of ***CH_2Cl_2-soluble/Et_2O-soluble*** portion: ^{19}F NMR (376 MHz, CD_2Cl_2, δ from $CFCl_3$): -137.70, -138.02, -158.62, -159.26, -163.49, -163.85. ^{11}B NMR (128 MHz, CD_2Cl_2, δ from externally referenced BF_3•Et_2O): -2.16, -3.81, -11.08. FTIR (KBr pellet) ν_{max} (cm^{-1}): 3441 (br vw), 2961 (vw), 1646 (m), 1517 (s), 1462 (vs), 1364 (vw), 1278 (m), 1087 (s), 976 (s), 921 (m), 857 (vw), 810 (vw), 771 (m), 764 (m), 744 (vw), 694 (m), 671 (m), 621 (vw), 606 (vw), 576 (vw), 480 (vw), 425 (vw), 413 (vw). Characterization of **7** (***CH_2Cl_2-soluble/Et_2O-insoluble***): ^{1}H NMR (500 MHz, CD_2Cl_2, δ from protio solvent): 63.79 (br s), 51.38 (br s), 27.28 (br s), 26.44 (br s), 25.87 (br s), 25.31 (br s), 23.89 (br s), 22.87 (br s), 19.50 (br s), 16.44 (br s), 14.53 (br s), 12.94 (br s), 12.14 (br s). ^{19}F NMR (376 MHz, CD_2Cl_2, δ from $CFCl_3$): -133.78, -157.94, -163.92. ^{11}B NMR (128 MHz, CD_2Cl_2, δ from externally referenced BF_3•Et_2O): 12.33, -4.19. FTIR (KBr pellet) ν_{max} (cm^{-1}): 3445 (br vw), 2930 (w), 2869 (w), 1628 (s, ν_{CO}), 1517 (s), 1468 (vs), 1412 (m), 1380 (m), 1312 (w), 1282 (m), 1215 (vw), 1095 (s), 1044 (w), 980 (s), 937 (w), 879 (w), 794 (m), 765

(w), 750 (w), 694 (w), 674 (w), 609 (vw), 576 (vw). Anal. Calcd for $C_{60}H_{44}B_2F_{30}N_6Ni_3O_4S_4$: C, 39.84; H, 2.45; N, 4.65. Found: C, 39.51; H, 2.50; N, 4.65

4.5.5 General Reaction of 4 with O_2 (air), $O_2^{\bullet-}$, and N_3^-

All reactions of **4** with O_2 (air), NaN_3, KO_2 (solubilized with 18C6 in some cases) were performed in quartz UV–vis cuvettes and monitored by UV–vis spectroscopy and/or LR-ESI-MS under anaerobic conditions MeOH at 25 °C.

*Reaction of **4** and O_2 (air) in MeOH*

A 100 μL aliquot from 30.6 mM stock of **4** in MeOH was added to a cuvette containing 3000 μL of MeOH to yield a solution of **4** with the final concentration of 0.987 mM. The cuvette was exposed to ambience air for 1 min then closed back up. The difference spectra in UV-vis was recorded immediately and monitor for 14 hours at 30 min interval. LR-ESI-MS was recorded at 14-hour mark.

*Reaction of **4** and KO_2 (1 mol-equiv and 10 mol-equiv) in MeOH*

A 50 μL aliquot (1 mol-equiv) of a 66 mM DMSO solution of KO_2 (containing 84 mM of 18C6) was added to a cuvette containing **4** (3100 μL, 0.987 mM) to yield a final concentration of 1.05 mM for KO_2 and 0.971 mM for **4**. The UV–vis spectrum was recorded immediately and monitored at 30 min interval for 13 h. LR-ESI-MS was recorded at 13-hour mark.

A 500 μL aliquot (10 mol-equiv) of a 66 mM DMSO solution of KO_2 (containing 84 mM of 18C6) was added to a cuvette containing **4** (3100 μL, 0.987 mM) to yield a final concentration

of 9.17 mM for KO_2 and 0.850 mM for **4**. The UV–vis spectrum was recorded immediately and recorded again after 24 h.

*Reaction of **4** and NaN_3 (1 mol-equiv and 10 mol-equiv) in MeOH*

A 10 μL aliquot (10 mol-equiv) of a 272 mM stock solution of NaN_3 in MeOH was added to a cuvette containing **4** (3100 μL, 0.877 mM) to yield a final concentration of 0.875 mM of **4** and 0.875 mM of NaN_3. The UV-vis spectrum was recorded immediately and monitored at 30 min interval for 18 h.

A 100 μL aliquot (10 mol-equiv) of a 272 mM stock solution of NaN_3 in MeOH was added to a cuvette containing **4** (3100 μL, 0.877 mM) to yield a final concentration of 0.850 mM of **4** and 8.50 mM of NaN_3. The UV-vis spectrum was recorded immediately and monitored at 30 min interval for 18 h.

4.5.6 AR-HRP Assay for H_2O_2 Detection

The AR-HRP assay was prepared using the protocol described by Haugland and co-workers.[71] Milli-Q grade water (18.0 MΩ cm) was used to prepare 50 mM HEPES (pH 7.4) buffer, which was treated with Chelex 100 for 24 h to remove trace metals. The experiments were monitored by UV-vis. The stock solutions for **4**, **6**, and **KO_2** were prepared anaerobically with degassed solvents. Solid samples of **4** and **6** were dissolved in MeOH to yield 480 μM and 240 μM stock solutions, respectively. A 160 μM stock solution of KO_2 in DMSO was prepared in a 10-mL volumetric flash (containing 345 μM of 18C6). As AR and HRP are stable to air, all solutions for the standard curve were prepared under aerobic conditions. A 100 μM solution of AR

was prepared by diluting aliquots of a 10 mM stock of AR in DMSO (stored at −20 °C) with HEPES. A stock solution of HRP was prepared by dissolving the powdered HRP into HEPES to yield a 10 U/mL HRP stock solution. The blank consisted of a 3.000 mL solution of 10 μM AR and 1 U/mL HRP in HEPES. Due to the air sensitivity of **2**, all solutions were prepared with degassed solvents. The reaction mixture contained a total volume of 3.000 mL with 10 μM of AR, 1 U/mL of HRP, 8 μM of KO_2/18C6 (1:2), and 8 μM of **4** or 4 μM of **6**. The UV-vis spectra of the aforementioned mixture was compared to a control sample with no complex: i.e., 3 μM KO_2/18C6 (1:1) with 10 μM of AR and 1 U/mL of HRP.

4.5.7 Computational Details

Density functional theory (DFT) calculations were performed with the ORCA electronic structure package, version 3.0.3.[75] Geometry optimization and frequency analysis of all models were performed using the BP86 functional[76,77] along with resolution of the identity (RI) approximation[78] and Grimme's D3(BJ) dispersion correction[79,80] with coordinates from the crystal structures of **1**·DAA and **2**. Ahlrich's triple-ζ basis set def2-TZVPP[81,82] and the auxiliary basis set def2-TZVPP/J were selected for all atoms. The integration grid was set at GRID5 with NOFINALGRID. No imaginary frequencies were found. Natural population analysis (NPA) charges on the optimized structures of **4***, **4^{ox}***, **6***, and **6^{ox}*** were obtained from the program JANPA.[83]

Single-point energy (SPE) calculations were performed on the optimized structures using the OLYP functional (OPTX exchange functional of Cohen and Handy[84] coupled with Lee, Yang, and Parr's correlation functional[85]) with RI approximation.[78] Ahlrich's triple-ζ basis set def2-

TZVPP[81,82] and the auxiliary basis set def2-TZVPP/J were selected for all atoms. The integration grid was set at GRID5 with FINALGRID7. The conductor-like screening model (COSMO)[86] was utilized to model solvent environments of DMF (ε = 38.3, n = 1.430). UCSF Chimera[87] was used to generate model structures and to visualize isosurface plots of MOs with isodensity values of 0.05. Spin density plot for **4^{ox*}** and **6^{ox*}** were visualized with isodensity values of 0.0015 and 0.002 a.u., respectively.

4.5.8 X-ray Crystallographic Data Collection and Structure Solution and Refinement

Red plates of **4** with the acetone self-condensation product diacetone alcohol ($C_6H_{12}O$ = DAA; **4**•DAA) were grown by slow diffusion (2 weeks) of Et_2O into a saturated solution of **4** in acetone/MeOH (4:1) at -20 °C. Slow diffusion (3 weeks) of Et_2O into a saturated solution of **5** in ^{i}PrOH at -25 °C yielded clear prism crystals of **5**•^{i}PrOH. Dark-red needles of **6**•4MeOH were obtained by slow diffusion (12 days) of Et_2O into a saturated solution of **6** in MeOH/CH_2Cl_2 (1:1) solution at RT. Dark-brown plates of **7** were obtained by slow evaporation (19 days) of a saturated solution of **7** in CH_2Cl_2. Suitable crystals of **4**•DAA, **6**•4MeOH, and **7** were mounted on a glass fiber. For **4**•DAA, **6**•4MeOH, and **7**, the X-ray intensity data were measured at 100 K on a Bruker D8 Quest PHOTON 100 CMOS X-ray diffractometer system with Incoatec Microfocus Source (IμS) monochromated MoKα radiation (λ = 0.71073 Å, sealed tube) using phi and omega-scan technique. The data were corrected for Lorentz and polarization effects and integrated with the manufacturer's SAINT software. Absorption corrections were applied with the program SADABS.[88] Subsequent solution and refinement was performed using the SHELXTL-2014[89,90] solution package operating on a Pentium computer. The structure was solved by direct methods

using the SHELXTL-2014 software package. Non-hydrogen atomic scattering factors were taken from the literature tabulations.[91] Non-hydrogen atoms were located from successive difference Fourier map calculations.

To eliminate the complications encountered due to a disordered water molecule in the structure of **4**•DAA, after the initial solution and refinement, the structure was re-refined with data obtained after the SQUEEZE operation provided within the PLATON program.[92]

For **5**·^{i}PrOH, The crystal was mounted in the 100 K nitrogen cold stream provided by an Oxford Cryostream low temperature apparatus on the goniometer head of a Bruker D8 Venture Kappa DUO diffractometer equipped with Bruker Photon 100 CMOS detector. Data were collected with the use of CuKα (λ = 1.54178 Å) microsource. A multi-scan absorption correction was applied with the program SADABS.[93] The structure was solved by a dual space method, (SHELXT)[94] and refined by full-matrix least-squares on F^2 (SHELXL-2017).[95] During refinement the O-H distance was restrained to 0.90(2) Å.

For **6**•4MeOH, the non-hydrogen atoms were refined in anisotropic displacement parameters. Except for two hydrogen atoms (H(3)) bonded with O(3) and H(4)) bonded with O(4)) located from difference Fourier map and refined with proper restraints, the rest of hydrogen atom positions were calculated and allowed to ride on the carbon to which they are bonded assuming a C–H bond length of m Å (m = 0.990 for CH_2 groups, m = 0.980 for CH_3 groups). Hydrogen atom temperature factors were fixed at n (n = 1.2 for CH_2 groups, n = 1.5 for CH_3 groups) times the isotropic temperature factor of the C-atom to which they are bonded.

For **7**, data reduction was performed using the *SAINT* (Bruker, V8.37A)[96] software, which corrects for Lorentz and polarization effects. The final completeness is 99.4% out to 36.479° in θ. A multi-scan absorption correction was performed using SADABS 2016/2.[93] The absorption coefficient μ of this complex is 1.268 mm^{-1} and the minimum and maximum transmissions are

0.5580 and 0.7471.the structure was solved in the space group P-1 (#2) by intrinsic phasing using the ShelXT[94] structure solution program and refined by Least Squares using ShelXL[95] embedded within the Olex2 graphical user interface.[97] All non-hydrogen atoms were refined anisotropically. Hydrogen atom positions were calculated geometrically and refined using the riding model. The value of Z' in the present case is 0.5. This means that only half of the formula unit is present in the asymmetric unit, with the other half consisting of symmetry equivalent atoms.

Selected data and metric parameters for these complexes are summarized in Table 4.2 and Table 4.S1. in the SI.

4.6 Supporting Information

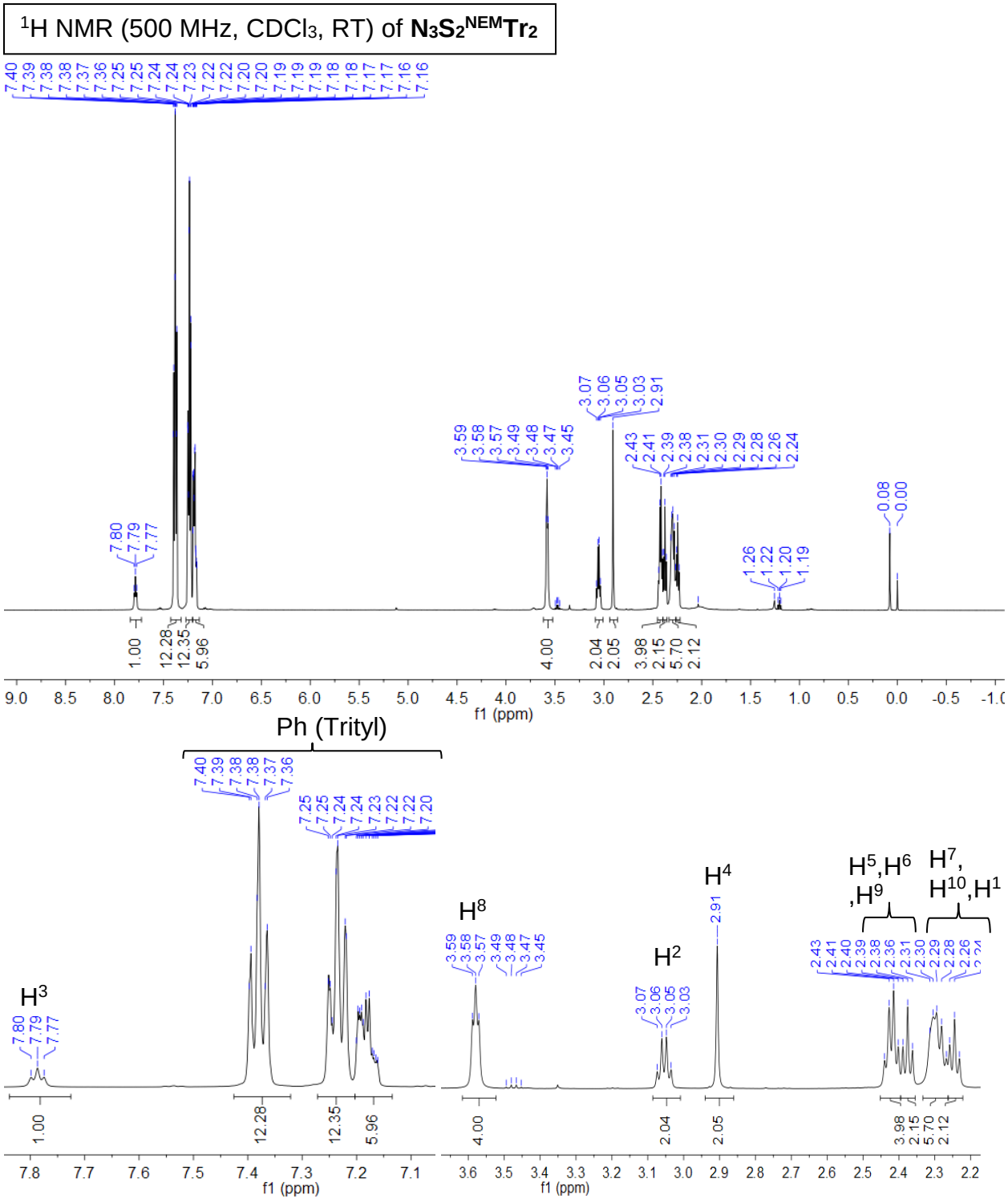

Figure 4.S1 *Top*: ^{1}H NMR spectrum of $N_3S_2^{NEM}Tr_2$ in $CDCl_3$ containing 0.05% v/v TMS at RT (δ vs. TMS). Trace amount of grease (0.08 ppm), EtOAc (1.20, 2.04, and 3.48 ppm), and water (1.26 ppm) are also present. *Bottom*: expansion of aromatic and aliphatic regions.

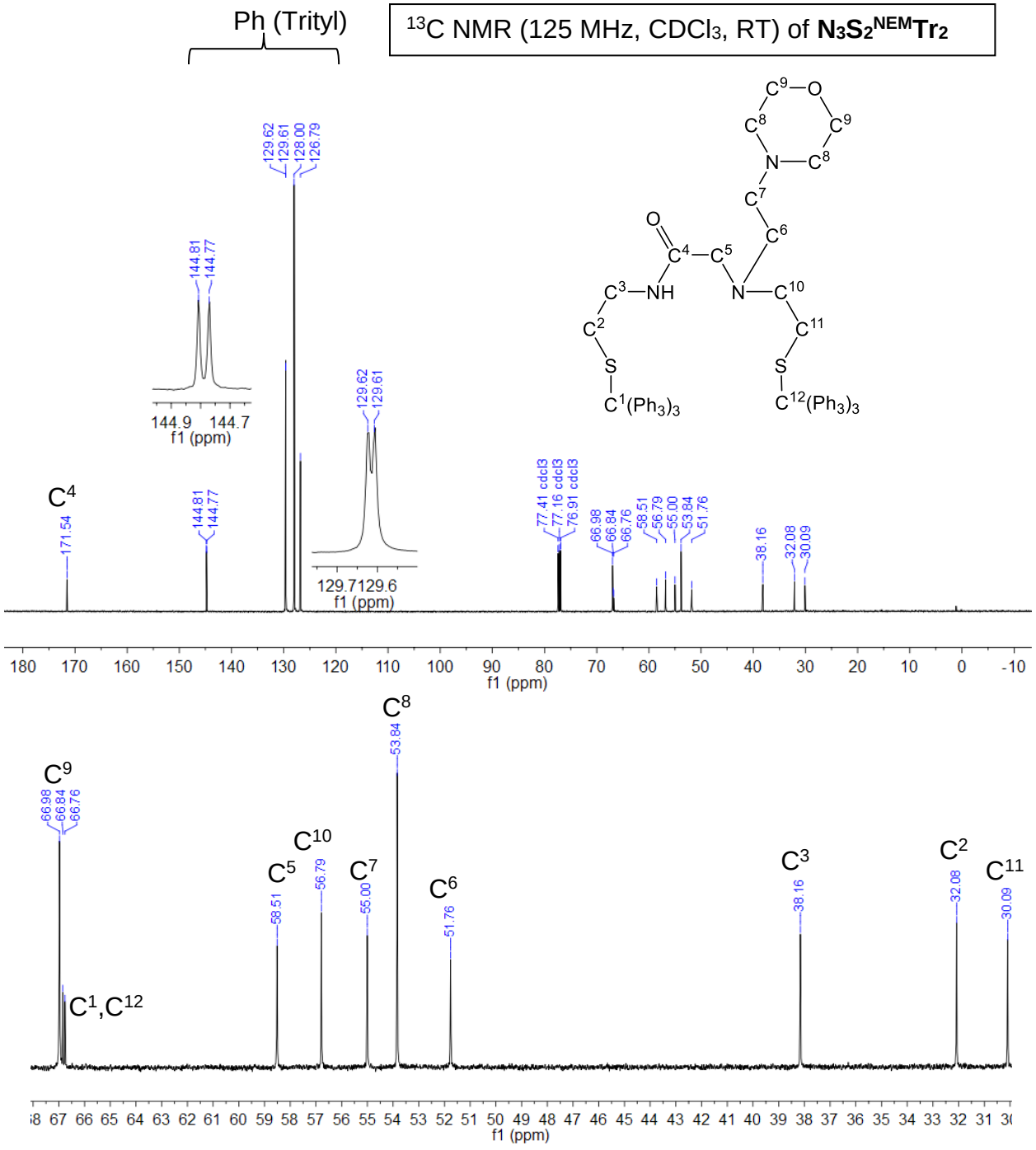

Figure 4.S2 *Top*: ^{13}C NMR spectrum of $N_3S_2^{NEM}Tr_2$ in $CDCl_3$ containing 0.05% v/v TMS at RT (δ vs. protio solvent). *Bottom*: expansion of the 127-172 ppm (left) and expansion of 30-68 ppm (right).

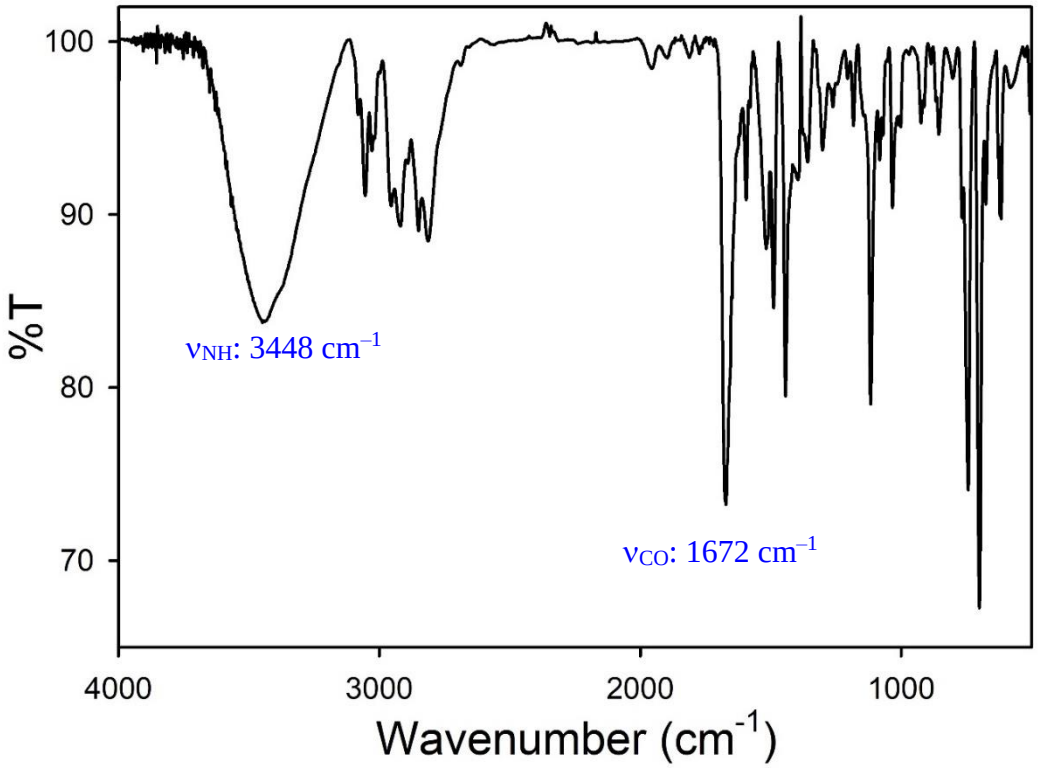

Figure 4.S3 Solid-state FTIR spectrum of $N_3S_2^{NEM}Tr_2$ in a KBr matrix at RT.

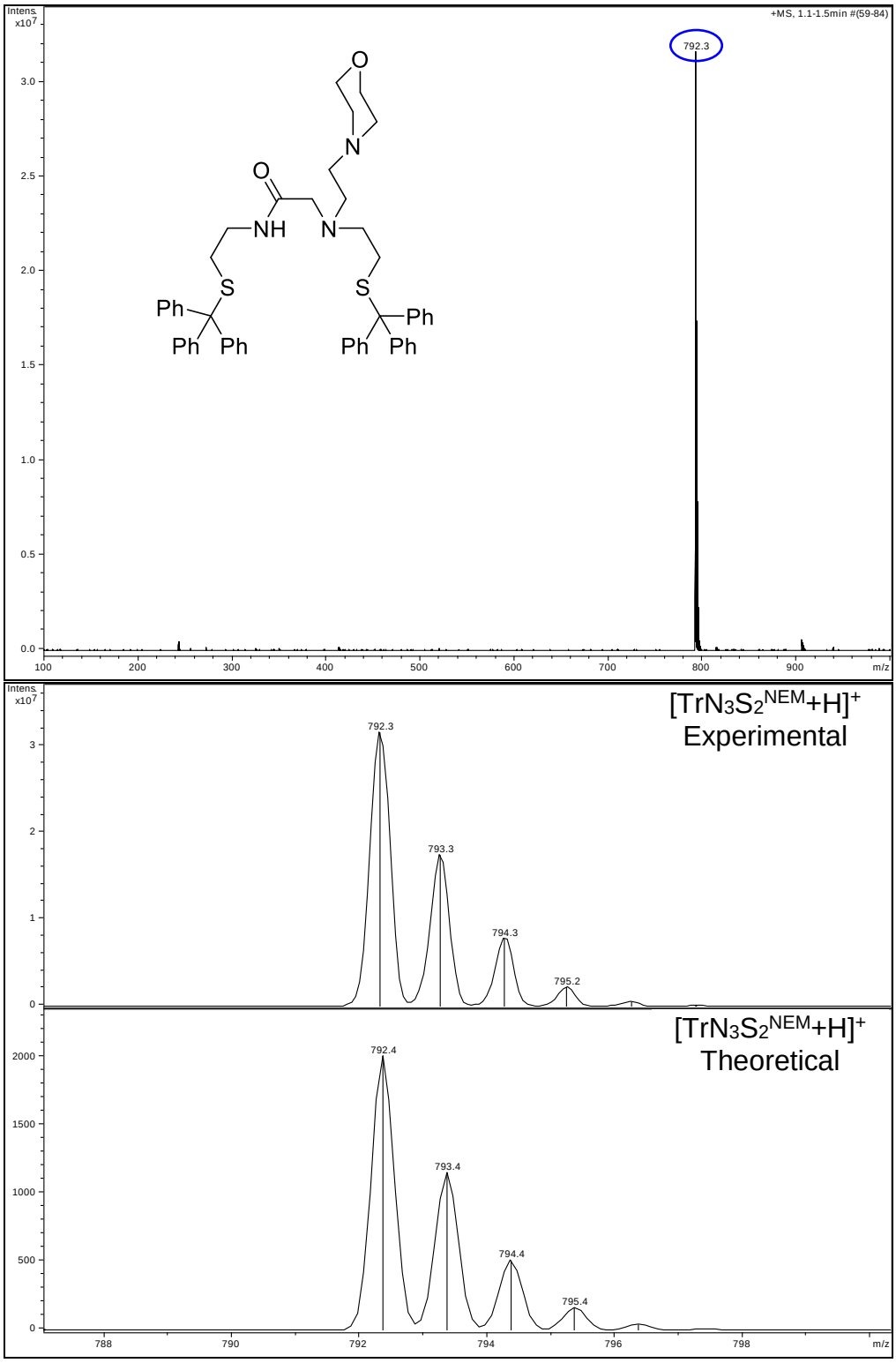

Figure 4.S4 *Top*: LR-ESI-MS(+) of $[N_3S_2{}^{NEM}Tr_2+H]^+$. *Bottom*: experimental versus theoretical isotopic distribution of $[N_3S_2{}^{NEM}Tr_2+H]^+$.

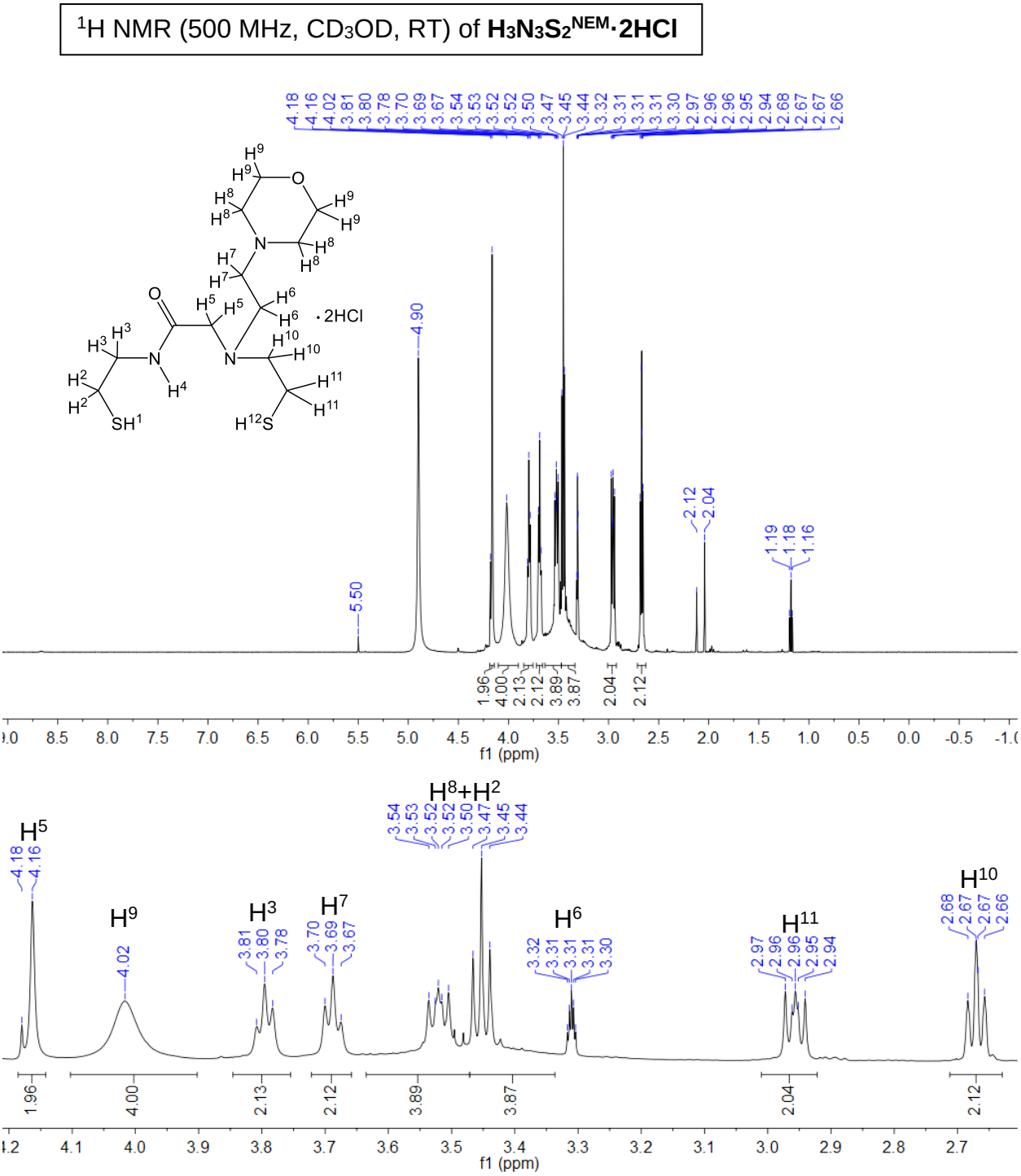

Figure 4.S5 *Top*: ^{1}H NMR spectrum of $H_3N_3S_2^{NEM}$·2HCl in CD_3OD at RT (δ vs. protio solvent). Trace amount of Et_2O (1.18 ppm and 3.49 ppm), CH_2Cl_2 (5.50 ppm), CH_3CN (2.04 ppm), and acetone (2.12 ppm) are also present. *Bottom*: expansion of 2.6–4.2 ppm region.

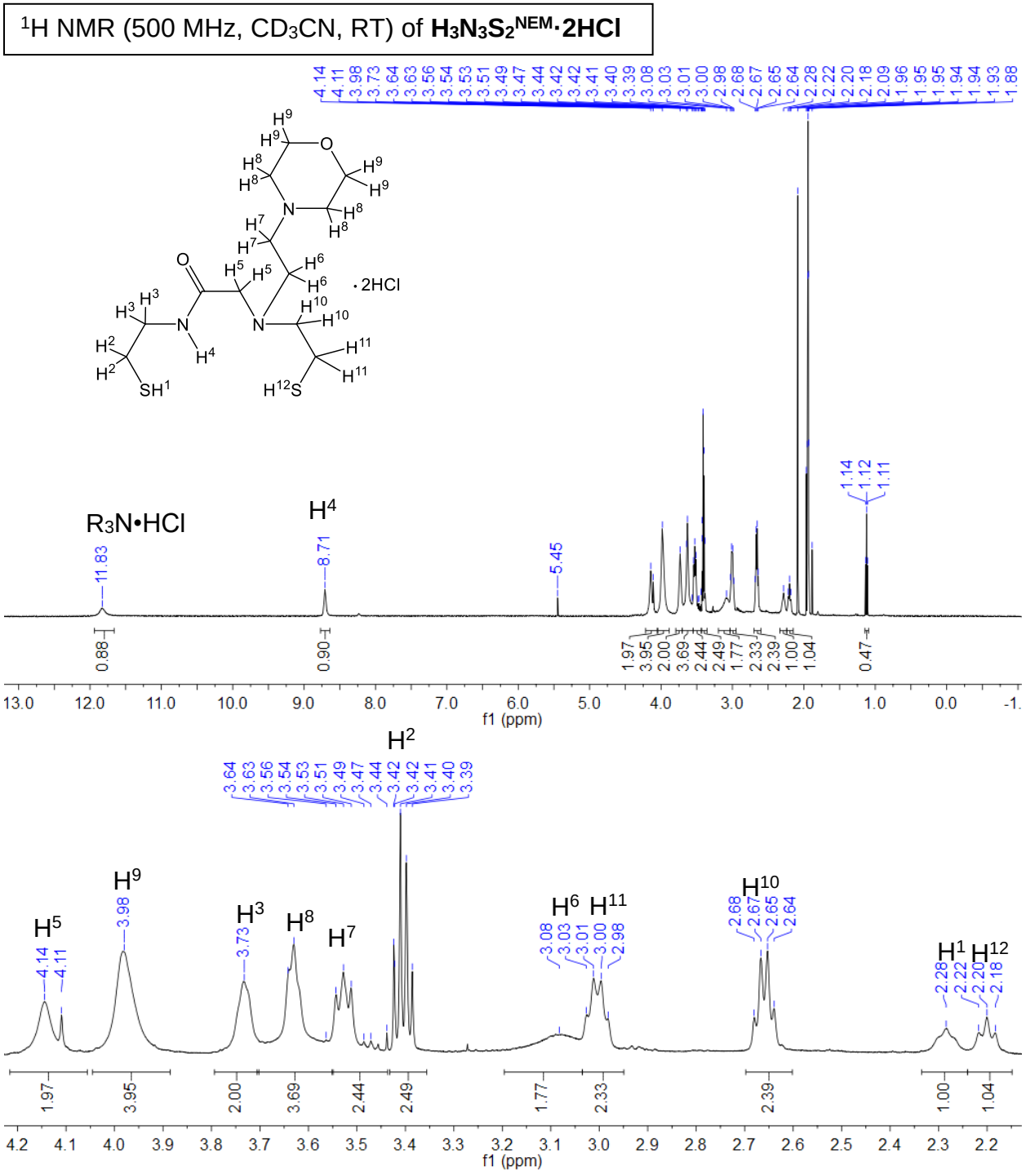

Figure 4.S6 *Top*: ^{1}H NMR spectrum of $H_3N_3S_2^{NEM}$·2HCl in CD_3CN at RT (δ vs. protio solvent). Trace amount of Et_2O (1.12 ppm and 3.42 ppm), CH_2Cl_2 (5.45 ppm), and CH_3CN (1.96 ppm) are also present. *Bottom*: expansion of 2.1–4.2 ppm region.

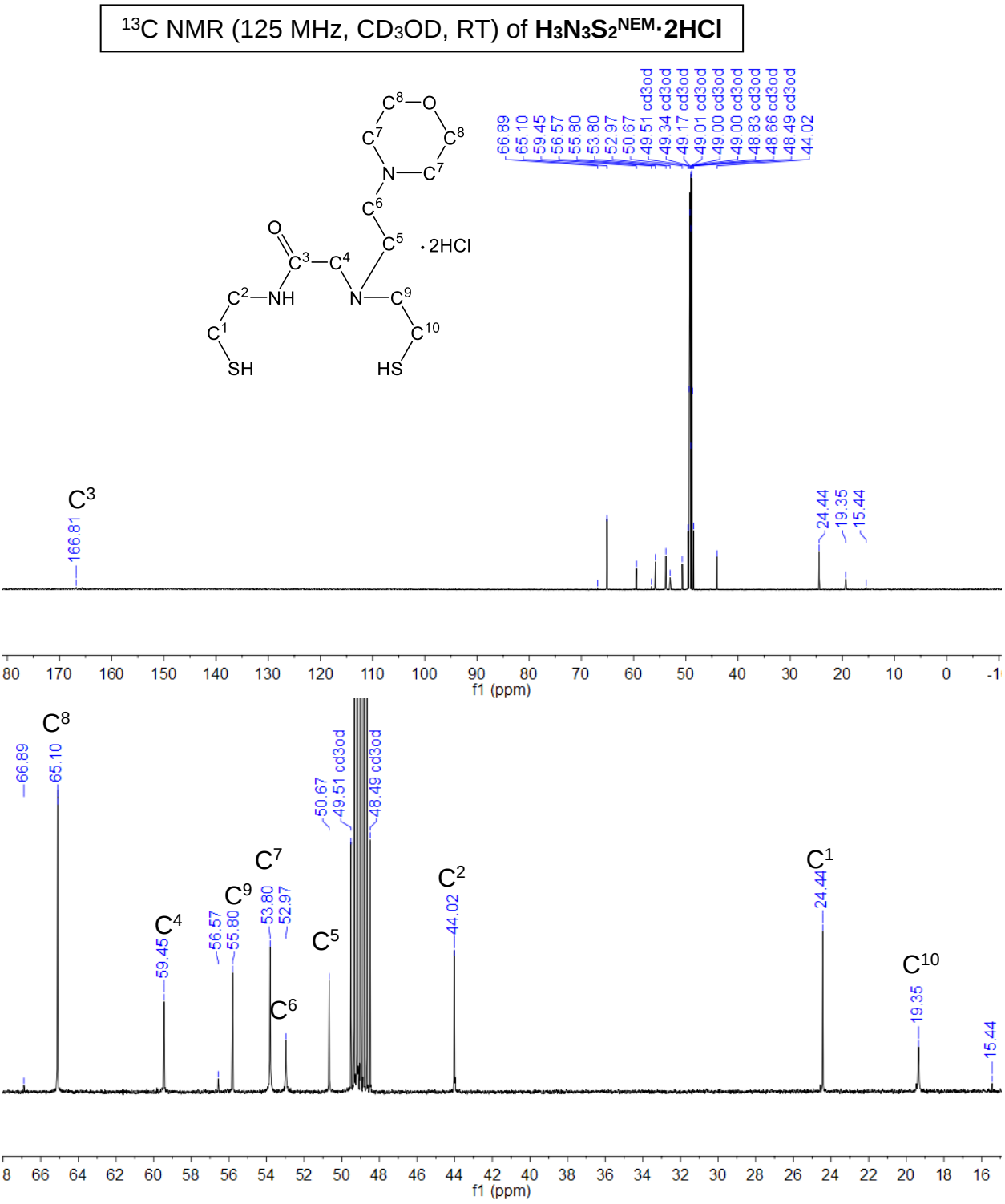

Figure 4.S7 *Top*: ^{13}C NMR spectrum of $H_3N_3S_2^{NEM}\cdot 2HCl$ in CD_3OD at RT (δ vs. protio solvent). Trace amount of Et_2O (15.44 ppm and 66.89 ppm) and CH_2Cl_2 (56.57 ppm) are also present. *Bottom*: expansion of 15–68 ppm region.

^{13}C NMR (125 MHz, CD_3CN, RT) of **$H_3N_3S_2^{NEM}$·2HCl**

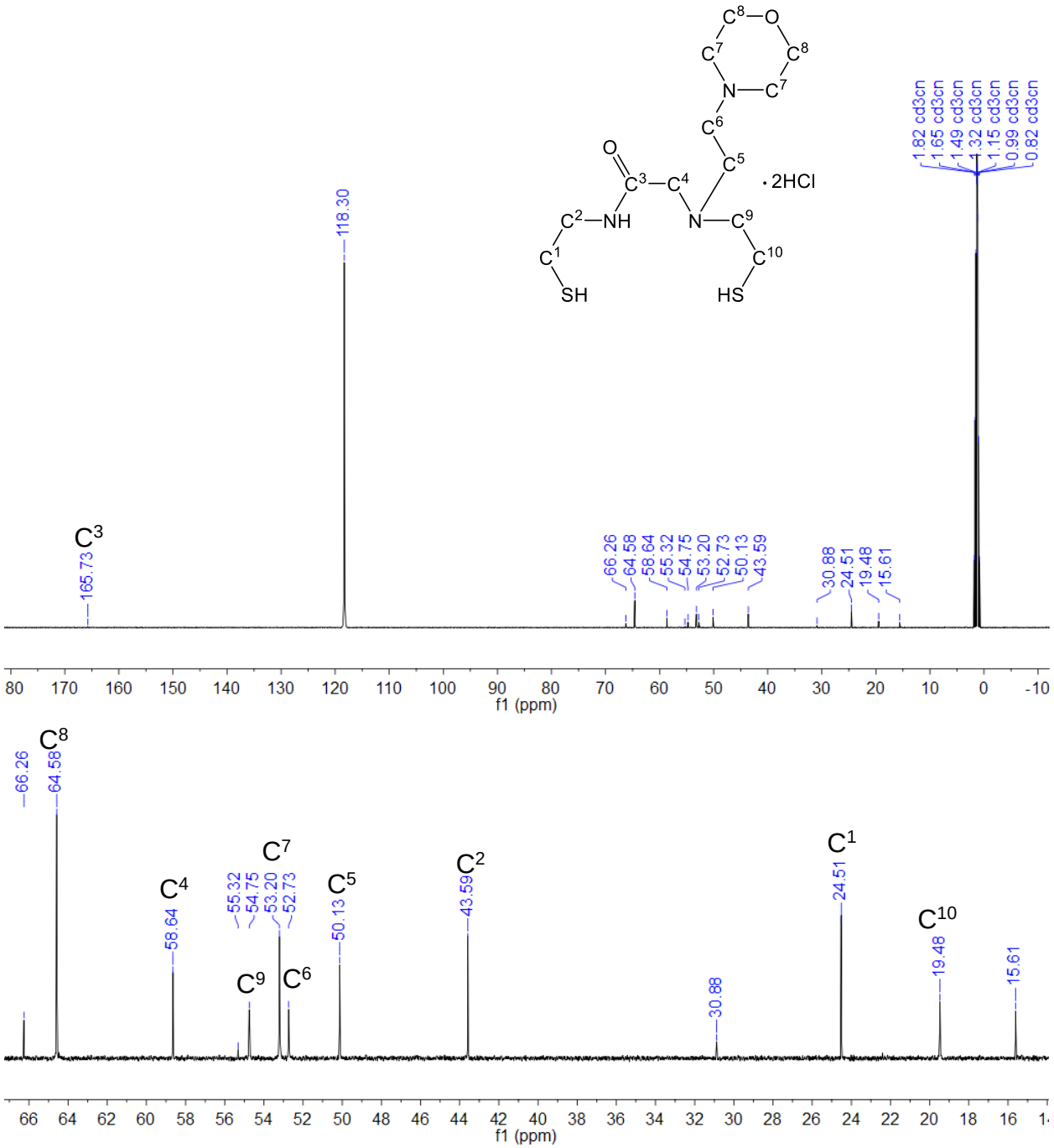

Figure 4.S8 *Top*: ^{13}C NMR spectrum of $H_3N_3S_2^{NEM}$·2HCl in CD_3CN at RT (δ vs. protio solvent). Trace amount of Et_2O (15.61 ppm and 66.26 ppm), acetone (30.88 ppm), and CH_2Cl_2 (55.32 ppm) are also present. *Bottom*: expansion of 14–69 ppm region.

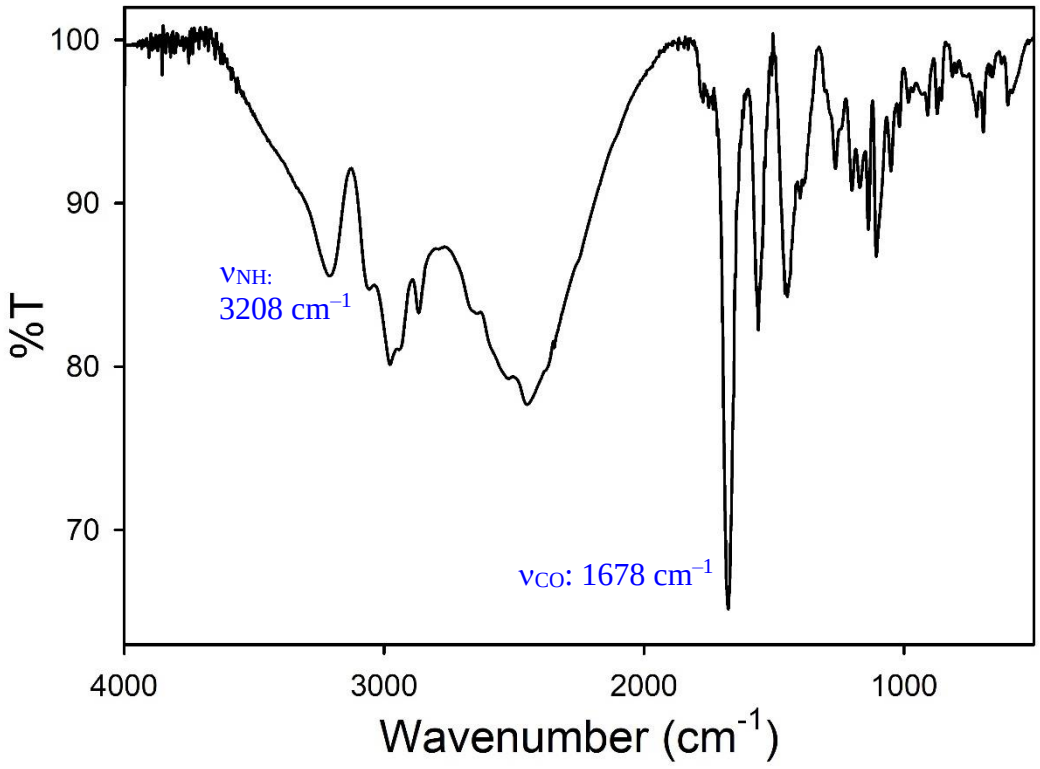

Figure 4.S9 Solid-state FTIR spectrum of $H_3N_3S_2^{NEM}\cdot 2HCl$ in a KBr matrix at RT.

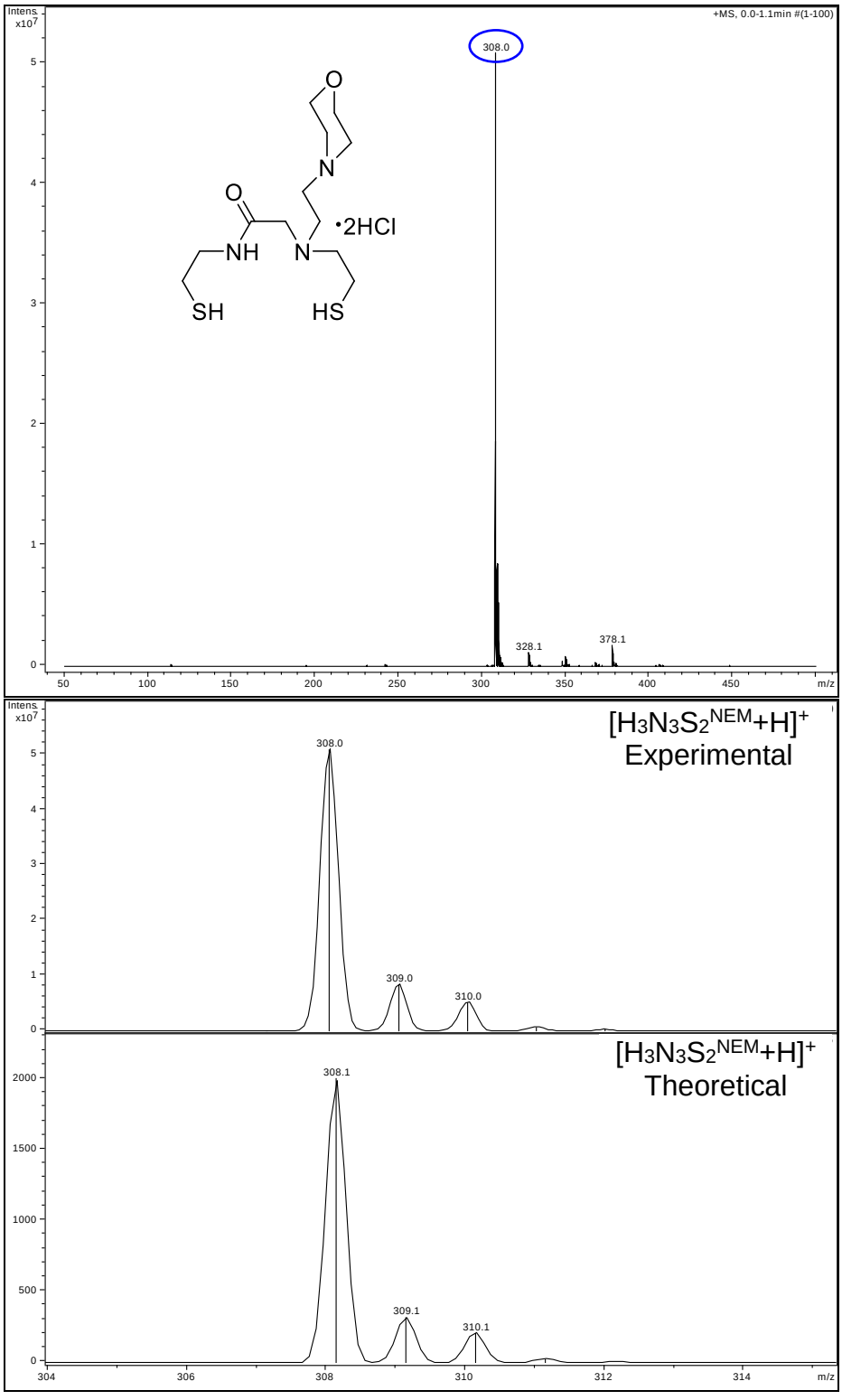

Figure 4.S10 *Top*: LR-ESI-MS(+) of $[H_3N_3S_2^{NEM}+H]^+$. *Bottom*: experimental versus theoretical isotopic distribution of $[H_3N_3S_2^{NEM}+H]^+$.

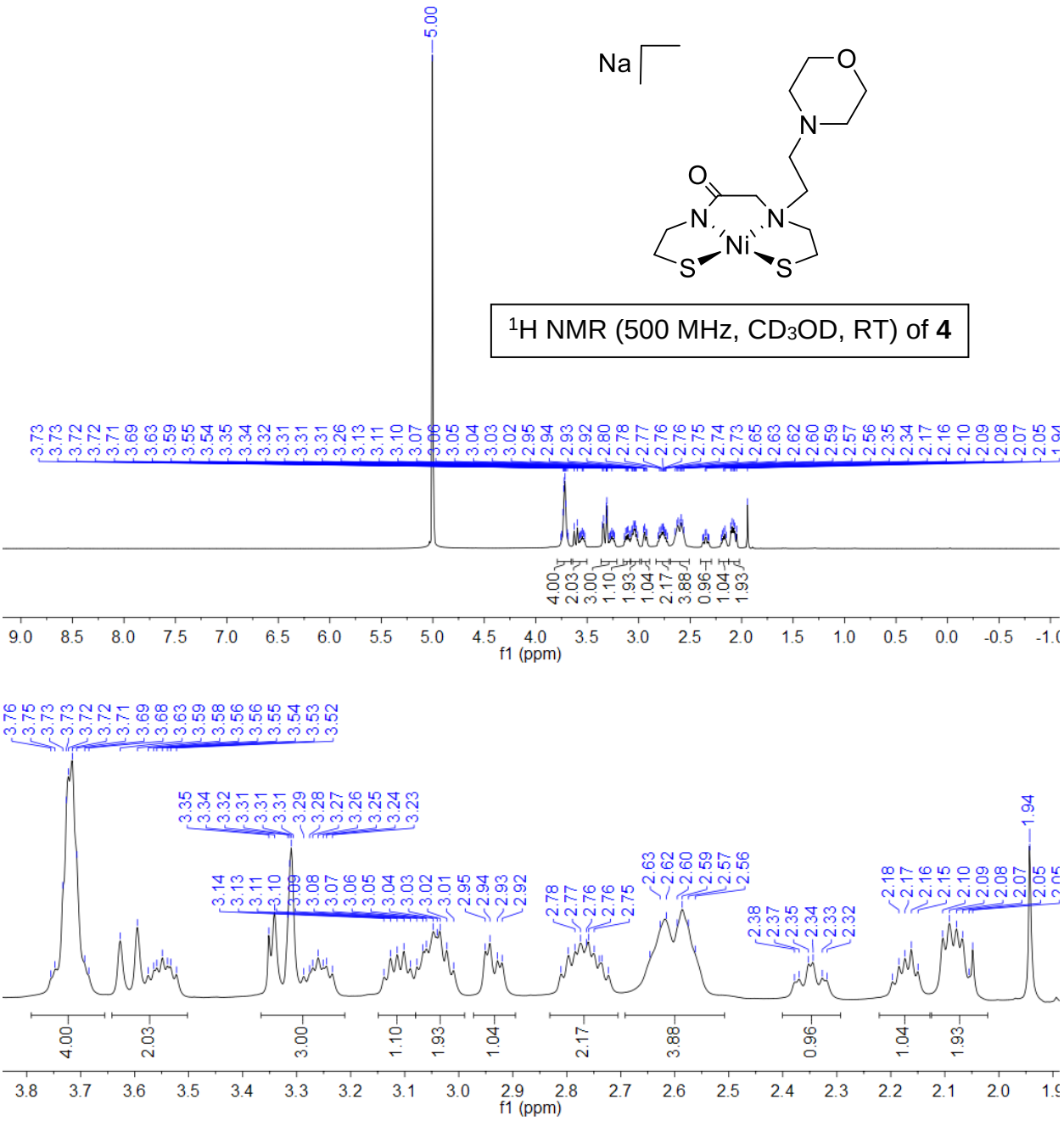

Figure 4.S11 *Top*: ^{1}H NMR spectrum of Na[Ni($N_3S_2^{NEM}$)] (**4**) in CD_3OD at RT (δ vs. protio solvent). Trace amount of MeCN (1.941 ppm) is also present. *Bottom*: expansion of the 1.5-3.9 ppm region.

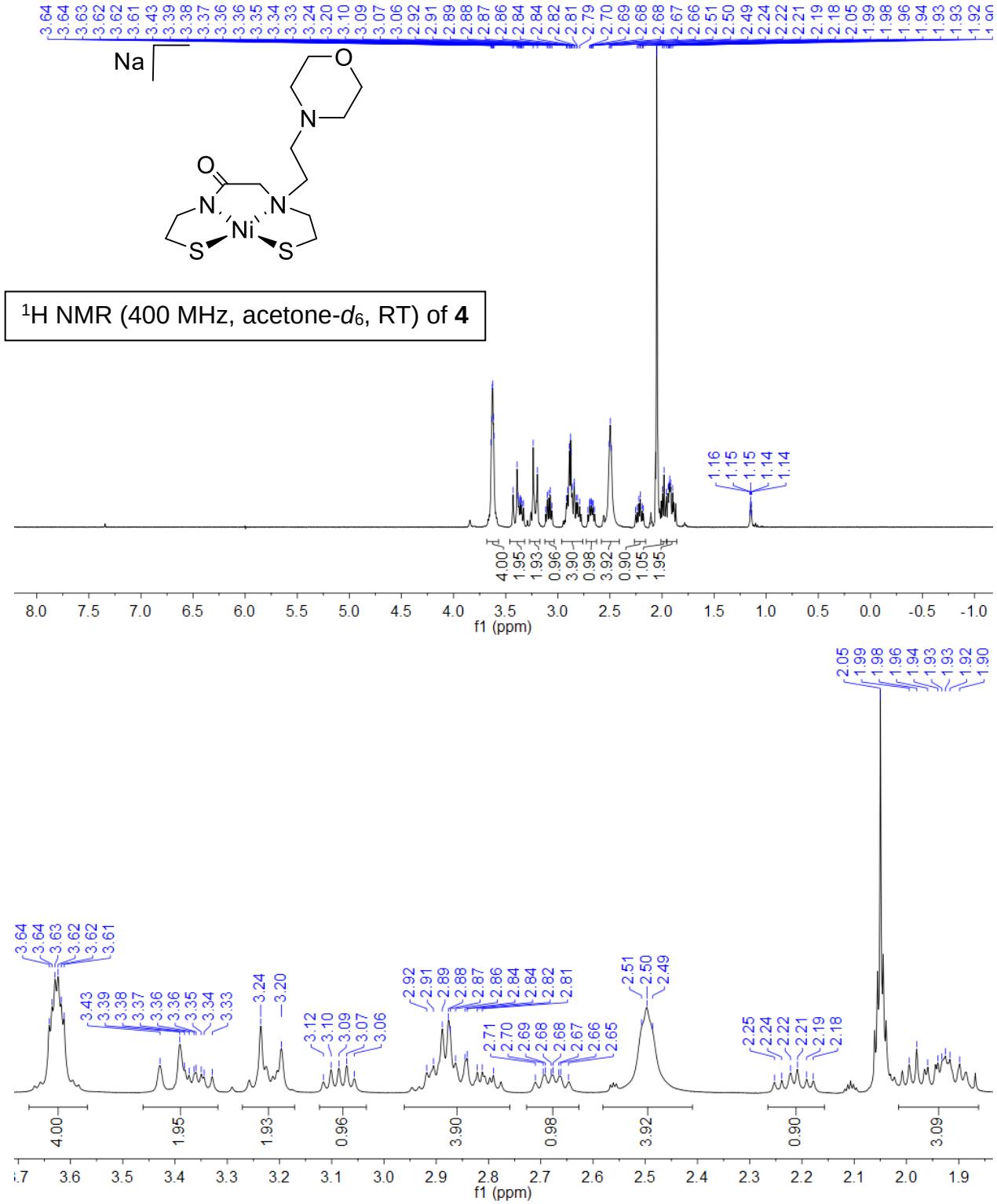

Figure 4.S12 *Top*: ^{1}H NMR spectrum of Na[Ni($N_3S_2^{NEM}$)] (**4**) in acetone-d_6 at RT (δ vs. protio solvent). Trace amount of Et_2O (1.15 and 3.41 ppm) is also present. *Bottom*: expansion of the 1.8-3.7 ppm region.

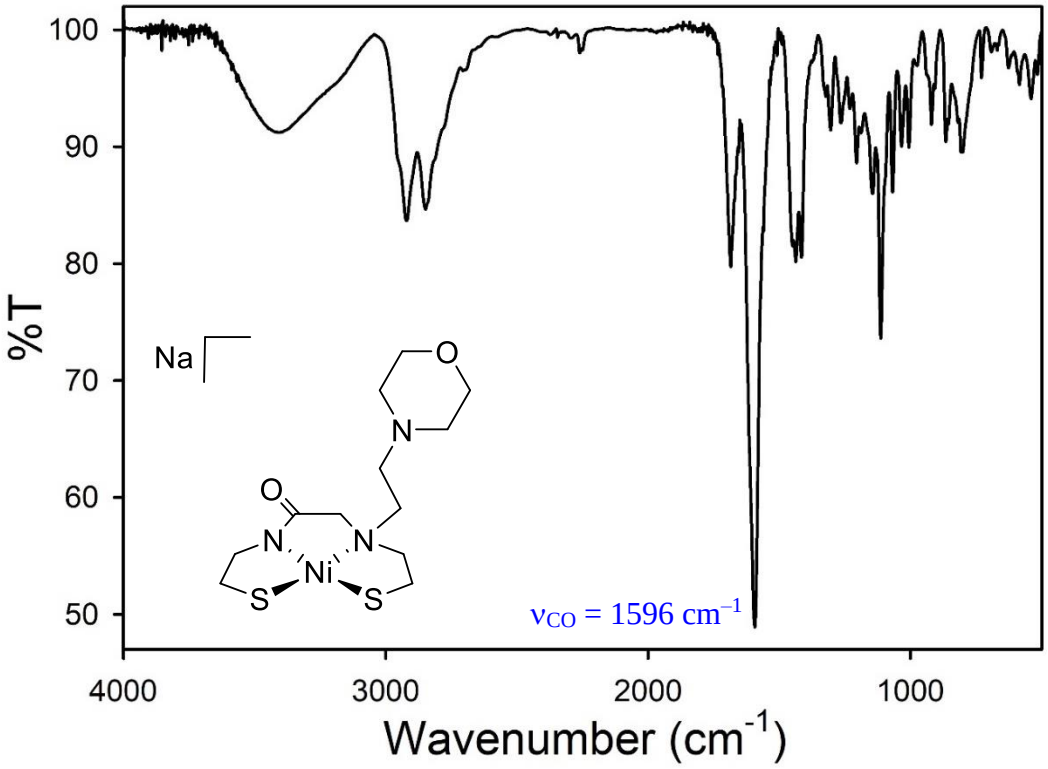

Figure 4.S13 Solid-state FTIR spectrum of Na[Ni($N_3S_2^{NEM}$)] (**4**) in a KBr matrix at RT.

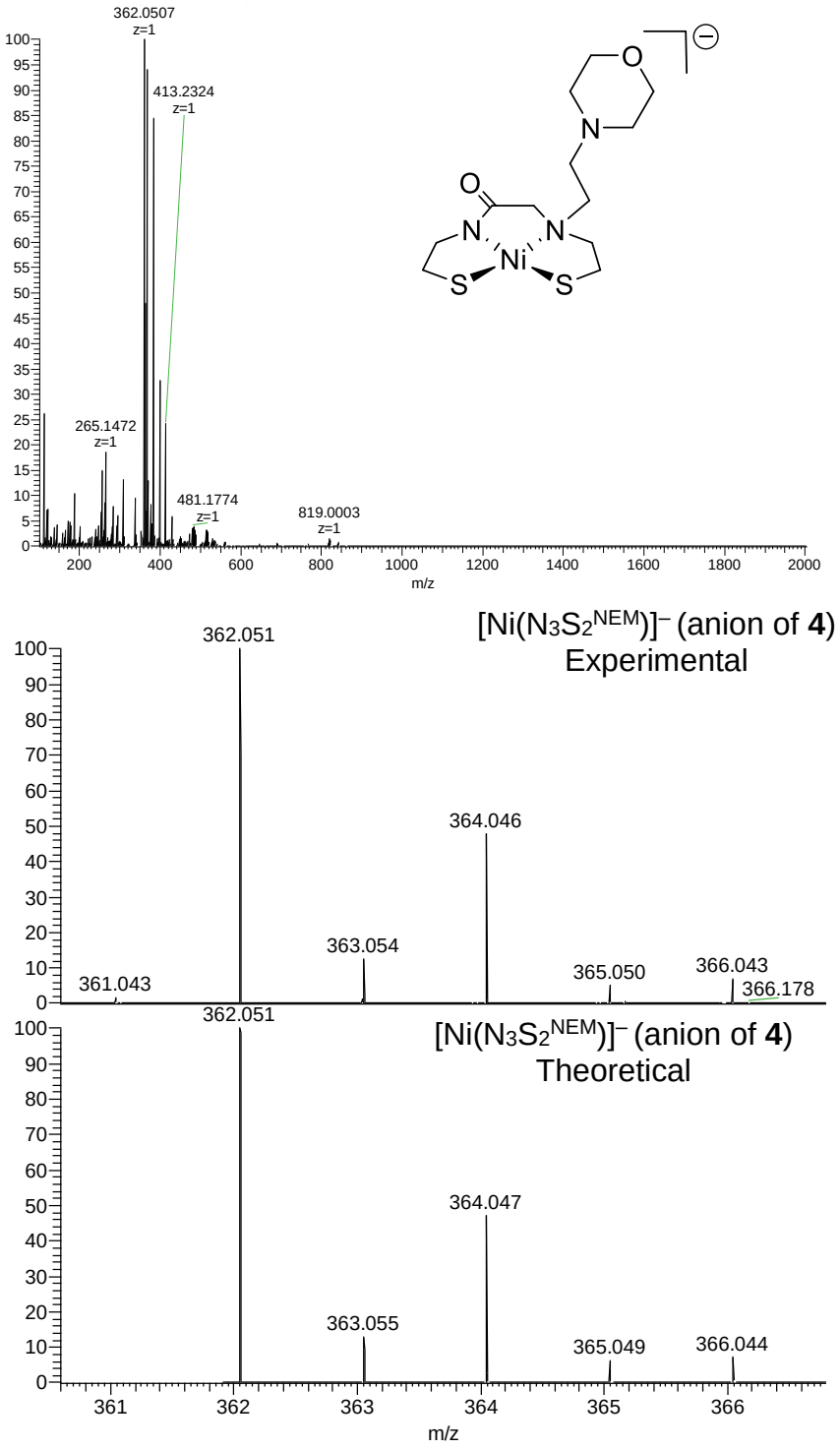

Figure 4.S14 *Top*: HR-ESI-MS(–) of the anion of Na[Ni($N_3S_2^{NEM}$)] (**4**) [M-Na]$^-$. *Bottom*: Experimental vs. theoretical isotopic distribution.

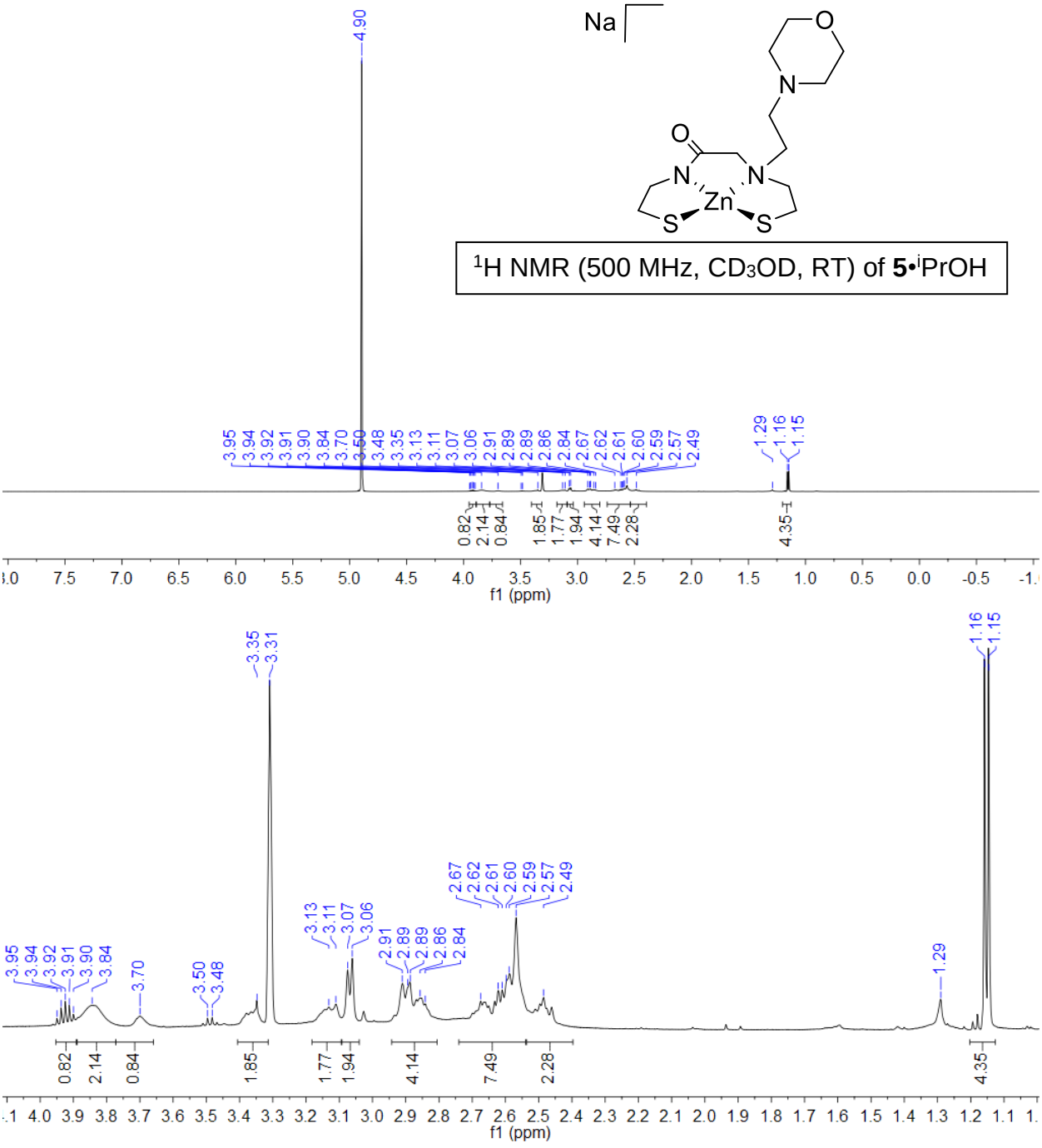

Figure 4.S15 *Top*: ^{1}H NMR spectrum of Na[Zn($N_3S_2^{NEM}$)]•^{i}PrOH (**5**•^{i}PrOH) in CD_3OD at RT (δ vs. protio solvent). Solvent of crystallization ^{i}PrOH (3.92 ppm and 1.16 ppm), trace amount of grease (1.29 ppm) and Et_2O (1.18 and 3.48 ppm) are also present. *Bottom*: expansion of 1.1-4.1 ppm region.

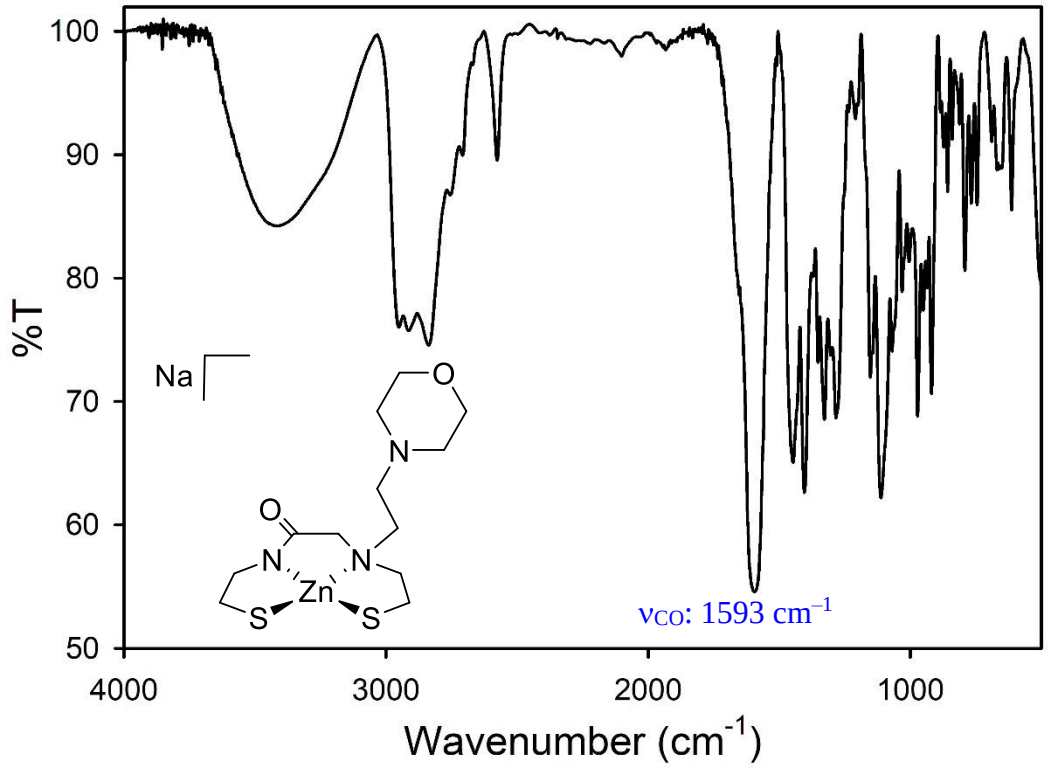

Figure 4.S16 Solid-state FTIR spectrum of Na[Zn($N_3S_2^{NEM}$)] (**5**•^{i}PrOH) in a KBr matrix at RT.

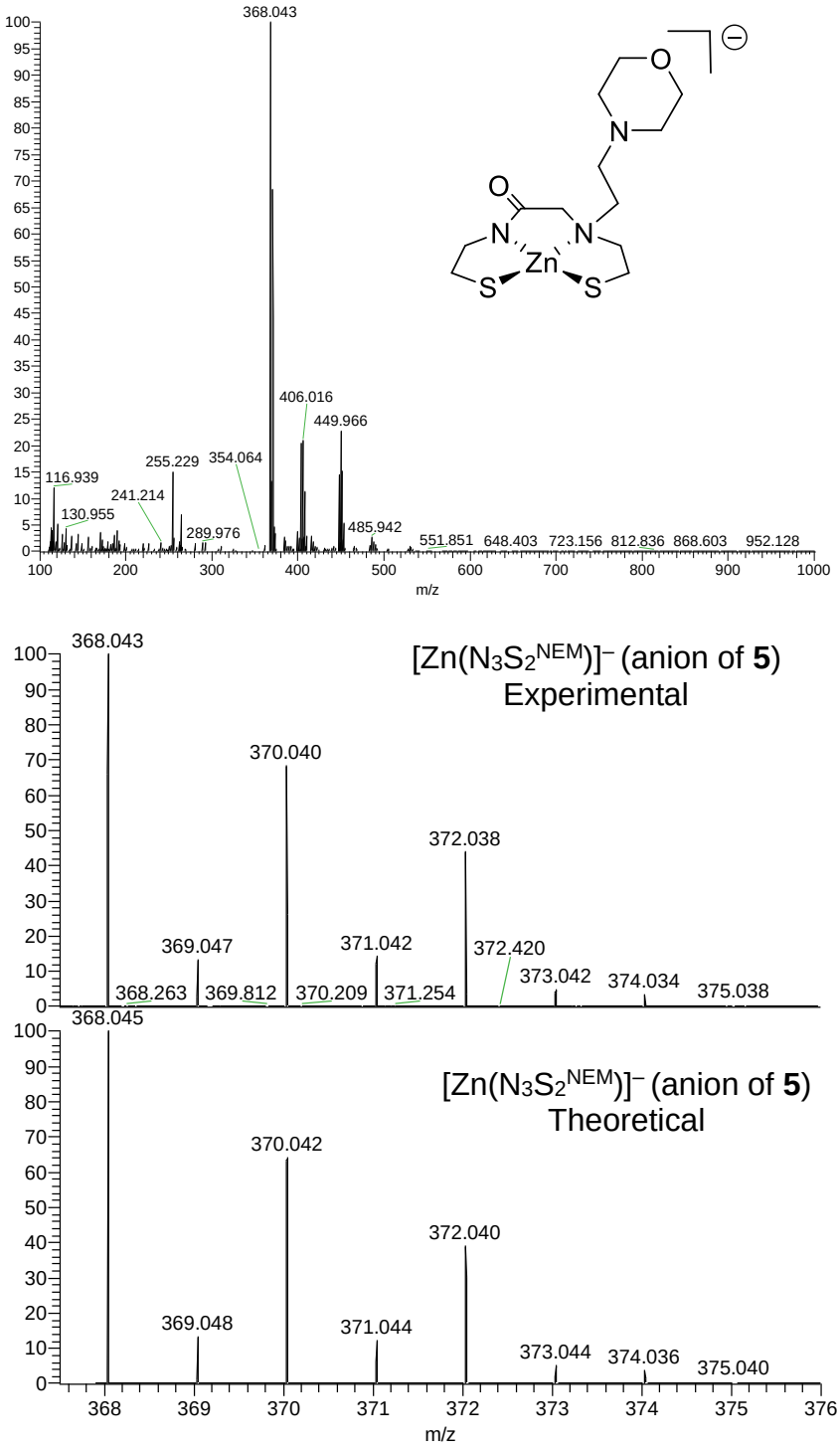

Figure 4.S17 *Top*: HR-ESI-MS(–) of the anion of Na[Zn($N_3S_2^{NEM}$)] (**5**) [M-Na]$^-$. *Bottom*: Experimental vs. theoretical isotopic distribution.

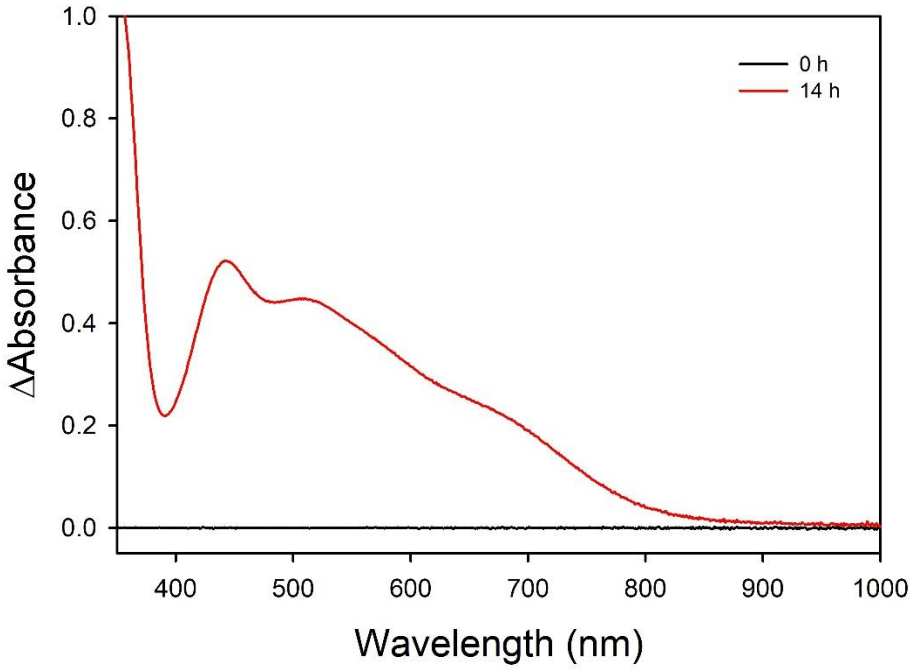

Figure 4.S18 UV-vis difference spectrum of **4** (0.987 mM) after 1 min exposure to air in MeOH at 25 °C at t = 0 h (black) and t = 14 h (red).

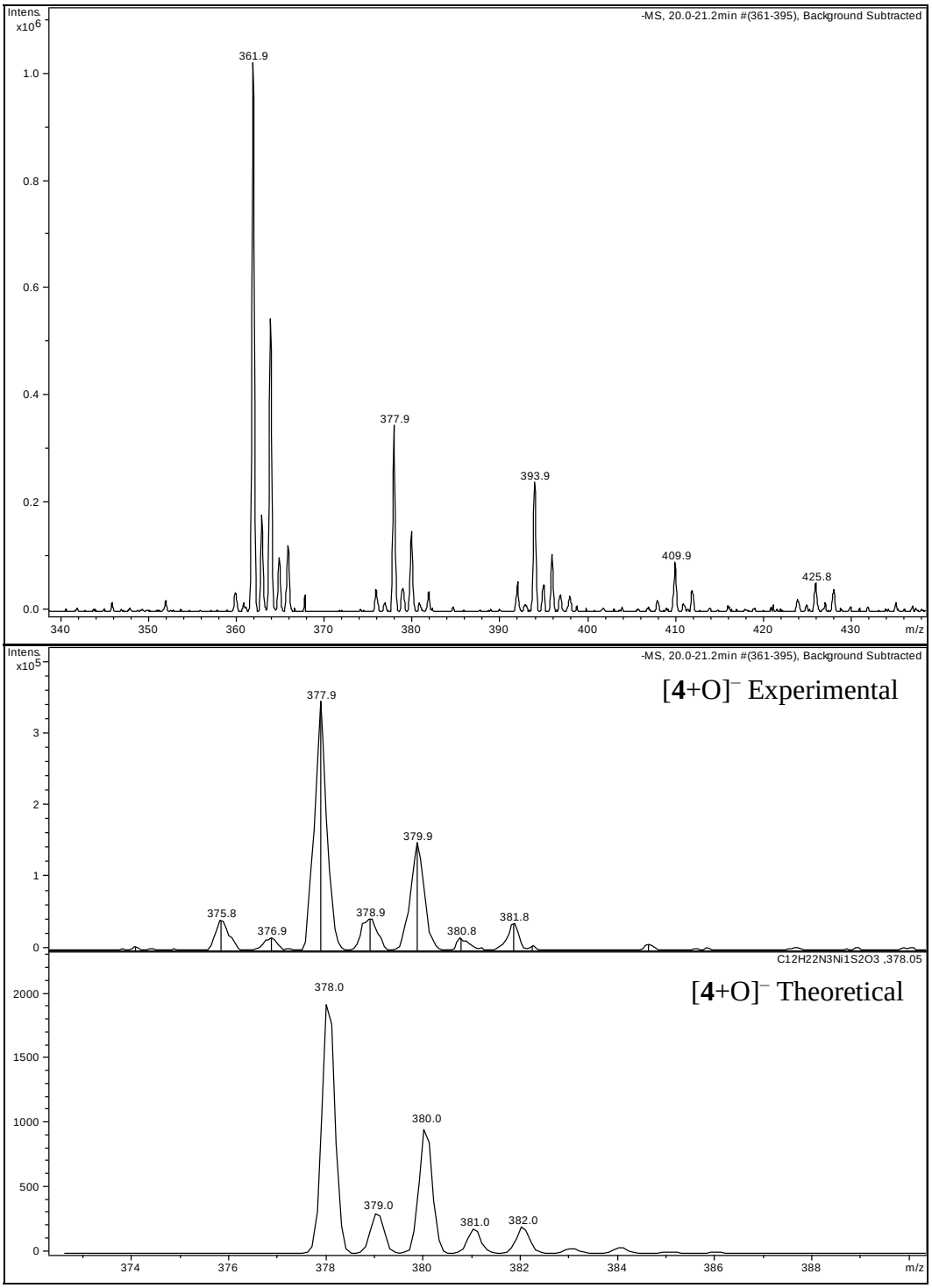

Figure 4.S19 *Top:* LR-ESI-MS(–) of solution of **4** after 1 min exposure to air in MeOH. Peaks corresponds to oxygenated products at *m/z*: 378 (+1O), 394 (+2O), 410 (+3O), and 426 (+4O)) along with unreacted **4** (*m/z*: 362). *Bottom*: experimental and theoretical isotopic distribution of [**4**+O]⁻.

Scheme 4.S1 Workup flowchart for oxidation of 4 by $FcPF_6$

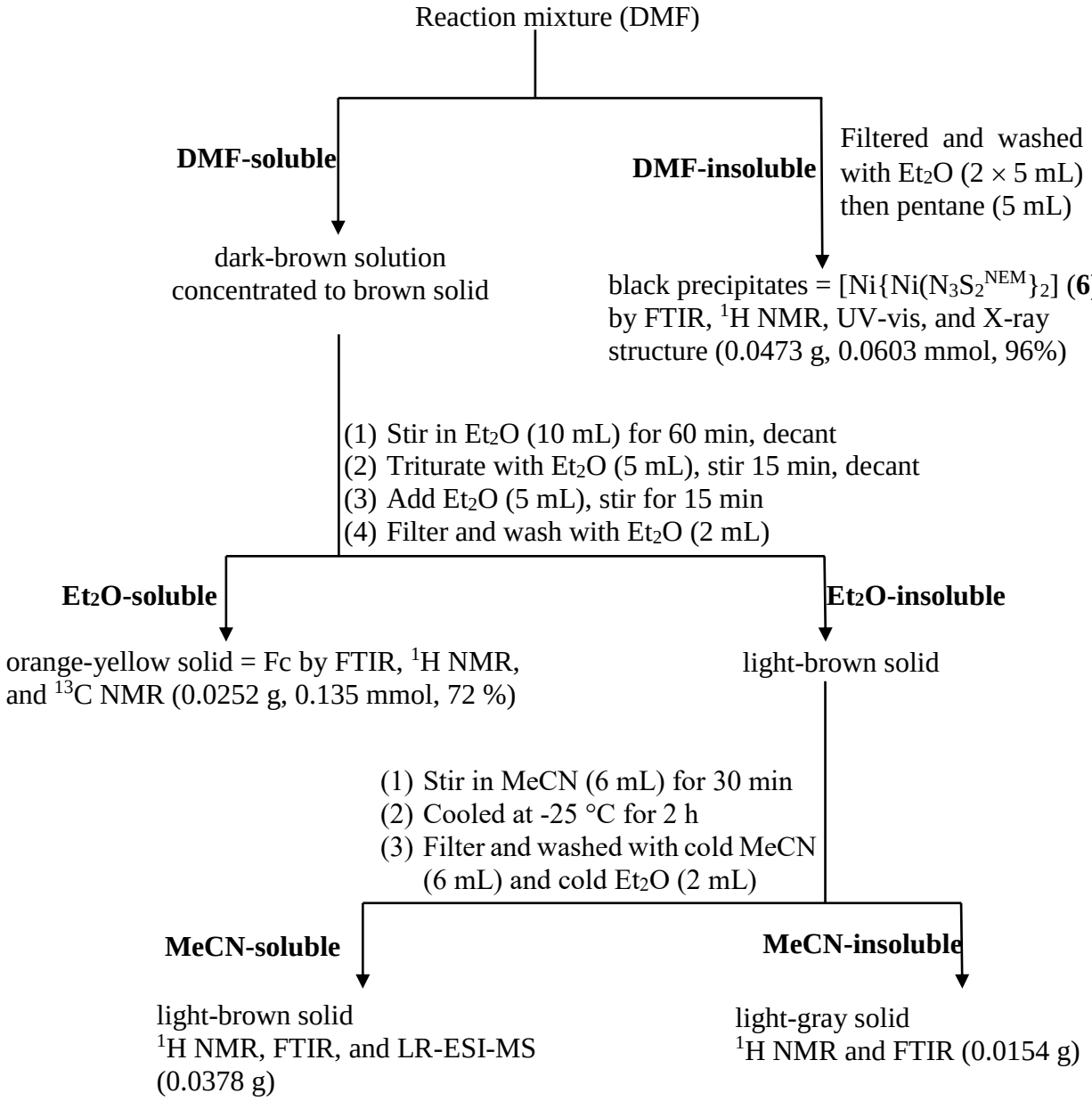

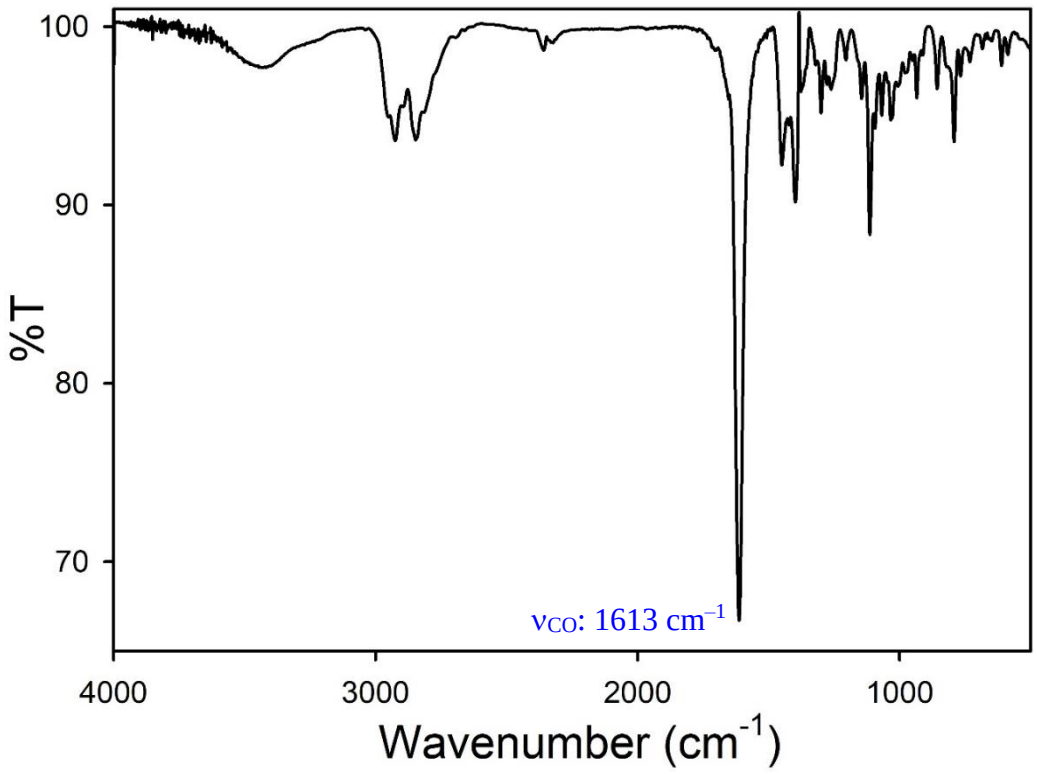

Figure 4.S20 Solid-state FTIR spectrum of **DMF-insoluble** black precipitates from oxidation of **4** by $FcPF_6$ at RT.

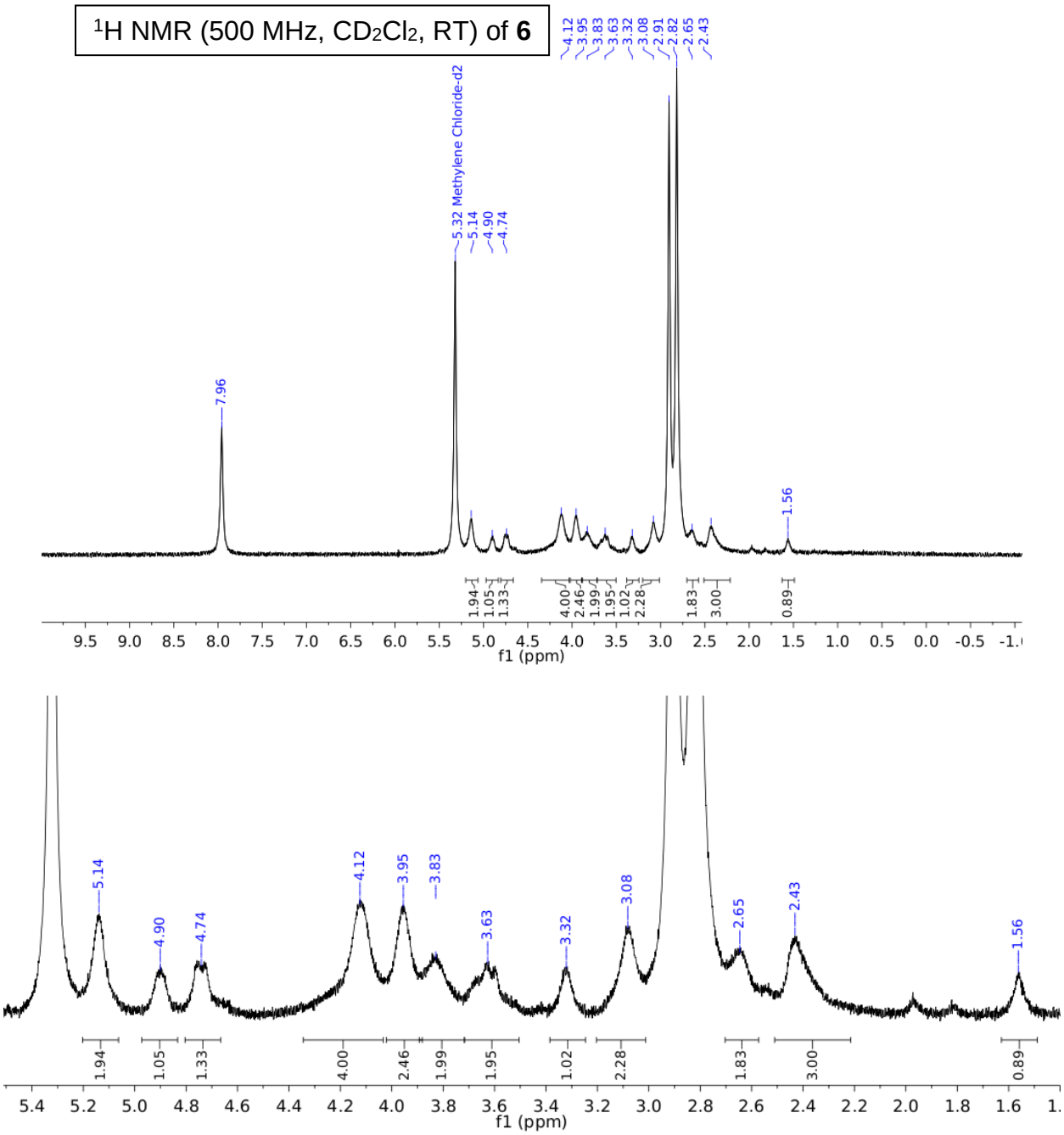

Figure 4.S21 *Top*: ^{1}H NMR spectrum of **DMF-insoluble** black precipitates from oxidation of **4** by $FcPF_6$ in CD_2Cl_2 at RT (δ vs. protio solvent). DMF (2.82, 2.91, and 7.96 ppm) is also present. *Bottom*: expansion of 2.5-11 ppm region.

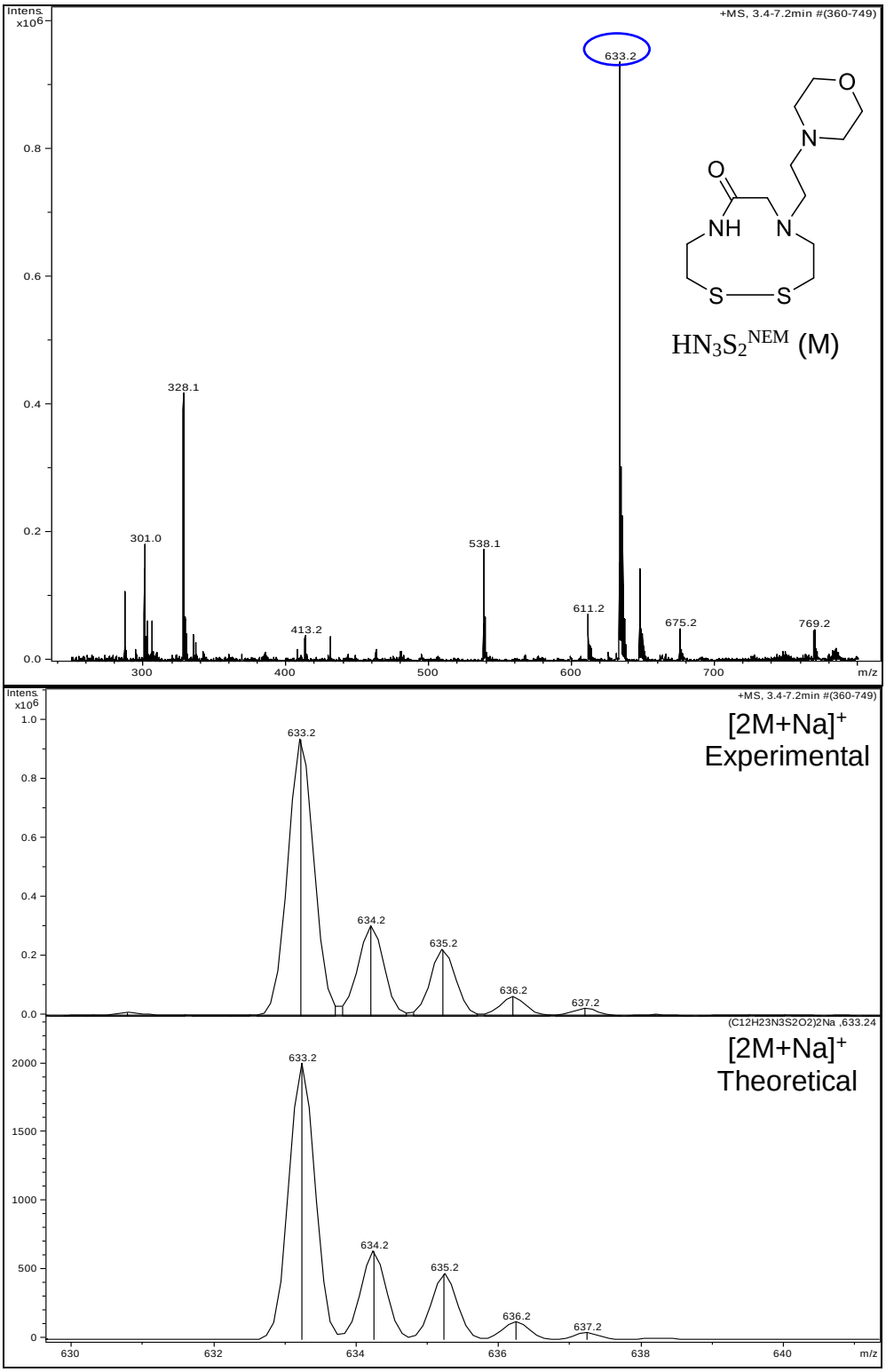

Figure 4.S22 *Top*: LR-ESI-MS(+) of **DMF-soluble/Et$_2$O-insoluble/MeCN-soluble** component from oxidation of **4** by $FcPF_6$. *Bottom*: experimental versus theoretical isotopic distribution of $[2M+Na]^+$.

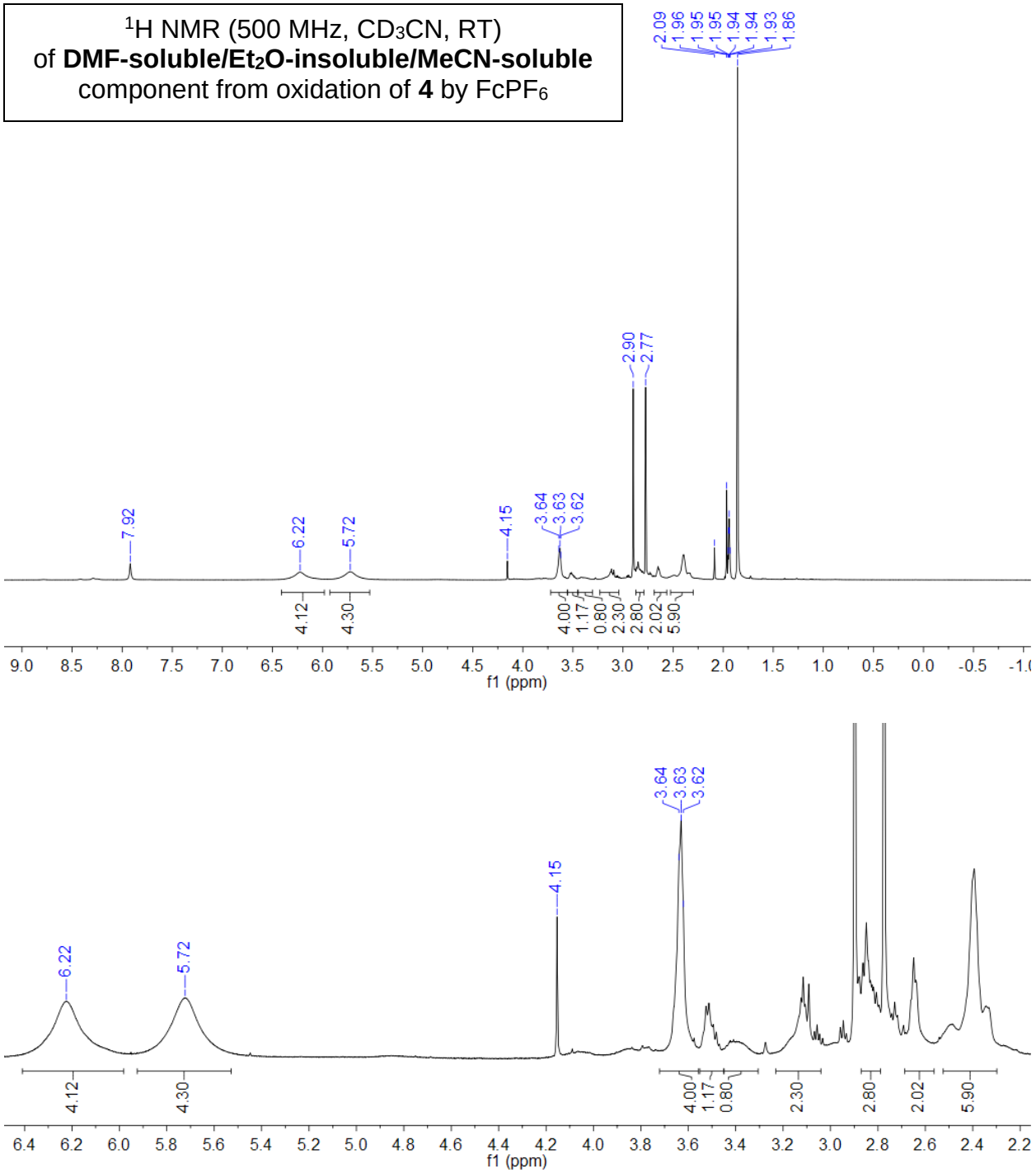

Figure 4.S23 *Top*: ^{1}H NMR spectrum of **DMF-soluble/Et_2O-insoluble/MeCN-soluble** component from oxidation of **4** by $FcPF_6$ in CD_3CN at RT (δ vs. protio solvent). DMF (2.82, 2.91, and 7.96 ppm) and trace amount of CH_3CN (1.95 ppm) and H_2O (2.09 ppm) are also present. *Bottom*: expansion of 2.2-6.4 ppm region.

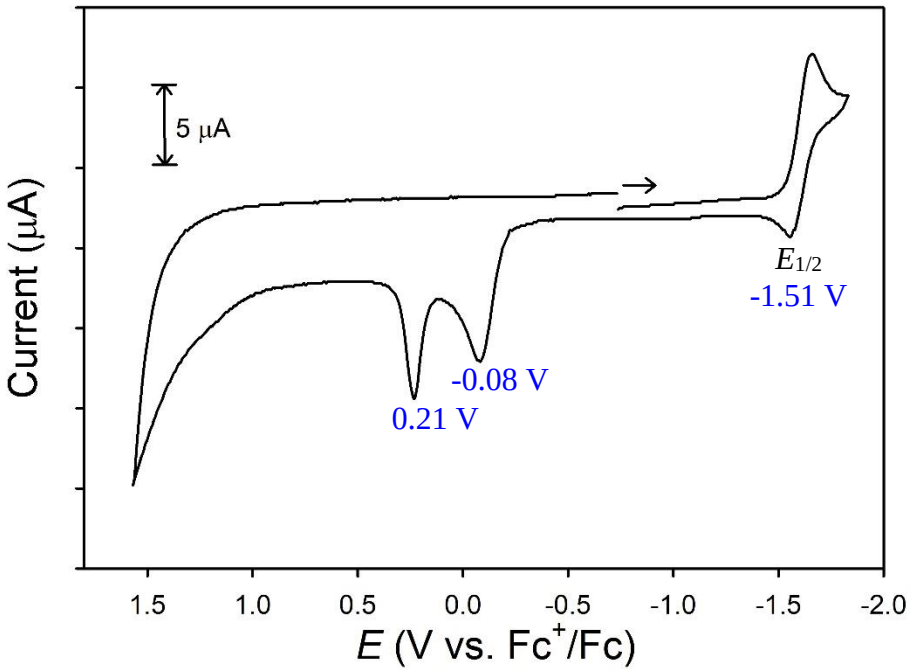

Figure 4.S24 CV of **6** (2.9 mM) in CH_2Cl_2 at RT (0.1 M $^nBu_4NPF_6$ supporting electrolyte, glassy carbon working electrode, 100 mV/s scan rate). Arrow displays scan direction.

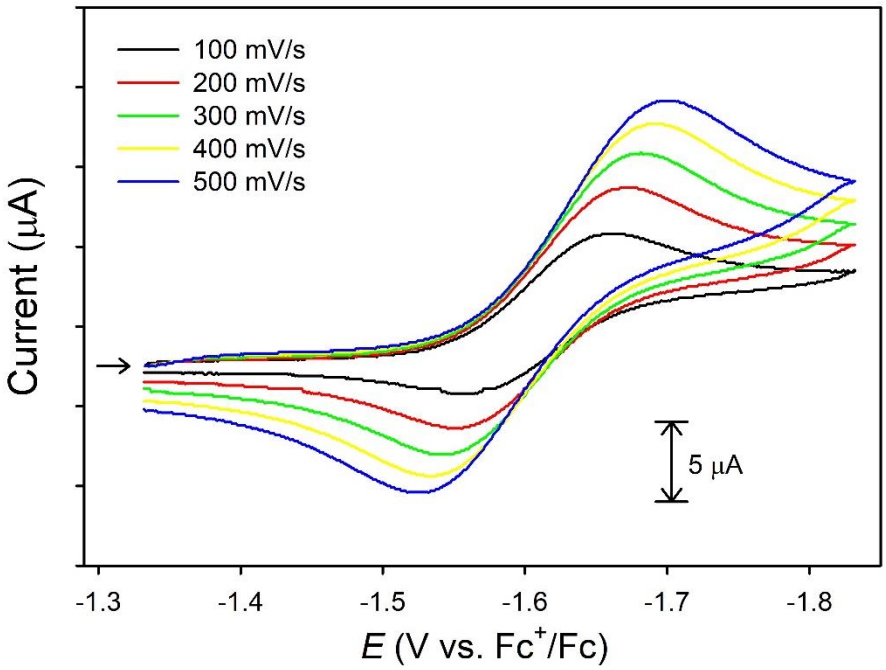

Figure 4.S25 CV of **6** (2.9 mM) in CH_2Cl_2 at RT at various scan rate centered at $E_{1/2}$ = -1.61 V (0.1 M ^{n}Bu$_4$NPF$_6$ supporting electrolyte, glassy carbon working electrode). Arrow displays scan direction.

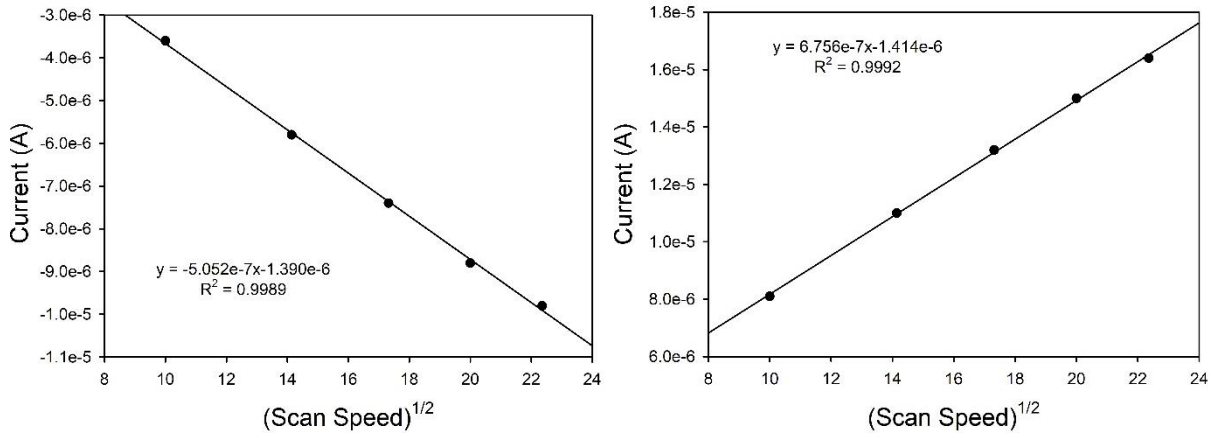

Figure 4.S26 Plots of the square root of scan rate vs. current (A) for the anodic (*left*) and cathodic (*right*) current for the reversible redox couple for **6** (2.9 mM) at $E_{1/2}$ = -1.61 V in CH_2Cl_2 at RT (0.1 M ^{n}Bu$_4$NPF$_6$ supporting electrolyte, glassy carbon working electrode).

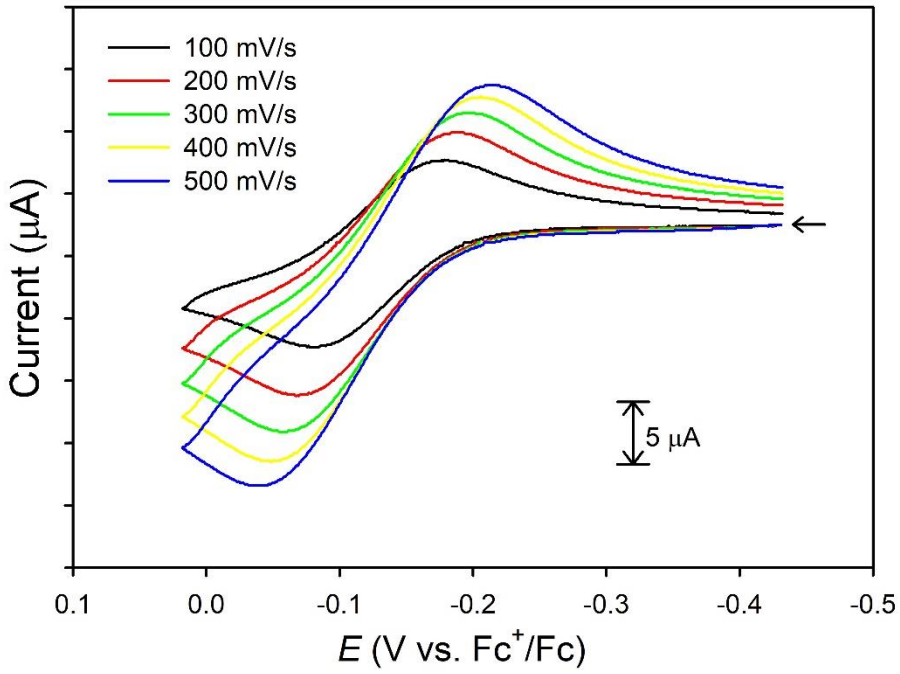

Figure 4.S27CV of **6** (2.9 mM) in CH_2Cl_2 at RT at various scan rate centered at $E_{1/2}$ = -0.13 V (0.1 M $^nBu_4NPF_6$ supporting electrolyte, glassy carbon working electrode). Arrow displays scan direction.

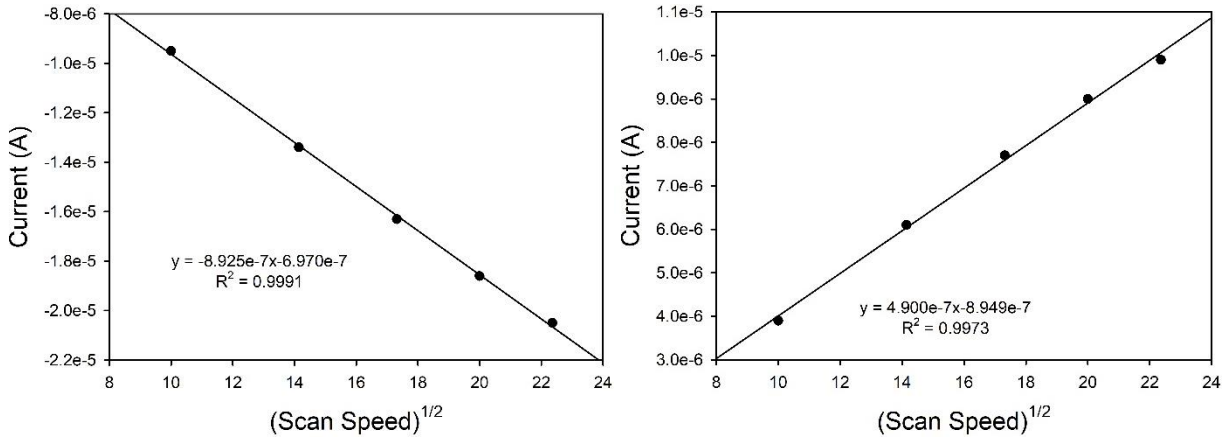

Figure 4.S28 Plots of the square root of scan rate vs. current (A) for the anodic (*left*) and cathodic (*right*) current for the reversible redox couple for **6** (2.9 mM) at $E_{1/2}$ = -0.13 V in CH_2Cl_2 at RT (0.1 M $^nBu_4NPF_6$ supporting electrolyte, glassy carbon working electrode).

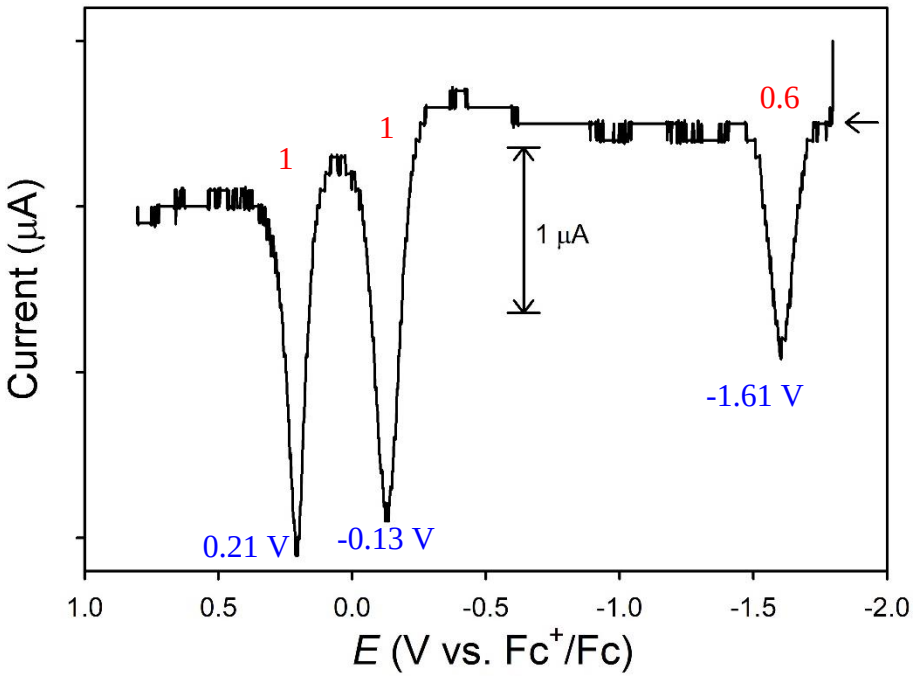

Figure 4.S29 DPV of **6** (1.2 mM) in CH_2Cl_2 at RT and ratio of area-under-the-curve between the peaks in red (0.1 M ^{n}Bu$_4$NPF$_6$ supporting electrolyte, glassy carbon working electrode, 20 mV/s scan rate, amplitude = 25 mV, frequency = 10 Hz, E_{step} = 2 mV). Arrow displays scan direction.

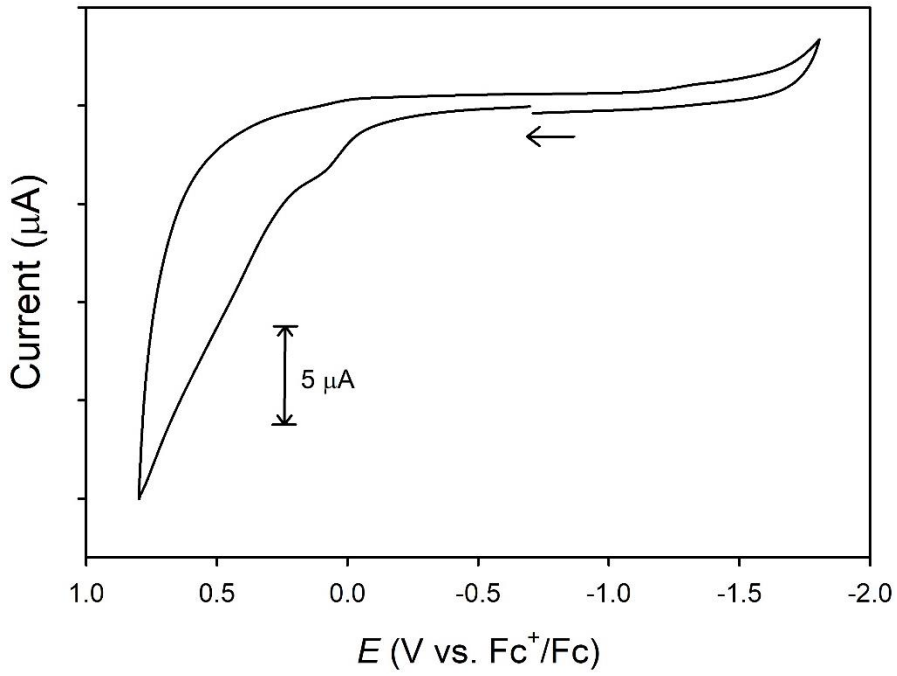

Figure 4.S30 CV of **5** (2.8 mM) with $Ni(PPh_3)_2Cl_2$ (1.4 mM) in CH_2Cl_2 at RT (0.1 M ^{n}Bu$_4$NPF$_6$ supporting electrolyte, glassy carbon working electrode, 100 mV/s scan rate). Arrow displays scan direction.

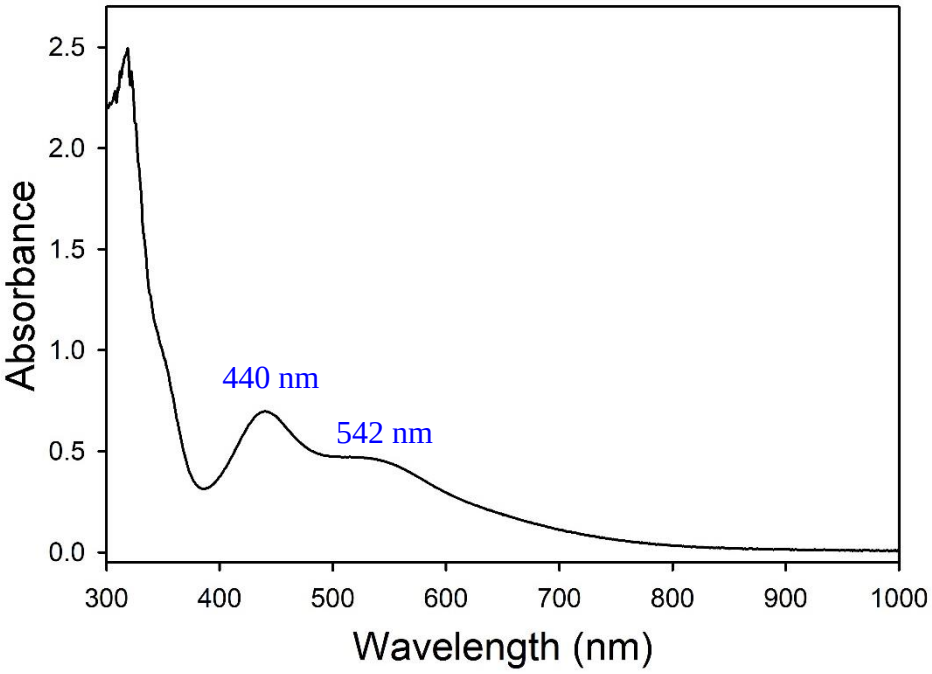

Figure 4.S31 Qualitative UV-vis in CH_2Cl_2 at RT of **CH_2Cl_2-soluble/Et_2O-insoluble** component from reaction of **4** with stoichiometric BCF.

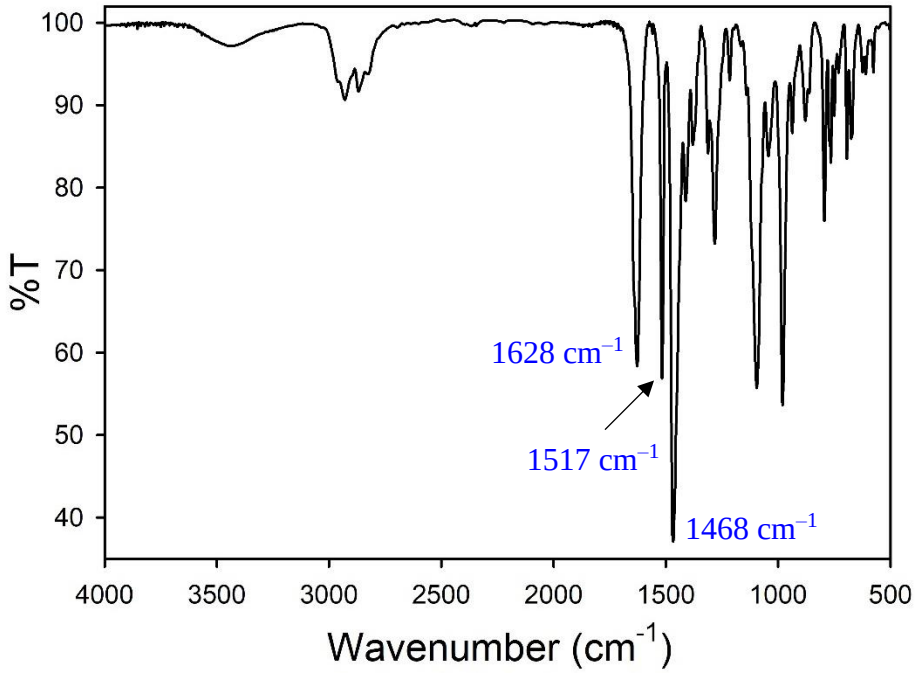

Figure 4.S32 Solid-state FTIR spectrum of **CH_2Cl_2-soluble/Et_2O-insoluble** from reaction of **4** with stoichiometric BCF in CH_2Cl_2 at RT.

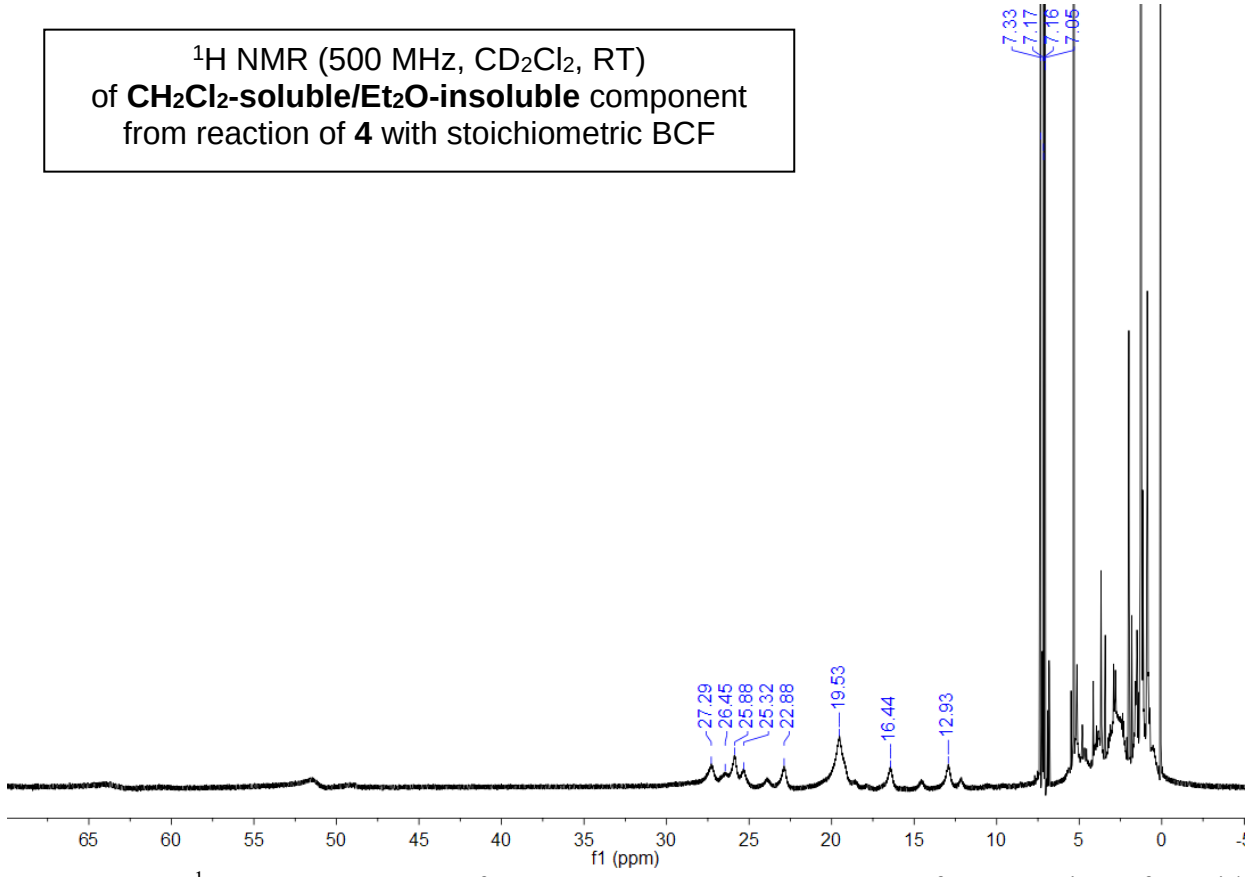

Figure 4.S33 ^{1}H NMR spectrum of **CH_2Cl_2-soluble/Et_2O-insoluble** from reaction of **4** with stoichiometric BCF in CD_2Cl_2 at RT (δ vs. protio solvent).

^{19}F NMR (376 MHz, CD_2Cl_2, RT)
of **CH_2Cl_2-soluble/Et_2O-insoluble** component
from reaction of **4** with stoichiometric BCF

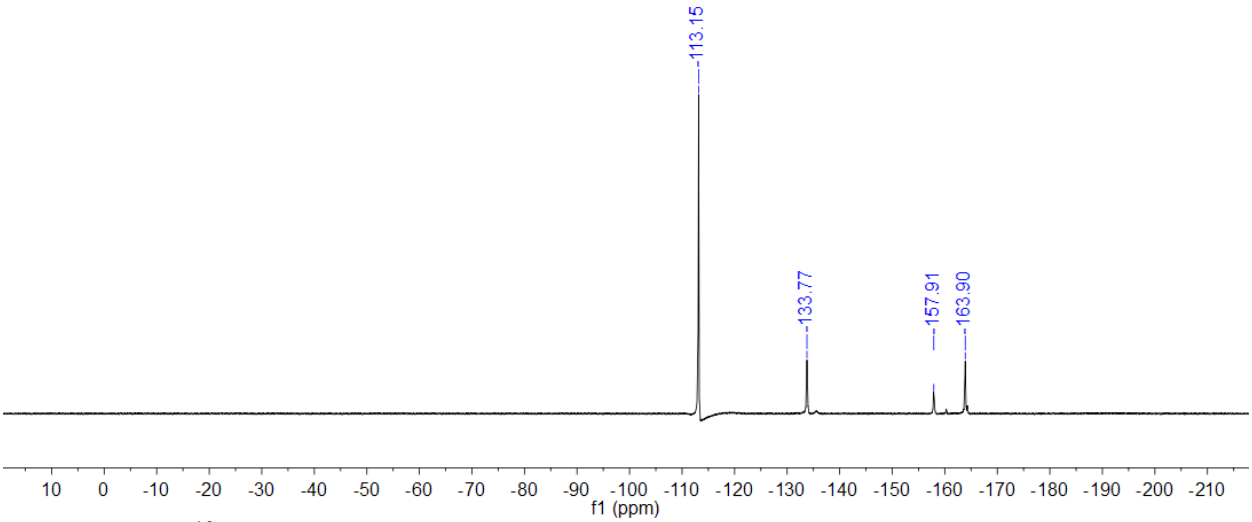

Figure 4.S34 ^{19}F NMR spectrum of **CH_2Cl_2-soluble/Et_2O-insoluble** from reaction of **4** with stoichiometric BCF in CD_2Cl_2 at RT (δ vs. $CFCl_3$). Fluorobenzene (20 μL) was added as internal reference (δ = -113.15 ppm).

^{11}B NMR (128 MHz, CD_2Cl_2, RT)
of **CH_2Cl_2-soluble/Et_2O-insoluble** component
from reaction of **4** with stoichiometric BCF

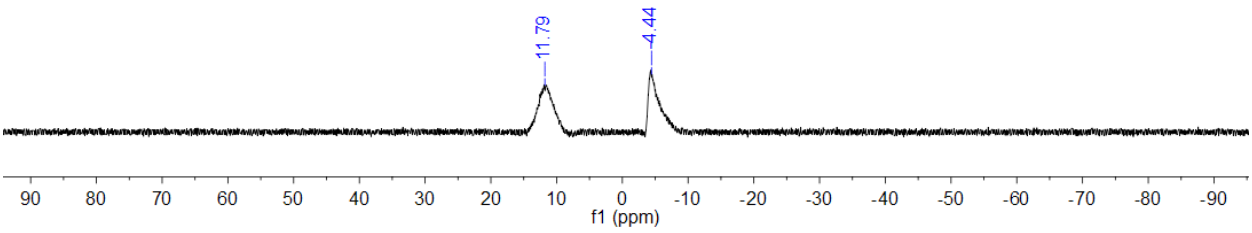

Figure 4.S35 ^{11}B NMR spectrum of **CH_2Cl_2-soluble/Et_2O-insoluble** from reaction of **4** with stoichiometric BCF in CD_2Cl_2 at RT (δ vs. BCF_3•Et_2O externally referenced).

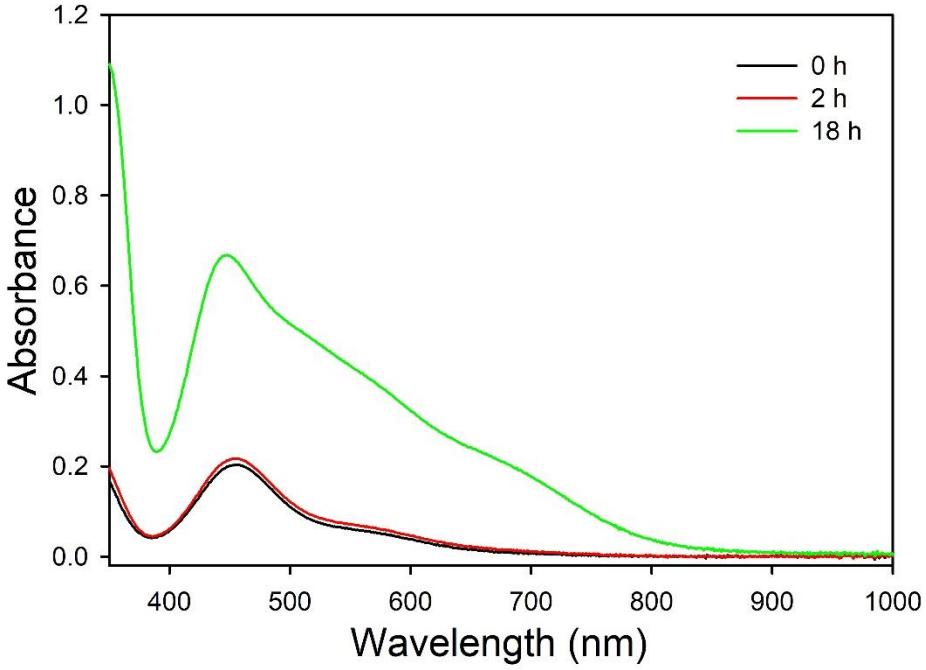

Figure 4.S36 UV-vis spectrum of **4** (0.875 mM) with 1 mol-equiv of NaN_3 (0.875 mM) in MeOH at 25 °C at t =0 h (black), t = 2 h (red), and t = 18 h (green).

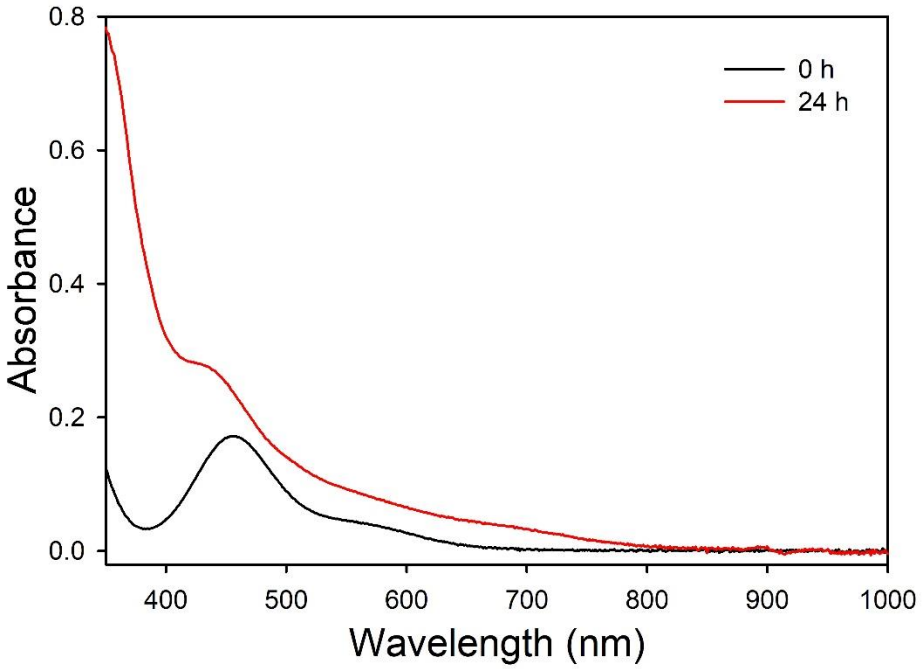

Figure 4.S37 UV-vis spectra of **4** (0.850 mM) with 10 mol-equiv of KO_2 (9.17 mM, stabilized by 18C6) at 25 °C at t = 0 h (black) and t = 24 h (red).

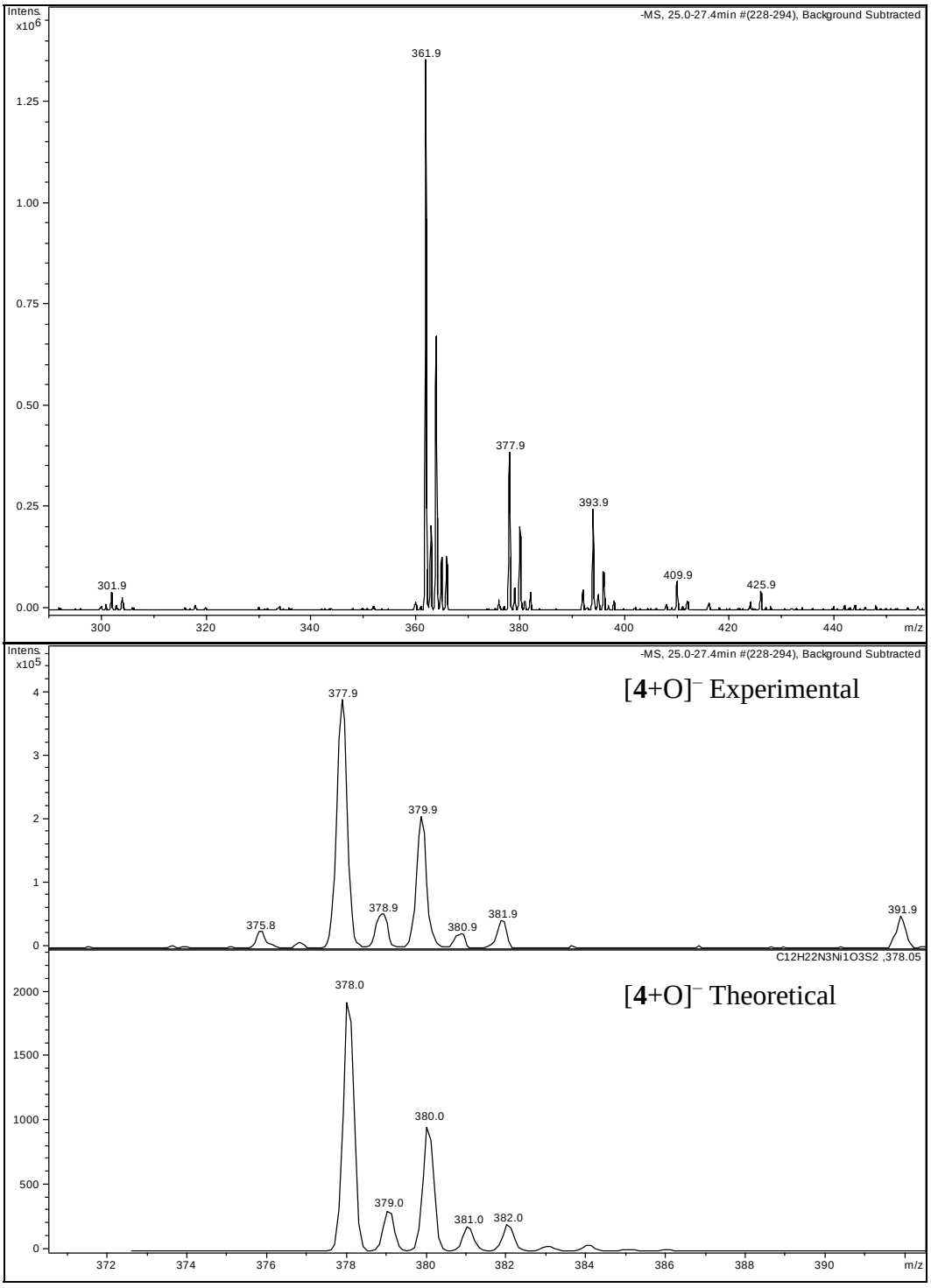

Figure 4.S38 *Top:* LR-ESI-MS(–) of solution of **4** after reaction with 1 mol-equiv of KO_2 for 13 h in MeOH. Peaks corresponds to oxygenated products are *m/z*: 378 (+1O) and 394 (+2O) along with unreacted **4** (m/z: 362). *Bottom*: Simulated spectrum of [**4**+O]$^-$ at *m/*z 378.

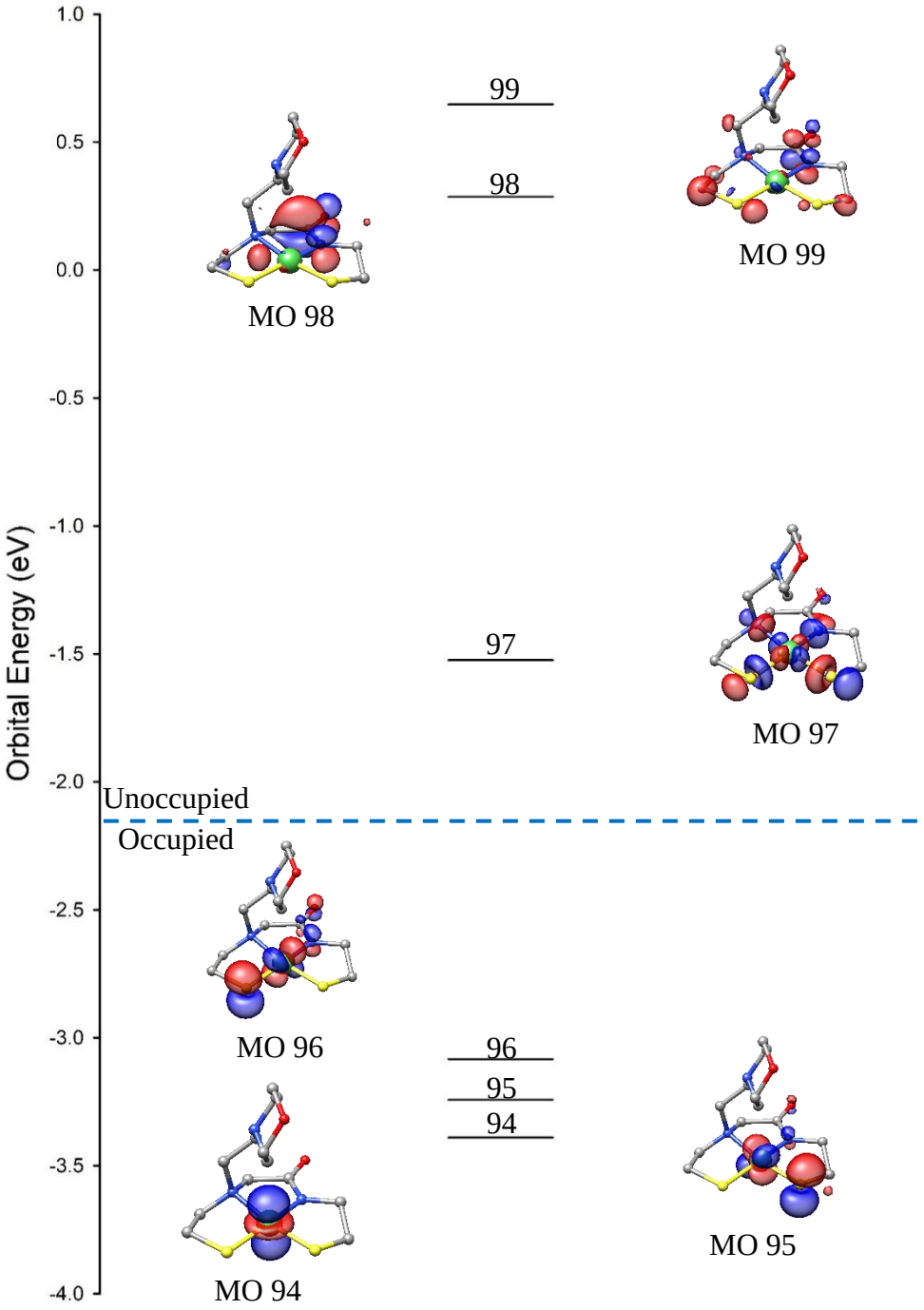

Figure 4.S39 DFT-generated isosurface plots (OLYP/def2-TZVPP) of the frontier MOs of **4***. The MOs descend in the order of LUMO+2, LUMO+1, LUMO, HOMO, HOMO-1, HOMO-2.

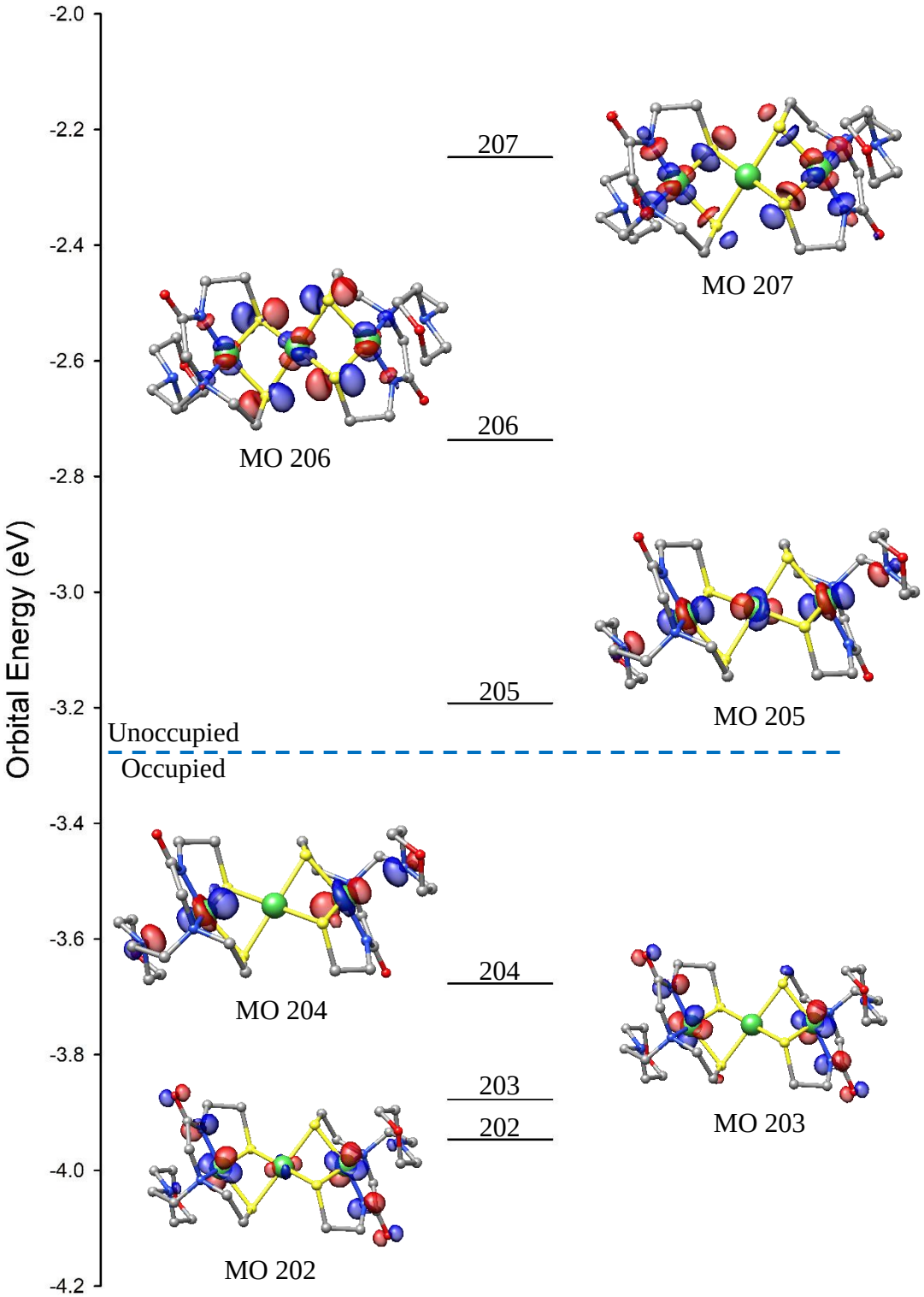

Figure 4.S40 DFT-generated isosurface plots (OLYP/def2-TZVPP) of the frontier MOs of **6***. The MOs descend in the order of LUMO+2, LUMO+1, LUMO, HOMO, HOMO-1, HOMO-2.

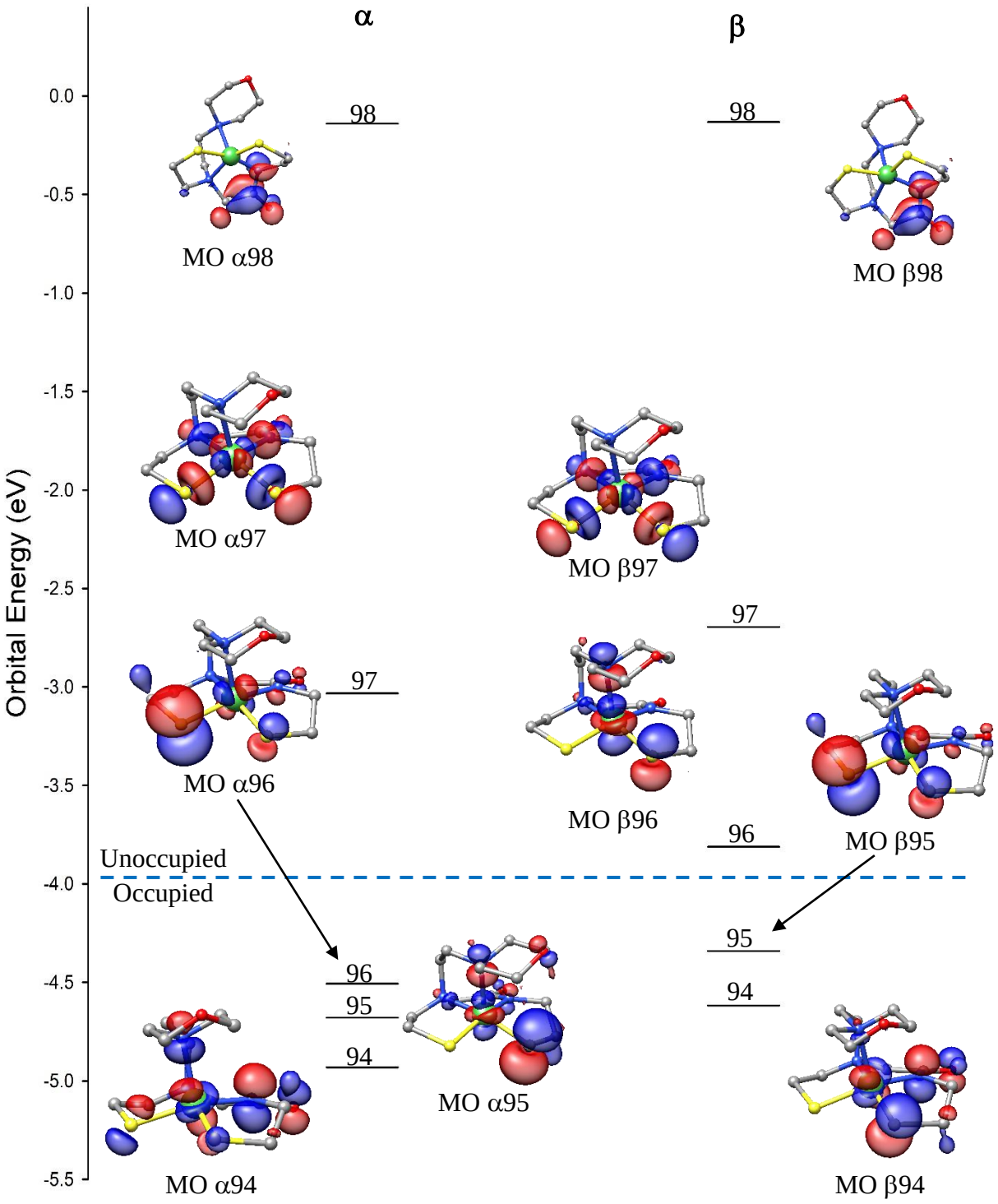

Figure 4.S41 DFT-generated isosurface plots (OLYP/def2-TZVPP) of the frontier MOs of **4^{ox}***. Spin-up (α) MOs (*left*); spin-down (β) MOs (*right*).

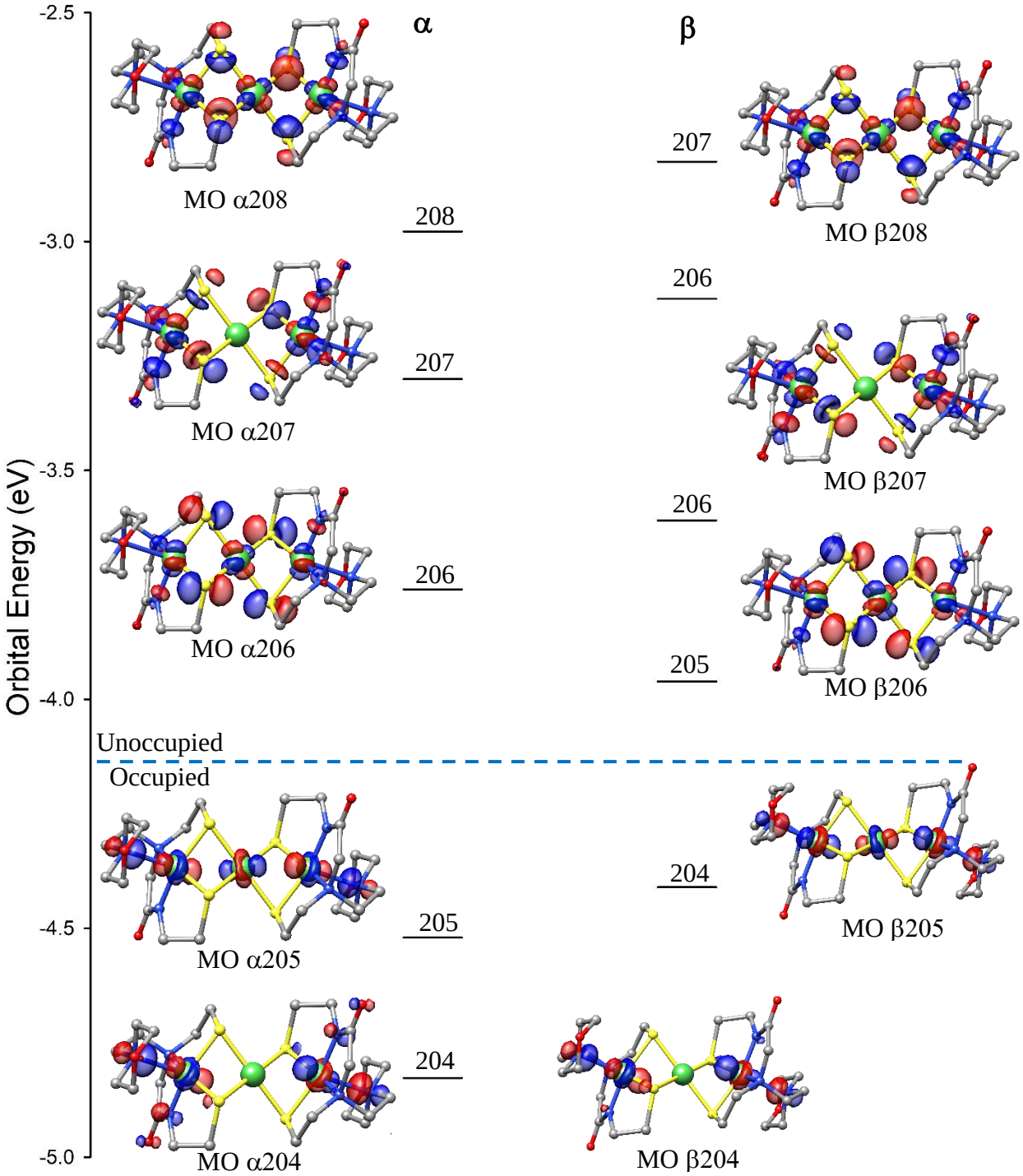

Figure 4.S42 DFT-generated isosurface plots (OLYP/def2-TZVPP) of the frontier MOs of **6^{ox}***. Spin-up (α) MOs (*left*); spin-down (β) MOs (*right*).

Table 4.S1 Summary of Crystal Data and Intensity Collection and Structure Refinement Parameters for Na[Ni($N_3S_2^{NEM}$)]·diacetone alcohol (DAA) (**4**•DAA), Na[Zn($N_3S_2^{NEM}$)]•^{i}PrOH (**5**•^{i}PrOH), {Ni[Ni($N_3S_2^{NEM}$)]$_2$}•4MeOH (**6**•4MeOH), and {Ni[Ni($N_3S_2^{NEM}$)]$_2$}•2(BCF)•6(CH_2Cl_2) (**7**•6CH_2Cl_2)

Parameters	**4**•DAA	**5**•^{i}PrOH	**6**•4MeOH	**7**•6(CH_2Cl_2)
Formula	$C_{18}H_{36}N_3NaNiO_5S_2$	$C_{15}H_{30}N_3NaO_3S_2Zn$	$C_{28}H_{60}N_6Ni_3O_8S_4$	$C_{66}H_{56}Cl_{12}F_{30}N_6Ni_3O_4S_4$
MW	520.30	452.90	913.18	2318.55
Crystal system	Monoclinic	Monoclinic	Monoclinic	Triclinic
Space group	*P*2(1)/c	*P*2(1)/c	*P*2(1)/c	$P\bar{1}$
Crystal color, habit	red, plate	colorless, prism	dark-red, needle	brown, plate
a, Å	8.5383(6)	12.4661(6)	8.0110(4)	10.9809(9)
b, Å	19.3707(12)	7.4080(3)	15.5029(8)	12.9747(11)
c, Å	14.8157(10)	23.8154(11)	15.3112(8)	15.2912(13)
α, deg	90	90	90	78.259(2)
β, deg	97.501(2)	105.123(2)	91.2320(10)	83.331(2)
γ, deg	90	90	90	80.381(2)
V, Å^3	2429.4(3)	2123.16(17)	1901.12(17)	2095.4(3)
Z	4	4	2	1
$\rho_{calcd,}$ g/cm^3	1.373	1.417	1.595	1.837
T, K	100(2)	100	100(2)	100(2)
abs coeff, μ (Mo Kα), mm^{-1}	1.015	3.80	1.744	1.27
θ limits, deg	2.406-28.282	3.7-72.4	2.661-39.389	2.4-36.4
total no. of data	75664	36635	109286	106158
no. of unique data	6024	4192	11327	20444
no. of parameters	266	232	233	574
GOF of F^2	1.048	1.100	1.067	1.047
R_1,[a] %	0.033	0.048	0.0294	0.0497
wR_2,[b] %	0.088	0.128	0.0817	0.1367
max, min peaks, e/Å^3	0.542, -0.421	1.09, -0.66	1.509, -0.809	2.82, -2.88

[a]$R_1 = \Sigma| |F_o| - |F_c| | / \Sigma |F_o|$; [b]$wR_2 = \{\Sigma[w(F_o^2 - F_c^2)^2]/\Sigma[w(F_o^2)^2]\}^{1/2}$

Table 4.S2 Löwdin population analysis derived from the DFT calculations for selected MOs of **4*** from OLYP/def2-TZVPP with COSMO(DMF). Only s and p contributions were tabulated for N and S atoms. Bonding interactions are represented with a + and antibonding interactions are denoted with a –. N1 = amino-N; N2 = carboxamido-N; N3 = morpholine-N; S1 = $S_{trans\text{-carboxamide}}$; S2 = $S_{trans\text{-amine}}$.

	MO#	Energy (eV)	%Ni	%S1	%S2	%N1	%N2	%N3	Type of Interaction
LUMO+2	99	0.65	9.9	4.2	2.6	0.8	4.0	0.2	N2(π)– S1(σ)–S2(σ)
LUMO+1	98	0.29	11.2	1.0	0.5	0.3	6.1	0.3	N2(π)–C(π)–O1(π)
LUMO	97	-1.52	50.8	9.7	13.3	5.6	5.7	0.0	Ni(d_σ)–S1(σ)–S2(σ)–N1(σ)–N2(σ)
HOMO	96	-3.08	62.9	20.2	2.8	0.0	2.8	0.0	Ni(d_π)–S1(π)–N2(π)–O1(π)
HOMO-1	95	-3.24	65.5	0.0	23.6	0.2	1.8	0.0	Ni(d_π)–S2(π)–N2(π)
HOMO-2	94	-3.39	88.7	1.0	4.0	0.4	0.9	0.2	Ni(d_σ)

Table 4.S3 Löwdin population analysis derived from the DFT calculations for selected MOs of **6*** from OLYP/def2-TZVPP with COSMO(DMF). Only s and p contributions were tabulated for N and S atoms. Bonding interactions are represented with a + and antibonding interactions are denoted with a –. N1 = amino-N; N2 = carboxamido-N; N3 = morpholine-N; S1 = $S_{trans\text{-carboxamide}}$; S2 = $S_{trans\text{-amine}}$.

	MO#	Energy (eV)	%Ni1	%Ni2	%S1	%S2	%N1	%N2	%N3	Type of Interaction
LUMO+2	207	-2.25	25.0	0.1	4.6	6.0	2.7	3.4	0.0	Ni1(d_σ)–S1(σ)–S2(σ)–N1(σ)–N2(σ); Ni1′(d_σ)–S1′(π)–S2′(π)–N1′(σ)–N2′(σ)
LUMO+1	206	-2.74	11.9	24.7	7.6	7.7	1.3	1.5	0.0	Ni1(d_σ)–S1(π)–S2(π)–N1(σ)–N2(σ)–Ni2(d_σ)–Ni1′(d_σ)–S1′(π)–S2′(π)–N1′(σ)–N2′(σ)
LUMO	205	-3.19	26.1	27.0	1.4	1.7	0.3	0.3	3.2	Ni1(d_σ)–N3(σ)–Ni2(d_σ)–Ni1′(d_σ)–N3′(σ)
HOMO	204	-3.68	31.6	2.4	1.5	2.5	0.5	0.4	5.6	Ni1(d_σ)–N3(σ)–Ni1′(d_σ)–N3′(σ)
HOMO-1	203	-3.88	32.9	0.6	3.2	0.8	0.0	4.4	0.1	Ni1(d_π)–N2(π)–O1(π)–Ni1′(d_π)–N2′(π)–O1′(π)
HOMO-2	202	-3.95	32.3	5.5	0.2	0.4	0.0	4.6	1.2	Ni1(d_π)–N2(π)–O1(π)–Ni2(d_σ)–Ni1′(d_π)–N2′(π)–O1′(π)

Table 4.S4 Löwdin population analysis derived from the DFT calculations for selected MOs of **4^{ox}*** from OLYP/def2-TZVPP with COSMO(DMF). Only s and p contributions were tabulated for N and S atoms. Bonding interactions are represented with a + and antibonding interactions are denoted with a –. N1 = amino-N; N2 = carboxamido-N; N3 = morpholine-N; S1 = $S_{trans\text{-carboxamide}}$; S2 = $S_{trans\text{-amine}}$.

	MO#	Energy (eV)	%Ni	%S1	%S2	%N1	%N2	%N3	Type of Interaction
α									
LUMO+1	98	-0.14	4.0	0.6	0.6	0.6	8.0	0.1	N2(π)–O1(π)
LUMO	97	-3.03	40.9	14.7	15.6	6.0	7.8	0.3	Ni(d_σ)–S1(σ)–S2(σ)–N1(σ)–N2(σ)
HOMO	96	-4.51	22.7	53.3	7.2	0.0	2.4	0.1	Ni(d_π)–S1(π)–S2(π)–N2(π)–N3(σ)
HOMO-1	95	-4.68	23.9	2.0	41.8	1.6	2.5	6.0	Ni(d_π)–S2(π)–N1(σ)–N2(π)–N3(σ)
HOMO-2	94	-4.93	31.9	8.6	5.4	0.3	17.1	8.6	Ni(d_π)+S1(π)+S2(π)–N2(π)–O1(π)–N3(σ)
β									
LUMO+2	98	-0.13	3.6	0.5	0.7	0.6	8.4	0.1	N2(π)–O1(π)
LUMO+1	97	-2.70	46.3	12.8	13.6	5.8	7.2	0.3	Ni(d_σ)–S1(σ)–S2(σ)–N1(σ)–N2(σ)
LUMO	96	-3.81	55.0	2.8	16.9	1.5	0.3	10.5	Ni(d_σ)–S2(π)–N1(σ)–N3(σ)
HOMO	95	-4.34	29.6	45.4	9.8	0.0	1.9	0.2	Ni(d_π)–S1(π)–S2(π)–N2(π)–N3(σ)
HOMO-1	94	-4.62	37.3	1.3	23.6	0.0	12.6	1.6	Ni(d_π)–S2(π)–N2(π)–O1(π)

Table 4.S5 Löwdin population analysis derived from the DFT calculations for selected MOs of **6^{ox}*** from OLYP/def2-TZVPP with COSMO(DMF). Only s and p contributions were tabulated for N and S atoms. Bonding interactions are represented with a + and antibonding interactions are denoted with a –. N1 = amino-N; N2 = carboxamido-N; N3 = morpholine-N; S1 = $S_{trans\text{-carboxamide}}$; S2 = $S_{trans\text{-amine}}$.

	MO#	Energy (eV)	%Ni1	%Ni2	%S1	%S2	%N1	%N2	%N3	Type of Interaction
α LUMO+2	208	-2.98	14.3	19.7	6.8	8.3	1.7	2.3	0.1	Ni1(d_σ)–S1(σ)–S2(σ)–N1(σ)–N2(σ)–Ni2(d_σ)–Ni1′(d_σ)–S1′(σ)–S2′(σ)–N1′(σ)–N2′(σ)
LUMO+1	207	-3.30	22.7	0.1	4.9	6.6	3.2	4.0	0.1	Ni1(d_σ)–S1(σ)–S2(σ)–N1(σ)–N2(σ)–Ni1′(d_σ)–S1′(σ)–S2′(σ)–N1′(σ)–N2′(σ)
LUMO	206	-3.76	10.8	22.1	8.4	8.5	1.6	1.9	0.0	Ni1(d_σ)–S1(π)–S2(π)–N1(σ)–N2(σ)–Ni2(d_σ)–Ni1′(d_σ)–S1′(π)–S2′(π)–N1′(σ)–N2′(σ)
HOMO	205	-4.52	22.2	19.5	1.9	2.3	0.6	0.3	6.4	Ni1(d_σ)–N3(σ)–Ni2–Ni1′(d_σ)–N3′(σ)
HOMO-1	204	-4.83	21.8	1.5	1.1	2.8	0.8	2.6	8.5	Ni1(d_σ)–N3(σ)–N2(π)–Ni1′(d_σ)–N3′(σ)–N2′(π)
β LUMO+3	208	-2.83	15.7	19.1	6.3	7.8	1.8	2.3	0.1	Ni1(d_σ)–S1(σ)–S2(σ)–N1(σ)–N2(σ)–Ni2(d_σ)–Ni1′(d_σ)–S1′(σ)–S2′(σ)–N1′(σ)–N2′(σ)
LUMO+2	207	-3.13	23.9	0.1	4.7	6.2	3.2	3.8	0.1	Ni1(d_σ)–S1(σ)–S2(σ)–N1(σ)–N2(σ)–Ni1′(d_σ)–S1′(σ)–S2′(σ)–N1′(σ)–N2′(σ)
LUMO+1	206	-3.61	10.9	24.5	8.3	8.1	1.2	1.7	0.0	Ni1(d_σ)–S1(π)–S2(π)–N1(σ)–N2(σ)–Ni2(d_σ)–Ni1′(d_σ)–S1′(π)–S2′(π)–N1′(σ)–N2′(σ)
LUMO	205	-3.96	25.4	21.1	1.5	1.9	0.5	0.2	4.8	Ni1(d_σ)–N3(σ)–Ni2–Ni1′(d_σ)–N3′(σ)
HOMO	204	-4.41	26.8	2.7	1.7	2.8	0.7	0.9	7.2	Ni1(d_σ)–N3(σ)–Ni1′(d_σ)–N3′(σ)

Table 4.S6 Cartesian coordinate (Å) of DFT optimized **4***.

Ni	4.48609609433245	11.68968907348400	2.47340346478486
S	4.30709764187950	13.84775822389110	2.41532922805342
S	6.34873811650550	11.64971556916060	3.62314219566947
N	2.97640527627158	11.56101484687770	1.36229129677383
N	4.35861726320509	9.71612816233213	2.59613984059623
N	2.24492481665037	10.45347669315960	5.51162585252243
O	1.57798215234086	10.04596972112470	0.26208873027685
O	1.53176893272065	12.32026825192080	7.57191383616932
C	2.92863403050596	11.75070245123010	5.63890055381506
C	2.88054232372205	12.21089286130410	7.08387001057700
C	0.84908673392487	11.07977783333170	7.40725976328423
C	0.86474097130005	10.60533852327500	5.95745457165356
C	2.32896615806952	9.93956783609345	4.13923694450471
C	3.71760273799599	9.33311993296269	3.88526703882007
C	3.14303776713422	13.92850660688960	0.98471784675786
C	2.18806288422039	12.74675983996940	1.04856615115019
C	2.57098567320725	10.34897989867010	0.95819767508042
C	3.54714436207860	9.25857401141994	1.43428991046943
C	5.74499214087832	9.17168861075799	2.55641999475891
C	6.61798552465280	9.82355337951833	3.61751868218776
H	3.97464824503454	11.66525543191020	5.30258529304940
H	2.46110836006249	12.51273090381820	4.98062435061487
H	3.32357807404066	13.20962054127560	7.18442189556151
H	3.44219573735957	11.49973926510650	7.72126408619899
H	1.32161115857427	10.30286604481190	8.04267372006667
H	-0.18153071074515	11.24494284023630	7.75287702119593
H	0.30171966035376	11.33384720515720	5.33005007469428
H	0.35249044491445	9.63210417264520	5.88406678004206
H	1.54970897317315	9.17301006292691	4.01785486770168
H	2.13026608072986	10.73637733444500	3.40053600331660
H	3.66886524415411	8.22715392976594	3.93241989451363
H	4.38234772815696	9.67048136014295	4.68588017862043
H	3.71971739270875	13.89267833728170	0.04756722235240
H	2.60314992806836	14.88718999172200	1.02210493025114
H	1.63261535242337	12.59548133960420	0.10745831505161
H	1.44613692325379	12.92198600882200	1.85204471386030
H	4.23304795184045	9.03468141689808	0.60445451177764
H	2.99440647878613	8.33455040434268	1.67153896833184
H	5.71401469579288	8.06660144778016	2.66881552272978
H	6.13888154002818	9.41493689568556	1.56095115271491
H	6.41888887245166	9.39003912200216	4.61063517272589
H	7.67287026724175	9.61476361624552	3.38590173672284

Table 4.S7 Cartesian coordinate (Å) of DFT optimized **6***.

Ni	3.61279079286021	9.08625406934373	5.35769078634044
Ni	3.84089960457320	7.75144871758593	7.65382951014851
Ni	4.06900761947568	6.41664480828860	9.94996975013786
S	3.02914106947131	7.04459181853669	5.69919198619996
S	5.45953982953188	8.61685769936674	6.39629882795461
S	4.65265747209344	8.45830677053845	9.60846678069068
S	2.22225919507360	6.88603975547380	8.91135999607384
N	4.40924282629168	9.59068250324879	2.96838730992325
N	1.86657961999826	9.50824468874777	4.88667952479104
N	3.90659525176678	11.04333600791580	5.55305468823765
N	3.27255215799877	5.91221926804494	12.33927253871730
N	5.81521840423833	5.99465476407814	10.42098303219720
N	3.77520346143661	4.45956269566071	9.75460769124190
O	5.02463729293935	7.13424944921782	1.63781853238408
O	0.30396218094668	11.22416418009420	4.84212591943348
O	2.65715517067492	8.36865293776794	13.66983917540710
O	7.37783598670286	4.27873557121930	10.46553959281410
C	5.79388061020366	9.16228032926841	2.75709517619559
C	5.86204141822368	7.64229533834750	2.67743867969999
C	3.67091961411634	7.52214935284647	1.88486413320691
C	3.52934963590970	9.03643299960908	1.93477644261424
C	4.26303843624891	11.03805810508900	3.07896572696391
C	4.73907838270203	11.55416107490270	4.43051958226271
C	1.18641234045471	7.31633843833276	5.61870566681408
C	0.91927517672867	8.43368380090837	4.61940918362846
C	1.44392460152390	10.77888237310240	5.03456867613289
C	2.55950039145992	11.69395478118170	5.56029443561633
C	4.60218194161588	11.21377244784610	6.86553139314023
C	5.83228280915266	10.33054697820390	6.97697392840900
C	1.88791399513659	6.34062111665644	12.55056275848130
C	1.81975236617594	7.86060609944803	12.63021844928480
C	4.01087326811850	7.98075356930669	13.42279490461100
C	4.15244408540948	6.46646996642487	13.37288385087830
C	3.41875689341194	4.46484358807147	12.22869589768670
C	2.94271867327840	3.94873900258208	10.87714206472400
C	6.49538608918994	8.18655994256255	9.68895422417617
C	6.76252276480137	7.06921597277310	10.68825240454410
C	6.23787359997801	4.72401699832868	10.27309565782190
C	5.12229819770677	3.80894375401334	9.74737057273400

C	3.07961876083245	4.28912504903627	8.44213014051156
C	1.84951782168203	5.17235008427877	8.33068508564839
H	6.41033041713764	9.49219435774733	3.60615661105116
H	6.21164359053348	9.60773990096273	1.82823814144859
H	6.88377805143087	7.31667685068380	2.44506922463528
H	5.55917692896436	7.21552334654317	3.65037353068708
H	3.32911818475744	7.09076609840234	2.84346506956393
H	3.07099245332187	7.10624713205735	1.06538540952455
H	3.76490858269929	9.46246898754721	0.93596276812640
H	2.49428731483571	9.30695443645462	2.18968624266512
H	3.19884741942063	11.27883805222760	2.94633875657220
H	4.81778789227415	11.57385664903570	2.28007629339980
H	5.77243237037661	11.23388099918890	4.60319379966566
H	4.72736758014576	12.65806600030470	4.43800147417470
H	0.71665545398110	6.37028529938164	5.31812764375742
H	0.85064085252725	7.59536207674173	6.62475660720104
H	1.05352932145952	8.05048084625423	3.59263699012821
H	-0.11031484770210	8.81465341604845	4.70532889921748
H	2.57605129912759	12.63223908578240	4.98752426130622
H	2.29767193629980	11.94868947136690	6.59586815113645
H	3.88612932574838	10.91212695670850	7.63980344939598
H	4.86219886022718	12.27813512419080	7.01853139057537
H	6.16856791491207	10.29583758415450	8.01941725529818
H	6.67170212210605	10.69456819638820	6.36963959923492
H	1.27146544788337	6.01070649931220	11.70150076180100
H	1.47015006073594	5.89516182005013	13.47941940653260
H	0.79801536205012	8.18622409135468	12.86258671562710
H	2.12261753746904	8.28737777553343	11.65728377330770
H	4.35267516592065	8.41213624278090	12.46419398469620
H	4.61079957657624	8.39665674142542	14.24227373708680
H	3.91688443402353	6.04043463480375	14.37169757772420
H	5.18750668985503	6.19594889007217	13.11797530209030
H	4.48294767435414	4.22406395374587	12.36132440702210
H	2.86400657415130	3.92904594255111	13.02758523135130
H	1.90936501621867	4.26901885077908	10.70446601871550
H	2.95442947018537	2.84483414958503	10.86966154064630
H	6.96514303479592	9.13261340726531	9.98953110532627
H	6.83115794353827	7.90753488643470	8.68290384976635
H	6.62826816573706	7.45242034811679	11.71502390326870
H	7.79211277042100	6.68824622306645	10.60233366434570
H	5.10574655439587	2.87066056028103	10.32014241443880

H	5.38412765614048	3.55420714063187	8.71179765456756
H	3.79567240064574	4.59077008797917	7.66785898355661
H	2.81960239234912	3.22476222045899	8.28913063577722
H	1.51323467666068	5.20705897635329	7.28824113762325
H	1.01009756117270	4.80832882099507	8.93801794748195

Table 4.S8 Optimized Cartesian coordinate (Å) of **4^{ox}***.

Ni	3.07786473157751	8.31630888570236	6.00902991827874
S	2.79903332673738	7.63501536516682	8.02895939626280
S	1.17933801725488	7.38818568237058	5.34282030578432
N	4.91607912717779	8.61578357858411	6.42210346583797
N	3.74205759070085	8.40433473871065	4.09772837188418
N	2.41343367296843	10.44369734974360	5.70544070339954
O	7.04716218846292	8.20404037473808	5.59279533542671
O	1.62424829794268	11.69766531725700	8.19503588131366
C	1.41208669836714	7.65049929394127	3.54174796493309
C	2.88769748970275	7.56871629799663	3.19459796914052
C	5.14191231617492	7.90183369338380	4.14698553147834
C	5.81802333263239	8.27882345188980	5.47092958208212
C	5.34766878629996	8.70034430512765	7.81504810022869
C	4.55202398667437	7.67837390971562	8.61543505925034
C	3.77750218788609	9.84662800678475	3.72658743993120
C	2.57458234730280	10.60943961823490	4.24682612267921
C	0.99565279153985	10.71399603249500	6.06339279600745
C	0.78396311456459	10.72564032550940	7.56600150451588
C	2.98512660877703	11.35770344368210	7.94275049337064
C	3.30094819599203	11.36996093702270	6.45166009169425
H	0.88077851616739	6.83949425409991	3.02321838679255
H	0.95612746274476	8.59068601963581	3.20095588841795
H	3.21432578016756	6.53268239842415	3.34347664074502
H	3.08791868621645	7.84984418889619	2.14392605339848
H	5.73294745400708	8.26746893774085	3.29343325103145
H	5.11849711376475	6.80517348317193	4.09913816769472
H	5.16812632436890	9.71237198265874	8.20997788991775
H	6.42915221268217	8.50600133767675	7.87097515480266
H	4.54617113401743	7.90092284612220	9.69116748339020
H	4.96193348406703	6.66977356753802	8.46971587102530
H	3.85113800895631	9.94958469098763	2.63082976887264
H	4.69474814121762	10.26242410543900	4.16198627745248
H	2.68061423739977	11.67943068530330	3.98993227204499
H	1.65496698671129	10.25529557463730	3.77117718511320
H	0.38567375200318	9.92175469807816	5.60818541347383

H	0.70660719350536	11.69847447608090	5.64897369696819
H	-0.25188541475534	11.00715072058570	7.79200396330783
H	0.98630082499496	9.72388899808802	7.98433294806477
H	3.19505413965644	10.35923824732890	8.36275272797528
H	3.60398436618312	12.10455547492950	8.45618092506047
H	3.15557375777474	12.39559390003760	6.06198972954010
H	4.34247228411265	11.06627290438190	6.28520185531042

Table 4.S9 Optimized Cartesian coordinate (Å) of **6^{ox*}**.

Ni	3.67453958253071	9.03639029597235	5.37466854604394
Ni	3.84089950535036	7.75144832593037	7.65382900179785
Ni	4.00725777070859	6.46650809521198	9.93299114850606
S	3.08138589668209	6.97714900466757	5.70250013925556
S	5.52197259450181	8.54549818916494	6.43082660531213
S	4.60041315117121	8.52574847950484	9.60515740101434
S	2.15982588735903	6.95739967986469	8.87683103845317
N	4.36933484333306	9.49096661207991	3.19845135682565
N	1.90256052675094	9.46105873259333	4.98811028845403
N	3.93480126073026	11.00224928131860	5.67971043751017
N	3.31246087604612	6.01193589023019	12.10920905235330
N	5.77923613025809	6.04183887449548	10.31955144411460
N	3.74699443666503	4.50064883481937	9.62795280243782
O	5.05683757881513	7.06442343571789	1.80295149757532
O	0.30827239765393	11.12470759972030	5.13025987323681
O	2.62496257545899	8.43848245742489	13.50470512893610
O	7.37352267298484	4.37818822567313	10.17740673319700
C	5.77256056710776	9.08587581351012	2.95990381434545
C	5.87907270056184	7.57024692560860	2.85028424250104
C	3.69466207561281	7.40822856775529	2.04330581949286
C	3.51100962657238	8.91521697105885	2.13843894931356
C	4.21082229686698	10.95621091311650	3.21717147484233
C	4.70813554267628	11.54247704228970	4.52543949053851
C	1.23614109926420	7.22656894356980	5.60129824178167
C	0.96165696158585	8.39396704353898	4.66755963950948
C	1.46401153270412	10.71589911765480	5.24598477155127
C	2.58021106750321	11.62888107125200	5.76834798601184
C	4.69167097624549	11.14851168351380	6.95914308603598
C	5.91781305753867	10.25664866534090	6.99590420511343

C	1.90923594286587	6.41703026477238	12.34775481249460
C	1.80272739501730	7.93265955728667	12.45737215016410
C	3.98713752671177	8.09467381622124	13.26435272716250
C	4.17078663845586	6.58768489841735	13.16922134496680
C	3.47097020483503	4.54669124171445	12.09049112822200
C	2.97365736389784	3.96042434528278	10.78222331266290
C	6.44565772765861	8.27632711748777	9.70635984669263
C	6.72014066064043	7.10893026595220	10.64010034917800
C	6.21778401754975	4.78699748864088	10.06168022361790
C	5.10158395758351	3.87401516663678	9.53931886787104
C	2.99012695004558	4.35438513195016	8.34851895414638
C	1.76398546942010	5.24624886602295	8.31175435220701
H	6.40045326185846	9.43239803997552	3.79169708008558
H	6.14173232446566	9.55096105044137	2.02606060652369
H	6.90985284553246	7.28326532278230	2.61031696822144
H	5.59693309291908	7.10728479699924	3.81314892562688
H	3.34553230426375	6.92722092572266	2.97566723214730
H	3.11496048559633	7.01125438319560	1.20112519728338
H	3.76646444985140	9.37512641484378	1.16487973669568
H	2.46860647601298	9.16609262971073	2.37316074146540
H	3.14282854699533	11.17716955075700	3.08760775670941
H	4.74819536284022	11.42589557268890	2.37334842555475
H	5.76307071627697	11.28692662591410	4.67222749699074
H	4.63162387720627	12.64115211610970	4.50986173448044
H	0.79719876805957	6.28886120789813	5.23778548663625
H	0.87735444498343	7.44421467336172	6.61402794768974
H	1.08281775595841	8.06996065751011	3.62125892233043
H	-0.06761071153933	8.76402721281087	4.78635693625419
H	2.55794505554422	12.58598665578770	5.23013461629995
H	2.35431771171697	11.84033227178670	6.82132292880278
H	4.01142265512957	10.85108317487170	7.76593374463787
H	4.97115268861181	12.20597913436250	7.11089023136571
H	6.32222047097860	10.21927110066500	8.01307199092913
H	6.72433956240510	10.60968638446600	6.34016427961359
H	1.28134323576049	6.07050839602807	11.51596144790870
H	1.54006220354350	5.95194727789977	13.28159829719970
H	0.77194770495486	8.21964409747663	12.69733773826470
H	2.08486938180861	8.39561955275832	11.49450717149490
H	4.33626952909179	8.57567975179295	12.33199129809300
H	4.56683906014348	8.49164745633370	14.10653360533560
H	3.91533017525293	6.12777713094986	14.14278086193130

H	5.21318937478389	6.33680672988134	12.93450051423820
H	4.53896326542795	4.32573040034325	12.22005650065220
H	2.93359508147518	4.07700894878277	12.93431411108940
H	1.91872299027191	4.21597685079756	10.63543352622300
H	3.05016663702924	2.86174918254946	10.79780273844700
H	6.88460078741027	9.21403499419332	10.06987131368490
H	6.80444426896486	8.05867968820592	8.69363047212260
H	6.59897998220779	7.43293846145980	11.68640049173250
H	7.74940797492747	6.73886893593688	10.52130383414910
H	5.12384829703436	2.91691139639152	10.07753545965810
H	5.32747819650284	3.66256008575693	8.48634493059968
H	3.67037696947474	4.65181211833529	7.54172915389207
H	2.71064494356864	3.29691766778548	8.19677274104696
H	1.35958037061905	5.28362574017602	7.29458564999001
H	0.95745737815734	4.89321230051806	8.96749287045339

4.7 References

(1) Youn, H.-D.; Kim, E.-J.; Roe, J.-H.; Hah, Y. C.; Kang, S.-O. A novel nickel-containing superoxide dismutase from *Streptomyces* spp. *Biochem. J.* **1996**, *318*, 889-896.

(2) Barondeau, D. P.; Kassmann, C. J.; Bruns, C. K.; Tainer, J. A.; Getzoff, E. D. Nickel Superoxide Dismutase Structure and Mechanism. *Biochemistry* **2004**, *43*, 8038-8047.

(3) Wuerges, J.; Lee, J.-W.; Yim, Y.-I.; Yim, H.-S.; Kang, S.-O.; Carugo, K. D. Crystal structure of nickel-containing superoxide dismutase reveals another type of active site. *Proc. Natl. Acad. Sci. U. S. A.* **2004**, *101*, 8569-8574.

(4) Herbst, R. W.; Guce, A.; Bryngelson, P. A.; Higgins, K. A.; Ryan, K. C.; Cabelli, D. E.; Garman, S. C.; Maroney, M. J. Role of Conserved Tyrosine Residues in NiSOD Catalysis: A Case of Convergent Evolution. *Biochemistry* **2009**, *48*, 3354-69.

(5) Johnson, O. E.; Ryan, K. C.; Maroney, M. J.; Brunold, T. C. Spectroscopic and computational investigation of three Cys-to-Ser mutants of nickel superoxide dismutase: insight into the roles played by the Cys2 and Cys6 active-site residues. *JBIC, J. Biol. Inorg. Chem.* **2010**, *15*, 777-793.

(6) Ryan, K. C.; Johnson, O. E.; Cabelli, D. E.; Brunold, T. C.; Maroney, M. J. Nickel superoxide dismutase: structural and functional roles of Cys2 and Cys6. *JBIC, J. Biol. Inorg. Chem.* **2010**, *15*, 795-807.

(7) Fiedler, A. T.; Bryngelson, P. A.; Maroney, M. J.; Brunold, T. C. Spectroscopic and Computational Studies of Ni Superoxide Dismutase: Electronic Structure Contributions to Enzymatic Function. *J. Am. Chem. Soc.* **2005**, *127*, 5449-5462.

(8) Bryngelson, P. A.; Arobo, S. E.; Pinkham, J. L.; Cabelli, D. E.; Maroney, M. J. Expression, Reconstitution, and Mutation of Recombinant *Streptomyces coelicolor* NiSOD. *J. Am. Chem. Soc.* **2004**, *126*, 460-461.

(9) Ryan, K. C.; Guce, A. I.; Johnson, O. E.; Brunold, T. C.; Cabelli, D. E.; Garman, S. C.; Maroney, M. J. Nickel Superoxide Dismutase: Structural and Functional Roles of His1 and Its H-Bonding Network. *Biochemistry* **2015**, *54*, 1016-1027.

(10) Broering, E. P.; Truong, P. T.; Gale, E. M.; Harrop, T. C. Synthetic Analogues of Nickel Superoxide Dismutase: A New Role for Nickel in Biology. *Biochemistry* **2013**, *52*, 4-18.

(11) Shearer, J. Insight into the Structure and Mechanism of Nickel-Containing Superoxide Dismutase Derived from Peptide-Based Mimics. *Acc. Chem. Res.* **2014**, *47*, 2332-2341.

(12) Shearer, J. Use of a Metallopeptide-Based Mimic Provides Evidence for a Proton-Coupled Electron-Transfer Mechanism for Superoxide Reduction by Nickel-Containing Superoxide Dismutase. *Angew. Chem., Int. Ed.* **2013**, *52*, 2569-2572.

(13) Shearer, J.; Peck, K. L.; Schmitt, J. C.; Neupane, K. P. Cysteinate Protonation and Water Hydrogen Bonding at the Active-Site of a Nickel Superoxide Dismutase Metallopeptide-Based Mimic: Implications for the Mechanism of Superoxide Reduction. *J. Am. Chem. Soc.* **2014**, *136*, 16009-16022.

(14) Shearer, J.; Long, L. M. A Nickel Superoxide Dismutase Maquette That Reproduces the Spectroscopic and Functional Properties of the Metalloenzyme. *Inorg. Chem.* **2006**, *45*, 2358-2360.

(15) Neupane, K. P.; Shearer, J. The Influence of Amine/Amide versus Bisamide Coordination in Nickel Superoxide Dismutase. *Inorg. Chem.* **2006**, *45*, 10552-10566.

(16) Neupane, K. P.; Gearty, K.; Francis, A.; Shearer, J. Probing Variable Axial Ligation in Nickel Superoxide Dismutase Utilizing Metallopeptide-Based Models: Insight into the Superoxide Disproportionation Mechanism. *J. Am. Chem. Soc.* **2007**, *129*, 14605-14618.

(17) Shearer, J.; Neupane, K. P.; Callan, P. E. Metallopeptide Based Mimics with Substituted Histidines Approximate a Key Hydrogen Bonding Network in the Metalloenzyme Nickel Superoxide Dismutase. *Inorg. Chem.* **2009**, *48*, 10560-10571.

(18) Shearer, J. Dioxygen and superoxide stability of metallopeptide based mimics of nickel containing superoxide dismutase: The influence of amine/amidate vs. bis-amidate ligation. *J. Inorg. Biochem.* **2013**, *129*, 145-149.

(19) Schmidt, M.; Zahn, S.; Carella, M.; Ohlenschläger, O.; Görlach, M.; Kothe, E.; Weston, J. Solution Structure of a Functional Biomimetic and Mechanistic Implications for Nickel Superoxide Dismutases. *ChemBioChem* **2008**, *9*, 2135-2146.

(20) Tietze, D.; Breitzke, H.; Imhof, D.; Kothe, E.; Weston, J.; Buntkowsky, G. New Insight into the Mode of Action of Nickel Superoxide Dismutase by Investigating Metallopeptide Substrate Models. *Chem. - Eur. J.* **2009**, *15*, 517-523.

(21) Tietze, D.; Tischler, M.; Voigt, S.; Imhof, D.; Ohlenschläger, O.; Görlach, M.; Buntkowsky, G. Development of a Functional *cis*-Prolyl Bond Biomimetic and Mechanistic Implications for Nickel Superoxide Dismutase. *Chem. - Eur. J.* **2010**, *16*, 7572-7578.

(22) Tietze, D.; Voigt, S.; Mollenhauer, D.; Tischler, M.; Imhof, D.; Gutmann, T.; González, L.; Ohlenschläger, O.; Breitzke, H.; Görlach, M.; Buntkowsky, G. Revealing the Position of the Substrate in Nickel Superoxide Dismutase: A Model Study. *Angew. Chem., Int. Ed.* **2011**, *50*, 2946-2950.

(23) Krause, M. E.; Glass, A. M.; Jackson, T. A.; Laurence, J. S. Novel Tripeptide Model of Nickel Superoxide Dismutase. *Inorg. Chem.* **2010**, *49*, 362-364.

(24) Krause, M. E.; Glass, A. M.; Jackson, T. A.; Laurence, J. S. MAPping the Chiral Inversion and Structural Transformation of a Metal-Tripeptide Complex Having Ni-Superoxide Dismutase Activity. *Inorg. Chem.* **2011**, *50*, 2479-2487.

(25) Glass, A. M.; Krause, M. E.; Laurence, J. S.; Jackson, T. A. Controlling the Chiral Inversion Reaction of the Metallopeptide Ni-Asparagine-Cysteine-Cysteine with Dioxygen. *Inorg. Chem.* **2012**, *51*, 10055-10063.

(26) Liu, Y.; Wang, Q. L.; Wei, Y. Z.; Lin, Y. W.; Li, W.; Su, J. H.; Wang, Z.; Tian, Y.; Huang, Z. X.; Tan, X. S. Functional conversion of nickel-containing metalloproteins via molecular design: from a truncated acetyl-coenzyme A synthase to a nickel superoxide dismutase. *Chem. Commun.* **2013**, *49*, 1452-1454.

(27) Ma, H.; Chattopadhyay, S.; Petersen, J. L.; Jensen, M. P. Harnessing Scorpionate Ligand Equilibria for Modeling Reduced Nickel Superoxide Dismutase Intermediates. *Inorg. Chem.* **2008**, *47*, 7966-7968.

(28) Ma, H.; Wang, G.; Yee, G. T.; Petersen, J. L.; Jensen, M. P. Scorpionate-supported models of nickel-dependent superoxide dismutase. *Inorg. Chim. Acta* **2009**, *362*, 4563-4569.

(29) Ma, H.; Petersen, J. L.; Young, V. G., Jr.; Yee, G. T.; Jensen, M. P. Solid-State Spin Crossover of Ni(II) in a Bioinspired N_3S_2 Ligand Field. *J. Am. Chem. Soc.* **2011**, *133*, 5644-5647.

(30) Mullins, C. S.; Grapperhaus, C. A.; Frye, B. C.; Wood, L. H.; Hay, A. J.; Buchanan, R. M.; Mashuta, M. S. Synthesis and Sulfur Oxygenation of a (N_3S)Ni Complex Related to Nickel-Containing Superoxide Dismutase. *Inorg. Chem.* **2009**, *48*, 9974-9976.

(31) Herdt, D. R.; Grapperhaus, C. A. Kinetic study of nickel-thiolate oxygenation by hydrogen peroxide. Implications for nickel-containing superoxide dismutase. *Dalton Trans.* **2012**, *41*, 364-366.

(32) Jenkins, R. M.; Singleton, M. L.; Almaraz, E.; Reibenspies, J. H.; Darensbourg, M. Y. Imidazole-Containing (N_3S)-Ni^{II} Complexes Relating to Nickel Containing Biomolecules. *Inorg. Chem.* **2009**, *48*, 7280-7293.

(33) Gale, E. M.; Patra, A. K.; Harrop, T. C. Versatile Methodology Toward NiN_2S_2 Complexes as Nickel Superoxide Dismutase Models: Structure and Proton Affinity. *Inorg. Chem.* **2009**, *48*, 5620-5622.

(34) Gale, E. M.; Cowart, D. M.; Scott, R. A.; Harrop, T. C. Dipeptide-Based Models of Nickel Superoxide Dismutase: Solvent Effects Highlight a Critical Role to Ni–S Bonding and Active Site Stabilization. *Inorg. Chem.* **2011**, *50*, 10460-10471.

(35) Gale, E. M.; Narendrapurapu, B. S.; Simmonett, A. C.; Schaefer, H. F., III; Harrop, T. C. Exploring the Effects of H-Bonding in Synthetic Analogues of Nickel Superoxide Dismutase (Ni-SOD): Experimental and Theoretical Implications for Protection of the Ni–SCys Bond. *Inorg. Chem.* **2010**, *49*, 7080-7096.

(36) Broering, E. P.; Dillon, S.; Gale, E. M.; Steiner, R. A.; Telser, J.; Brunold, T. C.; Harrop, T. C. Accessing Ni(III)-Thiolate Versus Ni(II)-Thiyl Bonding in a Family of Ni–N_2S_2 Synthetic Models of NiSOD. *Inorg. Chem.* **2015**, *54*, 3815-3828.

(37) Lee, W.-Z.; Chiang, C.-W.; Lin, T.-H.; Kuo, T.-S. A Discrete Five-Coordinate Ni^{III} Complex Resembling the Active Site of the Oxidized Form of Nickel Superoxide Dismutase. *Chem. - Eur. J.* **2012**, *18*, 50-53.

(38) Chiang, C.-W.; Chu, Y.-L.; Chen, H.-L.; Kuo, T.-S.; Lee, W.-Z. Synthesis and Characterization of Ni^{III}N3S2 Complexes as Active Site Models for the Oxidized Form of Nickel Superoxide Dismutase. *Chem. - Eur. J.* **2014**, *20*, 6283-6286.

(39) Snider, V. G.; Farquhar, E. R.; Allen, M.; Abu-Spetani, A.; Mukherjee, A. Design and reactivity of Ni-complexes using pentadentate neutral-polypyridyl ligands: Possible mimics of NiSOD. *J. Inorg. Biochem.* **2017**, *175*, 110-117.

(40) Nakane, D.; Funahashi, Y.; Ozawa, T.; Masuda, H. A Square-planar Ni(II) Complex with an Asymmetric N_2S_2 Donor Set as a Model for the Active Site of Nickel-containing SOD: Structural Conversion Driven by Addition of a Strong Donor Ligand in the High Oxidation State. *Chem. Lett.* **2010**, *39*, 344-346.

(41) Gale, E. M.; Simmonett, A. C.; Telser, J.; Schaefer, H. F., III; Harrop, T. C. Toward Functional Ni-SOD Biomimetics: Achieving a Structural/Electronic Correlation with Redox Dynamics. *Inorg. Chem.* **2011**, *50*, 9216-9218.

(42) Shearer, J.; Zhao, N. $[Me_4N](Ni^{II}(BEAAM))$: A Synthetic Model for Nickel Superoxide Dismutase That Contains Ni in a Mixed Amine/Amide Coordination Environment. *Inorg. Chem.* **2006**, *45*, 9637-9639.

(43) Mathrubootham, V.; Thomas, J.; Staples, R.; McCraken, J.; Shearer, J.; Hegg, E. L. Bisamidate and Mixed Amine/Amidate NiN_2S_2 Complexes as Models for Nickel-Containing Acetyl Coenzyme A Synthase and Superoxide Dismutase: An Experimental and Computational Study. *Inorg. Chem.* **2010**, *49*, 5393-5406.

(44) Nakane, D.; Wasada-Tsutsui, Y.; Funahashi, Y.; Hatanaka, T.; Ozawa, T.; Masuda, H. A Novel Square-Planar Ni(II) Complex with an Amino–Carboxamido–Dithiolato-Type Ligand as an Active-Site Model of NiSOD. *Inorg. Chem.* **2014**, *53*, 6512-6523.

(45) Senaratne, N. K.; Mwania, T. M.; Moore, C. E.; Eichhorn, D. M. Ni complexes of N_2S ligands with amine/imine and amine/amide donors with relevance to the active site of Ni superoxide dismutase. *Inorg. Chim. Acta* **2018**, *476*, 27-37.

(46) Truong, P. T.; Gale, E. M.; Dzul, S. P.; Stemmler, T. L.; Harrop, T. C. Steric Enforcement about One Thiolate Donor Leads to New Oxidation Chemistry in a NiSOD Model Complex. *Inorg. Chem.* **2017**, *56*, 7761-7780.

(47) Rayer, A. V.; Sumon, K. Z.; Jaffari, L.; Henni, A. Dissociation Constants (pK_a) of Tertiary and Cyclic Amines: Structural and Temperature Dependences. *J. Chem. Eng. Data* **2014**, *59*, 3805-3813.

(48) Linnell, R. Notes- Dissociation Constants of 2-Substituted Pyridines. *J. Org. Chem.* **1960**, *25*, 290-290.

(49) O'Neil, J. P.; Wilson, S. R.; Katzenellenbogen, J. A. Preparation and structural characterization of monoamine-monoamide bis(thiol) oxo complexes of technetium(V) and rhenium(V). *Inorg. Chem.* **1994**, *33*, 319-323.

(50) Nakamoto, K., *Infrared and Raman Spectra of Inorganic and Coordination Compounds, Applications in Coordination, Organometallic, and Bioinorganic Chemistry*. Wiley: 1997.

(51) Marlin, D. S.; Mascharak, P. K. Coordination of carboxamido nitrogen to tervalent iron: insight into a new chapter of iron chemistry. *Chem. Soc. Rev.* **2000**, *29*, 69-74.

(52) Yang, L.; Powell, D. R.; Houser, R. P. Structural variation in copper(I) complexes with pyridylmethylamide ligands: structural analysis with a new four-coordinate geometry index, τ_4. *Dalton Trans.* **2007**, 955-964.

(53) Wei, C. H.; Dahl, L. F. Structural Characterization of Crystalline Tetrakis(2-aminoethanethiol)trinickel(II) Chloride, $[Ni\{Ni(NH_2CH_2CH_2S)_2\}_2]Cl_2$. A New Basic Trinuclear Metal System Containing Nickel(II)-Nickel(II) Interactions. *Inorg. Chem.* **1970**, *9*, 1878-1887.

(54) Barrera, H.; Suades, J.; Perucaud, M. C.; Briansó, J. L. METAL COMPLEXES OF MERCAPTOAMINES–I. SYNTHESIS AND CRYSTAL AND MOLECULAR STRUCTURE OF TETRAKIS(3-AMINO-1-PROPANETHIOLATO) TRINICKEL(II)CHLORIDE. *Polyhedron* **1984**, *3*, 839-843.

(55) Turner, M. A.; Driessen, W. L.; Reedijk, J. Synthesis, Structure, and Properties of a Trinuclear and a Mononuclear Nickel(II) Complex of *N,N'*-Dimethyl-*N,N'*-bis(β-mercaptoethyl)ethylenediamine. *Inorg. Chem.* **1990**, *29*, 3331-3335.

(56) Farmer, P. J.; Solouki, T.; Mills, D. K.; Soma, T.; Russell, D. H.; Reibenspies, J. H.; Darensbourg, M. Y. Isotopic Labeling Investigation of the Oxygenation of Nickel-Bound Thiolates by Molecular-Oxygen. *J. Am. Chem. Soc.* **1992**, *114*, 4601-4605.

(57) Musie, G.; Farmer, P. J.; Tuntulani, T.; Reibenspies, J. H.; Darensbourg, M. Y. Influence of Sulfur Metalation on the Accessibility of the NiII/I Couple in [N,N‘-Bis(2-mercaptoethyl)-1,5-diazacyclooctanato]nickel(II): Insight into the Redox Properties of [NiFe]-Hydrogenase. *Inorg. Chem.* **1996**, *35*, 2176-2183.

(58) Wang, Q.; Blake, A. J.; Davies, E. S.; McInnes, E. J. L.; Wilson, C.; Schroder, M. Structure and electronic properties of an asymmetric thiolate-bridged binuclear complex: a model for the active site of acetyl CoA synthase. *Chem. Commun.* **2003**, 3012-3013.

(59) Hatlevik, Ø.; Blanksma, M. C.; Mathrubootham, V.; Arif, A. M.; Hegg, E. L. Modeling carbon monoxide dehydrogenase/acetyl-CoA synthase (CODH/ACS): a trinuclear nickel complex employing deprotonated amides and bridging thiolates. *JBIC, J. Biol. Inorg. Chem.* **2004**, *9*, 238-246.

(60) Golden, Melissa L.; Jeffery, Stephen P.; Miller, Matthew L.; Reibenspies, Joseph H.; Darensbourg, Marcetta Y. The Construction of $(N_2S_2)Ni{-}Pd$ Clusters: A Slant-Chair, a Basket and a C_4-Paddlewheel Structure. *Eur. J. Inorg. Chem.* **2004**, 231-236.

(61) Rao, P. V.; Bhaduri, S.; Jiang, J.; Holm, R. H. Sulfur Bridging Interactions of Cis-Planar $Ni^{II}–S_2N_2$ Coordination Units with Nickel(II), Copper(I,II), Zinc(II), and Mercury(II): A Library of Bridging Modes, Including $Ni^{II}(\mu 2\text{-}SR)_2M^{I,II}$ Rhombs. *Inorg. Chem.* **2004**, *43*, 5833-5849.

(62) Harrop, T. C.; Olmstead, M. M.; Mascharak, P. K. Binding of CO to structural models of the bimetallic subunit at the A-cluster of acetyl coenzyme A synthase/CO dehydrogenase. *Chem. Commun.* **2004**, 1744-1745.

(63) Rao, P. V.; Bhaduri, S.; Jiang, J.; Hong, D.; Holm, R. H. On $[Fe_4S_4]^{2+}–(\mu_2\text{-}SR)–M^{II}$ Bridge Formation in the Synthesis of an A-Cluster Analogue of Carbon Monoxide Dehydrogenase/Acetylcoenzyme A Synthase. *J. Am. Chem. Soc.* **2005**, *127*, 1933-1945.

(64) Duff, S. E.; Barclay, J. E.; Davies, S. C.; Evans, D. J. Homonuclear dinickel complexes: structural mimics for the dinickel subsite of the A-cluster of acetyl-CoA synthase. *Inorg. Chem. Commun.* **2005**, *8*, 170-173.

(65) Ito, M.; Kotera, M.; Song, Y.; Matsumoto, T.; Tatsumi, K. Structural Models for the Active Site of Acetyl-CoA Synthase: Synthesis of Dinuclear Nickel Complexes Having Thiolate, Isocyanide, and Thiourea on the Ni_p Site. *Inorg. Chem.* **2009**, *48*, 1250-1256.

(66) Hirotsu, M.; Kuwamura, N.; Kinoshita, I.; Kojima, M.; Yoshikawa, Y. Bis(μ_2-4,7-dimethyl-4,7-diazadecane-1,10-dithiolato)trinickel(II) bis(perchlorate). *Acta Crystallogr. Sect. E: Struct. Rep. Online* **2012**, *68*, m307.

(67) Denny, J. A.; Darensbourg, M. Y. Metallodithiolates as Ligands in Coordination, Bioinorganic, and Organometallic Chemistry. *Chem. Rev.* **2015**, *115*, 5248-5273.

(68) Gibson, D.; Lippard, S. J. Preparation and structural characterization of a novel hexanuclear complex of platinum(II) with 2-aminoethanethiolate. *Inorg. Chem.* **1986**, *25*, 219-222.

(69) Parks, D. J.; Piers, W. E.; Parvez, M.; Atencio, R.; Zaworotko, M. J. Synthesis and solution and solid-state structures of tris(pentafluorophenyl)borane adducts of PhC(O)X (X = H, Me, OEt, N^iPr_2). *Organometallics* **1998**, *17*, 1369-1377.

(70) Kitagawa, T.; Dey, A.; Lugo-Mas, P.; Benedict, J. B.; Kaminsky, W.; Solomon, E.; Kovacs, J. A. A Functional Model for the Cysteinate-Ligated Non-Heme Iron Enzyme Superoxide Reductase (SOR). *J. Am. Chem. Soc.* **2006**, *128*, 14448-14449.

(71) Zhou, M.; Diwu, Z.; Panchuk-Voloshina, N.; Haugland, R. P. A Stable Nonfluorescent Derivative of Resorufin for the Fluorometric Determination of Trace Hydrogen Peroxide: Applications in Detecting the Activity of Phagocyte NADPH Oxidase and Other Oxidases. *Anal. Biochem.* **1997**, *253*, 162-168.

(72) Bueno, C.; Villegas, M. L.; Bertolotti, S. G.; Previtali, C. M.; Neumann, M. G.; Encinas, M. V. The Excited-State Interaction of Resazurin and Resorufin with Amines in Aqueous Solutions. Photophysics and Photochemical Reaction. *Photochem. Photobiol.* **2002**, *76*, 385-390.

(73) Fulmer, G. R.; Miller, A. J. M.; Sherden, N. H.; Gottlieb, H. E.; Nudelman, A.; Stoltz, B. M.; Bercaw, J. E.; Goldberg, K. I. NMR Chemical Shifts of Trace Impurities: Common Laboratory Solvents, Organics, and Gases in Deuterated Solvents Relevant to the Organometallic Chemist. *Organometallics* **2010**, *29*, 2176-2179.

(74) Dungan, C. H.; Van Wazer, J. R., *Compilation of Reported F^{19} NMR Chemical Shifts, 1951 to Mid-1967*. John Wiley & Sons, Inc.: New York, 1970.

(75) Neese, F. The ORCA program system. *WIREs Comput. Mol. Sci.* **2012**, *2*, 73-78.

(76) Becke, A. D. Density functional calculations of molecular bond energies. *J. Chem. Phys.* **1986**, *84*, 4524-4529.

(77) Perdew, J. P. Density-functional approximation for the correlation energy of the inhomogeneous electron gas. *Phys. Rev. B: Condens. Matter Mater. Phys* **1986**, *33*, 8822-8824.

(78) Neese, F. An Improvement of the Resolution of the Identity Approximation for the Formation of the Coulomb Matrix. *J. Comput. Chem.* **2003**, *24*, 1740-1747.

(79) Grimme, S.; Antony, J.; Ehrlich, S.; Krieg, H. A consistent and accurate *ab initio* parametrization of density functional dispersion correction (DFT-D) for the 94 elements H-Pu. *J. Chem. Phys.* **2010**, *132*, 154104.

(80) Grimme, S.; Ehrlich, S.; Goerigk, L. Effect of the Damping Function in Dispersion Corrected Density Functional Theory. *J. Comput. Chem.* **2011**, *32*, 1456-1465.

(81) Weigend, F.; Ahlrichs, R. Balanced basis sets of split valence, triple zeta valence and quadruple zeta valence quality for H to Rn: Design and assessment of accuracy. *Phys. Chem. Chem. Phys.* **2005**, *7*, 3297-3305.

(82) Schäfer, A.; Horn, H.; Ahlrichs, R. Fully optimized contracted Gaussian basis sets for atoms Li to Kr. *J. Chem. Phys.* **1992**, *97*, 2571-2577.

(83) Nikolaienko, T. Y.; Bulavin, L. A.; Hovorun, D. M. JANPA: An open source cross-platform implementation of the Natural Population Analysis on the Java platform. *Comput. Theor. Chem.* **2014**, *1050*, 15-22.

(84) Cohen, A. J.; Handy, N. C. Dynamic correlation. *Mol. Phys.* **2001**, *99*, 607-615.

(85) Lee, C.; Yang, W.; Parr, R. G. Development of the Colle-Salvetti correlation-energy formula into a functional of the electron density. *Phys. Rev. B: Condens. Matter Mater. Phys* **1988**, *37*, 785-789.

(86) Klamt, A.; Schüürmann, G. COSMO: A New Approach to Dielectric Screening in Solvents with Explicit Expressions for the Screening Energy and its Gradient. *J. Chem. Soc., Perkin Trans. 2* **1993**, 799-805.

(87) Pettersen, E. F.; Goddard, T. D.; Huang, C. C.; Couch, G. S.; Greenblatt, D. M.; Meng, E. C.; Ferrin, T. E. UCSF Chimera—A Visualization System for Exploratory Research and Analysis. *J. Comput. Chem.* **2004**, *25*, 1605-1612.

(88) Sheldrick, G. M. *SADABS, Area Detector Absorption Correction*; University of Göttingen: Göttingen, Germany, 2001.

(89) Sheldrick, G. M. *SHELXTL-2014, Crystallographic Computing System*; Bruker Analytical X-Ray Instruments: Madison, WI, 2014.

(90) Sheldrick, G. M. A Short History of SHELX. *Acta Crystallogr., Sect. A: Found. Crystallogr.* **2008**, *64*, 112-122.

(91) Cromer, D. T.; Waber, J. T., International Tables for X-ray Crystallography, Vol. IV, Table 2.2B. The Kynoch Press: Birmingham England, 1974.

(92) Spek, A. L. PLATON SQUEEZE: a tool for the calculation of the disordered solvent contribution to the calculated structure factors. *Acta Crystallographica Section C-Structural Chemistry* **2015**, *71*, 9-18.

(93) Krause, L.; Herbst-Irmer, R.; Sheldrick, G. M.; Stalke, D. Comparison of silver and molybdenum microfocus X-ray sources for single-crystal structure determination. *J. Appl. Crystallogr.* **2015**, *48*, 3-10.

(94) Sheldrick, G. M. SHELXT - Integrated space-group and crystal-structure determination. *Acta Crystallographica A-Foundation and Advances* **2015**, *71*, 3-8.

(95) Sheldrick, G. M. Crystal structure refinement with SHELXL. *Acta Crystallographica Section C-Structural Chemistry* **2015**, *71*, 3-8.

(96) Bruker *SAINT V8.37A*; Bruker AXS Inc.: Madison, Wisconsin, USA.

(97) V., D. O.; J., B. L.; J., G. R.; K., H. J. A.; Horst, P. OLEX2: a complete structure solution, refinement and analysis program. *J. Appl. Crystallogr.* **2009**, *42*, 339-341.

CHAPTER 5

CONCLUSIONS

We have successfully designed, synthesized, and characterized Ni complexes that mimic the active site of NiSOD structurally and electronic with alkylthiolate N_3S_2 ligand systems containing pendant N-ligand poised to coordinate to the Ni center in the axial position. Even with the axial N-py poised to coordinate to the Ni center, oxidation resulted in formation of disulfide-bridged complex for the first-generation model as reported previously. The first half of my dissertation is on the design, synthesis, and characterization of the second-generation model with the incorporation of *gem*-$(CH_3)_2$ moiety adjacent to S *trans* to carboxamide. The steric enforcement provided by the *gem*-$(CH_3)_2$ moiety is expected to prevent disulfide formation at the S *trans* to carboxamide and promote Ni-based redox. In contrast, a new oxidation pathway was observed that yielded a thioazolidine ring rearrangement product as a result of the steric enforcement provided by the *gem*-$(CH_3)_2$ moiety.

The latter half of my dissertation is on the design, synthesis, and characterization of the third-generation model, which features a pendant *N*-ethylmorpholine moiety containing a more Lewis basic axial N-donor. The more basic axial N-ligand is expected to coordinate to both Ni^{2+} and Ni^{3+} center to promote facile Ni-based redox. Unexpectedly, oxidation of the third-generation model resulted in the formation of a stair-step trimetallic species with a Ni^{2+} coordinated to four S-thiolates provided by two monomeric Ni complexes at the terminal locations. X-ray structure of the trimetallic species show N-NEM is poised to coordinate to the Ni center at 2.59 Å away, similar to Ni---N-His1 in NiSOD (2.3-2.6 Å). Reaction between the third-generation model and the Lewis

acid, tri(pentafluorophenyl) borane, is expected sequester the electron density on the S-thiolates to similar to Ni^{2+} on the trimetallic species to yield a discrete five-coordinated Ni complex, but another trimetallic complex was obtained with borane interacting with carbonyl-O. The resulted trimetallic species exhibited multiple reversible Ni-based redox events that were not observed in other NiSOD model complexes from our lab. The sequestration of S-thiolate lone pairs by Lewis acid (i.e., Ni^{2+}) effectively lowered S contribution in the Ni(dπ)/S(pπ) filled/filled anti-bonding interactions, which promotes Ni-based redox.

In summary, this work highlights the challenges in promoting facile Ni(III/II) redox in synthetic analogues of NiSOD with alkylthiolates in the ligand frameworks for $O_2^{\bullet-}$ disproportionation. In addition, the incorporation of axial N-ligand did not ensure coordination to form five-coordinate Ni complexes. However, trimetallic species that formed from sequestration of lone pairs from S-thiolates by with Lewis acid (i.e., Ni^{2+}) highlight the importance of 2° and 3° interactions in NiSOD active site. While the N_3S_2 donor set is important in tuning the redox of Ni, it is the H-bonding network that fine-tune the electronic properties of the NiSOD active site for catalysis. With this in mind, the addition of the synthetic analogues from this study into an apoprotein with the proper H-bonding interactions can promote facile Ni-based redox for $O_2^{\bullet-}$ disproportionation. Furthermore, the bridging Ni in the trimetallic species is reminiscence the strategy employed by nature to harness the redox-active Ni-S system for catalysis in the [NiFe] site of [NiFe] H_2ase and Ni_C site of CODH, where the S-coordinated redox-active Ni center is also bridged via S-ligands to a Lewis acid (Fe^{2+} or Ni^{2+}). As such, it will be worth-while to explore the ability of the trimetallic species obtained in this work to catalyze reversible conversion of H_2 to H^+ or CO_2 to CO.